MAX-PLANCK-INSTITUT FÜR PLASMAPHYSIK
GARCHING BEI MÜNCHEN

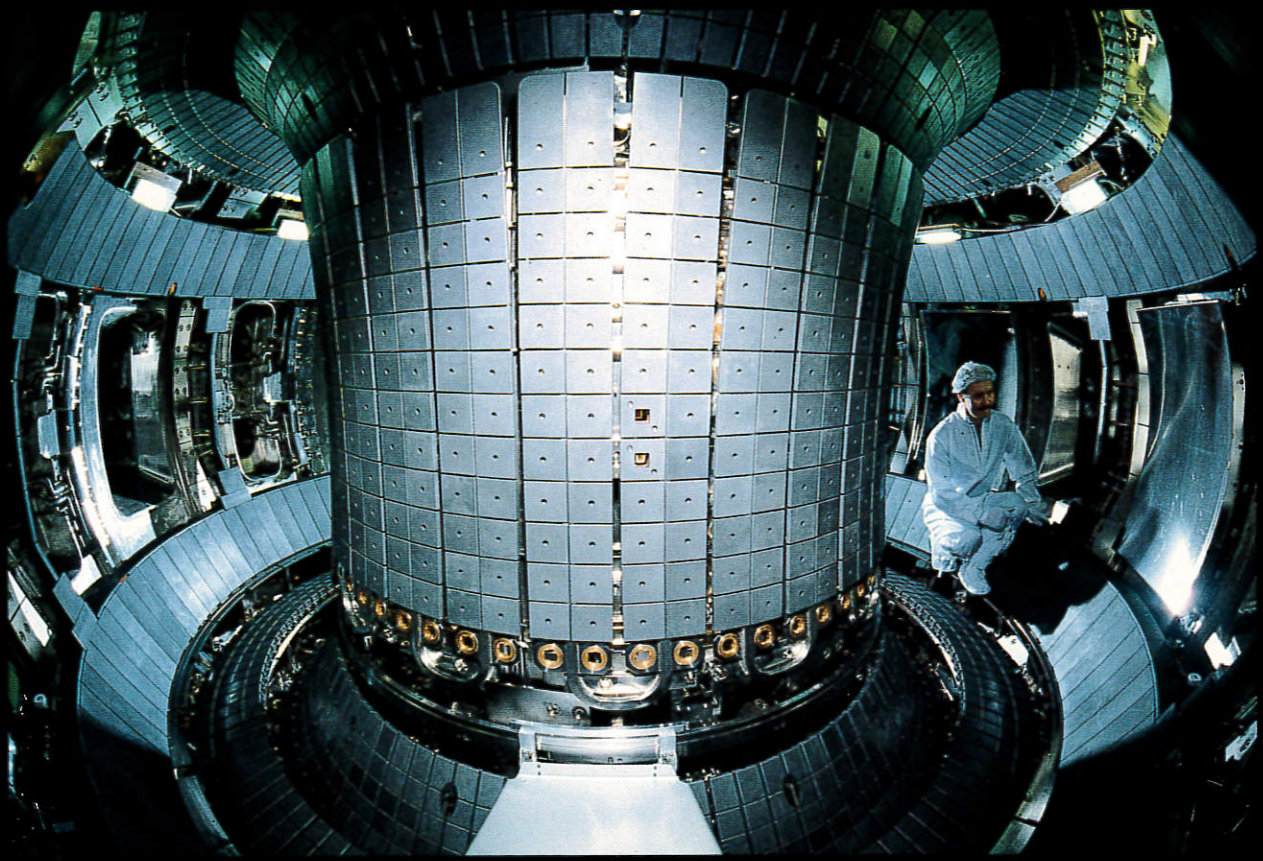

IPP

ANNUAL REPORT 1990

COVER ILLUSTRATION

Interior of the vacuum vessel of the ASDEX Upgrade, fusion experiment: The walls are covered with graphite tiles; the divertor plates are located at the top and bottom. Technical operation started in 1990.

MAX-PLANCK-INSTITUT FÜR PLASMAPHYSIK
GARCHING BEI MÜNCHEN

Annual Report 1990

CONTENTS

PREFACE

Fusion experiments of two types are conducted within the Max-Planck-Institut für Plasmaphysik (IPP), the tokamak and the stellarator: After ten years of successful operation the ASDEX tokamak experiment was finally shut down on 10 August 1990. Important contributions of ASDEX to fusion research have been the establishment of the poloidal divertor concept and the discovery of the H-mode. On the basis of the pioneering studies on ASDEX, future tokamaks throughout the world will operate with up-down divertors in the H-mode. During the final operation period ASDEX was run with closed divertor geometry and boronized walls. The resulting high reduction of impurities extended the limits of the H-mode and improved its good confinement properties. The achievement of H-phases with moderate or vanishing ELM frequency allowed detailed studies of H-mode physics. It was possible to operate in stationary H-modes lasting for 3.5 seconds, determined only by technical limits. A major part of the experimental work was devoted to the lower hybrid programme in cooperation with ENEA, Frascati, and PPPL, Princeton. The lower hybrid system let the full plasma current be driven.

After termination of the ASDEX programme IPP are now continuing their divertor investigations on the ASDEX Upgrade tokamak. The aim of this experiment is to realize a reactor-compatible, open divertor, which in contrast to the closed divertor of ASDEX is formed with distant poloidal field coils. In March 1990 assembly of the tokamak was completed and technical operation started. First plasma experiments in ASDEX Upgrade are scheduled for March 1991.

IPP's stellarator experiment, WENDELSTEIN 7-AS, was continuously operating at full field in 1990; neutral injection and electron cyclotron resonance heating were being routinely applied up to their full power. Reliable operation of the modular coils afforded proof of the technical feasibility of the Advanced Stellarator concept. One of the theoretical principles of stellarator optimization - the reduction of Pfirsch-Schlüter currents, manifested by a reduced Shafranov shift - was demonstrated up to the highest beta value hitherto achieved in this device.

Progress was made in planning WENDELSTEIN 7-X, the follow-up experiment for demonstrating the reactor relevance of the Advanced Stellarator principles first tested in WENDELSTEIN 7-AS. This new experiment will be a 5-period Helias configuration with a superconducting coil assembly, which promises good equilibrium, stability and transport properties as well as a small bootstrap current. The device should allow convincing predictions on the performance of an ignited stellarator. In 1990 the proposal for the device was finished and submitted to the European authorities for approval.

On the national level, IPP coordinate their research effort with Kernforschungsanlage Karlsruhe within the "Entwicklungsgemeinschaft Kernfusion" and also with National Research Centres involved in fusion research. IPP also closely cooperate with a number of German universities. The collaboration with the University of Stuttgart in the field of electron cyclotron resonance heating has been especially successful. The research conducted at IPP is part of the European fusion programme: IPP are involved in JET, the joint European experiment. The ASDEX Upgrade tokamak and the alternative stellarator concept as embodied in the WENDELSTEIN experiments provide essential information for preparing the next steps in the overall European programme. Furthermore, IPP act as host to NET, the European study group, who have been working here since 1983 on the design of the next European large-scale experiment.

Coordination of research activities also extends to the worldwide level. IPP are party to two Implementing Agreements with the USA: The one regulates cooperation in the joint stellarator programme, to which the WENDELSTEIN experiments make a major contribution; the other covers cooperation in the ASDEX Upgrade divertor tokamak. Since April 1988 IPP have provided the technical site for the American-European-Japanese-Soviet group responsible for planning ITER, the International Thermonuclear Experimental Reactor. On completion of the conceptual design of the ITER device in December 1990, Europe proposed IPP as technical site for the ITER Engineering Design Phase as well.

Klaus Pinkau

Projects

Tokamaks

The greater part of the capacity at IPP is devoted to investigating confinement in the tokamak configuration, this line being the furthest advanced towards application in a fusion reactor. With ASDEX, in operation till August 1990, and ASDEX Upgrade, which started technical operation in the same year, IPP have concentrated their tokamak research on the divertor principle.

Besides conducting their own tokamak experiments, IPP have been involved in JET, the joint European large-scale project at Culham (U.K.) since the planning phase. IPP have constructed and put into operation a large fraction of the JET diagnostics and participate in exploitation of the JET experiment. The results of JET, IPP and the other associations form the groundwork for planning the next step, for which IPP are hosting the NET ("Next European Torus") Team, a group of scientists and engineers called together to prepare the design of an experimental test reactor. In addition, the NET group are steering the European fusion technology programme. IPP are contributing to NET activities both by direct secondment of personnel to the NET team and by performing supporting work, partly via NET study contracts.

Meanwhile, the European Community, Japan, the USA and the USSR have agreed to prepare a possible next step as a joint venture. A conceptual design study called ITER (International Thermonuclear Experimental Reactor) is being carried out by a joint team of the four partners invited to Garching by the Federal Republic of Germany and the European Community. IPP are actively supporting this activity and have made substantial contributions through participation of their scientists in the numerous ITER expert group meetings. The ITER study group agreed to a common set of goals and parameters for the ITER design work. At the end of 1990 the ITER group finished the conceptual design phase and presented an ITER proposal. Continuation of this work as a design study, EDA ("Engineering Design Activity"), is now being discussed by the four partners. EURATOM and the Federal Republic of Germany have proposed Garching as host to the EDA team of 200 professionals.

The work on NET/ITER has demonstrated the reactor requirements to be met by the divertor configuration and the H-mode. The divertor configuration was developed at IPP in the pioneering work on ASDEX, and the H-regime was discovered there in 1982. The H-regime yields an increase in the plasma energy content typically by a factor of 2 in relation to the standard tokamak operation regime. An improvement in the confinement quality by a factor of 2 seems to provide a reasonable ignition margin for ITER. One of the successes of 1990 was the attainment of values close to Q=1 on JET with divertor operation in the H-mode. This implies that a deuterium-tritium plasma in JET under these conditions would produce as much energy as needed to heat it to yield a fusion power of about 20 MW. The final operation of JET with tritium is envisaged for the mid- nineties. The importance of IPP's strategy - to develop the physics of divertor tokamaks - is also borne out by the decision to remodel the magnetic configuration of JET to a full divertor - a divertor configuration based on ASDEX and other divertor experiments.

ASDEX was in operation till August 10, when it was finally shut down. During the final operation period ASDEX was run with closed divertor geometry and boronized walls. The resulting high reduction of impurities greatly extended the limits of the H-mode and improved its good confinement properties. The achievement of H- phases with moderate ELM

frequency or without ELMs allowed detailed studies of H-mode physics. It was possible to run stationary H-modes (with ELMs) lasting 3.5 s (determined only by technical limits).

To obtain a reliable data base for theoretical models for the density limit, the most important series of discharges were repeated under optimum and identical purity conditions (boronized wall) and with a full set of diagnostics. Deuterium and helium discharges were performed in a wide q-range with and without neutral beam injection.

About one-third of the discharges were devoted to lower hybrid experiments. These experiments with a frequency of 2.45 GHz (subject of trilateral cooperation with ENEA at Frascati and PPPL at Princeton) concentrated on the various aspects of current drive. It was shown that under certain conditions the energy confinement can be improved if the m=1 mode is stabilized. Noteworthy is the observation that a combination of different wave spectra affords the possibility of improving the local influence exerted on the current profile.

Already during an early phase of ASDEX operation in 1981 IPP proposed to continue and extend its divertor investigations by designing and constructing ASDEX Upgrade. Experimental results from ASDEX and theoretical studies of boundary problems in a tokamak reactor showed the divertor to be *the* candidate for solving the problems of plasma/wall contact such as energy transfer to the wall, erosion, pumping of hydrogen and helium and limitation of impurity production. In particular, ITER, necessary to reach ignition, leads to a rising energy flow density in the boundary. This increases the problems of energy transfer to the wall and of impurity control. The aim of ASDEX Upgrade is to realize a reactor-compatible, "open" divertor with distant poloidal field coils, in contrast to the ASDEX closed divertor.

The " open" divertor promises solutions because:

- the temperature at the plasma edge (typically 100 eV) can be decoupled from the temperature at the target plates (below 10 eV desired);
- a dense and cold plasma in front of the target plates limits erosion and impurity flow into the bulk plasma;
- this dense plasma is the ideal source region for pumping of hydrogen and helium;
- this plasma also offers the chance to reduce the energy flow to the target plates caused by radiation.

Parallel to simulation of the appropriate open divertor configuration, ASDEX Upgrade affords the possibility of investigating a reactor-compatible poloidal field configuration. Plasma control in the unstable position and a programme to prevent disruptions can be most realistically tested in ASDEX Upgrade.

After completion of the assembly of ASDEX Upgrade technical operation was started in 1990. The peripheral assembly, first-day diagnostic data acquisition and the plasma control system were completed to such an extent that physical operation can start in early 1991.

ASDEX PROJECT

(Head of Project: Dr. Friedrich Wagner)

1. EXPERIMENTAL RESULTS AND COMPARISON WITH THEORETICAL STUDIES

R. Aratari, R. Bätzner[4], R. Bartiromo[12], G. Becker, S. Bernabei[9], M. Bessenrodt-Weberpals[19], B. Bomba, H.S. Bosch[19], K. Büchl[19], R. Büchse[1], A. Carlson[19], C.C. Chu[19], T.K. Chu[9], R. De Angelis[12], G. Dodel[3], F. Dollinger[2], A. Eberhagen, M. Endler[1], M. Engelhard[2], W. Engelhardt, H.-U. Fahrbach[19], G. Fussmann, O. Gehre, K.W. Gentle[11], J. Gernhardt, L. Giannone, O. Gruber[20], G. Haas, T. Hartinger[2], R. Harvey[8], W. Herrmann[19], J.V. Hofmann, H. Hohenöcker[19], E. Holzhauer[3], K. Hübner[4], A. Izvozchikov[5], G. Janeschitz, E. Kakoulidis[6], A. Kallenbach[19], O. Kardaun[20], F. Karger, M. Kaufmann[19], A. Khoudoleev[5], O. Klüber†, M. Kornherr, M. Krämer[13], K. Krieger[1], J. Kucinski[17], B. Kurzan[2], G. Kyriakakis[6], K. Lackner[20], R. Lang[19], S.I. Lashkul[5], U. Leinberger[2], F. Leuterer[22], G. Lisitano, R. Loch[19], M.E. Manso[10], J. Matias[10], H.-M. Mayer, K. McCormick, D. Meisel, V. Mertens[19], E.R. Müller, H. Murmann, J. Neuhauser[20], H. Niedermeyer, J.-M. Noterdaeme[22], V. Petrzilka[18], W. Poschenrieder[21], J. Qin[14], H. Röhr[19], J. Roth[21], A. Rudyj, N. Ruhs, F. Ryter[22], W. Sandmann[19], F. Schneider, U. Schneider, R. Schubert[1], F. Serra[10], S. Sesnic[9], G. Siller, A. Silva[10], E. Simmet[1], F. Söldner, E. Speth[22], A. Stäbler[22], K.-H. Steuer, J. Stöckel[18], U. Stroth, E. Taglauer[21], G. Theimer[2], D. Thomas[8], N. Tsois[6], A. Tucillo[12], H. Verbeek[21], O. Vollmer[22], K. Ushigusa[15], K. Wira[16], B. Wolle[1], H.R. Yang[7], D. Zimmermann, H. Zohm[1]

1 Doctoral fellow
2 Undergraduate
3 Guest, University of Stuttgart, FRG
4 Guest, University of Heidelberg, FRG
5 Guest, Ioffe Institute, Leningrad, USSR
6 Guest, Demokritos, Attiki, Greece
7 Guest, Southwestern Inst. of Physics, Leshan, China
8 Guest, GA Technologies Inc., San Diego, USA
9 Guest, Princeton University, USA
10 Guest, IST, Lisbon, Portugal
11 Guest, University of Texas, Austin, USA
12 Guest, ENEA, Frascati, Italy
13 Guest, University of Bochum, FRG
14 Guest, Institute of Physics, Beijing, China
15 Guest, Japan Atomic Research, Ibaraki, Japan
16 Guest, University of Washington, Seattle, USA
17 Guest, Institute for Nuclear Studies, Otwock-Swierk, Poland
18 Guest, Institute of Plasma Physics, Prague, ČSFR
19 Experimental Plasma Physics Division 1
20 Theory Division 3
21 Plasma Wall Interaction Group
22 Technology Division
† 03.06.90

1.1 Overview

ASDEX was in operation till August 10, at which point it was finally shut down. One of the most successful and influential fusion experiments came to an end. The most important contributions of ASDEX were the establishment of the poloidal divertor concept for tokamaks and the discovery of the H-mode. Based to a large extent on the pioneering studies of ASDEX, future tokamaks will operate with up-down divertors in the H-mode. As a consequence of ASDEX performance, JET will be fully modified into a divertor experiment. Furthermore, JET has achieved its maximum performance in its present divertor configuration and under H-mode conditions. Also the ITER study has clearly highlighted the uncompromising need for divertor operation in the H-mode.

During the final operation period ASDEX was run with closed divertor geometry and boronized walls. The resulting high reduction of impurities (heavy impurities by closing the divertor, oxygen by boronization) led to a large extension of the limits of the H-mode with its good confinement properties. Depending

on parameter settings, H phases with moderate ELM frequency or without ELMs could be obtained for detailed studies of H-mode physics, e.g. for fluctuation studies. It was possible to run stationary H-modes (with ELMs) for durations of 3.5 s (determined only by technical limits). The large improvement in the accessibility of the H-mode by divertor closing and boronization indicates that the H-mode is not compatible with backstreaming of neutral gas in a strongly localized divertor like that of ASDEX.

As a key to the transition to the H-mode, in many recent theories the radial electric field is considered. In order to calculate this field, the poloidal rotation was determined. It was found that the rotation velocity is small at or outside the separatrix, but a few centimetres inside the velocity increases up to 10 km/s in the H phase.

Concerning the other modes with improved confinement (with peaked density profiles) the counter-NI-mode could still be reproduced after wall boronization, whereas the improved ohmic confinement (IOC) did not appear spontaneously. But it has been found that puffing of neon could produce the IOC-mode. It is believed that the edge density, which can be controlled by the power flow across the separatrix, is a critical parameter.

To obtain a reliable data base for theoretical models for the density limit, the most important series of discharges were repeated under optimum and identical cleanness conditions (boronized wall) and with a full set of diagnostics. Deuterium and helium discharges were performed in a wide q-range with and without neutral beam injection. In contrast to hydrogen and deuterium, the helium discharges do not develop marfes at high q-values and the density limit is much higher. This confirms the detrimental effect of marfes on the density limit at high q-values.

About one-third of the discharges were devoted to lower hybrid experiments. These experiments with a frequency of 2.45 GHz (subject of trilateral cooperation between the US, Italy and Germany) concentrated on the various aspects of current drive. A suitable choice of wave spectrum allows the spatial profile of the current density to be influenced, thus making it possible to affect a certain class of instabilities. It was shown that under certain conditions the energy confinement can be improved if the m=1 mode is stabilized. Noteworthy is the observation that a combination of different wave spectra affords the possibility of exerting an improved local influence on the current profile. The wave of the one type locally conditions the plasma so that the second wave is particularly effective at the location concerned.

1.2 Divertor and Scrape-off Layer Studies

It has become increasingly apparent that plasma boundary conditions (wall coating, divertor geometry, asymmetries) are important components in determining plasma edge properties. Section 1.2.1 considers some simple edge physics to illuminate the connections between edge density and temperature and global plasma properties such as n_e, I_p, and B_t. Empirical scaling laws for two different wall-conditioning procedures (carbonization, boronization) are presented to document these connections. Section 1.2.2 addresses scaling laws in divertor parameters for evaluating the validity of edge physics models. Sections 1.2.3 and 1.2.4 are concerned with Improved Ohmic Confinement discharges, which arise when a particular constellation of plasma boundary conditions exists. Finally, Secs. 1.2.5 and 1.2.6 discuss effects of divertor geometries, and asymmetric energy deposition on the target plates, both of which are important in dictating general plasma performance.

1.2.1 Edge scaling laws

Based on extensive parameter scans (carbonized and boronized walls; hydrogen and deuterium filling gases), scaling laws have been derived for the separatrix density n_{es} and temperature T_{es} in the midplane as a function of the operational parameters A (isotope mass), n_e, I_p, and B_t. Table 1 shows that T_{es} exhibits neither an important isotopic nor wall-conditioning dependence. In contrast, the isotopic dependence of n_{es} is markedly stronger for carbonized wall conditions, with hydrogen having the higher edge densities.

These differences may be elucidated by considering a simple energy balance model for the scrape-off layer (SOL). The power flowing into the SOL, $P_{SOL} = P_{OH} - P_{RAD}$, and then along open field lines into the divertor is equated to the power losses by radiation in the divertor, power losses through recycling near the target plate, and finally power transmitted to the plate:

$$P_{SOL} = P_{RAD,div} + \\ + (n_{ed} c_s \lambda_E W e(E_i+E_r)) + (n_{ed} c_s \lambda_E W \delta_t e T_{ed}),$$

where $n_{ed} c_s$ is the particle flux at the sheath, $c_s = \sqrt{2e\,T_{ed} / m_i}$ is the ionic sound speed at the sheath, $\lambda_E W$ is the cross-sectional area of the energy-carrying layer at the target plate, E_i+E_r is the energy dissipated by the plasma in sustaining each recycling event, and δ_t is the sheath energy transfer coefficient. From momentum balance one may obtain the relation $n_{es} T_{es} = 2 n_{ed} T_{ed}$, so that in combination with the above,

$$n_{es} T_{es} T_{ed}^{0.5} [1 + (E_i+E_r) / \delta_t T_{ed}] = \\ (2 / \lambda_E W \delta_t e) (m_i / 2e)^{0.5} P_{div} \qquad (1)$$

is obtained, where $P_{div} = P_{SOL} - P_{RAD,div}$. In other words, the product on the left-hand side of the equation is predicted to scale with the power flux density into the divertor. Or, if λ_E is not a function of P_{div}, the product will scale directly with P_{div}. Section 1.2.2 presents evidence that indeed λ_E is independent of P_{SOL}, and Sec. 1.2.3 shows that a linear relationship between the left and right-hand sides of the above equation exists. Hence, one can have some confidence that this simple physics relationship contains at least some of the essential elements governing plasma edge physics.

This equation identifies the leading elements in determining $n_{es} T_{es}$ to be P_{SOL}, A, and λ_E. Constructing scaling laws (Table 2) on such a basis leads to a unifying isotopic dependence of n_{es}, T_{es}, and $n_{es} T_{es}$ for both carbonized and boronized conditions, with deuterium having the higher values - as predicted. The different multipliers might be related to different recycling conditions for the hydrogen and deuterium cases. B_t has also been included as a regression parameter in order to partially account for the variation of W with q_a. Examining the

TABLE 1:		const	A		$\bar{n}_e$		I_p		B_t		Z_{eff}		R
P_{OH}	B	5.80E-04	-0.18	0.01	0.26	0.02	1.13	0.02	-0.35	0.03	0	0	0.99
	C	8.90E-04	-0.21	0.03	0.35	0.04	1.05	0.03	-0.39	0.07	0	0	0.98
P_{RAD}	B	2.15E-04	0.69	0.04	0	0	1.05	0.05	-0.71	0.09	0.41	0.13	0.96
	C	3.60E-03	0.28	0.05	0.55	0.08	0.48	0.05	0	0	0.39	0.08	0.83
P_{SOL}	B	3.64E-04	-0.43	0.02	0.37	0.03	1.15	0.02	-0.25	0.04	0	0	0.99
	C	1.45E-05	-0.58	0.04	0.28	0.05	1.72	0.05	-0.59	0.10	0	0	0.97
n_{es}	B	4.70E-02	-0.32	0.02	1.11	0.03	0.24	0.03	0.17	0.04	0	0	0.98
	C	1.70E-02	-0.73	0.03	1.18	0.05	0.48	0.06	0	0	0	0	0.96
T_{es}	B	1.33E-01	0	0	-0.52	0.04	1.16	0.03	0	0	0	0	0.97
	C	8.10E-02	0.24	0.03	-0.66	0.04	1.25	0.05	0	0	0	0	0.94
$n_{es}T_{es}$	B	1.23E-02	-0.29	0.03	0.58	0.05	1.30	0.04	0.21	0.07	0	0	0.97
	C	1.41E-03	-0.49	0.04	0.53	0.06	1.73	0.08	0	0	0	0	0.94

TABLE 1:
Parametric dependence of edge parameters on global quantities for ohmic heating. Exponents are given for regression fits of the form:
const $A^{\alpha}\ \bar{n}_e^{\beta}\ I_p^{\gamma}\ B_t^{\delta}\ Z_{eff}^{\varepsilon}$, *A (ion mass),* $\bar{n}_e$ *(*10^{13} *cm*$^{-3}$*),* I_p *(kA),* B_t *(T). The standard error is in the adjacent column. R is regression coefficient. C = carbonized walls, B = boronized. Parameter ranges: (B)* $\bar{n}_e = 2.5 - 5.8 \times 10^{13}$ *cm*$^{-3}$, $I_p = 250 - 450$ *kA,* $B_t = 1.9 - 2.8$ *T; (C)* $\bar{n}_e = 2.6 - 5.3 \times 10^{13}$ *cm*$^{-3}$, $I_p = 150 - 430$ *kA,* $B_t = 1.9 - 2.6$ *T.*

TABLE 2:		const	A		n_{es}		T_{es}		P_{SOL}		B_t		R
n_{es}	B	91.4	0.27	0.03			-0.92	0.06	1.21	0.05	0.5	0.07	0.95
	C	123	0.21	0.05			-0.88	0.05	1.16	0.04	0.33	0.09	0.94
T_{es}	B	115	0.27	0.03	-0.82	0.05			1.15	0.04	0.46	0.07	0.96
	C	160	0.24	0.05	-0.81	0.05			1.08	0.06	0.45	0.09	0.89
$n_{es}T_{es}$	B	126	0.25	0.03					1.18	0.03	0.51	0.07	0.97
	C	192	0.19	0.05					1.23	0.04	0.48	0.10	0.93

TABLE 2: Regressions for n_{es}, T_{es}, $n_{es}T_{es}$ *(*10^{13} *cm*$^{-3}$*, eV) of Table 1 in terms of:*
const. $A^{\alpha}\ n_{es}^{\beta}\ T_{es}^{\gamma}\ P_{SOL}^{\delta}\ B_t^{\varepsilon}$

scalings for P_{OH} and P_{RAD} (the components of P_{SOL}), one finds that P_{RAD} has an isotopic dependence, this then accounting for a substantial part of the differences between hydrogen and deuterium when regressing on the operational parameters of Table 1.

The importance of P_{SOL} in determining $n_{es}T_{es}$ also provides an explanation for one of the basic conditions necessary to produce IOC discharges. This is discussed in Sec. 1.2.3.

1.2.2 *Divertor and scrape-off layer studies by Langmuir probes*

The reciprocating Langmuir probe was used to study the flow of non-ambipolar currents in the SOL. The divertor probe in ASDEX is in close proximity to the upper-outer target plate, hence a probe tip electrically connected to the target plate should collect about the same current as that flowing to the target in the absence of the probe.

High currents with absolute values reaching the probe ion saturation current (1 - 10 A/cm^2) were observed to flow close to the separatrix, with significant changes in profile at the L/H transition and with different field polarities. These are interpreted as thermoelectric currents driven by the poloidally asymmetric power flow to the target plates as measured by calorimetry.

During the L phase an ion current is mainly flowing to the upper-outer target for both co- and counter-injection, whereas in the H phase the dominant current is seen to be parallel to the main plasma current, thus changing sign with the polarity of the plasma current in co- and counter-injection cases.

A divertor database with Langmuir probe measurements has also been incorporated into parametric studies of the scrape-off layer. Figures 1a,b,c show a subset referring to NI-heated D_2 discharges, with varying P_{NI} (= 0.25 - 1.8 MW). Within the framework of a classical heat flow model in the SOL, whereby heat conducted along field lines is balanced against volume radiation in the divertor, recycling processes and power convected through the target sheath (see Sec. 1.2.1), a linear dependence of the power flux to the probe on the SOL power influx is predicted, provided the width of the power-carrying layer is constant with P_{SOL}. Such a linear relationship is indeed observed experimentally (Fig. 1a).

The characteristic widths D_W, for the energy flux in the scrape-off layer, calculated from Langmuir probe power-flux profiles in the divertor, are found to be independent of the power influx to the SOL (Fig. 1b), consistently with the observed linear scaling of Fig. 1a. The power widths are defined as the ratio of the line integral of the power-flux profile and the peak value of the measured power flux. For slab geometry this definition conserves the total power in the layer as this is transformed from an exponential-shaped profile in the midplane to an approximately Gaussian-shaped profile in the divertor.

With the assumptions of Spitzer heat conductivity along field lines and heat diffusivity across field lines, the constancy of the power widths implies an increase of $n\chi_e$ with P_{SOL} (Fig. 1c), where $n\chi_e$ is calculated from measured values of P_{SOL} and D_W (power-flux widths from divertor probe measurements). Values of χ_e (SOL) are found to lie in the range 1 - 5 m^2/s, which are also typical of the edge region of the main plasma.

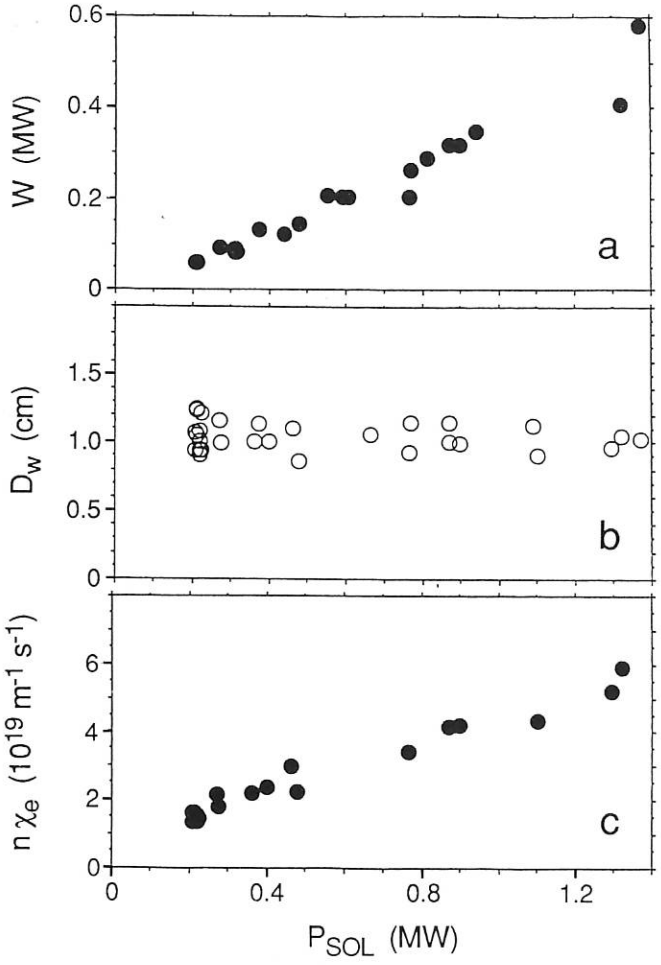

FIG. 1: a) Divertor-target power load from Langmuir probe measurements as a function of SOL power influx, $P_{SOL} = P_{tot} - P_{RAD}$.
b) Characteristic radial width of energy flux in the SOL, calculated from Langmuir probe measurements, versus P_{SOL}.
c) Calculated electron diffusivity in the SOL as a function of the power influx P_{SOL}.

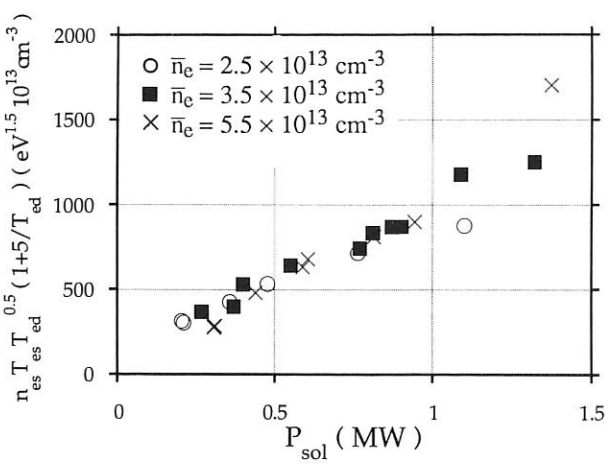

FIG. 2: The left-hand side of Eq. (1) in Sec. 1.2.1 vs. P_{SOL} for a P_{NI} power scan (P_{NI} = 0.25 - 1.8 MW) with $\bar{n}_e$ as a parameter. The points to the left for each density range arise from ohmic heating.

1.2.3 *Role of the edge conditions for the attainment of Improved Ohmic Confinement (IOC)*

The IOC regime on ASDEX was found in DVII with open bypasses, which resulted in higher edge radiation, increased recycling, and, concomitantly, reduced gas consumption. The gas puff fuelling rate dropped by a factor of two. IOC appeared during density plateaus above the LOC region. The transition from SOC to IOC was triggered by the sharp drop of external gas flux associated with the transition from a density ramp to a density plateau.

The improvement in energy confinement depends on the wall conditions. The highest values, extending the linear scaling $\tau_E \propto \bar{n}_e$ up to the density limit, were obtained with uncovered stainless-steel walls and with carbonization in a mixture of deuterized methane and nitrogen and subsequent glow discharge conditioning. The discharges in these cases had a high level of radiation. With clean walls after fresh carbonization or boronization or with hydrogen as the working gas, nearly no enhancement of τ_E above SOC values was obtained. In these cases the density profile also remained broad. This suggested a link between IOC, density profile shape, and heat flow into the SOL, whereby a reduction of the edge density is needed to trigger the steepening of the density gradient in the confinement region.

To motivate a physical understanding of the edge dynamics, we simply consider the SOL power balance expressed by Eq. (1) in Sec. 1.2.1. As a first approximation ($T_{es} = T_{ed}$, λ_E = const.) one may write

$$T_{es} \propto n_{es}^{-2/3} P_{div}^{2/3} \qquad (1)$$

as a function of the electron density n_{es} at the separatrix and the net target load P_{div} at the divertor plates. The fundamental relation between edge parameters and net power flux within the SOL as given by Eq. (1) in Sec. 1.2.1 was checked in a power scan:

The total heating power was varied from 0.25 to 1.8 MW; $\bar{n}_e$ was varied in the range $2.0 \leq \bar{n}_e$ (10^{13} cm^{-3}) ≤ 5.5. Figure 2 gives the left-hand side of the model solution as a function of P_{SOL} with $\bar{n}_e$ as parameter. Measurements of both the edge and the divertor parameters were available. Evidently, the model appears to describe the situation well, with some scatter for $P_{SOL} > 1$ MW. The empirical relation

$$T_{es} = 92\, n_{es}^{-0.77 \pm 0.04}\, P_{SOL}^{0.65 \pm 0.05} \quad [\text{eV}, 10^{13}\ \text{cm}^{-3}, \text{MW}]$$

for these results is also quite similar to that expected from the simplified model considerations above.

Equation (1) in Sec.1.2.3 leads one to expect that n_{es} can be influenced by varying P_{SOL} through the addition of impurities or by changing wall conditions (boronization vs. carbonization). In fact, boronized wall conditions are found to lead to higher edge densities virtue of the increased P_{SOL}, owing to a reduction of radiated power in the main plasma. Further, a reduction of the edge density and consequent narrowing of the density profile along with an improvement in confinement time can be provoked by introducing impurities into a clean deuterium plasma.

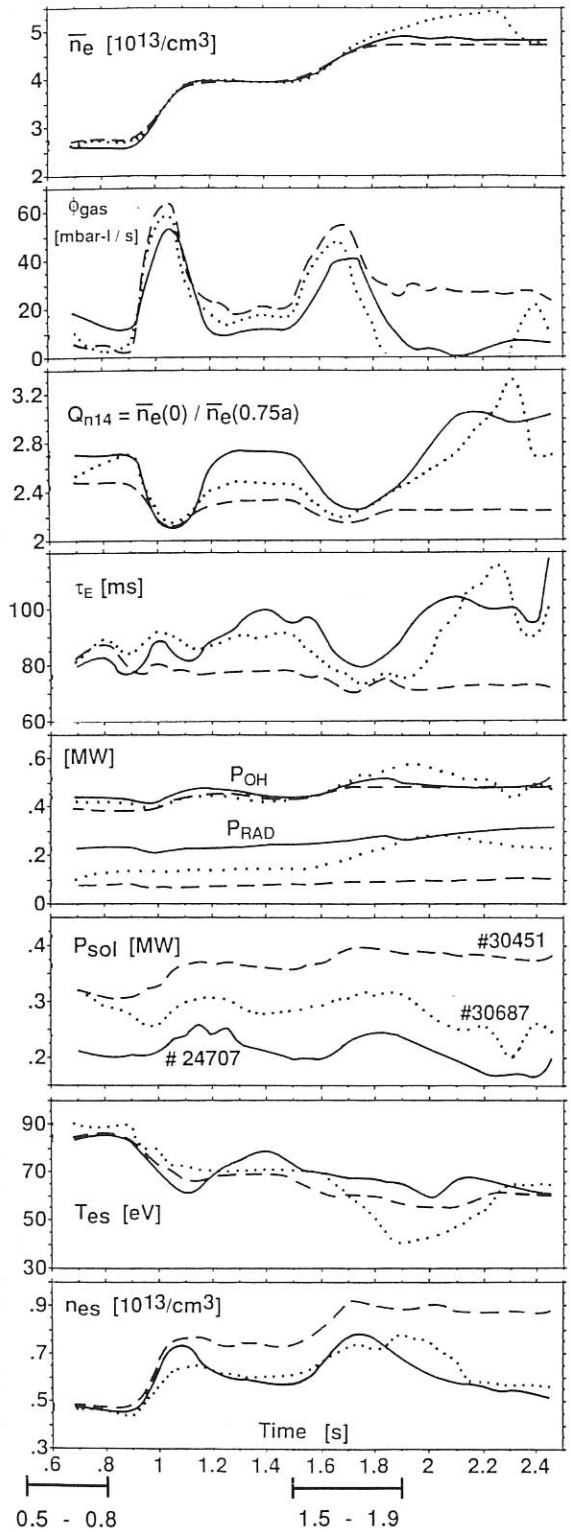

FIG. 3: The temporal behaviour of: $\bar{n}_e$, the gas puff rate ϕ_{gas}, the density peaking factor Q_{n14}, energy confinement time τ_E, P_{OH}, and P_{RAD} in the main chamber, $P_{SOL} = P_{OH} - P_{RAD}$, T_{es} and n_{es} for three different situations: —— IOC behaviour for stainless-steel walls #24707; ----- the SOC reaction of plasma to the same global settings ($\bar{n}_e$ = 2.7, 4.5 × 10^{13} cm^{-3}, I_p = 380 kA, B_t = 2.2 T) for boronized walls and one divertor by-pass closed #30451; ····· the production of IOC behaviour by puffing neon into a discharge identical to #30451 during the times 0.5 - 0.8 s and 1.5 - 1.9 s, #30687.

A series of experiments were performed where small amounts of various impurity gases were added to the main working gas deuterium. A discharge consisting of three density plateaus in the regions of LOC and SOC/IOC with density ramps in between was used to document intrinsic IOC behaviour as well as the effect of impurities.

First, discharges with moderate impurity puffing of various gases were carried out in order to choose the most effective impurity. The rare gases neon, argon, and krypton were separately injected in short pulses between 0.5 - 0.8 s and during the density ramp between 1.5 - 1.9 s (see Fig. 3). Neon provided peripheral radiation losses, giving rise to the favourable situation of a small energy loss in the core plasma with a low power deposition to the divertor plates.

A second series of discharges concentrated on optimization of the amount of neon. Neon contributed a few per cent to the total particle fluxes, which is comparable to the CO contamination of the recycling gas during the IOC discharges of the open divertor. In Fig. 3, the evolution of various plasma parameters is compared for three discharges with different wall conditions. Discharge #24707 with uncovered stainless-steel walls gives typical IOC transitions. Discharge #30451 with boronized walls remains in the SOC regime at high density. In discharge #30687 with boronized walls (as #30451) additional neon puffing is applied from 0.5 - 0.8 s and with higher flux between 1.5 - 1.9 s. The neon puffing yields high energy confinement times of up to $\tau_E \approx$ 120 ms as in IOC discharge #24707 at the highest density. In both discharges with IOC transitions the improvement of the confinement time is correlated with peaking of the density profile. This is seen from the increase of the ratio Q_{n14} of the HCN interferometer signals from the central channel and the channel at r/a = 0.75 plotted in Fig. 3. The ohmic power input given in the fifth row slightly increases during neon injection. But after the neon puff is cut off, the ohmic power decreases and beta increases to values comparable with IOC reference discharge #24707. The same holds for the loop voltage since the plasma current is kept constant. Here, the radiation losses exceed 50 per cent of the ohmic input power, whereas the pure deuterium discharge with boronized walls radiates only about 20 per cent of its ohmic heating power away. This high edge radiation results in a low power load at the target plates and simultaneously a small energy loss in the bulk plasma. Moreover, the flux of neutrons attains the same high value of 5 × 10^{10} neutrons s^{-1} both for the IOC and the neon-puffed discharge at the highest density plateau compared with 3 × 10^9 neutrons s^{-1} with boronized walls and without any impurity puffing.

1.2.4 Behaviour of the low-energy neutral flux to the wall for IOC/SOC conditions

The low-energy charge-exchange fluxes are very sensitive to changes in the confinement regimes. As an example, the development of the IOC regime for two discharges with different wall conditions is discussed in Fig. 4. For these shots n_e was ramped up to a plateau of 4.5 × 10^{13} cm^{-3}. During ramp-up the discharge enters the SOC regime, where the energy confinement time τ_E is observed to roll over. After a strong reduc-

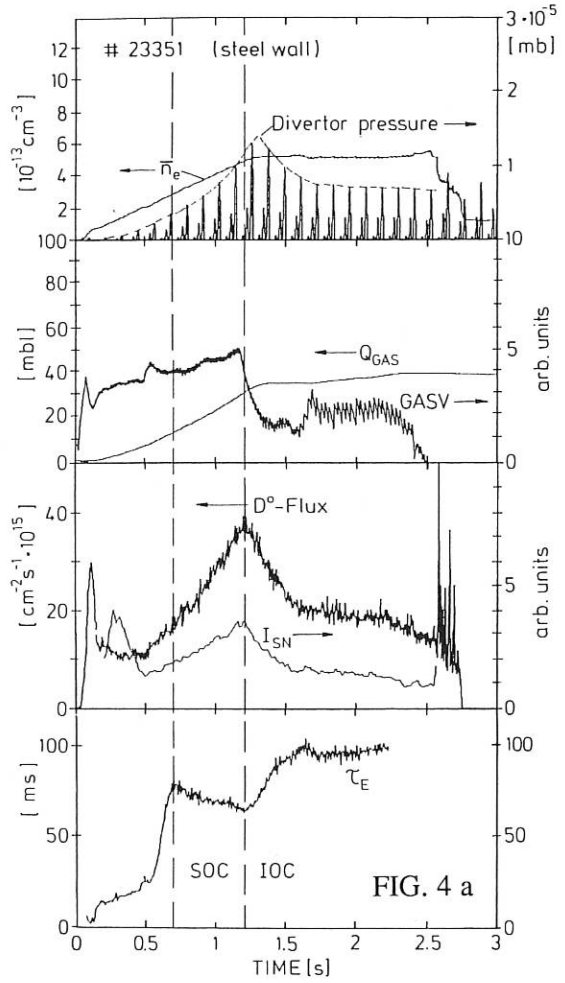

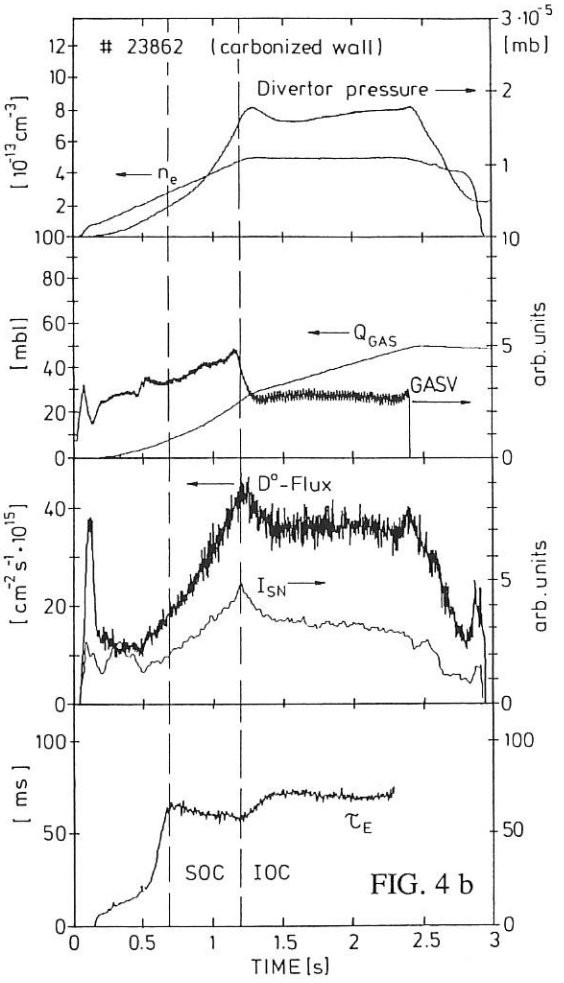

FIG. 4: Time evolution of the line-averaged density $\bar{n}_e$, the pressure in the lower divertor P_D, the voltage at the controlled gas valve GASV, the consumed amount of gas Q_{gas}, the D^oflux Γ^o, the electron current from the sniffer probe I_{SN}, and the energy confinement time τ_E for D_2 discharges with steel walls (a) and carbonized walls (b) but otherwise equal parameters. (For #23351 P_D was measured in the scanning mode, the envelop ----- of which is discussed here).

tion of the external gas feed (GASV) the IOC regime develops with an accompanying increase of τ_E. At the same time there is a strong reduction of the neutral D^0 flux, the ion flux in the scrape-off layer ISN as measured by the sniffer probe, and - with some delay due to the vacuum time constants involved - also of the divertor pressure measured by a mass spectrometer. These features are much less pronounced with carbonized walls, as shown in Fig. 4b. Under very clean conditions (boronization) intrinsic IOC cannot be achieved.

Considering the results of Secs. 1.2.3 and 1.2.4 leads to the conclusion that the reduction of the external gas feed is not the primary cause of the establishment of IOC. Rather, it is associated with the reduction of power flow into the SOL brought about by high edge radiation losses as detailed in Sec. 1.2.3.

1.2.5. Comparison of single- and double-null discharges for open and closed divertors

In summer 1988 the upper divertor by-passes, which allowed gas reflux from the divertor dome to the main chamber, were closed as much as technically feasible. It was then possible to compare at the same time two different divertor geometries (asymmetric configuration). In a second experimental period the by-passes were closed in the lower divertor too, resulting again in an up-down symmetric configuration. Comparison of the results from these two configurations enables one to discriminate between up-down asymmetries due to the difference in the divertor geometries and those induced intrinsically (e.g. by vertical drifts or owing to different recycling conditions in the two divertors).

The operational characteristics of these divertor configurations were studied by examining series of plasma discharges in which the plasma vertical position was varied by up to ± 4 cm in 1 cm steps (Δz series). In this way the plasma can be coupled either to the upper divertor (Single-Null (SN)-up) or to the lower one (SN-down) or to both (Double-Null (DN)).

Every discharge with constant Δz consists of an OH phase followed by an NI phase. In the middle of the NI phase the density is rapidly increased by about 60% via additional gas puffing in order to obtain two density plateaus of length 0.4 s at the beginning and end of the NI pulse. Thus, comparisons

between OH- and NI-heated plasmas at the same density and plasmas with different densities at the same NI power are realized. The density is always well below the density limit. Discharge parameters used are: $B_t = 2.2$ T, $I_p = 320$ kA, ($q_a = 3.1$), $P_{NI} = 1.4$ MW and $\bar{n}_e = 2.1 \times 10^{19}$ m^{-3} or 3.5×10^{19} m^{-3} for the low and high-density plateaus, respectively.

The main plasma as well as the divertor plasma and neutral gas accumulation were analyzed with the diagnostics shown in Fig. 5. For each diagnostic, data referring to the OH phase and to the two NI phases with low and high density (NI_L and NI_H respectively) are represented by a bar in the diagram.

The relative change in diagnostic signals measured in the lower divertor between closed and open geometry is shown in Fig. 5a, where the ratios of intensities for the closed divertor to the open one, in an SN-down configuration, are presented. In order to take into account the effect of different wall conditioning (boronization), these ratios are normalized to (i.e. divided by) the corresponding ratios measured for SN-up discharges in the upper divertor (which was always closed and is used then as "reference"). The only exception is the results from C III spectroscopy, which are not normalized because no measurement was available in the upper divertor (for this reason the carbon bars are hatched differently). Figure 5a shows that closing the divertor produces in most signals an increase of a factor of 2 to 3. For the radiated power P_{RAD} the increase is only 20 to 40%. The observed increase of the neutral density n_0 by a factor of 2 to 3 in the closed divertor is in good agreement with the estimated reduction of the by-pass gas conductance between the divertor and main chamber.

Figure 5b shows the relative change from open SN-down to closed SN-up of several main plasma characteristics measured under identical wall conditioning (asymmetric geometry) for the same phases of the discharges as in Fig. 5a. As expected, the signals from X-ray and Cu diagnostics have a very similar evolution, showing that Cu is one of the main heavy impurities in ASDEX. Also the loop voltage (which is feedback-controlled in order to sustain a constant plasma current) shows a similar behaviour, although less pronounced. We observe also that the largest difference between closed and open divertor appears in the phase of low-density NI-heated plasma. During this phase the plasma temperature is higher and, consequently, sputtering of wall material is enhanced. The impurity retention of the closed divertor is then even better for this less favourable condition. Q_{gas} is the total gas puffing used to sustain the discharge till the time corresponding to each phase considered: a closed SN-up discharge "consumes" about 60% more gas than an open SN-down, demonstrating the lower recycling conditions of the closed divertor.

The above results are interpreted by considering that the increase of the neutral density causes more energy to be lost by the divertor plasma via radiation and the plasma fan tends therefore to become narrower and the temperature is also slightly reduced. As a consequence, a) less energy is deposited to the divertor plates, reducing therefore the impurity production via sputtering, and b) there is a narrower channel along which the impurity can enter (or re-enter) the main chamber. Owing to the non linear energy dependence of the sputtering process it is conceivable that the DN configuration has worse performance than the SN ones, as already reported in the Annual Report 1989.

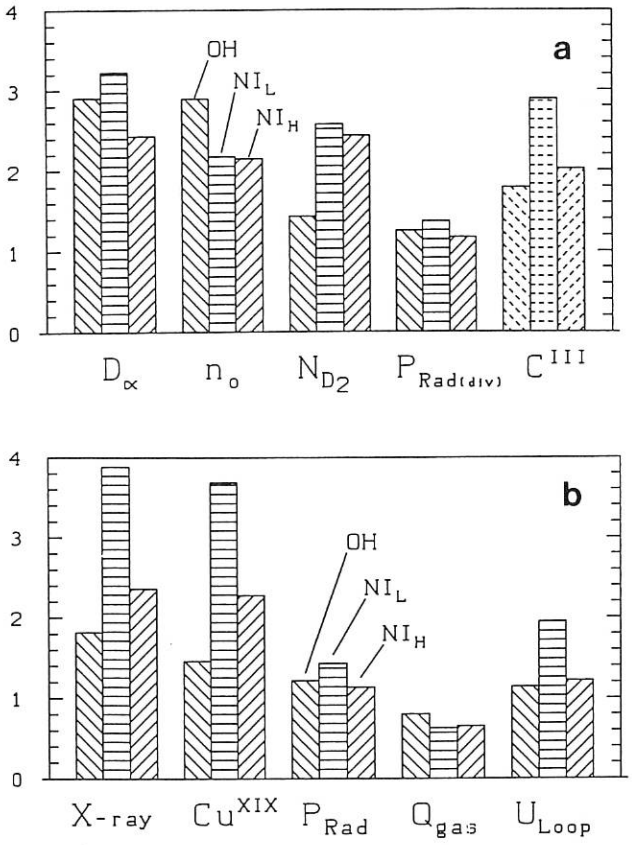

Fig. 5: a) Intensity ratios for closed and open divertor geometries measured for SN-down discharges in the lower divertor, normalized (except for C III) to the corresponding ratios measured in the upper divertor for SN-up discharges. OH: ohmic phase, $\bar{n}_e = 2.1 \times 10^{19}$ m^{-3}, NI_L, and NI_H: 1.4 MW NI-heated plasma with $\bar{n}_e = 2.1$ and 3.5×10^{19} m^{-3}, respectively. b) Intensity ratios measured in the main chamber for open SN-down and closed SN-up discharges. OH, NI_L and NI_H are the same as in Fig. 5a.

1.2.6 *Poloidal and toroidal energy deposition asymmetries on the divertor target rings*

(in collaboration with T. E. Evans, General Atomics)

Toroidally resolved divertor power loading measurements on each of the 4 copper target rings substantiate the existence of large poloidal and toroidal asymmetries in auxiliary-heated ASDEX discharges. The characteristics of these heat flux asymmetries depend primarily on the vertical position of the plasma, the edge safety factor (q_a), and the type of heating being applied (including the input power level). In addition, the amplitude and toroidal location of an individual loading peak as well as the poloidal distribution of the power flow into the divertors can be influenced by plasma density and vertical position variations. Weaker power loading distribution effects are also observed with changes in many of the other plasma parameters. An analysis of the divertor energy loading patterns during lower hybrid wave injection experiments at different q_a values suggests

a correlation between the positions of the loading peaks and changes in the expected locations of stationary magnetic island x-points. These intrinsic magnetic islands are produced in the vacuum field of a tokamak by unavoidable, small, random misalignments of the field coils (i.e., shifts of order 2 - 5 mm of some coils from their ideal positions).

Divertor energy loading measurements are made by recording an increase in the temperature of the cooling water flowing to individual divertor segments during a discharge. A careful calibration of the system provided a temperature-to-energy conversion factor of 30 ± 3.3 kJ/^{o}K. Owing to the relatively long time constants inherent in the divertor calorimetry measurements, data from the system represent the total energy deposited on a segment during an entire plasma discharge. Three categories of data analysis with differing degrees of spatial resolution are used. In the first a summation of the energy collected on each of the 40 calorimetry segments provides a measure of the total energy exhaust to the divertors during a particular shot. By carefully selecting plasmas with similar discharge conditions, we were able to make comparisons of the total energy flowing into the divertors with different heating methods at various input energy levels. There is a substantial change in the fraction of the energy collected by the divertors with each method of heating. For example, in both the ICRH and NBI-heated cases a lower percentage of the total input energy is collected in the divertor than in the ohmic case, and in the LHCD case this fraction is much higher. The second category of data analysis involves poloidally resolved measurements (obtained by summing over individual toroidal but not poloidal segments). This method facilitates the study of parametric plasma variations on individual poloidal target rings and shields. It is particularly

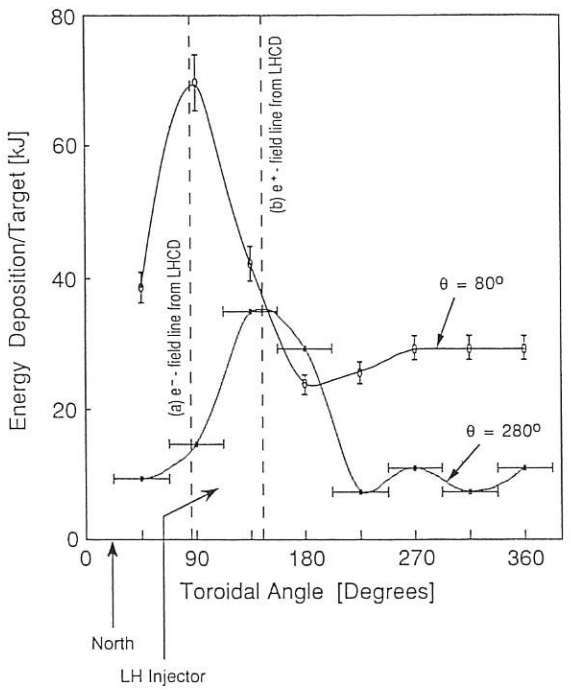

FIG. 6: Toroidally resolved energy deposition pattern on the upper-outer ($\theta = 80^{o}$) and the lower-outer ($\theta = 280^{o}$) target rings for a shot with a 0.7 s lower hybrid pulse producing 1.7 MW of absorbed power.

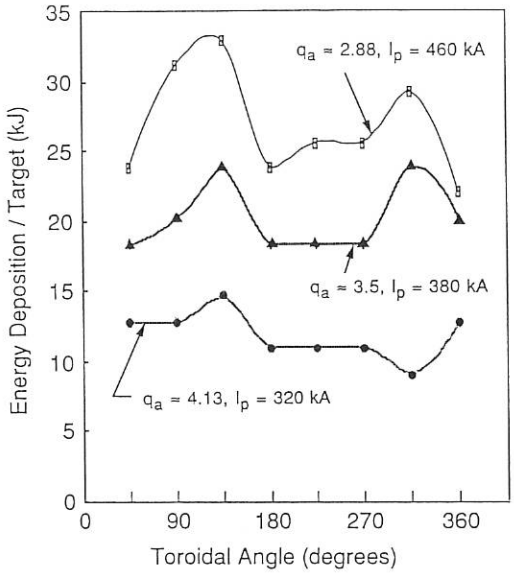

FIG. 7: Toroidal energy deposition patterns on the upper-outer ($\theta = 80^{o}$) target ring for three different values of q_a during otherwise similar ICRH shots with a 0.75 s heating pulse resulting in 1.3 MW of absorbed additional power.

useful in establishing a link between poloidal power loading asymmetries and impurity production in the divertors. The final category of analysis involves toroidally resolved measurements on each divertor ring and shield. The target rings as opposed to the divertor coil shields provide the most valuable information in this case because of their higher spatial resolution and larger energy loadings. We typically find, from the poloidally resolved measurements, that most of the energy absorbed in the divertors is collected by two of the four target rings. For most discharge conditions these are the upper-outer and lower-outer rings. An example of these toroidally resolved data from a lower hybrid discharge with an edge q_a of 2.5 is shown in Fig. 6.

The open data points in Fig. 6 represent the energy collected by individual ring segments. The north position and the lower hybrid wave injection port are referenced to the positions of individual segment centres (e.g. located at toroidal angles of 45^{o}, 90^{o}, etc.). The lower set of points, with horizontal bars attached to indicate the toroidal extent of an individual segment, is for data collected on the lower-outer target ring (located at a reference angle of $\theta = 280^{o}$). The upper curve, labelled $\theta = 80^{o}$, represents data from the upper-outer target ring. Interpolated curves are used to approximate a smooth distribution from one segment to the next. For this particular shot we calculated the toroidal connection angle which an m/n = 5/2 magnetic island passing in front of the lower hybrid launcher would have with the upper and lower divertor x-points. Assuming some fraction of the lower hybrid energy couples to fast electrons in the x-point of this intrinsic magnetic island and that this energy is lost to the outer target rings during a first pass near the divertor x-points, we calculate the positions at which we expect to find direct target plate loading due to lower hybrid wave injection. These points are indicated in the figure with

vertical dashed lines. Line (a) shows the deposition point in the electron drift direction (i.e. corresponding to a low-field side directed heat flux collected on the upper-outer target ring), while line (b) designates the ion drift direction loading point from the LHCD grill. These calculated positions match the deposition peaks on these two rings very well. This calculation was repeated for another shot with an edge $q_a = 3.2$. The loading peaks observed in that case corresponded to the toroidal connection angle of an m/n = 3/1 magnetic island. From the data given in the figure we can estimate the direct energy coupling required to produce these peaks . This analysis suggests that approximately 27% of the lower hybrid input power is directly coupled to the electron drift direction divertor and 12% to the ion drift direction divertor at this injection power level.

The loading peaks seen in Fig. 6 while reproducible are also very sensitive to changes in the edge safety factor. As q_a is changed the positions of the peaks are modified and the number of peaks can sometimes change. In addition, the average level and the amplitudes of the peaks can also change. Figure 7 shows a set of data from three similar ICRH shots with different q_a values. At lower q_a values the average power to the upper-outer target ring is higher and the amplitude of the loading peaks is larger. In the ICRH case the positions of the peaks are not as sensitive to changes in q_a as is the average value of the energy loading. The difference is expected to be related to the effects which intrinsic magnetic islands and ergodicity have on particles of different energies. Higher energy particles (i.e. such as suprathermal electrons produced during LHCD experiments) are more sensitive to magnetic field line trajectories and island structures because of their larger parallel velocities. Thermal particle transport, on the other hand, is primarily dominated by collisions and thus tends to smear out magnetic irregularities.

1.3 Impurity and Plasma-Wall Interaction Studies

(in collaboration with S. Adamson, R. Behrisch, K. Desinger, V. Dose, A.-P. Martinelli and V. Prozesky [Atomic Energy Corporation Pretoria, South Africa])

1.3.1 Optimization of boronization

Since April 1989 the ASDEX plasma chamber has been boronized seven times in DC glow discharges with various diborane-containing gas mixtures. The first five boronizations were performed in 10% B_2H_6 + 10% CH_4 + 80% He (method A), the last two of them with tripled gas throughput to improve deposition and homogeneity of the layers (see Sec. 2.1). During the 6th and 7th boronization runs a gas mixture with 90% H_2 or He + 10% B_2H_6 (methods B and C) was used. The tripling of the throughput of the working gas and the use of gas mixture C resulted in highest coverage and best homogeneity. The divertor chambers are not accessible to the glow discharge. All boronization runs were done with the vessel walls at room temperature.

Boronization provided considerably improved plasma conditions. The partial pressures in the upper divertor chamber measured by a quadrupole gas analyzer in a pumping port during the flat-top of standard ohmic discharges ($\bar{n}_e = 3 \times 10^{19}$ m^{-3}, $I_p = 0.32$ MA, $B_t = 2.17$ T, $q_a = 3.3$), showed a remarkable decrease of CO (Sec. 1.3.3). Simultaneously, the partial pressures of the hydrogen isotopes in the divertors were increased by a factor of ≥ 2 in relation to typical values of a well-conditioned uncovered machine (Fig. 13, Sec. 1.3.3).

Comparison of spectroscopic data showed a significant decrease of the line radiation from the plasma after fresh boronization. Spectroscopic measurements yielded a high reduction of the light impurities oxygen and carbon, with the strongest suppression after deposition method C, where oxygen and carbon disappeared from the spectra. Iron, too, vanished from the spectra and even copper, the target plate material, was significantly reduced. The oxygen-diminishing effect of boron/carbon and pure boron layers was found to be long lasting in comparison with the suppression of metal impurities. Deteriorated wall conditions occurred only after hundreds of discharges, including numerous additional heating shots with ICRH, NI, LH and combined scenarios, but pre-boronization conditions were never reached.

As a consequence of the reduction of light impurities, Z_{eff} obtained by bremsstrahlung was strongly reduced. The strongest reduction of Z_{eff} was observed after boronization C; even in standard ohmic discharges Z_{eff} was close to 1. The plasma edge values of Z_{eff}, too, were strongly decreased, with the lowest and broadest radial profiles after boronizations B and C (Fig. 8). The reduction of Z_{eff} with increasing density correlated well with the observed decrease of CO in relation to hydrogen within the divertors because of the high dilution of the light impurities after boronization. Z_{eff} increased again in the course of machine operation, interspersed by strong reduction after each boronization run, as shown for ASDEX fiducial shots ($\bar{n}_e = 3 \times 10^{19}$ m^{-3}, $I_p = 0.32$ MA, $B_t = 2.17$ T, $q_a = 3.3$). The overall tendency, however, was a permanent reduction of Z_{eff} with the best results after boronization C.

Investigations of the density limit as a function of wall conditioning were based on specially dedicated density limit shots where the density is slowly ramped up by feedback control until the plasma disrupts. The typical density limit in standard ohmic density limit discharges ($I_p = 0.32$ MA, $B_t = 2.17$ T, $q_a = 3.3$) was 5×10^{19} m^{-3} before boronization. After boronization A the density limit was 6.2×10^{19} m^{-3}, which further increased to 6.7×10^{19} m^{-3} (boronization B) and 7.3×10^{19} m^{-3} (boronization C), (Fig. 9). The increase in density limit was closely correlated with the decrease of the partial pressure in the divertor, mainly of CO. This is a rather clear indication that the density limit in ohmic discharges was most strongly influenced by the light impurities C and O, and that oxygen recycling is mainly via CO. A more detailed description of the density limit with boronized walls is given in Sec. 1.5.

For boronized wall conditions the fraction of radiated power compared with the input power P_{RAD}/P_{tot} was about 25%. This was an important difference to carbonization with $P_{RAD}/P_{tot} \approx 50\%$. A comparison of radiation profiles showed, for carbonization as well as for boronization, highly depressed central radiation in relation to a clean metal machine. For the carbonized case, however, the radiation profiles showed higher edge radiation as compared with the clean metal case. With boronization, however, the radiation from the plasma edge was significantly decreased to values below those of a metal machine.

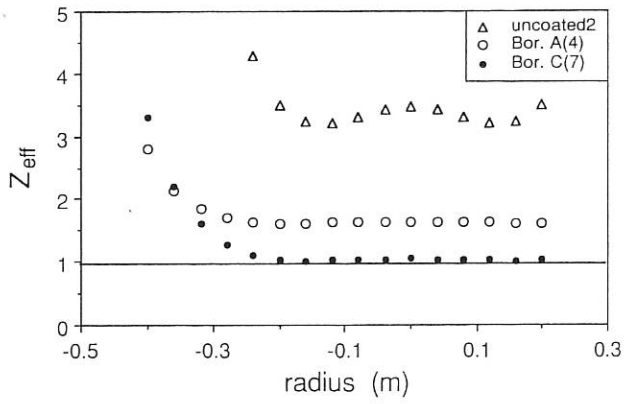

FIG. 8: Radial Z_{eff} profiles in standard ohmic plasma discharges before (uncoated 2) and after boronization A (Bor. A(4)) and C (Bor. C(7)).

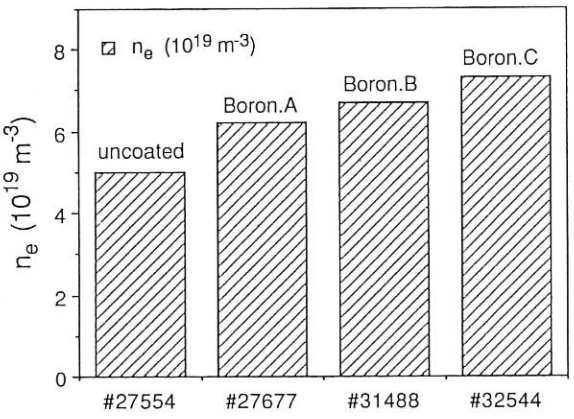

FIG. 9: Improvements on density limit in standard ohmic density limit discharges after boronization method A (#27677), B (#31488) and C (#32544). Discharge #27554 shows the typical density limit with uncoated vessel walls.

Boronization provided very good conditions for the H-mode which could be obtained over a wide range of plasma current, magnetic field and injection power. After boronization B and C the power threshold for the H-mode was significantly reduced (e.g. P_{NI} = 1.05 MW, I_p = 0.45 MA, B_t = 1.8 T, double null). For quiescent H-phases (lasting up to 190 ms) the plasma energy increase was terminated by the occurrence of Edge Localized Modes (ELM) and not by excessive radiation losses. The previously observed beta limit values were reproduced, however, at lower power. Long (> 3.5 s, limited by the NI pulse) and very stationary H-phases with ELMs could be achieved. The ELMs were extremely regular with less than 10% variation in frequency, which was probably an effect of the stable and reproducible edge conditions provided by the boronization.

Boronization was found to be an excellent wall-conditioning method. The effective particle confinement τ_p was high, as is typical of metallic walls. The oxygen- and carbon-diminishing effect of boronization remained over long periods (>1000 discharges) and older layers could be partly reactivated by plasma discharges even after venting of the vacuum vessel and maintenance work inside it (March 1990). When operation was resumed in April 1990 there was still some residual activity of the old boron layer. After just one day of operation good conditions for plasma discharges were reached (e.g. Murakami parameter = 4.3×10^{19} m^{-2} T^{-1} at q_a = 3.3 and H-mode formation).

Boron/carbon and pure boron layers were found to be more durable than pure carbon layers because boron is resistant to chemical erosion. Boron, supposedly removed by sputtering, was partly transported into the divertors, as indicated by collection probe data, and might also yield favourable action there. All observations on ASDEX support the assumption that the positive effect of boronization is not simply based on a reduction of H_2O in the vacuum vessel. More likely, the reaction of boron with atomic oxygen from the plasma, forming boron / oxygen compounds, and activation of the layer by the plasma itself are the true reasons.

1.3.2 Long-term Z_{eff} profile behaviour on ASDEX

Z_{eff} is an overall measure of the impurity content in a plasma and can be directly derived from bremsstrahlung emission. It should be close to 1 to minimize both fuel dilution and radiation losses. It is known that Z_{eff} strongly depends on wall coatings, stainless steel (s.st.), carbonization (carb.) and boronization (bor). The lowest values of Z_{eff} are obtained with fresh boronization, leading to flat radial profiles with values near 1 over most of the plasma radius (see Sec. 1.3.1, Fig. 8). Figure 10 shows the improvements in Z_{eff} on axis for standard ohmic discharges and different wall conditions. The strong reduction of Z_{eff} from uncoated to boronized walls results mainly from the elimination of metals and oxygen. With each new boronization the central Z_{eff} was improved and reached 1 after the last boronization, which was performed without CH_4 addition. The effectiveness of the boron layer is maintained over a long operation period; after about 1,000 plasma discharges Z_{eff} increases to about 1.3. This increase is faster when strong additional heating is frequently applied (bor. 5).

Close to the separatrix Z_{eff} rises to 3 in standard ohmic discharges, which is considerably less than for non-boronized wall conditions. At higher densities ($\bar{n}_e \geq 4.5 \times 10^{19}$ m^{-3}) the boundary Z_{eff} is even less than 2. This is in agreement with the observed reduction of the boundary radiation, which seems to be the main reason for the disappearance of the Improved Ohmic Confinement (IOC) in boronized plasma. The improvement in Z_{eff} correlates well with the rise of the density limit (see Sec. 1.5).

A strong reduction of Z_{eff} was also observed in plasmas heated with ICRH, LH and neutral beam injection, both in the L and H-mode. As an example, Fig. 11 shows the power dependence of the central Z_{eff} in an LH-heated plasma ($\bar{n}_e = 3 \times 10^{19}$ m^{-3}) before and after boronization. During LH operation the excursion of Z_{eff} is halved from values between 3 and 6 (non-boronized) to 1.5 and 3 (boronized), resulting in improved current drive efficiency.

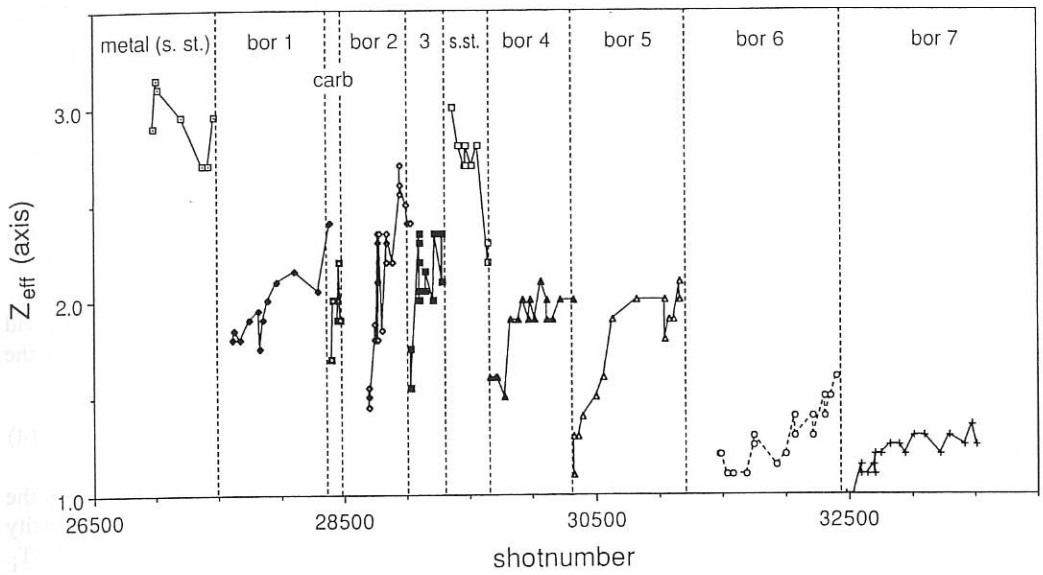

FIG. 10: Long-term dependence of Z_{eff} on ASDEX in standard ohmic discharges ($\bar{n}_e = 3 \times 10^{19}$ m^{-3}) with stainless-steel (s.st.), carbonized (carb.) and boronized (bor 1-7) walls.

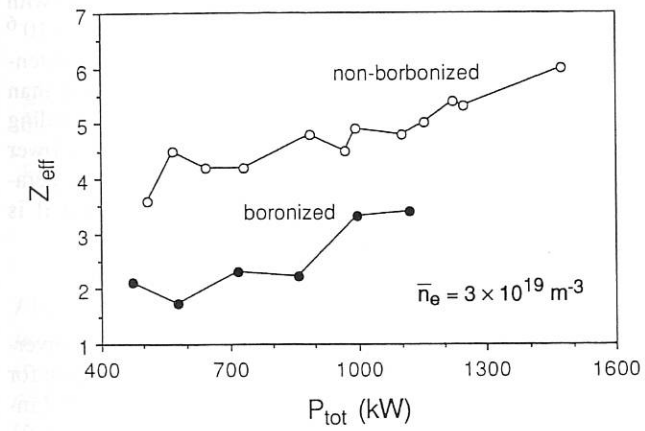

FIG. 11: Improvement of Z_{eff} due to boronization in LH-heated plasmas for different heating powers.

1.3.3 *Gaseous impurity recycling*

Partial pressures of impurity gases during the discharges were monitored in the ASDEX divertors almost from the commissioning date. Water vapour, methane and carbon monoxide were found to be the most abundant gases, usually adding up to between 10 and 25% of the partial pressure of the fuelling gas H_2 or D_2. Only with Ti-gettering in the divertors was it possible to achieve a significant reduction of water vapour and especially of carbon monoxide. The reduction agreed well with the spectroscopically determined reduction of oxygen in the plasma. These observations strongly suggested that oxygen was essentially recycled by these two gases. Moreover, the fluxes, which can be calculated from the measured partial pressures and the known conductances of the divertors to the main chamber, agreed well with those deduced from spectroscopic data. With carbonization a reduction of water vapour was observed, but a somewhat increased partial pressure of carbon monoxide remained as the source of oxygen.

With the boronization of ASDEX such investigations once more gained interest. As in the case of previous Ti-gettering, a strong reduction of carbon monoxide by a factor 5 to 10 was found. An assessment of the contribution of water vapour and methane, however, turned out to be difficult because at this time the machine was operated mostly with D_2 with a 10 to 30% contribution of H_2 from outgassing. Under these conditions a serious interference problem exists for the typical ion mass peaks of the two gases at M = 18, 19, 20, corresponding preponderantly to H_2O^+, HDO^+, D_2O^+ and CD_3^+, CD_3H^+, CD_4^+, respectively. Disentangling the contribution of methane versus water vapour to the impurity flux becomes crucial in discharges not dominated by recycling of carbon monoxide, in order to asses the virtues of boronization. An isotope-mixing model set up for the specific situation in the divertor was used to calculate the ratios of the various isotope molecules of water vapour and methane as a function of the concentration of hydrogen atoms in the molecules making up the pressure in the divertor. The result for methane, including the known cracking pattern of the mass spectrometer ion source, is shown in Fig. 12.

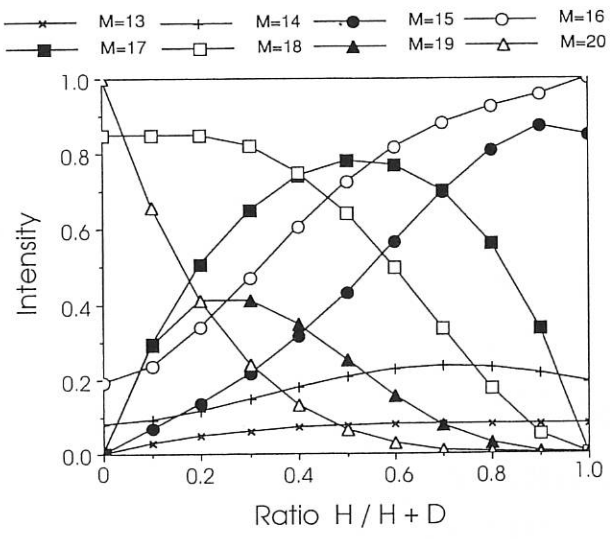

FIG. 12: Calculated intensity distribution for the methane peaks as a function of hydrogen atom concentration obtained from the partial pressures of H_2, HD and D_2 in the divertor.

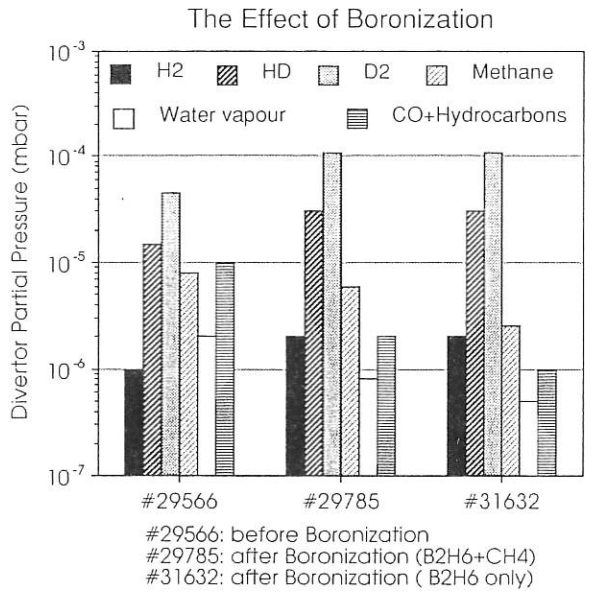

FIG. 13: Partial pressures of the hydrogen isotopes and of the main contaminant gases in the divertor before boronization (#29566), after boronization with $B_2H_6 + CH_4$ (#29785) and after pure boronization in B_2H_6 only (#31623). The reduction of "CO + hydrocarbons" from #29758 to #31623 is mostly due to the amount of hydrocarbons contributing to the signal at the corresponding mass.

The investigations showed that water vapour was indeed negligible after the boronization, but methane was hardly reduced (Fig. 13). This was somewhat in contrast to expectations as laboratory experiments predicted a significantly reduced chemical erosion of carbon. The data showed that the performance of the machine was now essentially limited by the radiation of carbon, recycling via hydrocarbons, produced by the reaction of the atoms of the fuelling gas with the still abundant carbon everywhere in the machine.

1.3.4 Impurity retention of the divertor

The retention capability of the divertor for target-produced impurities and noble gases has been extensively studied in ASDEX for several years. In 1990 we concentrated on the influence of some crucial parameters on the retention of noble gases. In particular, the connection length of the field lines is such a critical parameter which must be optimized to achieve sufficient exhaust of helium in a reactor .

Trying to interpret our observations, we invoked a very simple model which allows an analytical treatment of the problem. In this model the impurity fluxes parallel to the magnetic field lines are described by diffusive and convective parts:

$$\Gamma = D_{\|} \frac{\partial n_z}{\partial s} - V_{\|}\, n_z \qquad (1)$$

with $D_{\|} = D_{class}$ and $V_{\|} = M\, V_{sound}$. The stationary solution $\Gamma = 0$ for the source-free region leads to

$$n_z = n_{z,div} \exp\left(-\int_{s_d}^{s_x} \frac{v_{\|}}{D_{\|}}\, ds\right) . \qquad (2)$$

Defining the characteristic length

$$\lambda_{\|} \equiv \frac{D_{\|}}{V_{\|}} = \frac{8.84 \times 10^{12}}{(1 + m_i/m_z)\, \ln\Lambda} \frac{T_i^2}{M\, Z^2\, n_i(cm^{-3})} \quad (cm) \qquad (3)$$

and the connection length $L_{\|} = s_x - s_d$ as the length of the field lines from the divertor throat to the x-point, we obtain for the ratio $P = n_{z,x\text{-point}} / n_{z,divertor}$

$$P = e^{-\langle L_{\|} / \lambda_{\|} \rangle} = e^{-\text{ const } L_{\|} \langle Z^2\, M\, n_i / T_i^2 \rangle} . \qquad (4)$$

This expression predicts a pronounced dependence on all of the five parameters: connection length $L_{\|}$, background-ion density n_i, Mach number M, charge number Z and ion temperature T_i. An extreme sensitivity is particularly to be expected with respect to Z and T_i, which enter with the square in the exponent.

A more quantitative analysis for He shows that P can vary with T_i changing from $20 < T_i < 60$ eV from very small values $\approx 10^{-6}$ (excellent retention) to rather large values of ≈ 0.2 (poor retention). The model predicts that the retention of He is less than that of other gases which are in higher charge states. Including the necessity of being opaque for neutrals, which poses a lower temperature limit, there is a limiting interval for the ion temperature to provide good retention. For helium this interval is approximately given by

$$10 \text{ eV} \le T_i \le 10\, Z\, [10\, M\, n_i\, (10^{19}\, m^{-3})\, L_{\|}\, (m)]^{1/2} \text{ eV}$$

The above considerations suggest that the rise of T_i in the divertor with increasing additional heating is the essential reason for the breakdown of retention that is seen in the case of neutral injection.

In Fig. 14 we show experiments with short Ar pulses. The above effect of degrading the retention is here seen in the increase of the Ar XVI signal (emitted from the main plasma) with the onset of the second NI heating interval for the $q_a = 3.3$ shot. In a quantitative study, however, where the beam power was systematically varied and the electron temperature in the divertor measured (10 - 22 eV), relation (4) could not be confirmed when assuming $T_i = T_e$ and $M > 0.1$. Higher ion temperatures ($T_i \approx 2T_e$) have to be claimed to attain agreement. According to findings from JET such an enhancement of T_i in the divertor region may be realistic.

The effect of varying the connection length $L_{\|}$ - being proportional to the safety factor q_a - was systematically studied by varying the toroidal magnetic field, thus changing q_a between 2.2 and 4.4. In Fig. 14 we show the results for the two cases $q_a = 3.3$ (with NI) and 2.2 (pure ohmic). The expected degradation of the retention by lowering q_a is clearly demonstrated.

Again, however, problems arise within a quantitative analysis when the temporal behaviour of the signals is interpreted in terms of a simple dynamic model. The model describes the coupled system of all impurity ions in the main plasma N^+ and the corresponding neutrals in the divertor N^0 by means of the two differential equations:

$$\frac{\partial N^+}{\partial t} = -\frac{N^+}{\tau_{par}} + \frac{N^0}{\tau_{div}} \quad ; \quad \frac{\partial N^0}{\partial t} = \frac{N^+}{\tau_{par}} - \frac{N^0}{\tau_{div}} - \frac{N^0}{\tau_{pump}}$$

where τ_{par} , τ_{div} are the characteristic times for plasma- and divertor-confinement and τ_{pump} is the pumping time of the divertor. A reduction of $L_{||}$ is expected to enhance first of all the divertor outflux, thus decreasing τ_{div} . The above coupled system has two eigentimes τ_{fast} and τ_{slow} (being complicated functions of τ_{par} , τ_{div} , τ_{pump}) that describe the decay of the pulses in the main plasma by the sum of two exponentials. Consistently, the measured signals can also be well fitted by two exponentials. From these fittings τ_{par} , τ_{div} can be obtained provided τ_{pump} is known. Unfortunately, this quantity is not known to the accuracy needed to determine τ_{div} reliably, and even a falling or rising dependence of τ_{div} on q_a can be obtained within the uncertainties. On the other hand, we find contrary to expectation that τ_{par} is also affected by changing q_a and rises from $\tau_{par} \approx 60$ ms ($q_a = 4.2$) to about 130 ms ($q_a = 2.2$). This result is consistent with laser blow-off investigations using titanium (non-recycling), where a similar behaviour of the particle confinement time with q_a is found. An example showing signals of Ti XX emission for $q_a = 3.8$ and 2.7 is presented in Fig.15. In particular, these findings indicate that the above dynamic model is still a too simple description of the impurity transport between the main plasma and divertor. Further theoretical and experimental investigations on the matter are therefore needed.

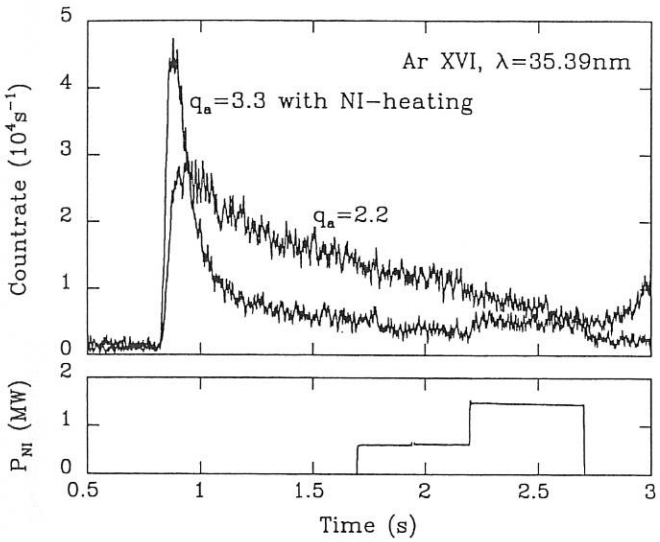

FIG. 14: Temporal behaviour of Ar XVI intensities after injection of short Ar pulses into the main plasma chamber. Two traces for different values of B_{tor} , corresponding to q_a = 2.2 and 3.3, are shown. In the q_a = 3.3 case additional NI heating (bottom insert) was applied.

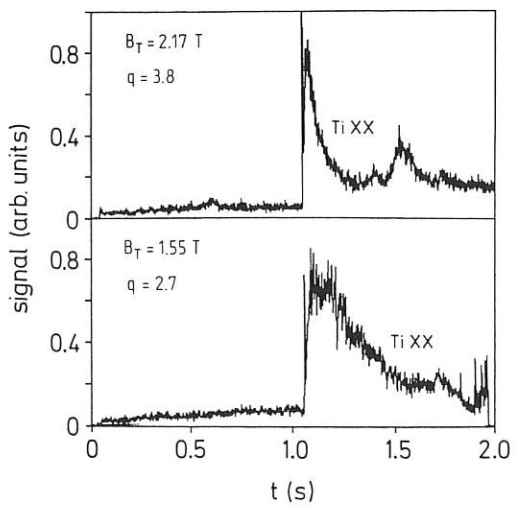

FIG. 15: Traces of Ti XX in the case of titanium laser blow-off for q_a = 2.7 and 3.8. As in Fig. 14, we notice a reduction of the decay time for the lower q_a value.

1.3.5 Collector probe measurements within the divertor

(in collaboration with S. Adamson, G. Staudenmaier and E. Taglauer, Surface Physics Division)

A newly designed divertor collector probe was used to study the divertor retention of impurities released from the divertor plate as well as the flux of wall impurities into the divertor. The new probe head consists of a rotatable high-purity graphite cylinder housed in a fixed molybdenum shield which contains an exposure slit.

Improvements on the previously used head with attached Papyex strips are: The graphite collectors contain a lower level of bulk impurities, the greater bulk of the massive graphite cylinders allows it to sustain higher heat loads, and - most important - continuous spatial sampling across the SOL is now possible.

The main results were as follows:
The dependence of collected impurities on the vertical plasma position Δz was further investigated (see Annual Report 1989, page 20, Fig. 10). For standard ohmic discharges changing the magnetic configuration from single-null down to double-null to single-null up produces a progressive increase in collected Cu fluxes (Fig. 16) released from the divertor plates. Further upward shifts (Δz = +2 and +3 cm) produce no significant increase in collected fluxes over the Δz = +1 cm case. As with the earlier Papyex measurements, a large "background" Cu deposit is found for the Δz = -3 cm discharge. Measurements made immediately after boronization of the main vessel gave a large boron deposit (5×10^{16} atoms/cm^2) which was sharply peaked in the middle of the SOL consistently with the main chamber wall being the source. Boronization reduced the total amount of collected Fe by only a factor of two, implying the existence of Fe sources at the divertor throat or in the divertor chamber. Deposited oxygen was seen to increase after boronization. Time-resolved measurements show that collected Fe and Cu impurities increase with NBI power (Fig. 17). During the NBI phase the peaks shift towards the divertor plate. In the case of Fe a second peak appears. This second Fe peak relates to the outside edge plasma. This behaviour would not have been apparent with the very limited spatial information obtainable from the Papyex probe.

The Cu deposition on the divertor probe was analyzed with a numerical code which models the plasma sheath in front of the target plate in two dimensions. This code reproduces well the Cu erosions as measured spectroscopically in front of the divertor plate. Subsequently, the Cu ionization is calculated in the divertor plasma and it is assumed that ionized Cu atoms are deposited along the magnetic field lines. The integrated amounts of Cu determined experimentally are almost a factor of 6 higher than calculated. The measured radial distributions of Cu on the probe, however, are well reproduced by the code calculations.

1.3.6 Impurity sputtering by ELMs

An important question for future tokamaks is whether the edge localized modes (ELMs) that occur during the H-phase of NI heating cause excessive sputtering. This question was addressed in ASDEX by measuring the Cu I intensity emitted

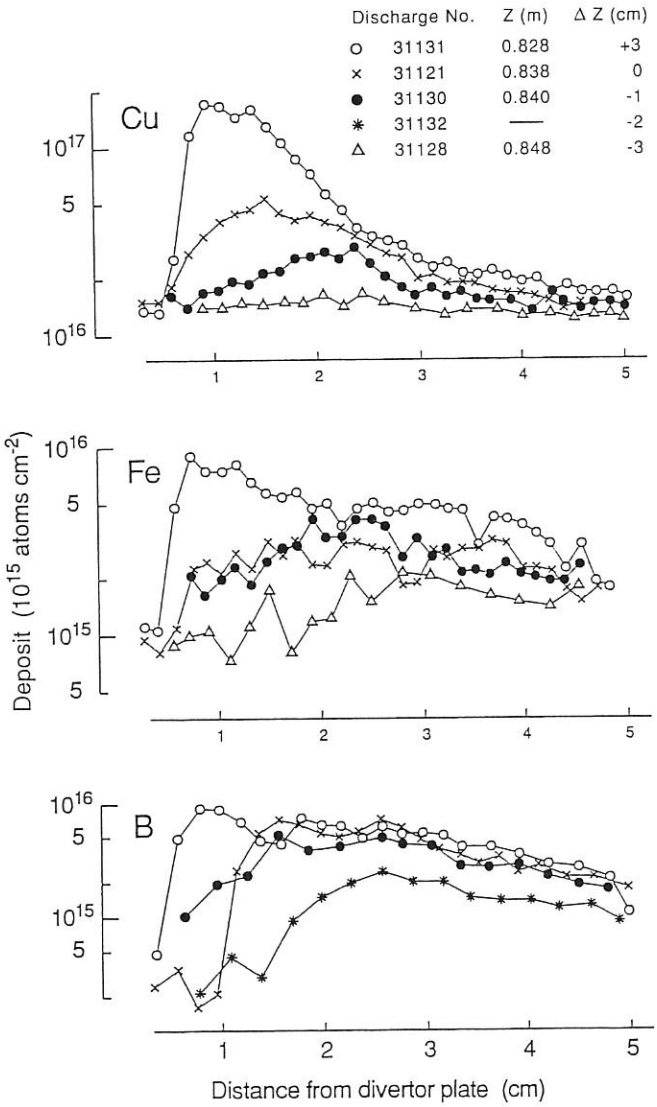

FIG. 16: Radial distributions of Cu, Fe and B deposits (integrated over the discharge) as functions of the vertical plasma shift Δz. I_P = 320 kA, $\bar{n}_e = 2.8 \times 10^{13}$ cm^{-3}.

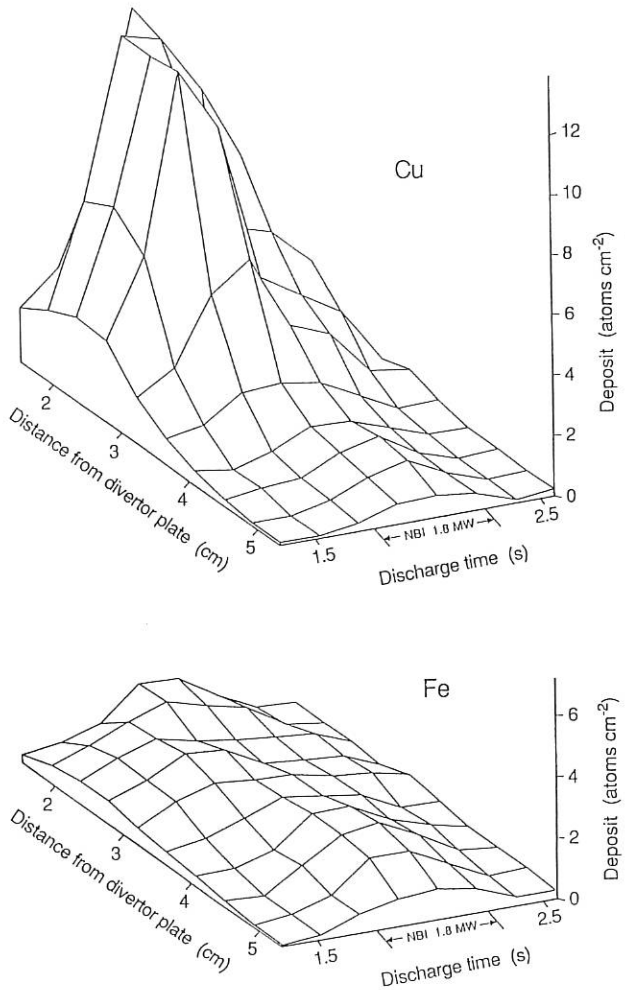

FIG. 17: Radial and time dependences of retained Cu and Fe deposits for discharge #30677. I_P = 380 kA, $\bar{n}_e = 2.8 \times 10^{13}$ cm^{-3}, NBI = 1.8 MW (1 → 2 s). The probe's time resolution was 0.3 s.

from the copper target plates in the lower divertor. The Cu I line intensity is proportional to the eroded Cu fluxes. In Fig. 18 this signal is plotted together with the D_α emission in the divertor and the Cu XIX intensity from the bulk plasma for an H-mode showing typical ELM activity. The strong correlation between the Cu I and D_α signals can be seen from the zoom plot in Fig. 18. On the other hand, no ELM correlation is found with the Cu XIX signal. The D_α and Cu I light is recorded at sampling rates of 5 kHz and 1 kHz, respectively, whereas the ELM duration is of the order of 100 μs only. Hence, one must be aware of aliasing and pulse-broadening effects.

We find that the total amount of copper sputtered during the ELM is a factor of more than two larger than the integral between the ELMs. Moreover, an enhancement factor of about 10 for the true peak value is estimated. These large peak values are consistent with the strong nonlinear sputtering yield as a function of temperature. Since the Cu I signals shown were recorded in the lower divertor under conditions where the plasma had been shifted upwards by 2 cm in order to attain the H-

phase, the pronounced peaking during an ELM may indicate not only an increase of T_i but also an additional widening of the ion temperature profile.

In summary, the strong non linear response of sputtering to T_i must be considered as an important effect when estimating the target erosion during ELMy H-phases.

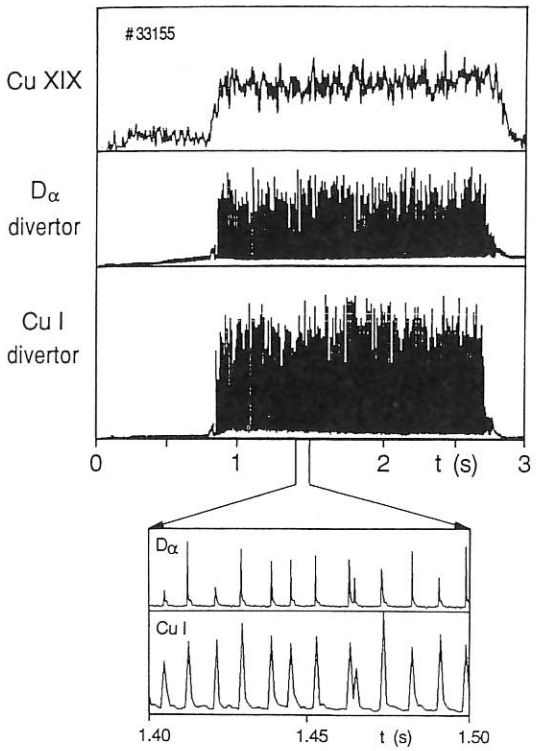

FIG. 18: Time dependence of the D_α light emission in the upper-outer divertor, copper sputtering at the lower-outer target (Cu I), and the intensity of a copper line from the bulk plasma (Cu XIX) for a quasi-stationary, ELMy H-mode.

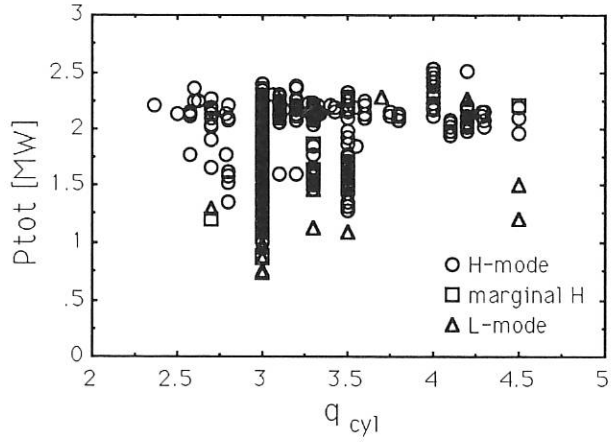

FIG. 19: H-mode power threshold for 280 kA and 320 kA versus safety factor q_a, $H^o \rightarrow D^+$, single-null configuration with $0.5 \leq z \leq 2$ cm, horizontal plasma position between 1.63 m and 1.69 m, averaged density at the L-H transition between 2.5×10^{19} m^{-3} and 3.5×10^{19} m^{-3}.

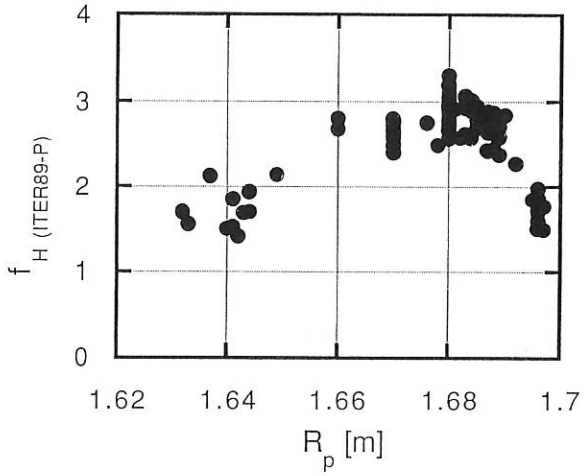

FIG. 20: H-confinement time enhancement factor normalized to ITER 89-P L-scaling versus horizontal position for 0.5 cm ≤ z ≤ 1.5 cm.

1.4 Confinement Studies

1.4.1 H-mode studies

1.4.1.1 Operational window of the H-mode

H-mode power threshold: With the new closed divertor, the power threshold to obtain the H-mode was lower than with the open configuration. The power threshold (P_H) for co-NI H-mode was analyzed for 200 kA ≤ I_p ≤ 460 kA and 1.1 T ≤ B_t ≤ 2.8 T. The threshold values for deuterium and hydrogen injection into a deuterium plasma are very similar. In the I_p-B_t operational diagram, the threshold shows a clear minimum along the $q_a = 3$ line. This is illustrated in Fig. 19 for I_p = 280 kA and standard H-mode parameters.

In the most recent scans with boronized walls the power threshold increases approximately linearly with B_t for $q_a \geq 3$. The B_t-dependence (and not the I_p- or q_a-dependence) is confirmed by the fact that the increases with B_t at constant I_p and along $q_a = 3$ are similar. In these cases the dependence is $P_H \approx \alpha B_t^{-\delta}$ in MW and Tesla with $\alpha = 1 \pm 0.25$ and $\delta = 0.5 \pm 0.5$. For $q_a \leq 3$, the power threshold increases very steeply and this could be related to the strong degradation of the divertor retention factor for $q_a < 3$. The power threshold clearly decreases with increasing density, which could also be related to the divertor retention, which increases with density. No further analysis has been done so far. For ctr-NI, no detailed studies have been performed but, confirming earlier observations, the threshold is about 20% lower than for co-NI.

ELM-free operation: The plasma position plays a key role for the H-operation. It has been known for a long time that upper single-null operation is favourable. The horizontal plasma posi-

tion (R_p) also influences the H-mode discharges as illustrated in Fig. 20, showing the H-confinement time enhancement factor compared with the mass-corrected ITER 89-P L-scaling versus horizontal position for a selection of the best discharges.

The highest confinement times in this picture (1.68 m ≤ R ≤ 1.69 m) correspond to ELM-free discharges, whereas the other values correspond to ELMy discharges, for which ELMs degrade the confinement. This figure shows indirectly how the ELM behaviour is affected by the plasma position, speculatively linked to the stabilizing effect of the outer wall. For R > 1.69 m, the intensified plasma-wall interaction with installations of the vacuum vessel, giving rise to limiter effects, could be the cause of more frequent ELMs and finally leads to L-mode operation for R > 1.70 m.

The ELM-free H-discharges (H*) are reproducibly obtained in a narrow range of the plasma position: z = 1 ± 0.5 cm and R_p = 1.67 ± 1 cm. The power threshold for ELM-free operation is higher than that described in section "H-mode power threshold" but has similar behaviour versus B_t and q_a. The lowest threshold value (1.5 MW at q_a = 3) is the same for H⁰ and D⁰ injection into deuterium plasmas. However, the I_p-B_t range for H* is narrower for H⁰ than for D⁰ injection.

Stationary H-discharges: An important feature of the plasma positioning is the ability to obtain ELM-controlled stationary H-discharges lasting for many confinement times. By precise vertical and horizontal positioning of the plasma column (z = 2 ± 0.5 cm and R_p = 1.66 ± 1 cm), the ELM period can be optimized in such a way that the confinement time is as high as possible ($\tau_E^H / \tau_E^{ITER\ 89\text{-}P} \cong 1.9$), whereas the ELMs maintain the impurities at low level. Such discharges have been sustained under stationary conditions at least over more than 80 confinement times at various plasma currents from 280 kA to 420 kA and $q_a \approx 3$. An example at 280 kA for an H-phase lasting more than 3 s (80 τ_E limited by the heating pulse length) is given in Fig. 21. The regular behaviour of the ELMs, which allowed steady-state H-operation, was presumably made possible by the boronization.

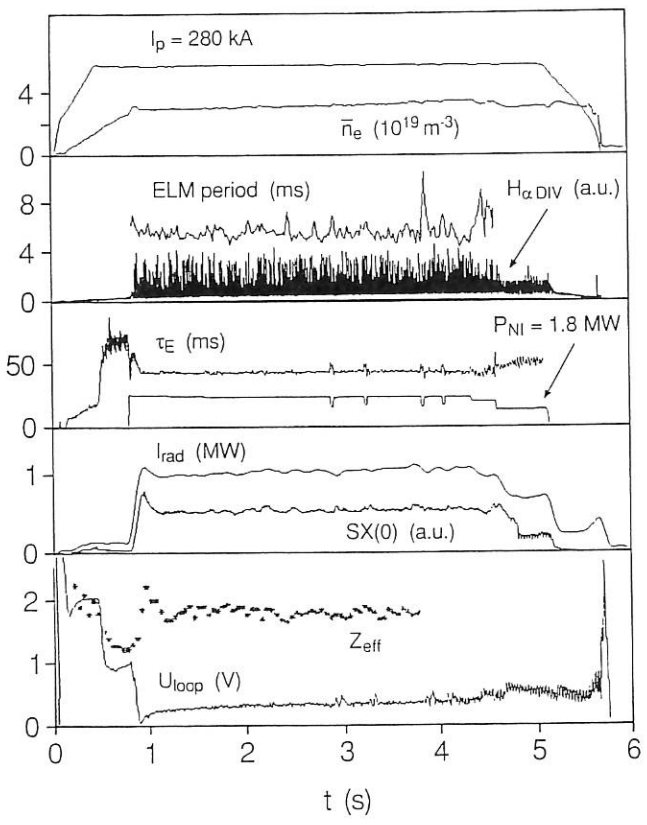

FIG. 21: Stationary H-discharge, I_p = 280 kA, B_t = 1.74 T, single null with z = +2 cm.

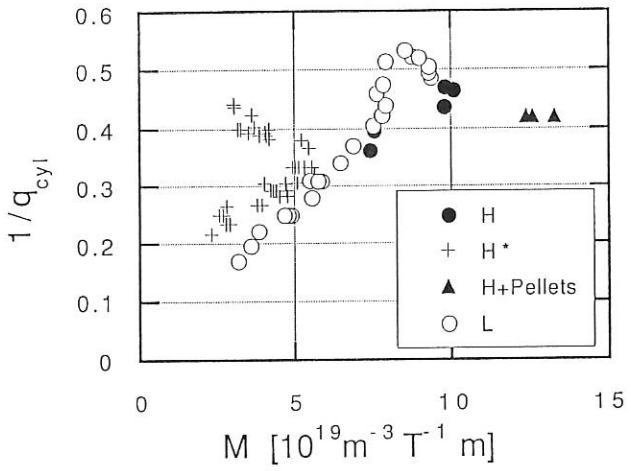

FIG. 22: Murakami operation diagram for H-mode, L-mode and pellet injection in H-mode.

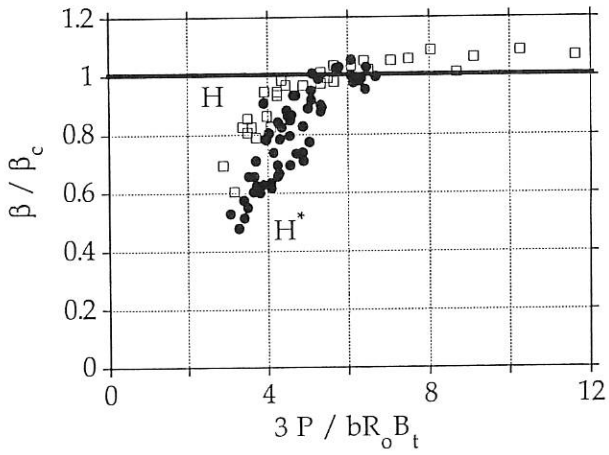

FIG. 23: Troyon factor versus normalized power.

Density window: The density operational window was not explored in detail with the new configuration. The earlier observation that the H-mode can only be obtained above a minimum density of about 2 × 10^{19} m^{-3} under standard conditions was confirmed. New results obtained at high density, near the L-mode density limit, are shown in Fig. 22 and discussed in more detail in Sec. 1.5.

Also shown is the high-density boundary reached in H*-discharges owing to the density increase, the gas valve being closed. The highest density values reached in this case are not determined by a density limit phenomenon but by the occurrence of ELMs and switch back to the L-regime.

Beta limit: With the available heating power (2.7 MW for D^0 injection), the beta limit could only be reached in H*-phases. The comparison with earlier results obtained in ELMy discharges (Fig. 23) shows that the Troyon factor does not depend on the type of discharges.

1.4.1.2 Measurement of poloidal rotation at the plasma edge

The drift velocity vectors of the light impurity ions B IV, C III and He II were determined at the plasma periphery in L- and H-mode NBI-heated plasmas. Components of the drift velocity $\underline{v}$ in the poloidal (v_θ), perpendicular ($v_\perp$) and toroidal (v_t) directions were inferred from the Doppler shift of the impurity line emission measured with a visible spectrometer / scanning mirror system. The velocity components were obtained from the differential Doppler shift between spectra measured along opposite viewing directions.

Drift velocity vectors constructed from the measured perpendicular and toroidal components are plotted in Fig. 24 for L- and two quiescent H*-phases with opposite B_t directions. (For technical reasons I_p was reversed with B_t and so the negative B_t case is studied in a H*-phase with ctr-NI.) v_t is approximately equal for the three cases. In the L-mode $v_\perp$ is small and in the direction of B×∇p; in the two H-phase cases $v_\perp$ is large and in the -B×∇p (electron drift) direction. The direction of $v_\perp$ reverses when B_t is changed.

The high perpendicular velocity cannot be explained in terms of the pressure gradient of the impurity species investigated but, rather, implies the existence of a strong inwardly directed radial electric field of magnitude $|E_r| \leq 25$ kV m^{-1} (confirming findings on DIII-D). Detailed consideration of the principle of this measurement confirms that, when measuring emission from low ionization states of low-Z ions confined to narrow shells at the plasma periphery, E_r can be determined directly from the measured $v_\perp$ without having to correct for possible contributions from the diamagnetic drift and radial gradients of the excitation probability. Measurement conditions did not allow determination of the gradient of E_r inside the separatrix. There is evidence, however, that there must be a steep gradient of E_r close to the separatrix since the perpendicular drift velocity of the C III ions (which are localized at or just outside the separatrix) is always observed to be small (≤ 2 km s^{-1}).

$v_\perp$ and v_θ gradually increase after the L→H-mode transition, showing a temporal variation similar to that of the edge pressure gradients. As an example, the edge B IV ion temperature (from Doppler measurements) and ∇p_e (from Thomson scattering data) are plotted along with $v_\perp$ in Fig. 24a. When ELMs occur, or in ELMy H-phases, $v_\perp$ and v_θ decrease to small values although remaining in the -B×∇p direction. The highest values of $v_\perp$ and v_θ (reached near the end of the H*-phase) rise with NBI heating power. The edge drift velocities were also studied at different B_t values (I_p was also changed to keep q_a constant); no distinct difference was observed between the two cases. These observations indicate that the origin of E_r may be related to temperature or density gradients at the plasma edge.

The value of E_r^* corresponding to $E_r^* = \nabla p_i / n_i e$ (∇p_i being the deuterium pressure gradient estimated by assuming $\nabla p_i = \nabla p_e$) is ≤ 50% of the measured value of E_r. Similarly, the deuteron poloidal drift velocity predicted by neo-classical theory $v_\theta = k \nabla T_i / eB$ is approximately 50% of that measured (assuming k = -1.7 as appropriate for the collisional regime). The collisionalities at the edge prior to the transition are typically $\nu_e^* > 5$ and $\nu_i^* > 10$. Apart from reflectometry (yielding n_e), however, none of the edge diagnostics can resolve the actual gradients. Thus, we cannot conclude whether the measured B IV drift velocities are consistent with the assumptions of a) the deuterons not rotating poloidally

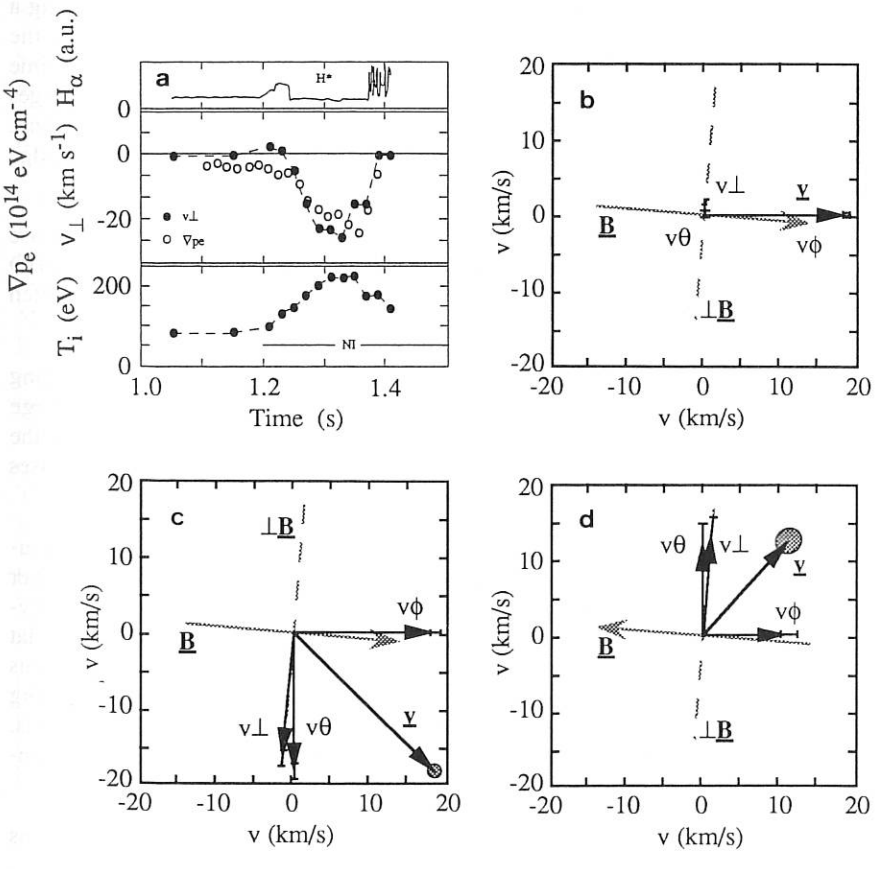

FIG. 24: Poloidal (v_θ), perpendicular ($v_\perp$) and toroidal (v_t) B IV drift velocity components measured at the plasma edge. (a): Time dependences of the H_α intensity within the divertor, perpendicular B IV drift velocity ($v_\perp$), B IV ion temperature and the electron pressure gradient within the thermal barrier. (b, c, d): B IV drift velocity vectors (constructed from $v_\perp$ and v_t) in the L-phase (b) and in H-modes with opposite directions of B_t (c,d).*

and being confined by the radial electric field, or b) the B IV ions rotating poloidally together with the deuterons at the velocity predicted for the deuterons by neo-classical theory.

1.4.1.3 H-mode fluctuation studies by reflectometry

(in collaboration with IST, Lisbon and University of Aveiro, Portugal)

Several signatures of the L-H mode transition have been reported, in particular the formation of a transport barrier and the sudden reduction of the fluctuation level at the plasma edge. In order to interpret theoretically the H mode, it is of crucial importance to determine the spatial extent of the edge barrier and its location with respect to the separatrix.

We have studied the L-H mode transition and in particular the formation of the edge transport barrier, using a novel technique based on microwave broadband reflectometry. In broad-band operation it is possible to determine from single-shot measurements both density profiles and the radial pattern of fluctuations and both turbulent and coherent MHD activity. The steep edge density gradients are resolved.

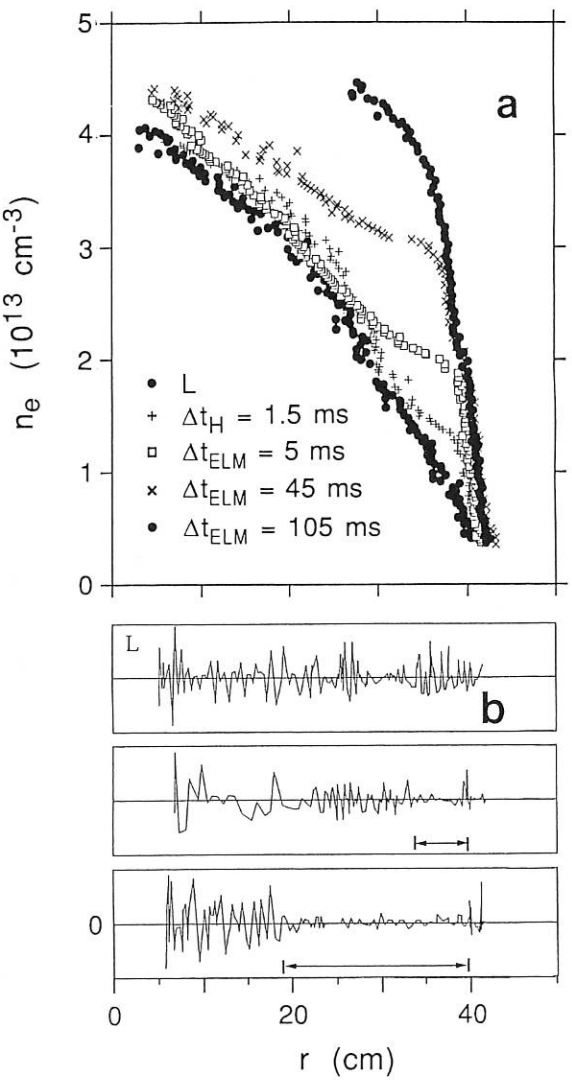

FIG. 25: a) Development of density profile from the L-phase into a quiescent H-phase.
b) Fluctuation level in the L-phase and H-phase at two different time points.

OH and L-phases: In the OH-phase fluctuations are present both in the edge plasma (between 35 and 40 cm) and in the central region (close to and within the $r_q = 1$ rational surface). In the intermediate zone ($16 \leq r \leq 35$ cm), MHD modes can be observed close to the expected locations of $q = 3/2$ and $q = 2$, while the turbulent fluctuation level is low. In the course of the L-phase, the density and fluctuations increase; no dramatic changes are observed.

L-H transition: At the onset of the H-phase, the level of fluctuations decreases as fast as the H_α radiation drops in the divertor chamber, to levels even well below those observed in the OH phase. The edge gradient steepens; density shoulders were detected $\approx$ 0.4 ms after the L-H transition. At the edge, a region with reduced fluctuations is formed that extends radially beyond the steep gradient zone. Figure 25 shows the development of the plasma density during the H-mode along with the fluctuation level in the L and H-phases. However, within this region two narrow zones of coherent fluctuations remain, spaced 1 - 2 cm apart, and probably located inside and outside the separatrix. The location of the fluctuation zones do not significantly vary during the H-phase, regardless of the great changes in plasma density; however, the width of the zone greatly varies, attaining a maximum shortly after the L-H transition. No dependence of these phenomena on the plasma conditions (B_t, I_p, $q_a \equiv 3.3$ is kept constant) was found, suggesting that their values should depend on the q-profile.

After the rapid formation of the edge shoulder at the L-H transition, the interior plasma profile ($r < 35$ cm) flattens along a much slower time scale, while fluctuations decrease to the levels observed in the OH phase. The observation of a fast time scale for the density rise at the edge and a slow one for changes in the bulk plasma, suggests that the improvement of the bulk confinement, is rather a consequence of the changes in the edge conditions, whose effects slowly propagate inward.

ELMy phase: Fluctuations at the edge in many cases increase to the levels observed in the L-phase, and coherent MHD modes that had been suppressed after the L-H transition often reappear.

H^* quiescent phase: A great increase of density occurs during the quiescent phase; contrary to expectation, however, large fluctuations can occur inside the edge density shoulder. At the onset of these fluctuations the edge T_e is reduced and decreases thereafter until the end of the H-phase.

H^*-L back transition: Prior to the H-L back transition, fluctuations increase and recover the pattern of the L-phase. A further increase of both incoherent density fluctuations and MHD activity is observed after the back transition. However, in the flat part of the profile a region with a very low level of fluctuations remains for some time ($\geq$10 ms) after the transition, suggesting that particle confinement is still improved in the interior plasma. This is in agreement with the observed slow time scale for density changes in the interior of the plasma.

Density fluctuations and MHD activity: Turbulent fluctuations

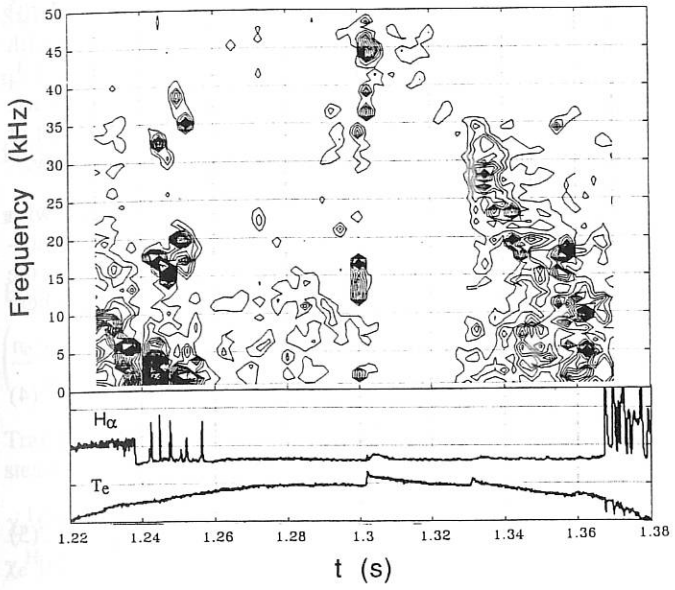

FIG. 26: Contour plot of frequency distribution during the H-phase as indicated by the divertor H_α radiation and the peripheral electron temperature. (#32283, I_P = 280 kA, B_t = 1.75 T)

and MHD activity were further studied with fixed-frequency reflectometry, providing radial wave number integrated measurements ($0 < k < 25$ cm^{-1}), with good spatial resolution (< 3 cm) and high sensitivity (≤ 1.5 mm). Three reflectometers were used to probe simultaneously density layers that are located: (i) in the scrape-off layer; (ii) close to and within the separatrix; (iii) in the central plasma region.

Spectra of fluctuations (in the range 0 - 50 kHz) show an exponential decrease with frequency, both in the OH and L-phases. At the L-H transition, fluctuations decrease preferably at higher frequencies.

Several MHD coherent modes can be observed in the OH and L-phases close to the rational surfaces with q = 1, 2, 5/2. Prior to the L-H transition a coherent mode is detected in the signals of the two outer channels, with f ≅ 7 kHz. After the transition MHD modes are strongly reduced, they again appear during ELMs with higher frequencies (f ≅ 15 kHz). MHD modes during the quiescent phase (f ≅ 17 kHz) are present until the end of the H-phase. In some cases they can grow to very large amplitudes; their frequency rapidly (≤ 20 ms) evolves to higher frequencies (f ≅ 22 kHz), keeping the same narrow band pattern. These modes are also detected with the FIR scattering diagnostic. Their frequency agrees with the central m=1 activity.

Prior to the back H-L transition an edge coherent mode at f ≅ 7 kHz, as previously seen at the L-H transition, appears that vanishes after the back transition.

Figure 26 summarizes the frequency distribution of coherent and turbulent fluctuation during an NI pulse from the L-phase of an ELMy H-phase followed by a quiescent H-phase and a bad transition of the L-phase.

1.4.1.4 Energy confinement of high-density pellet-fuelled H-mode plasmas

Previous investigations on ASDEX revealed that repetitive pellet injection (PI) can significantly improve the plasma performance, especially the energy confinement τ_E. However, the achieved enhancement in τ_E degrades, as shown earlier, from about 2 in the ohmic regime down to ~1.3 in the high auxiliary-power-heated L-mode case.

H-mode discharges, on the other hand, exhibit even at the highest auxiliary heating powers a confinement gain of 2 compared with the corresponding L-mode.

The object of this section is to examine the possibility of combining the favourable confinement properties of both regimes (PI, H-mode) by means of injecting pellets into H-mode discharges.

Both discharge types are characterized by strong deviations of their electron density profile shape from the "standard" profile. The PI discharges show markedly peaked profiles, but H-mode discharges relatively flat ones. If the confinement behaviour of both regimes is linked to the density profile shape, these beneficial properties may be difficult to combine.

Parameter scans in the experiments are concentrated on $1.7 \leq B_t$ (T) ≤ 2.0 and $320 \leq I_p$ (kA) ≤ 420. The line-averaged density exceeds $\bar{n}_e = 1 \times 10^{20}$ m^{-3}. The neutral beam heating power was limited to $P_{NBI} = 2.0$ MW. Up to 30 D_2 pellets, each contributing 2×10^{19} m^{-3} to the volume-averaged density, are injected into a single discharge at time intervals of 33 ms, yield ing penetration depths of roughly half the plasma radius.

The resulting H-phases with PI last up to 400 ms (~8 confinement times). They are always plagued by high-frequency ELMs, which, however, do not prevent the accumulation of impurities. The related central radiation can lead to significant plasma cooling.

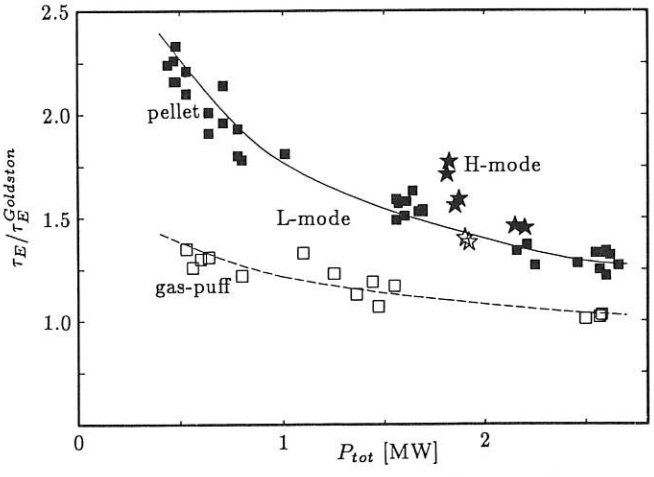

FIG. 27: τ_E normalized to the Goldston scaling vs. total heating power. The open symbols correspond to standard gas-puff (GP) fuelled discharges and the solid ones to PI discharges, the stars to ELMy H-modes ($q_a \leq 2.4$), and the squares to OH and L-modes ($q_a \sim 2.8$).

Despite successful peaking of the central density profile from Q_n^{GP} ~1.1 to Q_n^{PI} ~1.5 only τ_E enhancements of 10% to 15% (see Fig. 27) could be achieved compared with the corresponding high-density gas-puff-fuelled ELMy H-mode discharges. Additionally, in contrast to the standard H-mode, the τ_E improvement with PI seems to be more favourable at low q_a. The achieved confinement times do not exceed the values of standard ELM-free H-phases. This lack of further improvement can be attributed to the just moderate peaking of the profile shape, which might not be enough to suppress the η_i-mode driven transport.

Up to now one can say that PI is able to improve the quality of the H-mode energy confinement, but the simultaneously increased central particle confinement aggravates the problem of central radiation losses.

1.4.1.5 Studies of the origin of the improved bulk transport in the H regime

Possible processes causing the reduced electron heat diffusivity χ_e and diffusion coefficient D in the core of H-mode plasmas are explored. Simulations of ASDEX discharges with neutral-beam heating (tangential co-injection of hydrogen into deuterium targets) and with injection powers much higher than the ohmic input before auxiliary heating yielded the following empirical scaling laws:

$$\chi_e(r) = C_o\, q(r)\, B_t^{-1} \ \mathrm{cm^2\, s^{-1}} \tag{1}$$

$$D(r) = 0.4\, \chi_e(r) \tag{2}$$

$$v_{in}(r) = 0.5\, D(r)\, T_e^{-1}(r)\, \frac{\partial T_e}{\partial r} \ \mathrm{cm\, s^{-1}} \tag{3}$$

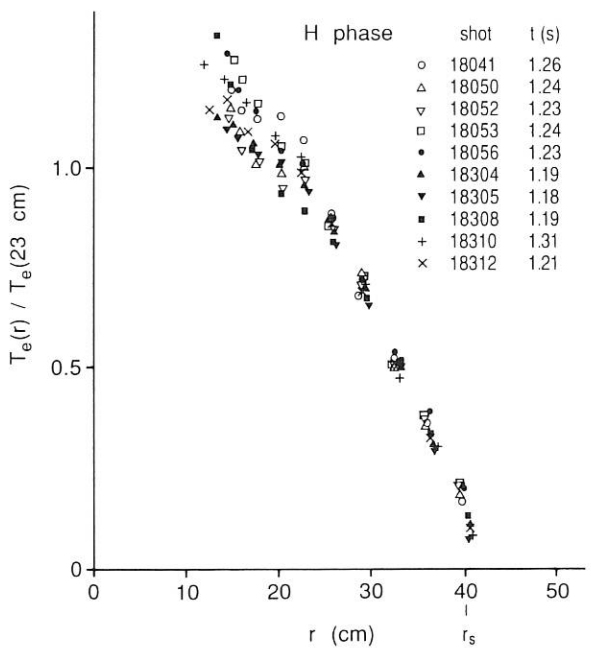

FIG. 28: Invariance of the T_e-profile shape in H discharges with neutral co-beam power P_{NI} = 3.45 MW ($H^o \rightarrow D^+$).

Here, C_o is a regime-dependent factor equal to $C_L = 6.2 \times 10^5$ in the L regime and to $C_H = 2.5 \times 10^5$ in the H regime with ELMs (edge-localized modes), B_t is in kG, $q\, B_t^{-1} = r\,(B_p\, R)^{-1}$, with the major radius R, and v_{in} is the inward drift velocity. The use of different constant factors contradicts the concept of a local transport law, i.e. a scaling with local parameters only.

The electron temperature profiles during the H phase with ELMs of ten discharges with constant heating power and variable current, B_t and q are shown in Fig. 28. As can be seen, the profiles linearly vary with the radius over a wide range where they can be approximated by

$$\frac{T_e(r)}{T_e^*(0)} = 1 - \frac{r}{a_T} \tag{4}$$

The electron temperature scale length reads

$$r_{T_e}(r) = -\frac{T_e}{\frac{\partial T_e}{\partial r}} = a_T - r \tag{5}$$

It is obvious that the T_e-profile shape is invariant for $r/a \geq 0.6$, i.e. $r_{T_e}(r)$ is conserved in the confinement zone. Here, $a = r_s$ = 40 cm is the plasma or separatrix radius. In the central region, however, the profile shape is not constant.

The ten discharges belong to a database consisting of electron temperature profiles from 38 H-mode discharges with ELMs from one operating period (closed divertor, double-null configuration). The injection power was kept constant at P_{NI} = 3.45 MW ($H^o \rightarrow D^+$). The plasma current I_p, the toroidal magnetic field B_t, the cylindrical edge q_a and the line-averaged density $\bar{n}_e$ were varied in the following ranges: I_p = 320 to 380 kA, B_t = 1.69 to 2.55 T, q_a = 2.5 to 3.3 and $\bar{n}_e = (3.2 - 3.9) \times 10^{13}$ cm^{-3}. Statistical analysis of the temperature profiles measured during the L phase yields a mean value $\bar{a}_T$ = 42.90 cm and a standard deviation s = 0.79 cm of the a_T values from $\bar{a}_T$. During the H phase $\bar{a}_T$ = 43.54 cm and s = 0.68 cm are obtained. We thus conclude that a constant a_T value and a canonical T_e-profile shape for $r/a \geq 0.6$ are present in the L and H phases.

An example of the time evolution of the electron temperature profile in an H discharge (#18310) is presented in Fig. 29. The L–H transition takes place at 1.169 s. Evidently, a_T is constant in the L and H phases, so that

$$r^L_{T_e}(r) = r^H_{T_e}(r) = a_T - r \tag{6}$$

Deviations from the canonical T_e-profile shape given in Eq. (4) occur in the inner plasma.

Figure 30 shows the development of the electron temperature profile in the pre-transition L phase and in the ELM-free H phase of discharge #18041. The L-H transition occurs at t^* = 1.231 s. As can be seen, constancy of the T_e-profile shape for $r/a \geq 0.6$ is also present in the ELM-free H phase. The poloidal beta becomes constant in the L phase of this discharge, so that a steady-state temperature gradient is reached and ∇T_e is known at t^*. From the steeper gradient at 1.244 s it follows that the χ_e in the bulk already improved at an early stage, i.e. less than 13 ms after t^*.

Starting from diffusive electron heat transport

$$q_e = -n_e \chi_e \frac{\partial T_e}{\partial r} \tag{7}$$

it follows that

$$r_{T_e}(r) = \frac{n_e(r)\,\chi_e(r)\,T_e(r)}{q_e(r)} \tag{8}$$

Profile invariance for r/a ≥ 0.6 (see Eq. (6)) yields

$$\left(\frac{n_e\,\chi_e\,T_e}{q_e}\right)_L = \left(\frac{n_e\,\chi_e\,T_e}{q_e}\right)_H \tag{9}$$

Transport simulations show that $q_e^L(r) \approx q_e^H(r)$ holds during steady-state L and H phases. We thus obtain

$$\frac{\chi_e^L(r)}{\chi_e^H(r)} \approx \left[1 + \frac{\Delta T_e}{T_e^L(r_s - \Delta)}\right] \frac{n_e^H(r)}{n_e^L(r)} \tag{10}$$

where ΔT_e is the temperature "pedestal" and Δ is the width of the steep gradient zone (see Fig. 31).

According to Eq. (10), the amount of χ_e reduction in the bulk plasma depends on the temperature pedestal and density rise. For typical ΔT_e values observed the term in brackets is about 1.5. The resulting change in χ_e by a factor of 2.2 with $n_e^H/n_e^L = 1.5$ agrees with the ratio $C_L/C_H \approx 2.5$ determined by transport analysis (see Eq. (1)). The radial dependence of χ_e^L/χ_e^H predicted by Eq. (10) is rather weak in the range $0.6a \le r \le a-\Delta$ since the measured n_e^H/n_e^L is a slowly varying function of radius. This explains the χ_e reduction by an r-independent factor C_L/C_H as expressed by Eq. (1). Moreover, a canonical T_e-profile shape is compatible with the fast transition from L to H confinement in the core, which occurs on a time-scale much shorter than the energy confinement time $(\tau_E^L \approx 20\ \text{ms})$.

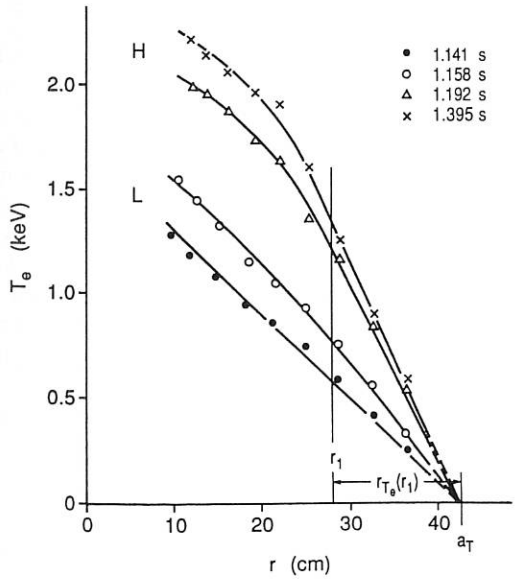

FIG. 29: Measured electron temperature profiles during the L and H-phases of an H discharge. $r_{T_e}(r)$ is conserved in the outer plasma.

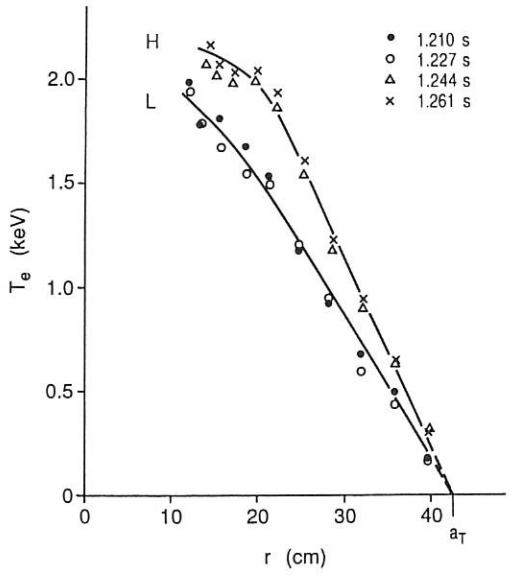

FIG. 30: Profile invariance in the outer region during L and ELM-free H-phases.

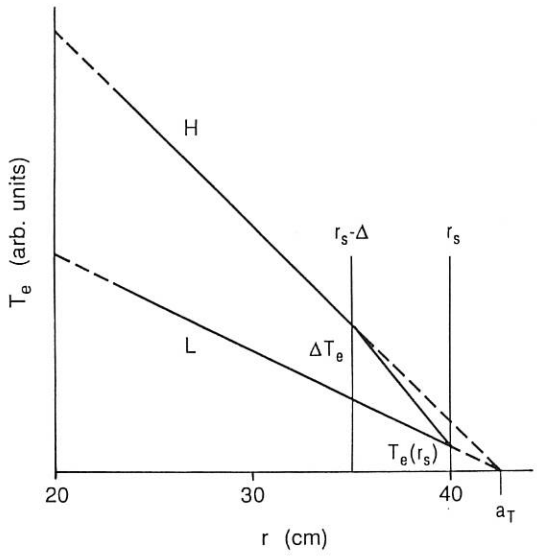

FIG. 31: Schematic diagram of the temperature profiles in the outer plasma during L and H-phases.

It is concluded that the T_e-profile invariance for r/a ≥ 0.6 is capable of explaining the magnitude, weak radial dependence and fast time-scale of the χ_e reduction in the H-mode plasma bulk. It introduces a non-local component into the empirical scaling laws for χ_e and D. The transport behaviour in the central region (r/a < 0.6) cannot, however, be attributed to profile invariance.

Another study looks for local parameters which might cause smaller diffusivities χ_e and D in the interior of H-mode plasmas. From the evolution of many local parameters during the L and H phases it is concluded that only the density scale length

$r_n = -n_e / (\partial n_e/\partial r)$ is a possible candidate. The r_n-values are larger in the H phase, whereas the electron temperature scale lengths remain unchanged. The primary process for density profile broadening is the increase of the density gradient near the edge in the initial H phase. It causes the build-up of a density pedestal and raises r_n at all radii in the inner plasma. A local transport law for χ_e and D based on the r_n increase is tested by self-consistent transport simulations. It works for ASDEX H-mode discharges with ELMs but is incompatible with the broad density profiles observed in other devices. Hence, a universal local parameter governing the bulk L and H confinement was not identified.

1.4.2 L-mode

The global energy confinement time of additional heated tokamak plasmas is empirically well described by a power law scaling. The physical processes, however, which make the transport in a tokamak plasma behave according to a simple law are not understood. We studied the specific aspects of the dependence of τ_E on density, electron temperature and current density profile and re-analyzed ICRF-heated discharges.

1.4.2.1 Studies on Density Scaling

An interesting question to be clarified is why ohmically heated (OH) and neutral beam (NI) heated L-mode plasmas exhibit a different dependence of τ_E on the line-averaged density: at low densities, τ_E increases linearly with density in OH plasmas and is independent of it in L-mode plasmas. Drift wave theories predict τ_E to be proportional to the ratio between density and heating power. This prediction can only hold for L-mode discharges if in a density scan the heating power changes linearly with the density.

To investigate this point, we performed transport calculations for OH and L-mode phases at different densities. The energy confinement times are plotted in Fig. 32 as squares with an approximately linear density dependence in the OH plasmas and no dependence during L-mode. A major difference in both phases is how electrons and ions contribute to the total plasma energy content: while the energy is about equally partitioned in L-mode plasmas, during LOC phases the ion energy content only slowly approaches the electron energy content as the coupling increases with density. The amount by which this effect contributes to the τ_E scaling with density can be seen from the triangles in Fig. 32a, which were calculated by setting the ion energy equal to the electron energy. The remaining τ_E improvement with density can be explained by an improvement of χ_e with density.

The absence of a density dependence in the L-mode cannot be explained by the shape of the NI power deposition profile, which is not essentially broader at the high density in Fig. 32 than at the low one. Because of secondary fast-ion recombination in the plasma centre, in the low-density case less power is absorbed. Therefore, the L-mode density scan also exhibits aspects of a power scan. Correcting for the power degradation ($\tau_E \sim P^{-0.58}$), one gets the triangles in Fig. 32b and a dependence of τ_E on density which is still smaller than in the OH-

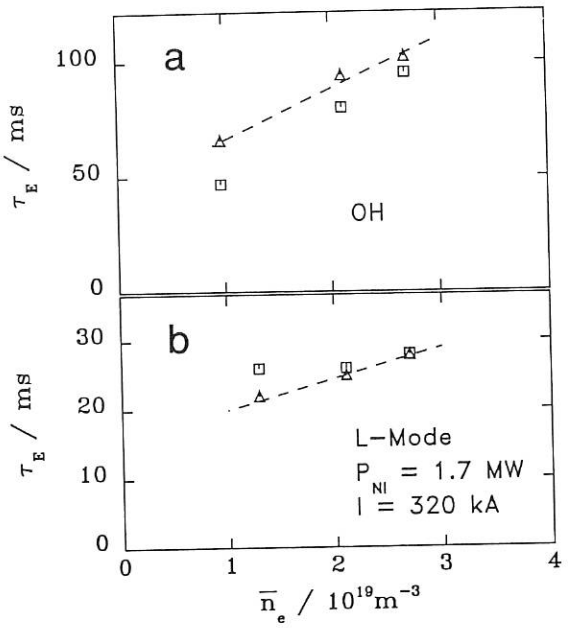

FIG. 32: Kinetic energy confinement times of OH (a) and L-mode (b) low-density discharges. In the L-mode, the transverse contribution from the fast ions is included. The triangles represent the confinement times obtained when the ion energy in the OH phase is set equal to the electron energy (a) or when we correct for the fact that at low densities less additional power is absorbed in the L-mode (b).

phase. Also the transport coefficients for electron and ion energy and angular momentum (see Fig. 33) are independent of density. The different behaviour compared to the transport coefficients in OH plasmas is not yet understood. The low-density L-mode plasmas resemble rather the high-density OH plasmas which do not show a dependence of τ_E on density either.

The local transport coefficients, obtained from calculations using the *TRANSP* transport code, are plotted in Fig. 33. Two regions are discussed: In the plasma centre ($r \leq 10$ cm) the ion energy diffusivity (χ_i) is of the order of the neoclassical prediction (see insert). There, the angular momentum diffusivity (χ_ω) is much smaller than χ_i and also neoclassically one expects smaller values for χ_ω than for χ_i. This changes in the confinement region ($20\text{ cm} \leq r \leq 30$ cm), where all the transport coefficients are of comparable size (1 to 2 m^2/s), indicated by the horizontal dotted lines. In this region an anomalous transport mechanism has to be taken into consideration which predicts comparable magnitudes for all transport coefficients. In the case of the ions, the anomalous transport is 3 to 4 times higher than predicted by neoclassical theories.

1.4.2.2 Studies on temperature scaling

For fusion research, the origin of the degradation of the confinement time with power is a major issue. According to drift wave theories, it would be due to the increase of the electron temperature. In order to clarify this question, we tried to estab-

lish discharges where the energy increase by additional heating is either realized at constant density and increasing temperature or by increasing density at constant temperature. Experimentally, this could be done by starting the NI heating phase with feedback to keep either the density or the electron temperature constant. In the second case we use the control ECE temperature channel instead of the line-averaged density as input for the density feedback system. Power scans were performed by this technique. Discharges at 1.5 MW heating power were established with half-radius density and temperature of 2.5×10^{19} m^{-3} and 900 eV, respectively, in the first case and 4.5×10^{19} m^{-3} and 700 eV in the second. It is known that L-mode energy confinement only weakly depends on the plasma density. Hence, a strong dependence of the transport coefficients on the temperature should show up in very different τ_E values for the discharges above. This is not the case, as is shown in Fig. 34. The full squares represent the diamagnetic τ_E for the discharges with constant temperature and therefore higher density. The fact that the squares lie above the circles, which represent τ_E of the discharges with lower density, can be perfectly explained by the weak dependence of τ_E on the density ($\tau_E \sim n^{0.26}$) . The confinement times of both ensembles of discharges obey a Goldston scaling law with an enhancement factor of 1.1. Contrary to the predictions of drift wave theories, the electron temperature does not seem to be a key parameter in energy confinement.

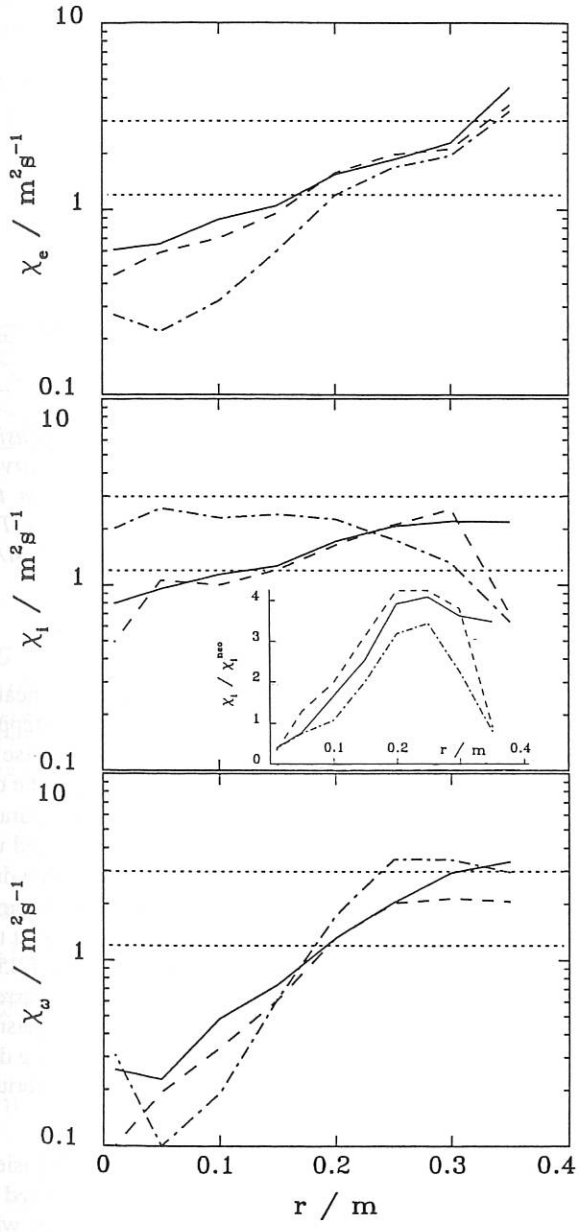

FIG. 33: Local transport coefficients for the L-mode discharges of Fig. 32b at the line-averaged densities of 1.3 (dashed-dotted), 2.1 (full) and 2.7 × 10^{19} m^{-3}, (dashed lines). The horizontal lines indicate the margin of the size of anomalous transport coefficient which could equally describe electron and ion heat as well as angular momentum transport in the confinement region.

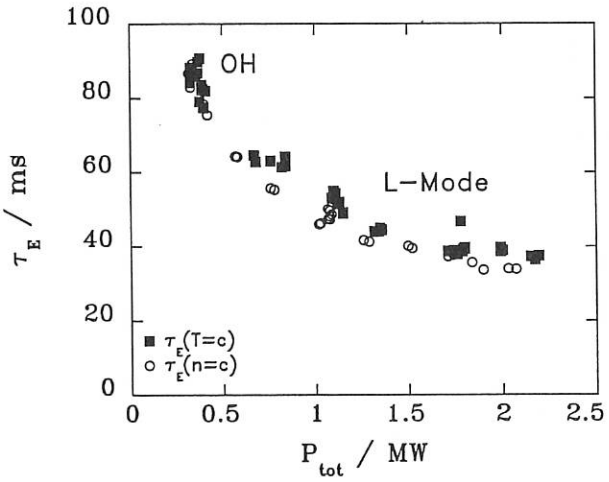

FIG. 34: Diamagnetic energy confinement times for NI power scans with discharges where either the electron temperature (full squares) or the density (circles) was fixed to the level before additional heating. Data for the preceding ohmic phases are also shown. There, the distinction is pointless.

1.4.2.3 ICRH L-mode

The ICRH results are reviewed to obtain the confinement time scaling law for ICRH experiments in ASDEX. Up to now, the most important L-mode discharge series with hydrogen second-harmonic heating, combined or not with neutral beam injection, were analyzed. As observed earlier (Annual Report 1989), no difference could be measured between ICRH alone or combined with neutral injection over the parameter range of ASDEX and no distinction is made in the following result. At present, the confinement time scaling, deduced from 180 discharges, is summarized by the expression:

$$\tau_E = 0.123\ A_i^{0.45\pm0.06}\ I_p^{0.56\pm0.08}\ P^{-0.4\pm0.02}\ n_e^{0.09\pm0.05}.$$

The ranges for the different parameters are: 245 kA $\leq I_p \leq$ 460 kA, 2.4×10^{19} $m^{-3} \leq \bar{n}_e \leq 6.2 \times 10^{19}$ m^{-3}, $1.2 \leq A_i \leq 1.6$, 0.43 MW $\leq P_{tot} \leq$ 3.24 MW.

This result must be considered with caution and further analysis

is still needed to confirm it. However, the behaviour observed in experimental scans of a single parameter confirms the above scaling law. The isotope dependence appears clearly. The measurement error on this parameter (30%) is much larger than the given statistical error. The weak current dependence is attributed to the confinement degradation which is observed at q_a below 3. The q-dependence could not be evaluated owing to the fact that the experiments were performed at constant magnetic field strength. The weak power dependence reflects the offset linear behaviour which is currently observed in power scan series. An offset linear scaling analysis is under way, as well as analysis for minority heating.

1.4.2.4 T_e-profile invariance under current ramp conditions on ASDEX

The resilience of the electron temperature profile in a tokamak plasma is a well-known phenomenon. On ASDEX it was found that the electron profile, normalized at half-radius, can be represented as a fairly straight line with constant slope outside the q=1 surface; the different T_e-profile shapes at various q_a-values are only due to changes within the q=1 surface. This early analysis, carried out under steady-state conditions, was extended to transient ASDEX plasmas with the plasma current being stepped up and down during the discharge. The conductivity of the plasma column was calculated radially and time-resolved, including neoclassical trapped particle effects, using measurements of $T_e(r,t)$ and $n_e(r,t)$ with the 60 Hz Nd:YAG laser scattering system. Current profiles were then calculated with a diffusion code starting with a radially constant electric field from a steady-state discharge and the electric field at the plasma edge derived from the measured loop voltage around the torus as boundary condition.

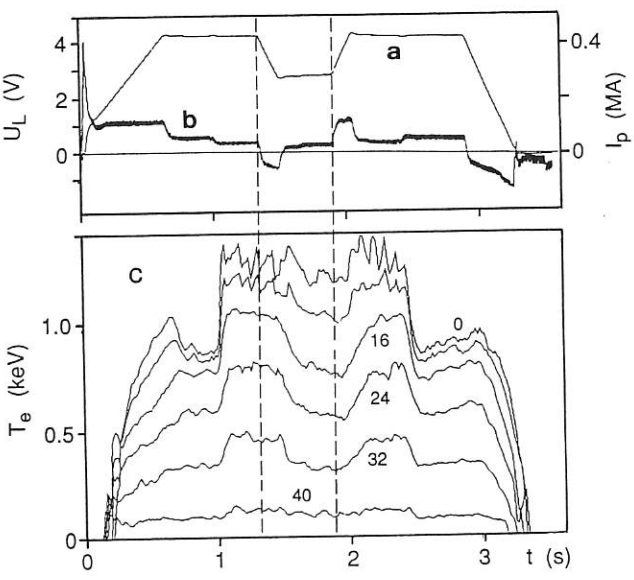

FIG. 35: Plasma current (a), loop voltage (b), electron temperatures (c) at different plasma radii versus time, measured with the Nd:YAG laser system;
r = 0, 8, 16, 24, 32, 40 cm; neutral beam heating from 1 s - 2.4 s, P_{NI} = 2 MW.

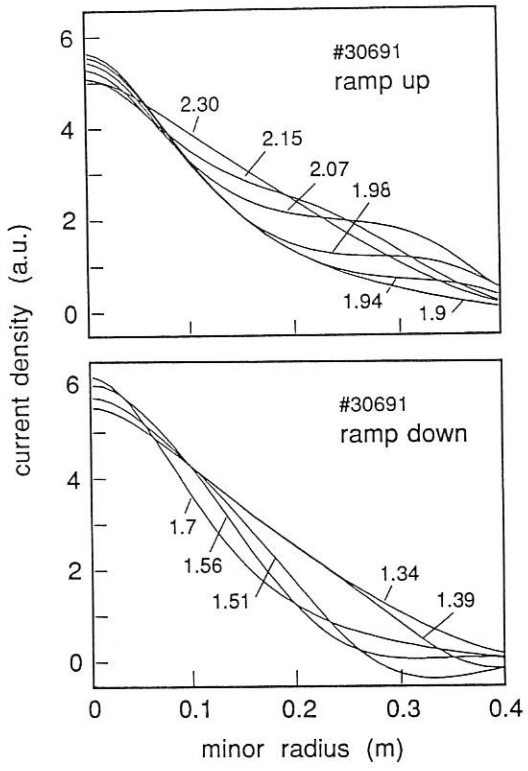

FIG. 36: Current densities j(r,t) calculated from a diffusion code at different times t (s), given as parameter in the curves. The plasma conductivity σ(r,t) was calculated from the measured electron temperatures and densities and Z_{eff}. The plasma current was ramped down and up again (0.42 MA / 0.28 MA) during the discharge.

Experimental results: Figure 35 shows a neutral-beam-heated discharge with a plasma current I_p of 0.42 MA being stepped down within 0.15 s to 0.28 MA and after a plateau phase of 400 ms up again within the same discharge. In Fig. 36 the development of the current distribution j(r,t) is displayed separately for the two cases when the current is ramped down and up. The beam heating power was 2 MW and basically constant during the ramp phases. In the first case the loop voltage becomes negative, which is reflected in a negative current density at the plasma edge at the beginning of the current change at t = 1.35 s. When I_p has reached its minimum value at t = 1.5 s, the current density also takes its maximum negative value at the plasma boundary. Within the next ~200 ms the current disturbance diffuses towards the hot centre until it reaches another equilibrium at about t = 1.7 s.

The development of temperature profiles during this transient phase is quite different, as shown in Fig. 37. Normalized to about half-radius, the profiles exhibit the usual invariance, with changes only inside the q=1 surface as a consequence of the changing plasma current. These profile changes, however, do not follow the external q_a-value but rather the amplitude of the current density at the core. The temperature profile is certainly not coupled rigidly to the current density as in a stationary state, but the profiles do have a tendency to show a slight deformation at the edge in the same manner as j(r) after a disturbance of the total current.

During the current decrease the electron temperature profile remains unchanged. The decrease of $T_e(0)$ does not begin before j(0) begins to drop at t ~ 1.5 s, which is the time when the current disturbance has reached the plasma centre during its diffusion process. This phenomenon is also reflected by the integrated thermal energy content of the electrons (E_e), as shown in Fig 38. It also begins to decrease at t = 1.5 s, when I_p is already down to 0.28 MA. Thus the energy confinement time stays constant while the current is being ramped down, and the relation $\tau_E \sim I_p$ certainly does not hold in this transient phase. This is also demonstrated in the overshooting of the poloidal β (β_p) shown in Fig. 38. τ_E remains at the high value corresponding to the initial current typically 2-3 energy confinement times before it rapidly decreases.

The observed delay of the change of the electron energy against the plasma current change is much less when I_p is ramped up again (see Figs. 35c and 38). This can be understood if one considers the difference in the j(r,t) profiles in the two cases of a negative and a positive current step in Fig. 36. In the first case with dI/dt < 0 , the power deposition, mostly neutral beam heating, remains unchanged in the centre until the diffusion process has come to an end and the plasma centre is affected. The ohmic power is also deposited mainly in the centre because the current density at the boundary is negligible. Thus the energy transport from the centre to the edge is not very much affected and the temperature profiles and gradients remain unaltered until the confinement properties of the inner confinement zone are changed owing to the reduced current density j(0).

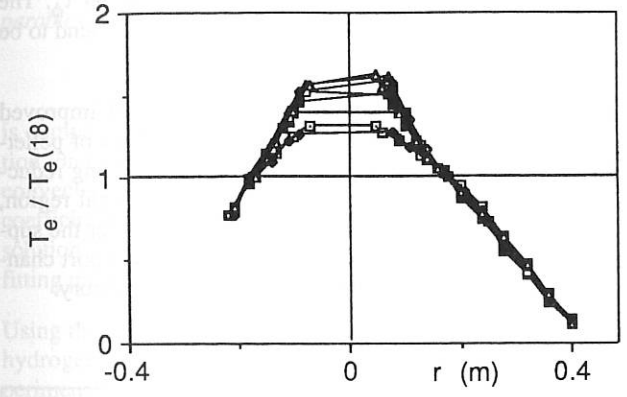

FIG. 37: Electron temperature profiles normalized at r = 18 cm (the influence region of the q = 1 surface) within the time interval 1.3 s ≤ t ≤ 2.2 s, covering the current ramping phase 0.42 MA / 0.28 MA. The normalized profiles are invariant for r ≥ 18 cm also in the transient phase.

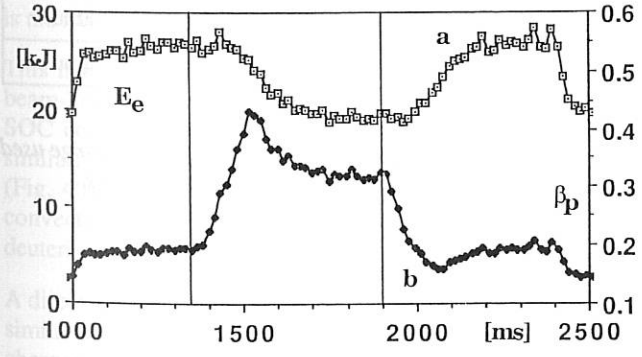

FIG. 38: Total integrated electron thermal energy (a) and the poloidal beta of the electrons as measured with the Nd:YAG system versus time. The change of the total energy is delayed against the onset of the current change by about 200 ms during ramping down. When the current is ramped up again, the delay is much shorter. This is also manifested in the overshoot of β_p.

When dI/dt is positive, on the other hand, there is an instantaneous rise of the current density at the edge with localized additional ohmic heating of the electrons at the boundary and subsequent instantaneous hampering of the heat outflow from the plasma centre. In this case the total energy rises with much less delay against the plasma current, which is also seen in Fig. 38. This delay time disappears in the case of pure ohmic heating. In our opinion this effect indicates the important influence of edge gradients on the global confinement.

Conclusions:
- The invariance of the electron temperature profile prevails also during a transient plasma phase when the total plasma current is strongly varied;
- the dominant parameter is not q_a, but rather the central current density, which influences the profile at the q=1 surface;
- the current density is certainly not an invariant quantity when the plasma is not stationary;
- τ_E is no longer a linear function of I_p, when dI/dt ≠ 0;
- profile gradients at the plasma boundary play a decisive role for the global confinement behaviour;
- the mechanism which governs profile invariance is not simply dominated by q_a or other local parameters.

1.4.3 Edge fluctuation studies

Density and potential fluctuations are considered as the cause of at least the major part of the particle and energy transport at the edge of tokamaks. In ASDEX they were investigated by measuring the fluctuations of the H_α light at the edge and of the ion saturation current and floating potential of Langmuir probes. Arrays with 16 observation points distributed in the poloidal direction were used to obtain information about the spatial structure.

Numerical methods were developed to calculate temporal and spatial correlation functions, the corresponding spectra and also mixed functions (cross-power k-spectra with the time delay as a variable). k-ω-spectra of the fluctuating particle flux are calculated as well as the spectral distribution of the various contributions to the net particle flux. Figure 39 shows the k-ω-spectrum of the contributions to the net particle flux.

k-spectra of the density fluctuations decay with a power law from a plateau at a k-value probably determined by the width of the scrape-off layer.

It is attempted to characterize the statistical functions by a set of scalar parameters, such as the propagation velocity. One hopes

to get more insight into the physical nature of the fluctuations from the parameter dependence of these characteristic scalars. For this reason systematic measurements were performed under various discharge conditions. Evaluation of these data has still to be performed.

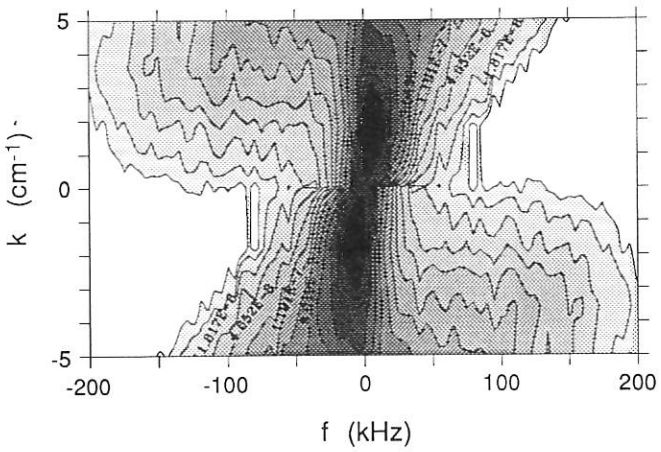

FIG. 39: k-ω-spectrum of the contributions to the net particle flux.

1.4.4 Angular momentum transport studies

A database has been constructed with the results of angular momentum transport studies of about 50 ASDEX discharges covering a variety of experimental conditions. For L mode conditions, scaling laws for the dependence on experimental parameters were derived for the central rotation speed v_0, the angular momentum confinement time τ_ϕ, and the radially averaged momentum diffusivity χ_ϕ (8 cm < r < 34 cm). The corresponding scaling of the global energy confinement $\tau_{E,dia}$ in the database is given for comparison. Table 3 shows the experimental data range covered by the statistical analysis using ordinary least-squares after a logarithmic transformation.

The following power-law dependences were obtained (L mode):

$$v_0 = 29.4\,(M / \bar{n}_e)^{0.61}\, I_p^{0.3}$$

[10^4 m/s, Nm, 10^{19} m^{-3}, MA]

$$\tau_\phi = 36\, P_{tot}^{-0.7}\, \bar{n}_e^{0.45}\, I_p^{0.85}\, A_{eff}^{1}\, A_{beam}^{-2}\, (B_\tau / 2.2)^{-0.8}$$

$$\tau_E = 37\, P_{tot}^{-0.58}\, \bar{n}_e^{0.35}\, I_p^{0.5}\, A_{eff}^{0.65}$$

[ms, MW, 10^{19} m^{-3}, MA, amu, Tesla]

$$\chi_\phi = 1.69\, P_{tot}^{0.65}\, \bar{n}_e^{0.73}\, I_p^{-0.65}\, A_{eff}^{-0.8}$$

[m^2/s, MW, 10^{19} m^{-3}, MA, amu]

M is the torque of the neutral beams and A_{eff} is the mean plasma mass number per electron. The close correlation between energy and momentum confinement indicates the existence of a common transport channel for momentum and energy. The density dependence of τ_E as well as the relatively high power degradation is owing to the inclusion of low NI-power shots in the database. A well-developed isotope effect shows up in the momentum transport results, which is supposed to be connected to anomalous ion transport in general. The most striking difference in the parameter dependences of τ_E and τ_ϕ is the B_t-dependence of the latter. To investigate its origin, we also derived a scaling law for the rotation velocity v_{35} at r = 35 cm (only the dominant parameters were taken into account since the relative scatter of the near-edge velocities is quite large):

$$v_{35} = 50\,(M / \bar{n}_e)^{0.55}\, I_p^{1}\, B_t^{-1.6}$$

[10^4 m/s, Nm, 10^{19} m^{-3}, MA, Tesla]

The scaling law indicates considerably increased momentum losses near the edge for higher toroidal fields. These losses are the origin of the B_t-dependence found for the global τ_ϕ. The momentum confinement time for radii r < 35 cm is found to be independent of B_t.

The studies of momentum transport in regimes of improved confinement conditions were completed by analysis of pellet-fuelled discharges. As in the counter-NI case, a strong reduction of momentum transport was found in the central region, where electron density profile peaking occurred after the suppression of sawteeth. This reduction in the ion transport channel is consistent with the prediction of the η_i-mode theory.

exp. parameter	mean value	min. value	max. value	standard deviation	unit
P_{tot}	1.44	0.58	2.3	0.51	MW
M	1.52	0.22	3.4	0.82	Nm
$\bar{n}_e$	3.43	1.6	7.6	1.16	10^{19} m^{-3}
I_p	0.38	0.25	0.45	0.05	MA
B_t	2.22	1.87	2.8	0.26	T
A_{eff}	1.77	1.26	2	0.22	amu
A_{beam}	1.13	1	2	0.33	amu

Table 3: Description of the experimental parameter range used to derive the momentum transport L-mode scaling laws.

1.4.5 Perturbation transport

1.4.5.1 Isotope dependence of electron particle transport

The isotope dependence of electron particle transport in the ASDEX bulk plasma was investigated using gas oscillation techniques. Small density perturbations about equilibrium, induced by sinusoidal modulation of the gas valve, were analyzed for different radial channels of the ASDEX HCN-laser interferometer. The measured pattern of amplitudes and phase shifts

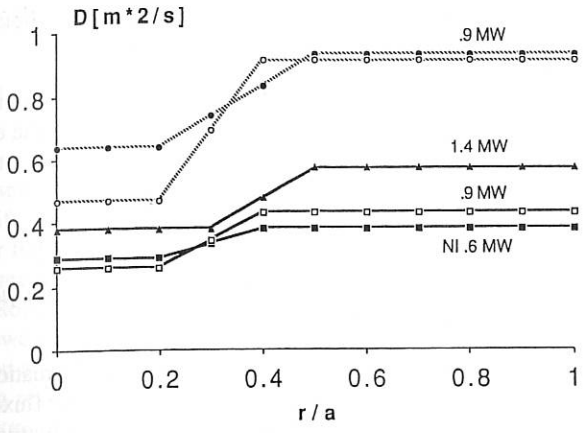

FIG. 40: Comparison of diffusion D versus normalized plasma radius, shown for NI (hydrogen beam, different power levels) into a hydrogen (broken lines, same power to test reproducibility) and a deuterium (solid lines) target plasma at comparable parameters.

is compared with solutions of the particle conservation equation, $\partial n/\partial t = -\nabla\Gamma + P$. A transport law with a diffusive and a convective flux component $\Gamma = -D\nabla n - Vn$ is assumed. The coefficients D(r) and V(r) are determined with a crude radial resolution for the central and outer plasma regions by a numerical fitting procedure.

Using this method, the transport of electrons was compared for hydrogen and deuterium discharges, and some additional experiments were carried out in helium.

Density scans, including the range of linear ohmic confinement (LOC) to saturated ohmic confinement (SOC), were performed for standard values of plasma current and main field (320 kA / 2.17 T). A clear isotope effect in both diffusion D and inward convection V was found in all plasma regions, except for V in the outer zone, which was comparable for the two isotopes. Particle confinement for deuterium is superior to that for hydrogen at all densities. Quantitatively, the diffusion roughly follows a law $\propto A_i^{-1/2}$ in LOC and $\propto A_i^{-1}$ in SOC, where A_i is the isotope mass.

This isotope effect is continued into the L-mode of neutral-beam-heated plasmas. For target densities corresponding to SOC conditions and NI heating powers of up to 1.4 MW, similarly to the ohmic phase an A_i^{-1} dependence was found (Fig. 40). In addition, in contrast to the ohmic case, inward convection in the confinement region was clearly larger for deuterium, which further improves the particle confinement.

A direct comparison between deuterium and helium has shown similar values for the transport parameters. As both A_i and the charge Z are increased by a factor of 2 for the transition to helium, these results seem to indicate that the isotope effect cannot be described by a pure mass dependence, but rather follows a pattern $\propto Z A_i^{-1}$.

1.4.6 Heat pulse analysis

The local electron temperature is measured outside the mixing radius by the ECE diagnostic and the signal is sampled at 20 kHz to provide sufficient time resolution of the sawtooth crash and the resultant heat pulse. Boxcar averaging of the temperature perturbation permits the electron thermal conductivity, χ_e, to be determined. The time-dependent temperature perturbation at each radial position is fitted by the numerical solution of the heat pulse propagation equation as a forced boundary value problem. The first channel outside the mixing radius is used as the time-dependent boundary condition.

Assuming a transport law $Q = -n\,\chi\,\partial T/\partial r$ for electrons and ions, heat pulse values of χ_e in ohmic discharges in ASDEX are generally a factor of 3 higher than equilibrium values. In this approximation the density pulse associated with a sawtooth crash is neglected, because the relative amplitude of the density perturbation in these ohmic discharges is considerably smaller than the relative amplitude of the temperature perturbation ($\delta n/n \approx 0.1\,\delta T/T$). It has been proposed that the inclusion of finite density perturbations in the models of heat pulse propagation could resolve the difference between the heat pulse and equilibrium values of χ_e.

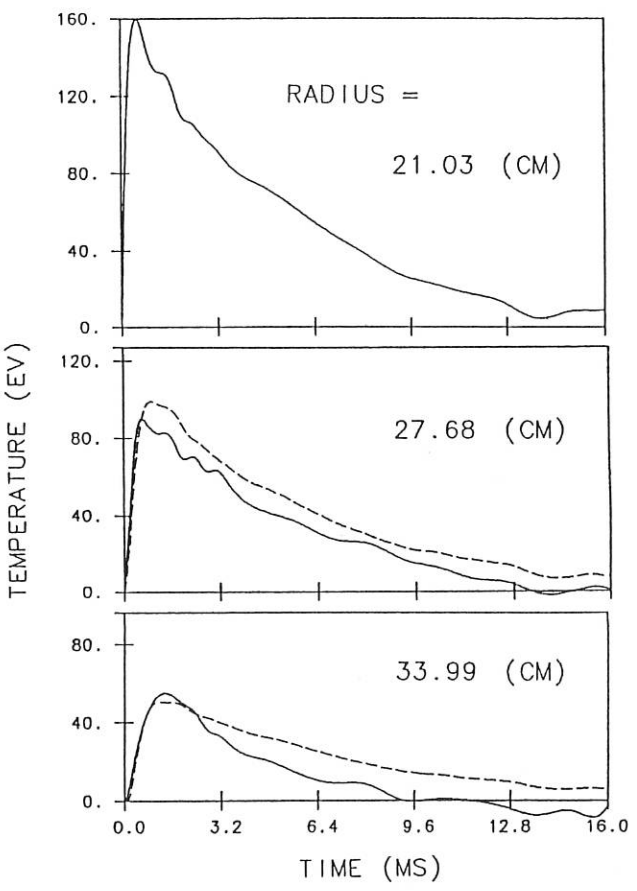

FIG. 41: Heat pulse evolution at three radial positions (solid line) and best-fit curve (dotted line) with the given parameters. ($D = 3\ m^2\ s^{-1}$, $\chi_e = 20\ m^2\ s^{-1}$, $\alpha_n = -0.8\ m^2\ s^{-1}$, $\alpha_T = 0\ m^2\ s^{-1}$).

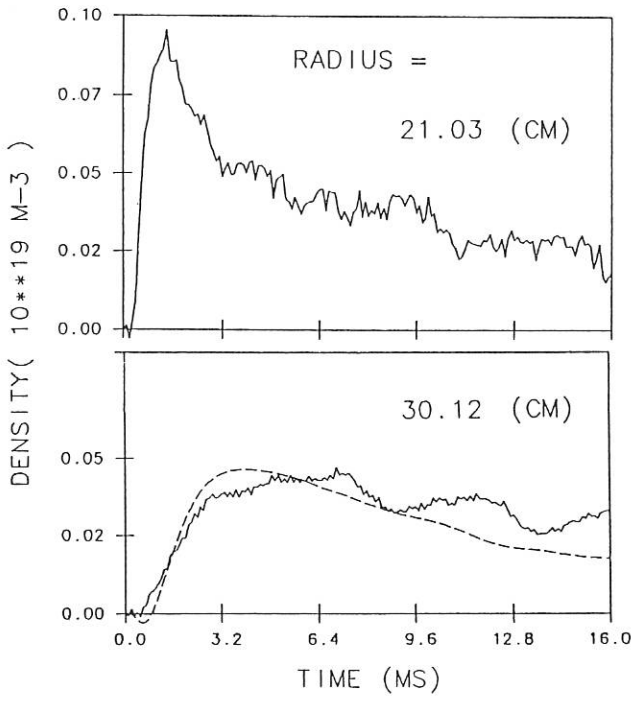

FIG. 42: Density pulse evolution at two radial positions (solid line) and best-fit curve with the given parameters. ($D = 3$ $m^2 s^{-1}$, $\chi_e = 20$ $m^2 s^{-1}$, $\alpha_n = -0.8$ $m^2 s^{-1}$, $\alpha_T = 0$ $m^2 s^{-1}$).

By considering a particle and heat flux of the form $\Gamma = -D\,\partial n/\partial r - Vn$, $Q = 3/2\,\Gamma T - n\chi\,\partial T/\partial r$, where D is the particle diffusion coefficient and V is the inward particle drift velocity, it is then possible to include the enhanced heat flux due to a finite density perturbation. The equilibrium values of D and V are determined from the zero-order particle flux as described above. Allowance for an increased value of D and a relative perturbation value of $\delta n/n = 0.2\,\delta T/T$ show that the enhanced heat flux due to finite density perturbation could only lead to a reduction of 20% in the inferred value of χ_e. The case in which the temperature and density perturbations are coupled by the off diagonal terms of the transport matrix was also considered. In this case particle and heat flux terms take the form

$$\Gamma = -D\,\partial n/\partial r - \alpha_n\, n/T\,\partial T/\partial r\ ,$$

$$Q = -\alpha_T T\,\partial n/\partial r - n\chi\,\partial T/\partial r + 3/2\,\Gamma T\ .$$

The extent to which particle fluxes and heat fluxes are driven by temperature and density gradients, respectively, depends on the coefficients α_n and α_T. In Fig. 41 the resultant heat pulse from a sawtooth crash in a neutral-beam-heated discharge (I_p = 320 kA, $B_0 = 2.17$ T, $n_e = 2.0 \times 10^{19}$ m^{-3}, $P_{NI} = 1.8$ MW) is shown. With $\alpha_T = 0$, a value of $\chi_e = 20$ m^2/s yields the best fit to the measurements. Non-zero values of α_T and lower values of χ_e do not yield better fits. The equilibrium values of χ_e at the radial position of the measurements range from 2 m^2/s to 4 m^2/s. In Fig. 42 the associated density pulse in the same discharge is shown. The pulses are obtained by Abel inversion of the line-integrated densities measured by the HCN laser. The best fit is found when $\alpha_n = -0.8$ m^2/s. This is equivalent to an inward drift velocity of 2.5 m/s. The value of D is then about a factor of three greater than the equilibrium value.

The decoupling of the density and heat pulses inferred from the ratio of $\chi_e/D \approx 7$ and the best fit for $\alpha_T = 0$ implies that the enhanced values of χ_e in heat pulse experiments cannot be attributed to the effects of finite density perturbations.

1.4.7 Empirical transport coefficients compared with quasi-linear fluctuation-induced transport

The quasilinear effects of electric and magnetic field fluctuations (connected with plasma turbulence) on particle and heat fluxes, bootstrap current, Ware pinch flux and electrical conductivity have previously been studied. On the basis of the drift kinetic equation, these transport quantities were calculated for given fluctuation spectra of $\tilde{\Phi}$ and $\tilde{A}_{\parallel}$, where $\tilde{\Phi}$ is the fluctuating electrostatic potential and $\tilde{A}_{\parallel}$ is the fluctuating parallel component of the vector potential. Quasilinear theory can help to understand the scalings of transport coefficients and the relations among various coefficients. It must be noted, however, that quasilinear theory neglects nonlinear terms, which are important at saturation so that, with some applications, incorrect conclusions will result.

Neglecting the equilibrium radial electric field term and the ω_{mn}/m term in the electron particle flux Γ_e and electron heat flux q_e yields

$$\Gamma_e = -\frac{\sqrt{\pi}}{4}\rho_{pe}^2\frac{v_{te}}{Rq}n_e \times \qquad (1)$$
$$\left[\sum_{m,n}\left(\frac{e\Phi_{mn}}{\sqrt{2}\,T_e}\right)^2\frac{m^2}{|m - nq|}\right]\left(\frac{1}{n_e}\frac{\partial n_e}{\partial r} - \frac{1}{2}\frac{1}{T_e}\frac{\partial T_e}{\partial r}\right)$$

$$q_e = -\frac{\sqrt{\pi}}{4}\rho_{pe}^2\frac{v_{te}}{Rq}n_e T_e \times \qquad (2)$$
$$\left[\sum_{m,n}\left(\frac{e\,\Phi_{mn}}{\sqrt{2}\,T_e}\right)^2\frac{m^2}{|m - nq|}\right]\left(\frac{13}{4}\frac{1}{T_e}\frac{\partial T_e}{\partial r} - \frac{3}{2}\frac{1}{p_e}\frac{\partial p_e}{\partial r}\right)$$

The corresponding fluxes due to magnetic fluctuations are obtained by replacing $\tilde{\Phi}$ by an expression proportional to $\tilde{A}_{\parallel}$. Here, ρ_{pe} is the electron poloidal gyroradius, v_{te} is the electron thermal speed, R is the major plasma radius and m(n) is the poloidal (toroidal) mode number of

$$\tilde{\Phi} = \sum_{m,n\neq 0}\Phi_{mn}\exp\left[i\omega_{mn}t + i\left(m\theta - n\zeta + \eta_{mn}\right)\right]$$

with mode frequency ω_{mn} and random phase angle η_{mn}.

Equations (1) and (2) can be expressed by

$$\Gamma_e = -D\frac{\partial n_e}{\partial r} + \frac{1}{2}D\frac{1}{T_e}\frac{\partial T_e}{\partial r}n_e \qquad (3)$$

$$q_e = -\frac{13}{4}D\,n_e\frac{\partial T_e}{\partial r} + \frac{3}{2}D\frac{\partial p_e}{\partial r} \qquad (4)$$

with the diffusion coefficient

$$D = \frac{\sqrt{\pi}}{4}\rho_{pe}^2\frac{v_{te}}{Rq}\left[\sum_{m,n}\left(\frac{e\,\Phi_{mn}}{\sqrt{2}\,T_e}\right)^2\frac{m^2}{|\,m\text{-}nq\,|}\right] \qquad (5)$$

Identification with the usual transport coefficients yields

$$v_{in} = 0.5\, D \frac{1}{T_e} \frac{\partial T_e}{\partial r} \quad (6)$$

$$\chi_e = 3.25\, D \quad (7)$$

where χ_e is the electron heat diffusivity and v_{in} is the inward drift velocity. The ratio $\chi_e/D = 3.25$ agrees with that derived for trapped-electron modes. A quasilinear calculation does not determine the saturated fluctuation level of Φ, and hence the absolute magnitude of the anomalous fluxes Γ_e and q_e. It does, however, yield the ratios $q_e/(T_e\,\Gamma_e)$ and χ_e/D since the saturation amplitude cancels. It should be mentioned that corresponding relations and $\chi_e/D = 3.25$ also result for magnetic fluctuations with small amplitudes. In contrast to that, high magnetic fluctuation levels leading to stochastic magnetic fields can give rise to χ_e/D ratios considerably above three.

For comparison, we present the scalings of the empirical transport coefficients χ_e, D and v_{in} determined by transport simulations of many series of ohmic, L and H discharges in ASDEX:

$$\chi_e = (2.5 - 5)\, D \quad (8)$$

$$v_{in} = 0.5\, D \frac{1}{T_e} \frac{\partial T_e}{\partial r} \quad \mathrm{cm\ s^{-1}} \quad (9)$$

These relations were found to be valid in all confinement regimes. The electron heat diffusivity for deuterium plasmas reads

$$\chi_e = 1.14 \times 10^{16}\, B_t\, n_e^{-1}\, T_e^{-1}\, q^{-1} \quad \mathrm{cm^2\ s^{-1}} \quad (10)$$

in the ohmic regime and

$$\chi_e = C_o\, q\, B_t^{-1} \quad \mathrm{cm^2\ s^{-1}} \quad (11)$$

in the neutral-beam-heated L and H regimes (tangential co-injection of hydrogen into deuterium target plasmas). Here, B_t is in kG, n_e is in $\mathrm{cm^{-3}}$ and T_e is in keV. The factor C_o is regime-dependent and is equal to $C_L = 6.2 \times 10^5$ in the L regime and $C_H = 2.5 \times 10^5$ in the H regime with ELMs (edge-localized modes).

The ion heat diffusivity χ_i in the ohmic, L and H regimes was found to exceed Z_{eff} times the neoclassical coefficient from Chang and Hinton (1982) by a factor of about 2.5. This corresponds to an enhancement factor χ_i / χ_{ineo} of only about 1.3 with respect to Chang and Hinton (1986).

According to Eqs. (1) and (2), it is a general result of quasilinear fluctuation-induced transport that the fluxes Γ_e and q_e depend in the same way on the fluctuation spectrum. This is also true of the diffusivities D and χ_e (see Eqs. (5) and (7)) and can explain the empirical result that χ_e and D proceed in parallel in each confinement regime and in transitions between different regimes. In the ohmically heated case, the same variation with density was found for χ_e and D (see Eq. (10)). In the L and H regimes, both χ_e and D scale inversely with the current or poloidal magnetic field (see Eq. (11)). Starting from the OH phase, both diffusivities are found to rise by a typical factor of 2 to 3 in the L phase and to decline in the bulk plasma by a factor of about 2 in the H phase with ELMs. It is interesting that a model which does not specify the electrostatic or magnetic fluctuations and a model based on trapped-electron modes yield $\chi_e/D \approx 3.3$ in agreement with the empirical result given in Eq. (8). This suggests that electron heat conduction in stochastic magnetic fields resulting in higher χ_e/D ratios is not present, at least in the confinement zone. It is concluded that the coupling between χ_e and D and $\chi_e/D \approx 3$ are fundamental properties of all confinement regimes and are supported by models based on fluctuation-induced transport.

The scaling of the inward drift velocity $v_{in} = 0.5\, D\, T_e^{-1}\, \partial T_e/\partial r$ given in Eq. (9) was shown to be valid for ohmic, L and H plasmas. It is interesting that an identical relation is a general result of quasilinear fluctuation-induced transport (see Eq. (6)), i.e. it can be derived from general electrostatic or magnetic fluctuation spectra. One important issue of this scaling is that v_{in} is proportional to D, which makes the ratio v_{in}/D insensitive to variations of D.

1.5 Density Limit

(in collaboration with K. Borrass, ITER Team)

The study of the density limit has been an ongoing experimental programme on ASDEX for many years. Specially dedicated density limit shots were performed to determine this limitation of the tokamak operational space. During the last year these investigations were continued and brought to a certain end by measurements in helium plasmas, some neutral beam power scans, additional divertor measurements and, for the first time, by extending these studies to H-mode plasmas.

1.5.1 Radiation at the density limit

It has been reported from other tokamaks that the density limit is connected to a situation where almost all the input power is lost by radiation mainly from the outer region of the main plasma. Such a description is not valid for ASDEX. With increasing density in ASDEX the main plasma radiation increases more or less proportionally to the density, but at the density limit or at the onset of a marfe (which precedes a density limit disruption for $q_a > 3$) this radiation amounts to only 30 – 40% of the total input power under boronized wall conditions. Radiation from the divertor region decreases during a density ramp to around 20% of P_{input} at the density limit. During a marfe the main plasma radiation can increase to around 70% of the input power but still some 10% is found to be radiated in the divertor region. The main plasma radiation, therefore, cannot be considered generally as the direct cause of the density limit in ASDEX.

The ASDEX results, however, strongly indicate that the density limit is a limit to the edge density and that this limit is a consequence of the physics governing the scrape-off layer and divertor region. This will be shown in more detail when discussing the experimental results to be presented in the following.

1.5.2 *Edge density limit*

The density limit in He plasmas was investigated under boronized wall conditions by performing a q-scan ($1.9 \leq q_a \leq 7.6$) in which I_p ($450\ kA \geq I_p \geq 180\ kA$) and B_t ($1.8\ T \leq B_t \leq 2.8\ T$) were changed simultaneously in small steps from shot to shot. A similar q-scan was performed earlier on for D_2 plasmas (see Annual Report 1989). With He as the discharge gas no marfes occur over the whole q-range, contrary to the observations in D_2 discharges. The results of the density limit in ohmically heated plasmas of both experiments are presented in a Hugill diagram in Fig. 43. Whereas for low q-values the achievable densities of the two plasmas are rather similar, significant differences develop with increasing q_a. Here, He plasmas allow much higher line-averaged densities and the Murakami parameter $\bar{n}_e R/B_t$ is no longer proportional to $1/q_a$. This result, however, is mainly a consequence of the different development of the density profiles. In deuterium only a slight increase in profile peakedness is observed when going to higher q_a, whereas He plasmas become very strongly peaked. When taking the density averaged over a chord at r = 3a/4 as representative of the density close to the plasma edge and replacing $\bar{n}_e$ in the Murakami parameter by this edge density, as done in Fig. 43, it becomes obvious that the edge density limits for both types of discharges are not very much different. Furthermore, a linear dependence of the edge density limit is recovered for He as well.

When applying neutral injection (D^0 beams) into a He plasma no increase in the line-averaged density is obtained at the highest q-values. This again is an effect of the density profile.

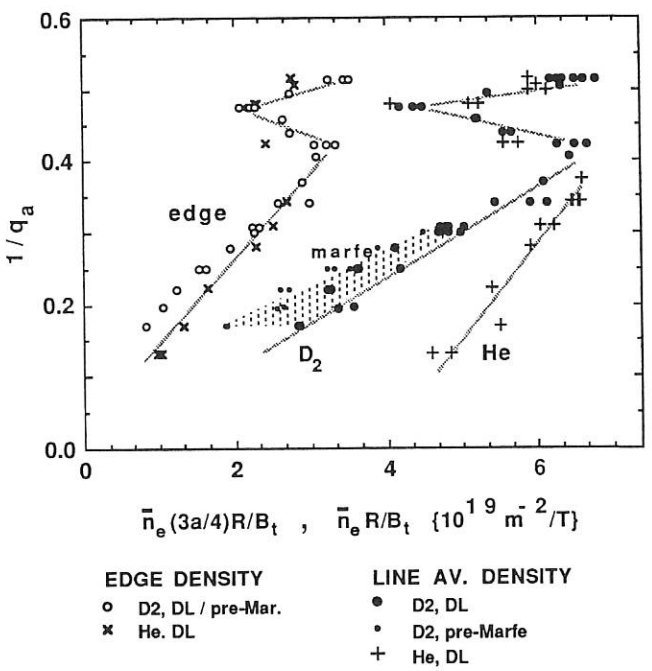

FIG. 43: Density limit and edge density limit for OH deuterium and helium plasmas under boronized wall conditions presented in a Hugill diagram. The region where marfes develop only in deuterium is indicated.

Additional heating causes the profiles to broaden significantly. If again the $\bar{n}_e(3a/4)$ is taken as a reference, it turns out that the edge density limit with NI heating is considerably above the one in OH plasmas for all q-values.

Similar results have already been observed when comparing the density limit in discharges with the usually obtained broad density profiles with that achieved in discharges developing peaked profiles (pellet injection, counter-NI, IOC). Peaked density profiles allow much higher line-averaged densities. This is especially true of pellet fuelling where Murakami parameters ($\bar{n}_e R/B_t$) of about $11 \times 10^{19}\ m^{-2}\ T^{-1}$ in ohmic plasmas and of $14 \times 10^{19}\ m^{-2}\ T^{-1}$ with NI heating (both at q_a around 2.3) were found, exceeding the values of the corresponding gas-fuelled discharges by a factor of around 1.7. Despite these strong differences in line-averaged density, the results of corresponding discharges with broad and peaked density profiles are rather well described by a common edge density limit.

The results discussed above are taken as a strong indication of the existence of a limit to the density at the plasma edge rather than to the line-averaged density.

1.5.3 *Development of divertor and edge parameters*

Such an edge density limit has been predicted by modelling calculations of the SOL and divertor region. In its simplest form these calculations relate the plasma at the separatrix and the divertor plasma in front of the plates by taking into account pressure balance, classical heat conduction along field lines, the energy transfer to the divertor plates and the energy needed for sustaining recycling. This leads to a separatrix density (n_{es}), when expressed as a function of the divertor temperature (T_{ed}), with a maximum at low but finite T_{ed} (≈ 5 eV). This maximum in n_{es} can be naturally considered as an edge density limit. Its absolute value depends on the power flow into the SOL and various divertor conditions. It has been shown in Sec. 1.2 that such a model can describe ASDEX edge results rather well.

Langmuir probe measurements of divertor density and temperature in density limit shots show the development of a cold dense divertor plasma during the density ramp. In the range where $\bar{n}_e R/B_t$ linearly depends on $1/q_a$ the density limit is observed when the divertor temperature has dropped to low values around 5 eV. These results are generally confirmed by measuring the C III radiation from the divertor. This also indicates a strong decrease of T_{ed} during the density ramp. At the plasma edge the temperature drops with increasing density and the density limit is reached in OH discharges (linear range) when $T_{e,edge}$ has decreased to about 35 – 40 eV; in NI-heated plasmas ($P_{NI} = 1.15$ MW) this minimum edge temperature increases to around 50 eV. These results are in agreement with classical heat conduction along field lines and the additional assumption that the density limit occurs at the same low divertor temperature. They therefore confirm the model mentioned above.

A further support of this model is obtained from the density limit values obtained in neutral beam power scans. The results for three different q_a-values are shown in Fig. 44. They demonstrate a q-dependent increase of the density limit with additional heating. For $q_a = 2.95$ (which is representative of

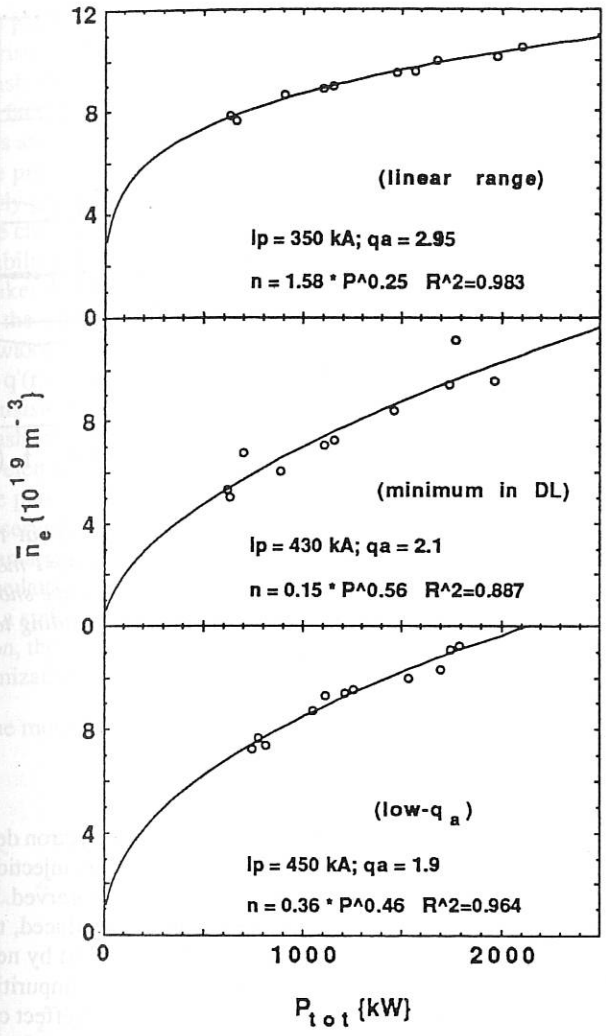

FIG. 44: Results from NI power scans at three q_a together with fits through the data points.

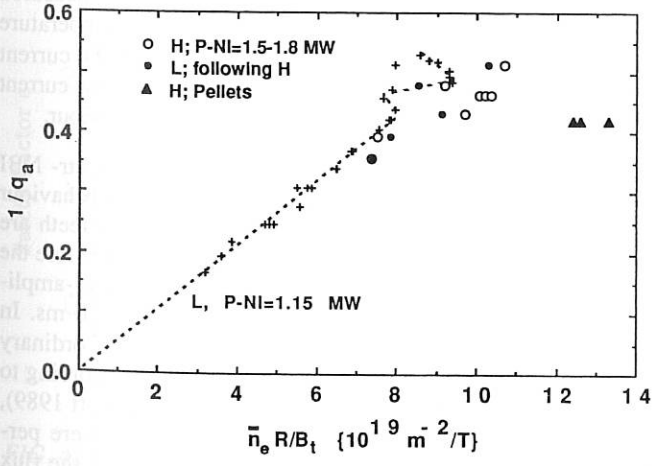

FIG. 45: Hugill diagram of maximum densities during the H-mode, the density limit in the L-mode following the H-mode, H-mode densities with pellet fuelling, and the L-mode density limit at somewhat lower power.

the linear range of $\bar{n}_e R/B_t$ with $1/q_a$) a $\bar{n}_{e,DL}$ dependence of $P^{0.25}$ is found. From P_{NI} scans at different densities far below the density limit, scalings of the edge parameters with the power flow into the SOL can be derived. With the assumptions that these scalings hold up to the maximum density and that the density limit occurs at the same low divertor temperature, $\bar{n}_{e,DL} \propto P^{0.22}$ is predicted, which is rather close to the experimental value.

Given the above results the description of the density limit as a consequence of the SOL and divertor physics is in rather good agreement with experimental results found on ASDEX.

1.5.4 H-mode and density limit

The design of next-step tokamaks such as ITER is based on H-mode confinement. The densities attainable in this mode of operation, therefore, is of particular interest. On ASDEX long quasi-steady H-modes with frequent ELMs were obtained after closing the divertor by-passes and boronization of the walls. Under these conditions density limit shots during the H-mode over a restricted parameter range have been performed in gas-fuelled as well as pellet-fuelled discharges. The density could be ramped up to rather high values but in almost all cases a transition back into the L-mode accompanied by a drop in density was observed prior to the density limit disruption. In cases were this final L-phase lasts for a longer time the maximum attainable density during the H-phase can be compared with the L-mode density limit in one shot. Figure 45 shows pellet H-mode results, maximum H-mode densities with gas fuelling, the density limit of L-modes following an H-mode and, for reference, the results of a q-scan in L-mode at a somewhat lower power. Obviously, the H-mode can be operated at densities comparable to the L-mode density limit values determined under the same conditions.

1.6 MHD Studies

1.6.1 ELMs

In ASDEX, long-pulse H-mode discharges have been performed. In order to achieve stationary conditions, it was necessary to have ELMs at a repetition rate of about 200 Hz to provide screening against the influx of impurities. The position of the ELM can be deduced from the T_e inversion point and is found to be at r/a = 0.88. To explore further, a fast data acquisition system capable of sample frequencies of up to 3 MHz was used to analyze the magnetic fluctuations connected with them.

Figure 46a shows the H_α trace for an H-mode discharge in which single ELMs as well as grassy ELMs occurred. Figure 46b shows an H_α and a magnetic (Mirnov) signal of a single ELM. It can be seen that the ELM (characterized by the increase in H_α emission) has a growing magnetic precursor. This precursor is always found to have a frequency of 100-200 kHz and a growth time of typically 50 µs, indicating an ideal rather than a resistive MHD process. Figure 46c shows a contour plot of the temporal evolution of the magnetic fluctuation frequency

spectra during an ELM. The precursor can be seen as a narrow frequency band; the ELM itself appears as a broadband turbulent phase reaching up to 300 kHz. These features are generally observed during ELMs. No difference is found between singular ELMs and grassy ELMs although these phenomena occur at different edge pressure gradients.

As the magnetic measurements were all made at a single location, the topology of the precursor could not be determined (such as mode numbers). Nevertheless, it is clear that ELMs are not a local phenomenon but rather occur in the whole edge region. During an ELM, H_α rises simultaneously within 20 μs at all toroidal positions and also in the divertor.

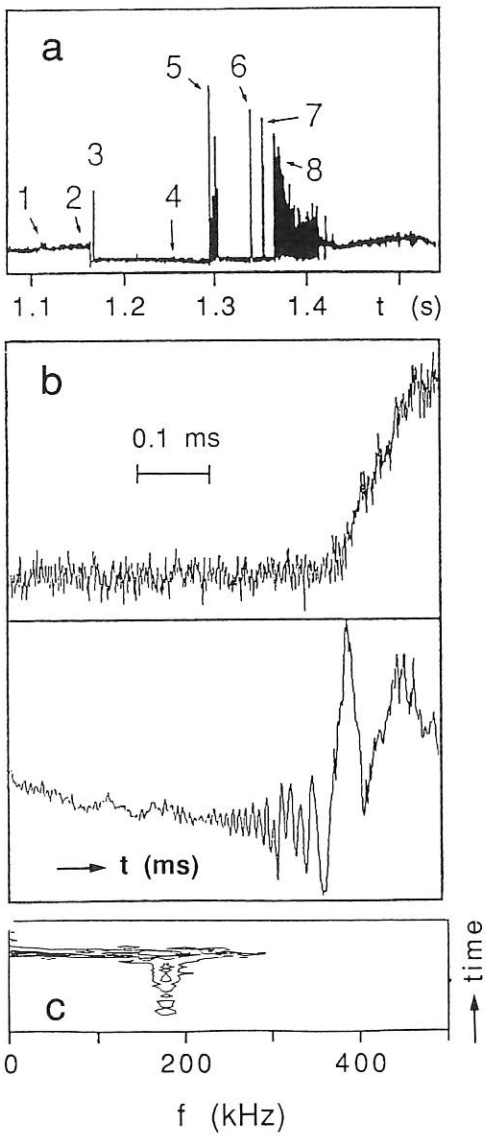

FIG. 46: a) H_α trace of an ASDEX H-mode shot showing a single ELM directly after the L-H transition (3), a set of giant ELMs (5) and the grassy H-mode (8).
b) H_α (upper) and Mirnov (lower) trace of the single ELM (3) in Fig. a). The magnetic precursor can be clearly seen.
c) Temporal evolution of the Fourier spectrum of the magnetic fluctuations of the same event; the precursor is seen as a narrow frequency band, the ELM itself as a broad turbulent phase.

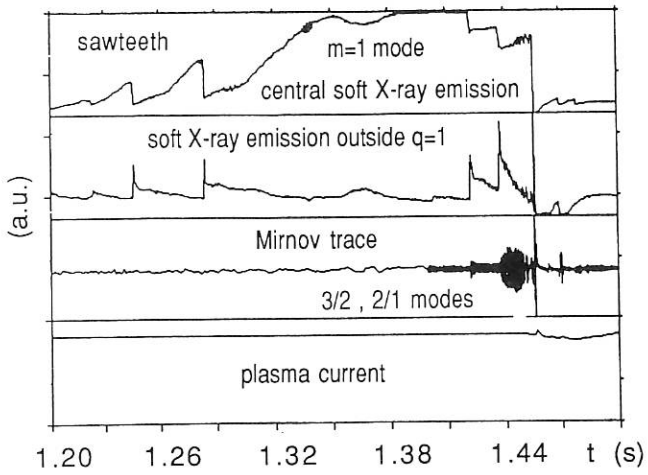

FIG. 47: MHD activity during counter injection: at t = 1.29 s sawteeth are suppressed, at t = 1.35 also the m=1 mode vanishes. At t = 1.42 s and t = 1.44 s the Mirnov trace shows the onset of (3,2) and (2,1) oscillations, the later leading to a minor disruption at t = 1.455 s.

1.6.2 Impurity accumulation and central modes

In the enhanced confinement regimes with peaked electron density profiles (i.e. IOC, ctr-NBI heated shots and pellet injection) an increase in the impurity content is generally observed. In these scenarios, when the anomalous transport is reduced, the observed accumulation of impurities is well predicted by neoclassical theory. In most cases, the accumulation of impurities leads to disruptive termination of the discharge. This effect can be ascribed to the modification of the current profile j(r) due to the change in Z_{eff}. During the accumulation process peaking of the Z_{eff} profile in the centre is observed. This leads to broadening of the current profile and therefore steepening of the gradient of j(r) at the edge. This in turn can lead to destabilization of MHD modes, leading to disruption. The process was analyzed using a current diffusion code based on the measured temporal evolution of the profiles of the electron temperature and Z_{eff}. With this code the temporal evolution of the current profile can be determined; a Δ' stability analysis of these current profiles is in agreement with the observed MHD behaviour.

Figure 47 shows an example of this analysis. For a ctr- NBI heated discharge the temporal evolution of the MHD behaviour is shown: the sawtooth period is enlarged, then sawteeth are suppressed. It is commonly seen that the last collapse before the suppression of sawtooth activity is followed by a large-amplitude (m=1,n=1) mode, which is present for a few 10 ms. In order to compare the crash mechanism with that of ordinary crashs, for which reconnection of the helical flux according to the model of Kadomtsev was found (see Annual Report 1989), SXR tomography studies of this kind of collapse were performed. It follows that the temporal development of the flux surfaces is the same as that seen in the early phase of crashs with complete reconnection. The hot plasma core within the q=1 surface undergoes a radial shift with a helical m=1 symmetry. After a fast increase of the shift from 3 cm to 8 cm within 100 μs the process stops and the hot core moves back into

the plasma centre on a slow time scale of a few 10 ms. A comparison of the SXR-, T_e- and n_e-profile changes during the crash shows that mixing of plasma in the vicinity of the q=1 surface takes place but does not reach the plasma centre. From this and from the flux surface topology it can be concluded that the process taking place during the crash is the same as in the early phase of crashs with complete reconnection. Thus the profile changes during the early phase of the crash are sufficient to stabilize the plasma against further reconnection. This result makes the shear at the resonant surface rather than the value of the safety factor on axis, q(0), a probable candidate for the sawtooth crash trigger: The crash starts at a certain critical value of $q'(r_s)$ and is stopped at another value of $q'(r_s)$. This is also consistent with the fact that these incomplete reconnection crashs are seen in plasmas with central accumulation of impurity elements, corresponding to a small radial variation of q in the plasma core. Finally, the onset of two MHD modes can be observed: In a first step, an (m=3,n=2) mode is destabilized, then also an (m=2, n=1) mode can be seen on the Mirnov trace. The latter mode leads to a minor disruption which is manifested as a spike on the plasma current signal. After the minor disruption, the mode activity is no longer observed; obviously, a reorganization of the current profile has occurred.

The mode numbers were obtained for the decomposition of the magnetic signal shown in Fig. 47. It was performed by projection of Mirnov data from 16 different coils onto eigenvectors that represent the (3,2) and (2.1) mode activity.

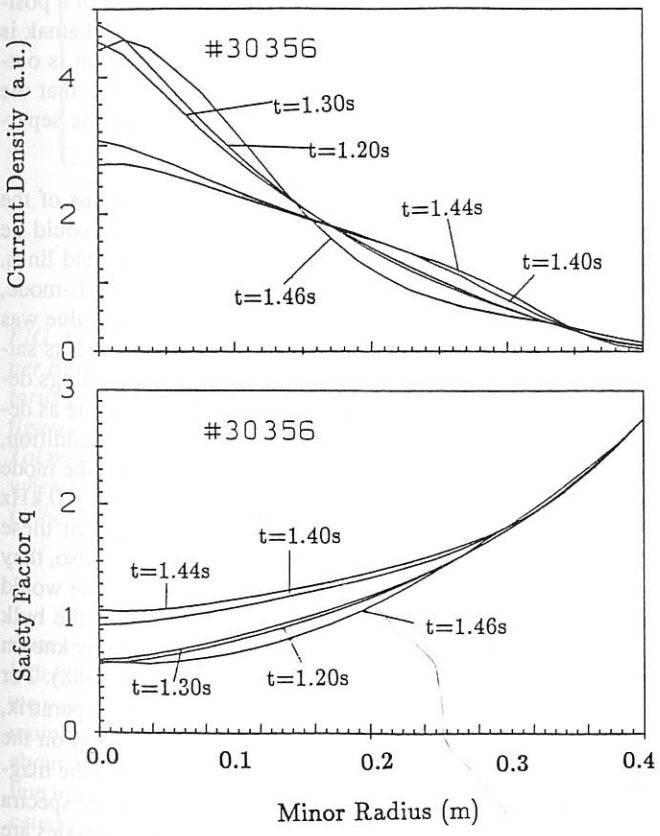

FIG. 48: Profiles of the current density and the safety factor at different time instants. The lowering of the central current density leads to a rise of the central safety factor above 1. Note that after the minor disruption (t = 1.46 s) the profiles return to the shape before the onset of the improved confinement (t = 1.2 s).

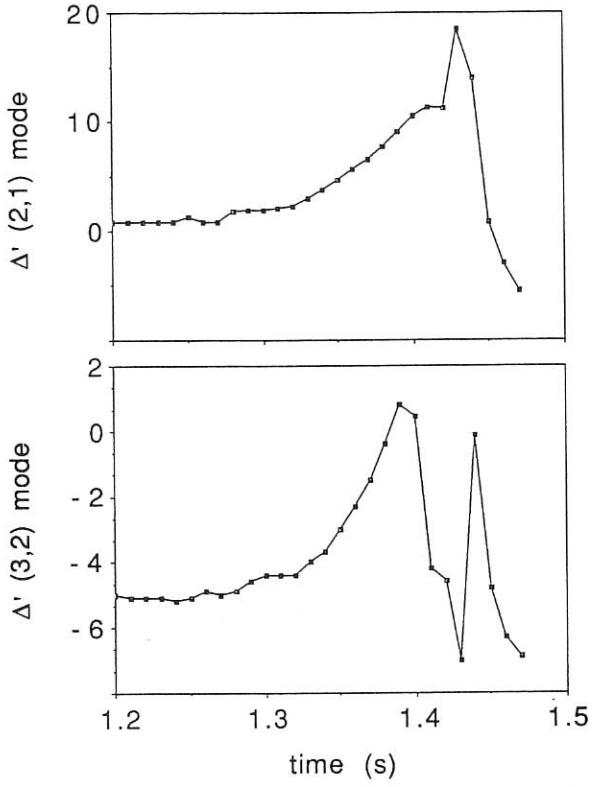

FIG. 49: Δ' stability analysis of the current profiles shown in Fig. 48 for the (3,2) and (2,1) modes.

Figure 48 shows the temporal evolution of the current and safety factor profiles as deduced with the current diffusion code based on the actual Z_{eff} profiles. In the first phase, the safety factor on axis, q_0, is calculated to be 0.6, which is lower than expected. This might be due to the fact that in this phase sawteeth are not yet suppressed and the code does not take into account any effect of the sawtooth transport on the current profile. In general, this effect would be to increase q_0 by lowering the current density on the axis. Nevertheless, in the later phase, when sawteeth are suppressed, this problem does not occur. Taking into account the peaking of the Z_{eff} profile we find a broadening of the current profile as shown in Fig. 48, and thereby an increase in q_0. Also, the current profile shows a steepening of the gradient at the edge (t = 1.44 s). At t = 1.46 s, the minor disruption has taken place and the current profile returns to the old shape. This phase is not well described by the diffusion code.

Figure 49 shows the results of a Δ' stability analysis of the current profile against the destabilization of the (3,2) and (2,1) tearing modes. It can be seen that the temporal evolution of the (3,2) mode is reproduced in quantitative agreement: Δ' stays below 0 as long as the mode is experimentally stable; as soon as the mode is seen to be destabilized, the Δ' analysis yields Δ' > 0. Also, the destabilization of the mode leads to a reduction

of Δ'; from this nonlinear effect we can understand the saturation of the growth of the mode. For the (2,1) mode, the agreement is only qualitative since the trend of the temporal behaviour is reproduced, whereas the absolute value of Δ' indicates instability at times when experimentally the mode is still stable. This discrepancy can be attributed to the fact that the Δ' code we used for the analysis is a simple one-dimensional cylindrical code which still describes the (3,2) mode but not the (2,1) mode, which is located at r/a = 0.9.

The scenario described above is found to be a severe limit to the regimes with peaked electron density profiles: as the confinement is improved, the accumulation of impurities leads to disruptive termination. In contrast, the ELMy H-mode with its broad density profiles can be kept stationary since ELMs provide effective screening against the influx of impurities.

1.6.3 m=1 satellite in the SOL

During periods of strong NBI heating often a large central m=1, n=1 mode is observed. Owing to its special topology (internal kink) it cannot be seen on the Mirnov coils but is detected by the soft-X-ray diagnostic. Nevertheless, in a plasma with strong NBI (above 1 MW), a mode rotating with the same frequency is detected by the magnetic coils. This so-called 'm=1 satellite' is not seen during LH or ICRH, even if comparable m=1 activity is observed in the centre and β comes close to the value with NI. The frequency of the m=1 and its satellite, which is typically of the order 10 - 20 kHz with strong NBI, is always found to be close to the central plasma rotation velocity measured by CXRS measurements. Therefore, the motion of the coupled modes seems to be essentially a toroidal one; also, it is in the ion diamagnetic drift direction, which is opposite to the direction of mode rotation observed without beams.

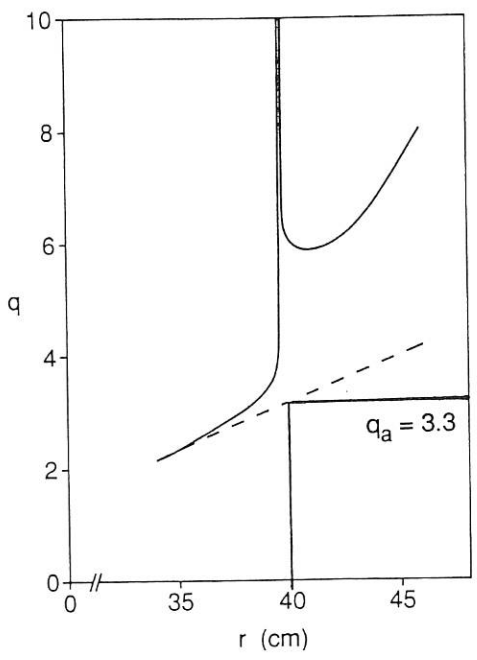

FIG. 50: Safety factor profile in the edge region of ASDEX (solid line) and for a limiter tokamak having the same cylindrical edge q (dashed line).

The amplitude of the satellite mode detected by the Mirnov coils is much bigger on the outside of the torus, the typical amplitude ratio between outside and inside being 5 - 10. Generally, we find that the poloidal mode number m of the satellite, determined from the magnetic probes, is equal to the next integer number above q_a. Therefore, the mode must be located very close to the separatrix, where the q-value, in an ideal configuration, becomes infinitely large. Calculations using realistic assumptions about the magnitude of the errors in position and shape of the multipole coils show that q-values of at least q = 10 can occur close to the separatrix. Figure 50 shows a calculated q-profile for q_a = 3.3. The figure also shows the q-profile of a limiter tokamak with the same edge q-value (dashed line).

To correctly interpret the mode number determined with the Mirnov diagnostic, one has to be aware of the fact that in ASDEX there are no magnetic coils in the vicinity of the X-points. On the other hand, only in this region does the local pitch angle come close to zero (as the large q-value indicates). In the region equipped with Mirnov probes, the local pitch angle varies like it does in a limiter tokamak. Therefore, the value of m=4 as determined for the poloidal mode number with the Mirnov diagnostic is misleading. If we take into account the geometry of the measurements as described above, we arrive at the conclusion that the mode is located in a position where the q-value as calculated for a limiter tokamak is equal to 4. As can be seen from Fig. 50, this location is outside the separatrix, and therefore we have to assume that the m=1 satellite is located on open field lines outside the separatrix which reach into the divertor.

To test this assumption, we measured the fluctuations of the poloidal magnetic field in the divertor chamber. It could be moved along the straight line perpendicular to the field lines. As an example we present the results of shot #27671 (L-mode, P_{NBI} = 1.8 MW). In this shot, the cylindrical edge q-value was q_a = 4.4. We observed the central m=1,n=1 mode and its satellite rotating at 15.6 kHz. In agreement with the findings described above, the poloidal mode number of the satellite as determined from the Mirnov diagnostic was 'm=5'. In addition, we observed two independently rotating modes with the mode numbers (m=4,n=1) and (m=3,n=1) at frequencies of 6.0 kHz and 2.0 kHz. From the mode numbers it is clear that these modes are located close to, but inside, the separatrix; also, they rotate in the electron diamagnetic drift direction, as one would expect in the edge region where the contribution of the bulk rotation is small. These modes are phenomenologically known as 'Toi modes' (see, for example, Annual Report 1988). For these three modes, which are all located close to the separatrix, we now look at the frequency spectra of a Mirnov coil on the outside of the torus, one on the inside of the torus and the magnetic probe in the divertor. Figure 51 shows these three spectra at two different time instants: In both phases, the Toi modes are present and are manifested on the two Mirnov coils (2.0 kHz and 6.0 kHz). At the later time (t = 1.37 s, right side of Fig. 51), also the m=1 mode and its satellite were present. According to the strong in/out contrast as mentioned above, the satellite is seen only on the Mirnov coil on the outside of the torus. If we now look at the spectra from the divertor coil, we find that only the satellite is seen in the divertor chamber although the

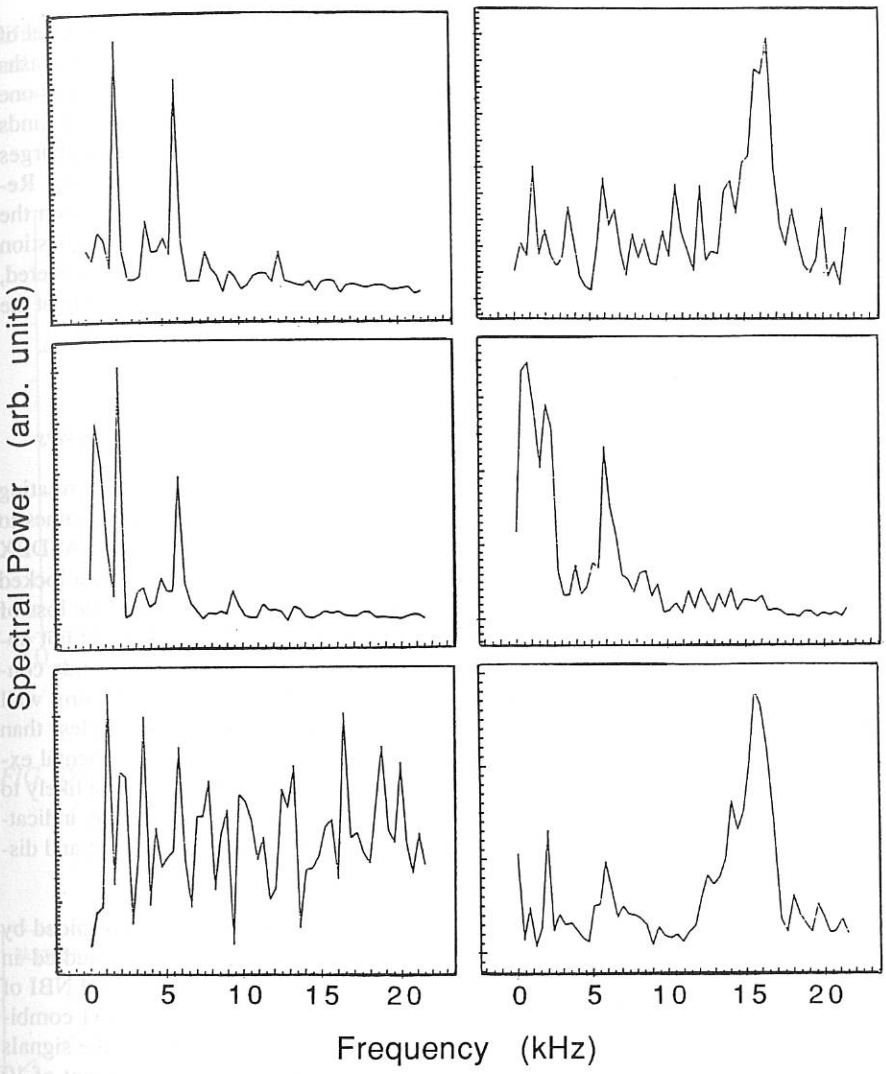

FIG. 51: Fourier spectra of a Mirnov coil on the outside (upper figures) and one on the inside (figures in the middle) of the torus in the main chamber and in the divertor chamber (lower figures). The left-hand side shows a time instant when only the Toi modes are present, the right-hand side shows a time instant when also the satellite mode is present. Only the satellite is seen in the divertor.

three modes are located close together and, moreover, the decay index of the satellite is the highest of the three modes. Also, if we vary the position of the divertor probe we can detect a maximum of the amplitude of the fluctuating field within a region of about 1 cm, indicating that the perturbation is coupled to a field line in the divertor. We therefore conclude that the satellite is located outside the separatrix on open field lines reaching into the divertor. Therefore, we cannot attribute a poloidal mode number m in the sense of a Fourier decomposition in the poloidal angle. Attempts were made to find a link between the in/out ratio of the satellite amplitude and the separatrix configuration (in the single null configuration, the inside and the outside of the torus are connected which is not the case in the double-null configuration) but no clear correlation was found.

These experimental findings have not yet been explained by a theoretical model. Such a model should explain the fact that the m=1,n=1 couples to a mode outside the separatrix but cannot be seen on the magnetic probes; moreover, the Toi modes stay unaffected. Therefore one should find eigenfunctions of the m=1, n=1 that have a local maximum outside the separatrix.

1.6.4 Compound sawteeth

In addition to the SXR tomography studies concerning sawtooth crashs with complete (see Annual Report 1989) and incomplete reconnection (see this report, Sec. 1.6.2), analyses of a further kind of sawtooth relaxations, so-called *compound sawteeth*, were performed in order to complete the picture of the sawtooth instability gained so far.

An example of a discharge with a compound sawtooth is given in Fig. 52. The instability occurs in between two ordinary sawtooth relaxations and is manifested in rather small amplitude changes in central SXR channels. The irregular appearance of compound sawteeth, which are also reported to appear in ohmic discharges in large tokamaks, shows that the trigger condition for the collapse depends very sensitively on small changes in plasma profiles. Inversion of the line-integrated raw data shows that a significant decrease in radiation amplitude takes place only off-axis, the centre of the plasma staying almost unaffected by the collapse. This finding, combined with the fact that compound sawteeth are seen in plasmas with flat or slightly

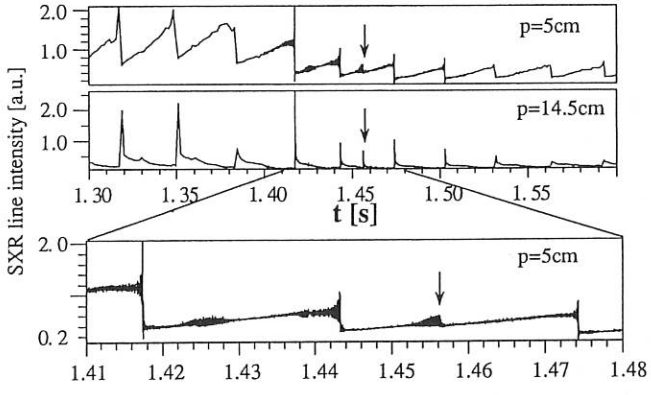

FIG. 52: Counter-NBI-heated discharge exhibiting compound sawtooth activity. The compound sawtooth crash takes place at t = 1.456 s and is preceded and followed by ordinary sawteeth.

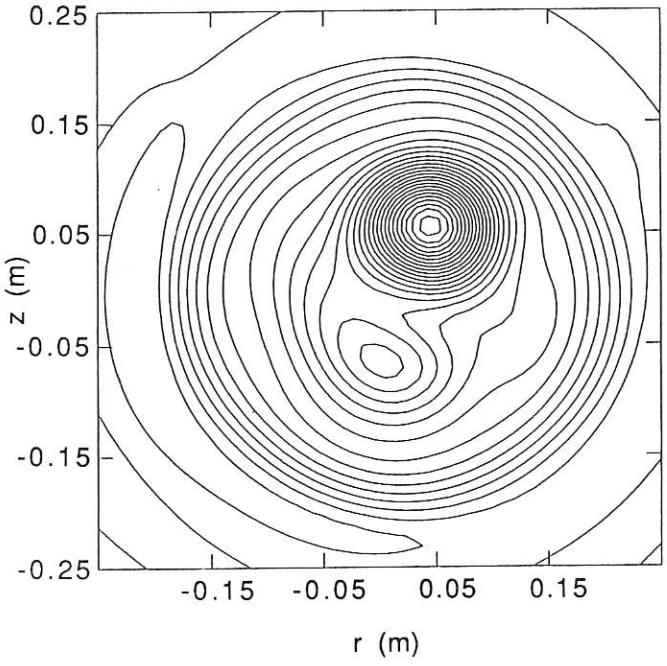

FIG. 53: Contours of constant soft-X ray emissivity during the reconnection phase of a compound sawtooth.

hollow T_e and n_e profiles and accordingly flat current profiles (ctr-NBI-heated ASDEX discharges) led to the presumption that compound sawteeth are connected with the presence of nonmonotonic current profiles with q(0)>1 and two off-axis q=1 surfaces. A detailed analysis of the MHD oscillations advancing the collapse (precursor mode) in fact gives a mode structure different from the (1,1) precursors commonly seen: it is consistent with the existence of two (1,1) modes located at different radii, which is a rather direct hint of the presence of two q=1 surfaces. This picture is clearly supported by tomographic analysis, which gives additional information on the dynamics of the crash: The SXR contours shown in Fig. 53 clearly display two oppositely located radiation maxima. From a sequence of contour plots taken during the whole precursor phase it is seen that the large inner hot spot moves outwards, whereas the outer one moves inwards. This kind of plasma mixing as well as the flux surface topology shown is consistent with the prediction of the model of resistive reconnection of the helical flux in the presence of two q=1 surfaces. Another confirmation of this result comes from the existence of one (1,1) mode immediately after the crash: The reconnection model predicts a q=1 surface after reconnection at a radius which is about a factor 4/3 larger than the original outer q=1 radius. This is in very good agreement with the experimental findings.

The reconnection time of 2 ms, which is very large compared with the 100 μs reconnection time of ordinary crashs, is in agreement with MHD theory, which states that the growth rate of resistive modes decreases with decreasing shear at the resonant surface.

In conclusion, it can be stated that with the help of SXR tomography the process of reconnection at two q=1 surfaces could be shown experimentally. In addition, this is indirect confirmation of the finding that reconnection according to the model of Kadomtsev is the process underlying ordinary ASDEX crashs in NI-heated plasmas since both types are special cases of one particular model. Combining all the results for different kinds of sawtooth phenomena in NBI-heated ASDEX discharges yields a rather consistent picture of the crash mechanism: Resistive reconnection of the helical flux is consistent with the majority of the experimental findings. Of course, the question concerning the triggering of the instability is still not answered, but there are some experimental indications that the shear at the resonant surface plays an important role.

1.6.5 Disruption control by unlocking of locked modes

Normally, disruptions in ASDEX are preceded by a rotating (m=2,n=1) mode. Often, this mode slows down and comes to rest. This so-called mode locking has been studied in ASDEX in detail (Annual Report 1989). Theory predicts that a locked mode should have an enhanced growth rate due to the loss of wall stabilization. This enhanced growth, however, is not observed in ASDEX. Stability calculations using a Δ' code confirm this result: The presence of a perfectly conducting wall reduces the instability parameter Δ' only marginally (less than 5%) in the ASDEX geometry. Nevertheless, experimental experience shows that a shot with a locked mode is more likely to disrupt than one with a rotating mode of the same size, indicating a more complex connection between mode locking and disruption.

The question therefore arises if disruptions can be avoided by forcing locked modes to rotate again. This was studied in ASDEX by using the triggered onset of unidirectional NBI of sufficient power (i.e. about 1.5 MW). We used an n=1 combination of saddle loops to detect the locked modes: the signals from the saddle loop are integrated with a time constant of 10 ms, which is long compared with the inverse of the normal mode rotation frequency (0.1 - 1 ms). Therefore rotating modes are not detected. A locked mode leads to a change in the flux

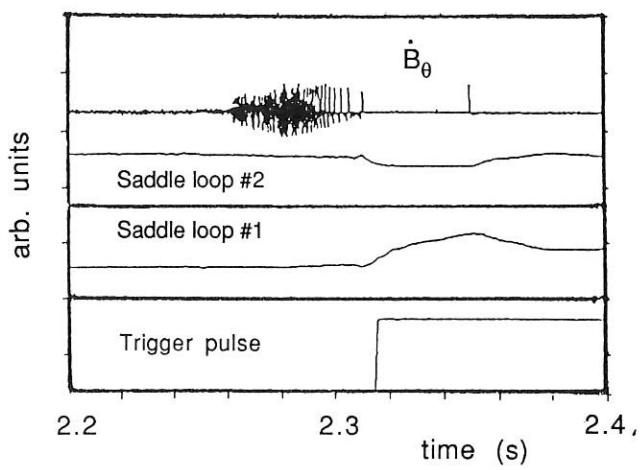

FIG. 54: Generation of a trigger pulse due to a locked mode: The locked mode leads to a change in the flux difference of the two saddle loops shown in the figure. Above a certain level a trigger signal is generated.

difference between the saddle loops which is detected online and is used to trigger an NBI pulse. Figure 54 shows an example.

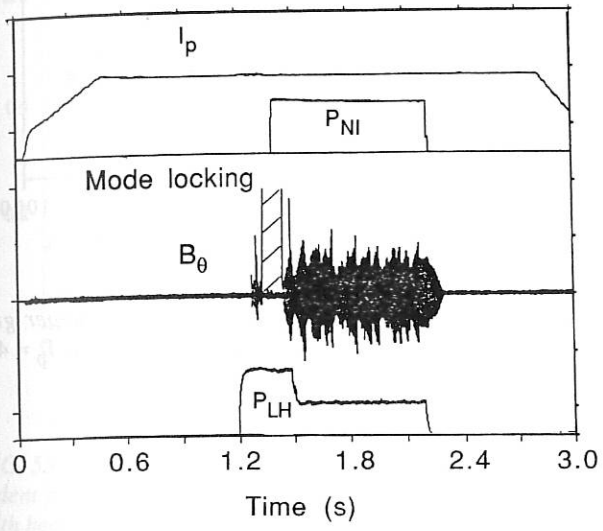

FIG. 55: Unlocking of a locked mode during LHCD.

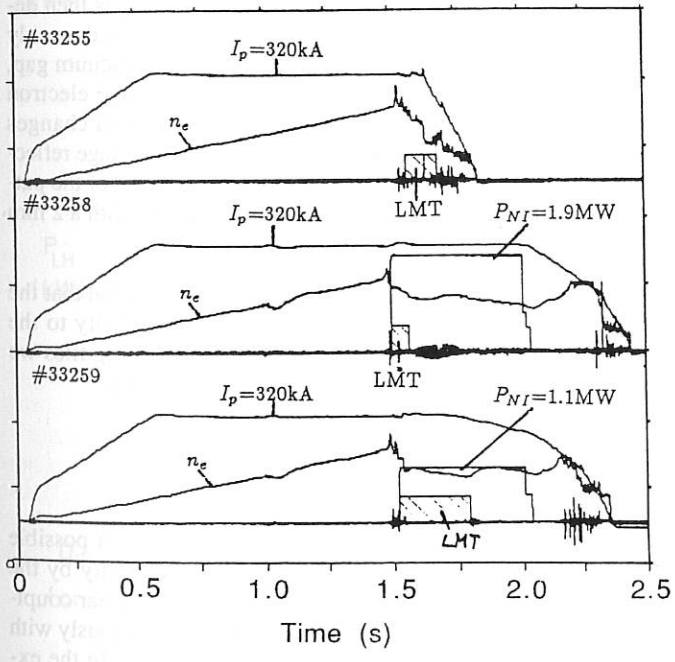

FIG. 56: Triggered unlocking of locked modes occurring at the density limit disruption: The upper traces show a normal density limit shot; in the two shots shown in the middle and lower figure the NBI was triggered by the occurrence of a locked mode at the onset of a marfe leading to the loss of density. The current disruption can be avoided; the duration of the locked mode (indicated by the locked mode trigger LMT) is dependent on the NBI power.

Figure 55 gives an example of the unlocking of a locked mode during Lower Hybrid Current Drive. As can be seen, the shot does not disrupt. Nevertheless, the m=2 amplitude does not decrease, even after a reduction of the LH power, so that further stabilization techniques should be applied. Figure 56 shows another example, this time during a density limit shot and for two different NBI powers. It can be seen that the NBI forces the mode to rotate again, thereby avoiding the density limit disruption even though a substantial loss of density occurs at the onset of the locked mode (which is also the onset of a marfe). In this case, the mode vanishes after unlocking. Here, it should be noticed that the NBI power (more than 1 MW) far exceeds the ohmic power supplied by the transformer (about 350 kW). Therefore the heating of the plasma by the beams is a dominant effect and we cannot apply the pure mechanical arguments of unlocking the mode.

In general, the technique has proved to be a possible candidate for disruption control if the disruption is preceded by a locked mode which persists for a time interval sufficient to detect and unlock the mode (i.e. about 10 - 50 ms in ASDEX). The application to bigger machines will be studied in further investigations using the coupled viscous and electromagnetic model of mode locking described in the Annual Report 1989.

1.6.6 "SNAKES" after injection of large pellets into OH discharges

(in collaboration with A. Weller)

The injection of large pellets (with 1.5×10^{20} atoms each) which penetrate close to the plasma centre is able to produce a striking resonance effect in ohmic D_2 discharges. A clear elevation can sometimes be observed on a symmetric soft X-ray emission profile (see Fig. 57) when the injection leads to reduced sawtooth dynamics. This "snake"-like perturbation with m=1,n=1 topology, first discovered in 1986 on JET, results from the rotation of a small region with enlarged X-ray emissivity. The rotation, unlike that of MHD oscillations in OH plasmas, is in the plasma current direction. It oscillates on ASDEX with frequencies of $\upsilon \lesssim 700$ Hz and lasts between 10 ms and 40 ms. The poloidal and radial widths (FWHM) of the elevation are found to be ≈ 0.09 m and 0.055 m, respectively. The central electron densities and temperatures measured by Thomson scattering lie around $n_e \sim 1 \times 10^{20}$ m^{-3} and $T_e \sim 500$ eV. The line-averaged density measured by the FIR interferometer point to local density enhancements in the snake region. With the radial width of the SX-ray elevation the density enhancement is estimated at $\Delta n_e \lesssim 1 \times 10^{19}$ m^{-3}. Temperature information in this region is not available, since the high density causes cutoff of the electron cyclotron emission.

Very weak sawteeth acting during the snake oscillation decelerate the rotation but do not terminate it. The crash promptly reduces its radial extent by up to 50%, which indicates that the q=1 surface does not completely disappear as a result of the weak sawteeth. The soft termination of the snake modulation after a time of $\lesssim 40$ ms probably reflects a gradual transition to $q \geq 1$ in the internal region. From this time the weak sawteeth are also absent. In parallel, these phases are characterized by an increase of the central radiation.

Model calculations can explain the local radiation enhancement by the deduced local density enhancement Δn_e and an undisturbed T_e . If T_e is coincidently decreased, as could be seen on JET, the calculated X-ray emissivity would be reduced. In contrast to JET, no structures with mode numbers m=3,n=2 and no characteristic dip in the H_α light from the ablating pellet, which is correlated to the q=1 radius, is diagnosed.

The unexpected local perturbation, which gives information on the radius of the q=1 surface and its time evolution, was explained by A. Weller et al. by the formation of a magnetic island at the q=1 surface with a new nonaxisymmetric equilibrium.

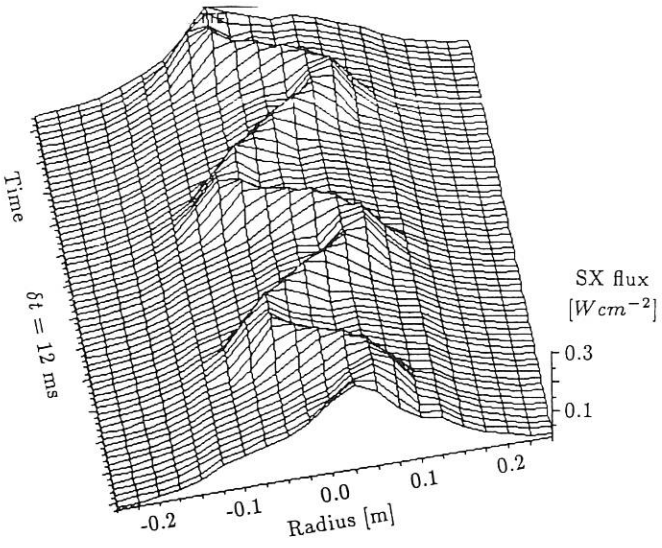

FIG. 57: Soft X-ray flux measured by the horizontal camera vs. time showing a "snake" oscillation after a deeply penetrating pellet.

1.7 Lower Hybrid

(in collaboration with H. Münich, M. Zouhar, F. Hassenplug, F. Munaco (Technology Division) and ENEA, Frascati and PPPL, Princeton)

Current drive and heating with lower hybrid waves were investigated on ASDEX in the second phase of experiments with an RF system at 2.45 GHz up to a power of 2 MW. The results on current drive efficiency agree well with theory, including the effect of a DC electric field. Global energy and particle confinement are improved in the presence of a large suprathermal electron population. Electrostatic fluctuations are reduced in this case. Stabilization of the m=1 mode gives rise to strong central electron heating and peaking of the $T_e(r)$ profile. Local control of the current profile is achieved by launching compound spectra from independent grill antennas. The LH power deposition profile and the modification of the current profile were modelled with a fully selfconsistent 3D Fokker-Planck code. Local transport analysis shows that in MHD-quiescent discharges with high central electron temperatures the electron heat conductivity drops close to neoclassical values.

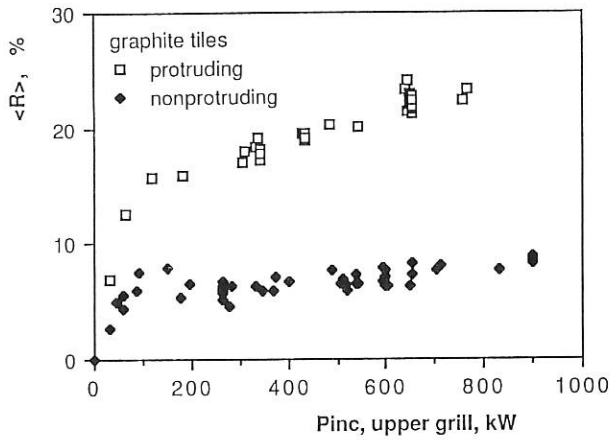

FIG. 58: Average reflection coefficient of the upper grill with protruding and nonprotruding tiles. (B_t = 2.8 T, I_p = 420 kA, n_e = 1.3 - 1.5 × 10^{13} cm^{-3}, bor.wall, D_ϕ = 90°)

1.7.1 Coupling

1.7.1.1 Linear coupling

The average reflection coefficient <R> was reduced by a factor of up to 3 by cutting back protruding structures around the grill, as shown in Fig. 58. The higher reflection can be explained by the linear coupling theory, assuming a vacuum layer of order 2 mm between the grill and the plasma. The coupling is then determined more by this gap than by the plasma and is thus only weakly dependent on the edge density. Without a vacuum gap, however, we find a strong dependence on the edge electron density. The whole structure of the reflection pattern changes when n_{edge} is varied through the value where the average reflection <R> is minimum. Such a change in the structure of the pattern is absent in the calculated patterns for the case with a 2 mm vacuum gap.

This is in agreement with the experimental observation that the coupling with protruding tiles showed little sensitivity to the main plasma parameters, whereas with nonprotruding tiles we found a clear dependence on the edge electron density.

1.7.1.2 Nonlinear coupling

The reflection coefficient <R> increases with power. A possible mechanism might be modification of the edge density by the ponderomotive force. This was studied with a nonlinear coupling code. The reflection coefficient <R> rises continuously with increasing power to high values, as seen in Fig. 59. In the experiment, however, <R> saturates at high power. Such a saturation can be obtained in the model if we allow the edge electron temperature to increase with the transmitted power. The rising plasma pressure counteracts the ponderomotive force, leading to a much reduced rise in the reflection coefficient and eventually to saturation, as seen in Fig. 59 (solid lines). Confirmation of this model is found in the variation of the reflection patterns with increasing power, indicating a reduction of the edge density in front of the grill as predicted by the ponderomotive force

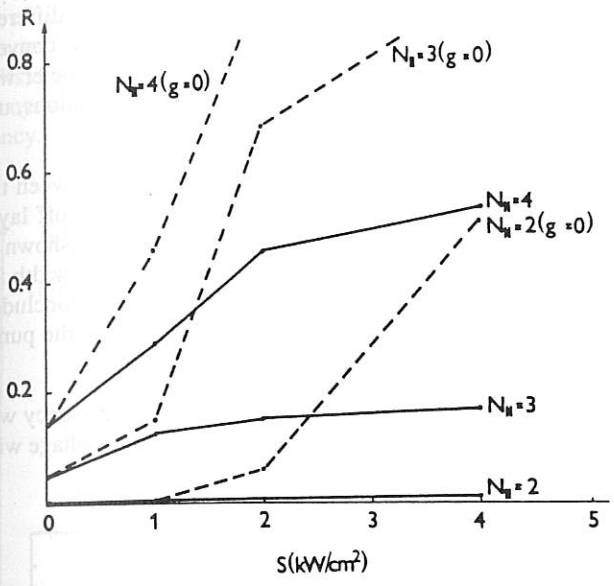

FIG. 59: Calculated reflection coefficient as a function of incident power density , $n_b/n_c = 4$, dashed / solid lines: without / with heating of the edge electrons

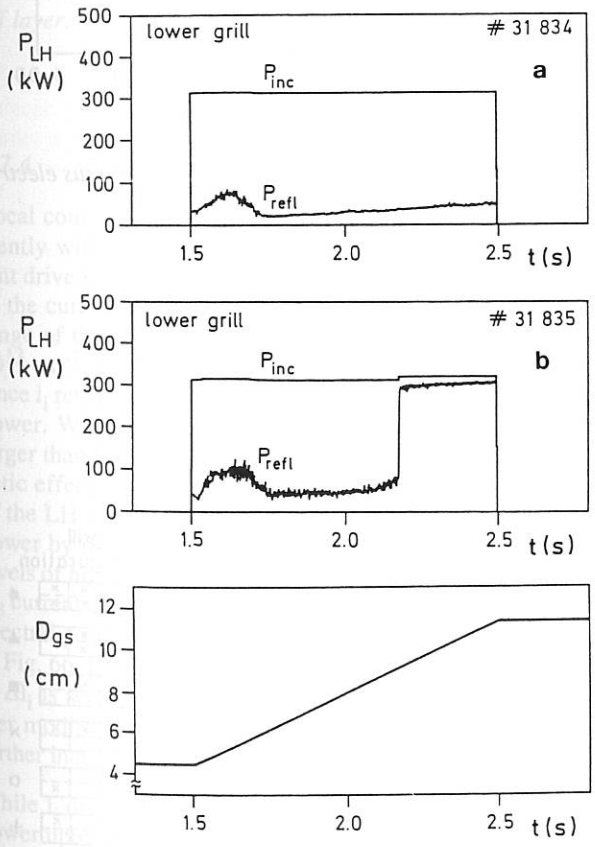

FIG. 60: Incident and reflected power vs. time while the plasma was moved away from the grill; a) gas valve near grill, b) gas valve far from grill.

effect, whereas away from the grill no clear variation could be found. Also, the ion saturation current to a Langmuir probe did rise considerably, indicating heating of the edge electrons.

1.7.1.3 Coupling at large grill-plasma distance

Good coupling was usually obtained with a distance between grill and separatrix $d_{g\text{-}s} = 4.5$ cm. For $d_{g\text{-}s} > 7$ cm nearly total reflection occurred. However, when $d_{g\text{-}s}$ was increased from 4.5 cm to 10 cm while the RF power was turned on, reasonably good coupling could be maintained, as shown in Fig. 60, when the gas feed was near the grill. But it could be abruptly lost when the gas feed was far away from it. Edge density profiles taken with an X-mode reflectometer show that a sufficiently dense edge plasma was maintained by the transmitted RF power with the gas valve near to the grill. But the density strongly drops over a distance of about 2 cm in front of the grill when the gas valve is far away.

Coupling could also be maintained or improved at large grill-separatrix distance during repetitive pellet injection. The rapid ablation of the pellets already near the plasma surface due to the fast electrons generated by the lower hybrid waves also creates a sufficiently dense edge plasma for good coupling.

1.7.2 Current drive efficiency

1.7.2.1 Efficiency at zero electric field

In addition to the results already given in the Annual Report 1989, we obtained some more data points at low phasing $\Delta\phi < 75^{o}$, i.e. $N_{||} < 1.8$. Under these conditions part of the wave spectrum is expected to violate the accessibility condition, resulting in strongly reduced efficiency. The experimental efficiencies are, however, considerably higher than estimated. The reasons are not understood.

Similarly, when only 2×8 instead of all 2×24 waveguides of the grill are fed with power, we launch a spectrum which is about a factor of 3 broader than usual. Here, too, part of the power at low $N_{||}$ should be lost owing to nonaccessibility. Nevertheless, the current drive efficiency obtained in experiments at low density was higher than that estimated for the broad spectrum.

1.7.2.2 Efficiency at nonzero electric field

We evaluated the RF-driven current independently in the following way: Using the measured electron temperature profiles, the central Z_{eff} and the loop voltage, we calculate the current density profile to obtain the inductively driven current. From this we can determine the fraction of inductively driven current I_{ind}/I_p, which is shown in Fig. 61 as a function of the residual loop voltage U_{LH} normalized to its value in the ohmic phase U_{OH}. The RF-driven current is $I_{RF}/I_p = 1 - I_{ind}/I_p$. The normalized efficiency is then $\eta/\eta_o = I_{RF} P_{LHO} / I_p P_{LH}$, where P_{LHO} is the power necessary to reach zero loop voltage. This has been compared with the analytic approximation by K.Yoshioka et al.:

$$\eta / \eta_o = \ln [(1-X_2)/(1-XX_2)] / (X - 1)X_2,$$

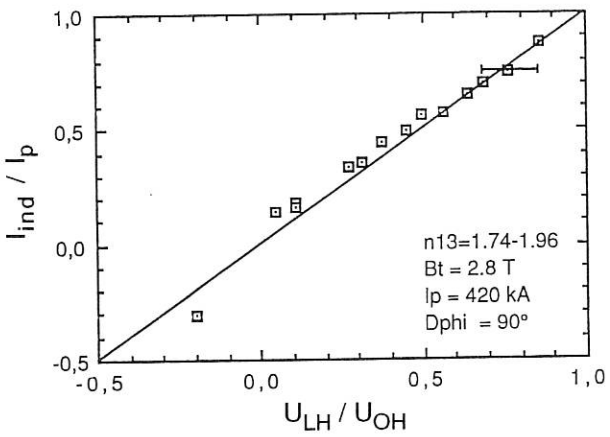

FIG. 61: Fraction of inductively driven current vs. normalized loop voltage.

where $X_2 = \alpha\, u_2^2\, E_N$, $\alpha = 12 / (Z_{eff}+7)$, $u = v_{ph}/v_{th}$, $X = u_1^2/u_2^2$ and $E_N = E/E_{Dreicer}$. The indices 1 and 2 refer to the lower and upper boundaries of the phase velocity spectrum. X_2 can be expressed as

$X_2 = A \cdot U_{LH}/U_{OH}$, with

$A = 65.7 \cdot U_{OH} / [(Z_{eff,LH}+7)\, N_{||2}^2\, n_{e13}]$.

In A all quantities can be measured except $N_{||}^2$, for which we take the lower limit of the calculated $N_{||}$ spectrum or the accessibility limit $N_{||acc}$ derived from the plane wave accessibility condition, whichever is larger. In Fig. 62 we show the result of a power scan. The dotted lines are the theoretical efficiencies for three different values of the spectrum width X : X = 1 corresponds to a very narrow spectrum ($N_{||1} = N_{||2}$) and X = 0 to a very wide spectrum ($N_{||1} = \infty$). The points seem to follow the characteristic with X = 1, instead of X ≈ 0.5 as given by the calculated spectrum. However, we have to realize that the error bars in the difference $I_{RF}/I_p = 1 - I_{ind}/I_p$ become quite large.

1.7.3 Parametric decay instabilities

The broadening of the LH pump frequency spectrum has previously been recognized to reduce the LHCD efficiency. Candidates for pump broadening are Parametric Decay Instabilities (PDI) involving ion sound quasimodes or scattering by density fluctuations at the plasma edge.

A PDI process should show three main characteristics:

1) a power threshold;
2) saturation above a certain power level;
3) evidence of convective effects due to the finite extent of the region where LH fields are excited.

To clarify the first two points, power scans down to 1 kW and up to ≈1.5 MW were performed, but no evidence of a threshold or saturation in the pump spectral width Δf_p was found. Rather Δf_p linearly increases with the total coupled LH power, as shown in Fig. 63. Different LH grill configurations were used in order to search for convective effects. By changing the excited segments inside the grill and arranging them in different ways, the spatial extent of the LH pump, and hence the convective losses, can be varied. The only significant parameter was found to be the total power for all the grill configurations, unlike in the ion cyclotron PDI case.

On the other hand, a good correlation was found between the pump spectral width and fluctuations in the scrape-off layer as measured by means of a Langmuir probe. This is shown in Fig. 64. Correspondingly, we observe that the pump width increases and CD efficiency decreases. Therefore we concluded that fluctuations rather than PDI are responsible for the pump broadening and the degradation of CD efficiency.

The influence of ion cyclotron sidebands on CD efficiency was investigated by comparing the decrease in the loop voltage with

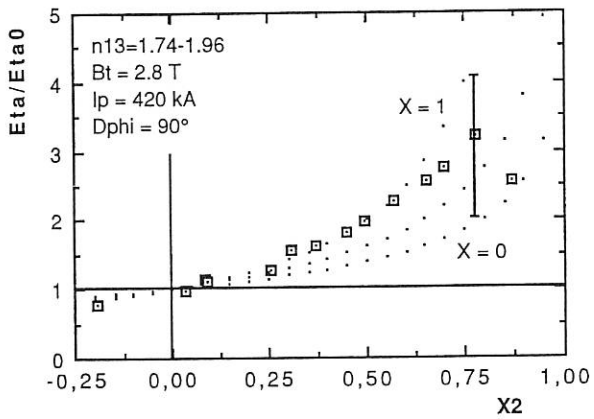

FIG. 62: Normalized current drive efficiency versus electric field.

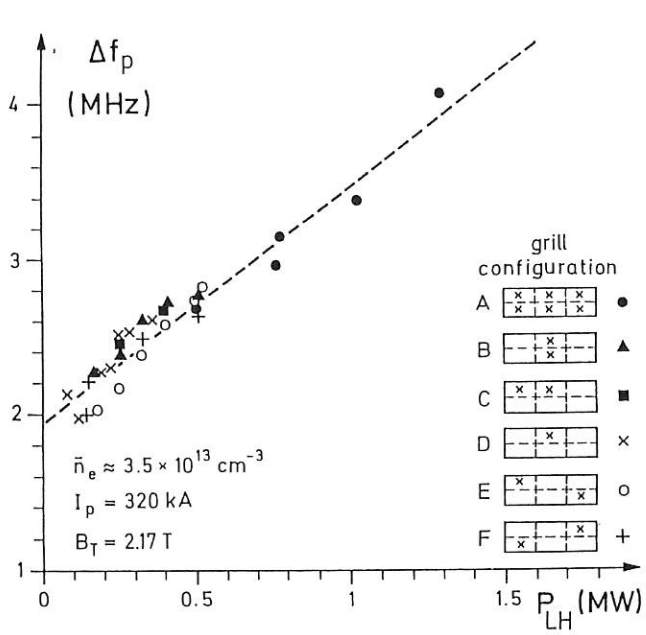

FIG. 63: Pump spectral width plotted versus total coupled LH power for different grill configurations.

the same total power either on one or on both LH grills. No difference is visible between the one grill, high PDI, and two grills, low PDI cases. Therefore the onset and development of ion cyclotron sidebands does not degrade the current drive efficiency.

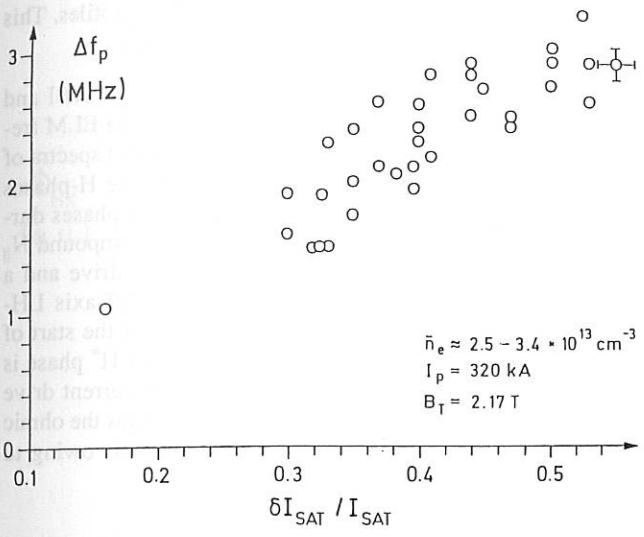

FIG. 64: Pump spectral width plotted versus the relative fluctuation level as measured by Langmuir probes in the scrape-off layer.

1.7.4 Profile control

Local control of the current profile j(r) is achieved most efficiently with compound wave spectra combining low-$N_{||}$ current drive spectra with high-$N_{||}$ spectra. Broadening or peaking of the current profile can be obtained in the whole parameter range of the current drive regime, up to densities of $\bar{n}_e = 5 \times 10^{13}$ cm^{-3}, as seen in Fig. 65. Changes in the internal inductance l_i remain small with LH-current drive at low $N_{||}$ up to high power. With compound low/high-$N_{||}$ spectra, reductions of l_i larger than from both spectra separately clearly reveal a synergetic effect. The results can only be explained by broadening of the LH deposition profile, with off-axis shift of the low-$N_{||}$ power by the superposed high-$N_{||}$ spectra. Already low power levels of high-$N_{||}$ spectra strongly change the deposition of low-$N_{||}$ current drive spectra. The variation of the drop in l_i with the spectral power composition of low and high-$N_{||}$ parts is shown in Fig. 66. For high power LHCD ($P_{LH} \geq 800$ kW) a saturation in Δl_i is seen for $P(180^o) / P(90^o) > 0.5$. It seems that no further modification of the power deposition profile results from further increasing the power in the high-$N_{||}$ spectrum.

While l_i drops and therefore j(r) broadens with increasing LH power upon injection of compound spectra, the central electron temperature increases and $T_e(r)$ peaks, even slightly more than in the normal current drive case if the power in the high-$N_{||}$ spectrum remains moderate (see Fig. 66). Current and electron temperature profiles can therefore be largely decoupled in compound spectrum operation with LH-current drive.

1.7.5 Hard X-ray emission

Bremsstrahlung emission from fast electrons was measured in the photon energy range from 40 keV to 500 keV on radial and tangential viewing chords. A typical spectrum from the central line of the radial system is shown in Fig. 67. The photon spectrum temperature and the flux intensity are used to characterize the LH wave interaction with electrons. Both are strongly correlated with the electron density, as shown in Fig. 68. There we note that fast electrons are still detected for an average electron density of $n_e = 4.5 \times 10^{13}$ cm^{-3}. A smaller decrease of the photon temperature is found with increasing $N_{||}$ in the case of current drive spectra. The photon temperature does not vary with power or working gas.

The hard x-ray intensity increases with decreasing $\overline{N}_{||}$. It is higher for the symmetric spectrum $00\pi\pi$ than for the 90 degree phasing with the same $\overline{N}_{||}$. This can be explained by the higher loop voltage and therefore stronger acceleration of fast electrons by the DC electric field with the $00\pi\pi$ spectrum. The photon temperatures are slightly higher in this case. It should be noted that the same intensity is obtained with $00\pi\pi$ phasing or launching two 90 degree waves in opposite toroidal directions with the two grills.

The tangential detector was used to record the HXR forward emission during LH power modulation. The emission in this condition is directly related to the LH-generated fast electrons. From the initial rise of each pulse information on the LH power deposition profile can be obtained. On a slower time scale information on the spatial diffusion of fast electrons is obtained. A

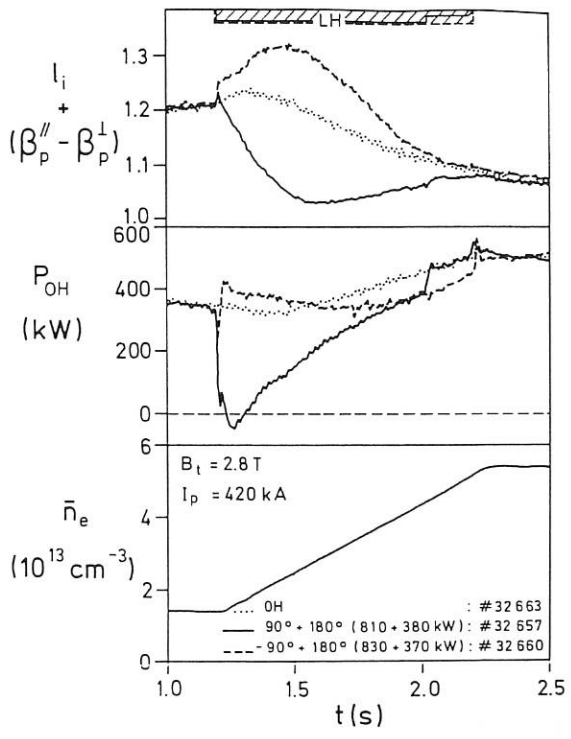

FIG. 65: Variation of internal inductance l_i and ohmic power input P_{OH} with injection of compound LH wave spectra during a slow density ramp.

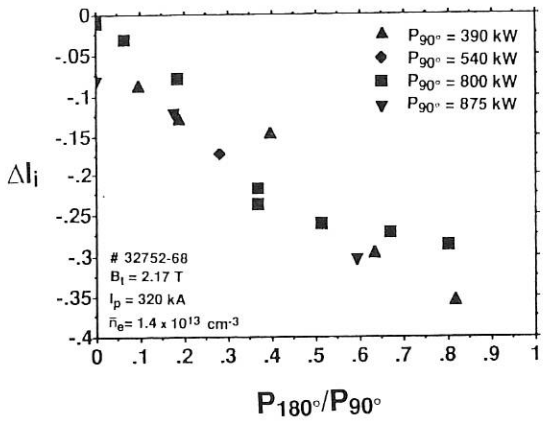

FIG. 66: Variation of the drop in the internal inductance Δl_i with the power composition of a 90° current drive and a 180° symmetric wave spectrum.

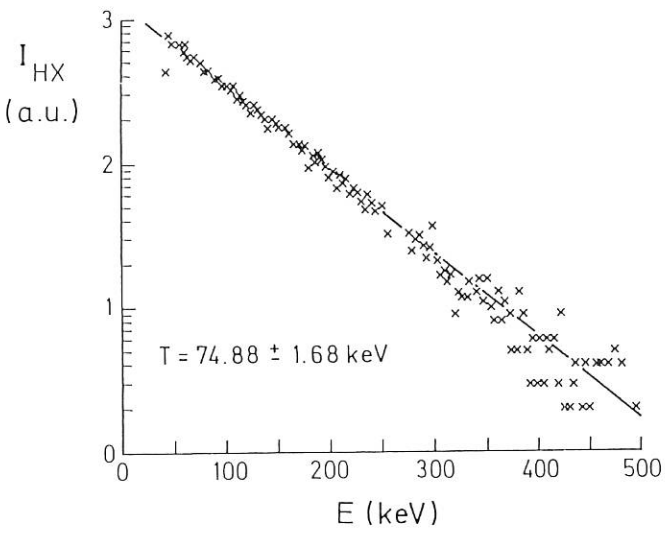

FIG. 67: Typical HXR spectrum from a central radial chord.

box car technique was used to increase the statistics. In Fig. 69 the value of the derivative is plotted versus the tangency radius of the tangential system viewing the outer part of the plasma. A clear indication of outward shift of the deposition with increasing electron density and increasing $N_{||}$ can be deduced.

1.7.6 Combined operation with neutral beam injection

Current drive and heating with lower hybrid (LH) waves were combined with heating by neutral beam injection (NBI) up to total powers of 4 MW. Absorption of LH power results in preferential electron heating up to densities of $\bar{n}_e \approx 5 \times 10^{13}$ cm^{-3}. At low densities ($\bar{n}_e < 3 \times 10^{13}$ cm^{-3}) NBI raises mainly the ion energy content. With both heating methods the energy confinement time decreases by increasing power with the same power law.

Peaked electron temperature profiles as attained with LH-current drive after suppression of the m=1 mode can be maintained during additional NBI heating. In some cases, however, enhanced MHD activity during NBI causes flattening of $T_e(r)$.

Current profile control with various LH wave spectra was studied together with high-power NBI heating. The energy confinement is improved with peaked current density profiles. This is achieved with off-axis opposite LH-current drive.

The H-mode was reached in combined operation of NBI and LH, both in current drive and symmetric mode. The ELM frequency could be modified by varying the power and spectra of the injected LH waves. Transitions into ELM-free H-phases were triggered by launching LH into stationary L-phases during NBI. An example is shown in Fig. 70. The compound $N_{||}$ spectrum, consisting of a low-$N_{||}$ (90°) current drive and a high-$N_{||}$ (180°) symmetric spectrum, provides off-axis LH-current drive. The DC electric field reverses after the start of LHCD. With short delay a 150 ms long quiescent H^* phase is established. With the sharply rising density the current drive efficiency decreases and the DC electric field regains the ohmic level. The energy content strongly rises and levels owing to enhanced central impurity radiation.

1.7.7 q- profile measurements

(in collaboration with IST, Lisbon and University of Aveiro, Portugal)

Broadband reflectometric measurements can provide local information about the characteristics of the MHD modes. This technique makes use of the fact that MHD modes produce density perturbations, which are detected and localized by reflectometry. As these modes are destabilized at the rational magnetic surfaces, information on the current profile may be obtained.

A detailed study was performed during LHCD discharges under conditions where locked modes (m=2) occurred, and in LHCD discharges with different compound launched spectra. Changes of j(r) are indicated by the temporal evolution of the radial position of the various modes as shown in Fig. 71. A clear shift in-

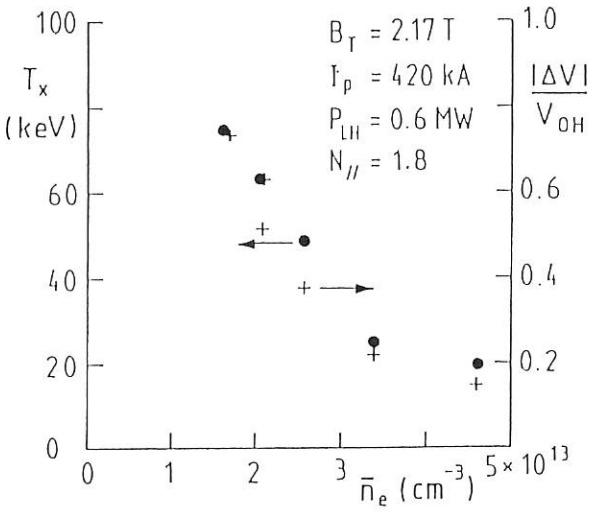

FIG 68: Photon temperature and loop voltage drop versus averaged electron density.

wards of the rational magnetic surfaces due to LHCD can be seen. Toward the end of the LH pulse this evolution stops and even a small regression is observed (t > 1.35 s). Based on the experimental results, the time evolution of the q-profile was estimated for different LH spectra (Fig. 72). Results are in good agreement with data from Li-beam measurements.

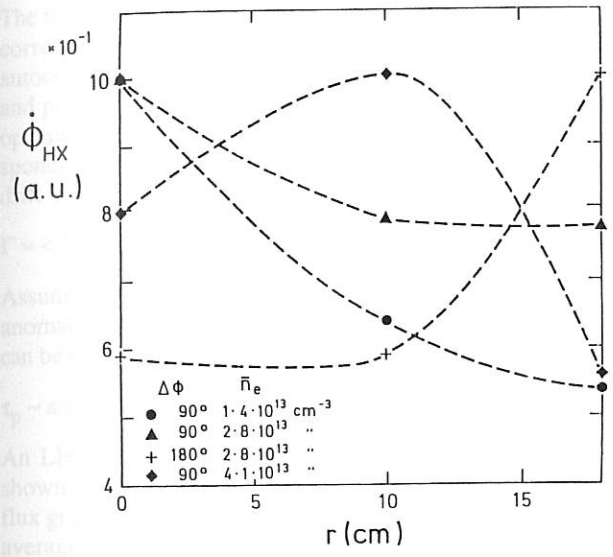

FIG 69: Derivatives of the HXR fluxes to the tangential detector at the onset of LH.

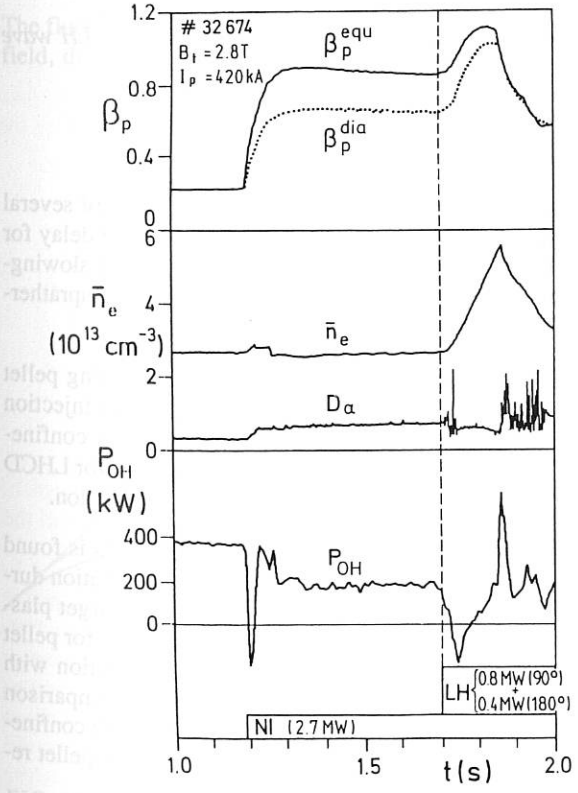

FIG. 70: H-mode transition triggered by LHCD during NBI.

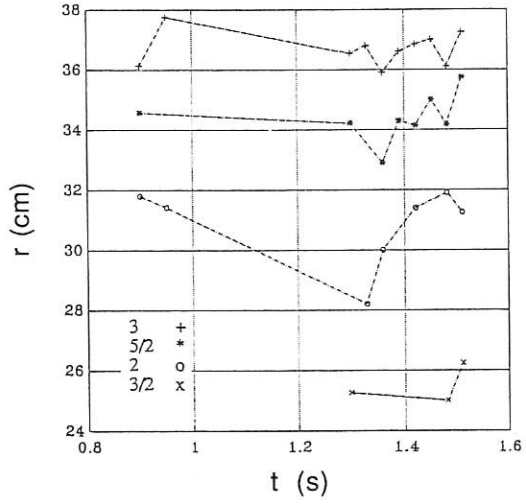

FIG. 71: Temporal evolution of the location of density perturbations on rational q-surfaces during LHCD (LH [1.0 s; 1.53 s]).

Numerical studies were performed in order to determine the limitations of this method. Difficulties with the identification of different MHD modes can arise; in this case the use of fixed-frequency reflectometry may be needed, where local spectra of the MHD fluctuations can be used to complement the broadband data.

The study confirms the potential of this new reflectometric technique: (i) the temporal evolution of the q-profile can be estimated in a single shot; (ii) the correlation between local changes of the q-profile and the suppression or excitation of MHD modes, due to LHCD, can be investigated.

1.7.8 Combined operation with pellet injection

Lower hybrid-current drive and heating were combined with repetitive injection of deuterium pellets. The evolution of various global plasma parameters with pellet injection during LHCD is shown in Fig. 73. The line-averaged density $\bar{n}_e$ increases immediately after injection of each pellet and continues to rise after the initial jump. The density profile $n_e(r)$, first flattened during the gas-puff-fuelled LHCD phase, gradually peaks during pellet injection, with the profile factor $Q_n = n_{eo} / \langle n_e \rangle$ rising from ~1.4 to ~1.8. Sawteeth are suppressed immediately after the start of LH. The m=1 mode is weakened and finally stabilized in a late phase after the last pellet. In the subsequent MHD-quiescent phase, the line-averaged density $\bar{n}_e$ stays nearly constant and the density profile strongly peaks. The neutron flux Φ_n then rises by a factor of about 2.

In ohmic target plasmas the small-size pellets penetrate to about half the plasma radius, as seen in Fig. 74a. With LH, the mass deposition profile strongly depends on the LH wave spectrum. With LH-current drive at low $N_{||}$ the pellets are ablated by the LH-generated fast electrons in a narrow zone near the plasma periphery, as seen from the sharp peak close to the separatrix in Fig. 74b. The additional broad wing of the H_α signal originates

from the gas cloud produced after evaporation of the solid pellet. With LH waves of higher $N_{||}$ the pellets are ablated further inside the separatrix, as shown in Fig. Fig. 74c. In this case fast electrons with lower mean energy are generated.

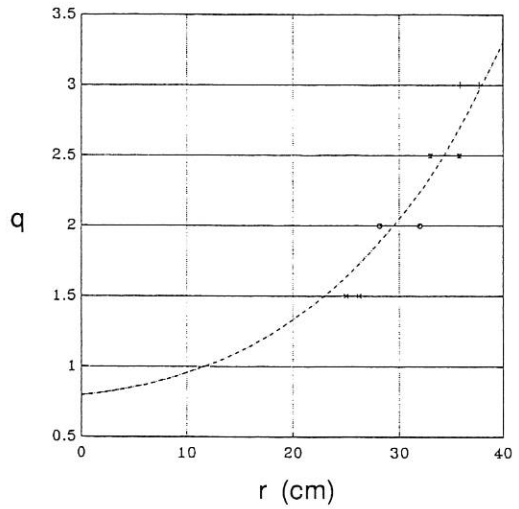

FIG. 72: Radial variation of the locations of density perturbations on q-surfaces during LHCD and the q-profile for the ohmic phase derived from the $T_e(r)$ profile.

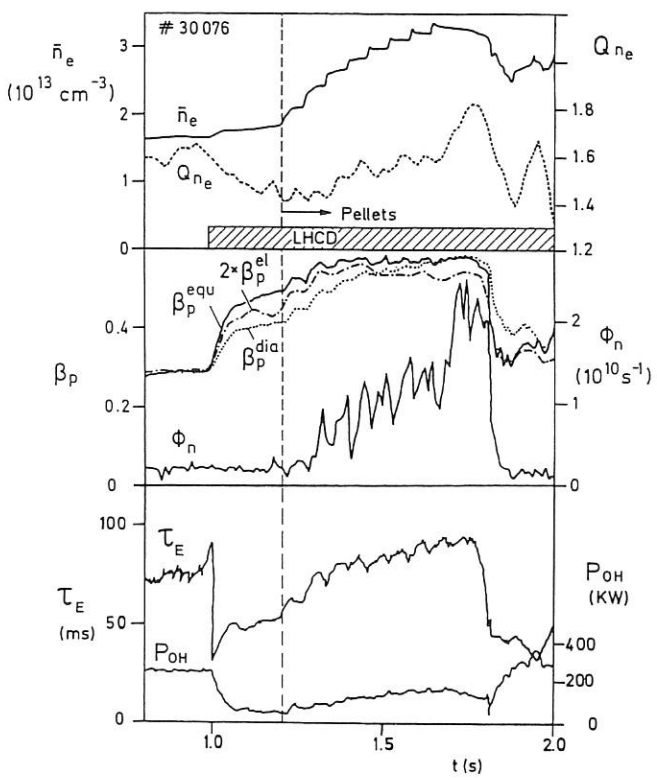

FIG. 73: Temporal evolution of various plasma parameters for a discharge with pellet injection during LH-current drive ($P_{LH} \approx 620$ kW, $\bar{N}_{||} = 1.8$).

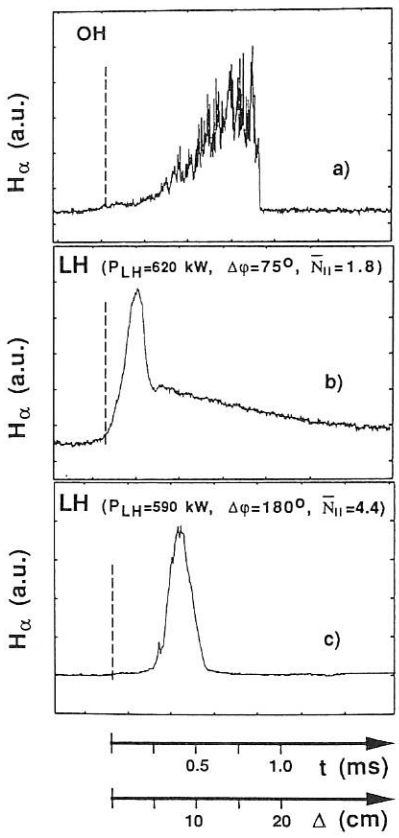

FIG. 74: Pellet ablation profiles as derived from H_α radiation. The dashed line indicates the position of the separatrix.
(a) Pellet injection into an ohmic target plasma.
(b) Pellet injection into LH-current drive with low-$N_{||}$ wave spectrum $\bar{N}_{||} = 1.8$).
(c) Pellet injection during application of a high-$N_{||}$ LH wave spectrum $\bar{N}_{||} = 4.4$).

Deep penetration is regained only with a long delay of several hundred ms after the end of the LH pulse. The time delay for recovery of deep pellet penetration corresponds to the slowing-down time of fast electrons near the upper end of the suprathermal tail distribution.

The energy confinement time rises with density during pellet injection into LHCD in the same way as with pellet injection into ohmic target plasmas. An increase of the energy confinement time with density can therefore also be regained for LHCD plasmas by peaking the density profile with pellet injection.

Approximately the same net inward flux of particles is found during the density build-up with peripheral pellet ablation during LH as with the deeper penetration into ohmic target plasmas. The bulk diffusion coefficient is about the same for pellet injection into ohmic target plasmas and in combination with LHCD. For both cases it is strongly reduced in comparison with purely gas-fuelled discharges. The central particle confinement is therefore also clearly improved with shallow pellet refuelling in combination with LH-current drive.

1.7.9 *Fluctuation measurements*

The electrostatic fluctuations were investigated near the plasma edge by means of a multiple-tip Langmuir probe. In most cases, the probe remained at a fixed position outside the separatrix radius. In a few cases the probe was also operated with fast radial movements. Radial profiles of fluctuating quantities are then determined during one single shot.

The fluctuating signals are recorded with a three-channel analog correlator, as seen in Fig. 75. Two channels operate in the autocorrelation mode measuring the rms values of density (n_e) and poloidal electric field (E_p) fluctuations. The third channel operates in a cross-correlation mode and its output signal corresponds to the radial turbulent flux Γ induced by the cross-field drift $E_p \times B_{tor}$,

$$\Gamma = < \delta n_e \, \delta E_p > / B_{tor}.$$

Assuming the turbulent transport as the dominant channel for anomalous particle losses from the plasma, the turbulent flux can be related to the global particle confinement time τ_p:

$$\tau_p \sim a \, n_e / \Gamma \quad (a = \text{minor radius})$$

An LH-power scan was performed in a single discharge, as shown in Fig. 76. During the first four power steps, the gas flux gradually decreases by a factor of up to two, while the line average density slightly increases. Also the D_α emission decreases for the low LH-power levels, while it increases for the high powers. Light and heavy impurity radiation decrease, as seen from CIII and soft X-ray radiation. Z_{eff} drops near the plasma edge for low levels of the LH power. Therefore, it can be concluded that the global particle confinement improves at low LH power.

The fluctuation levels, both of the density and poloidal electric field, decrease during the first LH power steps and increase with higher power. The jump after the fourth power step is related to the switching between the two LH antennas. During the second phase of the power scan the lower grill is activated, which is connected with the probe through the same magnetic flux tube. The much higher fluctuation level in this case seems

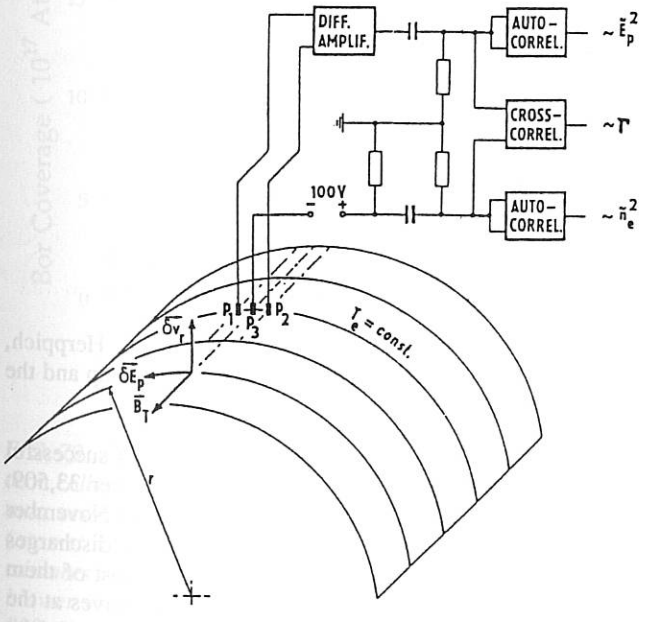

FIG. 75: Setup of fluctuation measurements with Langmuir probes.

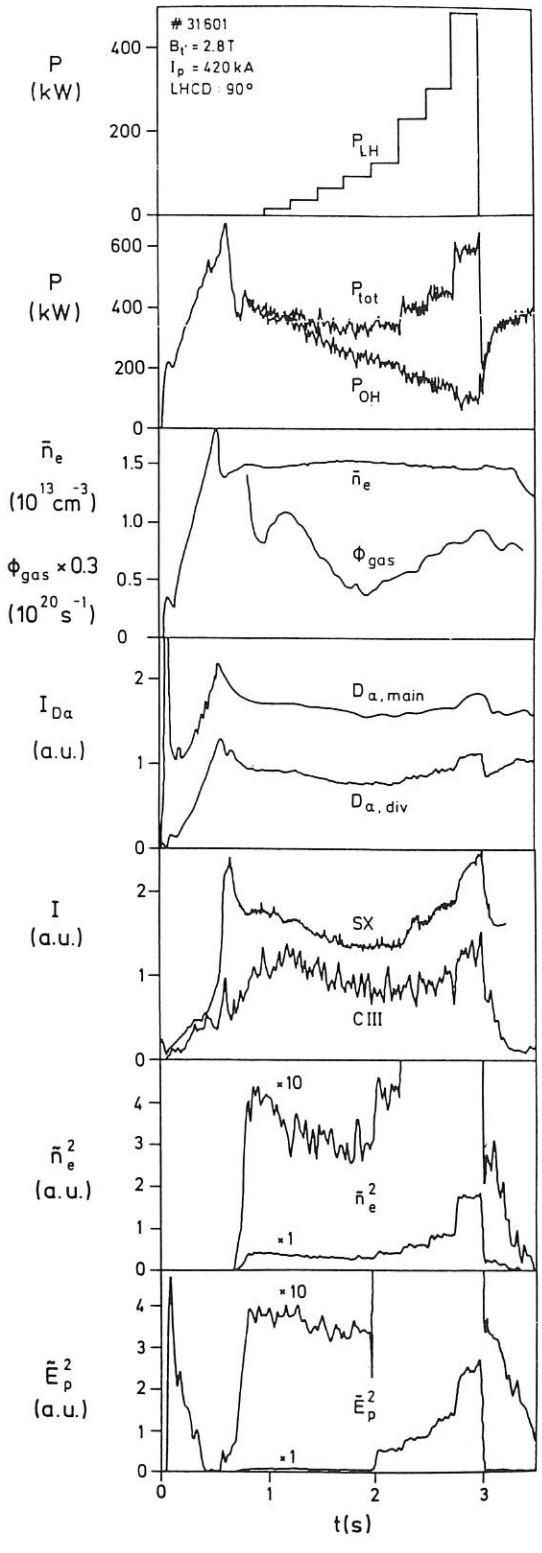

FIG. 76: LH-power scan in a single discharge with measurements of density and electric field fluctuations.

to be caused by local power deposition in front of the grill antenna.

The values for the particle confinement time τ_p determined from the global particle balance and from the turbulent flux agree well as long as the probe is not located inside a region of enhanced turbulence. The particle confinement time τ_p as well as the energy confinement time τ_E increase for the first LH power steps when the resulting total power input $P_{tot} = P_{LH} + P_{OH}$ remains below the initial OH power input. The highest confinement time is reached at the lowest value for P_{tot}. With higher total power, τ_E and τ_p gradually decrease.

1.7.10 Transport analysis

LH power deposition and heat transport in LHCD plasmas were modelled with the ASTRA 1.5D transport code developed at Kurchatov Institute. The code was run both in predictive and interpretive mode by using either a set of transport equations or the experimentally measured profiles of densities and temperatures as input. Broadening of the launched LH wave spectrum is obtained through a diffusive model approximating the result of separate ray-tracing calculations with the full wave equations. A power absorption coefficient as measured in the experiment is already reached after a few wave passes.

All coefficients were adjusted in parameter studies on one particular discharge. They were then kept unchanged for the simulation of experiments in the range $\bar{n}_e = 1.4 - 4 \times 10^{13}$ cm^{-3} and variation of the LH power with $P_{LH} \leq 1.1$ MW. The dependences of thermal electron heating, pressure anisotropy and current profile changes observed in the experiment are well reproduced by the code calculations. For the central electron temperature measured and calculated values are compared in Fig. 77. Radial profiles of the electron temperature and heat conductivity are shown in Fig. 78.

Suppression of sawteeth and the m=1 mode is modelled self-consistently in the code. With partial LH-current drive the current profile slightly broadens in the central region and q(0) rises close to 1. In recharging conditions with high-power LHCD the j(r) profile broadens further and the q=1 surface completely disappears. This behaviour agrees with the experiment where the m=1 mode is stabilized with high-power LHCD and broadening of the current distribution is inferred from a drop of l_i.

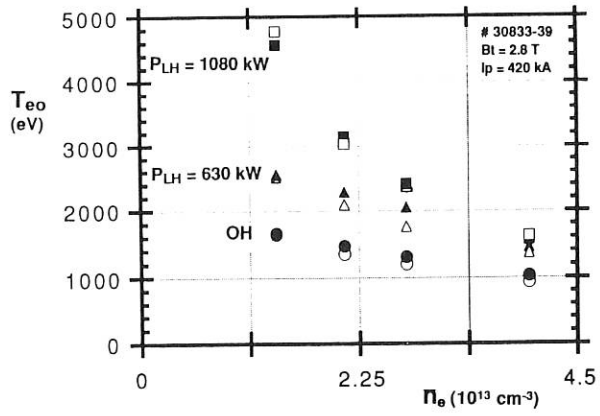

FIG. 77: Density dependence of the central electron temperature in OH and LHCD discharges. Closed symbols are measured, open symbols calculated values.

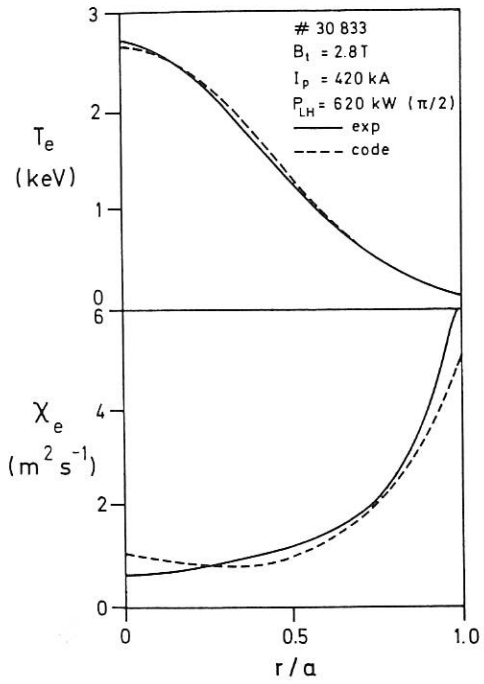

FIG. 78: Radial profiles of electron temperature and heat conductivity in experiment and transport code calculation.

Strong peaking of the electron temperature profile is obtained after suppression of the m=1 mode, as observed in the experiment. The electron heat conductivity in the central region then falls below the values of the ohmic phase and approaches the magnitude of neoclassical heat conductivity.

2. OPERATION OF ASDEX

2.1 Operation of the Experiment

(in collaboration with J. Gernhardt, F. Gresser, G. Herppich, G. Klement, P. Krüger, the ASDEX Assembly Group and the ASDEX Technical Team)

On Friday, 10 August 1990, more than ten years of successful operation of ASDEX ended with discharge number 33,509. The last experimentation phase of ASDEX began in November 1989. In this period a total number of 4,212 plasma discharges during 77 experimental days were carried out, most of them with neutral beam injection (NI) or by coupling waves at the lower hybrid frequency of 2.45 GHz (LH). In most cases the application of LH required again operation of the main field coils at the maximum value of 2.8 Tesla with long cool-down

times between the plasma discharges (11 min). All systems ran very reliably and the vacuum conditions were excellent. Only a break of one current lead to the ohmic heating coils at the end of February 1990 necessitated the dismounting of the whole north-west beamline together with the large sliding flange. The sophisticated and precise repair of the current lead as well as the remounting of the NI system took 6 1/2 weeks. In July 1990 a water leak occurred in an other OH current lead. A provisional but excellent arrangement allowed the operation of ASDEX with restricted parameters ($B_0 \leq 2.2$T, $I_{OH} \leq 20$ kA, flat-top time ≤ 2 s) till the scheduled shut-down. Fortunately the contacts between the multipole coils and the current leads showed no serious increase in contact resistance during the last experimental phase.

The majority of the plasma discharges were heated by NI, often together with LH. The first transition from co- to counter- operation with H^0 injection took place in the last experimental day of 1989 till 19 January 1990. Co-injection with D^0 started on 8 February 1990 till the unexpected shut-down in March 1990. Deuterium operation of the beamlines necessitated again covering of the ASDEX hall with the wooden ceiling to reduce the high neutron flux. During the last experimental phase since 19 April 1990 several transitions from co- to counter-operation with both H^0 and D^0 injection were done. In the last five weeks of ASDEX operation only with H^0 co-injection was possible because of the necessary reduction of the strain on the broken OH current lead and the need for accessibility.

As experienced in the preceding phases no severe temperature rise in or troublesome damage to the water-cooled copper target plates or the stainless-steel meanders could be observed in spite of the long heating pulses with high power of the heating systems (e. g. NI pulse lengths of up to 4.5 s) and very exotic discharges (e. g. $\Delta z = +0.14$ m). The water-cooled copper melting probe, placed near the upper neutralizer plate, showed in some cases, however, severe damage caused by thermal overload and by, perhaps, high-energy electrons.

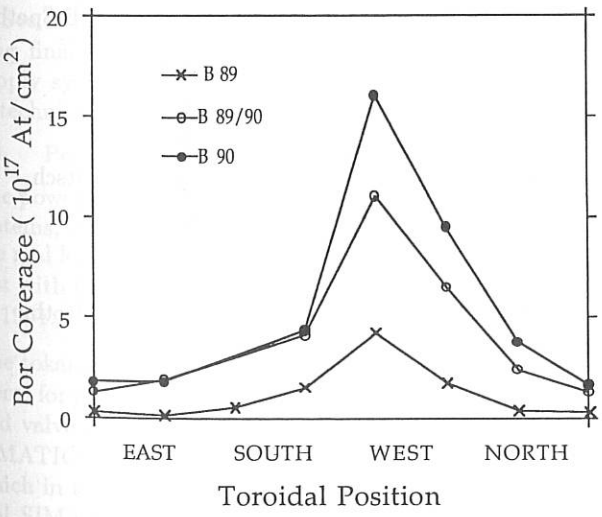

FIG. 79: The deposited boron layers as analyzed from long-term collecting probes toroidally distributed in the ASDEX vacuum vessel. Near the gas inlet the coverage of boron layers (atoms/cm^2) is highest. B89: three boronization runs in gas mixtures with 80% He + 10% B_2H_6 +10% CH_4 and no Roots blower in the exhaust system. B89/90: two boronizations in 80% He + 10% B_2H_6 +10% CH_4 and with Roots blower. B90: two boronizations in 90% H_2 or He + 10% B_2H_6, also with Roots blower.

The boronization system was modified in respect of gas throughput and safety aspects (the working gas diborane is toxic and explosive). By installing a Roots blower between the turbomolecular pump and thermal decomposer (700° C) the deposition of boron/carbon or pure boron layers resulted in improved deposition as analyzed by long-time collecting probes toroidally distributed inside the vacuum vessel (Fig. 79). The highest coverage was gained by using a gas mixture with 90% H_2 or He + 10% B_2H_6 without methane. To improve safety, the whole gas inlet for diborane and even the thermal decomposer were of coaxial design. A special gas case for the diborane bottle and a second diborane monitor completed the equipment. No diborane was detected outside the vacuum components of ASDEX during deposition phases. As expected, no diborane was detectable in the vented vacuum vessel, because during boronization runs B_2H_6 decomposed completely into harmless products. The impact on plasma parameters with boronized vacuum vessel walls is discussed in Sec. 1.3.1.

2.2 Long-pulse Beam System

(in collaboration with R. Bilau-Faust, J.-H. Feist, H. Lohnert, R.-C. Kunze, W. Ott, K. Wittenbecher (Technology Division), W. Melkus (Central Technical Services))

During the final 5 months of the experimentation phase in 1990, the majority of ASDEX discharges were again heated by neutral beams (about 300 discharges per month). Nearly 100% availability was achieved for this period: Only one ion source out of the set of 8 sources developed a vacuum leak but could be replaced within one week.

The extremely tight experimental programme of ASDEX could only be accomplished with high reliability of the ion sources. Not to jeopardize the tokamak programme as a whole, the neutral beam pulse length was restricted to 2 s and the power to about 80% of the nominal power level (3 MW) sufficient for most of the experiments. These restrictions were abandoned for the long-pulse H-mode programme (see Sec. 1.4), which was a major element in this phase. Pulse lengths of 4.5 s were achieved. The source behaviour during these experiments clearly indicated that an additional increase of the pulse length would have been possible by continuing the long-pulse operation.

To summarize the performance of the neutral beam system upgraded for long-pulse operation, the energy injected into the discharge was increased by about one order of magnitude. Long-pulse operation with pulse lengths close to $100\tau_E$ were achieved close to the maximal power level both for L and H-mode discharges.The high reliability of the system, on the other hand permitted numerous experiments with neutral injection as the main heating method with pulse lengths between 1 and 3 seconds, adequate for most ASDEX research topics.

ASDEX UPGRADE PROJECT

(Head of Project: Dr. Walter Köppendörfer)

ASDEX Upgrade Project Group:
Ch. Aubanel, A. Bauer, H. Bauer, K.Behler, A. Berg, H.J.Berger, A. Birkmeier, H. Blank, M. Blaumoser, H.Bruhns, E.Buchelt, S.Cha, Ch.Dorn, R.Drube, A.Field, D. Georgens, J.Gernhardt, J.Gruber, D. Haferkamp, M. Harnau, F.Hartz, J. Herrmann, H. Hohenöcker, D.Jacobi, E.Kaplan, G.Klement, H.Kollotzek, A.Krause, E.Lackner, G.Lieder, H. Lindner, K.Mattes[1)], R.Merkel, V.Mertens, J.Oswald, B. Pachur, M.Pillsticker, G.Prausner, G.Raupp, G.Reichert, H.Richter, Th.Richter, S. Sänftl, N.Salmon, J. Schaal, K.Schindr, H.Schneider, G.Schramm, G.Schrembs, S.Schweizer, U.Schweitzer, U.Seidel, H. Steidl, B.Streibl, W. Teufl, M.Troppmann, H.Vernickel, T. Wendt, F.Werner, A.Wieczorek, H. Wirth, W.Woyke, F. Wunderer, D.Zasche, T.Zehetbauer. G. Zimmermann,

[1)] Kernforschungszentrum Karlsruhe

Tokamak Theory Group:
O.Gruber, O.Kardaun, K.Lackner, P.J.McCarthy, P.Martin, H.P.Menzler, J.Neuhauser, R.Schneider, W.Schneider, R. Wunderlich, H.P.Zehrfeld

Central Technical Services:
N.Debudey, H.Gillhuber, H.Goss, R.Hadersbeck, A.Hasenmiller, H.Hofmann, W.Jakobus, S.Kamm, M.Kluger, H.Kosniowski, M.Kottmair, H.-J.Kutsch, T.v.Larcher, E.A.Maier, W.Melkus, S.Mukherjee, E.Peschl, E.Sebastian, R.Scherzer, B.Sombach, E.Trcka, R.Zanner

ASDEX Upgrade Diagnostic Group:
H. Röhr, U. Schumacher, C. Andelfinger, M. Bessenrodt-Weberpals, H.-S. Bosch, K. Büchl, A. Carlson, Ch.Ch. Chu, A.Eberhagen, H.-U. Fahrbach, D. Fieg[1], A. Field, Ch. Fuchs, G. Fußmann, O.Gehre, J. Gernhardt, S. Götsch, G. Haas, W. Herrmann, G. Janeschitz, F. Jenichen, A. Kallenbach, M. Kornherr, H. Krause, K. Krieger, R. Lang, G. Lieder, R. Loch, K.-F. Mast, H.-M. Mayer, D. Meisel, V. Mertens, H. Murmann, J. Neuhauser, H. Richter, N. Salmon, H. Salzmann, W. Sandmann, H.-B. Schilling, J. Schweinzer, F.X. Söldner, K.-H. Steuer, M. Ulrich, H. Vernickel, U.Wenzel, K. Wira, H. Zohm, W. Beck, H. Birkmeier, J. Bönisch P. Cierpka, W. Drechsler, J. Fink, H. Frischmuth, J. Herrmann, J. Krippner, E. Oberlander, M. Oswald, M. Oswald, D. Pohl, A. Roman, K. Schindler, E. Schmid, G. Schmitt, G. Stichs, A. Stimmelmayr, G. Weber, L. Zölch

Neutral Injection Group:
R.Bilau-Faust, J.L.Dunne, J.H.Feist, K.Freudenberger, B.Heinemann, W.Kraus, R.-C.Kunze, H.Lohnert, E.Morris, W.Ott, F.P.Penningsfeld, F.Probst, J.Sielanko[2)],E.Speth, A.Stäbler, R.Süß, O.Vollmer, K.Wittenbecher

[2)] University of Lublin, Poland

Ion Cyclotron Resonance Heating Group:
M.Ballico, J.Bäumler, W.Becker, F.Braun, R.Fritsch, F.Hofmeister, J.-M.Noterdaeme, S.Puri, F.Ryter, R.Schubert, H.Wedler, F.Wesner

Other Groups:
W.Amenda, G.Mannhardt, W.Poschenrieder, J.Roth, G.Venus

1. SUMMARY OF PROGRESS

1.1 Tokamak System

Assembly of the tokamak system proceeded on schedule. At the end of March 1990 assembly was completed and eight of 14 turbomolecular pumps were attached. In July the vacuum vessel was commissioned by pumping it down to a base pressure of 10^{-7} mbar and heating it up to 130 C in a 96-hour cycle. No graphite structures were installed at that time. From July on to the end of 1990 the TF magnet was energized in steps up to 3.25 T in flat-top pulses of up to 10 s. The temperature and displacement control

systems for the vacuum vessel and TF magnet were put into operation and tested for this purpose. These tests also encompassed part of the power supply system and cooling systems in conjunction with their respective SIMATIC preprogrammed control systems.

After re-opening of the vacuum vessel, installation of the graphite tiles for heat shields and divertor target plates was carried out and further in-vessel diagnostics were installed. The turbo molecular pumps were supplemented up to the total number of 14.

1.2 Periphery, in Torus Hall

The high-voltage and high-current connecting elements for the poloidal field (PF) coils suffered some delay due to certain fabrication and quality assurance problems. Their assembly and high-voltage testing was completed in November 1990 with satisfactory results. All PF coil-cooling circuits were completed and pressure tested, so that all supply circuits for all tokamak machine components were now available.

The cables for technical diagnostics and control circuits were installed in the torus hall by means of a modular prefabricated tube system. The cables for first-day physics diagnostics were also installed.

First diagnostics, mainly magnetic measuring probes and loops, spectrographs and cameras were installed and attached. The fabrication of the DCN interferometer was delayed by a few months, such that first density measurements and density feedback control have to be accomplished with a one-cord 2 mm microwave interferometer. The YAG laser Thomson scattering system is well under way.

In Sec.3 special features and events are described concerning final assembly of ASDEX Upgrade, completion of supply systems and auxiliary equipment, and first steps of technical operation.

1.3 Periphery, outside Torus Hall

The power supply systems including the SIMATIC control systems, have all been completed and tested either with the real loads or dummy loads or short circuited. The last test with the real loads (PF coils) will be carried out early in 1991.

The tokamak machine control and control of auxiliary systems for plasma heating, density control, pumping system and valve control and diagnostic control encompasses 15 SIMATIC subsystems (programmable logical controllers) which in turn are controlled and interconnected to a central SIMATIC control and visualisation system, the SLS (SIMATIC Leitsteuerung). Most of these systems and the central control systems are working and have been tested. Within this preprogrammed feedforward system a fast feedback plasma control system controls the discharge and plasma position. Overall control, discharge design, real-time technical control, plasma feedback control and monitoring and checking of control computers is managed by six real-time computers individually adjusted to their tasks. Fast plasma interpretation and feedback control have been tested, the tokamak simulation code TSC serving as plasma source and control object. This way the plasma control algorithm was also optimized for minimum effort and power load on the PF control coils.

The timing of all control and diagnostic events is set by a timing system which allows arbitrary time marks to be set in pace with a central clock. These signals can be individually addressed to local timer boards of control units and diagnostic systems. The timer system is installed and tested to the extent required for first plasma operation.

Thus at the end of 1990 the ASDEX Upgrade tokamak system, the electric power supplies, the cooling circuits, the vacuum pumping system, technical control and data acquisition system, the discharge control and plasma feedback control system, the required minimum of plasma diagnostics and the safety system were all essentially complete or in a status allowing first technical machine and discharge operation. This is planned for January and February 1991.

2. PHYSICS PROBLEMS AND OTHER CONSIDERATIONS

2.1 Precision of Plasma-relevant Machine Components

During assembly careful attention was given to the precise positioning of components which can influence the plasma shape and equilibrium properties. These are:

- the TF magnet, which determines the circles of toroidal field lines around the main axis;
- the vacuum vessel with the heat shield and divertor target plate structure;
- the position of the poloidal field coils with regard to the torus main axis.

Misalignment of the vacuum vessel and in-vessel components against the toroidal field line circles leads to toroidally inhomogeneous heat load distribution on divertor target plates and heat shield. Misalignment of the poloidal field coils, the position of their main axis with regard to the TF magnet axis and deviations of the coil currents from circles leads to magnetic islands within the plasma.

The basis for the tokamak component assembly was an optical measuring system in the centre with a theodolite. An equivalent system was used at the octant assembly stand. The torus main axis was determined by using an optical plummet with a marked mirror at the torus hall ceiling.

The toroidal field (TF) coil support structure could be positioned with an accuracy of 0.1 mm. The TF magnet axis, as defined by the straight inner legs of the 16 TF coils, is precise within 1 mm over a region of - 1.5 <Z< 1.5 m with regard to the ideal optical axis.

The vacuum vessel position measured at the eight big port flanges at R = 3420 mm towards the TF coil support structure is precise on the average within dR = 1.4 mm and dZ = - 0.14 mm, with maximum deviations of dR = 2 mm and dZ = 1.5 mm. This knowledge allowed to position

the console tables for target plates and heat shields to be placed inside the vessel with an accuracy of dR < 1 mm with regard to the ideal toroidal field line circle. The uncertainty of the circle of this structure compared with a real field line circle is therefore dR < 2 mm. This can be corrected to a certain extent, when a toroidally inhomogenous heat load distribution is observed, by adjusting the vacuum vessel.

The tolerances of the vertical field coil postions range up to 10 mm in dR and dZ owing to tolerances of the copper conductors in the winding packages and to tolerances in the positioning of the coils. This, however, already produces magnetic islands of tolerable radial extent. Figure 1 shows a comparison of islands produced by one V2 coil that was out of centre by 10 mm with the case of the same coil off centre by 30 mm.

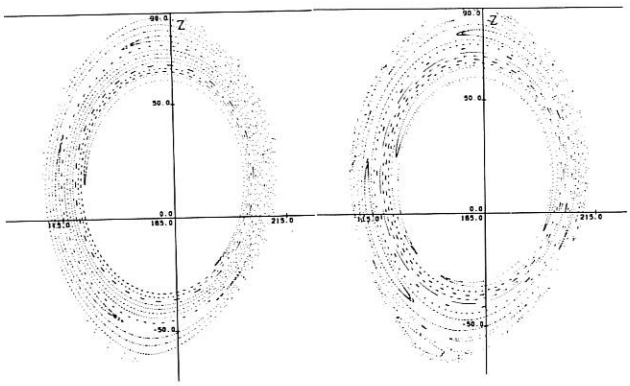

FIG.1 Magnetic islands produced by shifting the lower V2 coils horizontally out of center for a Single Null 1.6 MA plasma.
Left: by a shift of 10 mm;
right: by a shift of 30 mm.

2.2 Plasma Control

This year we concentrated on plasma formation and start-up under the constraints of the reactor-relevant PF system, development of discharge scenarios and improvement of our feedback methods.

The PF coils in AUG, being outside the TF coils, cause two problems for plasma start-up phase. Firstly, owing to the long ranging fields of the coils precharging of them - necessary to avoid overvoltage at the PF power supply rectifiers during breakdown (plasma loop voltages up to 35 V are produced by an OH circuit breaker) and helpful for reaching the currents necessary for divertor configurations within short times - results in undesired stray fields during the breakdown phase. Secondly, after breakdown the current ramp rates of the PF coils are not sufficient for obtaining divertor configurations during the initial plasma current rise. Therefore, we plan to start the discharge as a circular limiter plasma at the inner toroidal heat shield. The magnetic limiter is provided as early as possible to reduce plasma-wall interaction.

On breakdown the stray fields produced from the OH and PF currents and the induced currents in the passive elements (OH structure, vessel and PSL) were calculated with and without allowance for saddle currents due to high-resistance bellows in the vessel and to radial gaps in the OH supporting structure. The resulting stray fields can be compensated for currents in the inner active control coils. After current initiation the breakdown voltage will increase the plasma current up to 100 kA within 10-20 ms when the plasma is modelled by a rigid loop with variable resistance and inductance simulating the change in the plasma cross-section. After opening of the OH circuit breaker the plasma current and shape evolve at a much slower rate limited by the power supplies and the avoidance of unstable plasma current distributions.

During this start-up phase as well as in strong heating or ramp-down phases the feedback facilities for the plasma equilibrium control by PF coils - each producing all multipole moments - are usually incomplete with respect to the plasma position, shape and current and additionally suffer from the limited power capabilities. In this situation a systematic procedure is highly desirable to determine a complete set of the required control input for the PF coils as close as possible to the "correct" one corresponding to the equilibrium evolution wanted. Moreover, the available feedback capabilities are saved for unpredictable events.

To meet this need, the plasma control code PCC was developed and applied to the plasma discharge design for ASDEX Upgrade. Based on a large multidimensional variety of calculated equilibria, the program calculates the input voltages and currents of the PF coils, which move the plasma equilibrium along the desired trajectories of equilibrium parameters. The resulting trajectory of the equilibria is compatible with the given electromagnetic properties of the PF system, including the inductive couplings. Upper and lower limits for any variable can be applied and possibly contrary requirements are balanced to some extent by means of weight factors applied by the user.

The first applications to circular limiter and SN divertor discharges confirmed the ability of PCC to yield within a short computation time (below 20 s CRAY time for a real discharge time of 1 s) the required nominal input to the PF system of AUG. Within the exactness of the necessary estimation of the β_p and l_i evolution the results are in reasonable agreement with corresponding results from the Princeton tokamak simulation code TSC. A certain problem ensues from the ambiguity of the plasma position of inner limiter configurations, which injures the utilization of the equilibrium data basis to some extent. Despite this basic problem of a reactor-relevant PF coil system far away from the plasma, its practical consequences for the described method seem to be limited.

For the final feedback control the plasma control variables are determined by a function parametrization algorithm (FP) using magnetic measurements and are calculated together with the resulting control input to the PF system by a transputer computer. Both the FP method and the

control algorithm were extensively tested in the start-up, flat-top and additional heating phases using TSC.

A comparison of the plasma parameters obtained from FP with those from TSC showed excellent agreement in nearly all simulations. Tolerable differences occurred when the plasma evolves from a limiter to a divertor configuration or vice versa. In the early start-up, when the current in OH transformer is high and the induced plasma current still low (about 100 kA), non-negligible stray fields of the OH transformer at the probe positions have to be taken care of. Otherwise the radial plasma position reconstructed from FP - was about 6 cm off at these low currents compared with the TSC data.

In a next step the envisaged control algorithm was implemented in TSC and fed with the FP parameters to simulate the "closed loop" operation as it will be done online with the transputer system and the power supplies. The rules for tuning the parameters of the feedback algorithm were derived on the basis of low-order models, which are reduced forms of a multivariable lumped-parameter model (see also Annual Report 1989). The intensive tests in all plasma shot phases showed that the tuning of the control parameters had to be adapted owing to the different dynamic behaviour of the plasma column in the TSC simulations in order to optimize the control performance. The resulting parameter set could then be used for all discharge simulations and worked properly; especially parameter jumps occurring at limiter/divertor transitions as mentioned above did not seriously influence the feedback control. The additional heating phase was simulated with weak and strong anomalous thermal transport. It turned out that the feedback controller could cope well with the necessary control requirements owing to the changes in β_p.

As an example, Fig.2 shows the time history of the vertical position control variables during a TSC simulation of a plasma shot. The plasma current rises from 100 kA to 1.2 MA within the first 1.5 s. In the early phase the controller gets the command Z_c^{soll} to push the plasma 8 cm above the midplane while the plasma evolves from an inner limiter to a single-null lower divertor plasma owing to an additionally prescribed outward shift. During heat-up (1.5 - 2.5 s) with 12 MW of additional heating a further vertical shift to 12 cm is carried out and after the end of the additional heating, at 4 s, the plasma moves back to the torus midplane in the current ramp-down phase. In all phases the vertical position Z_c^{ist} follows the command Z_c^{soll} very closely. Severe perturbations in the early start-up and shut-down phases are controlled on a very fast time scale by the inner control coil currents I_{cz}^{ist}, which are well within their operational limits during the whole simulation. Each control coil has its own feedback control loop commanded by the vertical position controller (signal I_{cz}^{fb}) To relieve the inner control coils, their control currents are fed back the currents of the external PF coils V2 (I_{vz}^{ist}). This additional feed loop for the V2 coils uses the command signal I_{vz}^{fb}, which now represents online computed corrections for the preprogrammed V2 currents in order to track the vertical plasma position as defined by the command Z_c^{soll}. Therefore the control currents occur only transiently. The radial position and the plasma current control work similarly.

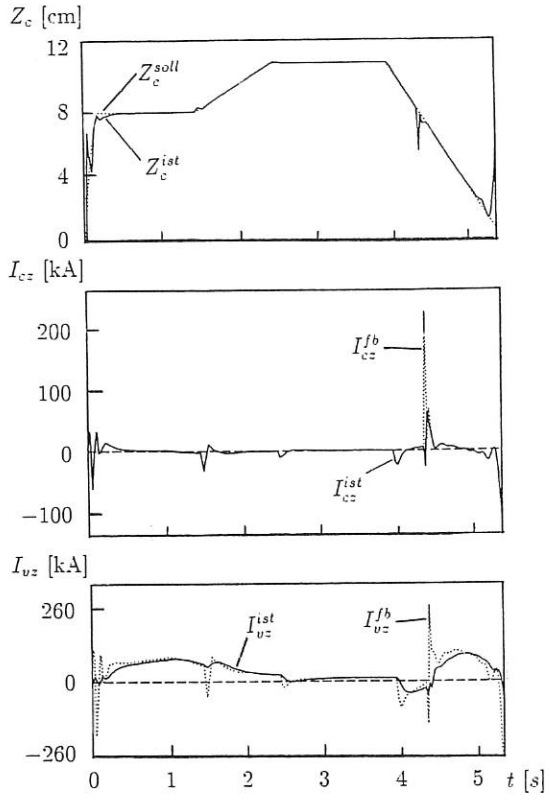

Fig.2 Command (indices ^{soll} and ^{fb}) and resulting (index ^{ist}) control variables for vertical position (Z_c) and coil currents (I_{vz}, I_{cz}).

2.3 Vertical Plasma Displacement, Halo Currents and Plasma Current Disruptions

The concept for calculating different loads on the vacuum vessel and internal structure was to study plasma disruptions at full current for vertical displacements in a region of the plasma axis between -0.15 < dZ < 0.15 m. For larger vertical displacements the plasma column was assumed to peel off with touching the vessel and installation structures. The current was thought to lose also the current density of the peeled-off layers, by being reduced this way.

Recent experience from JET and D III D, however, shows that during unstable vertical displacements of the plasma wall currents are induced which essentially flow in the plasma scrape-off layer and preserve the toroidal plasma current, although the plasma cross-section diminishes. The current bridge between the plasma and structure are so-called plasma halos. These poloidal halo currents produce vertical forces on the plasma and slow down the vertical displacement. Vice versa these forces lead to increased load on the vacuum vessel and structure. Installations such as holding fixtures for target plates and heat shield tiles, protection limiters and ICRH antenna structures can experience high loads when the currents in the structure are directed perpendicular to the toroidal magnetic field.

Measures decided to tackle these problems were:

- limitation of the plasma current during the first phase of operation and measurement of the currents within target plate consoles and other structures;
- development of calculational models for plasma equilibria including wall currents;
- development of reliable methods of disrupting the plasma current if a certain vertical displacement is exceeded;
- improved design and construction of enforced holding fixtures.

All this work has been initiated and is under way.

2.4 Time Schedule

During the second half of 1990 the vacuum vessel was commissioned, the vacuum pumping system put into first operation and the TF magnet energized and tested, including water-cooling circuits and all technical measurements. All electric power supplies were run and tested, controlled by their SIMATIC preprogrammed controllers. At the end of 1990 all poloidal field coils were connected to their power supplies and cooling circuits. All first diagnostics really necessary for first plasma operation had also been installed. The machine control system and the plasma control computers were progressing at a pace allowing early in 1991 first discharge and plasma start-up operations to the limited extent required.

The next steps of the programme are:

- January 1991
  leak test after last vessel opening, commissioning of pumping system and control, test of vertical field coils and supply controller adjustment;
- February
  test of OH transformer circuits, baking of vacuum vessel, glow discharge cleaning, first plasma breakdown experiments;
- March
  plasma start-up experiments, plasma experiments and plasma control with R2 plasma feedback control computer;
- April to end of 1991
  intermittent periods with open and closed vessel for: mounting and installation of next diagnostics, installation of ICRH antennas and coaxial lines, mounting of valve bellow unit of first neutral injector, plasma experiments with elongated divertor plasmas.

3. TOKAMAK SYSTEM

3.1 Toroidal Field (TF) Magnet

During 1990 the vault bladders of the assembled TF magnet were cured and the magnet was operated up to 3.26 T (70 kA). Both curing and operation were controlled by the R31 fast data processing computer, monitoring displacements, coil temperatures and the power supply. The cooling circuits were controlled by an additional SIMATIC system. Since assembly of the vacuum vessel and PF coils was running in parallel, the time for testing the TF magnet was severely restricted. However, the current control of the power generator could be optimized for the TF magnet load and the loading time of the generator flywheel determined as a function of its energy content. Both items are preconditions for reasonably arranging the time sequence of a plasma shot.

3.1.1 Hardening of the vault bladders

The inner legs of the 16 TF coils form a vault. There is no central column. To achieve homogenous force transfer within the vault region, resin-filled steel bladders are inserted between the inner coil legs. There are also resin-filled steel bladders between the turn over structure (TOS) and the coils. All these bladders were filled and precured at ambient temperature. The resulting mechanical strength is then still rather poor (10-20 Mpa for compression), but adequate for the TOS bladders. However, the vault bladders require additional curing at elevated temperature. For optimum strength a curing time of 12 h at 65 C was recommended for the resin. Its compressive strength then rises to about 200 Mpa.

For the final curing the coils were heated electrically. To avoid overheating, two independent temperature/current control systems were installed. The temperatures were monitored by 32 PT-100 resistors located adjacent to the upper and lower ends of the vault region. In steady state the heat losses were equivalent to a current of only 1.5 kA. The allowed maximum current of 6 kA caused a vault compression below 1 Mpa and yielded a sufficient temperature rise rate of 40 C per h.

3.1.2 Operation of the TF magnet

Since there is no central column, the main concern was whether the vaulted coils would return to their initial positions after a series of current pulses. Up to now no relevant vault distortions have been found. The vault, prestressed by external rubber springs (100 kN/coil), remained stable.

Figure 3 shows the measured radial displacements over B_o^2. The measurements were executed at field levels of 1.4, 2.05, 2.51, 2.91 and 3.26 T. The resistors measuring the displacements are located near the apex of each coil (top and bottom). Hence the measured displacements are a superpositioning of the actual vault deformations and bending effects within and beyond the vault. The plotted values are the average over all 16 coils. The top displacements are larger than the bottom displacements. The deviation from the least-squares straight line is about 15 %. Up to now there is no really plausible explanation for this tilting effect. Friction forces at the bottom coil support pads are negligible with respect to the vault forces. However, bending deformations resulting from them would have the right trend. Also shrinkage differences between top and bottom of the vault bladders are imaginable since the resin filling time is not negligible in relation to the precuring time. To assess the vault tilting effect in detail, the FE-model of the design phase, which assumed symmetry with respect to the torus plane, will be adequately extended.

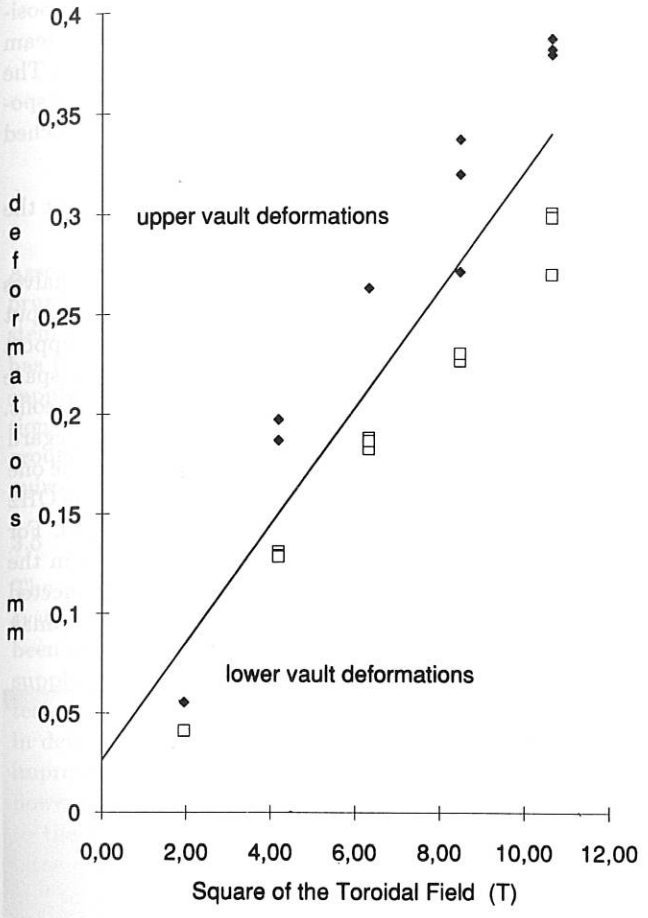

FIG.3 Measured displacements of the TF magnet as a function of the magnetic field to the square. The measurements were taken at B_o (T) = 1.4, 2.05, 2.51, 2.91 and 3.26

The original design computations predicted a slightly convex vault deformation shape and, as a consequence of this, much smaller deformations at the measuring position than within the vault. The deformations actually measured are larger than those computed. They amount to about 60 % of the computed vault deformations. This indicates, taking also the measured deformations on the outer leg of each coil into account, that the vault is less convex than predicted. Hence smaller shear stresses than computed should act.

3.1.3 Envisaged time sequence of a plasma shot

For plasma breakdown ASDEX Upgrade requires a breaker circuit for the current of the ohmic heating transformer (OHT). After the OHT is charged the charging current is transferred from the breaker to the parallel commutation resistor. This resistor, whose size can be varied, reduces the L/R time of the OHT adequately for generating a loop voltage of up to 35 V (design limitation). For Phase 0 only 19 V is at present released. The commutation process requires discharging of a capacitor to quench the breaker current. This capacitor has to be charged prior to the OHT. The charging of the capacitor and OHT and the breaker circuit are automatized by a SIMATIC control system and synchronized by the central timer system via 4 trigger signals. The maximum time for the whole process is limited to 60 s. Charging of the OHT and breakdown ought not last longer than 5.5 s.

The preparations for OH breakdown have to be closely synchronized with the generation of the flat-top current of the TF magnet, i.e. the generator flywheel has to be loaded in time. Tests have shown little scatter for the loading time. Its dependence on the flat-top number of revolutions, defining the available energy content, is sufficiently linear over the whole region of operation. The required energy can be predicted very accurately from the now well-controlled pulse shape of the TF current. With two further trigger pulses for the TF circuit it is thus possible to automatize the plasma breakdown. In the first stage all trigger pulses will be rigidly fixed to their calculated values (plus an adequate safety margin allowing for scatter). At a later stage signals from the OH and TF circuits will be taken into account by the central computer (R1) for more intelligent synchronization.

3.2 Poloidal Field Coil System

The poloidal field coils were assembled in their final position and adjusted within their holding fixtures. The assembly procedure is described in Sec. 3.4 and the positioning precission of coils discussed in Sec. 2.1.

Considerable effort went into the design and fabrication of the power feeding lines and the connecting elements to the coils. Owing to the limited space under the tokamak system and high voltage, up to 50 kV, careful adjustment was required. 125 water-cooling circuits had to be connected, each equipped with a flux controlling gauge. This work was completed at the end of 1990. A high-voltage testing of all electric circuits then followed.

3.3 Vacuum Vessel and Pumping System

As reported last year, construction of the plasma chamber was completed in 1989. The in-vessel components and the pumping system were installed. The plasma chamber proper is water-cooled during plasma operation. The same circuit is used for bake-out by charging it with hot, pressurized water. The bake-out temperature is 150 C. Connecting pieces and ports, added to the vessel after torus assembly, are heated electrically. A control system ensures homogeneous heating of the vessel during bake-out.

With the larger part of the pumping system being installed by mid-1990, a bake-out and pumping test was carried out. The interplay of the two heating systems worked alright. No leaks developed at the welding seams during or after bake-out. This was the final test in commissioning of the plasma vessel.

Mounting of the in-vessel components started with the electric and magnetic probes. This was followed by the heat shield, divertor plates, "additional limiters" and baffles preventing easy recycling of neutrals from the divertor chamber to the main plasma. As final step, all surfaces close to the plasma were equipped with graphite tiles. The vessel interior is now ready for plasma operation.

3.4 Completion of Tokamak System Assembly, Assembly of the Upper Spoked Wheel

At the end of 1989 the central ohmic heating coil OH1 and the upper vertical field coil V3 were put in place. The upper vertical field coil V2 and the outer control coil COA had been already put in position, resting provisionally on the TF magnet support structure.

The poloidal field coil support structure was also erected up to the sixteen 5 m vertical support beams. For final completion only the upper spoked wheel had to be put in place. This wheel is a separate component of the PF support structure, with a diameter of almost 9 m. It consists of 16 spokes (double-T beams) and the connecting beams which form the rim. It weights 30 tons.

The OH1 and the upper OH2 are connected to the nub and the upper V1, V2 and COA coils are attached to the spokes of the wheel so that the vertical forces acting on these coils are transferred to the wheel.

The assembly of this upper wheel together with the positioning of the coils was a challenge to the assembly team because of the large weight and the required precision. The load-carrying capability of the crane did not allow the spoked wheel to be hoisted together with the coils attached to it.

The particular circumstances made it necessary to put the spoked wheel into parking positions 3 times:

- The wheel was brought into the torus hall in halves because of the limited clearance of the door, put on top of the 16 vertical beams of the PF support frame and connected to a full wheel. All other space in the torus hall was occupied, mainly by PF coils.
- For proper adjustment of the OH2 coil with regard to current connections and water outlets on the one hand and to the spoked wheel on the other the OH2 coil was first test mounted to the spoked wheel. For this purpose the spoked wheel was taken from the PF support structure and the OH2 coil connected to it. Both were put back on top of the tokamak system for fitting adjustments.

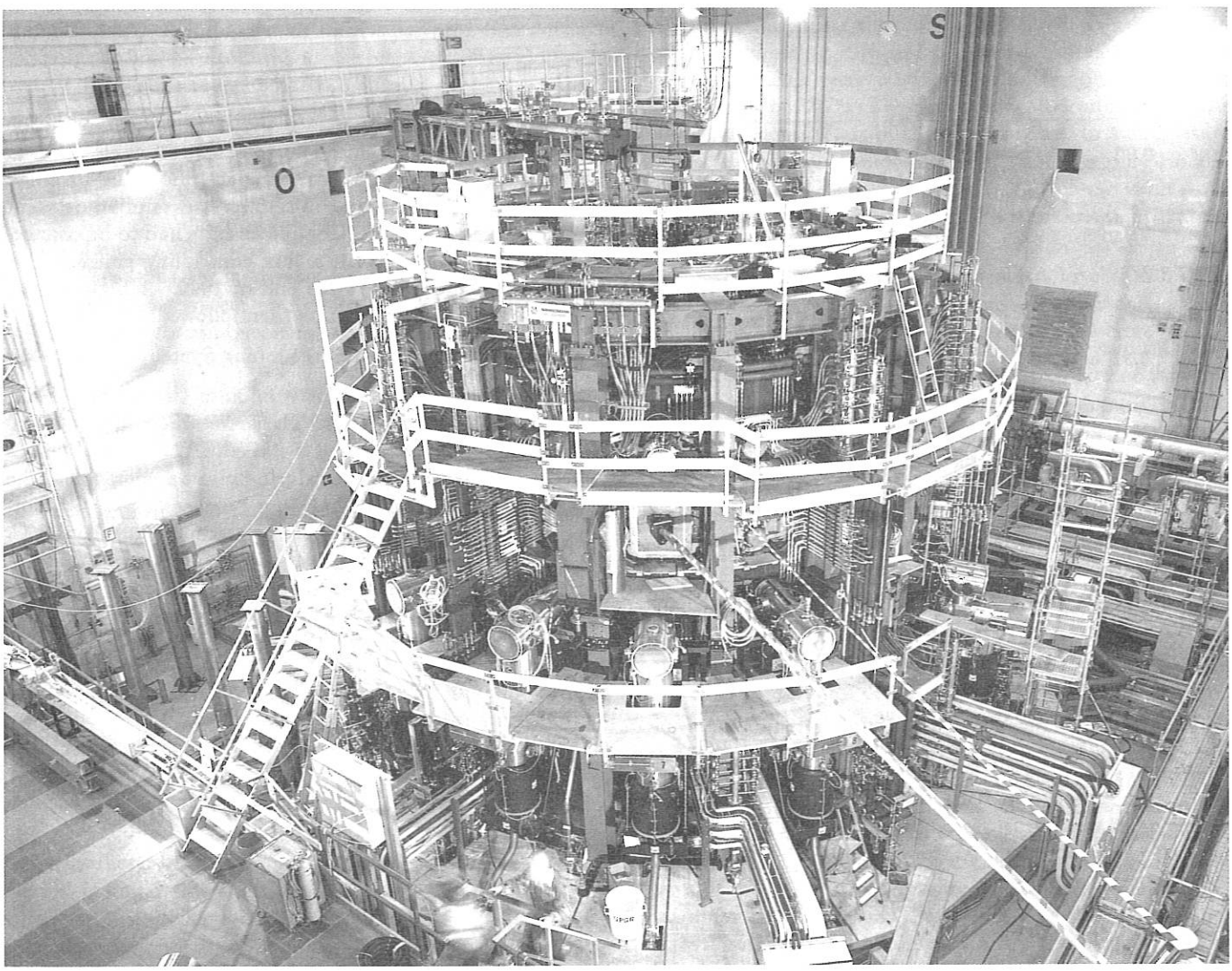

FIG.4 The ASDEX Upgrade Tokamak System at the end of 1990

- After this the spoked wheel had to be removed again for final mounting and adjustment of various components such as support connecting elements, water pipes and diagnostic gauges. Finally the spoked wheel was put back on top with the OH2 coil attached to it. After this the V1, V2 and COA coils were connected to the spoked wheel with their holding fixtures.

Assembly of the tokamak system was completed on February 20, 1990. A view of the completed tokamak system is given in Figure 4. Since then supplementary work has been carried out in the periphery: connections to all supply circuits, vacuum pumping system, cable connections for control and technical diagnostics, floors to cover ground installations and scaffoldings and installations required for auxiliary heating and diagnostic equipment.

3.5 Power Supply

The power supply systems for the TF magnet, the PF systems vertical field coils and ohmic heating coils had been all completed already at the end of 1988. The power supply for the fast control coils was completed in 1989 and tested with dummy load coils. This has been described in detail in the 1989 annual report together with certain improvements added in 1989. During the year 1990 the power supply control SIMATIC subsystems was connected to the master SIMATIC control system and tested. The interconnections to the fast discharge control workstations and to the timer system are described in Sec. 3.6.2.

3.6 ASDEX Upgrade Control System

3.6.1 Control systems overview

3.6.1.1 Basic Tasks

The ASDEX Upgrade control systems control a wide variety of technical and physical processes throughout the experimental setup and support diagnostic processes with additional services. There are many sophisticated features, such as plasma position control, preprogrammed event-dependent shot execution and central system timing. The control systems are heterogeneous and distributed. The main tasks are:

1. Feed-forward (ff) control for presetting before shots and controlling during shots physical and technical systems, such as power supplies, additional heating, etc.

2. Feed-back (fb) control of basic physical quantities, such as plasma position and shape, and density.

3. Monitoring and checking of control computers, power supply PLCs (programmable logical controllers), coil systems, and physical quantities, such as plasma current, plasma position, density, disruption- and runaway-indicating signals. Knowledge of these quantities is necessary for event-dependent shot execution.

4. The safety system's task is to protect persons and to keep away damage from the machine by initiating countermeasures in case of emergency situations.

5. Central system services for system-wide use comprise shot program editing, time definition and distribution, and system state and event distribution and protocolling.

3.6.1.2 Systems setup

The ASDEX Upgrade control system consists of groups of PLCs and specialized computers optimized for their tasks.

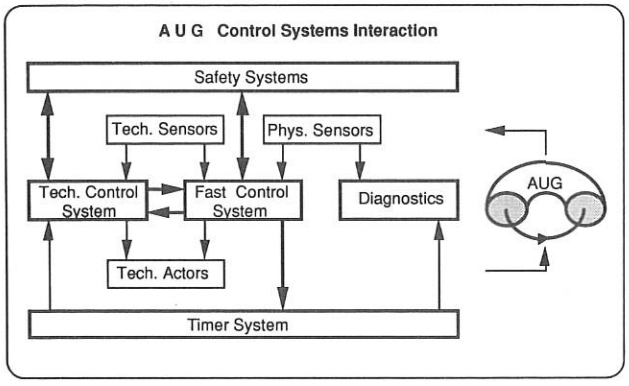

FIG.5 Overview of ASDEX Upgrade control systems

1. The technical control system is a group of 17 PLCs. The supervisor PLC is called SLS (Simatic Leitsteuerung). Its task is to coordinate a group of dedicated PLCs in star topology and organize the sequencing of technical processes. The 16 PLCs are related to autonomous technical processes, such as control of power supplies, additional heating, gas, vacuum, and cooling. They preset, control and monitor the slow technical processes on a hundredths of milliseconds time scale.

2. The SSR (Schnelle Steuerung und Regelung) fast control system is a group of 6 real-time computers optimized for their specific tasks. The computers control and monitor fast technical and physical processes on a milliseconds time scale. The most important processes are fb control of the plasma position and monitoring of disruption, runaways, coils and power supplies to provide event-dependent shot execution.

3. The timer system centrally defines a unique system time and distributes it fast to technical control systems and to diagnostics. The timer system is closely coupled to the SSR to provide the real-time information required within the SSR. The widespread timer system has additional tasks for the transfer of ff control signals and event information.

4. The safety system consists of independent safety loops for personnel and equipment. They distribute emergency information detected by one of the attached technical or fast control systems and synchronize a specific common reaction of all members.

5. The diagnostics consist of a wide variety of sensor electronics and controllers. They provide electrical representation of the measured physical and technical quantities.

The PLCs are commercially available systems. The fast control system, the timer system and part of the safety system were developed by IPP.

3.6.1.3 Systems actions and interactions

The system groups introduced above interact with each other, with the experiment and with operators.

The technical control system is preprogrammed by a technical operator, who selects one out of several parameter sets. If all intershot processes are finished, new parameters preset and no errors detected, then SLS sends a technical permission message including global technical parameters for the next shot to the fast control system. The technical control system is active during a discharge as well as between shots.

The fast control system is preprogrammed by the physical operator, who programs the time-dependent variation of controllable physical quantities. He also defines event-dependent conditions and related changes in the discharge sequencing. The complete set of quantities and conditions make up the shot program. It is executed by the fast control system during a discharge.

The timer system is preprogrammed as part of the fast control system. It is strongly coupled with one of the fast computers. The timer system transfers ff and event information to attached technical control and diagnostic systems which can be controlled ff as well as event-dependent. The timer system will become part of a general interlock system for future applications.

The safety loops are connected to important technical controllers and fast control computers. The safety systems accept emergency requests from attached systems and subsequently force all connected systems to carry out a synchronized distributed final reaction to shut down the shot. Diagnostic systems are informed via the fast control system and the timer system.

The sensor electronics distribute a large number of electric signals of technical and physical quantities to technical and fast control systems, and diagnostics. These perform data acquisition independently of each others, with their private hardware.

Both fast and technical control systems use the sensors and actuators of the technical control system and the sensors of the diagnostics. The systems I/O hardware is decoupled electrically. Fast control, technical control and timer systems are strongly coupled for shot execution, coordinated by the fast control system. The safety systems are superior to all these systems and may shut down both the fast and technical systems. Between shots, all systems are loosely coupled.

3.6.1.4 Status of control systems

The central technical and fast control systems hardware, timer system hardware and basic software have been commissioned. I/O hardware and software and distributed timer system hardware will be installed successively as required by the stepwise start of machine operation, with power supplies, coil and plasma position control first. Manufacturing of the plasma position backup system, commissioning of the machine safety systems and further installation of peripherals and PLCs for technical systems will continue during 1991. The graphic shot programming surface is under development, a preliminary first version now being operational. The main efforts for the future will be to complete the system installation of hardware and software and improve and expand the user surface according to the actual needs of physical and technical shot operation.

3.6.2 Technical control system

The technical plants and components are almost exclusively controlled by SIMATIC computer systems (Fig. 6). These systems are bidirectionally coupled via a bus system and coordinated by a master SIMATIC (SLS). The SLS works primarily offline, i.e. it sets the plant parameters and operational windows via the subsystems prior to a shot and registers the availability of all required plants. An overview of each subsystem can also be optionally visualized.

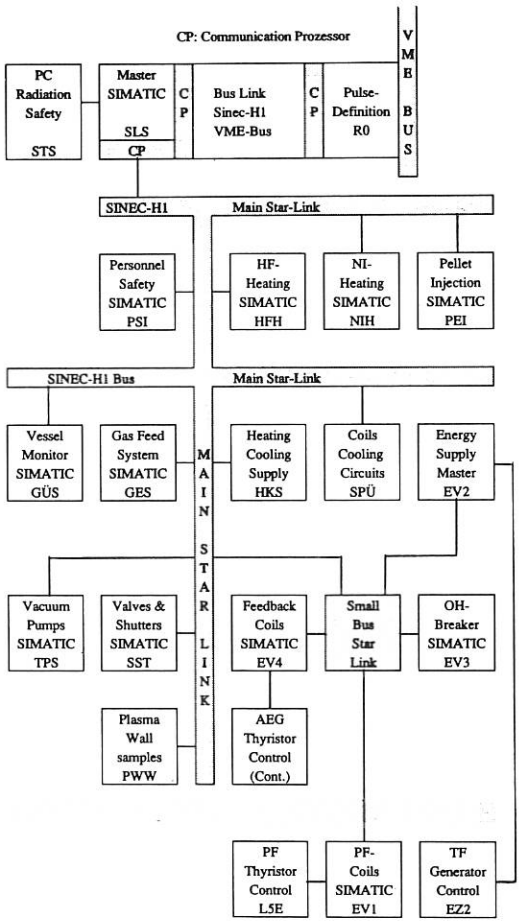

FIG.6 Scheme of technical control systems

During a shot the central computer (R1) takes over control and treats alarms and information coming from the

SIMATIC subsystems. In case of a fatal fault in a plant the responsible SIMATIC subsystem switches off by itself (e.g. energy supply). The SLS also mails the valid plant parameters and the overall plant availability to the second offline computer, the R0. The target of the R0, which is a UNIX system, is to set the online parameters and transfer them to the R1 (and R2). Hence, a special bus system had to be developed in order to link the SIMATIC and UNIX worlds.

The majority of SIMATIC subsystems required for the OH phase are now ready, i.e. the sensor inputs and control codes have been tested. In addition, more comprehensive tests under nearly operational conditions have been run. This applies to: the power supply control system (EV2 + subsystems EV1, EV3 and EV4); the HKS system, which controls the coil and vacuum vessel cooling supply and the vacuum vessel heating supply; the monitors for the vacuum vessel (GÜS) and the coil cooling circuits and temperatures (SPÜ) and the vacuum vessel pumping system (TPS). For the gas feed system (GES) the hardware is installed and partly tested. A reduced version will be operational in February 91. Plant components and computer hardware of the SST control-system (large vacuum valves and shutters of the vacuum vessel) have been installed. The SST software design is finished and programming in good progress. Due to severe manufacturing delays the installation of the PWW system for handling plasma-wall interaction samples is still open.

The personnel safety system (PSI), i.e. the system controlling mainly the access of persons at critical locations by means of an audio and video system, door interlocks and card reader terminals still requires a further testing and program documentation period. But it will be finished in time for the first experimental period.

All subsystems were designed to be as self-supporting as possible. Tasks requiring direct collaboration of a few subsystems are kept strictly inside them, i.e. the SLS is not involved. A few interlocks between subsystems provide basic operational safety for arbitrary situations. Each subsystem can store up to 499 named sets of plant parameters (recipes). The parameters for a recipe are gathered, stored and re-collected by a special utility program, which is identical for all subsystems. Released recipes can be directly loaded by the SLS. Each subsystem can generate recipes for arbitrary situations, i.e. testing, stand-alone operation, SLS operation, etc. For a particular experimental programme a compatible subset of up to 10 recipes will be selected and loaded into a special window. Only these recipes are then accessible from the SLS. The SLS also works with recipes. An SLS recipe is simply a collection of all subsystem recipes required for a special experimental condition. Only the recipe names are required, not the underlying subsystem parameters.

The general target of the recipe tool is to create a sort of learning system, i.e. out of a large number of possibilities the most successful ones will be filtered and stored in a way which permits quick re-collection and also quick modification. A further target is to collect and store the experience of the subsystem experts and readily make it comprehensively available for the operator of the experiment.

3.6.3 Fast control system

3.6.3.1 Introduction

The fast control system of ASDEX Upgrade consists of different computers. The first, R0, gives a graphic user interface to make the numerous definitions necessary for one shot as simple as possible. The second, R1, interprets these definitions during pulse execution. Thus it monitors, controls and feedback-controls the discharge. Additionally it provides a central and therefore unique definition of time. The third, R2, autonomously feedback controls plasma position and shape. The fourth, R3, monitors the mechanical and electrical stresses of the coils. Additional feedback systems, e.g. density control computer are possible within this system. The fifth, the timer system, distributes time and tokamak-relevant data called "events" during the shot. The sixth, safety system, cares for personnel and machine integrity. The interconnections between the computers are depicted in Fig. 7:

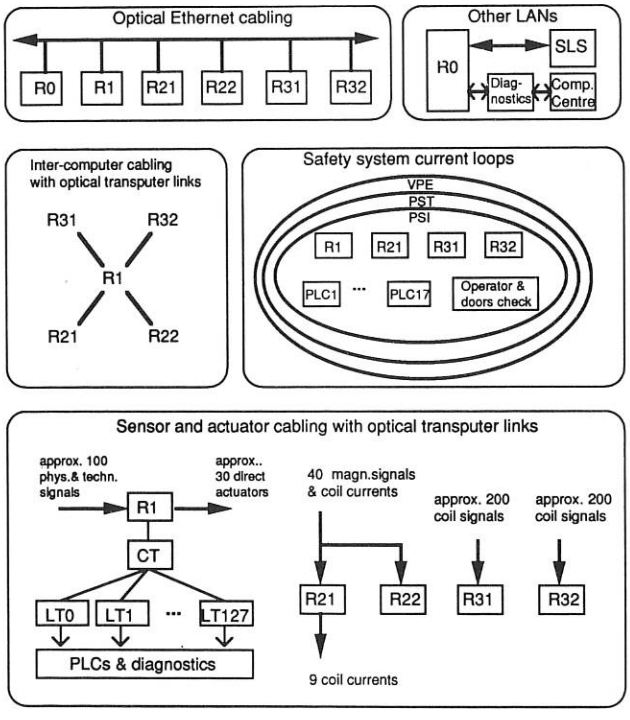

FIG.7 Cabling of the fast control system (SSR)

3.6.3.2 R0

The task of R0 is to convert the user input into an abstract data representation of the planned shot. Its output is the so-called "shot file". Therefore R0 has the following functions:

1. Input of the shot sequence with a nice user interface to reduce human error. This is done by segmenting the sequence and defining under what conditions the segments are to be concatenated. Within each segment several wave forms, switches and time bases can be defined.

2. Communicating with the central PLC to get global technical parameters for a final update of the shot file.

3. Sequencing the start and end of the R1 and R2 actions. This is performed by downloading the shot file to R1 and R2, signalling "start of shot" after having received shot permission from the central PLC and by collecting all protocol data from R1 and R2 after the shot.

4. Archiving protocol data in the computer centre.

5. Maintaining data base for shot file information.

R0 has point-to-point links to the central PLC, the further Rx systems and the computer centre. Its hardware is based upon a UNIX work station with VMEbus. The links are 2 optical Ethernets and a SINEC-PLC net.

3.6.3.3 R1

The task of R1 is the control, monitoring and protocolling of fast processes (approx. cycle time 10 ms). The control is event-dependent by online selection of the "next segment" within a set of predefined alternative segments in the shot program. The central timer is also part of the R1.

R1 performs its task by executing several real-time functions during the discharge:

1. Acquiring technical and physical data. There are about 100 different data "signals" which represent the plasma and coil currents, the plasma position, the plasma density and radiation and the status of the (slow) technical and fast control systems.

2. Preprocessing this data and compressing it into a "state vector" which represents the overall system state.

3. Evaluating the event-dependent conditions defined in the shot file.

4. Selecting the next segment by comparing planned shot with real shot.

5. Generating additional information about the events and distributing them via the timer system (see timer description)

6. Output of the next segment information to R2.

R1 has point-to-point links to the data acquisition peripherals and control outputs (sensors and actuators), to R2, R3 and the power supply PLCs. It outputs the data acquisition trigger via a star net to provide synchronous data input and it has an optical Ethernet to R0.

The hardware of the R1 is a UNIX workstation with VMEbus combined with a MULTITOP /HLR/ parallel computer using 29 transputers /IMS/. The MULTITOP architecture optimizes the benefit of parallel processing with transputers. Its modular design uses only two different types of boards: CPU0 boards with 4 transputers each for computing and MCPU boards with 1 transputer for coordinating. The transputers are fixed or variably interconnected.

/HLR/ H.Richter, "Multiprozessor mit dynamisch variabler Topologie", Dissertation Universität München 1988.
/IMS/ inmos, "Transputer Reference Manual", Prentice Hall 1988.

The R1 has 64 unidirectional inputs, 32+8 unidirectional outputs and 4 bidirectional links. Additionally, there are 16 unidirectional interlock links. All links are glass fibres with a communication speed of 10 MBit/s.

3.6.3.4 R2

The task of R2 is autonomous fb control of the plasma position and shape (1.7 ms cycle time), output status information to R1 for event-dependent shot sequencing.

This task can be fulfilled by real-time execution of the following processes:

1. Acquiring technical and physical data. There are about 40 signals from magnetic measurements and from the coil currents.

2. Executing function parametrization to determine the magnetic equilibrium state.

3. Executing ff and fb algorithms to control the 9 coil currents.

4. Output equilibrium state vector and R2 state to R1.

R2 has point-to-point links for data acquisition and triggering and to R1. It is connected with R0 by means of the optical Ethernet. All links are glass fibres with a communication speed of 10 MBit/s.

The hardware of R2 is a UNIX workstation with VMEbus, combined with a MULTITOP parallel computer using 14 transputers. The interconnection of the transputers is switched over via a programmable interconnection network 3 times every 1.7 ms to achieve maximum possible performance. It has 37 unidirectional inputs, 16 unidirectional outputs and 8 bidirectional links.

Because of the importance of proper position control the R2 is completely doubled and the two R2s are compared online by R1 to avoid fatal instabilities due to R2 defects.

3.6.3.5 R3

The task of R3 is autonomous monitoring of the TF and PF coils (cycle time 50 ms). Monitored are the currents, positions, temperatures and forces of the coils. This is done by real-time execution of the following:

1. Acquiring technical data. There are about 400 coil signals.

2. Computing forces on the coils.

3. Output of coil and R3 status to R1.

4. Alarming the safety system in case of coil overload.

The R3 has point-to-point links for data acquisitions and to R1. Data input is asynchronous. It is connected with R0 via the optical Ethernet. All links are glass fibres with 10 MBit/s.

The hardware of R3 is a UNIX workstation with VMEbus combined with a MULTITOP parallel computer using 5 transputers. It has 5 unidirectional inputs, 1 unidirectional output and 1 bidirectional link. The coil signals are multiplexed onto the links.

Because of the large number of signals the R3 is doubled and the two R3s perform separate monitoring of the PF and TF coil systems.

3.6.3.6 Additional Rx

The task of additional Rx computers is to build up autonomous fb controls for physical quantities which at present are only ff-controlled or fb-controlled by hardware, e.g. the density. The system integration of Rx computers is done analogously to that of R2.

3.6.3.7 Timer system

The task of the timer system is to make a central and therefore unique definition of what "tokamak time" is and when it begins and to distribute it system-wide. The timer system is additionally used for signalling the events of ASDEX Upgrade. It performs this by:

1. Real-time output of shotfile-predefined and online-detected events (central timer)

2. User-programmed reaction of local output signals to events (local timers)

3. Protocolling the reactions together with time stamps

4. Protocolling other user reactions (optional)

The central timer is point-to-point connected with every local timer and with the R1. The timer system is based on a transputer and a fibreoptic star net with up to 255 links and local timers connected to them. The transmission speed is 10 MBit/s, with Manchester modulation and error detection and correction. The signalling time for 1 event is 10 μs.

A detailed description of the timer system can be found in /AR89/.

3.6.4 Safety system

The task of the safety system is to ensure the safety of personnel and equipment. There are three safety scenarios:

1. decentralized voltage-free switching of main components (emergency off);

2. decentralized shutdown (immediate pulse stop);

3. premature pulse end under central control (not immediately).

This is done by the following functions:

1. accepting local alarm request

2. distributing alarm system-wide
3. granting alarm request system-wide.

The safety system consists of three independent loops which connect the control computers, the power supply PLCs, the heating systems and the operator console in a ring. The hardware is based on fail-safe technology and doubling of each module. The loops are current loops with constant current of 10 mA.

/AR89/ IPP, "Annual Report 1989"

4. DIAGNOSTICS

A large number of diagnostics has been designed and constructed to be operational for the first discharge, such as: the electromagnetic probe system, the 2-mm microwave interferometer, the H-alpha diagnostic, the TV-camera system, the hard X-ray monitor, spectroscopic diagnostics for overview spectra as well as for C and O monitoring, the mass spectrometers, deposition probes, Langmuir probes, the bolometer and soft X-ray pinhole camera system.

Another group is scheduled to be operational in the next six months: the DCN interferometer, the Thomson scattering system (vertical), combined with the Z_{eff}-profile measurement, the thermography system for divertor plates, the ECE 8-channel system as well as the heterodyne system for the boundary, the neutron flux and spectrum diagnostics, the CX diagnostic, and the pellet centrifuge.

In the last group design and, in part, construction have been started: Thomson scattering (combined with Z_{eff}-profile measurement) horizontally and in the divertor, high-resolution spectroscopic diagnostics, fast-moving plasma-wall interaction probes, fast-moving Langmuir probes, micro-wave reflectometry, time-of-flight neutral particle analyzer, and Li-beam diagnostic. A few diagnostics showing some new aspects are presented in the following in more detail.

4.1 Density Feedback Control with Bremsstrahlung

The line density $\bar{n}_e$ measured by laser interferometry is normally used for plasma density feedback control. Fast density changes, however, as in large sawteeth or during pellet injection, can cause counting errors in the interferometer signal. For cases where the interferometer system is disturbed one needs a reliable substitute to guarantee permanent density control. At ASDEX it has been shown that the bremsstrahlung signal can then be used instead of the interferometer. It is possible, furthermore, to realign the interferometer signal after the disturbed period.

An avalanche diode collects the bremsstrahlung along the central chord of the plasma in the near-infrared wavelength range between 850 and 980 nm. The output voltage U of the detector is proportional to

$$U \sim \frac{Z_{eff}}{\sqrt{T_e}} n_e^2 \quad \Rightarrow \quad n_e \sim \frac{\sqrt[4]{T_e}}{\sqrt{Z_{eff}}} \sqrt{U},$$

where Z_{eff} is the effective ion charge, and T_e the electron temperature. The relation between the line density $\bar{n}_e$ and U was investigated experimentally in wide density and heating ranges. /232/

In ohmic discharges at higher densities ($\bar{n}_e \geq 3 \times 10^{19}\ m^{-3}$) it was found that $Z_{eff}/\sqrt{T_e}$ is nearly independent of the density. This means that the electron density is directly proportional to $\sqrt{U}$ and an exact knowledge of Z_{eff} and T_e is not necessary. Although Z_{eff} and T_e depend on the heating method, the electron density dominates the bremsstrahlung emission in all cases.

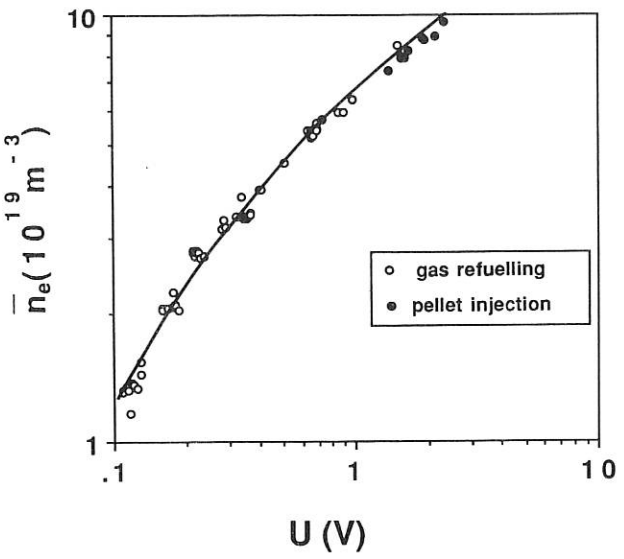

FIG.8 Relation between $\bar{n}_e$ and bremsstrahlung signal U for ohmic discharges with gas and pellet refuelling. The characteristic (solid line) is used for an online density control.

In Fig. 8 $\bar{n}_e$ is plotted versus the bremsstrahlung signal U for gas and pellet-refuelled ohmic discharges. Since the variations of U are sufficiently small, this also being valid for plasmas with auxiliary heating, one can represent the relation between $\bar{n}_e$ and U by one characteristic (depending on the heating method) which can be programmed into an analog computer and used for online density control. This method was successfully applied in ASDEX and will also be used in ASDEX Upgrade.

4.2 Microwave reflectometry

Design of a diagnostic system for microwave reflectometry has been started together with IST Lisbon and the University of Aveiro, Portugal, with the following goals:

1. measurements of the density profile $n_e(r)$ on the low and high-field sides near the equatorial plane and in the scrape-off plasma near the lower X-point region;

2. measurements of density fluctuations with the systems near the equatorial plane.

Ordinary and extraordinary-mode measurements will be performed on the low-field side in order to cover the complete density profile, starting at low values in the scrape-off layer plasma. On the high-field side extraordinary-mode waves cannot propagate into the plasma. Only ordinary-mode waves are used there.

The system will contain 5 frequency bands in the range 16-110 GHz with the capability of fast broad-band sweeps ($\geq$ 10 μs/sweep). Perturbations of the density profile measurements by fluctuations should be avoided. Solid-state varactor-tuned oscillators are used for all bands. In ordinary mode the microwaves are emitted and received with one single antenna per frequency band. Focussing fog-horn antennas will be placed on the low-field side of the vessel. On the high-field side only simple antennas can be used owing to space limitations. Density profile measurements are performed in homodyne detection; for fluctuation measurements the detection system will be extended to heterodyne detection. An additional system for measurements in extraordinary mode inside the ICRH antenna is envisaged. This should allow detection of local modifications of the density profile due to absorption of ICRH power near the plasma surface.

4.3 ECE Heterodyne Radiometer

Besides the 8-channel grating spectrometer for measuring electron temperature profiles via ECE in the bulk plasma, a heterodyne radiometer was designed to determine the electron temperature in the plasma edge region. This diagnostic will measure the temperature simultaneously at sixteen different locations on the mid-plane in the region 15 cm in from the separatrix. Each channel of this instrument will have a radial resolution of $\sim$1 cm in the plasma, a minimum detectable temperature variation of $\sim$4 eV and a time resolution of $\sim$10 μs. The diagnostic uses an array of GaAs balanced mixers to mix the cyclotron radiation down to an intermediate frequency band that extends from 3 GHz to 20 GHz. Silicon Schottky barrier detector diodes are then used to detect signals in this band.

4.4 Development for Spectroscopy on ASDEX Upgrade

Spectroscopic investigations on ASDEX Upgrade will be performed to determine the impurity concentrations, their spatial distributions and their transport in the plasma for different operational conditions, to measure the plasma rotation and to study the impurity behaviour in the plasma boundary and in the divertor region. Different spectroscopic devices will cover the wide spectral range from the visible down to the soft X-ray region.

Two devices, the Double-SPRED (Double Survey, Poor Resolution, Extended Domain) and the C- and O-Monitor, are ready to operate from the beginning of ASDEX Upgrade operation as impurity monitors. The Double-SPRED is designed to display two spectral regions of different width for identification, absolute concentration monitoring and time behaviour studies of the most prominent impurities in ASDEX Upgrade, viewing through a fixed line of sight through the plasma centre. Both channels of the SPRED were absolutely calibrated using the Lyman lines of HeII of an absolutely calibrated helium hollow-discharge lamp. The C- and O-Monitor is specifically designed to determine and monitor the most prominent impurities, carbon and oxygen, simply by measuring the intensities of the Lyman α lines of C and O with two flat crystals at just the appropriate Bragg angles.

The other six spectroscopic devices are devoted to investigations of the plasma and impurity behaviour in the boundary and in the divertor region as well as in the plasma centre.

A divertor spectroscopic system is at presently being designed with imaging systems, fibres and spectrometers in the visible region to determine - spatially resolved - the erosion from the divertor target plates, to measure the

energy distribution of the sputtered particles and their redeposition on the target plates, to study the ionization and recombination of the impurities in the divertor as well as their transport in the divertor region. Moreover, the spatial distributions of the ion temperature and the densities of neutral particles and molecules will be investigated, and measurements of the divertor retention and exhaust and flow speeds in the divertor and X-point region will be performed. This instrument will be partly combined with the plasma boundary spectrometer also being designed, a device to measure spectral line intensities and shapes with high spatial flexibility. This is obtained by a mirror which can be rotated and swivelled simultaneously to reflect visible and VUV radiation from different specific regions of the boundary (divertor plate surfaces, plasma boundary in the toroidal and poloidal directions, RF antenna boundary) throughout the discharge into an imaging system which focusses the central VUV radiation via a large Pt-covered ellipsoidal mirror onto a normal-incidence VUV spectrometer and - simultaneously - the outer visible radiation via a Cassegrain system onto a visible spectrometer. This new device will allow us to study impurity sources, impurity transport in the boundary and plasma rotation.

A charge exchange recombination spectrometer system is under construction to determine the spatial impurity distribution and rotation in the ASDEX Upgrade bulk plasma by applying a two-dimensional detector and camera at the spectrometer exit.

For impurity investigations in the plasma boundary as well as in the bulk a grazing-incidence-spectrometer is being constructed which allows measurements of two different spectral regions simultaneously (from about 1 nm to 100 nm) with spatial resolution on s shot-to-shot basis. For the spatial and spectral resolution of the soft X-ray spectrum for impurity distribution and transport studies of the bulk plasma a multi-bragg-spectrometer consisting of three moveable double-flat-crystal monochromators is being designed and constructed. It will allow us to study impurity accumulation problems of metallic and other impurities. Ion temperature determination from X-ray line Doppler profiles will accompany these measurements using a curved-crystal high-spectral resolution device (Johann spectrometer).

4.5 ASDEX UPGRADE DATA ACQUISITION AND DATA PROCESSING

Planning over 60 diagnostics around the ASDEX Upgrade tokamak it was clear that a big amount of physical data has to be mastered by the physicists. Therefore the Computer Science Division of the IPP designed a system for data acquisition and data processing which integrates UNIX workstations and an IBM mainframe via a fast network and provides a sophisticated archival system for data storage and backup for all participants. This so called AMOS/D system and its features are described in this and former IPP annual reports by the Computer Science Division.

However, to have own facilities near the ASDEX Upgrade project the ASDEX Upgrade data processing group has been established in 1990. This group in cooperation with the Computer Science Division put the system components near the experiment into operation and provides continuous support with operating, administration, programming, and developing power for diagnosticians and theoreticians.

Besides building up the data acquisition computers and CAMAC equipment for several diagnostics, the installation of a bundle of office workstations for scientists, and some minor software developments, three major software projects have been realized:

- The adaptation and redesign of an existing IBM oriented fullscreen menu package on the UNIX workstations now allows compatible programming of fullscreen dialogs in all three system environments (AMOS, CMS, and UNIX).
- A journal system for the experiment leader acquires and displays not only the main shot parameters from the experiment control system and the main physical and technical diagnostics, but allows also input of remarks by the physicist in charge concerning the physical goals of single or series of shots as well as about the more or less convenient behaviour of the discharge.
- The general purpose data display program OSIRIS (Open System for Interactive Retrieval of Information from Shotfiles) provides an interactive access to ASDEX Upgrade shotfile data for display of signals (graphically or tabulated). It is able to do unary (integration, differentiation, smoothing) and other mathematical operations on signals (scalar or between different signals), and also to cross-correlate them. OSIRIS can be configured to repeat the same operations and displays automatically on a series of shots. Storing from and recalling back such configurations into OSIRIS allows to work with it as with a special purpose plotting or even a simple analysis program.

5. ADDITIONAL PLASMA HEATING

5.1 Neutral Injection into ASDEX Upgrade

The highlights of the project in 1990 were the delivery of the first vacuum box in September, the subsequent start of operation of the test stand, and EURATOM approval of preferential support for the second injector in December.

5.1.1 PINIs

The continuation of tests with the RF plasma source and the first PINI structure revealed that, in contrast to the previously reported profile measurements without beam extraction, the plasma profile does not seem to be sufficiently uniform across the extraction area, and further optimization is needed (for details see Technology Division).

The assembly of bucket source plasma generators together with the PINI accelerator structures, has been completed and all units are at present being stored under vacuum.

One completely assembled PINI was installed on the test stand at the end of the year.

5.1.2 Beamline Design and Manufacture

The situation at the end of 1990 can be summarized in that the majority of components have been delivered and contracts have been placed for all of the remaining mechanical components with the exception of the external magnetic shield and its support, the design of which is still in progress. Those components whose fabrication is still under way will all be delivered within the next six months. The only exception is the delivery of the vacuum boxes. The first vacuum box was delivered in September 1990 with a total delay of 21 months. The second vacuum box was accepted in November 1990 at the contractor's premises. Owing to serious contractual complications, the contractor has refused to deliver the second box. An alternative contract for the fabrication of a further box was therefore placed in summer and is well advanced. Of the components delivered and accepted an example is shown in Fig. 9: the actively cooled, movable beamline calorimeter for stopping and measuring beam powers of up to 11.6 MW.

FIG. 9 Side view of the movable beamline calorimeter suitable for a power of 4×2.9 *MW. The view shows only two of the total number of four D-shaped calorimeter units, each of which receives one beam. The remaining two units are behind the large central copper wall. During operation the side facing the observer is also covered by a suitable large-area copper shield.*

5.1.3 Power Supplies, Controls and Data Acquisition

All supplies and controls necessary for the test stand have been installed and commissioned and are available, with the exception of the magnet power supply, which will become available in a few months' time. The corresponding systems for the injector have also been installed and commissioned to a large extent. Furthermore, the installation of the control room is progressing well. The control system for the injector has largely been delivered; the software will not involve considerable additional effort, since it is basically compatible with the test stand control software. Data acquisition for the test stand is operational, the computer for the injector is available.

5.1.4 Test Stand

After delivery of the test stand vacuum box in September, the vacuum system, the test stand calorimeter and the titanium evaporators were mounted and commissioned. Also the first PINI has been installed on the test stand and commissioning is in progress. The next steps will consist in commissioning the low-voltage and high-voltage power supplies together with the PINI and the conditioning of the first PINI up to full power. Subsequently, the four series PINIs will be conditioned.

5.1.5 Preparations for the Second Neutral Beam Injector

The application for preferential support concerning the second neutral injector was examined by a EURATOM ad hoc group in summer, and approval was guaranteed in December. This second injector will be identical to the first one with the exception of the plasma sources, which will be RF sources instead of bucket sources. Furthermore, the second injector will have additional PINIs suitable for 100 keV deuterium injection.

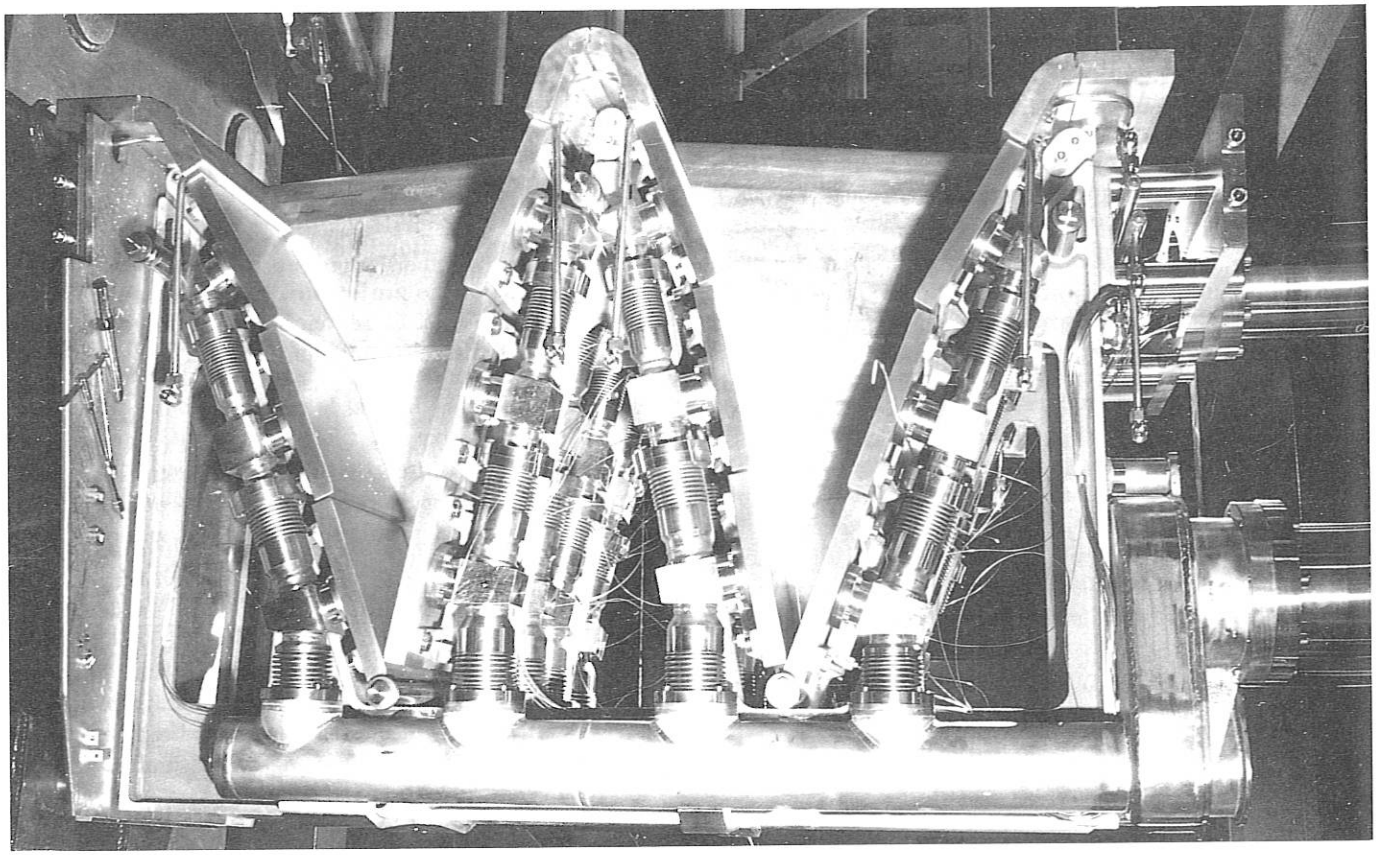

In order to demonstrate the advantage of 100 keV deuterium operation over the previous 65 keV deuterium and furthermore, the advantage of the RF sources over the bucket sources due to the higher atomic ion fraction, a number of neutral beam deposition calculations were made with the FREYA deposition code. An example is shown in Fig. 10, where an ASDEX Upgrade plasma with parabolic density profile (average density: 1.47×10^{14} cm^{-3}) is being considered. Clearly the higher beam energy and also the higher atomic ion fraction of the RF sources do considerably improve the deposition profile.

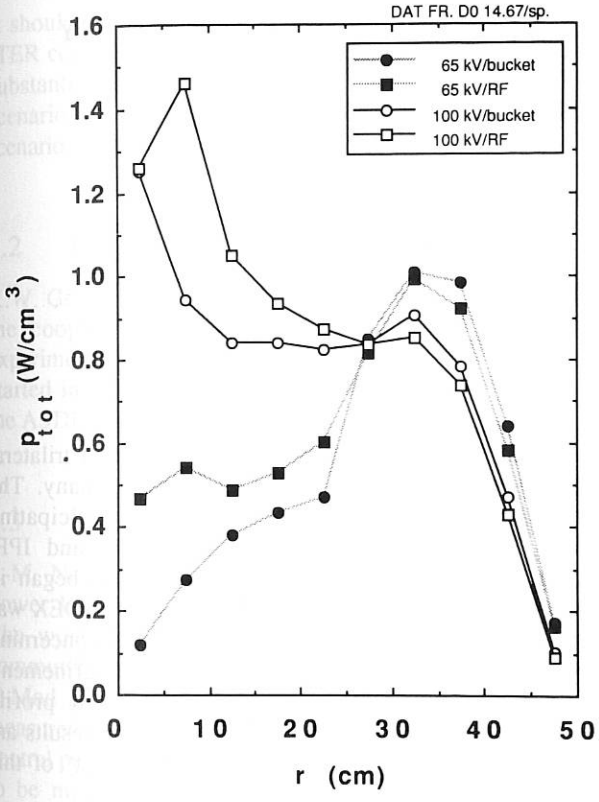

Fig. 10Power deposition profiles for a parabolic density profile at an average density of 1.47×10^{14} cm^{-3} *for the RF source 85 % of atomic ions are considered as opposed to 65 % of atomic ions in the bucket source; both values were measured. All four profiles were calculated from the same neutral power of 6 MW.*

For realization of this additional project, a considerable number of components has already been ordered by releasing the corresponding options in the contracts for the first injector (for example, calorimeter, vacuum system, water-cooled panels, bellows/valve adapter unit, magnet, ion dumps, beam steering, piping system). Furthermore, a call for tenders was sent out in summer for the additional high-voltage power supply system comprising 4 plus 1 units of 7 MW output each. Offers have been received and are at present being evaluated.

In collaboration with KFA Jülich, the RF plasma source was redesigned in order to include compatibility with long-pulse operation and a larger source width in order to improve the plasma uniformity. The manufacture of this source is nearly complete at KFA Jülich, and assembly tests can start very soon (see Technology Division). Furthermore, the specifications for the RF generators are being reviewed in a series of discussions with industry. The reviewed specifications will include regulation and modulation of the RF power and further features necessary for application to the tokamak experiment.

5.2 Ion Cyclotron Resonance Heating

The basic design of the ICRH system and the layout and data of its main components were already described in the annual reports of 1985-1989. In 1990 the main emphasis was put on the final definition of all components, on the fabrication of antenna and feeding line elements and on the control, measuring and data acquisition systems.

For the four antennas all housings were completed and two of them have already been installed in the vacuum vessel of ASDEX Upgrade. The fabrication of other antenna components such as loops, Faraday screens and side-walls is well advanced. The development of remaining parts such as antenna-protecting limiters and some fixing elements was completed for the manufacturing in the first half of 1991.

The vacuum-insulated antenna feeding lines, which are the last missing RF transmission line sections, are nearly completed. Final tests of the vacuum feedthroughs, being the most critical elements of these lines, showed a high electrical strength (see Technology, Section 2). The cryo pumping system for these lines, the development of which is described in the Annual Report 1989, was completely defined and ordered.

The programming of the central ICRH control system was continued. It combines the sub-controls of generators, coaxial switchgear, matching and vacuum systems etc. The measuring systems for all RF, electrical, temperature, and vacuum data were fixed and almost all elements were ordered. The implementation of the data acquisition systems is in good progress. For different diagnostics inside and in front of the antennas several pipes, waveguides and optical fibres were planned to be installed in the antennas.

The assembling of the antennas, feeding lines and pumping systems was planned in detail. Several devices necessary for the difficult installation of the antenna parts were designed, manufactured and tested.

IEA IMPLEMENTING AGREEMENT
for the joint work on the investigation of toroidal physics and plasma technologies in ASDEX and ASDEX Upgrade
EUROPEAN ATOMIC ENERGY COMMUNITY / US DEPARTMENT OF ENERGY

1. OBJECTIVES OF THE AGREEMENT

The Implementing Agreement which is in force since 1985 was signed aiming at conducting "a joint programme to investigate toroidal physics and plasma technologies in tokamaks with poloidal divertors" as a means of optimizing plasma performance as explicitly laid down in Article 1. The establishment of a common data base in these areas is also envisaged. Thus, the activities under the agreement include transfer of equipment, assignment of scientists, and exchange of information for investigating, for example, boundary theory, confinement incl. particle transport, impurity behaviour, plasma fuelling and control, resistive MHD modes, general tokamak physics including diagnostics and heating, and LH heating and current drive.

The collaboration was concentrated on experiments and data of ASDEX until August 10, 1990, when the facility was closed down. The cooperative programme is now being continued in ASDEX Upgrade, which has a reactor-relevant divertor configuration.

2. STATUS OF THE AGREEMENT

On December 12, 1990, the Executive Committee met for the sixth time in Frascati, Italy, to review the progress of the collaboration and to discuss the scientific programme for 1991, which is now directed towards ASDEX Upgrade. Parallel to the Executive Committee meeting the final LH workshop took place (December 11 and 12 , 1990), dealing with subjects such as power absorption, deposition profiles, coupling, current drive efficiency, confinement, MHD effects, current profile control, and edge current drive.

3. REPORT ON 1990 ACTIVITIES

3.1 Lower Hybrid Current Drive

The 2.45 GHz lower hybrid system was built in a trilateral collaboration between Italy, the U.S., and Germany. The hardware came from or was built in the participating laboratories (ENEA-Frascati, PPPL-Princeton, and IPP-Garching). In December 1988 LH experiments began in ASDEX and lasted until August 10, 1990, when ASDEX was closed down. New results have been obtained concerning current drive efficiency, heating, absorption, confinement, sawtooth stabilization, MHD behaviour, current profile control, and parametric decay instabilities. These results are described in detail in the section "ASDEX Project" of this annual report.

In the experimental phase up to now personnel delegated by the parties to the collaboration have substantially contributed to the exploitation of the experiment: six scientists from ENEA and seven from the U.S. stayed at IPP.

From ENEA, R. DeAngelis studied impurities during LH, A.Tuccillo investigated hard X-ray emission, R. Cesario and V. Pericoli worked on nonlinear wave propagation, and R. Bartiromo and F. Santini discussed and prepared the meeting of the LH Project Council. Their efforts amounted to about 11 man months in 1990.

From the United States T.K. Chu (PPPL) worked on studies of the preservation and change of electron pressure profiles during LH current drive and heating, H. Takahashi (PPPL) studied edge current drive, R. Harvey (GA) participated in theoretical work on LH current drive (LHCD modelling) and simulation of experimental results. D. Thomas (GA) and A. Hyatt (GA) continued work on the development of a high-current Li beam source which was tested on ASDEX. S. Sesnic (PPPL) performed HX measurements and, S. Bernabei (PPPL) participated in LHCD experiments and their evaluation. The combined effort amounted to nearly 17 man months.

It should be mentioned that the present proposal for NET or ITER considers LHCD as an essential means either to drive a substantial fraction of the plasma current in the steady-state scenario or to control the current profile in the pulsed operation scenario.

3.2 Confinement (incl. Particle Transport)

K.W. Gentle from the University of Texas, Austin, continued the cooperation in the area of analyzing gas oscillation experiments to investigate particle transport. This collaboration started in 1987. A publication on this subject comprising all the ASDEX results was also finalized.

3.3 Theory and General Tokamak Physics

J.-M. Noterdaeme participated in the 'Workshop on High Power ICRH Antenna Design for High Density Tokamaks'. The workshop brought together the expertise of the RF community in support of the design activities for the Alcator C-Mod antennas. G. Haas went to GA to discuss pressure measurements with 'ASDEX type' ion gauges in DIII-D - the neutral pressures inside the newly installed divertor baffle were to be measured - and to assist in putting the gauges into operation on DIII-D. W. Engelhardt also stayed at GA to participate in the cooperation of an advanced divertor concept. Issues relating to the pending collaboration in pellet ablation physics were discussed by L. Lengyel at GA. He and also V. Mertens went to ORNL to talk about subjects connected with a Nuclear Fusion Review Paper on pellet injection. Fluctuation studies are being performed by A. Rudyj, who went to PPPL for one year.

To discuss possible collaboration on ASDEX Upgrade in the frame of the Implementing Agreement, M. Kaufmann, W. Köppendörfer, and K. Lackner visited several laboratories in the U.S. (PPPL, MIT, GA, Univ. of Texas) in October 1990. Previously, R. Stambaugh (GA) and S. Cohen (PPPL) had been at IPP for the same reason in summer 1990. The results of the various discussions have been laid down in letters and also in a paper 'Plans for ASDEX Upgrade - US Collaboration 1991'. Also, a paper "Long-Range Planning US -ASDEX Upgrade Collaboration' has been set up, fixing the subjects of main interest and the laboratories possibly involved.

3.4 Publications

Thirty-four publications and conference contributions resulted from the collaboration in 1990 comprising themes of pellet imaging techniques, boronization, pellet ablation, fluctuations, transport in the scrape-off layer, LH current drive, LHCD efficiency, profile modification, confinement, parametric decay instabilities, electron pressure profiles during LH current drive and heating, transition from electron- to ion-interaction of LH waves, power absorption during LH injection, particle transport, momentum confinement, plasma instabilities, and edge modelling.

Abbreviations:

DoE	=	Department of Energy
GA	=	General Atomic Technology Incorp.
MIT	=	Plasma Fusion Center Massachussets Institute of Technology
ORNL	=	Oak Ridge National Laboratory
PPPL	=	Princeton Plasma Physics Laboratory

JET COOPERATION PROJECT

(Head of Project: Prof. Dr. Michael Kaufmann)

The JET Joint Undertaking was set up in 1978 and operation of the JET experiment started in 1983. In 1989 it was proposed to prolong the JET project by four years until the end of 1996 in order to introduce before the final two-year Tritium Phase a new Pumped Divertor Phase, the objective of which would be to establish the effective control of plasma impurities in operating conditions close to those of the Next Step. A proposal for such a prolongation has been submitted by the European Commission to the European Parliament and Council of Ministers and it is expected to be formally adopted during the first half of 1991.

Besides regular assignment of personnel to JET for specified tasks, some employees of IPP have been seconded to JET for long- term stays. They are members of the JET team. Various diagnostic devices essential for investigating the JET plasma have been built by IPP and installed in JET. These succesful diagnostic systems are: a bolometer array for measuring the total radiated power resolved in time and space, soft X-ray diode arrays to detect MHD instabilities and locate rational surfaces, two crystal spectrometers for the X-ray regime to investigate the impurity behaviour (especially the evolution of impurity density profiles), a surface analysis station to find out about plasma-wall- limiter interactions, and a pellet injection system for diagnostic purposes.

To run the diagnostic devices and contribute to the exploitation of JET in specific research areas, personnel are assigned to JET under several task agreements concluded with JET. Two of those agreements are still in force. The first one provides for the investigation of bulk impurity physics and for the use of impurity- related diagnostics. The second one refers to the study of plasma- wall interaction. Another task agreement relating to LH current drive experiments has ended. During 1990 the number of scientists working at JET within the frame of the JET cooperation was 22, including 3 members of institutes other than IPP.

During 1990 JET again made considerable progress, on both the technical and scientific sides. The plasma current of 7 MA in the limiter configuration and the current duration of up to 30 s at 3 MA are world records and are over twice the values achieved in any other fusion experiment. The currents of 5.1 MA and 4.5 MA are also the highest achieved in single-null and double-null divertor configurations, respectively. NBI heating has been brought up to full power ($\sim$21 MW) and the ICRH power has been increased to $\sim$22 MW in the plasma. In combination, these systems have delivered 35 MW to the plasma.

Improved plasma purity was achieved with a beryllium first wall by sweeping the X-point and using strong gas puffing in the divertor region. This resulted in high ion temperatures ($T_i(o)$ in the range 20 - 30 keV) and improved plasma performance, with the fusion triple product ($n_D(0)\tau_E T_i(0)$) significantly increasing. In the hot-ion H-mode regime, the central ion temperature reached 22 keV and the energy confinement time was 1.1 s, with a record fusion triple product of $8-9\times10^{20}\ m^{-3}\ keV$ s and $Q_{DD}=2.4\times10^{-3}$. A full D-T simulation of this discharge showed that an equivalent fusion amplification factor $Q_{DT}\sim0.8$ would have been obtained transiently, reaching near-breakeven conditions and within a factor of 8 of that required by a reactor. Similar results were obtained with ICRF at medium but equal temperatures $T_e(0)\sim T_i(0)\sim10\ keV$.

As a result of reduced impurity levels with the beryllium first wall, the general performance of JET improved. In particular

- the density limit increased, and a record peak density of $4 \times 10^{20}\ m^{-3}$ was achieved with pellet fuelling; the density is limited principally by fuelling and not by disruptions, as was found with carbon limiters;
- sawteeth were stabilized for periods exceeding 8 s;
- with beryllium antennae screens, H-modes were obtained for periods >1 s when ICRH alone was applied; the confinement characteristics were similar to those with NBI alone;
- β-values up to the Troyon limit were obtained in double-null X-point plasmas.

Thus, in JET, the parameters required for a reactor plasma have been reached individually, and near-breakeven conditions have been achieved in single discharges.

1. TASK AGREEMENT NO. 1

R. Barnsley[1], J. Fink, N. Gottardi[1], H.J. Jäckel[1], G. Janeschitz[1], K.F. Mast, U. Schumacher, D. Zasche

[1] JET Joint Undertaking, Abingdon, U.K.

The bolometer, the soft X-ray diagnostics, and the double-crystal monochromators for soft X-ray plasma spectroscopy were operated as JET diagnostic systems in 1990. These diagnostics contribute to the understanding of plasma radiation losses, impurity behaviour, and the fast behaviour of the plasma observed through its X-ray emission.

Bolometric measurements showed that from the very beginning of machine operation JET plasmas underwent long phases with strong internal radiation asymmetries (up-down and in-out asymmetries).

Internal asymmetries due to thermal instability (Marfes) and asymmetries due to contact of the plasma with machine structures or to the shape of the magnetic field (X-point configuration) are not considered here.

Internal asymmetries may be associated with the neoclassical impurity transport mechanism and the radial electric field. As a common feature, JET L-mode plasmas show strong up-down and/or in-out asymmetries. After transition to an H-mode plasma during NBI or ICRH additional heating these internal asymmetries may diminish or even disappear.

A sudden change of the electron temperature or poloidal rotation velocity of the bulk plasma near the plasma edge during the transition from L-mode to H-mode could explain the phenomenon. Generalized Abel inversion with the assumption of constant emissivity on flux surfaces is then applicable during the H-mode in order to reconstruct radiation profiles from bolometrically measured line-integrated intensities.

The active-phase double-crystal spectrometer was on line for most JET pulses during 1990, producing data integrated into the data set of line intensities obtained from the VUV spectrometers and used for analysis of the radiated power. Owing to its comparatively high sensitivity at wavelengths below about 2 nm, it gave useful information on the behaviour of oxygen after the introduction of Be in the JET vacuum vessel by monitoring the oxygen Lyman α intensity, usually too faint to be detected by the VUV instruments. In its high- resolution mode the instrument gave some preliminary results on the temperature of different ions located at various radii across the plasma discharge.

The double-crystal spatially-scanning monochromator gave radial profiles of line radiation from the nickel impurities.

2. EVALUATION OF LIDAR DATA

H. Fajemirokun[1], C. Gowers[1], P. Nielsen[1], H. Salzmann, B. Schunke[1]

[1] JET Joint Undertaking, Abingdon, U.K.

The LIDAR Thomson scattering diagnostic on JET is used to measure radial electron temperature and density profiles in a backscatter geometry. Owing to this geometry the scattered spectra are rather broad. At the electron temperatures achieved on JET the whole visible spectral range is covered. Therefore, the evaluation of LIDAR measurements can be endangered by chromatic deposits on the inside of the viewing window. To avoid these difficulties, monitoring the transmission of the window over the whole spectral range of the measurements is needed (and is done on JET using the plasma as a broadband light source). In addition, statistical methods can be used to identify and correct systematic errors on the assumption that the chromatic effects mentioned do not change over the period of time required to collect a representative set of scattering data.

The statistical approach is based on the fact that all calibrations relevant to temperature evaluation (the normalized spectral sensitivities of the spectrometer channels, the absolute sensitivities of the detectors and their noise properties), but that of the spectrally varying transmission of the collection optics can be done hands-on outside the biological shield. This transmission is assumed to vary slowly over the spectral range and can therefore be approximated by a constant value for each spectral channel.

Thus the signal S_i from each spectral channel is given by $S_i = R_i \cdot n_e \cdot f_i(T_e)$, where the temperature dependence $f_i(T_e)$ is determined by folding the spectral density function with the spectral sensitivities of the channels as measured outside the biological shield. It should be noted that for a LIDAR system where the solid angle of collection strongly varies along the line of sight, the values of R_i will vary for each spatial point according to this effect. However, the ratios R_i/R_1 used for determining the electron temperature should be constant for a well-aligned spectrometer.

The investigated procedure basically consists in simultaneously fitting electron temperatures and the values of $R_i \cdot n_e$ to a set of k measurements at a fixed spatial location. For example, 10 laser shots will yield 60 measurements of S_i, allowing one in principle to fit the 20 unknown parameters. To avoid this cumbersome procedure, iteration methods are applied where alternatively temperatures and densities are fitted, using fixed values of R_i, and then these fitted values are used to improve the values of R_i. It should be noted that this method will only restore the relative calibration of the scattering system needed to measure the electron temperature but not the absolute calibration required for the density evaluation. The method is applicable to all Thomson scattering systems using more than 2 spectral channels.

First encouraging results on JET LIDAR data have been obtained.

3. TASK AGREEMENT NO. 2

R. Behrisch, A.P. Martinelli, I. Hughes[1]

[1] DAAD scholarship holder from the University of Belfast, N. Ireland

A detailed analysis of a carbon limiter tile removed after the Be-evaporation phase of JET showed a Be/C deposition several μm thick containing some Ni, Cr, Fe, O and about 30 at % of D.

Time-resolved measurements of erosion and redeposition at limiter-like carbon probes implanted with Mo markers and mounted on the FTS showed deposition of carbon and Be with C/Be between 1 and 4 during the flat- top phase of a reference discharge. The deposition increased exponentially from $10^{16}\ at/cm^2s$ at a distance of 8 cm to $10^{19}\ at/cm^2s$ at a distance of 1 cm. The carbon and Be are probably eroded at the limiters and/or divertor plates and subsequently redeposited on the probe or the FTS at some distance from the area of erosion.

4. ELMy H-MODE SCALINGS BASED ON JET AND ASDEX DATA

O. Kardaun, K. Thomsen[1], J. Christiansen[1], J. Cordey[1], and the JET and ASDEX Teams

[1] JET Joint Undertaking, Abingdon, U.K.

The compilation and analysis of global confinement time scalings for ELMy H-mode discharges based on a combined data set from JET and ASDEX are described under NET/ITER Cooperation Project.

NET/ITER COOPERATION PROJECT

(Head of Project: Dr. Günter Grieger)

Since its foundation IPP host the NET Team, a group of scientists and engineers from the European countries participating in the EURATOM programme. They were called together to prepare the design of NET, the Next European Torus. NET is conceived as the next major step in the European fusion programme, and a considerable fraction of its objectives are in the technology area. IPP contribute to the NET activities both by direct secondment of personnel to the NET Team and by performing NET supporting work.

Since May 1988 IPP also host the ITER Team (International Thermonuclear Experimental Reactor), a project with objectives similar to those of NET but with equal participation of EURATOM, Japan, USSR and USA. IPP is strongly supporting the ITER activities through its support of NET.

1. INTRODUCTION

With the end of 1990 ITER has successfully finished its first phase with the completion of the ITER conceptual design report. IPP has contributed to this through three major channels: (i) direct participation of IPP scientists in the numerous expert meetings called together by ITER to deal with special subjects, (ii) handling of special tasks in support of NET/ITER and (iii) participating in various NET/ITER committees. It is the second part which will be described in this report.
NET/ITER oriented work of IPP was concentrated on performing particular experiments in ASDEX, on a number of scaling investigations and statistical profile analysis, on safety and environmental aspects, and on surface erosion of plasma facing materials.

2. ASDEX CONTRIBUTIONS

ASDEX has - like in the past - contributed to the physics requirement of ITER in the field of:

- power exhaust conditions
- characterization of low-Z materials for plasma-facing components
- steady-state operation in enhanced confinement regimes (H-mode and enhanced L-mode)
- control of MHD activities
- density limits.

Furthermore, the following topics were addressed in the assessment of theoretical transport models on the basis of ASDEX data:

- dependence of transport coefficients derived from quasi-stationary analysis on ion mass, density profile, confinement mode (L,H,H*)
- comparison of measurements with theoretically predicted energy transport coefficients for ions, electrons and toroidal angular momentum in different confinement regimes
- determination of off-diagonal transport coefficients
- transport coefficients derived from perturbation methods (gas-puff oscillations, heat and particle pulses created by sawteeth).

3. SCALING INVESTIGATIONS AND STATISTICAL PROFILE ANALYSIS

(O. Kardaun (Theory Division 3))

3.1 L-mode scalings for energy confinement

The ITER L-mode global confinement database, containing contributions from a large range of Tokamaks, and collected by Kaye et al., has been analysed with special attention to the derivation of global power-law scalings, and estimates of their statistical uncertainty. In cooperation with collegues from each of the 4 `nations` involved in the ITER project, this led to a joint publication in Nuclear Fusion (Yushmanov et al.). The major results of this article are in an ITER89-P (Power-law) and an ITER89-OL (offset-linear) scaling, which both give a prediction of about 2 seconds for the average ITER L-mode operation, with a roughly estimated uncertainty of 20 %. The geometrical scaling of ITER89-P is $\tau \sim R^{1.2}\, a^{0.3} k^{0.5}$. Moreover, two directions of small data variaton were identified, one corresponding to q_{cyl} and the other to $(R/a)a^{0.25}\, k^{0.5}$. More data in those two directions would increase the precision and reliability of ITER L-mode predicions. Moreover, a better distinction between diamagnetic and MHD measurements of the confinement time, and preparations to a future merge with the ITER H-mode database, would be further steps to improve these, already valuable, results.

3.2 Compilation of the ASDEX global H-mode dataset

This dataset was compiled as part of the ITER global H-mode database. It consists of a cross-section of all ASDEX H-mode discharges from 1982-1986 with NBI as the only additional heating method. Seven timepoints (`observations`) per discharge are provided (3 ohmic points, 1 L-mode point, and 3 H-mode points), the last H-mode point corresponding to $\dot{W} = 0$. The variable list for each observation consists of 76 global plasma parameters. Reliable determination of W_{dia}, and W_{mhd} for the first two H-mode points, and the ELM classification (no ELM`s, small ELM`s, large ELM`s) required time-intensive manual intervention. In the so-called `standard dataset`(which excludes observations with low $q_{cyl}$, high fast particle contributions, high radiation, or transient behaviour), there are 160 ASDEX observations with large ELM`s, 80 with small ELM`s and 16 without ELM`s.

3.3. H-mode scalings for energy confinement

In cooperation with colleagues from DIII-D, JET, JFT-2M, PDX and PBX/M the ITER H-mode database (`ITER HM-DB-90`) has been assembled and preliminary analyses of the confinement time scaling have been performed. This resulted in an IAEA contribution (Christiansen et al.), while a more extensive report is in preparation. The work at ASDEX concentrated on analysis of the condition of the dataset and performing global power-law type regression analyses. As the logarithms of B_t, I_p, P_{abs}, n_e, R, a and b (the symbols having their usual meaning) are used as regressors for the confinement time, the data are geometrically represented by a large number of points in 7 dimensional space. The condition of the dataset can now be looked at from two points of view, (a) the ratio between the data variation and the measurement errors (b) the ratio between the data variation and the distance from the database-average to ITER. Both ratios are considered along the principal directions, which point from the center of the database along the principal axis of the ellipse fitting the data-cloud. The first point of view indicates how reliable the individual regression coefficients can be estimated from ordinary least squares regression. From the second point of view, one can see how much the various principal directions contribute to the statistical uncertainty in the prediction for ITER, provided the condition is `good` from the first point of view. If the condition is `moderately bad`to `just good` from the first point of view (ratios between 1 and 4, say), then improved estimates can be obtained by errors-in-variable regression, and some other `advanced` techniques. The condition of both the ELMy and ELM-free datasets appears to be `just good`with respect to the above 7 variables from both points of view, provided that all Tokamaks are used in the regression. This implies, however, that no allowance is made for triangularity, `beam shapedness` (PBX/M), plasma-wall distance, and type of divertor (open/closed). In fact, the open divertor Tokamaks tend to have high kappa values, such that the effects of divertor type and kappa on confinement cannot be separated from the present dataset. Also, the isotope dependence can hardly be extracted from the present dataset. Finally, it appears that some Tokamaks are heavily represented by ELMy, and others heavily by ELM-free discharges.

A sensible choice seems to use diamagnetic confinement times for the Tokamaks with (roughly) parallel beam injection (ASDEX, JFT-2M) and mhd confinement times for the Tokamaks with perpendicular beam injection (DIII-D, PDX, PBX/M). For PDX and PBX/M, only τ_{mhd} is available. For JET, we consider both cases. Taking τ_{dia} for JET, one gets for the confinement time in seconds:

$$\tau_E = 0.022 I_p^{0.85}\, B_T^{0.65}\, (P_{abs}\text{-}W)^{-0.5}\, (A/Z)^{0.5} \cdot R^{1.9} k^{0.65}\, (a/R)^{-0.2} n_e^{0.1}$$

with a rmsq of 13.7 % for the ELM-free discharges, and

$$\tau_E = 0.028 I_p^{0.55}\, B_T^{0.50}\, (P_{abs}\text{-}W)^{-0.5}\, (A/Z)^{0.5} \cdot R^{2.5} k^{0.5}\, (a/R)^{-0.4} n_e^{0.25}$$

with a rmsq of 13.0 % for the ELMy discharges. The units are MA, T, MW, m and $10^{19}/m^3$. The result is obtained by standard regression of the so-called standard dataset (see above, in addition the shots from PDX where the ratio between the divertor and midplane H_α signal is less then 4 are excluded), and imposing the exponent of A/Z. The exponents are slightly rounded and satisfy,

within the family of power-law scaling, to good approximation the constraint imposed by the quasi-neutral, collisional, high-beta Fokker-Planck model, which states that τ_E equals the Bohm time times a function of 7 dimensionless parameters. The high coefficient of B_t is persistent under various variations of the regression set-up, but not in accordance with single parameter scans in some of the Tokamaks. Hence, this is a topic of further investigation. The above scaling gives confinement predictions of 7.0 (1 ± 0.2) sec for the ELMy and 8.5 (1 ± 0.15) sec for the ELM-free confinement time for ITER with I_p = 22 MA, B_t = 5 T, $n_e = 1.25 \cdot 10^{20}$ m^{-3}, P_{abs} = 160 MW, A/Z = 2.5, R = 6, a = 2.15, b = 4.75, where R, a and b refer to the plasma dimensions. In brackets an estimate of the uncertainty is given (3 std. dev. from OLV, roughly 2 std. dev. if the errors in the regression variables are taken into account) of the average ITER performance, under the assumption that the regression model is correct. However, if τ_{mhd} instead of τ_{dia} is used for JET, then one gets 5.3 (1 ± 0.2) s for ELMy, and 7.8 (1 ± 0.15) s for ELM-free ITER discharges. This is due to the fact that τ_{dia} is notably higher than τ_{mhd} for the ELMy shots at JET (on average about 25 %). Further activities are planned for more refined analyses, especially of the thermal energy confinement time.

3.4 ELMy H-mode scalings based on JET and ASDEX data.

The dataset consists of the ELMy H-mode dataset discussed in the previous annual report (which is, except for the JET shots from 1989, also included in `ITER HM-DB90`), extended with 52 boronized ASDEX shots from 1989 (20 of which D into D$^+$). In this analysis, only 1 point per shot is analyzed (where W_{dia} is maximal and, in any case $W_{dia} < 0.3\ P_{tot}$). The condensed results of the analysis have been presented on an EPS poster, which is also available as ITER-1L-PH-4-O-E-10. We discuss some particular aspects: (all results are based on simultaneous regression analysis, using q_{cyl}, B_tI_p, P_{tot} - W, n_e, L ~ $(Rab)^{1/3}$, A/Z and indicators for DN/SN, and wall conditioning (C, Bo, Be), as regression variables. All uncertainties, unless stated otherwise, indicate 1 std. dev.) $\tau_E \sim (A/Z)^{0.45\text{-}0.55}$ in the joint regression, and $\tau_E \sim (A/Z)^{0.55\text{-}0.65}$ in the regression of the ASDEX data alone. (The lower values correspond to τ_{dia}, and the upper values to τ_{mhd}; the JET data consisted exclusively of D into D$^+$ discharges). Each of the two datasets exhibited a negative curvature in the dependence of log τ with respect to log P_{tot} (log $\tau_E \sim$ (- 0.5 ± 0.15) $(\log P)^2$) not present in the joint regression. This suggests an interaction between the heating power and the size of the machine on confinement time. Both carbonized and boronized ASDEX ELMy H-mode shots have about 15 - 20 % (± 3 %) smaller confinement time than the standard stainless steel discharges in the old (closed, DV I) divertor configuration. It should be mentioned that the boronized ASDEX shots had partly carbonized walls and were all with the new (closed, DV II) divertor type. The DN shots at ASDEX had about 10 - 15 % (± 3 %) better confinement than the SN shots, whereas at JET no significant difference was observed. At ASDEX there seems to be a higher B_t and a smaller I_p dependence for $q_{cyl} < 3$ than for $q_{cyl} > 3$. This effect is less strong than the one presented in the previous annual report, possibly related to the simplifying assumption, now made, that the ratio of the confinement times of the boronized, DV II shots and the stainless steel, DV I shots is independent of the plasma parameters. For JET, the diamagnetic and mhd confinement times give conflicting results (for mhd as in ASDEX, for dia there was no difference between the two regions). In both cases, the drawing of any firm conclusions on this aspect of the scaling is hampered by the relatively small variation in q_{cyl}. The size scaling is $\tau_{dia} \sim L^{2.2}$ and $\tau_{mhd} \sim L^{1.8}$, with L ~ $(Rab)^{1/3}$. Given this somewhat primitive model for the scaling with R, a and b, the predictions for ITER at q_{cyl} = 1.8 are:
4.2 (1 ± 0.3) sec for τ_{mhd} and 6.9 (1 ± 0.3) sec for τ_{dia}. (In brackets roughly 2 std. dev. from OLS). The difference between these two results can be understood from the fact that τ_{mhd} at ASDEX is about 25 % larger than τ_{dia}, largely due to the parallel beam injection, whereas for the ELMy shots at JET (with perpendicular beam injection) about the reverse is true. Hence, from this JET-ASDEX comparison, one expects the ITER ELMy H-mode confinement time to be somewhere between 4 and 7 s.

3.5. Statistical profile analysis

(P. McCarghy, (Theory Division 3))

The work on statistical profile parameterisation has come to a temporarily conclusion by two IPP reports (5/34 and 5/35). The theoretical report gives a precise account of the statistical models and techniques to analyze the influence of plasma parameters on e.g. density and temperature profiles as measured by YAG-laser Thomson scattering experiments. Some continuous profile models are discussed with emphasis on (general) spline representations also describe the influence of the plasma variables on the profiles. Special attention is given to the modelling of the propagation of errors. An account is given of relevant estimation methods, and of statistical tests to decide whether various sub-models are in accordance with the data (with profile invariance, and the hypothesis of gaussian profile shapes as interesting special cases). A derivation and explicit formulas are given for local and global confidence bands for the underlying profile (for any specified values of the plasma parameters). Similarly, a discussion is given for prediction bands of new single profile measurements, and asymptotic confidence intervals are derived for volume averaged values of density, temperature and pressure, obtained by (numeric) integration of the measured n_e and T_e profiles. The addition of a running example of practical analyses is planned to make the report more accessible to a larger audience.

The practical report (Mc Carthy et al.) describes the analysis of 2 extensive ohmic datasets in the Saturated Ohmic Confinement regime (105 temporally compressed profiles from ´high density´, ´low q_a`, Ti-gettered discharges, and 38 from ´medium density`, ´medium q_a`, non-gettered discharges). An extended version of this report is submitted for publication. Global confinement scalings are given of all major plasma parameters,

$$W_{dia}, W_{mhd}, W_{th}, V_{loop}, Z_{eff}, \langle T_e \rangle,$$

confinement times, etc. A sensitivity analysis was made to investigate the influence of various assumptions on the scaling of the energy estimates. One aspect of these analyses is that, in contrast to the results some previous single scan experiments, in general no confinement degradation (only a saturation) at high values of n_e is observed. The scaling of the temperature peaking factor is rigorously shown to be in good agreement with the ansatz of classical resistive equilibrium, which implies that

$$\frac{\langle T^{3/2} \rangle_{r=0}}{\langle T^{3/2} \rangle_{r=a}} = \frac{q_{r=a}}{q_{r=0}}$$

A detailed profile analysis has been performed, with a careful analysis of the influence of outliers and of the propagation of the various error components. In addition to the regression formulae, the results are summarized by convenient graphical representations, from which one can quantitatively judge both the hypothesis of profile invariance and of gaussian profile shapes. It appears that q_{cyl} influences the profile shapes of T_e and n_e (and hence p_e) noticeably in the region $0.2 < r/a < 0.6$, and that the hypothesis of gaussian profiles is severely rejected.

4. Safety and Environmental Aspects

In the framework of the IPP/NET collaboration problems of safety and environmental aspects of the next step of fusion experiments are investigated. The predictions of doses following a continuous HTO release were analyzed and compared. On the basis of the Canadian and French tritium release experiments the accidental tritium release of a fusion reactor was investigated, too. Concerning the safety aspects of the next step problems of plasma chamber accidents are being treated, mainly reactions of the chamber components with oxygen or air and the consequences of high power run-away electrons for the plasma chamber. Moreover, the available results of investigations on the temperature development in a fusion reactor after loss of cooling were analyzed, and two-dimensional calculations of the temperature distribution for various parameter sets will be performed.

5. Surface Erosion of Plasma Facing Materials

Within the frame of a NET task agreement sputtering of high Z materials such as Mo and W at bombardment with H^+-, D^+-, He^+- and C^+-ions has been investigated in some detail, both with the computer simulation program TRIM and with the high current ion source. For bombardment with energy and angular distributions of the ions, corresponding to a Maxwellian distribution and acceleration in the sheath in front of wall plates, the threshold energies for sputtering are reduced by up to a factor 5 compared to the threshold at single energy normal ion incidence. C^+ at normal incidence causes a build-up of a C-layer with the known selfsputtering yield < 1. At angles of incidence > 45° the selfsputtering yield for carbon is > 1 and a continuous erosion of a carbon rich layer is found.

Stellarators

The IPP activities on Stellarators are now concentrated in two divisions. Experimental Division 2, headed by G. Grieger, comprises the WENDELSTEIN 7-X oriented activities of the former Experimental Division 2, together with those of the former Theoretical Division 2, after A. Schlüters retirement. The activities on running the experimental facility WENDELSTEIN 7-AS are now concentrated in the Experimental Division 3, headed by F. Wagner.

W 7-AS was operated continuously in 1990 (apart from the usual summer shut down) and produced a large amount of experimental results. Plasma operation was generally carried out at full field of 2.5 T; neutral injection and electron cyclotron resonance heating were routinely used up to their full power capabilities. Thus, W 7-AS and its infrastructure demonstrated full power operation over an extended period of time. In particular, the reliable and problem-free operation of the modular coils routinely at full parameters gives important proof of the feasibility of this coil concept.

The major results from the W 7-AS studies are:

◊ Reduction of Pfirsch-Schlüter currents indicated by a reduced Shafranov-shift up to the highest $<\beta>$ -values achieved, namely 0.8 %. Thus the principle of Stellarator optimization is demonstrated.

◊ Confinement times beyond 30 ms both for medium density - low power ECRF and high density - high power NI heated plasmas. In particular, the confinement studies reproduced the favorable density scaling which clearly points out a safe route to good confinement for Stellarators. The τ_E values of beam heated plasmas at high density are clearly beyond the expectations from Tokamak L-mode scaling relations. A confinement time data bank has been started.

◊ Wall optimization via carbonization or boronization increased the operational range of the experiment: Already with one gyrotron (180 kW) plasmas up to the ECRH cut-off density ($5 \cdot 10^{13}$ cm^{-3}) could be maintained. At full NI power, a density limit of $n_e \approx 3 \cdot 10^{14}$ cm^{-3} was achieved (corresponding to a Murakami-parameter of 20).

◊ Detailed studies addressed the development of bootstrap current I_b and the possibility to compensate it via ECRH current drive. Good agreement between the expected neoclassical value for I_b was found. Also ECRH current drive efficiency can be modelled rather well. Thus, to a large extent these crucial elements for the configuration of currentless and shearfree stellarators can be predicted and computed.

◊ The study of the plasma boundary, scrape-off layer and plasma-wall interactions has been intensified.

The work oriented on WENDELSTEIN 7-X was governed by the preparation of the EURATOM Phase-I Proposal for this device. Selection of the magnetic configuration forming the basis of that proposal was made and all the details were calculated. Extra coils were defined to allow sufficient flexibility for experimentation. Scientific aims were defined along with the dimensions of the device and the necessary heating power evaluated accordingly. Two industrial study contracts led to a conceptual design and a cost analysis of the facility. The Proposal was finished in August 1990 and submitted to EURATOM for Phase-I agreement.

The configuration of WENDELSTEIN 7-X is optimized for high-quality nested magnetic surfaces being rather insensitive to the plasma pressure, good equilibrium and good stability properties, neo-classical transport limited to acceptable values, good chances for anomalous contributions to the transport to be small, good alpha particle containment, small bootstrap currents, and a manageable coil arrangement. The main dimensions of W 7-X are: major radius 5.5 m, average plasma radius 0.55 m, maximum toroidal field on axis 3 T. The size selected is big enough for sufficient plasma-wall distance and should allow reaching reactor relevant plasma conditions with tolerable heating power of 10 to 20 MW. The results should allow convincing predictions on the performance of an ignition machine. Since long-term operation is a key issue for Stellarators, the device should allow demonstration of this capability. Consequently, the magnet will be superconducting.

Additional work was concentrated on divertor studies exploiting the properties of the Helias configuration, on predictions of the transport properties, on coil studies, on non-local MHD studies, and on studies on some reactor properties. On the engineering side, an R&D programme was defined to assure that all technologies necessary for the construction of W 7-X are at hand. A demonstration coil and a test section of the cryostat are essential elements of this R&D programme. The conductor development is ready to be started.

Details can be found in the reports below.

WENDELSTEIN 7-AS

(Head of Project: Dr. Hermann Renner)

W7-AS-Team

V. Afanasiev[6], J. Baldzuhn, N. Besedin[7], R. Brakel, R. Burhenn, G. Cattanei, A. Dodhy, D. Dorst, A. Elsner, K. Engelhardt, V. Erckmann, U. Gasparino, S. Geißler, L. Giannone, S. Grebenchtchikov[4], P. Grigull, U. Gutarev[7], H. Hacker, H.J. Hartfuss, D. Hildebrandt[8], A. Izvozchikov[6], R. Jaenicke, S. Jiang[3], J. Junker, F. Karger, M. Kick, J. Kholnov[4], K. Kondo[2], H. Kroiss, G. Kuehner, I. Lakicevic, A. Lazaros, H. Maassberg, C. Mahn, T. Mizuuchi[2], A. Navarro[1], H. Niedermeyer, M. Ochando[1], W. Ohlendorf, F. Rau, H. Renner, H. Ringler, J. Saffert, J. Sanchez[1], F. Sardei, U. Schneider, G. Siller, M. Tutter, F. Wagner, A. Weller, H. Wobig, H. Wolff[8], E. Würsching, M. Zippe, S. Zöpfel, H. Zushi[2].

ICRH (Ion Cycl. Resonance Heating)

M. Ballico, J. Bäumler, W. Becker, F. Braun, R. Fritsch, F. Hofmeister, J.M. Noterdaeme, S. Puri, F. Ryter, H. Wedler,
F. Wesner. (Technology Division)

NBI (Neutral Beam Injection)

J.H. Feist, K. Freudenberger, M. Liniers[1], W. Ott, F.-P. Penningsfeld, E. Speth
(Technology Division),
W. Melkus (ZTE)

Computer Centre

J. Gassmann, H. Lederer, I. Weidl

ECRH (Electr. Cycl. Resonance Heating)

W. Kasparek, G.A. Müller, P.G. Schüller, M. Thumm.
(IPF Stuttgart)

Pellet Injection

K. Büchl, R. Lang (Division 1)

Plasma-Surface Interaction Group

R. Behrisch, A. Martinelli, V. Prozesky, J. Roth, E. Taglauer

---

1) Guest from Ciemat, Madrid,
2) Guest from Kyoto University,
3) Guest from Southw. Institute of Physics, Leshan, China,
4) Guest from Institute of General Physics, Moskau
5) Guest from IPF, University of Stuttgart
6) Guest from Ioffe Institute, Leningrad
7) Guest from Inst. of Phys. and Technology, Kharkov
8) Guest from ZIE d. ADW, Berlin

1. STATUS

1.1. OVERVIEW

1.1.1 Status of the experiment

From the beginning of 1990 the W7-AS stellarator was routinely operated at the full specified parameters for the magnetic field of 2.5 T. The improvement of the support of the critical modular coils MF *3 and *4 restricts the deformation to a tolerable level. For about 5000 shots completely reversible behaviour of the magnetic system was observed, demonstrating the effectiveness of the measures to stabilize the coil system for a long lifetime.

The experiments were concentrated on optimizing plasma build-up and heating by means of ECF power at 70 GHz of up to 1 MW. With a pulse duration of up to 1.5 s plasmas with densities of $5 \cdot 10^{19}$ m^{-3}, close to the cut-off density, electron temperatures of $T_{eo} \leq 2.5$ keV and ion temperatures of $T_{io} \leq 0.45$ keV were achieved. The database for evaluation of local heat and particle transport in the plasma and for comparison with transport models (DKES) could be significantly extended. The results of sophisticated experiments with local power deposition for local current drive (ECCD) are in good agreement with theoretical models developed on the basis of a simplified Fokker-Planck code. Thus, even local control of the plasma current to optimize the magnetic configuration becomes predictable to minimize pressure effects.
By ECRH a target plasma for combined heating with neutral beam injection (NBI) and ion cyclotron heating (ICRH) became available. Pellet injection was used for a rapid increase of the density. However, first experiments showed a significant increase of the radiation losses towards higher densities. Even the quasioptical launch of ECF power leads to contamination of the plasma by carbon, oxygen, iron and titanium. Carbonization and boronization were applied to reduce the radiative power losses and influence the recycling of neutrals. With reduced impurity concentrations the energy replacement time τ_E could be improved up to 30 ms for both conditions, ECF and NBI heating. With NBI heating a maximum energy content of 33 kJ was obtained at very high densities of $n_e > 3 \cdot 10^{20}$ m^{-3} and temperatures of 0.5 keV. The central β at a magnetic field of 2.5 T exceeded 1.7%.

The integration of members of the ASDEX-team allows improvement of the diagnostics at W7-AS. Investigations of the plasma boundary and the analysis of fluctuations relating to transport phenomena will be extended.

1.2 RESULTS

1.2.1 Magnetic configuration

1.2.1.1 Rotational transform, shear, plasma current

As in the experiments at the low magnetic field of 1.25 T, a strong dependence of the confinement on the parameters of the magnetic configuration is found: Optimal confinement is obtained for values of the rotational transform ι at the boundary close to 1/3 and 1/2. Rational values of the transform have to be excluded from the entire plasma, if not sufficient shear is established. Such perturbations are indicated by local fluctuations as detected by means of ECE, soft-X measurements and reflectometry. The profile of the vacuum transform is modified by the secondary currents and pressure-driven net currents (bootstrap current) of up to 5 kA. Control of the current by induced voltages ($U_L < 0.1$ V), current drive (ECCD) of ECF by $k_{II} \neq 0$ and unbalanced neutral beam injection is necessary. So far, the condition $I_p = 0$, compensating the bootstrap current either by ohmic currents or by central current drive, leads at higher pressure and higher temperatures to positive shear, where "resonances" always exist inside the plasma. More sophisticated shaping of the current density profile by off-axis power deposition is possible and may allow further improvement. In order to reach a state of equilibrium long time constants of up to 300 ms have to be considered at electron temperatures $T_e > 1$ keV.

1.2.1.2 Equilibrium and stability

One of the aims of the partly optimized W7-AS field configuration was to reduce the Pfirsch-Schlüter (PS) currents. From the W7-AS optimization, a PS-current reduction by a factor of 2 was expected in relation to a standard stellarator. This leads to a reduced Shafranov shift. The outward shift of the magnetic axis with β_0 is confirmed by soft-X observations. Comparison with predictions based on the KW equilibrium code verifies the PS current reduction by a factor of 2. In addition, the B_z field component originating from the PS-currents, which is related to the volume-averaged $<\beta>$, is measured directly with magnetic loops and agrees with the relation $B_z \sim <\beta> B_0/\iota$ as simulated by the VMEC equilibrium code. Volume-averaged β values $<\beta>$ of up to 0.16 % and 0.28 % were found when using ECRH for B_0=2.5 T and B_0=1.25 T, respectively. The maximum peak β_0 values were 0.52 % and nearly 0.8 %. Maximum values of $<\beta>$=0.7% and β_0=1.7 % were found with NBI. So far, the maximum values of β seem limited only by the available heating power. The experimental $<\beta>$ values were much lower than the predicted $<\beta>$ limit of about 2 %. However, localized fluctuations and mode activities were found by the SX and the ECE diagnostics, from reflectometry and from H_α measurements. These activities mainly relate to configurational effects for discharges with resonances at ι=1/2 or ι=1/3 within the confinement region. Current profile analysis indicates that these fluctuations and mode activities not relating to the stability limit are stabilized by sufficient internal shear as generated by the internal currents.

1.2.2 Transport

The local analysis of electron heat transport is based on measured density and temperature profiles. Compared with the case of 1.25 T, a significant improvement of the confinement is obtained at the higher magnetic field. Typical values for the electron heat conduction χ_e are 0.2 - 0.9 m^2/s for densities of $4 \cdot 10^{19}$m^{-3} and temperatures of 1-2 keV. In the centre at low collisionality, the evaluated values do not differ much from neoclassical values. Especially at the boundary, however, the experimental values are one order of magnitude larger than the predictions of the DKES code. For experiments with reduced aperture (limiter) the rapid increase of χ_e at the boundary is

prevented. This may indicate that the transport is enhanced by destruction of magnetic surfaces at the boundary either by magnetic perturbations or by pressure effects on a geometric scale. A statistical analysis of the electron heat conduction including about 110 measured profiles delivers as significant scaling parameters: density, magnetic field, rotational transform and input power. Only a weak dependence on the local temperature is found. The global energy replacement time can be described fairly well in terms of the LHD scaling. Calculations of the bootstrap current on the basis of the DKES code are in fair agreement with the experimental data. The evaluation of the current-drive efficiency for ECRH using a simplified Fokker-Planck code describes the observed currents quite well if trapped particle effects due to the particular magnetic configuration of W7-AS are included.
Taking into account the W7-AS geometry calculations based on the DEGAS code and on H_α measurements yielded informations on the particle balance. Experimental diffusion coefficients $D = 1/2 - 1/10\ \chi_e$ with similar dependences on the ECF power, inversely dependences on density, magnetic field and rotational transform were derived at the boundary.

1.2.3 Boundary

As derived from analysis of exposed probes and the observed pattern of plasma-wall interaction, the edge region of W7-AS is highly inhomogeneous. Nevertheless, certain essential details can be reasonably described by guiding-centre orbit calculations with a Monte Carlo code. Such calculations may help to evaluate the particle fluxes to the wall in order to optimize and integrate divertor-like structures for density and impurity control.
Radial T_e and n_e profiles in the SOL were measured. Poloidal dependences of the radial decay length are related to the X-point structures of "natural islands" with a (5/m)-symmetry and a modification of the connection length caused by local limiting apertures depending on the particular value of ι. The reduction of low-Z impurities causes a significant increase of the edge temperature and hence an increase of the limiter load. Consequently, the short lifetime of the boron coatings of the limiter becomes crucial. For improvement the Ti-coated graphite tiles on W7-AS will be replaced during spring 1991 by boron/graphite ones (boron 20 %).

1.3 HEATING

1.3.1 ECF

The complete 70 GHz system consisting of 4 gyrotrons (200 kW, 3s) and a pulsed gyrotron (200 kW, 0.1s) was used. The experiments with the pulsed gyrotron for current-drive launching at the poloidal plane with a small inverted magnetic field gradient were terminated at the end of May 1990 as planned, to allow installation of the 140 GHz system. The pulsed gyrotron with its launching angle of 10° to the perpendicular was used to test models of ECF-current drive. For this purpose the magnetic mirror ratio was varied by particular values of the rotational transform.
The KfK successfuily operated the prototype gyrotron at 140 GHz and could demonstrate the specifications. During June 1990 the gyrotron was delivered to the IPP. The major part of the transmission line was already manufactured before by the IPF and the IPP workshops and installed at W7-AS by October 1990. Thus, first experiments using ECRH with 140 GHz will possibly be performed in March 1991.
In the meantime a proposal for replacement of the existing 70 GHz system by a 140 GHz one with increased power was submitted for approval.

1.3.2 NBI

During July 1990 the investigations at W7-AS were concentrated on experiments using neutral beam injection. After carbonization by glow discharges with a mixture of He and 30% CD_4 (or CH_4) the content of high-Z material (Fe und Ti) was significantly reduced. With reduced radiative losses the parameter range of plasmas was extended to much higher densities than before and to pulse durations of up to 300 ms. The target plasma is produced by 70 GHz ECRH at a main field of 2.5 T or 1.25 T. The full power of NBI
($P_N \leq 1.5$ MW) on W7-AS with injection of H^o with an accelerating voltage of 45 kV was used for further heating. With carbonized walls the recycling coefficient is larger than 1 and the evolution of the discharge is characterized by a steady increase of density. Before saturation the rate of density increase is determined by gas released by plasma-wall interaction rather than by the flux associated with NBI. The maximum energy content of 28 kJ ($\beta_O \approx 1.5$ %) at 1.4 MW absorbed power was achieved at 2.5 T and a plasma radius of 0.176 m for a rotational transform of $\iota = 0.34$. With balanced injection the observed bootstrap current of 1.2 kA agrees well with the calculated value. Unbalanced injection generates a change of the net current by a few kA, depending on the density. The maximum obtainable density, and consequently ß, seems related to the absorbed power, as long as the electron temperature stays above 350 eV to minimize radiative losses and prevent radiative collapse. After boronization a maximum density of $n_e > 3 \cdot 10^{20} m^{-3}$ was achieved
(Murakami parameter: $nR/B > 20\ m^{-2}\ T^{-1}$).
At present only a global description of the energy confinement is possible. He glow discharges and reduction of the input power allow the density to be stabilized close to
$n_{eo} = 1 \cdot 10^{20}\ m^{-3}$. At these densities a maximum energy replacement time of 30 ms was achieved.
In operation at the low field of 1.25 T discharges at similar densities and a slightly reduced temperature could be maintained. Using only 3 injectors ($P_N \leq 1.1$ MW), plasmas with an averaged <ß> of 0.65% and an energy replacement time of typically 10 ms were produced.
Due to the favourable scaling of the energy confinement with increasing density, upgrading of the available power to 3 MW by additional installation of 4 sources at the existing beamlines seems promising and is planned to continue high-ß experiments.

1.4 TECHNICAL STATUS

After improvements in the coil support structure and recommissioning in December 1989, the W7-AS machine was successfully run for about 5500 shots at 2.5 T and different iotas between 0.33 and 0.67.
The stresses in some of the coils were largest at low iotas when the magnetic field of the modular coil system (MF system) and of the toroidal coil system (TF system) were operated in the same direction.

The currents in both systems reached their maximum design values with $\iota_o = 0.67$ (MF system and TF system in opposite directions). To prevent mechanical overloads in the MF system if the power supply of the TF system fails, a fast protection system had to be installed to turn off the power supply of the MF system.
An additional regulated power supply with 80 kV/40 A was installed and is now being commissioned. More of such power supplies will be required when the 70 GHz gyrotrons have to be replaced by 140 GHz gyrotrons.

1.5 DATA ACQUISITION

Major developments in 1990 included:
- a fast hardcopy system for printing VAX workstation GKS images on an HP Laser Printer;
- installing a separate Ethernet segment for data analysis, parallel to the data acquision segment;
- setup of the pellet injection diagnostic system;
- upgrading the VAX operating systems to VMS version 5.4;
- installing 320 Mbyte system disks and new disk controllers on all diagnostic systems;
- replacing the "fast link" data transfer to the IBM 4381 with a TCP/IP connection:
- significant increases in the overall amount of acquired data.

The fast hardcopy system consists of a DRV11-W parallel DMA interface connected via a simple adapter card developed by the UDAS group to the Centronics interface of the HP-LaserJet IID printer. Additionally, software was written to read in the bitmap of a graphic workstaton image and transmit it to the printer via the DRV11-C interface. Units were installed on the ECRH and NBI diagnostic computers in January and February.

The groundwork was laid for the eventual expansion of the W7-AS computer network to include high-performance workstations for data analysis. A separate Ethernet segment, with its own connection to the main data acquisition system, was installed parallel to the existing data acquisition network segments. It is planned to extend this segment to reach the new office tracts in the I-building. This segment also connects directly to the IBM 4381 computer and via a bridge to the IPP network and to the W7-AS data acquisition network. The computers inherited from the ASDEX experiment as well as high-performance computers to be acquired in the future will be connected to this network, where they can be used for analyzing W7-AS online data (as well as old ASDEX shots).

The pellet injection diagnostic was completely set up and put into operation by May 1990. Its three ADC modules contributed 1.7 Mbytes to the total data acquired, which allowed the diagnostic to be included only when definitely necessary.

In May, work began on improving the performance and functionality of the VAX-based Data Acquisition System. A major goal was the support of on-line synoptic data analysis on all diagnostic computers. Introducing a Local-Area VAX Cluster (LAVC) with remote access to the experiment shot file was considered to be the most effective method. Since the existing version 4.5 of the VAX/VMS operating system was not compatible with the LAVC software, it was necessary to upgrade all systems to version 5.3. Additional reasons were the upgrade support for MicroVAX-III computers (not able to run VMS 4.5), the introduction of new software such as DEC windows and the VMS/ULTRIX Connection Internet software. After preparatory tests between May and July, it was planned to take advantage of the summer recess to install the new system on all experiment computers.

In August and September, all diagnostic computers were successively converted to the new system. At the same time, the peripheral hardware was reorganized, with new disk controllers and larger disks installed to provide a minimum of 320 MBytes of storage for each system, as well as the possibility of easily installing further disks if necessary. The conversion was completed in time to begin experimental operations in mid-October.

A number of unexpected problems, however, caused major delays in the conversion. Undocumented solutions had to be found to install and configure non-standard data acquisition hardware under the new operating system. The MEDAV soft X-ray diagnostic subsystem software did not work due to errors in the new version of the parallell interface software (purchased from DEC). Finally, the VAX Cluster concept had to be abandoned due to unacceptable side-effects experienced in the first two weeks of experimental operations: shutting down and restating one node caused unpredictable hangups and delays at other systems and unexplained system crashes frequently occurred.

These problems required a further upgrade to VMS 5.4 and several more weeks of work to achieve stable operations. The synoptic on-line analysis from the diagnostic computers could not be made available as planned.

The HSCC "fast link" data transfer system connecting the VAX 750 computer to the IBM 4381 was always a source of problems, often failing or causing system crashes or other hardware errors. The introduction of the UCX (VMS/ULTRIX connection) software - an internet protocol package for the VAX - provided a standard and reliable alternative for efficient data transfer. Adaption of the programs involved was completed in a cooperative effort involving the Garching computer centre and the W7-AS data acquisition team. The work was finished in time to start operations in the last quarter of 1990. Since then, the data transfer has been operating at almost 100 % reliability.

The overall load on the UDAS data acquisition system has grown far beyond the originally required one megabyte and even the two megabytes actually planned for. From 2.5 Megabytes at the beginning of 1990, the main shot file size grew to 4.3 Mbytes in the final phase of December 1990- This does not include the 400 Kbyte acquired by the NBI diagnostic (but not transmitted to the main acquisition computer) or the pellet injection diagnostic, capable of delivering up to 1.7 Mbytes. A number of shots including the pellet diagnostic with a total of 5.4 Mbytes of data were acquired in July.

2. HEATING

2.1 Electron Cyclotron Resonance Heating

2.1.1. General aspects

Electron cyclotron resonance heating (ECRH) was used as a standard method for plasma build-up and electron heating in more than 10000 plasma shots with a typical pulse duration of up to 1.5 s. The RF-power was generated by up to 5 commercially available VARIAN gyrotrons, located approximately 50 m from the experiment in a separate hall. Each of them delivers an output power of 200 kW at 70 GHz. This frequency corresponds to a resonant magnetic field of 2.5 T for 1st-harmonic ordinary mode heating and to 1.25 T for 2nd-harmonic extraordinary mode heating. Four of the five available gyrotrons had CW capability. The microwaves are transmitted to the stellarator by means of distinct circular oversized waveguides and the four long-pulse microwave beams are finally combined at one poloidal plane by a quasi-optical launcher. The beams are launched in the linearly polarized Gaussian mode from the low-field side with a mirror system inside the vacuum chamber. Each RF-beam hits a movable focusing mirror and can be directed into the plasma at arbitrary poloidal and toroidal angles with respect to the orientation of the stellarator magnetic field. Electron cyclotron current drive (ECCD) experiments as well as on/off-axis heating experiments can easily be performed without the necessity of tuning the magnetic field. The curvature of the mirror surface is chosen to position the beam waist with plane phase fronts in the plasma centre (normal incidence). An additional segmented graphite mirror is installed at the inner torus wall opposite the four launching mirrors which reflects the nonabsorbed fraction of the incident waves back to the plasma in a well-defined polarization. An array of 38 monomode waveguides is embedded in the central section, allowing direct measurement of the RF-beam quality with respect to beam deflection in the presence of a plasma. The fifth beam was launched at a different poloidal plane and was used for up-down shifted resonance current drive experiments in combination with the other four beams.

Whereas the first experimental campaign in 1989 was mainly dedicated to ECF investigations of 2nd-harmonic X-mode heating with B_{res} = 1.25 T and a corresponding cut-off density of $3 \cdot 10^{19}$ m^{-3}, the experiments in 1990 concentrated on 1st-harmonic O-mode heating at B_{res} = 2.5 T in an extended plasma parameter range given by the higher cut-off density of $6 \cdot 10^{19}$ m^{-3}. The extension of the pulse width towards 1.5 s, being limited by data acquisition reasons only, showed that the global plasma parameters could be maintained constant during the pulse by controlling the edge value of the rotational transform and the gas fuelling as seen from fig. 1.

The total radiated power remains constant and is typically 30 % of the heating power offering interesting prospects of a further extension of the pulse width. Such discharges are well suited to heat wave propagation analysis by power modulation of the incident microwaves, as can be seen on the bottom trace of fig. 1.

2.1.2 ECRH at 140 GHz

A pilot experiment at 140 GHz was installed in close collaboration with the gyrotron development group of the Kernforschungszentrum Karlsruhe (KfK) and the ECF group at the IPF Stuttgart.

The prototype gyrotron was developed at the KfK and transferred to the IPP after successful operation in the test bed at Karlsruhe. The frequency fits to the nominal W7-AS magnetic field at 2nd-harmonic heating and can be run together with the 70 GHz system described in the previous section. At 140 GHz the cut-off density for plasma operation is shifted to twice the value at 70 GHz ($1.2 \cdot 10^{20}$ m^{-3}), which will considerably extend the accessible parameter range for plasma investigations and allow plasma heating in combination with NBI heating if sufficiently high power is installed.

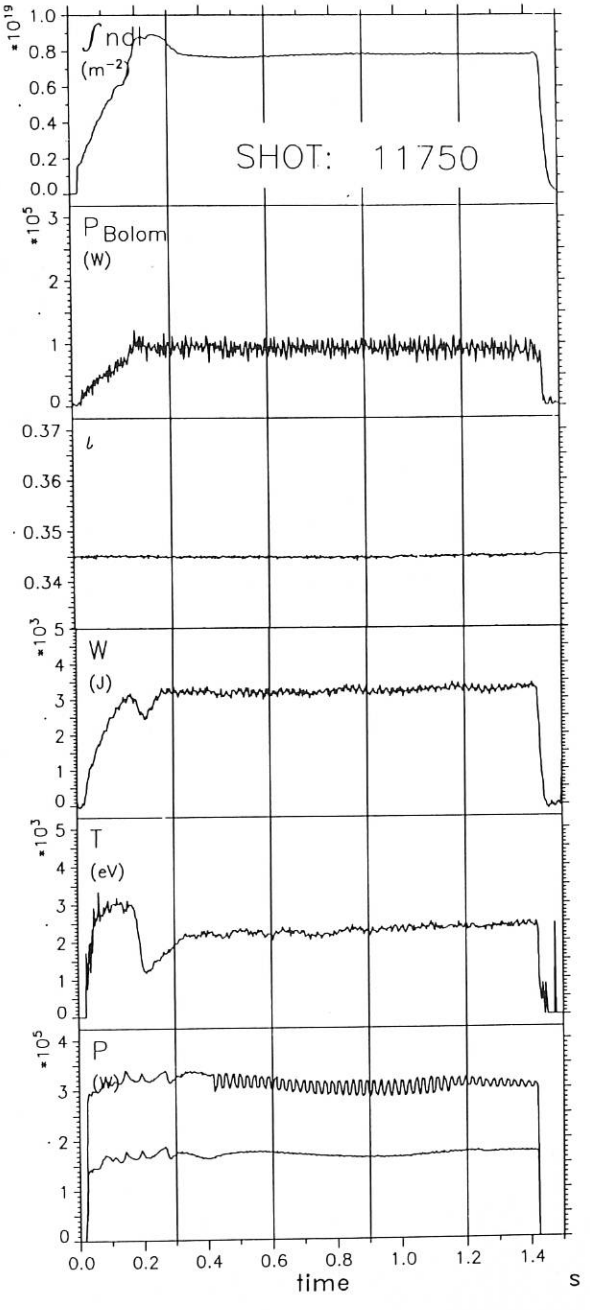

FIG. 1: *Line-integrated density $\int n_e dl$, total radiated power P_{Bolom}, rotational transform ι, total stored plasma energy W, electron temperature T_e from SX diagnostics, and ECF input power P as a function of time.*

The technical preparations at the IPP included a new series-regulator with 5 MW DC capability, the cryogenic system for the cooling of the superconducting magnet, the water-cooling system, the data acquisition and control system and were completed on schedule. The KfK-gyrotron was successfully operated together with the IPP peripherals and achieved the specified output power of 0.1 MW for a pulse duration of 0.1 s in the TE_{03} mode. The gyrotron and the superconducting magnet are shown in fig. 2.
The transmission line was designed by the IPF Stuttgart and is built as a pure open optical system, in contrast to the waveguide solution used for the 70 GHz ECRH system. Such optical systems theoretically provide the high power capability required for future RF-sources in the power range from 0.5 to 1 MW per gyrotron and are well adapted to the 2 mm wavelength of the microwaves. The short wavelength would enlarge the various mode converters necessary for a conventional oversized waveguide system to an intolerable size because the waveguide diameter can no longer be reduced at high power density.
In such an optical system the microwaves are guided from the RF-source to the plasma by an appropriate arrangement of mirrors. The TE_{03} gyrotron output mode is transformed to a circularly symmetric, linearly polarized Gaussian free-space mode by means of a Vlasov converter in combination with appropriately shaped imaging mirrors. The converter is partially seen on top of the gyrotron output waveguide in fig. 2. The efficiency of such Vlasov converters at present is not sufficiently high (typically 80 %) and intense investigations are under way to improve the efficiency.

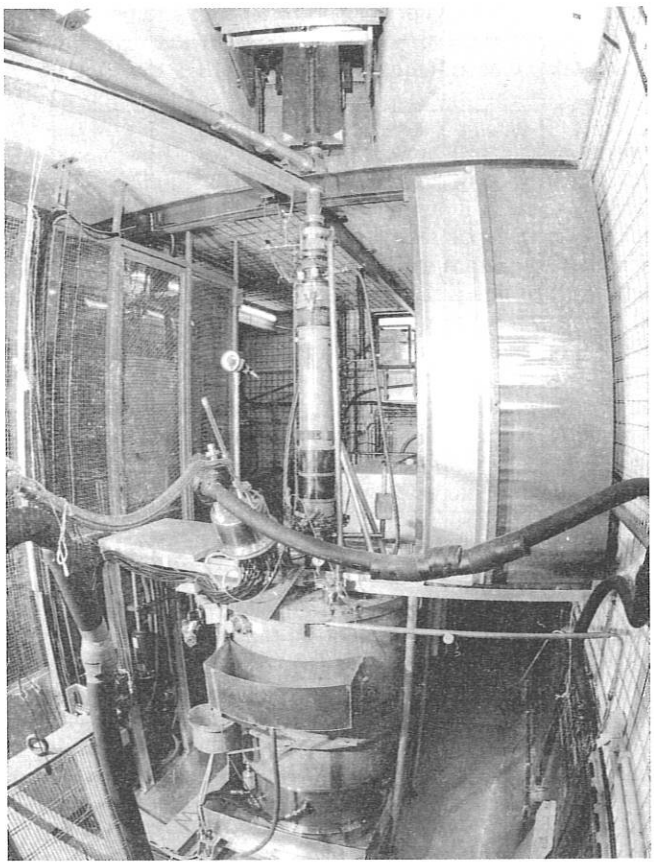

FIG. 2: *The 140 GHz KfK gyrotron and the superconducting magnet. A part of the quasi-optical Vlasov converter is seen at the top of the figure.*

The Gaussian beam is fed to the transmission line consisting of ellipsoidal reflectors which guide the beam towards the vacuum vessel and simultaneously perform appropriate focussing to the plasma centre in the extraordinary mode. The technical installation of the transmission system and the in-vessel launching mirrors was completed and the alignment was tested at low power. The launching structure gives access to on/off-axis heating and current drive experiments and the design is based on the launcher design used for the 70 GHz system. Because of the low RF-output power, the gyrotron will mainly be used for diagnostic purposes such as heat wave propagation experiments in high-density plasmas rather than for bulk plasma heating. First plasma experiments with modulated microwave power are scheduled for early 1991.

2.2 NBI

2.2.1 Status and performance of the NI system

Both NI boxes, each equipped with 2 sources were available during the whole year and fired about 1600 shots into the plasma using 1 to 4 sources with pulse lengths of up to 0.7 s. Some smaller faults mostly occurring in power supplies could be repaired very fast. A very high reliability of the NI-system of more than 95 % thus could be reached.
The standard working gas was H^o, but He^o, too, was injected. Table 1 gives an overview of the beam parameters measured with the torus calorimeter.

	Hydrogen (45 kV, 24 A)	**Helium** (50 kV, 20 A)
transmission	38 %	50 %
neutralization	66 %	75 %
neutral power	410 kW	500 kW

Table 1: beam parameters of NI/W7-AS for H^o and He^o

The torus calorimeters of both boxes had to be removed during the summer shutdown of W7-AS since space was needed for other diagnostics (ECE and an optical camera). An optical beam diagnostic using H_α Doppler spectroscopy was installed and the spectral data are now being routinely sampled for one source per shot. Standard evaluation of these data will be implemented soon, giving routinely divergence and species mix, including the oxygen content of the beams.
Two major faults occurred this year: firstly, a leakage of the water-cooled duct of the west box in January and, secondly, a leakage of the vacuum seal between this box and its valve in December.
The duct leak could not be repaired in situ. The duct therefore is no longer cooled. The maximal temperatures observed so far were below 90° C operating with both sources of this box at pulse lengths of up to 0.7 s. These temperatures are still in an acceptable range, but at least before doubling the NI power to 3.0 MW (see NI proposal of Dec 1990) the cooling jacket must be repaired or replaced.
The leakage of the metallic vacuum seal between the box exit and the valve was caused by a very high local heat load, which also melted the ceramic surface layer of the insulation flange nearby. This local power load could only be produced by re-ionized beam particles entering the duct region and being deflected by a stray field in the range of 0.5 T. Direct beam

losses cannot reach this point. The damaged seal now is replaced and additional copper shields are mounted in both boxes.

2.2.2 Experimental results with NBI heating

Beginning in February 1990, the NBI heating experiments were performed at a magnetic field strength of 2.5 T.
The discharges were usually started with a short ECRH pulse generating a target plasma for NBI with typical parameters: $n_e \approx 0.4 \cdot 10^{20}$ m^{-3}, $T_e \approx 1500$ eV. Starting from this target plasma several NBI scenarios were realized by combining different sources at various power levels, depending on the wall conditions, gas puffing and magnetic configuration used. In this way, balanced, unbalanced, pure co or pure counter injection could be studied.
In the 1990 W7-AS experimental period, the wall conditions of W7-AS were changed twice: starting with the pure stainless-steel wall, firstly by carbonization and secondly by boronization of the vessel. The maximum energy content obtainable strongly depended on the actual wall conditions.
Two types of discharges can clearly be separated: transient discharges running into highest density and energy contents and quasistationary discharges at lower density:

2.2.2.1 Transient NBI-discharges:

The optimum energy content and the typical plasma parameters obtained under very different conditions are listed in table 2. SS stands for the pure W7-AS wall, 1.C and 2.C for wall conditions after first and second carbonization, respectively, and 1.B (2.B) for the wall after first (second) boronization.
The pure wall (SS) only allowed a maximum energy content of ≈12 kJ at a density of $0.7 \cdot 10^{20}$ m^{-3} ($P_{NI} \approx 1.0$ MW), whereafter the discharge collapsed due to increasing radiation.
After the first carbonization and with the inner sources only ($P_{NI} \approx 0.75$ MW) about 17 kJ could be reached at optimum configuration, and with all four sources the record of 28 kJ was obtained at an averaged density of $2.66 \cdot 10^{20}$ m^{-3}. But the radiation, mostly from low-Z material, following the density increase terminated the discharge as well.
After the second carbonization, the NBI current-drive in the co and counter-directions was analyzed. The estimated beam-driven current in both directions is in the range of ≈1.0 kA for the inner sources (see also sec. 2.2.3).
The boronization at first did not give as good results as after carbonization, and the radiation of high-Z materials again increased. Probably, the boron layer was not sufficiently thick and, therefore quickly destroyed. But immediately after the second boronization the highest energy content in W7-AS was obtained: 33 kJ at a mean density of $\approx 3 \cdot 10^{20}$ m^{-3} with a heating power of ≈1.5 MW. This corresponds to $\langle\beta\rangle = 0.7$ % and $\beta(o) = 1.5$ %. The radiation was lowered in these discharges by reducing the edge temperature using gas puffing, which also shielded the plasma from impurity influx.
A common feature of all NBI discharges was that the energy content essentially followed the density increase, whereas the temperatures remained nearly constant (typically being $T_e = T_i \approx 500$ eV) and independent of the wall conditions. This can be seen in fig. 3, showing the increase of the energy content with the line-density for a series of transient discharges.

shot	iota	wall	W_{dia} [kJ]	P_{NI} [kW]	n_e [10^{20}m^{-3}]	I_p	P_{rad} [kW]
8255	.510	SS	4.8	520	0.47	free	400
8287	.507	SS	9.2	650	0.77	free	300
8947	.498	SS	12.0	1000	0.75	free	
9799	.326	1.C	16.0	1200	0.84	0	500
9866	.340	1.C	28.0	1470	2.66	free	500
10146	.340	2.C	17.0	750	1.31	free	200
10185	.340	2.C	10.5	400	1.24	free	150
10285	.340	2.C	9.0	380	1.13	free	180
10786	.345	1.B	23.0	1400	3.90	0	
10787	.344	1.B	23.0	1400	3.90	free	
11119	.344	2.B	23.0	800	2.50	free	500
11213	.344	2.B	33.0	1500	3.00	free	400

Table 2 : Overview of transient NBI discharges obtained under different wall conditions and heating scenarios for B = 2.5 T. All shots used by balanced injection with the exception of #10185 (only co-injection with one source) and #10285 (only counter-NI). The electron temperature stayed in the range of about 500 eV in all cases.

2.2.2.2 Quasi-stationary discharges

After boronization, a quasistationary discharge (#10777) of about 0.3 s could be realized with an energy content of 5 kJ at a density of $1.2 \cdot 10^{20}$ m^{-3} and $T_e \approx 300$ eV using only one source (inner east). The plasma current of this co-injection discharge was increased to ≈1.5 kA by the beam-driven current and the bootstrap current.
After the second boronizsation an even longer discharge of about 0.6 s was possible (see fig. 4)

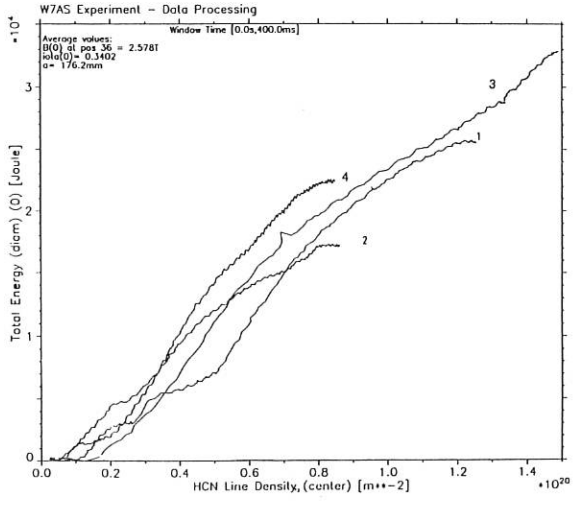

FIG. 3: *Total energy vs line-density for NI discharges*
(1) carbonized wall, all sources, shot 9866
(2) - - , inner sources, shot 10108
(3) boronized wall, all sources, shot 11213
(4) - - , inner sources shot 11119

and could be used to measure a poloidal rotation velocity of plasma ions for the first time in W7-AS (see sec. 4.10). In the following an actual status of corresponding calculations is given.

2.2.3 Simulation of NBI

The simulation of plasma heating by NBI may be separated into three topics:

a) heating profiles and heating efficiencies
b) beam-driven currents
c) local density of fast and thermal neutrals.

2.2.3.1 FAFNER code

FAFNER, an NBI code tracing the orbits of injected particles in spatial coordinates now is used routinely to calculate the heating power profiles for actual discharges. Input quantities are the measured electron density and temperature-profiles as well as the beam parameters. For each active source, one code-run per shot is used and the results are superimposed. The results are the global efficiency, losses (i.e. shinethrough, charge exchange and orbit losses), the birth profile and the heating profile. An example is given in figs. 5 a,b.
A problem occurred for the simulation of NBI into high-density discharges: many of the trajectories started in the outer plasma region ($r_{eff} > 15$ cm) where the field representation by Dommaschk potentials is not precise enough, resulting in very high orbit losses. Improvement was achieved by incorporating a grid representation of B and grad B into FAFNER. The guiding center orbits of test particles, calculated by this new FAFNER1 version, were checked by comparing them with orbits calculated by the GOURDON code using the same grid representation. Now the orbit losses calculated by FAFNER1 are much smaller than those calculated with the older version. An additional advantage of the new version is that the direction of grad ψ is also given on the grid and can be used to define the direction of a radial electric field. Therefore, in principle, the effect of an radial electric field now also can be included.
Figure 6 shows the global heating efficiency, defined as the heating power divided by the neutral input power, versus the effective line-density. Three regions with different loss mechanisms can be distinguished: at very low densities ($\int n_e dl < 1.5 \cdot 10^{19}$ m^{-2}) shinethrough losses dominate, mainly

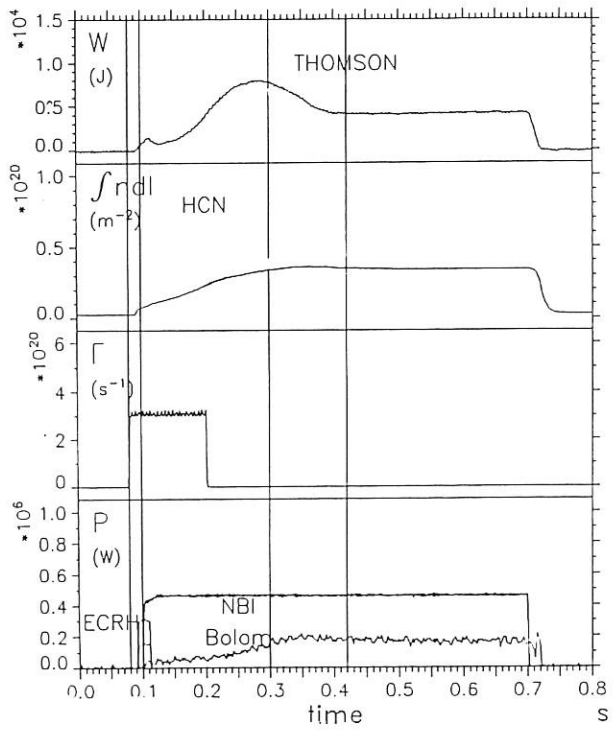

FIG. 4: *Example of a quasistationary discharge heated by one NI source (inner, co, #11459): The time histories of the diamagnetically measured energy content (W), line-integrated density (∫ndl), gas flux (Γ), NBI power and bolometrically measured radiation (P) are shown. Other parameters are: $I_p = 0.2$ kA, $\iota = 0.343$, $B_z = 0.0109$ T*

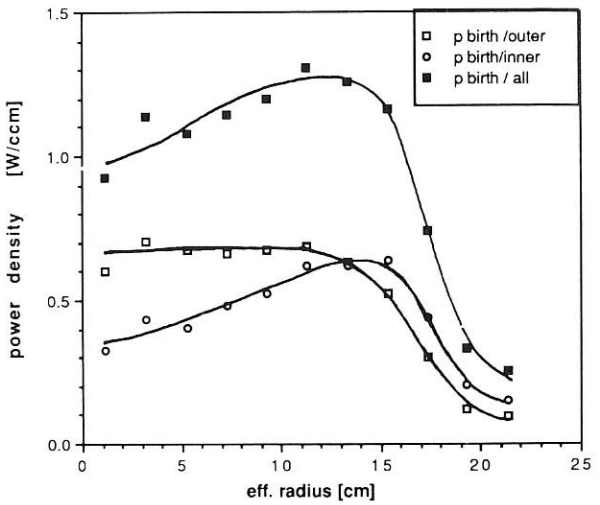

FIG. 5a: *Birth profiles calculated by FAFNER1 for shot 9867: $n_e(0) = 2.66 \cdot 10^{20}$ m^{-3} ; $T_e(0) = 550$ eV; $P_{NI} = 1.585$ MW; shine-through losses: 20 kW (1.3 %).*

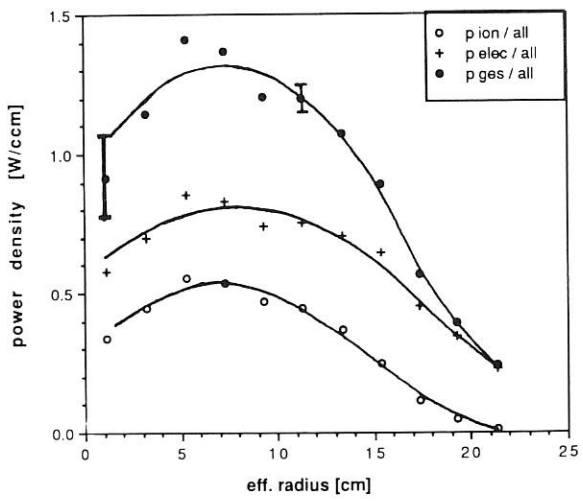

FIG. 5b: *Heating profiles for discharge 9867. 29 % of the total heating power of 1565 kW are directly coupled to the ions and 63 % to the electrons. The remaining 8 % are lost by charge exchange and by orbit losses during the slowing-down of the fast ions.*

for the outer but also for the inner sources injecting more tangentially. At moderate densities charge exchange losses depending on the actual neutral gas density at the plasma edge represent a significant loss channel, typically 10 to 15 % (see also annual report 1989, p. 145). At high densities ($\int n_e dl > 5.0\ 10^{19}\ m^{-2}$) the injected ions are slowed down very fast and therefore charge exchange losses are reduced, but orbit losses increase because the fast ions are deposited more and more off-axis.

2.2.3.2 Calculation of the NBI- driven current

From the known birth profile of injected fast ions given by FAFNER1, the radially resolved distribution function of fast ions can easily be calculated, assuming that the ions slow down within the radial layer in which they are ionized. By integrating this distribution function over the velocity space it is possible to calculate the fast-ion current density j_{fi}. The beam-driven current density j_{bd} can then be obtained using the trapped electron fraction $f_t = 1 - f_c$ for W7-AS:

$$j_{bd}(r) = j_{fi}(r)\ \left(1 - \frac{Z_b}{Z_{eff}}\ f_c(r)\right)$$

Integration of j_{bd} over the minor radius then gives the observable beam-driven current $I_{NB,max}$. After the beginning of injection this current develops with a time constant $\tau = L/R$ (≈ 0.1 s for typical W7-AS discharges) and the time dependence of this current may then be represented by

$$I_{NB}(t) = I_{NB,max}\ \left(1 - \exp[\,(t-t_o)/\tau\,]\right).$$

Figure 7a shows the result for co- and fig. 7b for counter-injection. In both cases one starts with balanced injection and switches off one source. In these examples, no ohmic current is induced, so that the measured current I_P is the sum of bootstrap current $I_{boot}(t)$ and $I_{NB}(t)$. By definition 'co'-injection means that the fast-ion current increases the rotational transform as does the bootstrap current for $B > 0$. The residual current obtained by subtraction of $I_{NB}(t)$ from the measured current $I_P(t)$ agrees fairly well with the bootstrap current calculated at that time where density and temperature profiles were measured, assuming $Z_{eff} \approx 3$.

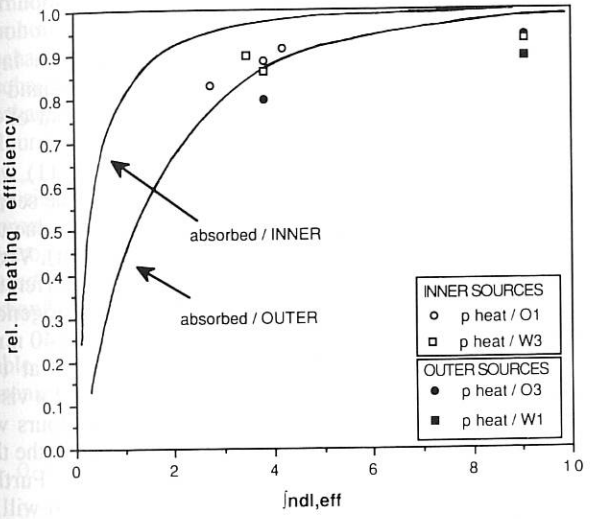

FIG. 6: *Global heating efficiency (P_{heat}/P_{NI}) calculated by FAFNER1 versus effective line-density given in $10^{19}\ m^{-2}$. The absorption of the inner and outer beams is shown. Some results for actual shots including CX and orbit losses are also indicated.*

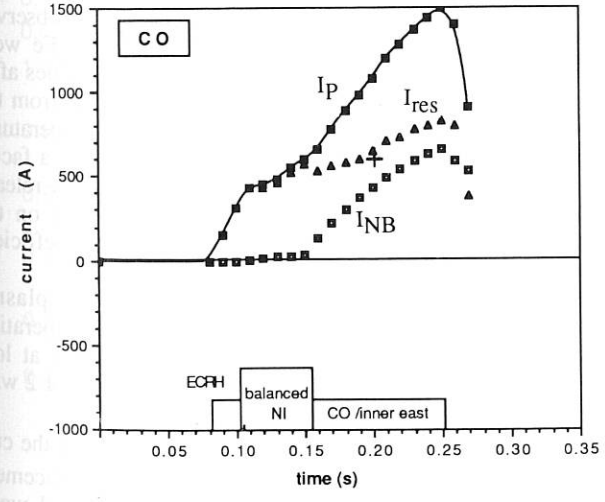

FIG 7a: *Comparison of the measured plasma current $I_P(t)$ with the beam-driven current $I_{NB}(t)$ for co-injection; (+) indicates the bootstrap current calculated with the profiles measured at $t = 200$ ms.*

2.2.3.3 Local density of fast and thermal neutrals

The absorption of the beams is done by electron and proton ionization processes as well as by charge exchange between thermal ions and injected neutrals. The last process generates thermal neutrals, their cloud beeing called the "beam halo". These in turn may be the cause of increased CX losses of fast and thermal ions. To estimate this effect, the source rate of

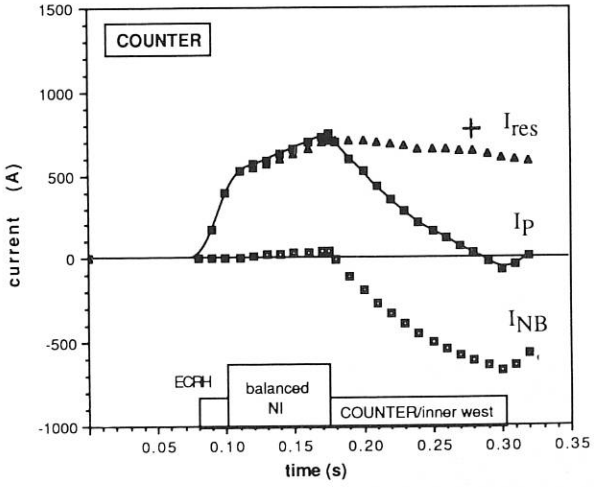

FIG 7b: *Comparison of the measured plasma current $I_P(t)$ with the beam-driven current $I_{NB}(t)$ for counter-injection;*
(+) indicates the bootstrap current calculated with the profiles measured at $t = 280$ ms.

halo neutrals was calculated for several actual discharges and will be included as an additional source of thermal neutral gas in the DEGAS code (see sec. 3.2.3).
The local density of fast neutrals of each neutral beam species injected - valuable information for CXRS diagnostics - now can be calculated for W7-AS also by using the NEUDEN code /IPP 4/229/ along any arbitrary chord across the beams.

2.3 ICRH on W7-AS

First experiments were performed on W7-AS in the H-minority regime at full field for different values of ι ($0.3 < \iota < 0.525$) in combination with ECRH. The system performed well technically: an RF power of up to 250 kW was achieved separately on each antenna, with 500 kW together for 80 ms and 400 kW for 400 ms.
However, in almost all cases the ICRH pulse resulted in a large plasma density increase and a plasma energy decrease. Impurities (light and/or heavy depending on the plasma-wall distance) increased. Because of the difficulty in controlling the minority density to sufficiently low values for good absorption, attempts were made to work at the 2^{nd}-harmonic frequency of H. There, however, technical difficulties occurred: at the frequency required for operation with ECRH the generators were unstable. Only by operating the generators on the antennas and a dummy load in parallel was it possible to stabilize them. Experiments at an RF power of up to 150 kW, $\iota \approx 0.3$ and in combination with ECRH showed a small antenna loading and plasma results similar to minority heating. Further experiments must be made in combination with NBI to increase the absorption, and in combination with boronized walls to reduce the impurity problems.

3. RESULTS AND THEORETICAL MODELS

3.1 Wall and boundary

3.1.1 Wall conditioning

In order to reduce recycling and impurity concentrations (oxygen, carbon, titanium and iron) various wall conditioning methods are being used:
- glow discharges in helium up to half an hour before every experimental day
- carbonization or boronization, resulting in a deposition of thin pure carbon or boron layers onto the plasma-facing vessel walls during glow discharges

Carbonization was done in gas mixtures of about 70 % He + 30 % CH_4 (after #9694) or CD_4 (after #9988), resulting in layer thicknesses of about 1000 Å after a deposition time of up to 5 h. The typical glow discharge pressure for carbonization is about $1 \cdot 10^{-2}$ mbar. The burn conditions for the three anodes toroidally displaced about 120° from each other are 3 A and 500 V. Carbonization showed a significant (about a factor of more than 10) and durable reduction of the metallic impurities. Oxygen again rapidly increased but could be shortly reduced to improved conditions by glow discharges in helium. Density control, however, was not possible after carbonization (recycling coefficient >1). Before venting the plasma chamber for the scheduled shut-down in summer the vessel walls were decarbonized in a glow discharge in hydrogen.

For further investigations of wall conditioning methods the plasma chamber was boronized twice in November 1990. The boronization-runs on W7-AS were done in glow discharges with 10 % B_2H_6 (diborane) + 90 % He at room temperature vessel walls. For safe handling of the diborane, being both toxic and explosive, the gas mixture is fed from a pressure bottle located in a special gas case to the gas inlets via a low-pressure tube system of coaxial design. In conjunction with the gas inlets an exhaust system was installed, comprising one of the standard turbomolecular pumps of W7-AS, backed by a thermal decomposer ($\approx$ 750° C), followed by a special chemical pump and a $KMnO_4$ filter. If there is any diborane in the exhaust system it will completely decomposed in the filters into harmless products. The two special instruments continuously monitoring for diborane during boronization runs never detected any B_2H_6 in the coaxial gasfeed system nor in the exhaust or in the air. To get homogeneity in layer deposition, up to five gas inlets toroidally located around the vacuum vessel, together with a Roots blower in front of the thermal decomposer were used.
The two boronization runs (after #10624 and #11111) were done under slightly different conditions (Table 1). The second deposition phase resulted in a smaller layer thickness due to a lower discharge pressure (zero drift of the instrument). Visual inspection of a removable collection probe by interference colours after boronization 1 yielded an inhomogenous deposition of 200 - 800 Å over the probe diameter (140 mm), confirmed by Nuclear Reaction Analysis (NRA) at two positions on the probe (Table 1). After boronization 2 a visual estimation of the layer thickness by interference colours was not possible due to the unexpected light-blue colour of the thin film, which may be due to metallic impurities. Further investigations of this not yet understood phenomenon will be done. The long-term behaviour of the layers will be investigated by probes poloidally and toroidally distributed inside the vacuum vessel.
Boronization resulted in a considerable reduction of impurities and reduced recycling coefficient (< 1) during plasma discharges. As compared to experiments with metallic walls oxygen and carbon, the dominant low-Z impurities were reduced, oxygen e. g. by a factor of more than ten as observed by spectroscopy. The high-Z components Ti and Fe were significantly reduced, but increased back to high values after some shots during which the boron film was eroded from the limiters (see also Sect. 4.4). Due to the high edge temperatures after boronization an increase of the limiter load by a factor of $\approx$ 3 was observed corresponding to higher impurity release from the limiters. The beneficial effects, however, on the oxygen and carbon concentrations and the recycling coefficient remained over a long time.
Boronizations provide significantly improved plasma conditions. After fresh boronization of W7-AS the operation mode for 70 GHz ECF - heated plasma discharges at low power level $P_N < 200$ kW was extended by a factor of 2 with respect to density and energy (rotational transform $\iota = 0.34$, $B_o = 2.57$ T). It was possible to operate near the cut-off density and a significant increase of the energy replacement time of up to 40 ms was achieved. With boronized walls discharges at stationary densities with constant gas influx were obtained (recycling coefficient < 1). The layers were further tested in NBI-heated scenarios. With two H° beam lines e. g. and an averaged density of 1.5×10^{20} m^{-3} the energy content was improved to 23 kJ without optimization arrangements. With four sources (absorbed power $\approx$ 1.1 MW) record values in

energy content of up to 33 kJ (<β> = 0.7 % at 2.5 T) at an averaged density of 3 x 10^{20} m^{-3} were observed. The energy confinement time was estimated to be 30 ms. For boronized wall conditions the fraction of radiated power compared with the input power P_{rad}/P_{tot} was about 35%. Some NBI-heated discharges, however, showed short-term breaks in plasma energy and temperature, correlated with an increase of the titanium flux, but energy and temperature increased again with a simultaneous decrease of the radiation to its former level. Boronization seems to be superior to carbonization because it does not pose a problem with density control. The reduction of oxygen and carbon is obviously durable and allows significantly improved plasma conditions over a long time. To avoid the metallic impurities in the discharges the replacement of all titaniumcarbide vessel components by boron-doped graphite material is planned. In addition, a careful protection by carbon tiles of those stainless-steel components acting as secondary limiters is envisaged.

	Boronization 1	Boronization 2
number of gas inlets:	4	5
number of anodes:	2	3
discharge current:	2.5 A	3.5 A
discharge voltage:	500 V	600 V
discharge pressure:	10^{-2} mbar	< 10^{-2} mbar
colour of layer:	transparent	light-blue
deposition on probe (Pos. 1/Pos. 2):		
[boron atoms/cm^2] · 10^{17}	5.4/7.7	3.8/5.2
[hydrogen atoms/cm^2] · 10^{17}	3.0/4.1	1.8/3.3
[carbon atoms/cm^2] · 10^{16}	3.7/3.2	6.8/3.2
carbon/boron	≈ 0.05	≈ 0.10

Table 1: Discharge conditions and deposition results of the two boronization-runs on W7-AS.

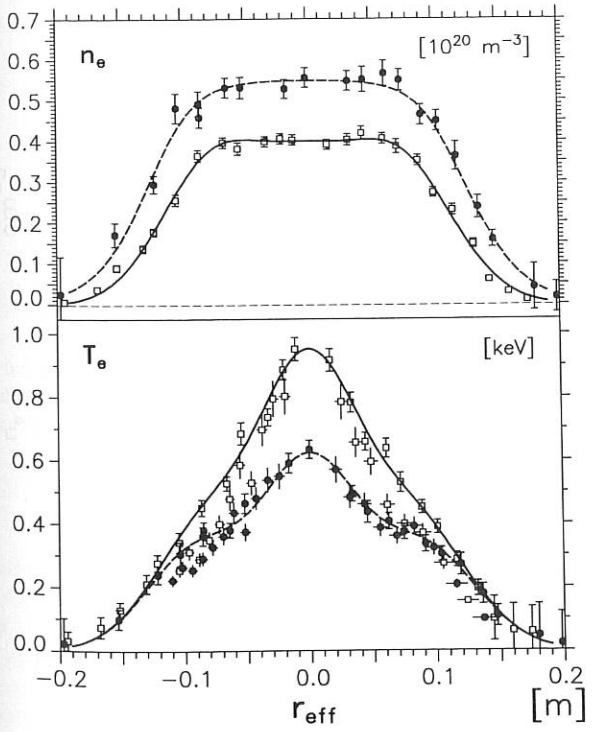

FIG. 8: *Electron density (Thomson data, upper plot) and electron temperature profiles (Thomson and ECE data, lower plot) for low-power (about 140 kW) ECRH discharges immediately after boronization (shots 10647-70, solid lines) and after carbonization (shots 11847-73, broken lines).*

3.1.2 Density Control and Wall Conditioning

ECRH discharges with high densities ($n_e > 4 \cdot 10^{13}$ cm^{-3}) at low heating power (one gyrotron) are most sensitive to recycling conditions and impurity influx. Low impurity levels were obtained immediately after boronization and after carbonization (with additional He glow discharge conditioning) of the machine, which allows access to the high-density regime at low heating power. In the unconditioned machine, this regime was partially accessible for reduced plasma radius (z_{lim} = 21.5 cm) or for high ι where the plasma is limited by the separatrix. The most pronounced difference between boronization and carbonization is found in the recycling properties, which are dominated by the limiter for small ι in the ECRH discharges. In fig. 8 the density and temperature profiles of ECRH discharges immediately after boronization (shots 10647-70, solid lines) and after carbonization (shots 11847-73, broken lines) are shown. In the former case, additional external gas puffing was necessary to get the high densities for stationary conditions. After carbonization with additional He glow discharge conditioning, the density increased to cut-off without external gas puffing, the density profiles being significantly broader indicating that the recycling (mainly from the limiter) is much larger in this case.

3.1.3 Plasma-edge, plasma-surface interaction

3.1.3.1 Patterns of enhanced plasma-wall interaction

Visual inspection of the inner surface of the W7-AS torus in the autumn of 1989 after about one year of operation showed characteristic stripes due to plasma-wall interaction. They follow a helical contour from the lower torus apex along the radial outside towards the upper apex, through each field period. The pattern is modified by local effects at the limiters and built-in components.

The origin of these patterns could be clarified /22,300/ by following numerically the behaviour of vacuum field lines and guiding center orbits (Monte Carlo code using pitch angle scattering of H^+ ions with 50 eV energy, normalized mean free path $L^* = \lambda t/\pi R = 0.1$, no electric field). The guiding center orbits are started at random toroidal and poloidal points, at a small distance inside the edge radius. Field lines starting not too far outside the edge give similar results. The helical shape of the interaction stripes at the wall and `hot spots´ at the limiters or other in-vessel components are recovered in these calculations (fig. 9).

At ι = 0.53 and an outward limiter position the edge topology is separatrix-dominated. From guiding center calculations the efficiency of the two main limiters is about 40 %, while another 35 % are found on the guard limiters of the ICF antenna. The remaining guiding center orbits end at the diamagnetic coil, the torus wall or the module separation limiters (fig. 10). Typical orbit lengths range between 270 and

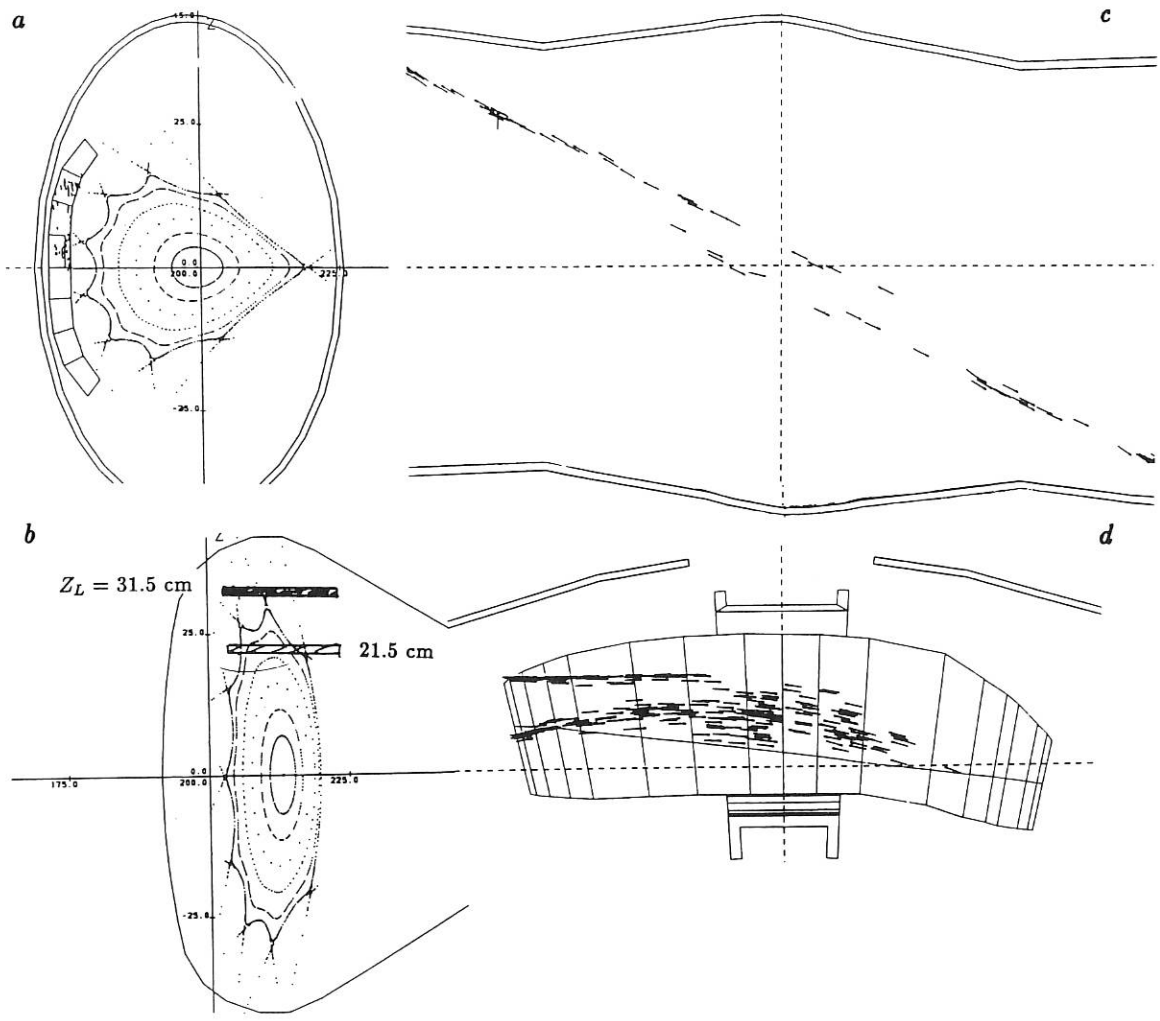

FIG. 9: *Vacuum field of W7-AS for $\iota = 0.53$ at $\varphi = 0$ with torus wall, probe limiter inserted (a), at 1/2 of the field period with vertical positions of top limiter shown (b); intersection patterns at outside wall (c) and at bottom limiter for $Z_L = 31.5$ cm (d);*

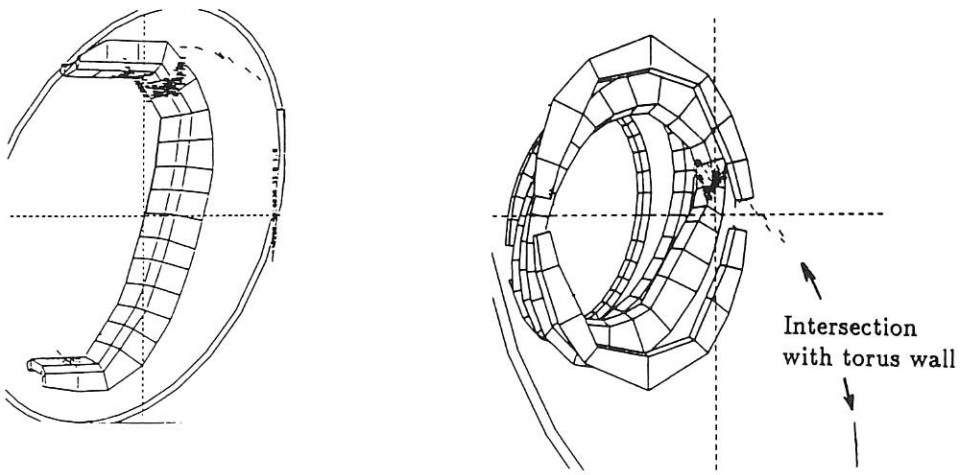

FIG. 10: *perspective views in the vicinity of one of the ECF guard limiters (left) and of the diamagnetic coil (right).*

420 m. For a vertical position of the limiters, with $Z_L < 28$ cm the configuration is limiter-dominated, and the percentages of the other in-vessel objects drop below 10 %. Configurations at low ι ($\iota = 0.34$) are always limiter-dominated.
For $Z_L = 31.5$ the limiter efficiency is only 66 %. It increases to about 100 % for the inward limiter position; then the aspect ratio is $A \approx 16$. Guiding center intersection lengths are shorter than at $\iota = 0.53$. A limiter efficiency > 90 % in a separatrix-dominated topology is obtained for high ι ($\iota = 0.71$) with the inward limiter position and at increased aspect ratio $A \approx 20$. The influence of the in-vessel objects is negligible, and the average orbit lengths until intersection, typically 500 to 1200 m, are maximum. This interesting case remains to be studied experimentally in W7-AS.

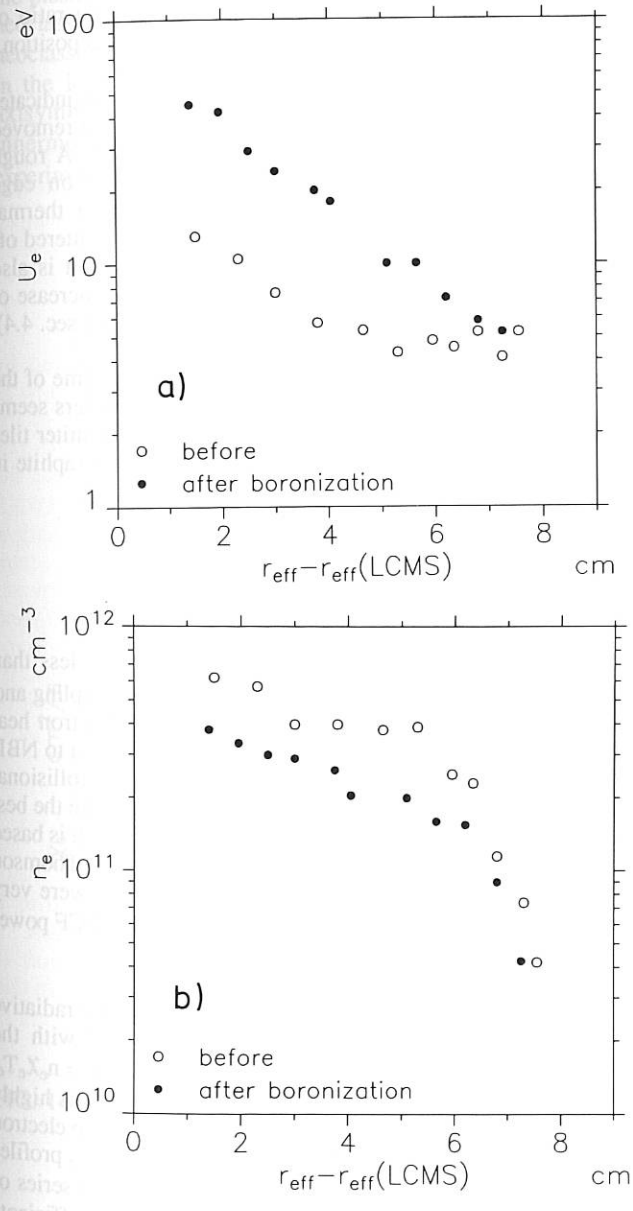

FIG. 11: *Radial decay of SOL temperature (a) and density (b) for ECRH reference discharges before (#10608 - 10619) and after (#10674- 10685) first boronization (from Langmuir probe).*
$P_{ECRH} = 180$ kW, $B_t = 2.5$ T, $\iota_a = 0.34$, line-density $5 \cdot 10^{18}$ m^{-2}.

3.1.4 Scrape-off layer, limiter action

Scrape-off layer (SOL) parameters and limiter action[1] were studied in some detail for ECRH with $B_t = 2.5$ T, $\iota \approx 1/3$, $\iota \approx 1/2$ and limiters at the inward position.

In the low-ι case magnetic surfaces exist within the whole SOL. Connection lengths are approximately constant and, from that point of view, local measurements can be taken representative for the respective magnetic surfaces. For the central density close to cut-off typical parameters at the last closed magnetic surface (LCMS) are $n_{ea} \approx 10^{13}$ cm^{-3} and $T_{ea} \approx 100$ eV with radial decay lengths of $\lambda_n \approx 3$ cm and $\lambda_T \approx 1.5$ - 2 cm (from Thomson scattering and/or Langmuir probes). DEGAS code modelling yielded $D_{\perp a} \approx 0.5$ - 2 $m^2 s^{-1}$, $(D_\perp/\chi_e)_a \approx 0.1$ - 0.3, $t_{pa} \approx 3$ - 9 ms and SOL refuelling contributions > 50 %.
Power depositions on the main limiters (from calorimetry) increase nonlinearly with the absorbed ECF power resulting in efficiencies of between 20 and 50 % ($P_{ECRH} = 180$ kW and 650 kW, respectively) in the low-ι case and 10 - 35 % for an ι

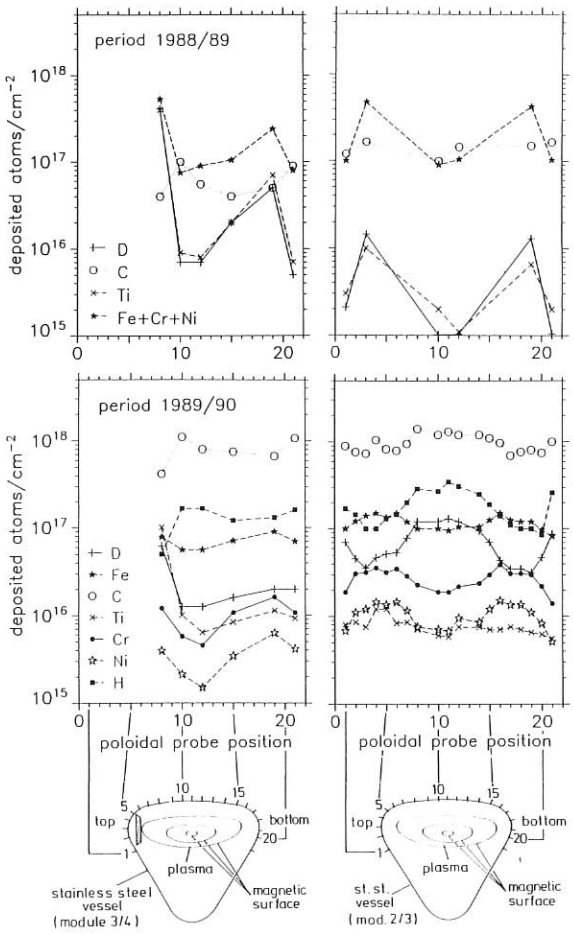

FIG. 12: *Distribution of deposited materials from long-term collector probe analysis.*

1) P. Grigull et al., Some aspects of the plasma edge properties of the Wendelstein 7-AS stellarator, J. Nuclear Materials 176, to be published.

of about 1/2. Lower efficiencies in the latter case can be partly explained by the occurrence of SOL regions with extremely large connection lengths depending strongly on the ι value at the magnetic surface under consideration (local limiter action). For stationary reference discharges the measured power deposition on the limiters was well reproduced by DEGAS code modelling taking absolute H_α fluxes for calibration and assuming sheath potentials of 3 kT_e. By adding measured total radiative losses (from bolometry) to the calculated transport power loss on the limiters and wall (the latter playing a minor role in this configuration), a deficiency of 25 - 50 % was found with respect to the total power accountability.
The effects of the first boronization were studied for ECRH reference discharges recorded before and after boronization with B_t = 2.5 T, P_{ECRH} = 180 kW, ι_a = 0.34, a line-density of $5 \cdot 10^{18}$ m^{-2} and limiters at the outermost position. The limiter thermal load was increased by a factor of 2.5 after boronization. As far as can be inferred from local Langmuir probe data this seems to be due to significantly increased SOL temperatures, see fig. 11 (prev. page).

3.1.5 Deposition probe analysis

Long-term collector probes were exposed during two operating periods of W7-AS in 1988/89 (about 6600 discharges mainly with ECRH at B_t = 1.25 T). The probes were poloidally distributed at two different planes, one of them close to the upper limiter, the other far from limiters.

Surface analysis of the probes revealed the distributions of elements shown in fig. 12 (prev. page). After the first period the deposition of Ti is approximately equal to the amount of deuterium collected and has a local maximum near the limiter (limiters are coated with TiC). The deposition of wall materials (Fe, Cr, Ni) shows maxima at the top and bottom of the vessel and near the limiter. It is assumed that the wall material deposition is caused at least partially by cleaning glow discharges (homogeneous deposition) and then modified by the plasma discharges (maxima at the top and bottom).

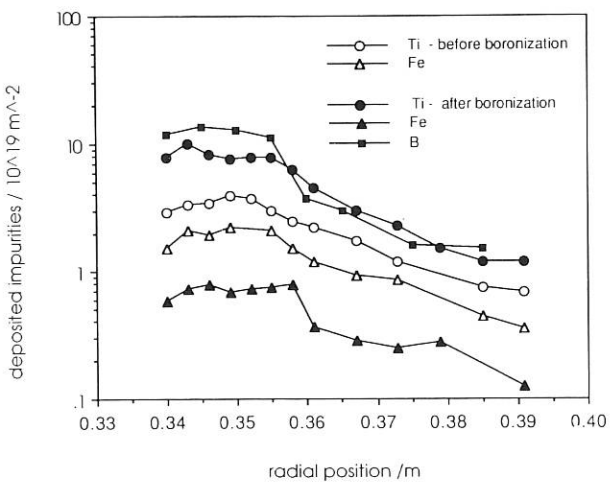

FIG. 13: *Deposited impurities as functions of the radial position (vertical distance from the torus midplane, limiter position is 0.315 m). The probe was exposed to 10 ECRH reference discharges before and after boronization.*

The erosion from the limiters is responsible for the increased deposition of all materials near the limiter. Probes from the second (high-field) period of operation show more homogeneous distributions. The effect of boronization on impurity fluxes within the SOL was studied by a retractable, radially resolving deposition probe (carbon) placed above the upper apex of the elliptic plasma cross-section. It was exposed to 10 ECRH reference discharges before and after the first boronization.
The amounts of Ti (originating from limiters), Fe (from stainless-steel walls and/or depositions on limiters) and B collected are shown in fig. 13 as functions of the radial position. Before boronization the Ti deposition exceeded that of Fe by a factor of 2. After boronization the Ti deposition is increased by a factor of 2.5, whereas the Fe deposition is decreased by the same factor, resulting in a Ti/Fe ratio of about 15. The deposited boron is as large as the Ti deposition.

The increase of the Ti flux after boronization strongly indicates that most of the boron layer on the limiters has been removed during the first few discharges after boronization. A rough estimate of the ion flux on the limiters, based on edge temperatures from Thomson scattering and limiter thermal loads, confirms that the boron coating should be sputtered off during the very first discharges. This consideration is also supported by spectroscopic data showing a rapid increase of Ti line radiation immediately after boronization (see sec. 4.4).

Due to the increased limiter load and the short lifetime of the boron coating medium-Z impurity influx from limiters seems to become crucial. Consequently, the TiC-coated limiter tiles will be replaced by tiles made from boron-doped graphite in May 91.

3.2 Transport

3.2.1 Transport analysis for ECRH discharges

For ECRH discharges, the electron densities were less than $6 \cdot 10^{13}$ cm^{-3}, so that the collisional electron-ion coupling and the radiative losses were rather small, and the electron heat conduction was the dominant loss channel. In contrast to NBI-heated discharges at rather high densities where the collisional electron-ion coupling dominates, ECRH discharges are the best candidates for electron energy balance analysis, which is based on density and temperature profiles measured by the Thomson scattering diagnostic. Furthermore, the n_e profiles were very broad and the T_e profiles highly peaked for central ECF power deposition.

The stationary electron energy balance equation with radiative losses and electron-ion power transfer is solved with the diffusive ansatz for the radial electron energy flux $q_e = n_e \chi_e T_e$ and an analytic ECF power deposition model which is highly peaked in agreement with ray-tracing calculations. The electron energy balance equation is solved and the measured T_e profiles are fitted by a least-squares technique using a power series of log (χ_e) in the normalized radius, the power series coefficients being the fit parameters. This integration method of the electron energy balance equations leads to a smoothed representation of the electron heat conductivity $\chi_e(r)$. For the n_e profiles a standard fit function is used. With these T_e and n_e profiles, all neoclassical transport properties are estimated with

the DKES-2 code[1]. The DKES code solves the monoenergetic drift kinetic equation for general magnetic field topology. Note that the W7-AS field topology is quite different to that of standard stellarators. Energy convolution yields the full neoclassical transport matrix.

In fig. 14, the electron temperature, density, heat conductivity and rotational transform profiles are shown for one of the high-density ECRH discharges at B_0 = 2.5 T with 200 kW ECF input power (1 gyrotron operating). The bootstrap current was compensated by an external loop voltage. The central β was about 0.35 %. The T_e profile is highly peaked due to central ECF power deposition; note that the T_e gradient is nearly constant. For the high electron temperatures, the bulk part of the plasma is in the long mean free path regime (LMFP), the neoclassical transport being dominated by ripple losses. The neoclassical χ_e estimated with the DKES code (the solid line in the lower left plot of fig. 1) significantly exceeds the axisymmetric contribution (dashed line). Only in the innermost part does the neoclassical χ_e approach the experimental value. The error bars of the experimental χ_e curve represent the standard errors of the fit given by the functional variance. Close to the effective separatrix radius of about 14.5 cm, the T_e profile becomes flat and the experimental χ_e strongly increases. In the bulk of the plasma, χ_e is much larger than the neoclassical value. For this condition of high n_e at low heating power, the experimental χ_e is one of the lowest found in W7-AS so far, the values of 2000 to 4000 cm^2/s in the main part of the plasma are in the range of the optimum χ_e values found in tokamaks.

The lower right plot of fig. 14 shows the effect of the bootstrap and compensating ohmic current densities on the rotational transform. Both current densities are estimated using the neoclassical DKES code and agree quite well with the experimental observations in ECRH discharges (see sec. 3.2.4). For the discharges of fig. 14 the internal current distribution leads to a rather strong positive shear $\Delta\iota = \iota(a) - \iota(0) \approx 0.1$, the resonance $\iota = 1/2$ being clearly located within the confinement region. The positive effect of internal shear on the energy confinement properties was

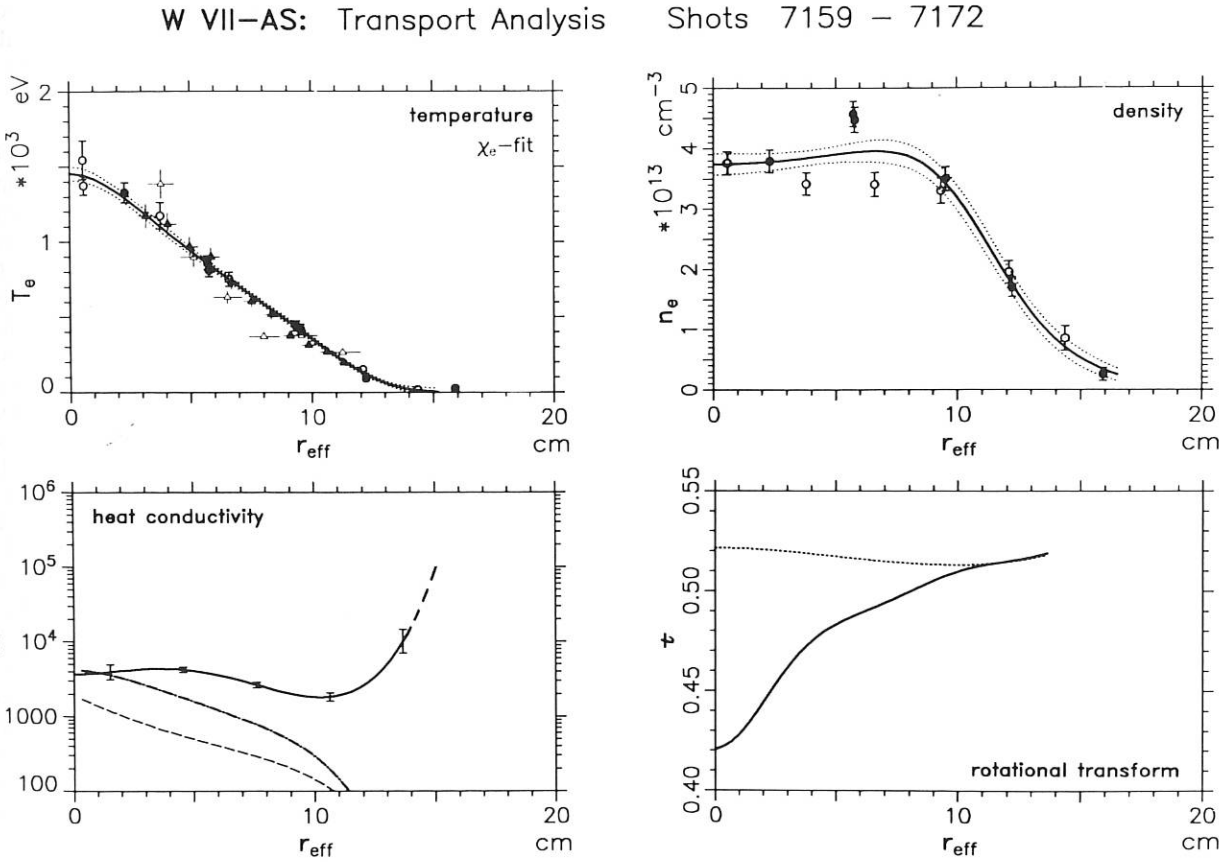

FIG. 14: *Transport analysis for a series of ECRH discharges (7159-72): the profiles of electron temperature T_e, density n_e, heat conductivity χ_e , and rotational transform ι are shown for B_o = 2.5 T and an input power of $P_{ECF} \approx$ 200 kW. N_e and T_e were measured by Thomson scattering (circles) and ECE (triangles); the central T_i was about 340 eV (passive CX neutral particle analysis).*
In the experimental χ_e (lower left plot, solid line) standard errors resulting from the least-squares fit of the T_e profile (in the upper left plot) are given; additionally, the χ_e from the DKES code (dot-dashed line) and from the Hinton-Hazeltine model (dashed line) are shown. The bootstrap current was compensated by a small external loop voltage. In the lower right plot, the resultant rotational transform profile due to the local current densities (solid line) is significantly decreased in relation to the ι profile without these internal currents (dotted line, β effects are included).

demonstrated within a heating power scan at a critical value of the edge rotational transform as well as by ECCD experiments / /. The optimization of the internal ι profile will be an important task for future experiments.

The dependence of the electron heat conductivity on the plasma parameters is analyzed by density and heating power scans as well as by statistical analysis of the Thomson series database. The local χ_e values decrease with both density and magnetic field strength and increase with the global heating power. In the statistical analysis, no conclusive regression with respect to the local electron temperature could be obtained.

3.2.2 Energy confinement times

The maximum energy confinement time was found in an NBI-heated discharge (one source with ~ 350 kW) at high density, where τ_E was slightly above 40 ms. The corresponding maximum τ_E for a series of ECRH discharges was obtained at very low power level (one gyrotron with about 120 kW) and $n_e(0)$ close to cut-off (nearly $6 \cdot 10^{13}$ cm^{-3}); τ_E was about 32 ms. Typically, the energy confinement time reduces significantly with heating power and increases with density. For the series of discharges with Thomson profile data a global scaling of τ_E was performed by means of multiple linear regression using the W7THDB database program:

$$\tau_E^{W\ 7\text{-}AS} = 1.23 \cdot a^{1.28} \cdot B^{0.73} \cdot \iota_a^{0.23} \cdot n_e^{0.53} \cdot P_{abs}^{-0.56}$$

with the effective plasma radius a in m, the line-averaged density n_e in 10^{20} m^{-3} and the absorbed heating power P_{abs} in MW. The rather weak dependence on the effective plasma radius in $\tau_E^{W\ 7\text{-}AS}$ (12 cm < a < 18 cm) is related to degraded confinement at outer plasma radii in a significant subset of discharges. For optimum confinement conditions, however, τ_E scales with a^2. The experimental energy confinement time $\tau_E^{W\ 7\text{-}AS}$, in comparison with the scaling, is shown in fig. 15

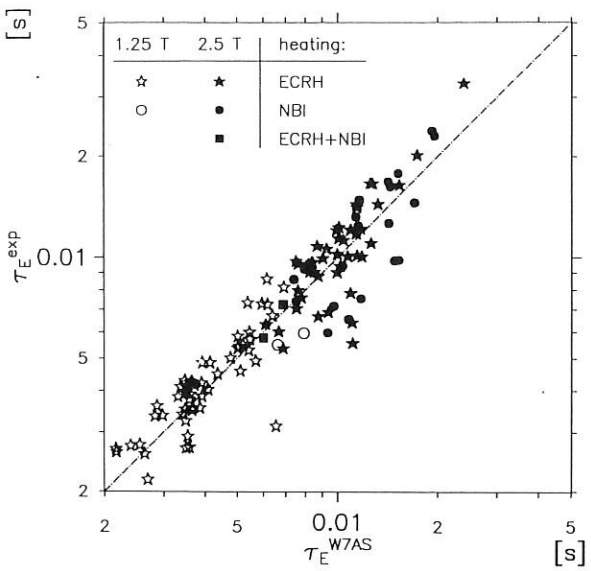

FIG. 15: *The experimental energy confinement time $\tau_E^{W\ 7\text{-}AS}$ versus the result of the regression formula $\tau_E^{W\ 7\text{-}AS}$ for different heating schemes.*

for the discharges with pure ECRH, pure NBI and combined heating. There is no significant difference in energy confinement time between ECF and NBI-heated discharges.

These results were also compared with various scaling laws (see Annual Report 1989). There is only a small difference to the Lackner-Gottardi scaling based on a model of neoclassical ion plateau transport, to the ATF scaling based on a model of drift wave turbulence and, finally, to the LHD scaling based on experimental results mainly obtained from Heliotron-E. For these scalings the average deviation is typically less than 50 %. However, replacing the plasma current in the Goldston L-mode scaling by the rotational transform leads to complete disagreement: the increase of τ_E with density is not described by this model (in tokamaks, the plasma current is related to the density).

3.2.3 Particle transport

The particle confinement in W7-AS was investigated for ECRH discharges at 1.25 and 2.5 T by coupling DEGAS code[2] simulations with H_α emissions measured at relevant toroidal positions. Radially resolved ion fluxes were obtained from calculated neutral particle distributions after calibrating them with the H_α signals / 209 /. Estimated Z_{eff} were used to derive the electron particle fluxes and diffusivities.

For a power scan at 2.5 T, ι(a) = 0.34, characterized by electron density profiles which get more and more hollow as the heating power is increased, the electron fluxes in the central region were compared with neoclassical predictions (see fig. 16). As a T_i profile information is lacking, only the neoclassical electron fluxes were estimated with the DKES code. In the 4-gyrotron case, for which the central hollow profile is most pronounced, the fluxes near the plasma center are in fairly good agreement (fig. 16, right side). This means that the observed hollow density profile can be explained reasonably well by the neoclassical temperature gradient driven particle flux (thermodiffusion) without need of additional anomalous contributions. This is consistent with the lack of major resonances in the central confinement predicted for large heating powers and fixed ι(a) ≃ 1/3. In this case it can be shown that the ohmic current needed to compensate the high bootstrap current leads to a strong positive shear which keeps the central region well below the ι = 1/3 resonance. By reducing the heating power to 1 gyrotron, the hollow density profiles disappear and the particle fluxes are enhanced by a factor of ≃ 5 over the neoclassical values (fig. 16, left side).
This poor particle confinement in the central region is consistent with a flattening of the measured T_e profile. In this case, an ι = 1/3 transition in the main confinement region is predicted.
In the density gradient region, as compared with the central region, the particle fluxes strongly increase, whereas the neoclassical fluxes are negligible due to the neoclassical T_e dependence. For solving the particle balance equation the diffusive ansatz, Γ = -Dn′, is used for the particle fluxes. The particle diffusivities D were evaluated for discharges operated at half and full field, the ι(a) values beeing close to the major

1) W.I. van Rij and S.P. Hirshman, 1989)

2) D.B. Heifetz et al., J. Comput. Phys. 46(1982), 309

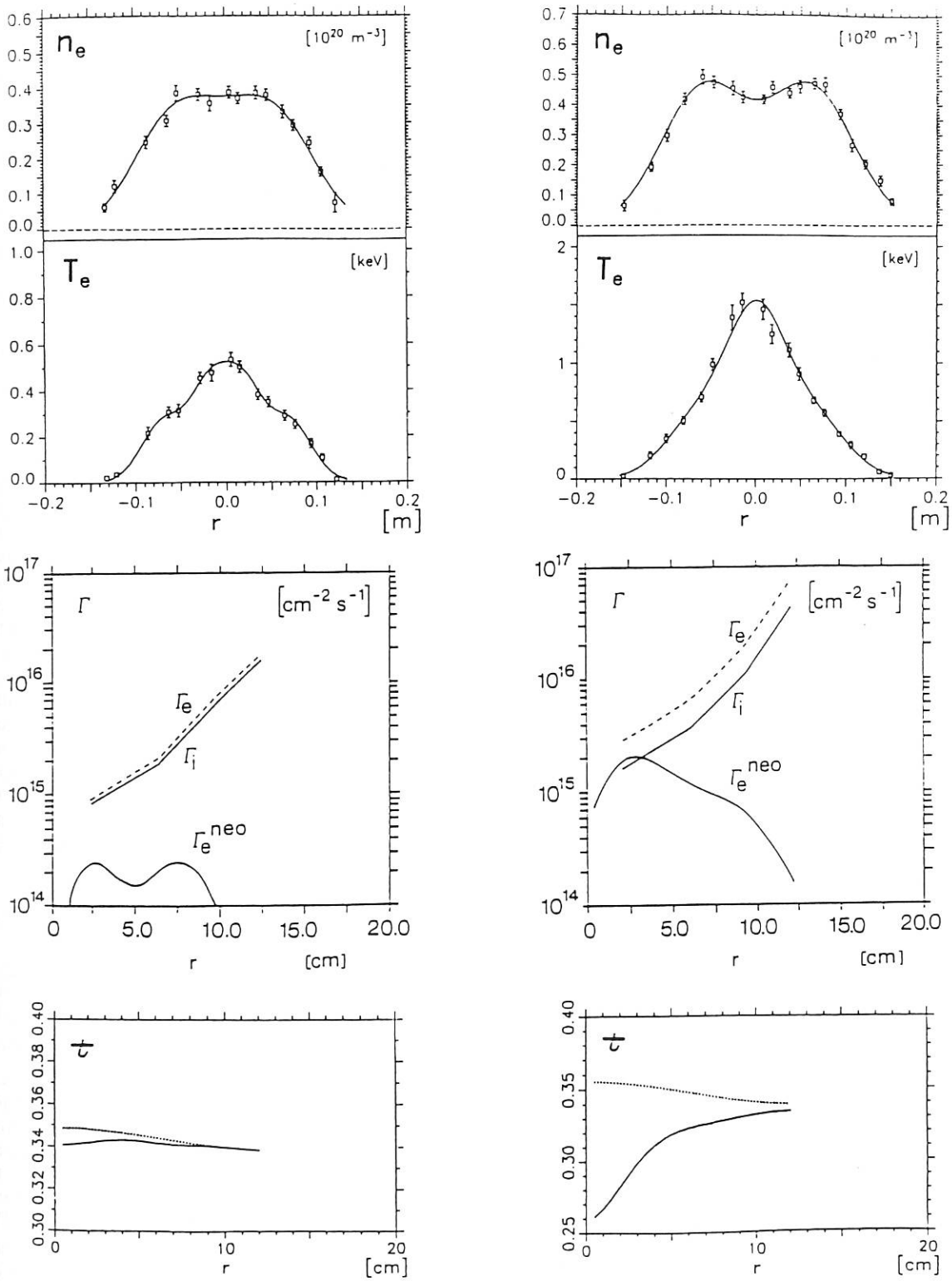

FIG. 16: *Radial profiles of electron fluxes Γ_e and of corresponding neoclassical predictions Γ_e^{neo} for small and large ECRH powers (left and right sides, respectively).*

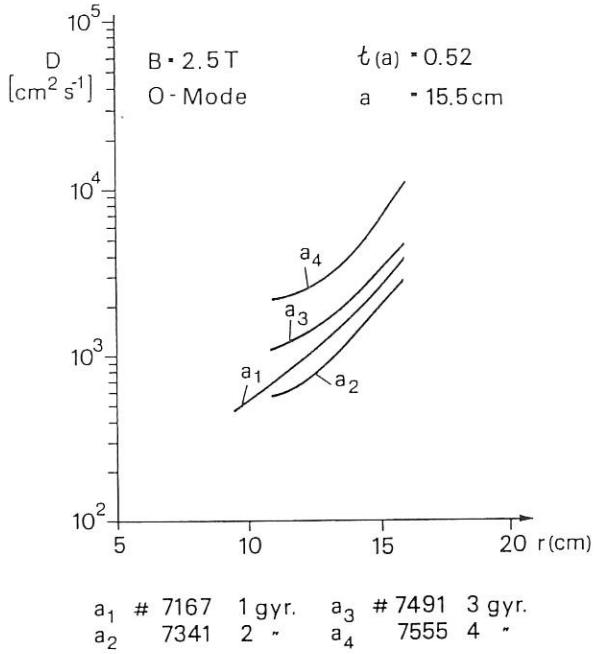

FIG. 17: *Ion diffusivity profiles D for ECRH discharges at B_o = 2.5 T for different ECR heating powers (number of gyrotrons operating). The line-averaged density of the 1-gyrotron case is lower than that of the other 3 cases.*

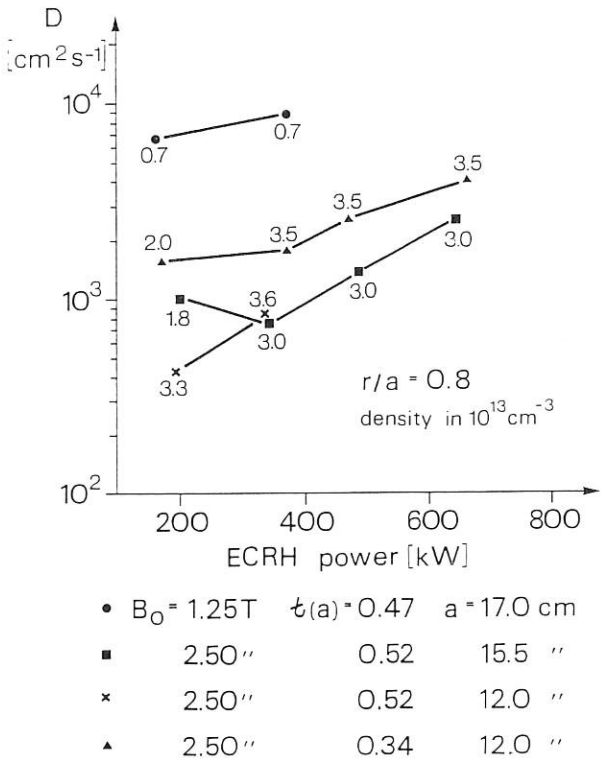

FIG. 18: *Dependence of ion diffusivity D on ECRH power at fixed r/a = 0.8. The numbers in the plot give the local electron density n_e in units of 10^{13} cm^{-3}.*

resonances 1/3 and 1/2, where optimum confinement has been found. The radial range of the diffusivities is restricted to the density gradient region up to the limiter (D cannot be determined for flat density profiles). Here, the density profiles can be explained by diffusive transport alone.

For the power scan at $\iota(a) = 0.34$ discussed above, the diffusivities in the outer confinement region ($r \simeq 10$ cm) increase with heating power for constant density ($D \simeq 1800 - 4000$ cm^2/s from 2 to 4 gyrotrons). The same behaviour is found for discharges operated at $\iota(a) \simeq 0.5$; see the 2,3,4-gyrotron cases of fig. 17 with $\bar{n}_e \simeq 2.8 \cdot 10^{13}$ cm^{-3}.
D also increases with decreasing density for constant heating power. A similar behaviour was found for the electron thermal diffusivity. In the 1-gyrotron case power scan with $\iota(a) = 0.52$ as shown in fig. 17, the expected reduction of D due to the small heating power is overcompensated by an enhancement due to a smaller local density. A comparison between the analyzed 1.25 and 2.5 T discharges indicate an average improvement of the particle confinement with the magnetic field by a factor of $\simeq$ 3 throughout the density gradient region.
Figure 18 shows the ECRH power dependence of the diffusivities in the outer confinement region (r/a = 0.8) for the discussed 1,2-gyrotron discharges at 1.25 T, the power scans at $\iota(a) = 0.52$ and 0.34 and two additional full-field discharges at $\iota(a) = 0.52$, a = 12 cm. The lowest values of the diffusivity are found at full-field, high-ι operation. In the low-ι power scan, the diffusivities are on the average twice as large as in the high-ι power scan. This ι dependence of D is not distorted by density effects since, at each power level, the densities between the two power scans differ by only $\simeq$ 15 %. The relatively high diffusivities in the 1-gyrotron case of both power scans can be explained by the 40 % smaller local densities than in the respective 2,3,4-gyrotron cases. All these results indicate that at least in the outer confinement region, D scales positively with the heating power and negatively with B, ι and the local plasma density. A comparison of D and χ_e for the analyzed discharges yields D/χ_e values between 0.1 and 0.3 in the outer confinement region at r/a = 0.8.

An interesting transition was observed in ECRH full-field discharges at $\iota(a) = 0.32$ (fig. 19, next page).
During the evolution of the electron density the energy content increases within 15 ms by about 30 % without any measures being taken from the outside. The transition takes place at a line-averaged density of $\bar{n}_e = 1.8 \cdot 10^{14}$ cm^{-3} corresponding to $\int n dl = 7.5 \cdot 10^{14}$ cm^{-2} in fig. 19, next page. The H_α signals show a maximum in the fluctuation level at the start of the transition and then relax to a lower level. From ECE measurements a small transient increase in Te is seen during the transition at all radial positions. This indicates that this phenomenon is not just restricted to the plasma edge, as one would conclude from the H_α signals alone. From Thomson scattering the temperature profiles during the steady phase after the transition turned out to be the same, but the electron density has increased, indicating better confinement, particularly since the external gas flux is even reduced. From energy and particle balance analysis, the transition to higher density is seen to correlate with an average reduction of χ_e by about 30 % over the whole plasma column and with a decrease of D by about 50 % in the density gradient region.

3.2.4 Bootstrap current

The bootstrap current was numerically evaluated by applying the DKES code[1] to the rather complex 3-D magnetic field topology of W7-AS. Concerning the determination of bootstrap current and plasma conductivity, two main limitations are intrinsic to this approach: in the DKES code the collision operator is taken in its pitch angle scattering limit, and terms related to external sources (simulating, e.g., the effects of auxiliary heating) cannot be included in the code. To compensate the loss of parallel momentum artificially introduced by the use of the simplified collision operator, an appropriate weight function was introduced in the energy convolution of the mono-energetic DKES results /88/. The current driven directly by auxiliary heating was treated separately and superimposed on the neoclassical bootstrap current. The effects of auxiliary heating on the neoclassical fluxes themselves (e.g. as a consequencce of the presence of suprathermal particles) were disregarded.

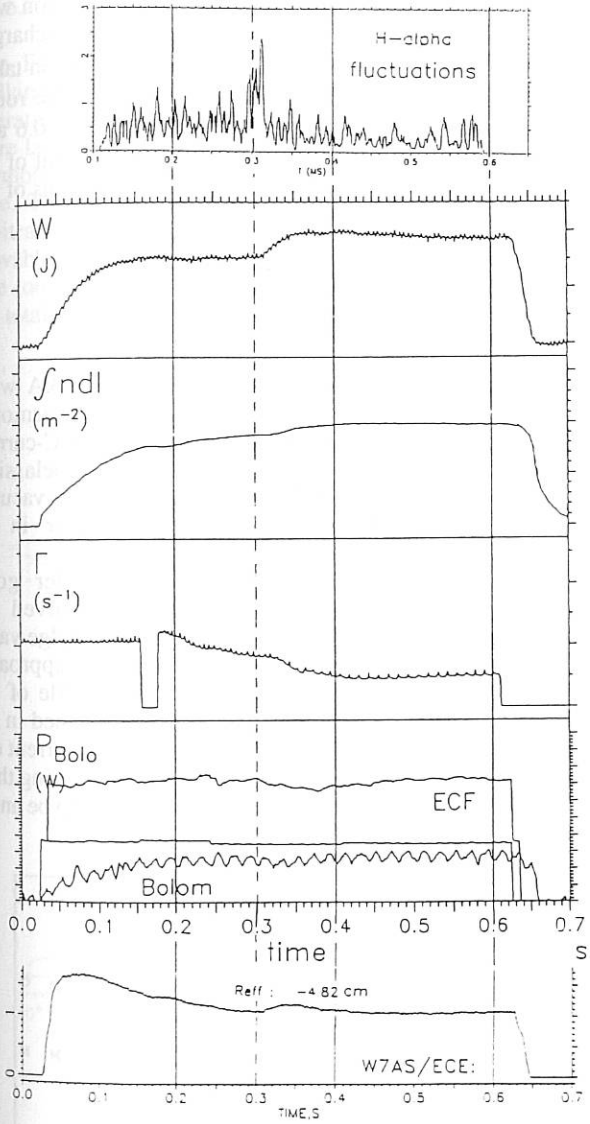

FIG. 19: *Transition to improved confinement in shot 8424: the energy content, line density, gas flux, ECF input power and radiation loss, and, in the lowest plot, the ECE electron temperature at about $r \approx 5$ cm are shown versus time. The H_α fluctuations (upper plot) peak at the transition (broken line) and decrease afterwards. T_e shows only a transient increase after the transition, unlike W and ∫ndl.*

In fig. 20 the behaviour of the net toroidal current for ECRH discharges with resonance on axis is reported. The ECRH beams are injected perpendicularly to avoid a directly driven current component (see sec. 3.2.6).
The central plasma densities and temperatures are in the ranges: $0.8 \cdot 10^{13} < n_{e,o} < 5.5 \cdot 10^{13}$ cm^{-3} and $0.4 < T_{e,o} < 2.5$ keV. These plasmas are characterized by very broad density profiles, peaked T_e profiles and $T_i << T_e$. Under these conditions, the main driving force for the bootstrap current is expected to be the T_e gradient. As the confinement in low-shear devices such as W7-AS is very sensitive to critical values of the edge rotational transform, the current in most discharges was controlled by an externally applied loop voltage U_l. The DKES prediction, based on measured temperature and density profiles, for the dominant electron component $I_{b,e}$ is compared with the experimental values defined as $I_p - U_l/R$ (where I_p and U_l are the measured net current and loop voltage and R is the predicted plasma resistance). The agreement with the neoclassical predictions is very good. For higher power levels and lower densities, suprathermal electrons induced by ECRH contribute to both the bootstrap current and the plasma resistance.

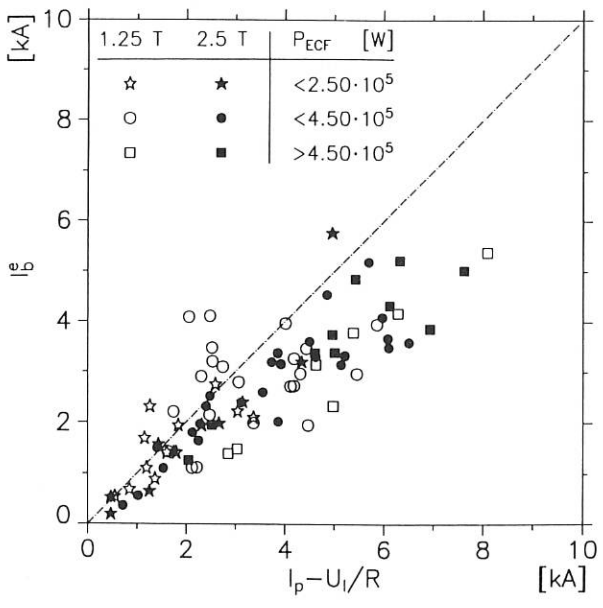

FIG. 20: *The electron component of the bootstrap current, $I_{b,e}$ calculated from the DKES code versus the experimental value $I_p - U_l/R$, for ECRH discharges (without ECCD) with central deposition. The sign of the current, as predicted by theory, reverses by reversing the magnetic field so that only the absolute value is reported.*

[1] S.P. Hirshman et al., Phys. Fluids 29 (1986), 2951

3.2.5 Electron heat transport analysis by modulated ECRH

The localized and narrow power deposition profiles in ECF-heated discharges allow application of a modulation method for direct measurement of the local electron heat diffusivity. The modulation of the incident microwave power generates a "heat wave" (T_e-modulation) which propagates radially outward. The phase shift of this heat wave with respect to the driving ECF-power modulation depends on the local heat diffusivity and can be measured by a space and time-resolving electron temperature measurement using SX or ECE diagnostics.
This perturbation method using power-modulated ECRH together with ECE diagnostics was applied for the first time in W7-A. It is of great importance for this method that the power deposition region is small compared to the cross-section of the plasma, and, in particular, that complete single-pass absorption is obtained. For all other cases where the power deposition region is smeared out or a second deposition layer has to be taken into account, analysis remains possible in principle, but does not allow straightforward interpretation. In order to illustrate this, two discharges are compared with incomplete and complete single-pass absorption. The measured data of the phase delay of the radially outward propagating heat wave (T_e modulation) from ECE diagnostics is shown in fig. 21 (left) for a discharge with a central electron temperature $T_{eo} \sim 0.5$ keV, corresponding to a single-pass absorption of only 50 %. In fig. 21 (right) the same data are shown for a discharge with $T_{eo} \sim 2.5$ keV and a corresponding single-pass wave absorption of 95 %.
In both cases, the phase shift increases radially outward. In the case of weak single-pass absorption, however, the phase shift again decreases at larger radii and is almost in phase with the driving microwave power modulation at the plasma edge. This is a clear indication of power deposition at the plasma centre and the edge as well. Additional edge deposition is expected if the single-pass absorption is weak and multiple reflections of the microwaves have to be taken into account. Note that even at infinite heat diffusivity the phase delay remains constant and independent of the radius, whereas inversion can only be due to edge power deposition. The analysis in this case is difficult and requires a precise knowledge of the power deposition profiles at the centre and at the edge.
In the case of strong single-pass absorption (fig. 21, right) a monotonic increase of the phase delay is measured from the plasma centre towards the plasma edge. A clear separation of the power deposition zone and the diffusive zone simplifies the analysis. An example of the derived electron heat diffusivity for the latter case is shown in fig. 22.

As seen in fig. 22, the experimental data scatter within the modelled boundary values of 1 and 2 m^2/s indicating an electron heat diffusivity of about 1.5 m^2/s. Comparison with the standard n_e and T_e profile analysis for the same discharges gives χ_e values of 1 ± 0.5 m^2/s within the radial region taken for the analysis, which is in fair agreement within the rough assumptions of the model (constant χ_e within $r/a < 0.6$ and increasing towards the plasma edge). An improvement of the analysis taking into account higher Fourier components of the modulation is being developed.

3.2.6 Electron cyclotron current drive (ECCD)

3.2.6.1 General considerations

In W7-AS small net currents in the range of 1-4 kA were observed for both 2nd-harmonic X-mode and 1st-harmonic O-mode heating with pure perpendicular launch (no EC-current drive). This net current was identified as the neoclassical bootstrap current (see sec. 3.2.4), which changes the vacuum magnetic field configuration of the stellarator in an uncontrolled manner.
In a first approach steady-state operation under good confinement conditions was successfully achieved by controlling the total net current thus controlling the edge value of the rotational transform. A more sophisticated approach, however, would aim at controlling the radial profile of the rotational transform (shear) by ECCD which is planned in the forthcoming experimental campaign. The bootstrap current can be balanced by application of inductive current drive using the OH transformer. EC-current drive was demonstrated to be an

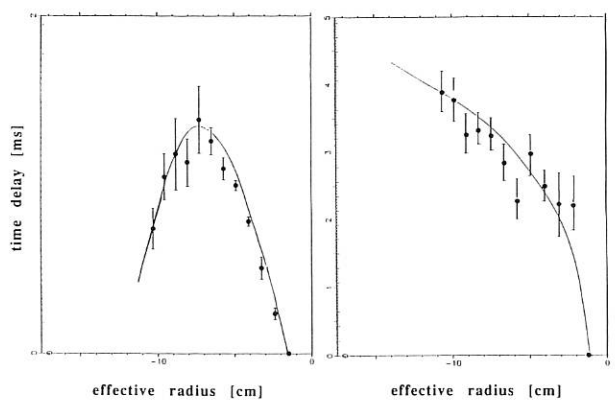

FIG. 21: *Left: phase delay of the T_e modulation measured by ECE diagnostics as a function of the minor plasma radius for a discharge with weak single-pass absorption of the microwaves at the given central electron temperature of 0.5 keV.*
Right: same for a discharge with high single-pass absorption at T_{eo} = 2.5 keV.

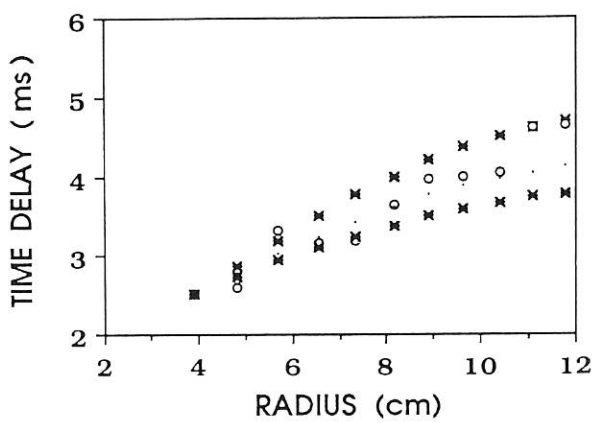

FIG. 22: *Modelling of the phase delay as a function of the minor plasma radius for assumed values of the electron heat diffusivity χ_e = 1.0 (upper set of crosses) and 2.0 m^2/s (lower set of crosses). The experimental data (circles) are also plotted.*

alternative powerful tool for current control. A complete compensation of the bootstrap current was achieved for 2nd- harmonic X-mode launch whereas at 1st-harmonic O-mode launch the bootstrap current could not be fully compensated by ECCD. This is explained by the incomplete single pass absorption at 1st-harmonic heating for the given electron temperature and density and the improved energy confinement at the higher magnetic induction, which in turn leads to higher bootstrap currents at the higher electron temperatures.

3.2.6.2 Launch angle variation

The ECCD experiments were performed at the W7-AS stellarator with up to 0.7 MW of RF-power in long-pulse operation (< 1.5 s). Up to four linearly polarized RF-beams were launched at both the 1st-harmonic ordinary and the 2nd-harmonic extraordinary-wave polarization from the low-field side. The RF-beams were directed towards the plasma at arbitrary toroidal launch angles by a set of independently movable focusing mirrors mounted inside the vacuum chamber The toroidal launch angle of the RF-beams was varied while the total net plasma current was kept close to zero

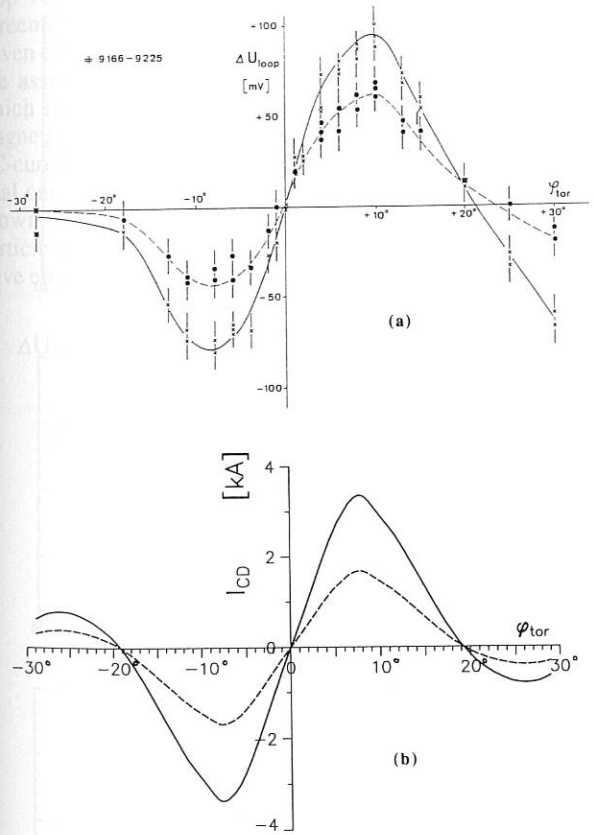

FIG. 23a: *Loop voltage increment ΔU as a function of the launch angle for 0.17 MW (dots) and 0.35 MW (crosses) of ECCD power. The EC-driven current is balanced by inductive current drive (OH-transformer feedback). The total input power for both cases is 0.35 MW.*

FIG. 23b: *ECCD modelling based on the measured n_e and T_e profiles for the same discharges at 0.17 MW (dashed curve) and 0.35 MW (solid curve).*

(I < 0.2 kA) by feedback control with the OH-transformer. The measured change of the required loop voltage ΔU with respect to perpendicular launch (no ECCD) is plotted in fig. 23a as a function of the launch angle at the resonance layer for a constant input power of 0.35 MW in 1st-harmonic O-mode. The dots refer to experiments with one beam (0.17 MW) at perpendicular launch (no ECCD) and one beam (0.17 MW) at oblique launch angles. The crosses refer to a variation of the launch angle of both beams. The right wing of the curve with positive loop voltage increment corresponds to a situation where the bootstrap current has the same direction as the EC-driven current. The left wing of the curve corresponds to ECCD in the direction counter to the bootstrap current. Equivalent experiments at B_0 = 1.25 T show similar results. The ECCD efficiency is evaluated in a 3-D ray-tracing code by means of the adjoint approach. In the limit of low collisionality, the evaluation of the local efficiencies was generalized to include trapped particle effects in W7-AS magnetic configurations. A comparison of the experimental data with this linear model is shown in fig. 23b. The experimental findings are well described by the model.

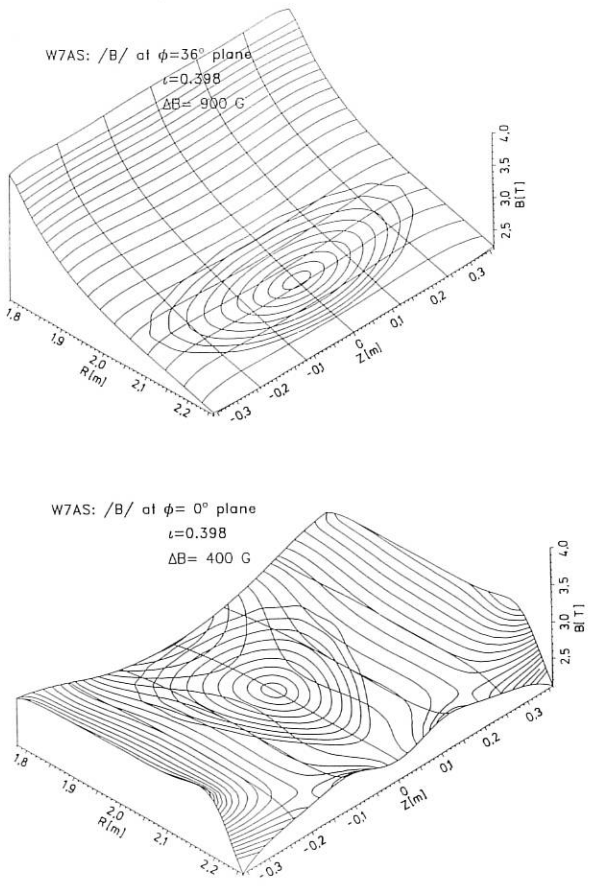

FIG. 24: *Top: Variation of /B/ in a poloidal plane with strong magnetic induction gradient. The elliptical plasma cross-section is indicated, too. Four microwave beams (0.8 MW) are launched in this plane.*
Bottom: Variation of /B/ in a poloidal plane with almost vanishing magnetic induction gradient. Here the plasma shows a triangular cross-section. A fifth microwave beam (0.2 MW) is launched at fixed toroidal angle in this plane.

In particular, the launch angle for maximum current drive and the linear increase of ECCD with RF-power agree well. The absorption layer is shifted radially outward with increasing oblique launch. The current drive efficiency decreases for large launch angles (far in the Doppler regime) because the absorption sensitively depends on T_e and the absorption layer is then within the T_e gradient region. The absolute value of the EC-driven current at optimum launch angle derived from the experiment is about 3 - 5 kA, which is in satisfactory agreement with the simplified assumptions of the theory and the experimental error bars.

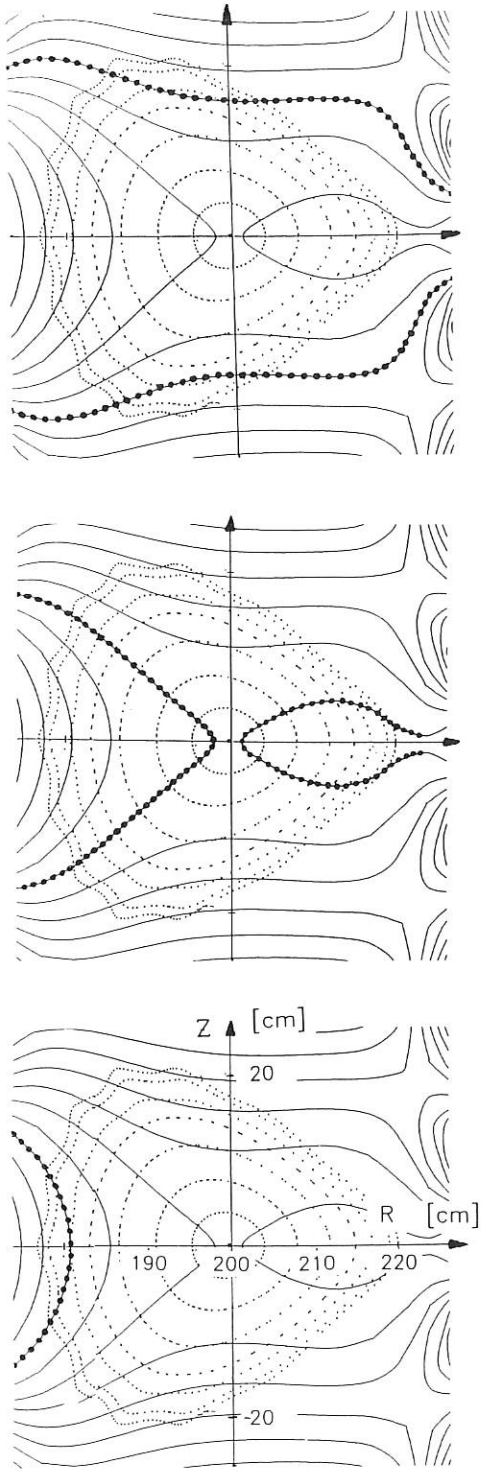

FIG. 25a: *Position of the resonance layer (dotted line) in a poloidal cross-section with small magnetic field gradient at B_o = 2.4 T (top), B_o = 2.5 T (middle) and B_o = 2.6 T (bottom). The solid lines indicate |B| = const. contours; the dashed lines give the nested flux surfaces.*

3.2.6.3 ECCD in the up/down- shifted resonance regime

ECCD in the up/down- shifted regime was investigated by making use of a peculiarity of the magnetic field configuration of W7-AS, i.e. wave launching at a poloidal plane with an almost vanishing magnetic field gradient. Under such conditions, sufficiently high single-pass absorption is obtained even at moderate electron temperatures of about 2 keV in the absence of the fundamental resonance.
The magnetic field topology, i.e. the variation of the magnetic field within the two selected poloidal planes is illustrated in fig. 24. The plasma cross-section is also indicated and will be referred to as "elliptical" and "triangular" plane for obvious reasons.
In the triangular plane a fifth microwave beam is launched at a fixed toroidal angle of 11° with respect to perpendicular launch.

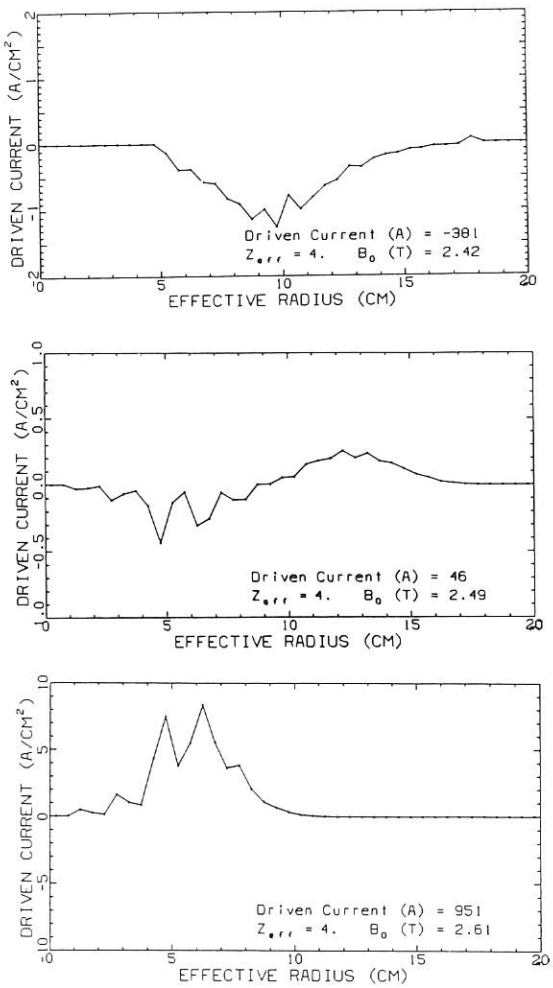

FIG. 25b: *EC-driven current density distribution from 3-D ray-tracing calculations for 0.1 MW of microwave power for the upshifted resonance (top), the resonant case (middle), and the downshifted case (bottom).*

Due to the weak gradient of the magnetic induction, the EC-resonance layer can be completely shifted out of the confinement region (last closed flux surface) by varying the magnetic induction from 2.4 to 2.6 T, as can be seen from fig. 25a, prev. page.
The target plasma is maintained by a perpendicular launch of 0.7 MW (no ECCD) in the poloidal plane with a strong tokamak-like magnetic field gradient, where the EC-resonance layer remains well within the confinement region for the given magnetic field variation. The calculated spatial current density distribution is given in fig. 25b, prev. page, for the three cases of B_o = 2.4 T (upshifted), 2.5 T (resonant), and 2.6 T (downshifted). For the resonant case (fig. 25b, prev. page, middle) an almost zero net-current is found because the vanishing magnetic field gradient and the corresponding broad power deposition profile create counterstreaming currents on both the low and high-field sides of the resonance layer. The current reverses the sign while varying the magnetic field from an upshifted scenario (fig. 25, prev. page, top) to a downshifted one (fig. 25, prev. page, bottom). The measured loop voltage increment required to balance the EC-driven current is given in fig. 26a for the full magnetic field scan. The change of the sign as well as the transition through zero loop voltage increment at the resonant magnetic field is in agreement with theory as shown in fig. 26b, where the EC-driven current is normalized to the launched microwave power.
We assume, however, that only the first transit absorption, which is given in fig. 27a, next page, as a function of the magnetic induction, contributes to current drive. The relevant EC-current drive efficiency is then obtained by normalizing the total current to the power absorbed in a single pass, which is shown in fig. 27b, next page. In all calculations trapped particle effects are taken into account. An improved current drive efficiency as compared with the two experiments mentioned first is clearly deduced.
The parameter dependence on the launch angle, the electron temperature, the plasma density and the microwave power for all types of ECCD experiments is in good agreement with a linear theoretical model which takes into account quasilinear and trapped particle effects. The results are confirmed by Fokker-Planck calculations.

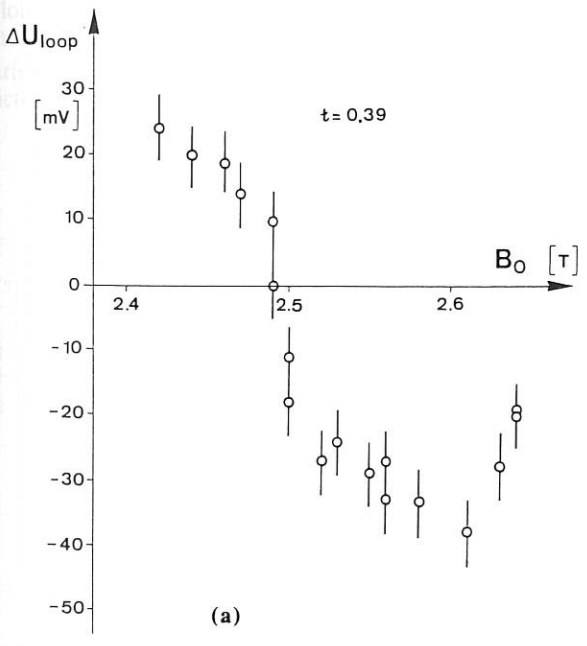

FIG. 26a: *Loop voltage increment ΔU_{loop} required to balance the EC-driven current as a function of the magnetic induction on axis. The left part (B_o~2.4 T) corresponds to an upshifted, the right part (B_o~2.6 T) to a downshifted scenario.*

4. DIAGNOSTICS

4.1 Density fluctuations and ECF beam power distribution

The Annual Report 1989 presented results of computer simulation of
i) ECE spectra near the cut-off density,
ii) power deposition profiles during ECRH,
iii) spatial distribution of ECF power after passing the plasma column.
These calculations were made with a certain amount of random plasma density fluctuations superposed on the density distribution as taken from Thomson measurements, which is, of course, smoothed.
The ray-tracing program used has now been extended to the introduction of additional coherent radial or poloidal density waves. The amplitudes of these disturbances are considered to be either proportional to the undisturbed density or to its gradient. The maximum possible k-value of the disturbances is $2\pi \cdot 0.33\ cm^{-1}$. Calculations with those waves were made for case (iii), which is briefly explained.
An array of microwave pick-up antennas is situated at the torus wall opposite each of the four ECF launching antennas. The signals received by these pick-up antennas indicate the spreading and the single-pass absorption of the incoming microwave beam.

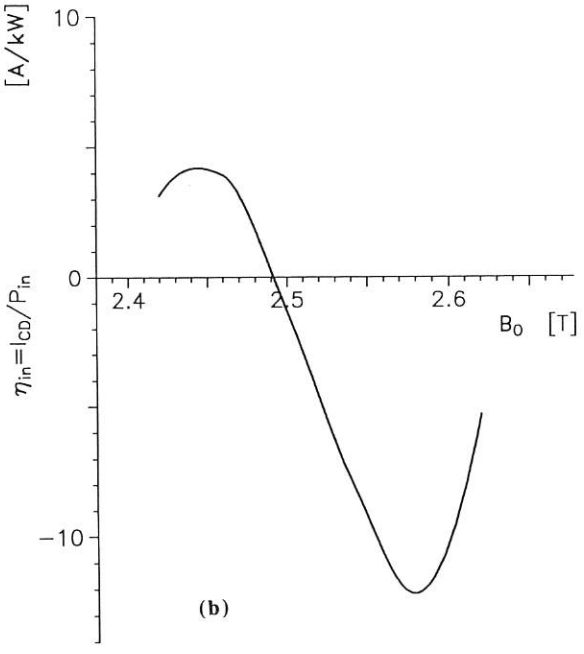

FIG. 26b: *ECCD modelling of the experiment. The current-drive efficiency η_{in} is defined as the driven current I_{CD} normalized to the launched power P_{in}.*

Fig. 28 shows the measured signals of the central channels of the two arrays in one poloidal plane, when only one gyrotron is working. The upper signal belongs to the array opposite the working launcher, which is directly hit by the beam. The dotted line is the line density. With increasing density the lower signal increases from very low values. The upper one decreases because a) the absorption grows and b) the microwave beam is bent away by diffraction. This bending goes in such a direction that the lower signal should also decrease. We can model the observed lower signal by ray-tracing superposing ripple on the smoothed density distribution.

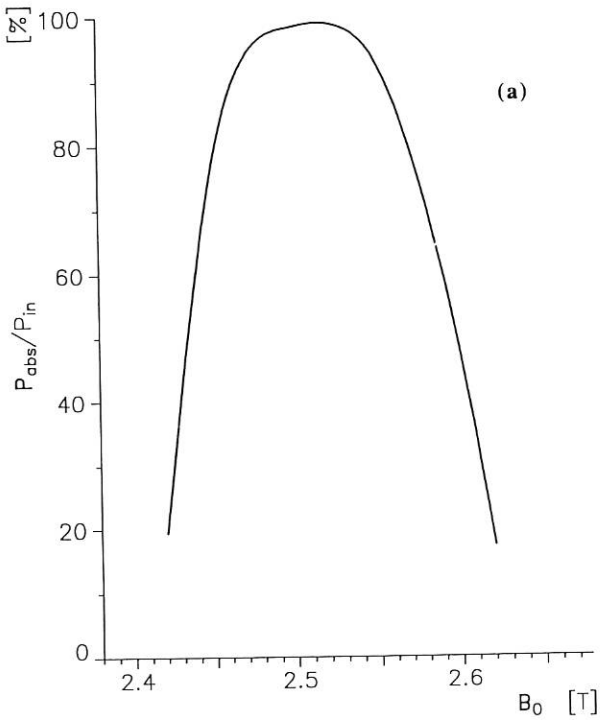

FIG. 27a: *The single-pass absorption P_{abs} normalized to the launched power P_{in} from ray-tracing calculations for the same discharges.*

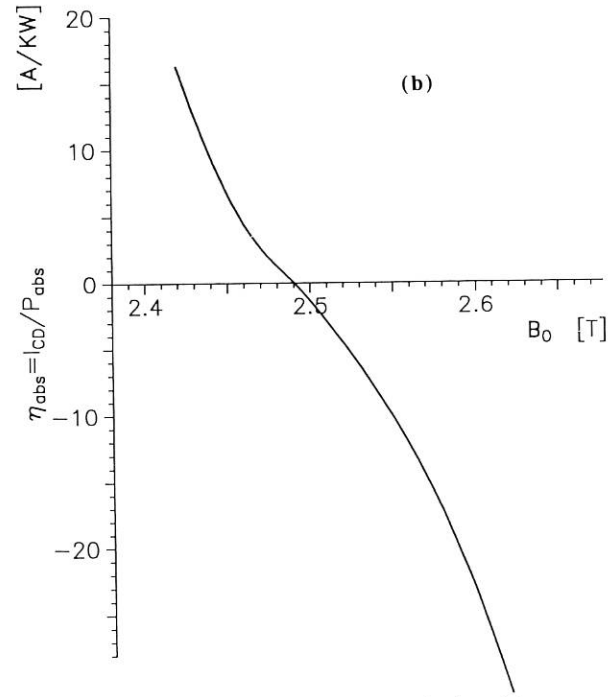

FIG. 27b: *ECCD efficiency η_{abs}, with the driven current I_{CD} normalized to the single-pass absorption P_{abs} for the same discharges.*

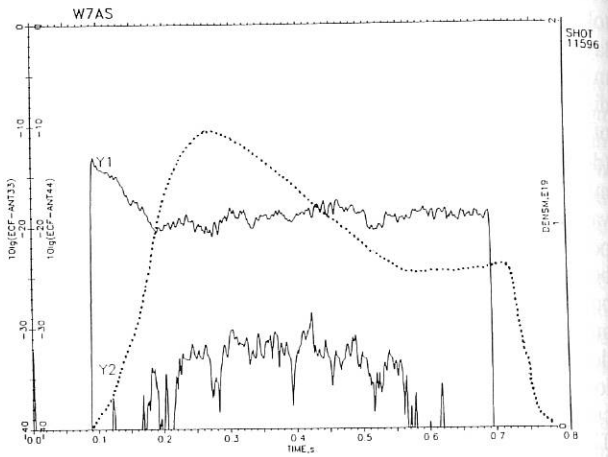

FIG. 28: *Measured signals of pick-up antennas and line-density (dotted) with one gyrotron working. The upper signal (Y1) is that of the directly-hit antenna.*

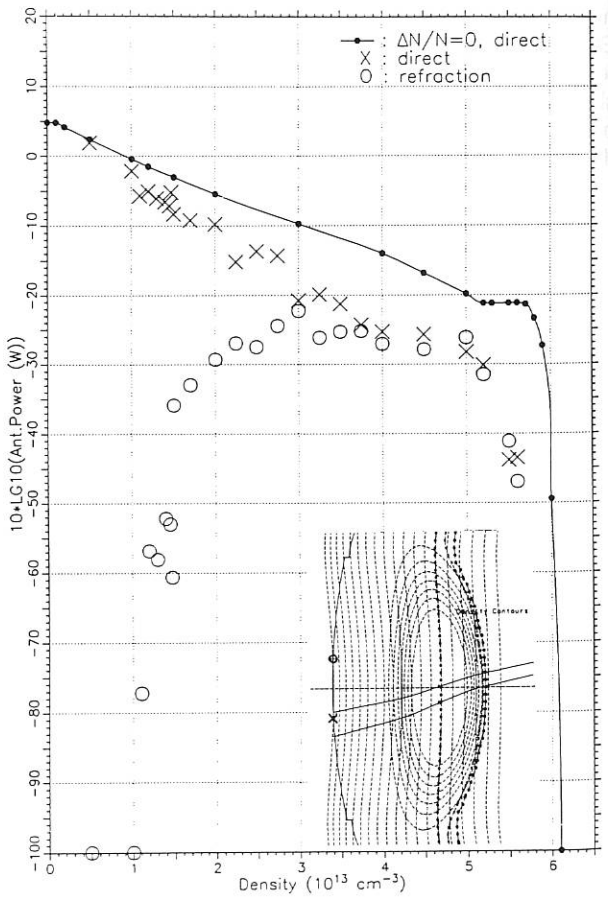

FIG. 29: *Simulated signals. The ECF beam together with the positions of the two antennas is sketched in the insert. Without fluctuations no signal is found in the upper antenna.*

It has been found that poloidal waves of high wave number as disturbance broaden the ECF beam similarly to random fluctuations, whereas radial waves (wave vectors mainly parallel to the beam) have only a weak influence.
Figure 29, prev. page, shows as an example results of simulation with random fluctuations of 30 % of the local undisturbed density. The solid line is the signal of the directly hit pick-up antenna without fluctuations.
Note that the direct signal and the refracted one become more and more equal with growing density, i.e. the power becomes more and more equally distributed at the left-hand side of the plasma.
From fig. 28, prev. page, we see a difference between the strong and weak signals of about 12 dB when the line-density is maximum ($\sim 1.5 \cdot 10^{19}$ m^{-2}). This corresponds to a central density of roughly $2.5 \cdot 10^{13}$ cm^{-3}, for which we find in fig. 29, prev. page, the same difference of about 12 dB between the direct and the refracted signal.
If we simulate with fluctuation amplitudes proportional not to the density but to its gradient, we need about double the amplitude for the fit.

4.2 ECE

Radiometry of the electron cyclotron emission (ECE) is routinely conducted using a 12-channel heterodyne receiver, monitoring the 2nd-harmonic emission in extraordinary-mode polarization. The system is absolutely calibrated and yields electron temperature $T_e(r_i, t)$ as a function of time at 12 different radii r_i. The temporal resolution corresponds to about 100 kHz video bandwidth but is restricted to about 10 kHz by the digitization rate of the data acquisition system. The temperature information is in good agreement with that obtained by Thomson scattering for both purely electron cyclotron heated (ECRH) and neutral beam injection (NBI) heated discharges. In the latter case ECE measurements are restricted to electron densities below about $1 \cdot 10^{20}$ m^{-3}, which is the cut-off density of the spectral region monitored.

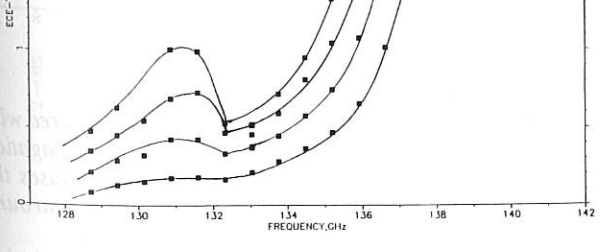

Fig. 30: *In the presence of a suprathermal electron population, an additional maximum in the electron cyclotron emission spectrum is found. The figure demonstrates how this feature becomes more pronounced with increasing ECR heating power between 160 and 650 kW.*

The viewing optics of the ECE was replaced by a new one, using corrugated horn antennas and elliptical mirrors which form a Gauss beam. This measure was necessary because no direct access to the plasma is possible in the new plane of observation which must be shared in part with an NBI beamline. The beam waist of the Gauss beam obtained in the plasma center is about 1 cm. Three different horn mirror combinations can be chosen, one mounted in the equatorial plane of the machine, the other ones 10 cm above and below. The central mirror is additionally used by a 1st and a 3rd-harmonic antenna. Only sporadic measurements have been made. They confirm the 2nd-harmonic measurements especially the information on the optical depth deduced.

In pure ECRH discharges a non-negligible amount of energy is stored in suprathermal electrons. The cyclotron emission of this population is red-shifted due to the relativistic mass increase, resulting in a significant deviation of the temperature profile on its low-field side. Figure 30 demonstrates this feature for different ECRH power levels. The suprathermal content in the plasma can be simulated on the bases of these observations. Peak densities of up to 1 % of the bulk density and an average energy of about 5-7 keV are necessary to explain the experimental data.

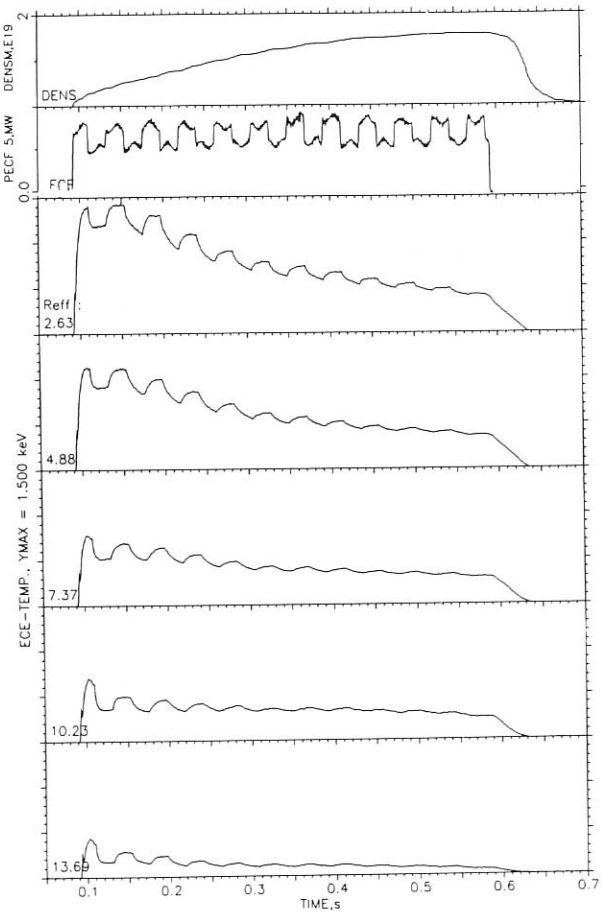

Fig. 31: *The figure gives the modulated ECF signal together with the temperature response observed in a few channels across the plasma radius. A density increase causes a decrease of the temperature modulation amplitude.*

The multichannel ECE radiometer was used for electron heat diffusivity studies. In these experiments the ECF power is modulated with an amplitude of about 10 % and frequencies between 20 and 200 Hz. Both the amplitude and phase of the resulting temperature modulation are measured as functions of the radius.
Figure 31, prev. page, gives as an example the temperature modulation as observed during a non-stationary discharge. It is obvious that the temperature modulation decreases with increasing electron density. Figure 32 gives these data as predicted by a transport code assuming a given profile for the electron heat diffusivity.

As with the temperature profiles mentioned above, phase or time delay information can be scrambled by an existing suprathermal electron population. Due to the fact that this population contributes with its red-shifted emission to the emission of electrons located in the gradient and edge region of the low-field side of the profile while it is located near the center of the plasma column in the power deposition zone, the clear phase relation with B is removed and the monotonic increase of the delay time with radius reflecting the propagation of the heat wave obscured. This effect becomes obvious just in those channels which correspond to the suprathermal feature in the temperature profile (see fig. 33).

4.3 Soft-X diagnostics

4.3.1 Soft-X cameras and PHA

The soft X-ray camera systems on W7-AS were used to study magnetic configuration effects (Shafranov shift, flux surface contours), MHD activities (identification of m = 2, 3 modes, location of rational surfaces) and electron temperature profiles (filter method) and to analyze impurity radiation. The diagnostics were completed in 1990 with two X-ray pulse height analyzer (PHA) systems.

4.3.2 MHD activity driven by NBI

The ideal MHD m=2/n=1, m=3/n=1 resonant modes were observed (Annual Report 1989) in the low-frequency band of 1-5 kHz by the soft-X diodes in W7-AS during iota scans around the resonant values of ι=0.5 and ι=0.33. These modes show no pronounced correlation with the operating conditions

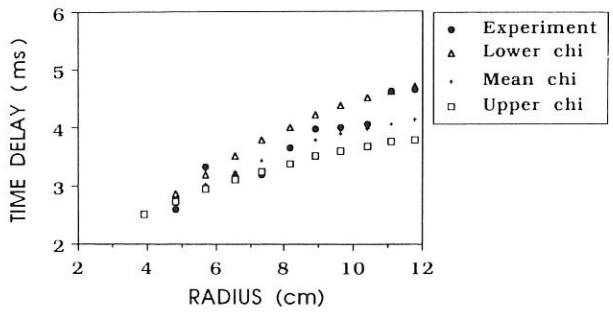

Fig. 32: *The time delay of the heat wave as function of radius. The modulation frequency used is 70 Hz. The figure gives for comparison the predicted time delay assuming a constant heat diffusivity coefficient of 1.5 ± 0.5 m^2/s.*

(i.e. ECF or NBI heating of plasma) or the plasma parameters. Their only precondition is the existence of the q=2, q=3 rational surface within the plasma volume at the location at which they were observed.

A different kind of resonance observed in the high-frequency range 20-40 kHz by the Mirnov coils and the X-ray diodes in low-iota operation (ι(a)=0.34) of W7-AS during balanced NBI and co-NBI only is shown in fig. 34, next page.

This may be described as follows:

- The mode always terminates immediately after the NBI is switched off (on a time scale of 0.5 ms, see fig. 34, next page), although the plasma remains for further 10-20 ms.

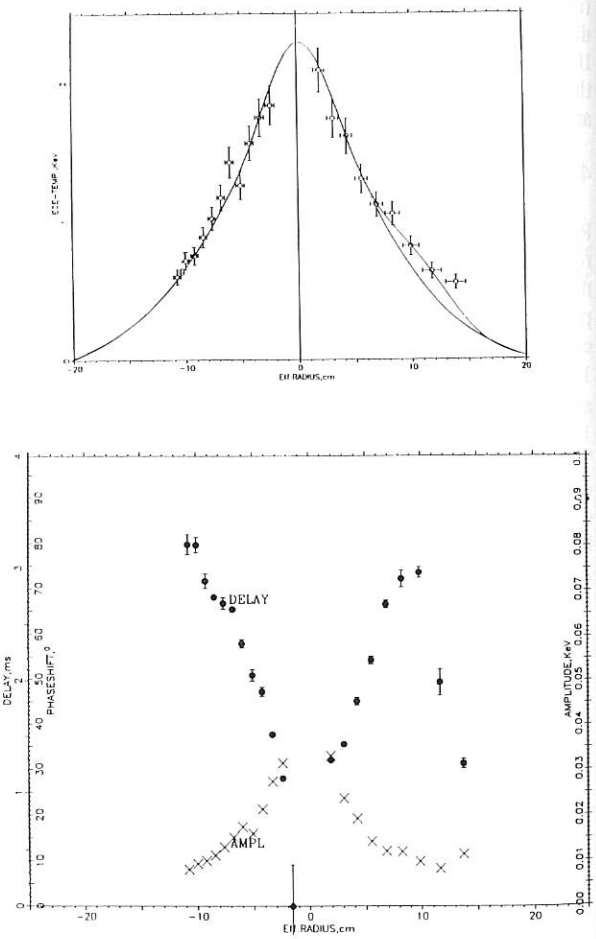

Fig. 33: *Upper figure: Temperatur profile as measured with the ECE radiometer during heat wave propagation studies. A small suprathermal content causes the deviations from a symmetric profile around + 10 cm.*
Lower figure: Time delay and modulation amplitude as function of radius under the same conditions. At radii greater than + 10 cm, the monotonic increase of the delay disappears, demonstrating that the observed emission in the suprathermal feature originates in the plasma center.

- The mode is identified by comparing the X-ray intensity fluctuation profiles with the simulated ones shown in fig. 35 for the saturated m=3 island in particular at r_{eff}=8 cm. Typical and well reproducible fluctuation profiles of the intense mode activity during balanced NBI and co-NBI are shown in fig. 36. One can see a similar structure (to that of the simulated profiles), apart from a relative displacement to the inside due to the applied positive vertical field. This mode analysis always indicates the same saturated m=3 structure at r_{eff}=7-10 cm. The well-defined location of the resonant surface within the confinement region may be due to the pressure gradient there, which drives bootstrap current contributing to the magnetic shear.
- The mode frequency vs. density plot (see fig. 37) shows an inverse relation in the frequency range 20-40 kHz. This was also confirmed by observation of the pellet-mode interaction. X-ray and magnetic fluctuations after the pellet is injected are shown in fig. 38. It is seen that the pellet immediately damps the fluctuations, which slowly grow again until 6 ms later the same dominant m=3 mode can be identified. Looking at the Fourier spectrum of the fluctuations before and after the pellet, however, one sees that the m=3 mode frequency is shifted from 35 kHz down to 25 kHz, apparently due to an increase in density (confirming the inverse relation between mode frequency and density).

The reproducibility of the mode characteristics and its correlation with the NBI operation lead to the conclusion that this is an NBI-driven effect different from the m=2, m=3 modes described earlier (the difference in the frequency spectrum is about 5-20 kHz). NBI heating is a definite precondition for the resonance, but it is apparently not the only one. The existence of the q=3 rational surface inside the plasma is a precondition, too. During the sustainment phase of the intense mode activity well-reproducible Thomson density and temperature profiles were obtained. Comparison of the diamagnetic energy content between series of shots at the same heating power with and without the resonance shows that this mode has no impact on global energy confinement, although the Thomson profiles can be different.

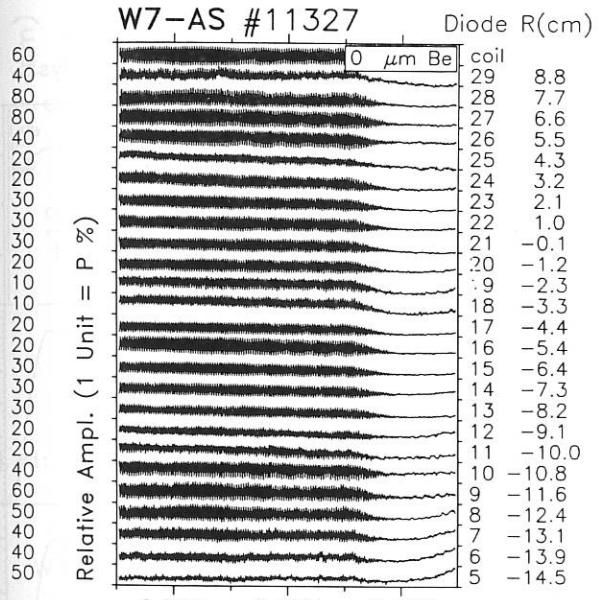

FIG. 34: *X-ray and magnetic fluctuations (top signal) in W7-AS. The fluctuations terminate within 0.5 ms immediately after the NBI is switched off.*

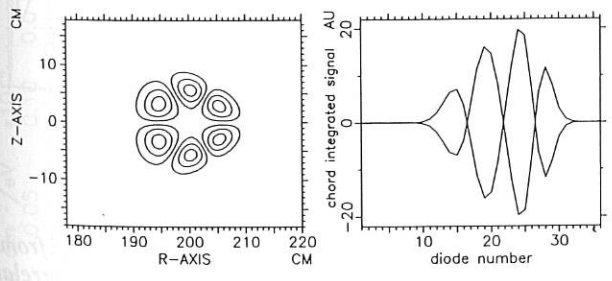

FIG. 35: *m=3 mode simulation at r_{eff}=8 cm for the field geometry of W7-AS at the toroidal location of the X-ray cameras (left), with the corresponding fluctuation profiles when the mode is at phases of 0° and 180° (at which the profiles simply turn upside down).*

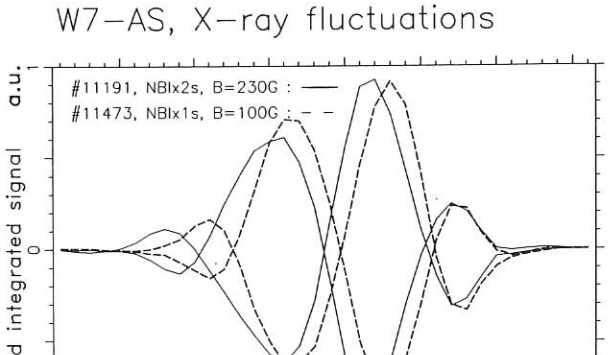

FIG. 36: *Typical and well-reproducible fluctuation profiles of the intense mode activity during balanced NBI and co-NBI.*

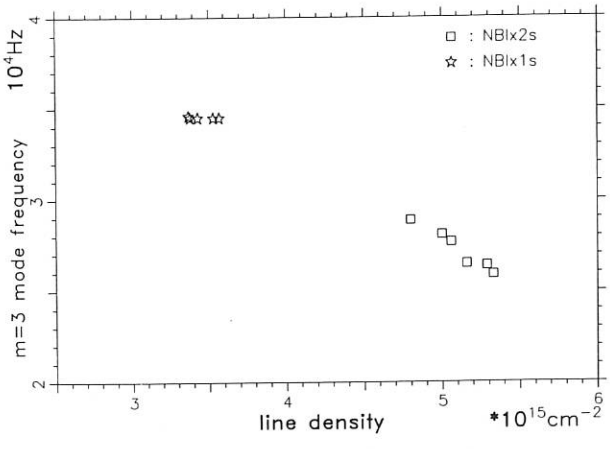

FIG. 37: *m=3 mode frequency vs. line-density in W7-AS.*

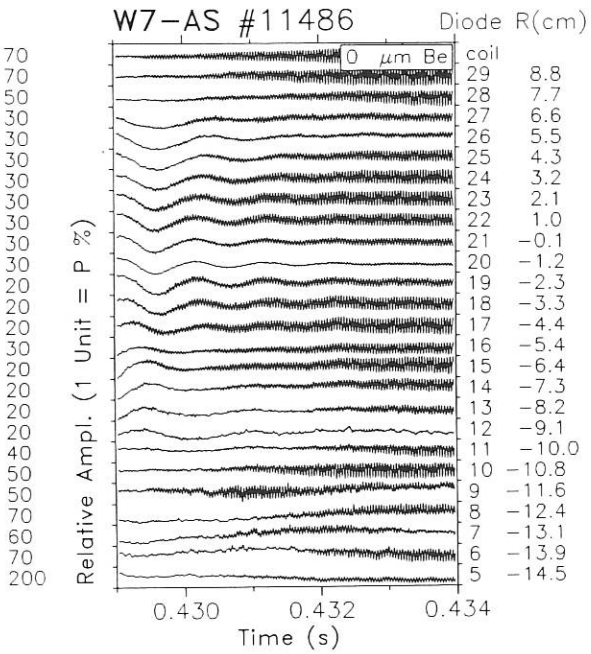

FIG. 38: *X-ray and magnetic fluctuations (top signal) after pellet injection in W7-AS. The pellet is fired 1 ms before.*

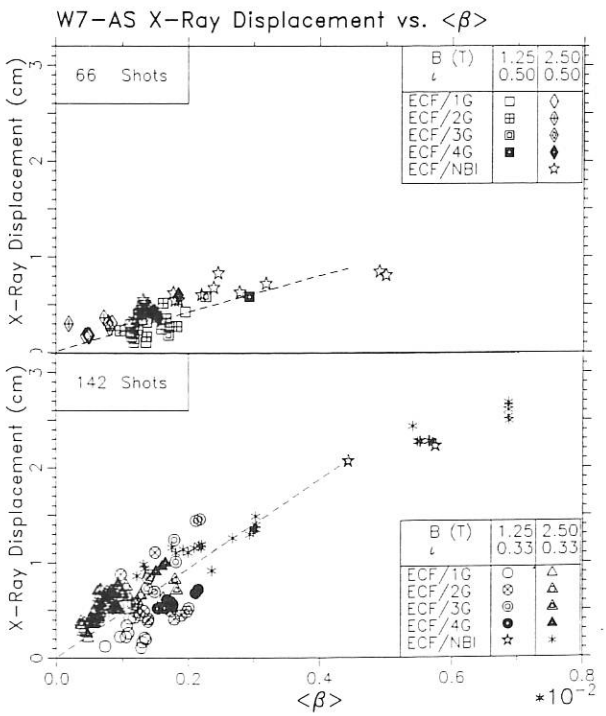

FIG. 39: *Statistical analysis of measured X-ray displacement (from T_e camera profiles) for representative shots and times used for Thomson profile measurements. The data are plotted versus the volume-averaged beta for ι~0.5 (top) and ι~0.33 (bottom). Comparison with predicted values confirm the reduced Shafranov shift in W7-AS (factor of ~2 compared with an l=2 stellarator).*

4.3.3 Equilibrium studies

Concerning the horizontal plasma displacement due to the equilibrium currents (Shafranov shift) a statistical analysis of X-ray profiles obtained with the X-ray T_e cameras was performed. In fig. 39 the observed shift of the radiation center is plotted as a function of the volume-averaged beta.
The database refers to the time of maximum plasma energy of different well-documented discharges heated by ECRH or NBI. For high rotational transform (ι ~ 0.5, upper figure) the observed displacement is clearly less than in the case of the lower transform (ι ~ 0.34, lower figure). The experimental points fit within the experimental errors to predicted values for W7-AS (dashed lines), which are reduced by a factor of ~ 2 compared to a conventional l=2 stellarator. The correlation of the X-ray plasma-shift signal with the plasma pressure is shown in fig. 40 for a particular NBI-heated discharge.

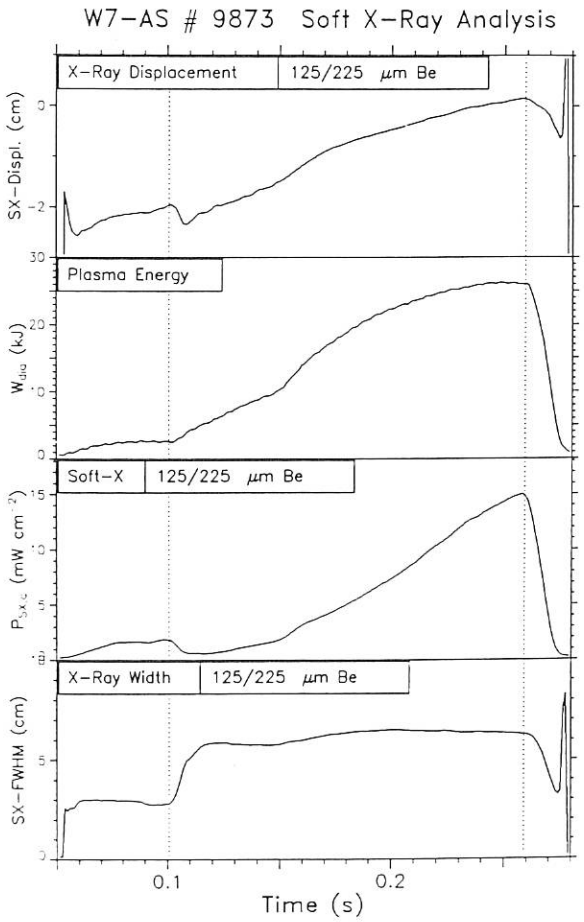

FIG. 40: *Displacement of the X-ray profiles derived from the T_e camera system (NBI starts at 0.1 s). Correlation with plasma energy, X-ray intensity and X-ray profile width.*

1) Navarro, A.P., Ochando, M.A., Weller, A., in Contr. Fus. and Plasma Phys. (Proc. 16th Europ. Conf. Venice, 1989), Vol. 13B, Part II (1989) 687-690

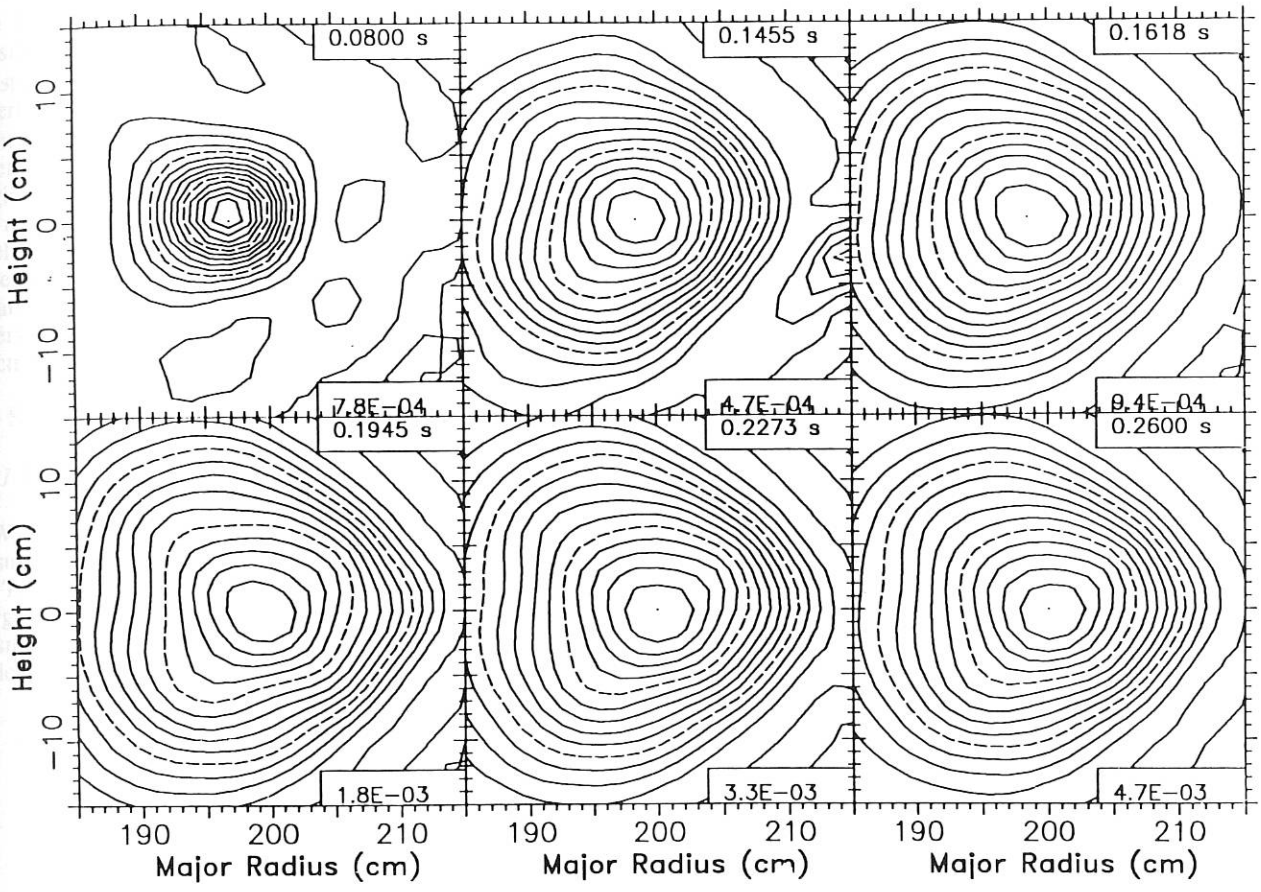

FIG. 41: *Displacement of the X-ray emissivity from tomographic reconstruction (EBITA code) of the two main camera data. Emissivity contours for different times.*

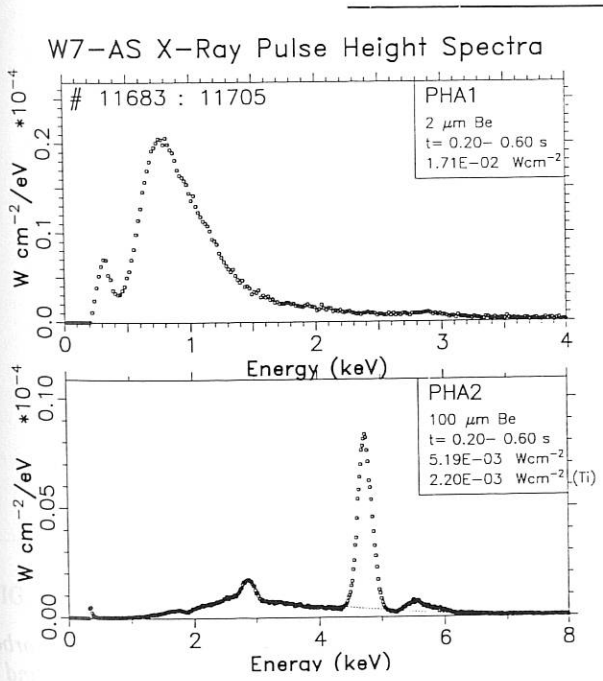

FIG. 42: *X-ray PHA spectra showing low-energy radiation (O, Ti, upper part) and pronounced Ti line radiation (lower part, Cl line at 2.7 keV).*

In addition, the effect is also seen in the tomographic reconstructions of the main X-ray imaging system (2 cameras, Annual Report 1989). The contour plots of the local X-ray emissivity were obtained by the EBITA iterative code[1)] (see fig. 41).
The latter two figures also show the significant broadening of the profiles at the transition between the ECRH and NBI phases (t=0.1 s).

4.3.4 Impurity analysis

X-ray intensity profiles and PHA spectra were measured with various low-energy absorber foils in order to enhance the sensitivity in particular energy and radial ranges, respectively. Typical PHA data are shown in fig. 42.
In the low-energy range (2 μ Be filter, upper part) the spectra are dominated by radiation below ~1 keV, mainly due to oxygen and titanium impurities (energy resolution ~300 eV). Simultaneously in the energy range ~ 2 keV (100 μ Be filter, lower part) very strong titanium radiation is seen (4.7, 5.5 keV) and also some chlorine (2.7 keV). In this case iron impurities are negligible. These measurements are also important for correction of the T_e analysis by the filter method (Annual Report 1988) for the impurity composition, but in addition central electron temperatures can be derived from the slope of the continuum radiation.

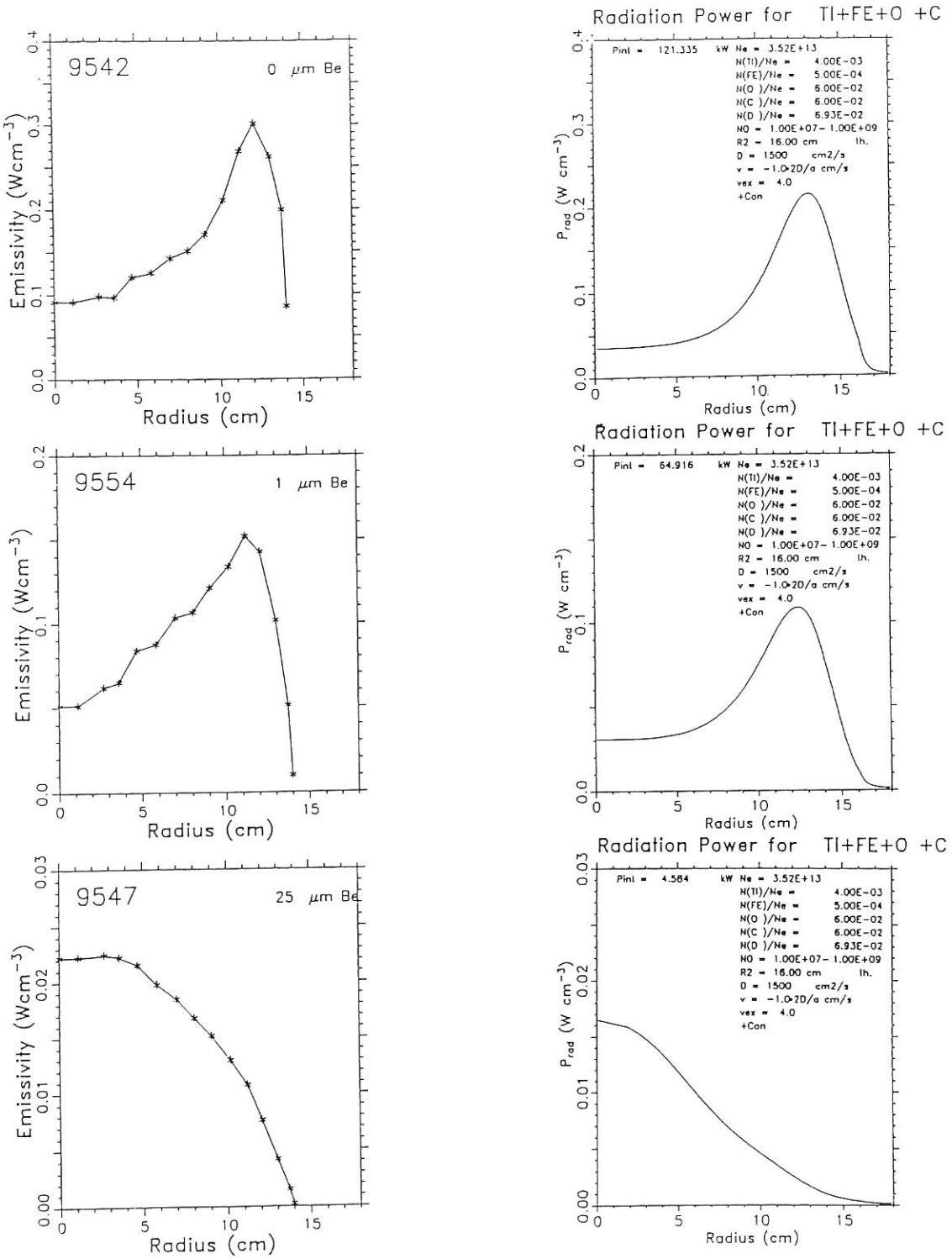

FIG. 43: *X-ray emissivity profiles from X-ray tomography (intensity averaged on flux surfaces) obtained with different absorber foils (left). Comparison with radiation simulation (IONEQ code, right) based on the composition of Ti, Fe, O and C impurities used to simulate the PHA spectrum. The calculations include impurity transport with transport coefficients derived from Al laser blow-off experiments)*

The impurity radiation analysis in terms of C, 0 Ti, Fe densities and Z_{eff} was performed by the IONEQ impurity transport and radiation code[2)3)]. The calculations are based on experimental T_e and n_e profiles, transport parameters as derived from Al laser blow-off experiments and additional spectroscopic data. The concentrations of Ti impurities, which originate from the TiC coating of limiting graphite structures can reach ~0.5 % of the electron density in ECRH discharges. Abel-inverted X-ray emissivity profiles were used in addition to determine absolute impurity densities.
Figure 43 compares measured profiles obtained for 3 different filters with total radiation calculations, consistent with spectroscopic data on individual impurity lines.

4.4 Soft X-ray and VUV spectroscopy

4.4.1 Impurity behaviour

In W7-AS oxygen, carbon, titanium, and iron are the dominant plasma impurities originating from the stainless-steel wall and the TiC-coated limiters and shieldings. For metallic walls the oxygen flux was minimized by He glow discharges and long plasma discharges (up to 1.5 s). ECF-heated plasmas are not critically affected by impurity radiation. However, when NBI-heating is used impurities play an important role (radiative collapse), due to the much higher plasma densities achieved.

With the aim of impurity reduction the machine was carbonized after shot #9694. Figure 44 shows the effect of carbonization on the impurity fluxes for ECRH discharges. The emission from intermediate ionization stages of the dominant impurities was observed in the VUV range by the SPRED spectrometer along a central viewing chord and normalized to the line-of-sight integrated electron density. The total emission in the spectral range of 80 - 1070 Å of the spectrometer is also included in the figure. Carbonization removed the metallic impurities durably and efficiently but density control was not possible. Oxygen could be retained only for a few discharges.

In a second step the machine was boronized after shot #10624 with preceding decarbonization. The evolution of the impurity fluxes in response to the boronization is shown in fig. 45 for ECRH operation. As compared with the experiments with metallic walls, boronization significantly reduced oxygen and carbon fluxes, whereas the metallic impurities rose to their former level after the first few shots during which the boron coating was removed from the limiter. Titanium even increased by a factor of ~ 2 above its pre-boronization value, whereas the final level observed for iron was a factor of ~ 2 lower than

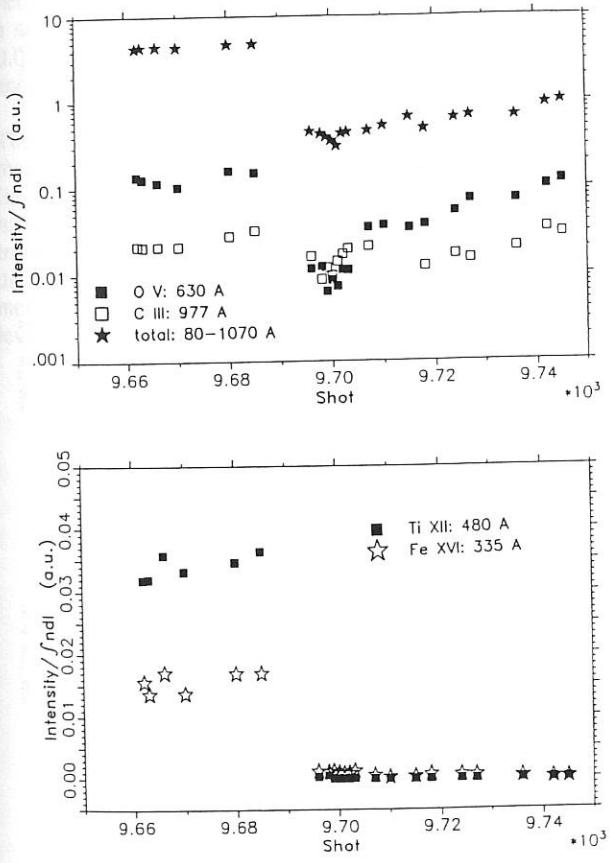

FIG. 44: *Evolution of impurity radiation from ECF-heated W7-AS plasmas in response to carbonization after shot #9694.*

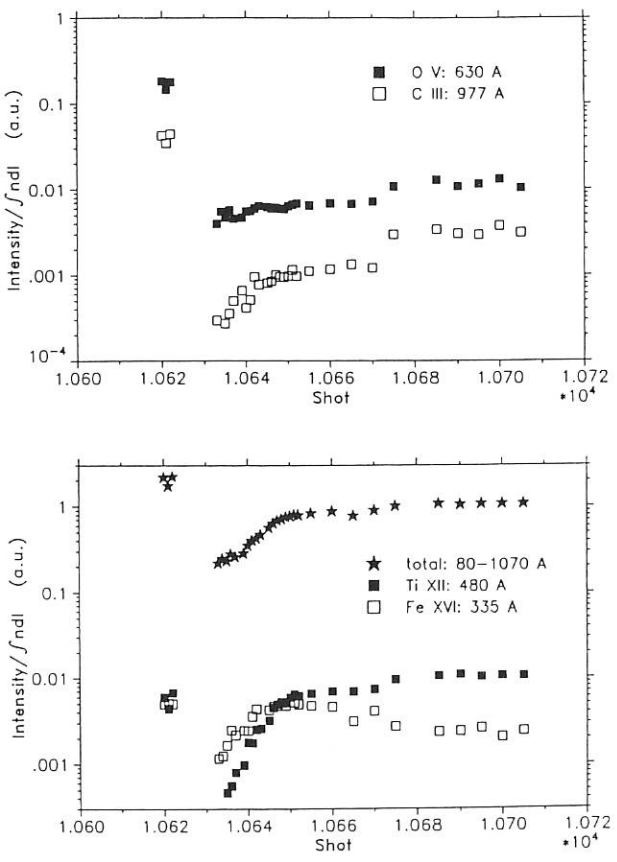

FIG. 45: *Evolution of impurity radiation from ECF-heated W7-AS plasmas in response to boronization after shot #10624.*

2) Weller, A. et al., JET-IR (87)10 (1987)
3) Behringer, K., JET-R (87)08 (1987)

before boronization (see also sec. 3.1.5). The latter observations are explained by higher edge temperatures after boronization due to reduced radiation losses in the plasma edge region, resulting in correspondingly higher limiter loads and impurity release from the limiters. They also support previous assumptions that at least part of the iron flux originates from iron which has been deposited on the limiters, in particular by glow discharge conditioning. Soft-X spectra show the same behaviour of impurities as observed in the VUV range (fig. 46).

VUV spectra from NBI-heated plasmas are compared for the three wall conditions in fig. 47. For the metallic wall the discharge terminates with a radiative collapse associated with an increase of Ti and Fe radiation. Carbonization removes almost completely the metallic impurities. Boronization reduces oxygen and carbon but Ti and Fe reappear in the spectrum. For the boronized case chlorine appears as additional impurity species when NBI heating is applied. The origin of chlorine is not yet clear. In conclusion, both wall conditioning methods considerably improved the performance of W7-AS by impurity reduction (low-Z with boronization, medium-Z with carbonization). Boronization seems to be most promising for further improvement. The Ti sources can be removed by replacing the TiC-coated in-vessel components.

4.4.2 Impurity transport

Impurity transport was investigated by the laser blow-off technique with aluminium as tracer impurity under various plasma conditions (different plasma apertures and ECF input powers, different rotational transforms). The temporal decay of the density of the injected tracer impurity was simulated by the STRAHL transport code[1] on the assumption of a radially constant diffusion coefficient D and a radially increasing convection velocity.

Compared with earlier experiments with ECF-heated plasmas at half the toroidal magnetic field (1.25 T) the operation at 2.5 T with higher electron density shows a significant increase by a factor of nearly 4, of the impurity confinement time to 40 - 70 ms and a similar decrease of the diffusion coefficient to 1000 - 2000 cm^2/s. Omitting the convective velocity in the transport calculations leads to a reduction of 20 % of the values for the diffusion coefficient. Additionally, a clear dependence of the confinement time on the plasma aperture (approximately to a^2) was observed, while the diffusion coefficient remained unchanged. Normalization by this scaling strongly reduces the scattering of the experimental values. Measurement of the confinement properties at different ECF input powers shows no clear dependence within the error bars. In experiments with combined ECF/NBI-heating the impurity transport seems to be similar to that of pure ECF-heated plasmas.

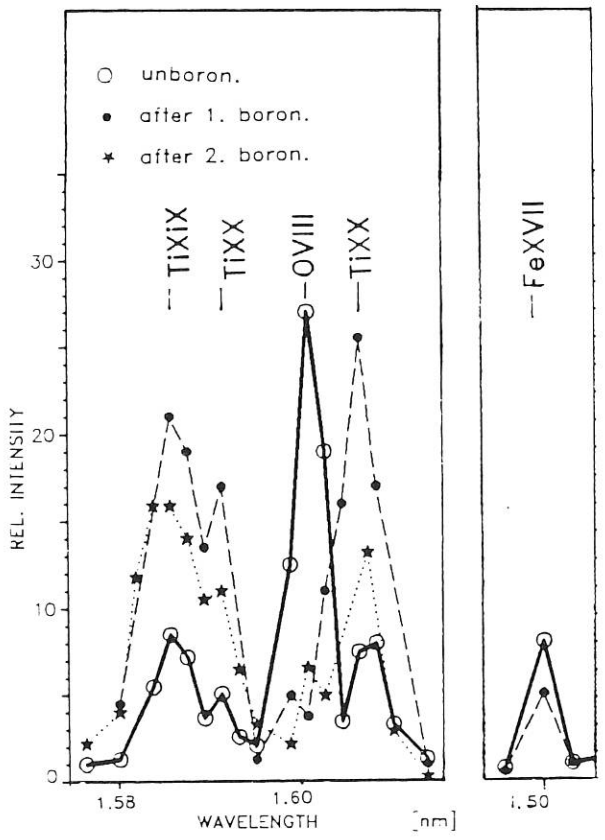

FIG. 46: *Soft-X-ray spectra from ECF-heated W7-AS plasmas before and after boronization.*

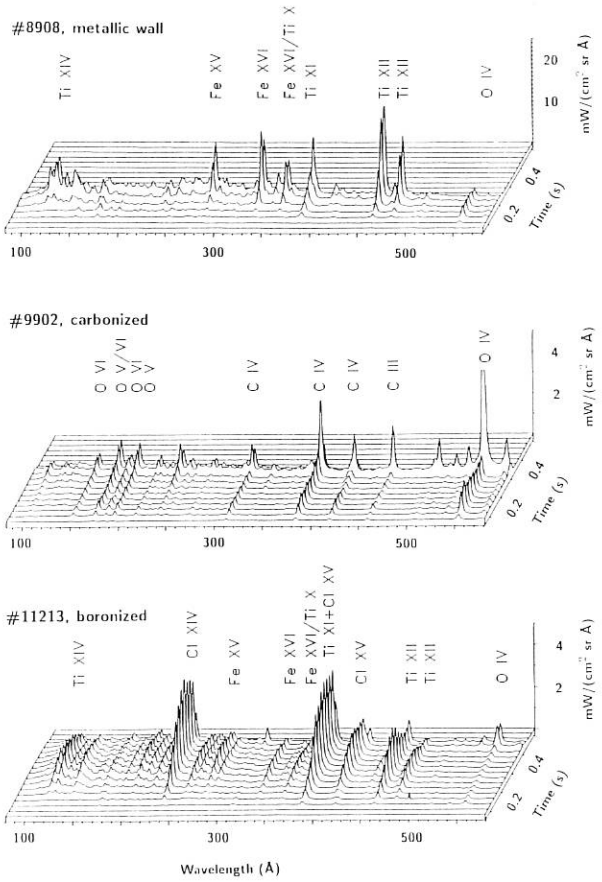

FIG. 47: *VUV spectra from NBI-heated W7-AS plasmas for metallic, carbonized and boronized wall. Note that the vertical scale is enlarged by a factor of 5 in the case of the metallic wall.*

[1] Behringer, K., JET Report, JET-R-(87)08(1987)

4.5 Bolometry

The radiation losses from the plasma are essentially governed by (a) the material and conditioning of the vessel wall, (b) the distance of the plasma from the wall, and (c) the ratio of the wall surface area to the plasma volume. These three operating conditions at the plasma edge can be appropriately characterized by the following data: (a) the impurity number Z_{eff} and the recycling factor, (b) the limiter concept, the gas programme, and the plasma position, and (c) the aspect ratio A. Whereas the aspect ratio is fixed by the size of the apparatus, $A_{W7\text{-}AS} \approx 10$, conditions (a) and (b) can be experimentally varied within limits and their influence on the radiation behaviour and energy content of the plasma be investigated.
As an example of the dependence of the plasma confinement on the plasma position fig. 48 shows the energy content and total radiation as functions of the plasma displacement by the vertical field, a radial inward displacement of 1 cm being equivalent to a change in the magnetic field of 0.01 T. As can be seen, the inward-shifted ECRH discharges have a somewhat elevated energy and simultaneously a somewhat lower total radiation. In this case the inward displacement is accompanied by an increase of the temperature and a decrease of the radiation density in the plasma core. Conversely, an outward displacement is accompanied by a slight decrease of the necessary gas input and energy content. One does also observe a similarly positive effect with a vertical field of 0.01 T to 0.025 T in neutral particle heated discharges, where the energies are an order of magnitude higher.

The effect of wall-conditioning on the plasma was studied by means of carbonization and boronization of the torus wall, limiters and installations. In agreement with spectroscopic measurements, the radiation powers recorded after appropriate treatment were lower than in not-conditioned reference discharges, with the carbonization preventing penetration of metal impurities and the boronization reducing the radiation levels of oxygen and carbon.

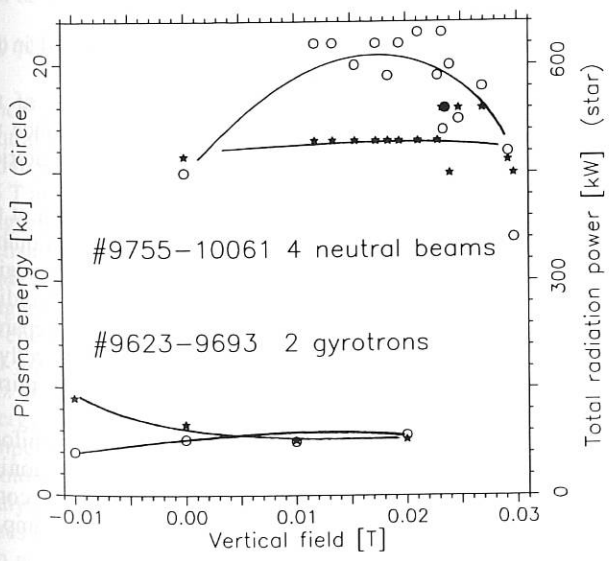

FIG. 48: *Plasma energy content and total radiation power versus plasma position shifted by different vertical fields. The variations in energy and radiation are shown for ECRH and NB discharges.*

The development of the plasma energy and total radiation after carbonization and boronization as functions of the line-density is shown in fig. 49. The lowest radiation level in conjunction with the highest energy is achieved after the boronization. It is seen that all discharges in the energy diagram follow the same linear development. The different conditioning processes have no influence on the plasma temperature. The high energies are obtained by means of the density alone.

Depending on the choice of discharge, it is possible during the non-stationary plasma build-up phase to reache a state in which the balance between heating power input and power loss through transport and radiation is critical. The result here may be a collapse or a further build-up of the discharge, depending on external control parameters such as gas feed, or on internal non-controllable particle dynamics. Figure 50, next page, shows two discharges with free internal plasma current which initially develop in the same way. With equal external control parameters, the current results in a critical magnetic confinement configuration in which the discharge bifurcates: the energy in the one discharge increases with decreasing radiation and vice versa in the other.

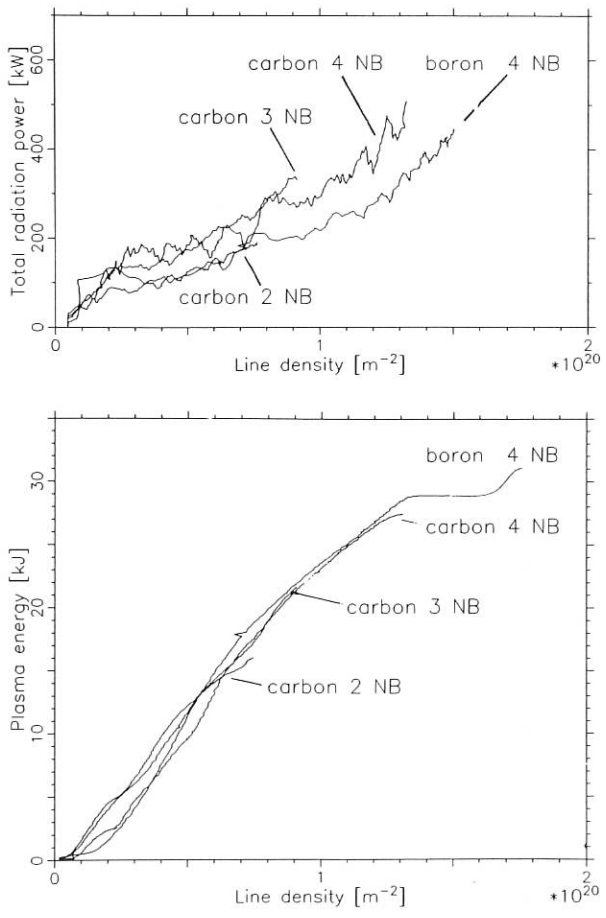

FIG. 49: *Plasma energy content and total radiation power as functions of the line-density. The plasma regime can be extended by means of wall-conditioning, i.e. carbonization and boronization.*

4.6 Reflectometry

A broad-band heterodyne reflectometer was developed and installed at the W7-AS stellarator, operating in the frequency range 75-110 GHz, in the extraordinary mode. It is designed to operate in the triangular plane of the stellarator, where the B-field is almost constant along the major radius, resulting in an almost constant electron cyclotron frequency. So in this case the X-mode cut-off frequency depends on the plasma frequency only. The resulting electron density range corresponding to the operating frequency range of the reflectometer is $5 \cdot 10^{18}$ to $6 \cdot 10^{19}$ m^{-3}. This covers a large part of the electron density gradient region in both ECF and NBI-heated discharges.

So far most of the reflectometers installed use single homodyne detection. This kind of detection allows broad-band operation which is useful to reach different plasma positions, but has shown severe limitations. These systems are only able to measure $V = A \cdot \cos \Phi$ and not directly the phase delay Φ, which is the relevant quantity in reflectometry. This leads to interpretation problems due to the coupling between phase and amplitude and to the nonlinearity and ambiguity of the cosine function. Attempts to perform direct phase measurements by dual sine-cosine detection, phase-locked heterodyne or fixed-frequency heterodyne detection have been kept to narrow-band operation, either single or multi-channel.

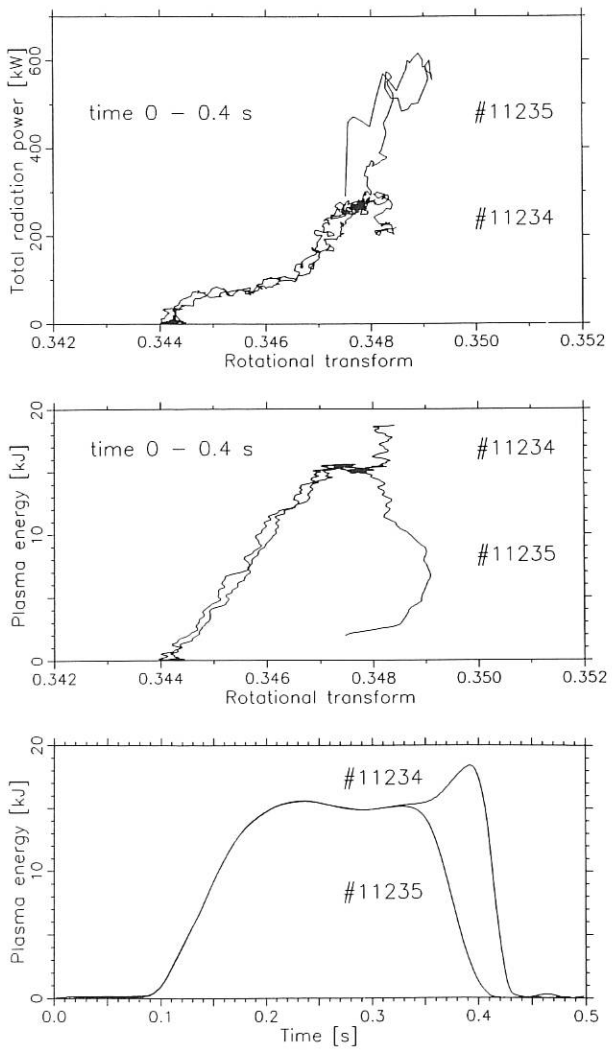

FIG. 50: *Two discharges with equal external control parameters and different developments established by various magnetic configurations resulting from free internal plasma currents.*

The system developed here was designed to operate in the full frequency range of 75-110 GHz without additional adjustments. Both the signal and the reference oscillators are of the BWO type. The special mixing scheme chosen cancels all frequency drifts and most of the wideband FM noise of the BWO's. The mixing scheme is based in principle on the feed-forward tracking circuit developed in Princeton[1]. The first intermediate frequency of the triple conversion system is allowed to drift between 5.6 and 8.2 GHz. It is defined by the frequency difference between the signal and reference oscillator. In a next step any signal in this band is down-converted to 4 GHz and in a third conversion to 60 MHz with quartz stability. At this last intermediate frequency two signals are delivered to a phase meter. One is the reference, the second contains the full phase information from the plasma phase delay. The fast phase meter is a conventional one with an input bandwidth of 20 MHz and a settling time of 70 ns. It has a dynamic range of more than 60 dB. Amplitude variations within this range do not affect the phase measurement.
Laboratory tests have been performed demonstrating the expected performance concerning stability and noise.
Tests simulating the plasma with a mirror have proved the ability of the system to measure the phase delay either with fixed frequency, as used for density fluctuation measurements, or in the sweeping mode as applied for density profile reconstruction. The system is installed on the two-antenna reflectometer of W7-AS, using separate antennas for wave launching and reception of the reflected ones.

4.7 Status of Thomson scattering diagnostics

The multipoint Thomson scattering system presented in the Annual Report 1989 is now nearly completed.
The last problem to be treated was the reduction of the parasitic light. This task is somewhat complicated since the space for the laser beam is very limited and the geometrical conditions for the observation optics are unfavourable:

i) As the power and energy density of the laser beam at the beam exit are rather high, several concepts of beam dumps had to be tested in order to prevent destruction of imaging components or influence on the plasma, thus avoiding unwanted vacuum breaks. Two possibilities were prepared: A weakly absorbing compound glass beam dump directly in the beam exit port and a high-performance laser mirror together with a remote glass beam dump.
ii) Further reduction of the parasitic light level and its uniform distribution were achieved by carefully positioning diaphragms and adjusting their diameter. A honeycomb structure made of stainless steel is used as viewing dump.

A big engineering task was the construction of the support for the observation optics and the light guides, the latter requiring

1) J.L. Doane, Rev. Sci. Instr. 51, 317 (1980)

five degrees of freedom for alignment. All components are now available and are already being installed at the experiment. The final alignment will be performed during the next vacuum break. At present the 20 polychromators are being assembled and tested. As the scattering light is introduced by light guides, their sensitivity to parasitic light can already be tested in the laboratory by means of the torus test piece.

4.8 Diagnostic injector

The diagnostic injector, as described before (Annual Report 1989), went into operation in 1990, thus allowing measurements of radial ion temperature profiles by charge exchange neutral particle analysis, CX, and charge exchange recombination spectroscopy, CXRS, as well as measurements of plasma rotation by CXRS.
In the first stage the diagnostic injector operated at an acceleration voltage of 30 kV with an extracted current density of 80 mA/cm^2. The installation of an additional magnetic field along the axis of the ion source close to the extraction region increased the current density up to 240 mA/cm^2.
Because the beam is injected along the major radius of the elliptical plasma cross section with nearly box-shaped radial ion density profiles, its penetration to the plasma center is limited to peak densities of about 10^{20} m^{-3}. For higher densities the beam would have to be injected horizontally thus making densities of about $3 \cdot 10^{20}$ m^{-3} accessible to measurements. Feasibility studies for a reconstruction to this geometry are under way, but are difficult to carry out because of the limited spatial access to W7-AS. Replacing of the DuoPIGatron ion source with a species mix of $H^+ : H_2^+ : H_3^+ = 20\ \% : 30\ \% : 50\ \%$ with energies of $E_o : E_{o/2} : E_{o/3}$ by an RF-source with a species mix of 90 % : 7 % : 3 %, demonstrated by the NBI-Group, (see Annual Report 1989) will increase the number of CXRS-photons by a factor of four, because this diagnostic is mainly sensitive to particles with high energies. An RF-source operating at frequencies of 2-4 MHz and a power of 20 kW will be delivered soon.

4.9 Neutral particle analysis

Since the diagnostic particle beam is now operational the neutral particle analysis (CX) has the possibility to evaluate an active particle flux. The magnetic field of W7-AS now beeing 2.5 T and because new 10-channel analyzers with new analyzer magnets were installed, the calibration of the 4 analyzers (two 5-channel and two 10-channel analyzers) was again checked and leads to a correction of the calibration and to a problem of magnetic screening for the 80 keV analyzer magnet in the 10-channel analyzers. The problem was overcome in using the old magnets, only beeing capable of measuring the particle flux in an energy range of up to 50 keV, this reduction of energy range not beeing relevant to the present range of ion temperature measurements. Other tests such as influence of photons, X-quants or run-away electrons for the particle analysis cause no problems, because their contribution in most cases is lower than 1 % of the signals. So the CX diagnostic can now use all analyzers to measure ion temperature profiles with error bars of the order of or lower than 10 %. For plasmas with high density over a large radial extend the measured spectra of the outgoing neutrals tend to overestimate the ion temperature. From detailed calculations of the absorption of the neutrals by charge exchange and ionization collisions from their origin at the diagnostic particle beam along the line-of-sight through the plasma one gets the spectrum which arrives at the particle analyzer. Fitting this spectrum - in particular its slope - to the measured one by iteratively adjusting the ion temperature leads to a corrected ion temperature which differs from the slope of the measured spectrum. When a halo extending over ± 0.15 m into a cylinder around the diagnostic beam is also included, a plasma density of $1.1 \cdot 10^{20}$ m^{-3} over a range of $r_{eff} = \pm 0.15$ m leads to a real ion temperature of 456 eV instead of the slope-deduced 492 eV.
To keep this correction below 10 %, it is necessary to restrict the measurement of the ion tempeature to plasma densities below $1 \cdot 10^{20}$ m^{-3} for density profile widths not exceeding ± 0.15 m. For ι near 1/3 this means that the interferometrically measured density signal has to be kept well below $6 \cdot 10^{19}$ m^{-2}.
Typical temperature profiles for ECRH and NBI discharges are shown in fig. 51 and fig. 52. Theoretical calculations of the ion temperature- and the electron temperature profiles (fig. 52, next page) show the possibility of the existence of electric fields inside W7-AS. This will be the main point of further investigations, especially for the CXRS diagnostic (see sec. 4.10).

4.10 Doppler measurements

In order to obtain ion temperatures and mass velocities, as functions of both radius and time, Doppler widths and shift measurements of impurity lines were made. The lines arising from interactions between the neutral beam of a diagnostic

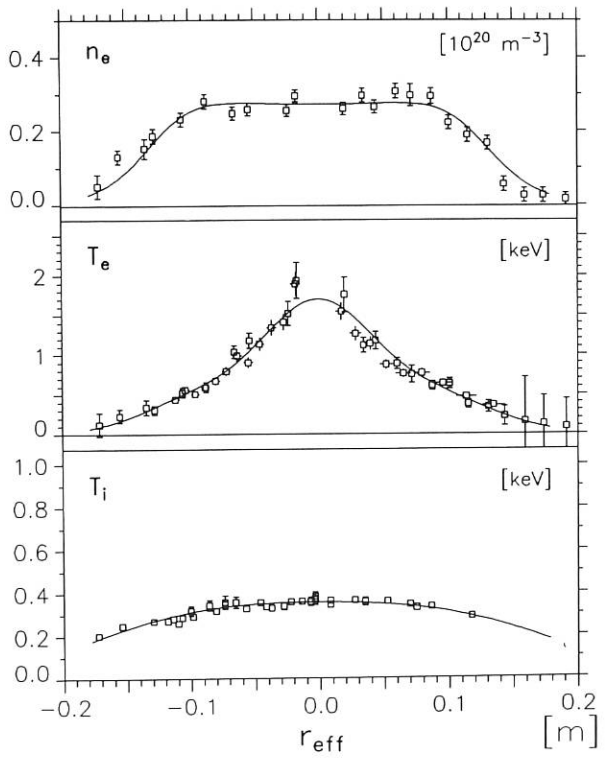

FIG. 51: *Comparison between the plasma density and the electron and ion temperatures of an ECRH-discharge ($B_0 = 2.57$ T, $\iota_a = 0.345$, $W_d = 3.24$ kJ, $P_h = 290$ kW, shots 11754-11800 at 400 ms).*

injector and background impurities (Charge Exchange Recombination, CXR) were measured with two set-ups. One, serving as a monitor, views the intersection volume of the diagnostic injector with the plasma centre. No radial scanning is foreseen.
The other provides radial scanning (almost perpendicular to the magnetic field) of the intersection volume of the diagnostic injector with the lower half of the plasma.(see fig. 53). For the time being, balanced NBI will be necessary to determine poloidal velocities and, hence, radial electric fields. First results obtained in an unbalanced NBI discharge show velocities comparable in rise-time and magnitude to those of W7-A (fig. 54). The ion temperature measurements yield values which agree reasonably well with those obtained from neutral particle analysis.

4.11 Z_{eff} from continuum measurements

Since the interference filter (for the visible green radiation, at 550 nm, 1 nm wide) had been delivered during the summer break and installed in the Thomson scattering detector system, bremsstrahlung radiation was recorded starting Nov. 90. In those cases where T_e and n_e radial profiles existed, this yielded "side-on" profiles of the radiation.

These profiles are being evaluated by means of a generalized form of Abel inversion (the emissivity being assumed to be constant on magnetic flux surfaces) in order to get the desired radial profiles of the continuum emission.

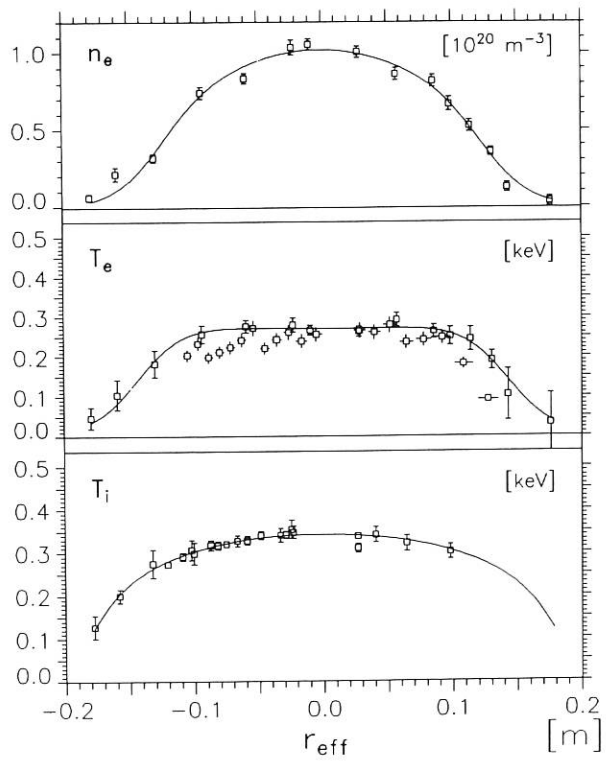

FIG. 52: *Comparison between the plasma density and the electron and ion temperatures of an NBI-discharge (B_0 = 2.59 T, ι_a = 0.344, W_d = 4.21 kJ, P_h = 400 kW, shots 11458-11485 at 420 ms).*

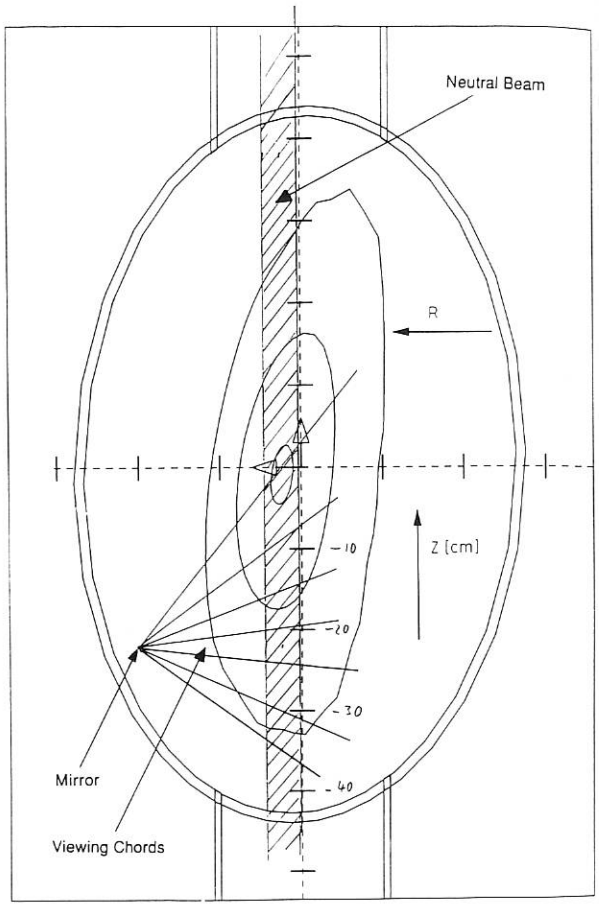

FIG. 53: *Plasma contours, viewing chords and diagnostic beam on W7-AS.*

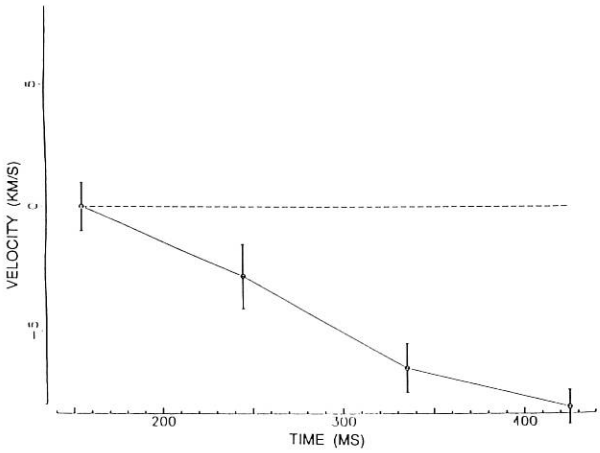

FIG. 54: *First determination of a mass velocity on W7-AS.*

Absolute calibration has not yet been done, which means that for the time being only relative radial distributions of Z_{eff} are being obtained. Furthermore, direct control of possibly perturbing line radiation is still lacking. A light pipe system to feed a monitor for this purpose has been ordered.

WENDELSTEIN 7-X

(Head of Project: Dr. Günter Grieger)

1. WENDELSTEIN 7-X STUDIES

C. Beidler, E. Harmeyer, F. Herrnegger, J. Junker, J. Kißlinger, H. Maaßberg, F. Rau, F. Sardei, M. Schlüter, M. Spada, H. Wobig.

1.1 Configuration Studies

In 1990 the Helias configuration HS 5-10 was selected as the basis for Wendelstein 7-X [1]. This configuration was already described in the Annual Report 1989 [2]. Ongoing activity in 1990 explored the vacuum field parameter range / 403 / of a device equipped with additional planar coils, shown in Fig. 1.1, and a current supply system which permits slightly different currents in each coil type. TABLE I gives the current distribution for the modular coils and the additional coils of some characteristic cases, and in TABLE II the corresponding vacuum field data are collected. For all cases the ratio of $\langle |j_{||}/j_{\perp}| \rangle$ is below 0.88 (low ι case), and a magnetic well exists.

1.1.1 Variation of the Rotational Transform

The variation of the rotational transform is achieved by superposition of toroidal field components generated by the planar coils A und B (see TABLE I, lines B and C). Together with the ι variation the magnetic well changes. In the high ι case the magnetic well deepens to 2.2%. It is flattened in the low ι case (0.65%). The respective Poincaré plots are shown in Fig. 1.2 for the toroidal plane at 1/2 field period, and the ι profiles in Fig. 1.3.

[1] W 7-X Proposal, 1990 (unpublished)

[2] see Annual Report 1989, p. 147 ff

TABLE I: Current distribution for modular coils 1...5 and planar coils A and B for different magnetic field configurations. The individual coil current $I_c = I_n F_c$, I_n [MA] is the nominal coil current for an average field strength of 2.5 T, and F_c is the individual factor for each coil type given in the table.

		I_n	F_c						
	Case		1	2	3	4	5	A	B
A	St. case	1.47	1.0	1.0	1.0	1.0	1.0	0.0	0.0
B	Low ι	1.31	1.0	1.0	1.0	1.0	1.0	0.31	0.31
C	High ι	1.68	1.0	1.0	1.0	1.0	1.0	-.30	-.30
D	Inward	1.47	0.90	0.95	1.04	1.02	1.09	0.23	-.23
E	Outward	1.47	1.03	1.10	1.06	0.89	0.92	-.23	0.23
F	Low mirr.	1.47	0.92	1.02	1.03	0.98	1.04	0.0	0.0
G	Hi. mirr.	1.47	1.07	1.06	1.03	0.91	0.93	0.0	0.0
H	Low shear	1.47	1.18	1.18	1.06	0.8	0.8	-.36	0.32
I	Hi. shear	1.63	0.90	0.95	1.0	1.02	1.08	0.0	-.45

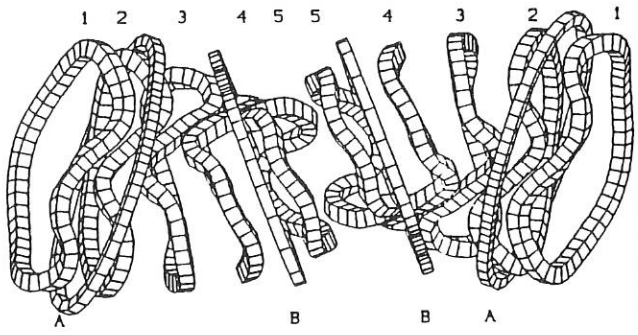

FIG. 1.1: View of one field period of the modular coils (number 1...5) and of the planar additional coils A and B from radially inside. Each coil type occurs twice per field period.

TABLE II: Characteristic vacuum field data of the different field configurations of TABLE I. $\langle|j_{||}/j_{\perp}|\rangle$ is the ratio of parallel and perpendicular current density, averaged over the flux surface. $J^{\star} = \langle(B_o^2/B^2)\cdot(1+(j_{||}/j_{\perp})^2)\rangle$ enters the stability criterion of resistive interchange modes and is a direct measure of the reduced secondary plasma currents. The factor $G_{b,lmfp}$ enters the relation for the bootstrap current in the lmfp regime, normalized to the value of an equivalent axisymmetric configuration with the same rotational transform and aspect ratio.

		Case →	A	B	C	D	E	F	G	H	I
Axis	Rotational transform	ι_o	0.84	0.72	1.02	0.79	0.87	0.83	0.86	0.91	0.91
	Secondary current ratio	$\langle\|j_{\|\|}/j_{\perp}\|\rangle$	0.73	0.88	0.60	0.70	0.78	0.78	0.62	0.67	0.60
	Stability parameter	$J^{\star}$	1.60	1.80	1.38	1.52	1.61	1.60	1.44	1.50	1.37
	Bootstrap current ratio	$G_{b,lmfp}$	0.10	0.17	0.05	0.10	0.12	0.08	0.10	0.20	0.15
Half Radius	Rotational transform	ι	0.87	0.74	1.05	0.82	0.89	0.86	0.89	0.92	0.95
	Secondary current ratio	$\langle\|j_{\|\|}/j_{\perp}\|\rangle$	0.73	0.88	0.60	0.69	0.77	0.77	0.61	0.67	0.59
	Stability parameter	$J^{\star}$	1.55	1.79	1.37	1.50	1.61	1.59	1.44	1.50	1.38
	Bootstrap current ratio	$G_{b,lmfp}$	0.0	0.06	-.04	-.02	0.0	-.07	0.0	0.0	-.04
Edge	Rotational transform	ι_a	0.99	0.83	1.2	0.98	0.98	0.98	0.98	0.98	1.2
	Magnetic Well Depth	$\frac{\delta V'}{V_o'}$ [%]	-1.4	-.65	-2.2	-1.4	-1.2	-1.7	-1.2	-0.7	-2.2
	Secondary current ratio	$\langle\|j_{\|\|}/j_{\perp}\|\rangle$	0.69	0.84	0.67	0.65	0.75	0.74	0.59	0.69	0.56
	Stability parameter	$J^{\star}$	1.51	1.76	1.48	1.48	1.60	1.56	1.43	1.55	1.36
	Bootstrap current ratio	$G_{b,lmfp}$	-.05	0.02	-.02	-.09	-.05	-.15	-.05	0.0	-.10

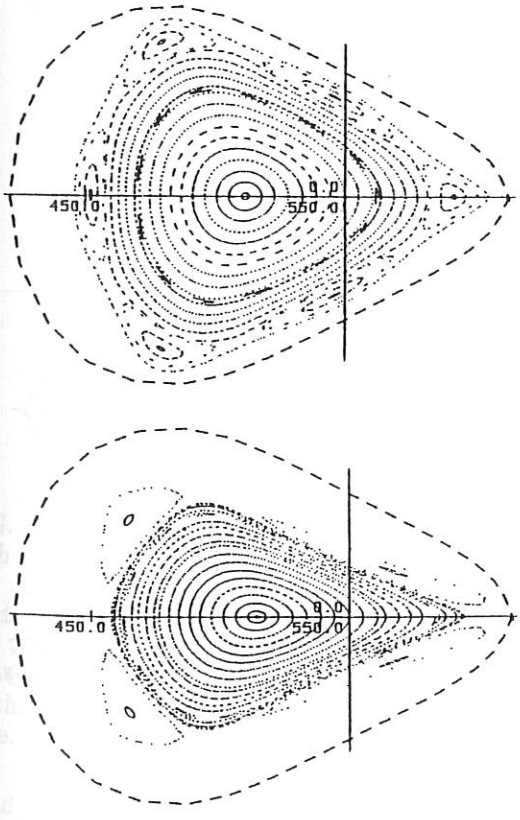

FIG. 1.2: Poincaré plot of vacuum magnetic surfaces at $\varphi = 36°$ of the low ι (top) and high ι (bottom) cases. The dashed line indicates the position of a tentative first wall.

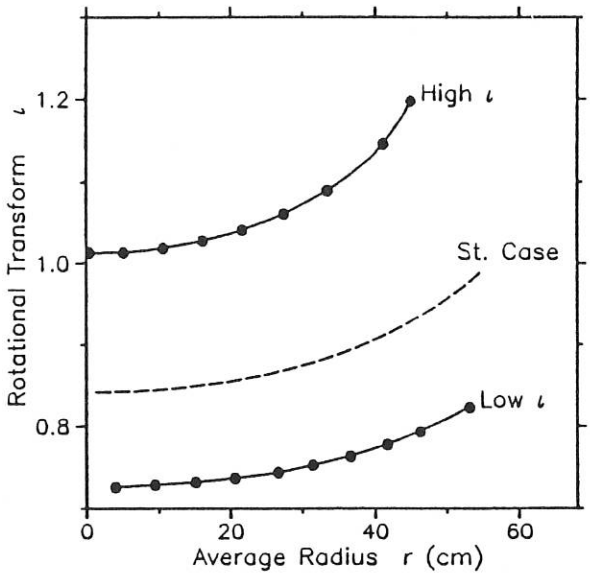

FIG. 1.3: Rotational transform ι as a function of the averaged minor radius r for cases A, B and C of TABLE I.

1.1.2 *Shift of the Magnetic Axis*

Because of the helical arrangement of the additional coils A and B, opposite currents in these coils generate a net vertical field which shifts the magnetic surfaces radially. At the same time, however, a toroidal modulation of the magnetic field strength is introduced. This effect can be considerably reduced by adjusting the currents in the modular coils.

For the current distributions given in TABLE I, lines D and E, a shift of the magnetic axis of ± 3.5 cm at toroidal angle $\varphi = 0^o$ and of ± 5 cm at $\varphi = 36^o$ is obtained. The axis value of ι is also influenced in these cases (outward shifted +5%, inward shifted -6%).

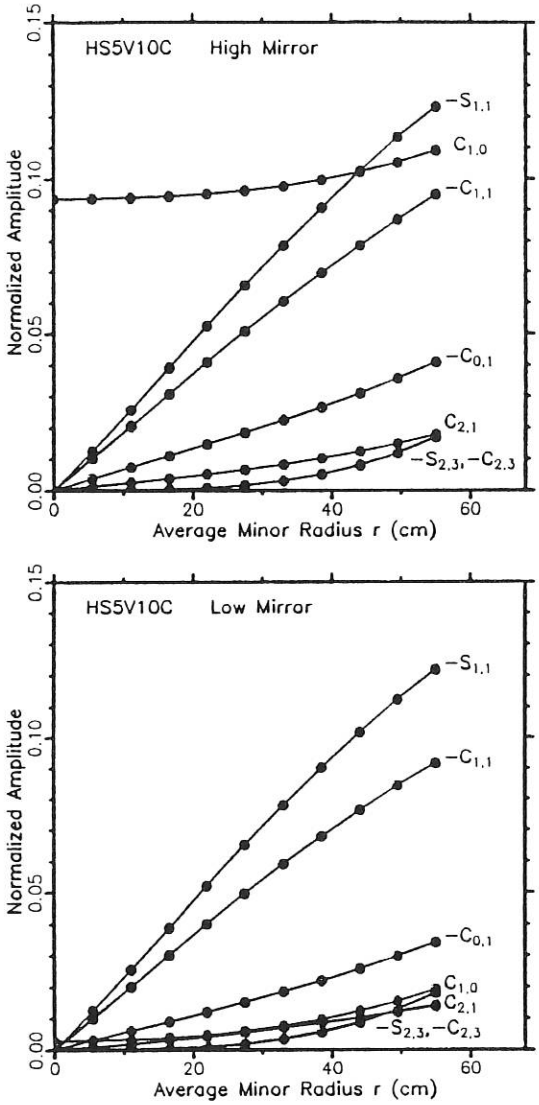

FIG. 1.4: Normalized Fourier components of the magnetic field $\frac{B}{B_0} = \sum C_{m,l}\ cos(m\varphi)cos(l\theta) + \sum S_{m,l}\ sin(m\varphi)sin(l\theta)$ *for the low-mirror (top) and high-mirror (bottom) cases. Not shown in this figure are components with an edge value below 1%,* $C_{0,0} \approx 1$, *and the components associated with the modular ripple* $C_{10,0}$ *and* $S_{9,1}$ *(about 1.5% at the edge).*

1.1.3 *Variation of the Magnetic Mirror*

The variation of the magnetic mirror ratio changes the number the location of the trapped particles and thus the neoclassical transport and bootstrap current. This can be done either by opposite currents in the planar coils A and B or by feeding the modular coils with different currents (see lines F and G in TABLE I). Feeding the coils so as to reduce the magnetic mirror component $C_{1,0}$ to a value of $< 1\%$ approximates a quasi-helically symmetric configuration for which the bootstrap factor G_b becomes negative (see TABLE II, row F, low mirror). If the magnetic mirror component is increased to about 10%, moving more towards a linked-mirror machine, G_b remains close to the value of the standard case but the averaged ratio of $\langle |j_{||}/j_{\perp}| \rangle$ decreases from 0.78 to 0.65. Other field components are nearly unchanged in these cases; see Fig. 1.4.

1.1.4 *Variation of Shear*

The shear can be varied by appropriately combining individually adjusted currents in the modular coils and planar coils A and B. The two cases H and I in TABLE I have the same rotational transform, on axis $\iota_0 = 0.91$, but their edge values differ. Both configurations are bounded by separatrices of low order rational values for $\iota = 5/5$ (low shear) and $\iota = 5/4$ (high shear); see Fig. 1.5. Together with the shear the magnetic well varies (low shear 0.7%, high shear 2.1%).

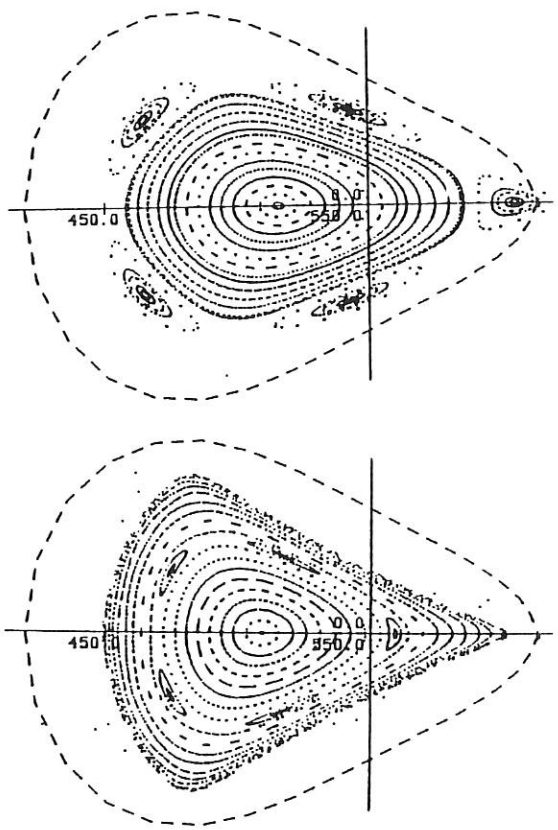

FIG. 1.5: Poincaré plot of vacuum magnetic surfaces at $\varphi = 36^o$ *of the low-shear (top) and high-shear cases (bottom).*

1.1.5 *Island Formation*

In the procedure for defining the coils for W7-X, special attention was paid to obtaining good vacuum magnetic surfaces, i.e. to avoiding magnetic islands. In the standard case small islands are seen at rational ι-values, e.g. $\iota = 10/11,\ 15/16,\ 20/21$, with average sizes of

about 0.8%, 0.2%, 0.15% of the minor radius, resp. Near the edge comparatively large islands are present for $\iota = 1$ at average radius $r \approx 55\ cm$ with $\delta r \approx 3.4\ cm$. The associated separatrix is of potential use for limiter and divertor applications. In the case of a divertor device a finite island size and X-points with given angle between the asymptotes of the separatrix hyperbolae are desirable at certain toroidal and poloidal positions. This can be achieved by using two current loops inside the vacuum vessel (trim coils) for each field period, which follow the tips of the magnetic surfaces just inside the $\iota = 1$ separatrix at toroidal angles φ between 12^o and 24^o (and, because of the stellarator symmetry, also between $\varphi = 48^o$ and 60^o). The influence of these small-amplitude fields on the $\iota = 1$ islands is shown in Fig. 1.6.

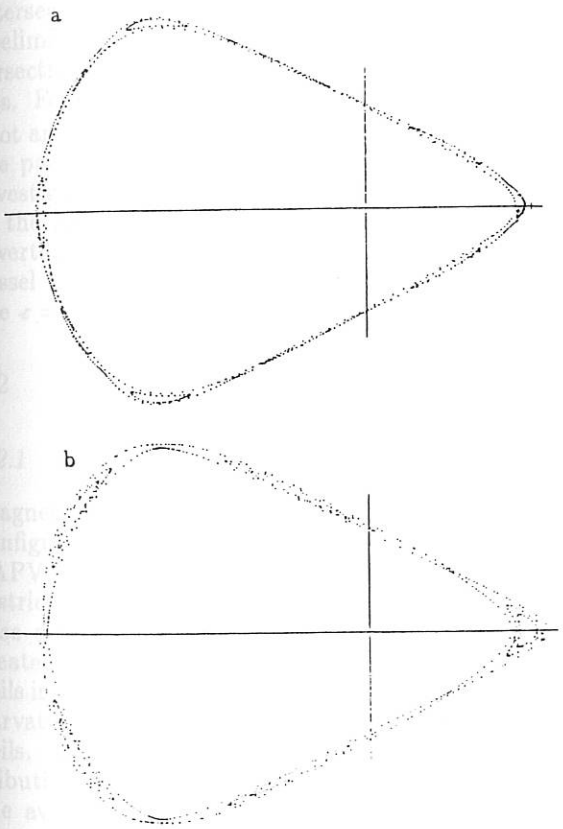

FIG. 1.6: Magnetic surfaces near the edge with different currents in the trim coils. a): Compensated case with 4.9 kA; 10 small islands remain, associated with the rational number 10/10, for which the trim coils are not effective. b): Current of 10 kA in the coils; the poloidal position of the X-point is changed in relation to the standard case.

1.1.6 *Perturbation Studies*

Symmetry-breaking perturbation fields (error fields) are studied for Wendelstein 7-X in order to estimate the required accuracy of the modular coil set. The 50 non-planar modular coils with 5 different coil shapes and the external coil system allow many degrees of freedom. To restrict the number of computations, perturbations with periodicities $M = 1$ and 2 have been applied so far to the standard case of HS 5-10. At irrational ι-values their effect is negligible. For rational ι they change 'natural' islands, introduce new islands, and enhance the ergodicity. As a consequence, the aspect ratio of the configuration rises.

The top part of Fig. 1.7 shows the effect of a tilt of one of the modular coils by about 0.5 cm at its periphery, modelled by two tilted dipole loops at the position and with the current of the coil of interest. The five O-points of the $\iota = 1$ islands are enclosed by a common separatrix with $M = 1$ symmetry. Its X-point is indicated in the figure. There is little change in the size of the natural island system at $\iota = 10/11$. Thin new islands at $\iota = 8/9,\ 9/10,\ 11/12$ appear, up to 15/16. They are separated by closed surfaces with irrational transform which are omitted in the figure for clarity. Near the edge, the islands at $\iota = 23/24$ can be localized.

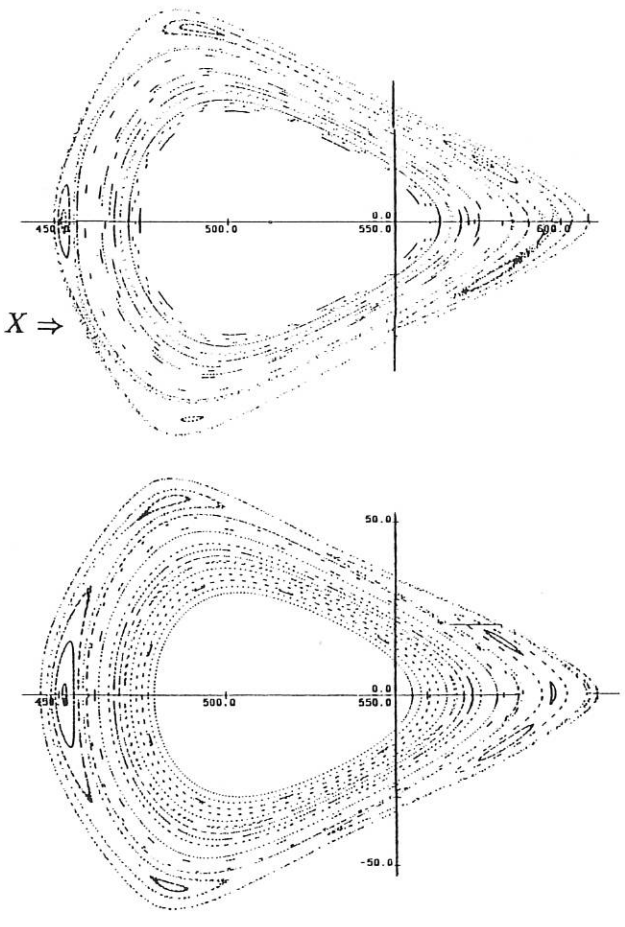

FIG. 1.7: Perturbed fields at $\iota = 1$. Top part: modular coil No. 13 tilted by 0.5 cm around a vertical axis, modelled by two tilted dipole loops. Lower part: elliptic offset of the radial positions of all modular coils with an amplitude of 1 cm . Such offsets might be comparable to achievable construction tolerances.

The lower part of the figure is obtained by an elliptic offset of the radial position for all modular coils, with an amplitude of 1 cm . This $M = 2$ perturbation changes the $\iota = 1$ islands into two groups of sub-islands. A total increase of the aspect ratio of about 15 % is estimated for either perturbation.

Other conceivable coil displacements or local deformations of the coil shapes have to be investigated, also at other transform values. Results performed for an earlier data set at $\iota = 5/4$ are given in [3] . It is well established that the superposition of a large number of randomly chosen different perturbations introduces only a rather small effect on the magnetic field. Also the possible compensation of perturbation islands by means of the trim coils (see preceding section) or other local fields is of interest. Compensation coils outside the cryostat would be preferable, but require substantially larger currents.

1.1.7 Edge Structure

Studies of plasma physics near the edge of the configuration are an essential topic of the experimental programme for Wendelstein 7-X in respect of effective impurity control. The present understanding of edge-plasma physics is competition of perpendicular and parallel transport of particles and energy, influenced by fluctuations and electric fields in a complex way. The boundary region is an important link between the bulk plasma and external material objects such as limiters, divertor plates or the vessel wall. The latter needs to be shielded in an experiment operating at large heating powers. Prototype calculations have been done in [4] using field line tracing and guiding centre orbits (Monte Carlo code with pitch-angle scattering of monoenergetic H^+ ions) in HS 5-8, an earlier configuration.

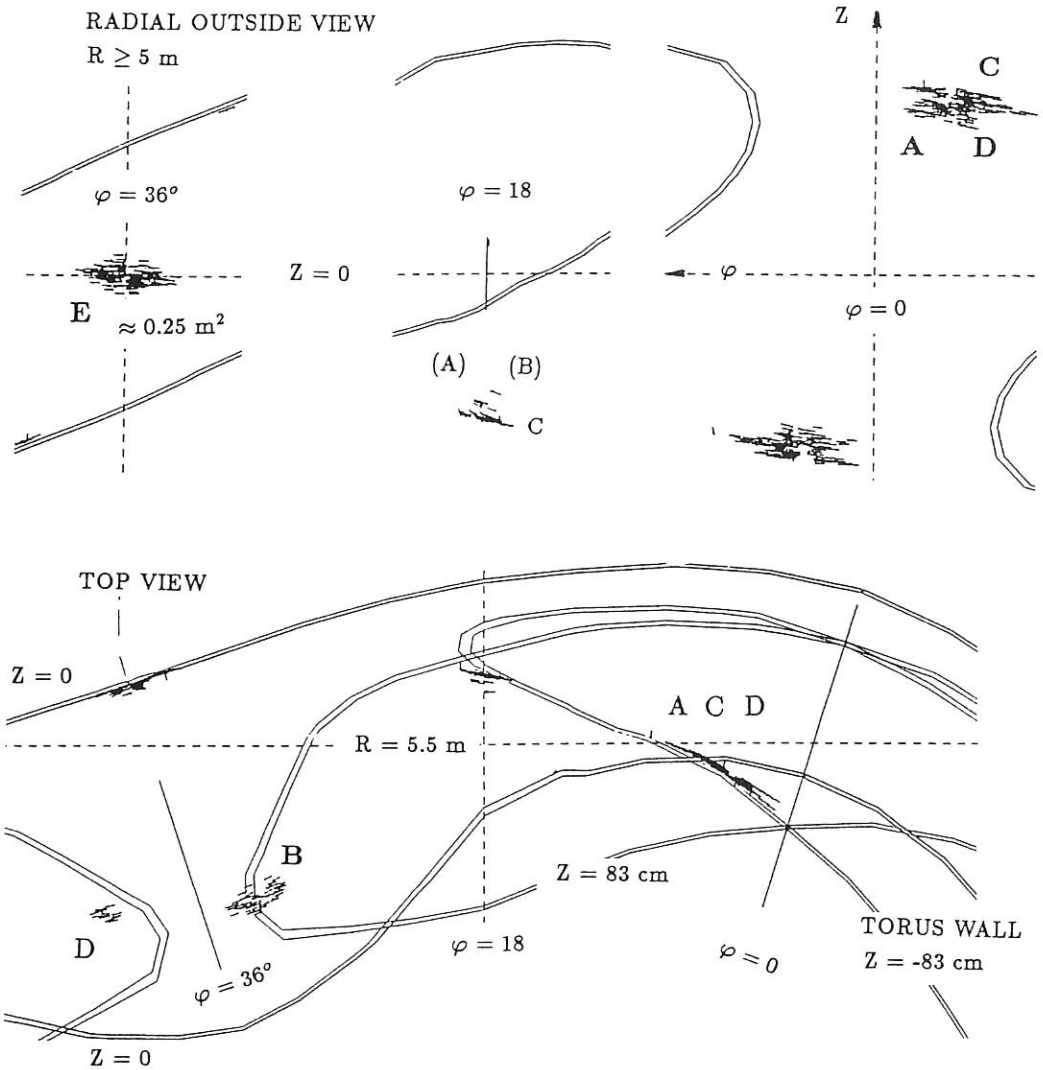

FIG. 1.8: Radial outside and top views of the intersection patterns of 200 eV H^+ ions. Monte Carlo code with pitch-angle scattering, normalized mean free path $L^\star = \lambda\iota/\pi R = 0.4$, and no electric field. The orbits are started inside the last closed surface of configurations 'A' to 'E' as described in TABLE I.

[3] see Annual Report 1989, p. 153

[4] see Annual Report 1989, p. 151

The method agrees in essential details with experimental observations of plasma-wall interaction in Wendelstein 7-AS; see / 22 / and / 300 /. Studies of the edge structure of the Wendelstein 7-X reference configuration HS 5-10 are in progress. In their first part they establish the regions of interactions with the segmented first wall of Wendelstein 7-X for configurations 'A' to 'I' described above. Preliminary results of a total of more than 1100 intersection points are shown in Fig. 1.8. For this ensemble, obtained from cases 'A' to 'E', several localized 'hot spots' are seen along characteristic contours. They start near the toroidal position of the bean-shaped cross-section radially inside the lower torus apex, extend helically towards the outside of the vessel, where the magnetic surfaces are nearly triangularly shaped, and end near the upper apex, symmetrically with respect to the starting region. Other intersection patterns are near 1/2 of the field period. Preliminary average values of the orbit lengths until intersection range between 3 and about 100 toroidal transits. For the whole torus (five field periods) total hot spot areas of 0.2 to 0.5 m^2 are estimated, depending on the particular configuration. The second part of this investigation aims at improving the spatial homogneity of the intersection pattern, and at studying limiter / divertor geometries. Another approach utilizes the in-vessel current loops, which allow the size and phase of the $\iota = 1$ islands to be varied.

1.2 Force and Stress Calculations

1.2.1 Toroidal Arrangement

Magnetic force and mechanical stress analyses of Helias configurations were continued by means of the EFFI, SAPV(2), and ADINA codes. The calculations were restricted to the configuration HS 5-10. The standard case and some of the cases listed in TABLE I were treated. The distribution of the magnetic forces in the coils is inhomogeneous because of the different local coil curvatures and the slightly helical arrangement of the coils. For different coil types there are different distributions of the magnetic force density. Calculating the average value of the magnetic force density over the coil cross-section, one obtains both a radial and a lateral force density component which vary along the circumference of the coil.

In a toroidal arrangement the volume integral of the magnetic force densities results in a net force for each coil in the assembly. Because of the slight helicity of the coil arrangement the vector of the coil net forces is of helical type and varies considerably in magnitude. For the standard case of the HS 5-10 configuration at $B_o = 3$ T the maximum amounts to about 4 MN. In Fig. 2.1 the radial and vertical net coil forces are shown. Under fault conditions – quenching of a coil – this force may increase to about 7 MN. For a whole toroidal field period the resulting net force vector is directed towards the torus centre because of the toroidal arrangement of the coils.

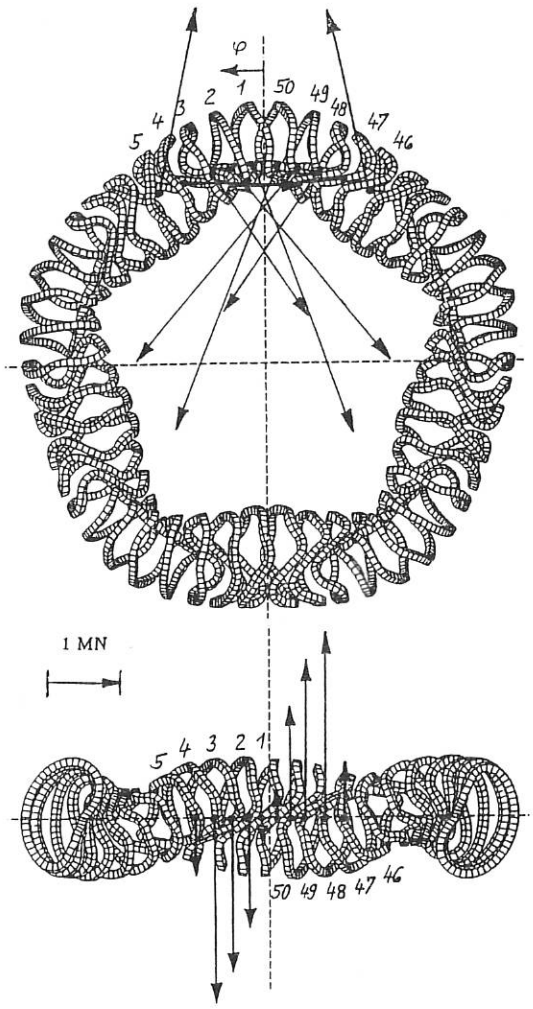

FIG. 2.1: Radial and vertical net coil forces for the standard case of the HS 5-10 coil configuration.

The mechanical stress and strain distributions were investigated by means of finite-element calculations. The orthotropic material data of the EURATOM LCT coil or of the ABB conductor are being used in the calculations as appropriate average values for the complex coil construction. As support scheme for the coil assembly in the Helias systems a concept of mutual support between adjacent coils has been used, as already [5] described. The results of the linear computations for the HS 5-10 configuration showed that the coils are feasible. The effect of the additional toroidal field for ι-variation was included in the calculations, but the coil systems have not yet been mechanically connected. The contact problem is being treated / 528 / and gap elements have been introduced between the winding pack and the coil housing. This investigation is being done by members of the ZTE division. So far, certain components of the stress tensor, particularly the normal stress components in the radial and lateral directions, considerably increase, while other components decrease when these gap elements are taken into account.

[5] see Annual Report 1989, p. 150

1.2.2 *Demonstration Coil*

In order to treat the complex overall engineering aspects of the nonplanar superconducting Wendelstein 7-X coils, construction and testing of a full-size *Demonstration Coil* is necessary. This coil will be installed in the TOSKA facility at KfK Karlsruhe, where the EURATOM LCT coil is used to generate the background magnetic field at a temperature of 4 K. From the 5 different coil shapes of the HS 5-10 configuration, coil No. 3 was selected as Demonstration Coil in the development and test programme because of its rather large toroidal excursions combined with finite indentation. Calculations of magnetic forces, mechanical stresses and strains of the superconducting Demonstration Coil in the test arrangement of the TOSKA facility were made. The mechanical stresses in the winding pack of the coil, in the coil housing, and in the supporting structure were computed by finite-element methods. The results were compared with that of the toroidal arrangement. They are described in / 378 /. In Fig. 2.2 the displacements of the Demonstration Coil in the test arrangement of the TOSKA facility are shown.

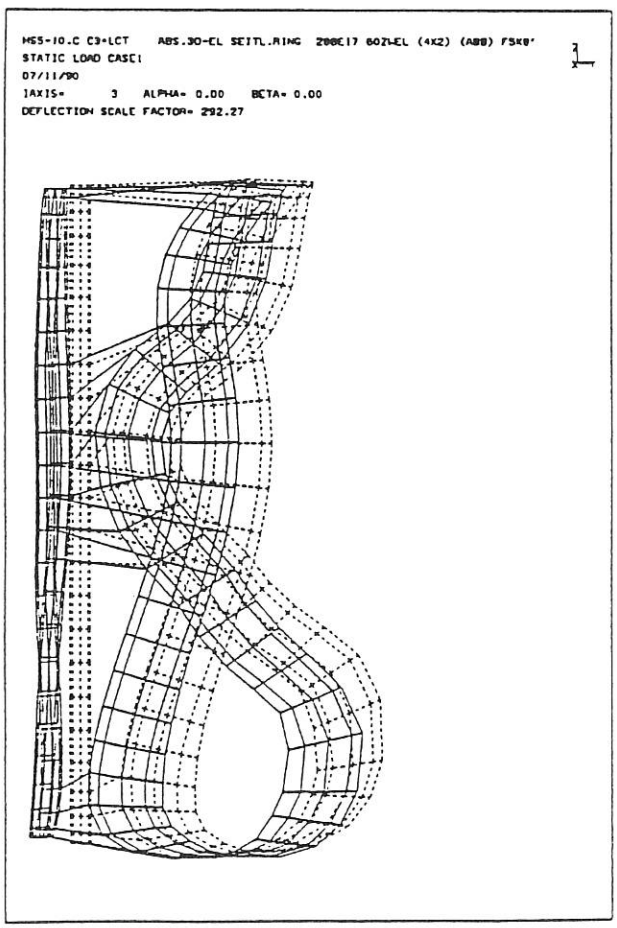

FIG. 2.2: Displacement plot for the Demonstration Coil and its support structure.

Although the load in the test arrangement is different from that in the toroidal arrangement of Wendelstein 7-X, the components of the stress tensor are of the same level. The maximum von Mises stress is of about 37 MPa, assuming the orthotropic material data of the conductor proposed for Wendelstein 7-X. The results for the normal stress values indicate that the test arrangement can already be considered as a slight overload case. In this way information can be obtained on the coil performance and the operational safety of the nonplanar superconducting coils of the Wendelstein 7-X experiment, before starting series production.

1.2.3 *Normal-conduction Coil System*

For comparison with the superconducting coil system, a pulsed normal-conducting version of HS 5-10 was designed in order to explore the limitations and restrictions of this approach. The main result, described in / IPP 2/310 /, is:

The power supply system at IPP Garching would have to be considerably upgraded to keep the magnetic field at $B_o = 3$ T. Assuming the frame of the installed power supply system at IPP Garching, Helias systems of the type HS 5-10 with a magnetic field on axis of $B_o \approx 2$ T would be obtained. Furthermore, the pulse length would be rather short, and the requested large number of pulses might affect the coil performance in regions of high stresses, because of the temperature dependence of the admissible stress levels in the insulation.

1.3 Physics Studies for Wendelstein 7-X

1.3.1 *Theory of Neoclassical Transport in General Toroidal Equilibria*

The complicated structure of Helias equilibria prevents simple classification of particle orbits and application of standard theory of neoclassical transport in stellarators. For this reason a new approach to neoclassical theory in general stellarator equilibria has been established which starts from the Fokker-Planck equation of a multispecies plasma and makes use of the properties of the plasma equilibrium. The basis of the new theory is decomposition of the distribution function $f(\mathbf{x}, \mathbf{v})$ into four orthogonal components $f = f_o^s + f_1^s + f_o^a + f_1^a$, where f^s is symmetric and f^a antisymmetric with respect to the transformation $\mathbf{v} \longrightarrow -\mathbf{v}$. The function $f_o^s(v^2, \mathbf{x})$ is spherically symmetric and f_1^s non-spherically symmetric in velocity space. The Fokker-Planck equation is transformed in 4 coupled equations for the four components. Neoclassical effects are described by f_1^s and its tensorial moments, which are the viscous stress tensors. In toroidal geometry with good confinement of particle orbits, the distribution is close to a Maxwellian, even in the regime of low collisionality. This property allows one to decouple the four equations to some extent and calculate the distribution function $F(\mathbf{x}, \mathbf{v})$ of the ideal equilibrium, the classical transport and the neoclassical transport. The distribution F is expanded in terms of the Laguerre-Sonine functions, its scalar moments P_k are functions of the magnetic surface and its vector

moments $\mathbf{U}_k$ describe the plasma flow in the magnetic surface, the diamagnetic flow and the parallel flow. The main result of the theory is an equation for f_1^s which relates f_1^s to components of the equilibrium function F. In the collisional limit the Braginskii theory of viscosity is obtained; in the low-collisional regime and after the gyro-kinetic approximation is taken the equations yield the standard neoclassical equations, but, the driving terms also include the Pirsch-Schlüter currents and the net toroidal currents. From the kinetic equations the generalized flux-friction relations and the matrices of transport coefficients are derived. The Onsager symmetry of the neoclassical transport matrix follows from the self-adjointness of the collision operator. A further result of the theory is the symmetry between bootstrap effect and pinch effect. It is shown that all neoclassical effects, except the modification of the resistivity, strongly depend on the Pfirsch-Schlüter currents and can be minimized by minimizing the Pfirsch-Schlüter currents in the plasma equilibrium. This can be explained by the close relation between Pfirsch-Schlüter currents and the radial drift of gyrating particles, which both depend on the poloidal gradient of mod B in the magnetic surface.

1.3.2 *Neoclassical Transport in Helical-axis Configurations*

Analytical calculations of neoclassical transport were extended to make exact allowance for all $m = 0$ and $m = 1$ magnetic field harmonics (m being the toroidal mode number) present in a general Fourier decomposition of a stellarator's magnetic field. These calculations may thus be used to obtain neoclassical transport coefficients for arbitrary Helias configurations as well as for the majority of present-day stellarator/torsatron experiments (e.g. ATF, Heliotron-E, CHS, Uragan-2M). The results conclusively show that the Helias concept leads to a significant reduction of transport rates for all collision frequencies with the reduction being particularly dramatic in the ν^{-1} regime. This is illustrated in Fig. 3.1. In particular, HS5V10C is found to have an effective helical ripple of $<\epsilon_h> \lesssim 0.01$ across the entire plasma cross-section even though the geometrical value of the helical ripple, ϵ_h, varies from 0.03 on axis to 0.12 at the plasma edge. This result is in stark contrast to those obtained for conventional stellarator/torsatron configurations where $<\epsilon_h>$ and ϵ_h are comparable in magnitude; this is illustrated in Fig. 3.2. Results from a Monte Carlo numerical simulation confirm these analytic estimates. Using the Monte Carlo method, it is also possible to investigate what effect the presence of $m \geq 2$ magnetic field harmonics has on the transport rate. For HS5V10C, it is found that these additional harmonics lead to a modest degradation of the neoclassical confinement with $<\epsilon_h> \lesssim 0.016$ across the entire plasma cross-section.

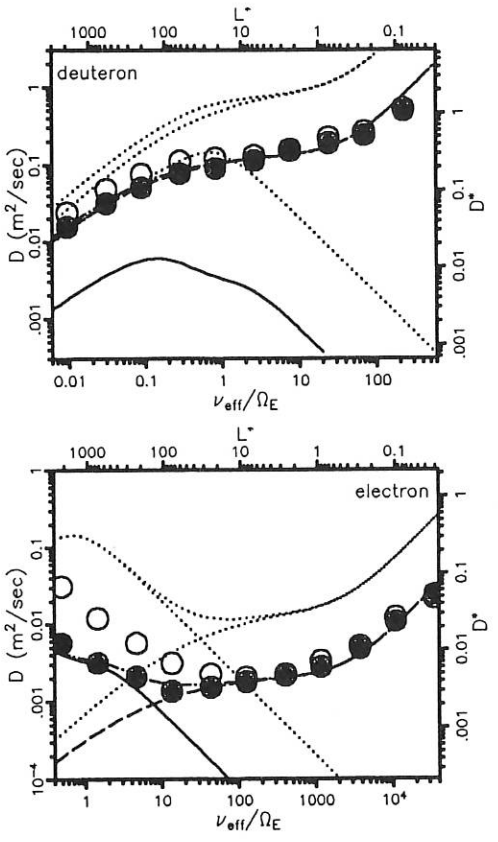

FIG. 3.1: The monoenergetic diffusion coefficient D is plotted versus normalized collision frequency ν_{eff}/Ω_E ($\nu_{eff} \equiv \nu/2\epsilon_h$ and Ω_E is the $\mathbf{E} \times \mathbf{B}$ precessional frequency) for deuterons and electrons in HS5V10C at half plasma radius. (The second set of axes presents the results in terms of the diffusion coefficient normalized to that of the equivalent tokamak in the plateau regime, D^*, versus the mean free path normalized to half the connection length, L^*.) The broken line is an analytic estimate of the expected axisymmetric transport, while the solid line was obtained from a general solution of the bounce-averaged kinetic equation and illustrates the expected helical-ripple transport. The dot-dash line is the sum of the dotted and solid lines. The dotted lines show these three transport curves for the equivalent 'ideal' stellarator, which is assumed to have the same aspect ratio, rotational transform and amplitude of the helical ripple as HS5V10C. Monte Carlo results are shown for simulations in which only $m \leq 1$ harmonics were taken (solid circles) as well as cases in which the full spectrum of magnetic field harmonics was considered (open circles). Simulation parameters: test particle energy 3 keV, major radius 5.5 m, minor radius 0.55 m, magnetic field on axis 2.5 T, rotational transform 0.869, electrostatic potential 3.375 kV.

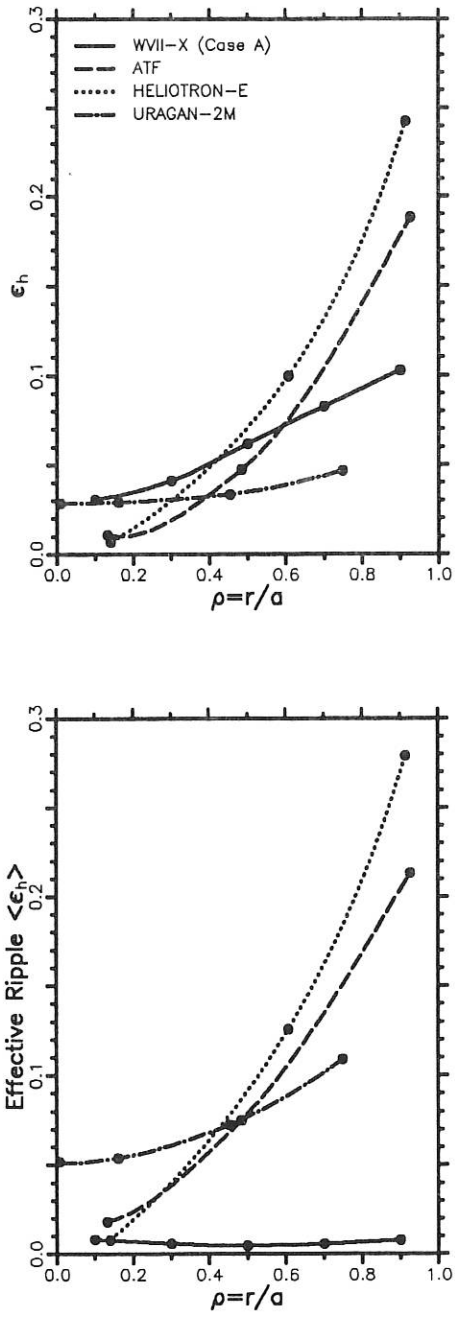

FIG. 3.2: The geometrical value of the helical ripple, ϵ_h, and the "effective" helical ripple for ν^{-1} transport, $<\epsilon_h>$, are shown as functions of the normalized minor radius for the standard case of Wendelstein 7-X and three other stellarator configurations. The results illustrated here for $<\epsilon_h>$ were obtained analytically; Monte Carlo simulations show a modest degradation of the results obtained for W 7-X when the full spectrum of magnetic-field harmonics is taken into account.

1.3.3 Drift Wave Instabilities

Drift wave instabilities in stellarator configurations are considered. A kinetic approach is used to perform a linear stability analysis. In order to discuss the influence of plasma quantities such as the Pfirsch-Schlüter currents, a representation of the equilibrium solution in its moments is suitable. A central problem especially in non-axisymmetric systems is the spatial structure of the drift wave fluctuations. With the presence of shear also taken into account, a modified ballooning mode formalism may be appropriate. As in the axisymmetric case, reduced shear damping due to toroidal effects is expected. Furthermore, trapped particles can contribute to destabilizing the drift waves.

1.3.4 Magnetohydrodynamic Plasma Equilibrium

The one-fluid dissipative model of a magnetohydrodynamic plasma equilibrium is considered. It includes inertial forces, finite resistivity and viscosity, and a particle source which sustains the pressure gradient in the plasma; the resistivity, viscosity and plasma density are assumed to be uniform. Thus, the equations are (in the absence of loop voltage):

$$\rho(\vec{v}\cdot\nabla)\vec{v} = -\nabla p + (\nabla\times\vec{B})\times\vec{B} + V\vec{v},$$

$$\eta\nabla\times(\nabla\times\vec{B}) = \nabla\times(\vec{v}\times\vec{B}),$$

$$\rho\nabla\cdot\vec{v} = S.$$

Here $V\vec{v}$ is the Braginskii viscous force per unit volume acting on the plasma. The fields are defined in a smooth 3D toroidal domain Ω. Boundary conditions are assigned by prescribing the value of the flow velocity $\vec{v}$ on Γ ($\equiv \partial\Omega$) and by requiring that the normal component of $\vec{B}$ and the tangential component of the electric field vanish on Γ. This dissipative model eliminates the topological constraints of the ideal MHD model ($\oint d\ell/B$ = const on rational magnetic surfaces), and is also applicable to non-axisymmetric equilibria with magnetic islands and stochastic regions. In particular, the model applies to the boundary regions of stellarators and tokamaks, where the plasma is collision-dominated and magnetic surfaces are destroyed.

The above model is studied by generalizing the mathematical techniques successfully used in hydrodynamics to investigate the existence and uniqueness of stationary solutions of the Navier-Stokes equations. Thus, after an appropriately weak formulation of the problem has been established, the latter is reduced to the study of a fixed-point equation in a (separable) Hilbert space; the operator appearing in such an equation is obviously nonlinear and is proved to be completely continuous. The main results are: (i) By using the Leray-Schauder fixed-point theorem, we prove the existence of at least one weak solution if the plasma source (or β) is sufficiently small and/or the resistivity and viscosity are sufficiently large; (ii) we obtain an estimate of the solution, the upper bounds of $\|\vec{v}\|$ and $\|\vec{B}\|$ being given in terms of resistivity, viscosity, plasma source (S) and constants

which depend only on the shape of the domain; (iii) we prove that, under a condition of the same kind as the afore mentioned for existence, but more stringent, the solution is unique; (iv) the condition for uniqueness holding for hydrodynamic stationary flow is obtained when the magnetic field is dropped. If resistivity and viscosity become small, uniqueness of the solution is no longer guaranteed; this introduces bifurcations and possibly exchange of stability. Work in progress includes the study of the stability of the bifurcating solutions. Moreover, it is planned to attempt to generalize the analysis by dropping the strong assumption of uniform density.

1.3.5 *Neutral Gas Behaviour in the Plasma Edge of Wendelstein 7-X*

The neutral density distribution in the plasma edge and the loading of the wall by charge exchange recycling neutrals were calculated with the DEGAS [6] code for a simple model plasma of the W 7-X, HS 5-10 configuration / 403 /. The plasma is modelled by parabolic profiles for the density and temperature, with $10^{14}\ cm^{-3}$, 2 keV on axis and $2 \times 10^{13}\ cm^{-3}$, 20 eV on the separatrix. The plasma outflow is assumed to be localized along the apex of the configuration, extending over a toroidal range of 12° between every two planes of symmetry. Here, the largest population of guiding centre orbits leaving the plasma was found from Monte Carlo pitch angle scattering calculations. In these regions, as well as on a narrow strip along the separatrix (see Fig. 3.3), the plasma density and temperature are set to half the values on the separatrix, whereas in the remaining volume behind the separatrix they are assumed to be very small ($10^{11}\ cm^{-3}$ and 1 eV).

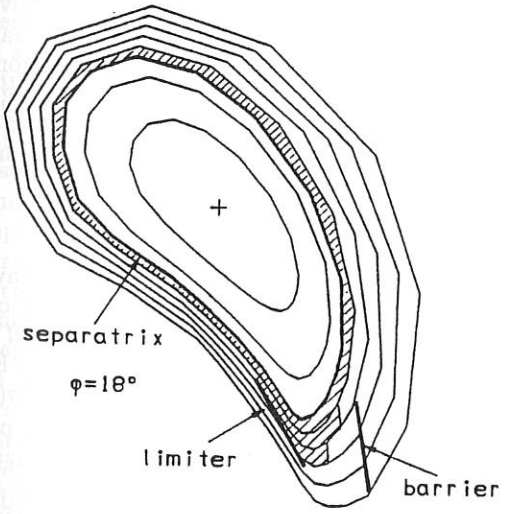

FIG. 3.3: Cross-section of the HS 5-10 configuration with limiter and barrier as used in the simulations. The shaded areas represent the regions of plasma outflow.

[6] D.B. Heifetz et al., J. Comput. Phys. 46 (1982), 309

The neutrals originate from 100% recycling at limiter plates (see Fig. 3.3), whose geometry is being optimized to catch most of the outflowing plasma [7]. The total recycling flux is obtained from an estimated global confinement time of 1 s. Recombination sources of neutrals are not included since their contribution to the neutral density in the plasma edge is negligible compared to that of the recycling sources.

The 2D distribution of the neutral densities in a cross-section centred between two planes of symmetry (at $\varphi = 18°$), as resulting from the neutral transport simulation, is shown in Fig. 3.4. The isolines clearly indicate a strong localization of the neutrals in front of the limiter face. Inside the plasma, the isolines are shown, in comparison with Fig. 3.3, to follow roughly the contours of the magnetic surfaces in the upper part of the cross-section, above the magnetic axis. In the lower, elongated part, however, the density is higher, owing to the superposition of the neutral fluxes laterally penetrating the plasma from both sides of the cross-section. The poloidal decay of the neutral density along the wall, where the plasma density and temperature are very small, is also shown to be much weaker than the radial drop inside the plasma. This implies that a non-negligible fraction of the neutrals escape along the wall via charge exchange and wall reflection, reaching the plasma edge at any poloidal position. The neutrals which penetrate the plasma in the regions where the separatrix is closest to the wall will, on the average, hit the wall with the highest charge exchange energies.

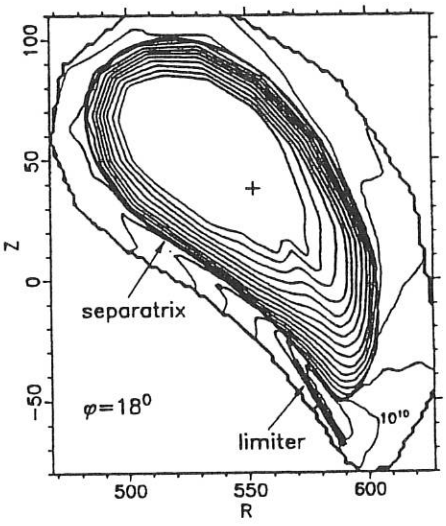

FIG. 3.4: Constant neutral density lines resulting from limiter recycling (increment: $\Delta \log n = 1/3$).

Trapping of the neutrals by material structures placed near the recycling source is expected both to reduce this effect and to increase the local plasma recycling with its favourable cooling effect on the outflowing plasma. The trapping efficiency was explored by placing a barrier

[7] Report IPP 2/302, Nov. 1989, p.115

close to the outflowing plasma (see Fig. 3.3). No additional barrier is needed at the inboard side of the wall, since the neutral flux in this poloidal direction is already substantially reduced by the limiter itself, which acts as a second barrier, as can be seen by comparing the isoline sequence on both sides of the limiter along the wall (Fig. 3.4).

Figure 3.5 shows the poloidal neutral density distribution in the boundary region outside the separatrix with and without barrier. By comparing the two profiles, the presence of the barrier is shown to cause compression of the neutrals between the limiter and the barrier (from $\theta = 260°$ to $330°$) and rarefaction behind the barrier (for $\theta > 340°$).

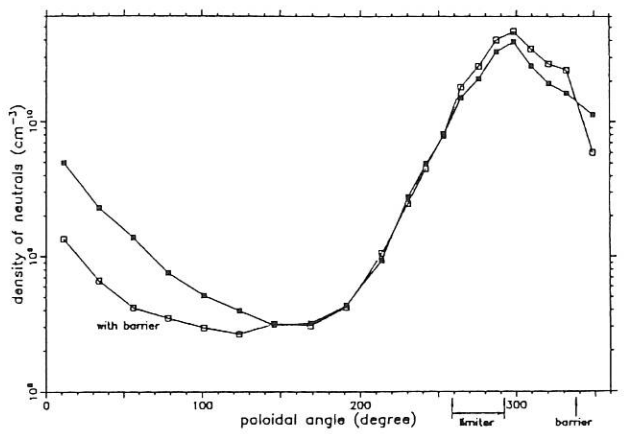

FIG. 3.5: Poloidal distribution of the neutral densities in the plasma/wall boundary region for the 2 cases without barrier (solid line) and with barrier (dottet line).

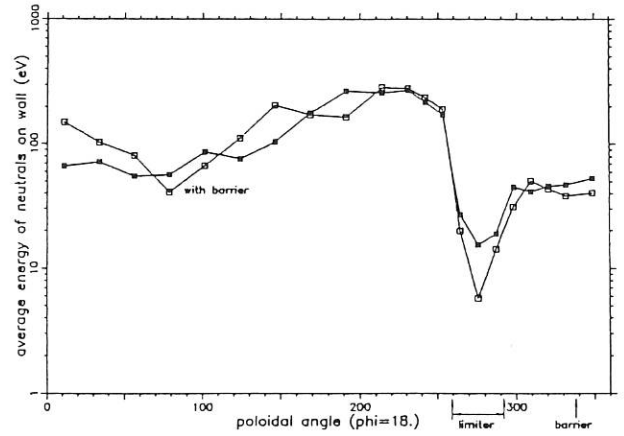

FIG. 3.6: Poloidal distribution of the average energy of the neutrals hitting the wall without barrier (solid line) and with barrier (dotted line).

However, the barrier does not significantly modify the poloidal distribution of the average energy of the neutrals hitting the wall (see Fig. 3.6). This energy has a minimum behind the limiter, which completely shields the wall from impact by high-energy charge exchange neutrals. A maximum of ≈ 300 eV is found at $\theta = 230°$, where the separatrix is closest to the wall and the plasma density and temperature are very low (poor screening of CX neutrals). This energy may be critical for impurity sputtering. Nevertheless, even in this region, the total neutral power flux to the wall is not larger than in the highest density region between the limiter and the barrier. This is due to the high trapping efficiency of the limiter, which results in a strong poloidal drop, by more than a factor of 10, of the neutral density away from the limiter.

1.3.6 Plasma Parameters in Wendelstein 7-X

Plasma parameters in Wendelstein 7-X were calculated using the TEMPL-code. This code solves the one-dimensional energy balance equations of ions and electrons and computes the temperature profiles as a function of the average plasma radius. Density profiles are not calculated self-consistently, the density being given and kept fixed instead; power deposition profiles are also given functions of radius. Since stellarator experiments do not show anomalous behaviour of ions, neoclassical transport is considered to be the only mechanism of ion energy loss. Ion heat conductivity is used in the analytic approximation given by C. Beidler. An important role is played by the radial electric field in reducing the loss of trapped particles. In principle, this radial E-field is determined by the condition of ambipolarity; here a simpler model is used where the electric field is balanced by the ion pressure gradient $\mathbf{E} = \nabla p_i / en$. This implies that the macroscopic ion motion $\mathbf{v}_i$ is slowed down to zero by ion viscosity. Charge exchange losses are taken into account in the the ion energy balance; for this reason a simple model of the neutral gas was established.

The thermal conductivity of electrons is the sum of the neoclassical coefficient and the anomalous coefficient $\chi_{e,L}$, which is the same coefficient used by K. Lackner to model the ASDEX L-mode confinement. To solve the energy balance equations, boundary conditions have to be imposed. Since appropriate boundary conditions require a model of the physics between the last magnetic surface and first wall - which is not available - a simple choice was made: the temperature at the boundary $r = a$ is fixed at 50 eV.

a) ECRH scenario

The purpose of ECRH in Wendelstein 7-X is to investigate a high-temperature plasma under quasi-stationary conditions. The density is limited by the cut-off density slightly above 10^{20} m^{-3}. In computing the ECR-heated plasma the parameters are: B=2.5 T and $n(0) = 10^{20}$ m^{-3}. The radial localization of the heating power can be varied within certain limits, a strong localization on the magnetic axis being is of special interest since in this case the highest temperature can be achieved. Although the power is deposited into the electrons only, coupling between electrons and ions is strong enough to equalize the temperatures, except in the central regions, where the heating occurs.

The ion and electron temperatures achievable with the highest heating power of 10 MW are $T_e = 4.5$ keV

and T_i = 2.5 keV, the power being deposited in the central region with diameter 10 cm. The anomalous electron thermal conductivity $\chi_{e,L}$ determines the electron temperature, it being larger than the neoclassical thermal conductivity. Reducing the anomalous conductivity leads to higher temperatures; in the case $\chi_{e,an} = 1/8\chi_{e,L}$, the electron temperature is doubled and reaches more than 8 keV. The normalized mean free path $\lambda\iota/R$ ranges between 500 and 1000, which is close to reactor conditions. Since the anomalous thermal conductivity scales with $T_e^{3/2}$, the temperature $T_e(0)$ increases only weakly with the heating power. The energy confinement time decreases with power and ranges between 0.4 and 0.15 s. These values are roughly 50% larger than those predicted by the global scaling laws. The reason for this result is the strong improvement of neoclassical ion confinement in Wendelstein 7-X . In contrast to present-day stellarator experiments, where in ECR-heated discharges ions play a small role in the energy balance, the stronger coupling between ions and electrons in Wendelstein 7-X leads to this effect of improved ion confinement on the overall confinement although the anomaly of electrons is not changed. Under the more optimistic assumption ($\chi_{e,an} \longrightarrow 1/8\chi_{e,L}$) the energy confinement time lies between 0.7 and 0.3 s.

Since the cut-off frequency limits the density to 10^{20} m^{-3}, the ECRH experiment is not suited to exploring the β-limit of the Wendelstein 7-X configuration. The achievable β-value in ECRH discharges is $<\beta>\approx 1\%$ at P = 10 MW, B = 2.5 T and $\chi_{e,an} = \chi_{e,L}$. Under improved conditions $\chi_{e,an} = 1/8\chi_{e,L}$, $<\beta>= 2.4\%$ can be reached.

b) NBI scenario

The aim of neutral beam heating in Wendelstein 7-X is to investigate the β-limits. The best method to reach high β-values is to run the discharge at the highest possible density and moderate temperatures. Also a smaller magnetic field than 2.5 T is preferable, but in that case the target plasma cannot be formed by the 140 GHz gyrotrons; ion cyclotron heating and neutral beam injection could be combined in these circumstances. In NBI-heated plasmas the density tends to increase during the discharge if beam fuelling and pumping at the wall are not in equilibrium. The density rises until radiative losses terminate the discharge. For computing temperatures in NBI-heated plasmas a density of $n(0) = 1.5 \times 10^{20}$ m^{-3} is considered to be a representative value. The power deposition is modelled by $p_{e,i} \propto (1-r^2)^\alpha, \alpha = 6$. The total input power P ($P_e = P_i = 1/2P$) ranges from 2 to 20 MW. Because of strong coupling between particle species the temperatures are nearly equal; this result does not depend on the fraction of power into the particle species.

For standard conditions in W 7-X (B = 2.5 T) with the total heating power of P = 20 MW, $<\beta>\approx 1.9\%$ can be achieved. Only the improvement of the confinement ($\chi_{e,an} \longrightarrow 1/8\chi_{e,L}$) would lead to $<\beta>= 4\%$ at a heating power of 20 MW. Although at lower magnetic fields confinement properties decrease and lower temperatures are obtained, the achievable β-values are larger. TEMPL calculations show that at B = 1.25 T, $<\beta> = 4.2\%$ can be reached with P = 20 MW and $\chi_{e,an} = \chi_{e,L}$. Therefore, the β-limit in Wendelstein 7-X at this low magnetic field can be investigated even if no reduction of anomalous transport occurs.

c) Bootstrap currents

Bootstrap currents in stellarators are net toroidal currents driven by the anisotropy of the pressure tensor. The origin of this anisotropy are the particle orbits in the inhomogeneous magnetic field leading to a non-Maxwellian distribution function. This deviation from a Maxwellian increases if collisions become rare, and therefore the most relevant regime for bootstrap currents is the long-mean-free-path regime.

Experiments in Wendelstein 7-AS have shown that bootstrap currents modify the rotational transform at the risk of arriving at a low-order rational magnetic surface, where confinement is deteriorated. For this reason bootstrap currents in W 7-X have to be minimized as much as possible. This is one of the criteria leading to the choice of the present configuration. Bootstrap currents in stellarators seem to follow neoclassical theory, with no major discrepancy reported as yet. This justifies the application of neoclassical theory in predicting the currents in W 7-X. Three methods are available to calculate the bootstrap currents in general stellarator geometry: analytic theory, DKES code, and Monte Carlo technique. Monte Carlo methods compute the distribution function $f(v_{||})$, its asymmetry indicating a parallel current [8] . The DKES code solves the drift-kinetic equation and provides the whole transport matrix in all collisionality regimes. Shaing and Callen [9] have derived an expression for j_b which holds in the lmfp regime and has the same shape as bootstrap currents in tokamaks, except for a geometrical factor $G_{bs} = f_t/f_c G_b$:

$$j_b = -2.96\frac{f_t}{f_c}G_b\{0.55(T_e+T_i)n' - 0.094nT_i' + 0.14nT_e'\},$$

where f_t is the number of trapped particles, and $f_c = 1 - f_t$. This numerical factor G_{bs} was evaluated numerically for the Wendelstein 7-X configurations. This result shows that the bootstrap current in Wendelstein 7-X is much smaller than in the equivalent axisymmetric tokamak with the same rotational transform and the same aspect ratio. The reduction of the bootstrap current in Wendelstein 7-X is caused by two counteracting effects. The toroidal effect leading to a tokamak-like bootstrap current is characterized by the $C_{0,1}$-coefficient in $B(\varphi,\theta)$; the helical terms $C_{1,1}, S_{1,1}$ are responsible for a negative bootstrap current. The toroidal mirror term allows the bootstrap current to be varied within certain limits.

---

[8] H. Wobig, *Z. f. Naturforschung*, **37a**, (1982), 906

[9] K.C. Shaing, J. Callen, *Ph. Fluids* **26**, (1986), 3315

Since the DKES code allows neoclassical effects to be computed for any collisionality, this method was used to evaluate the current density, the modification of the rotational transform and the total bootstrap current of the 6 cases described in TABLE III. The starting point is the vacuum field of the Wendelstein 7-X standard configuration. Finite-β effects only slightly modify the Fourier spectrum of $B(\varphi,\theta)$, except the $B_{0,0}$ term, which is changed by the diamagnetism of the plasma. As can be seen, everywhere in the lmfp regime the normalized bootstrap coefficient $D_{31}/D_{31,tok}$ is below 0.1, which confirms the analytic result given in G_{bs}. Therefore, in this regime the bootstrap current is a factor of more than 10 smaller than in the axisymmetric configuration. At higher collisionality (plateau regime and Pfirsch-Schlüter regime) the bootstrap current becomes negative. In the plateau regime analytic theory also provides a geometrical factor $C_{b,pl}$. In the various modifications of Wendelstein 7-X this factor, normalized to the equivalent tokamak, is around -1.2, indicating that in the plateau regime the bootstrap current is as large as in the equivalent tokamak, but the sign is opposite. Analytic theory and the DKES code yield results which roughly agree. The DKES code results were used to calculate the current density, modified ι-profile and the total bootstrap current for the various discharges. The total bootstrap current in this case is -8.9 kA. If confinement is improved ($\chi_{ean} \longrightarrow 1/8\chi_{e,L}$), collisionality decreases and the bootstrap current grows to +42 kA. In the NBI scenario a similar situation occurs. The largest bootstrap current was found at maximum NBI-heating power and $\chi_{e,an} = 1/8\chi_{e,L}$: $I_b = +54$ kA.

A toroidal current of this size would lead to a shift of the rotational transform $\delta\iota = 0.08$ at the edge, which is considered as being too large to be tolerable.

Two methods allow the bootstrap current to be controlled: ECRH current drive and modification of $B(\varphi,\theta)$ by mirror fields and ι-variation. An ECR current drive efficiency of 13 kA/kW heating power is expected in Wendelstein 7-X. Therefore, a maximum heating power of 10 MW should be sufficient to control and compensate bootstrap currents of up to 50 kA.

d) Summary

Because of the strongly reduced neoclassical transport the electron temperatures in Wendelstein 7-X are mainly determined by anomalous transport processes of the electrons. Since the physical mechanism of this process is not known, extrapolation towards Wendelstein 7-X is somewhat speculative. However, reduction of Pfirsch-Schlüter currents and small banana orbits suggest that anomalous transport may also be reduced in Wendelstein 7-X. Straightforward extrapolation of Wendelstein 7-AS results predict confinement times between 0.3 and 0.1 s and maximum temperatures of around 4 keV (L-mode confinement). Under optimistic assumptions the temperature would increase to 8 keV (10 MW ECRH). The highest β-value can be achieved at a low magnetic field ($B = 1.25$ T, 20 MW NBI $\longrightarrow < \beta > \approx 4\%$) and L-mode confinement. Bootstrap currents of up to 50 kA may arise in Wendelstein 7-X, ECR current drive is a possible method to control these currents. In TABLE III characteristic data of the 6 specific cases are summarized.

TABLE III: Results of the TEMPL code

Case	1	2	3	4	5	6
B [T]	2.5	2.5	1.25	2.5	2.5	1.25
$n(0)$ [m^{-3}]	1.0×10^{20}	1.5	1.5	1.0	1.5	1.5
P_e [MW]	10	10	10	10	12.5	10
P_i [MW]	0	10	10	0	12.5	10
$\chi_{e,an}$	$\chi_{e,L}$	$\chi_{e,L}$	$\chi_{e,L}$	$1/8\ \chi_{e,L}$	$1/8\ \chi_{e,L}$	$1/8\ \chi_{e,L}$
$T_e(0)$ [keV]	4.5	2.95	1.76	7.65	6.12	3.6
$T_i(0)$ [keV]	2.5	3.1	1.96	3.9	6.02	3.6
$\beta(0)$ [%]	4.5	5.8	14.4	7.4	11.7	27.6
$\langle\beta\rangle$ [%]	1.1	1.8	4.2	2.2	4.2	8.9
τ_E [s]	0.14	0.11	0.061	0.28	0.21	0.14
$\bar{n}\tau_E$	7.9×10^{18}	9.7×10^{18}	5.2×10^{18}	1.6×10^{19}	1.8×10^{19}	1.2×10^{19}
$\bar{n}\tau_E T_i(0)$	$2 \cdot 10^{19}$	$3.0 \cdot 10^{19}$	$1.0 \cdot 10^{19}$	$6.24 \cdot 10^{19}$	$1.08 \cdot 10^{20}$	$4.3 \cdot 10^{19}$
I_b [kA]	-5.3	-18.0	-36.2	20.0	57.5	-14
$\delta\iota(a)$	-0.008	-0.026	-0.11	0.03	0.084	-0.03
Job No. IFH	488	493	275	483	499	276

1.4 Reactor Considerations

1.4.1 *Coil Systems*

Helias configurations with an average field $B_0 = 5$ T on axis in the dimensions of a fusion reactor (HSR) or a burner experiment (HSB) were derived from the coil systems HS 5-8 and HS 50B [11], having major radii of about $R_0 = 20$ and 13 m for HSR58 and HSB58, respectively, with a typical plasma aspect ratio of 12.5. The system HS 50B has a larger coil aspect ratio than HS 5-8 and requires major radii of $R_0 = 26$ and 16 m since constant radial distances are to be observed in the scaling. The burner is shielded with a minimum distance of $\Delta_{cw} = 0.75$ m between the coil bore and the first wall, a value comparable with that specified for ITER [12]. For the reactor additional space is required for the neutron breeding blanket; a minimum distance of $\Delta_{cw} = 1.2$ m was utilized in the ASRA6C reactor study [13].

In TABLE IV characteristic data of the Helias reactor version HSR58 are compared with the data of STARFIRE [14] and ARIES-I [15], as well as with the ITER experiment.

The two commercial tokamak reactors have an electric power output of about $P_{el} = 1000$ MW. STARFIRE is characterized by a magnetic field on axis of $B_0 = 5.8$ T and a stored magnetic energy of $W = 70$ GJ in the TF coil system, whereas the ARIES-I study [16] "assumes a minimum extrapolation from current tokamak physics and incorporates technological advances that can be available in the next 20 to 30 years", and has a large field of $B_0 = 13$ T on axis. The peak field on the coils of about $B_{max} = 24$ T calls for $Nb_3(Al,Ge)$, a new superconducting material. Considerable mechanical loads are associated with the high stored magnetic energy of $W = 160$ GJ of the TF coil system. The ARIES-I reactor operates in steady-state, using ICRF fast waves to drive the current at the core plasma, lower-hybrid waves for the edge plasma, and bootstrap current. The current-drive power is estimated at 160 MW. Its efficiency, and also the thermal power plant efficiency need to be very high in view of the electric power output of 1 GW associated with the fusion power of about 2 GW.

For a stellarator reactor a single modular coil set can be envisaged. The Helias reactor is characterized by steady-state operation with current drive balancing the small bootstrap current effects on the transform profile. The system should be inherently safe from disruptions. The stored magnetic energy in HSR58 is $W = 70$ GJ. Fifty modular nonplanar coils generate the magnetic field of 5 T with a peak value of 10.7 T at the coils. This would allow supercritical helium at 1.8 K to be used for cooling the NbTi coils, a technology applied in, for example, the TORE SUPRA coil system in France. The moderate helicity of the magnetic axis in the Helias configuration and the toroidally varying shape of the coil bores cause a related helical geometry of the blanket and shield. An appropriate maintenance scheme may use techniques different to those favoured for tokamaks. One of the options discussed considers a system separated in half field periods for end-on maintenance. Further investigation in this field is necessary. The neutron wall load in HSR58 is relatively low compared with that of tokamak reactors because of the larger aspect ratio (first wall area of about 1900 m^2).

1.4.2 *Ignition and Stationary Burn*

The TEMPL code was used to investigate the parameter regime of ignition and stationary burn in the Helias reactor. Neoclassical and various anomalous losses are assumed; the peak density and a radial electric field are other input parameters. Figure 4.1 shows the start-up scenario for a particular case with an additional anomalous thermal conductivity according to the Horton drift wave model [17]. Reducing the field to 5 T results in an average β-value of 4.9% for the stationary burn at a peak density of $n(o) = 1.8 \cdot 10^{20}$ m^{-3}.

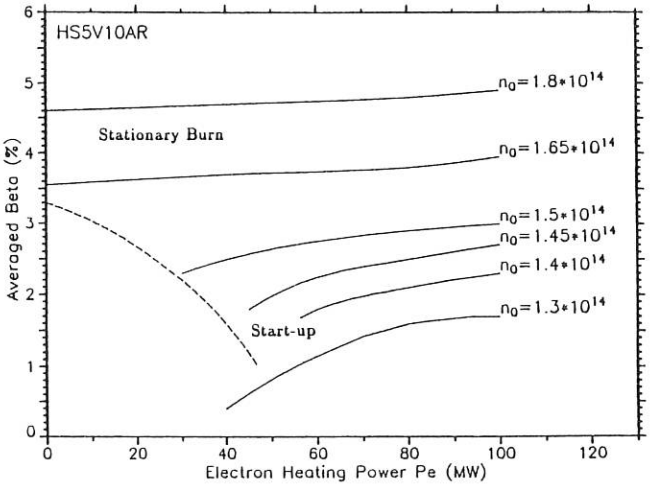

FIG. 4.1: Start-up scenario for a Helias reactor $B = 5.5$ T, $n(o) = 1.65 \cdot 10^{20}$ m^{-3}, $\bar{\beta} = 3.7\%$, fusion power $\geq$ 2.6 GW, effective ripple $\epsilon_0 = 0.5$ % on axis, rising to 1% at the edge.

[11] Annual Report 1989, p. 161 and 164, resp.

[12] ITER Conceptual Design: Interim Report, IAEA, Vienna 1990

[13] Böhme, G., et al., Report IPP 2/285, Mai 1987

[14] Starfire - A Commercial Tokamak Fusion Power Plant Study, Report ANL/FPP-80-1, Sept. 1980

[15] The ARIES Tokamak Reactor Study, Report UCLA/PPG-1274, Oct. 1989

[16] Najmabadi, F., Conn, R.W., et al., Proc. 13th Symp. on Fusion Eng., Knoxville, TN, (1989), 1021

[17] Horton, W., et al., Proc. 12th Int. Conf. on Plasma Physics, Nice 1988, Vol. 2, 211, IAEA Vienna 1989

With the same peak density, a lower level of $\bar{\beta} = 4.3\%$ and a fusion power ≥ 2.8 GW are seen if the anomalous electron heat conduction according to Lackner [18] is used, reduced by a factor of 8 in order to account for the expected improvement of anomalous losses in Helias fields. Figures 4.2 and 4.3 give pertinent radial profiles for a case where an additional edge radiation of 200 MW is assumed, causing the average β to rise to 5.3 % / 298 /.

These are acceptable parameters with respect to the stability limit of Wendelstein 7-X. Also the fusion power output, 2.8 to 4 GW, is compatible with the level of present-day power stations. Higher power output could be achieved by increasing the density. In Wendelstein 7-AS peak densities of $n(o) = 2.5 \cdot 10^{20}$ m^{-3} have been reported.

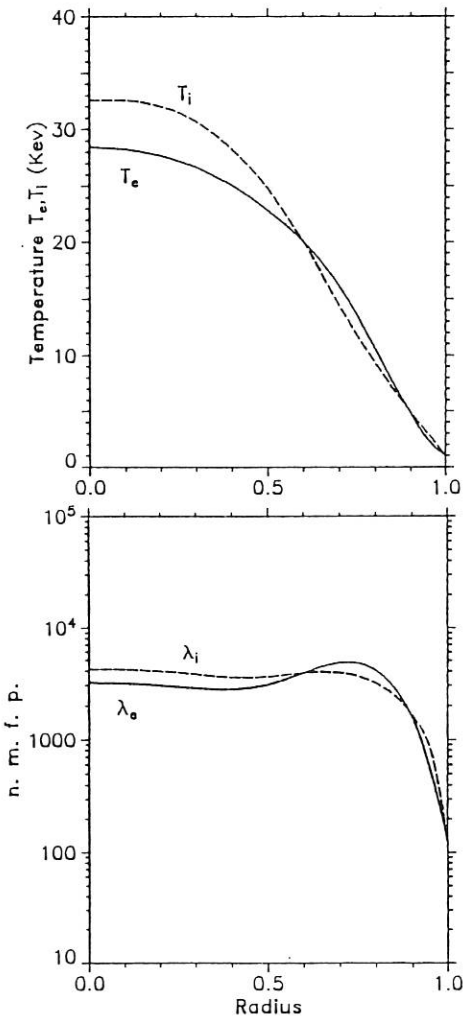

FIG. 4.2: Radial profiles of the temperature and the n.m.f.p. obtained by the TEMPL10 code; B = 5.0 T, $n(o) = 1.9 \cdot 10^{20}$ m^{-3} , radially constant effective ripple $\epsilon = 1$ %.

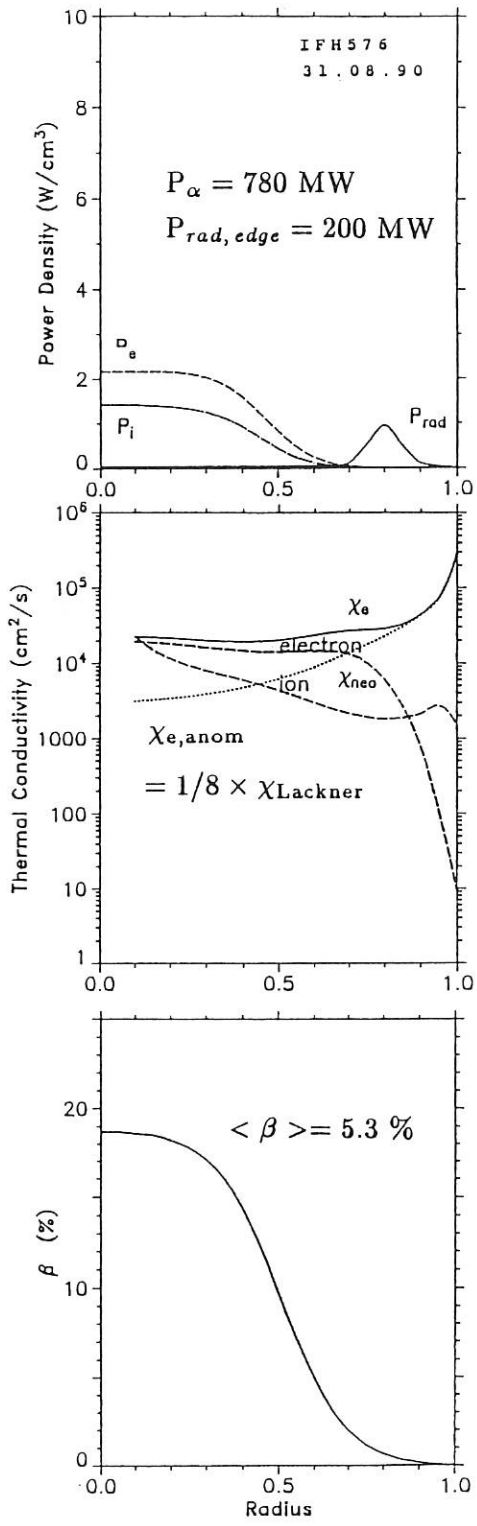

FIG. 4.3: Radial profiles of the power density, thermal conductivity, and resulting β obtained by TEMPL10 code; stationary burn with 200 MW edge radiation, fusion power 3.9 GW.

[18] Lackner, K., et al., Plasma Phys. and Contr. Fusion, **31**, (1989), 1629

TABLE IV: Characteristic data of the reactor version HSR58 derived from the Helias coil configuration HS58B (5 field periods, $\iota = 0.84$) in comparison with the STARFIRE, ARIES-I and ITER tokamaks.

			HSR58	STARFIRE	ARIES-I	ITER-TF 'Phys.Phase'
Year of inauguration			1989	1980	1989	1988
Average major radius	R_0	[m]	19.5	7.0	6.5	5.8
Average coil radius	r_c	[m]	3.9	6.0	4.3	5.3
Average coil volume	V_c	[m^3]	9.3	62.2	28.5	21.5
Min. distance coil-wall	Δ_{cw}	[m]	1.2	1.4	1.8/1.2	0.75
Coil number total	n		50	12	16	16
Total coil current	I_c	[MA]	10.4	16.9	25.1	9.
Overall current density	j_c	[MA/m^2]	31.5	10.2	25.1	14.
Total inductance (one-turn)	L	[μH]	1294.	490.	493.	820.
Stored magnetic energy	W	[GJ]	70.	70.+12.**)	160.*)	33.+10.**)
Induction on axis	B_o	[T]	5.	5.8	13.	5.
Maximum induction at coil	B_m	[T]	10.7	11.1	23.8	12.8
Average force density	$\langle f \rangle$	[MN/m^3]	86.	38.	188.	50.
Maximum net force (one coil)	F_{res}	[MN]	115.	772.	1442.	425.
Virial stress	σ_V	[MPa]	150.	94.	350.	96.
Superconductor			NbTi	Nb_3Sn	$Nb_3(Al, Ge)$	Nb_3Sn
Cooling			1.8K	4.2K	4.2K	4.5K
Average plasma radius	r_p	[m]	1.59	2.37	1.85	2.2
Plasma volume	V_p	[m^3]	1060.	781.	441.	750.
First-wall area	A_{fw}	[m^2]	~1890.	1070.	580.	800.
Average neutron wall load	P_{nw}	[MW/m^2]	1.5	3.6	2.8	1.
Fusion power	P_f	[MW]	3800.	3510.	1990.	1000.

*) TF coil system only **) TF + PF coil systems

2. STELLARATOR PHYSICS STUDIES

W. Dommaschk, F. Herrnegger, W. Lotz, P. Merkel, J. Nührenberg, E. Rittger, A. Schlüter, C. Schwab, U. Schwenn, E. Strumberger, L. Zheng
Guests: D. Anderson[1], A.H. Boozer[2], H.J. Gardner[3]

In 1990 the work of the Stellarator Physics Group was concentrated on preparing the Phase-I Proposal for W7-X and on beginning to extend the work to areas not yet fully covered there. Such areas were, for example, non-local (and non-ideal) MHD studies, W7-X coil studies, and divertor studies exploiting the Helias configurational properties.

2.1 Stellarator Optimizations

2.1.1 Optimizations in relation to W7-X

2.1.1.1 Optimizations by solving boundary value problems

In addition to the basic configuration for W7-X, variants were produced to afford flexibility in the device and for illustrative purposes.

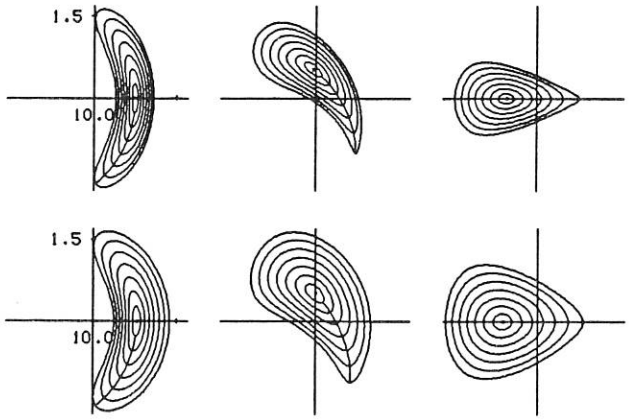

FIG. 1: Flux surfaces of Helias configurations. The first one represents the high-ι low-mirror case for W7-X, the second one the low-ι high-mirror case. The radial lines indicate the locations of strongest curvature of the flux surface sections. A "helical edge" at the plasma boundary is given by the half-helix like line along the line of strongest curvature connecting the bottom of the indented cross-section via the triangular cross-section to the top of the indented cross-section one period apart. Note that the position of this helical edge is nearly unchanged.

[1] Guest from University of Wisconsin-Madison

[2] Guest from College of William and Mary, Williamsburg

[3] Guest from Australian National University, Canberra

Figure 1 shows two examples: a high-ι case ($1 < \iota \lesssim \frac{5}{4}$) and a low-$\iota$ case ($\frac{2}{3} \lesssim \iota \leq \frac{5}{6}$) which were selected with the additional intention of giving the helical edge (see Sec. 2.6) an approximately constant location in space. Other examples concern configurations with various ratios of principal helical to toroidal curvature (see Fig. 2).

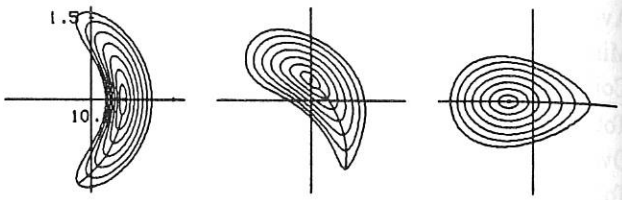

FIG. 2: Optimized Helias configuration with equal principal helical and toroidal curvature terms.

In these optimizations the same optimization procedure as for the basic configuration of W7-X was used: the magnetic curvatures are minimized and the geometrical shape of the configuration is a consequence of the structure of B which is realized /151, 175/[4].

2.1.1.2 Optimization of Analytic Stellarator Fields by Using Mapping Methods

An optimization code[5] to find vacuum stellarator fields with prescribed inherent properties was improved and supplemented. The vacuum magnetic fields are given analytically by a finite set of Dommaschk potentials[6] which essentially consists of finite power series in the cylindrical coordinates R and Z for each toroidal harmonic. The singularities of the individual magnetic fields are located at $Z = 0$ (main torus axis) and at infinity. The use of low-order and slowly varying multipole fields should guarantee that the position of the corresponding coils can be sufficiently far away from the plasma surface (last closed magnetic surface) of given aspect ratio A ($A = R_T/r_0 \approx 12$).

The inherent magnetic properties used in the optimization procedure are: the residues of two reference fixed lines and their aspect ratio A, the normalized magnetic flux between two closed field lines belonging to the same

[4] Lotz, W., Nührenberg, J., Schwab, C., Proc. 13th Int. Conf. on Plasma Physics and Contr. Nuclear Fusion Res., Washington 1990, paper IAEA-CN-53/G-I-6

[5] Dommaschk, W., Herrnegger, F., Schlüter, A., Proc. 16th Europ. Conf. on Contr. Fusion and Plasma Physics, Venice 1989, ECA, **13B**, Part 2, 583

[6] Dommaschk, W., Comput. Phys. Commun. 40 (1986) 203

rational ι- value and the Hamada condition that $\oint dl/B$ should have the same value for the X and the O fixed lines, the number M of field periods around the torus, the specific volume V', the twist ι, and the measure $\langle|j_{||}|/|j_{\perp}|\rangle$ of the Pfirsch-Schlüter current density. Geometric conditions on the shape of the magnetic surfaces and an analytic parametrization of the magnetic surfaces are not used in the optimization procedure.

The method of measure-preserving tangential mapping is applied in order to analyze the vicinity of the fixed points of the mapping. The internal properties used in the optimization code are evaluated at four different fixed lines; the outermost one is associated with the magnetic divertor, where the angle γ between the asymptotes at the X points should be of considerable size at certain positions in the toroidal direction. The O points have an elliptic neighbourhood where the ellipticity $\epsilon = (b/a-1)/(b/a+1)$ and the residues have been determined (a and b are the minor and major half-axes of the ellipses).

Figure 3 shows an optimized configuration of moderate shear given by 69 individual fields where the high-order harmonics are relatively small ($M = 5$ field periods, magnetic well $\Delta V'/V'_{ax} = -0.6\%$, $A = 11.8$, $\iota_{ax} = 0.65$, $\iota_b = 1.0$, $\langle|j_{||}|/|j_{\perp}|\rangle = 0.59$ at the boundary). Figure 4 shows the X-point angle along an X-point field line.

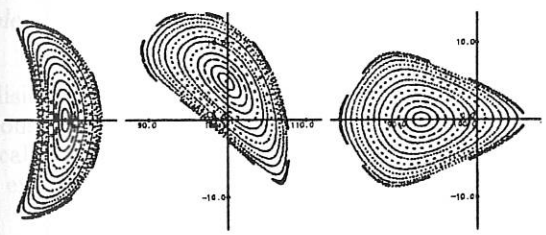

FIG. 3: Poincaré plot of an optimized configuration given by 69 Dommaschk potentials.

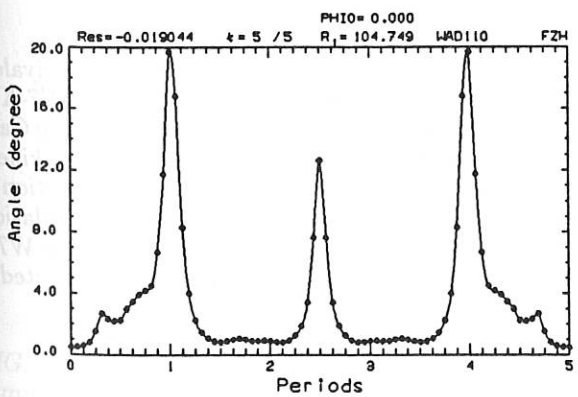

FIG. 4: X-point angle along the X-point field line.

2.1.2 *Quasi-helically symmetric stellarators*

A computational realization of quasi-helically symmetric stellarators with 4 periods and rather low aspect ratio is shown in Fig. 5. α-particles launched at aspect ratio 40 (corresponding to $\frac{1}{5}$ of the minor radius) and 20 are well confined; see Sec. 2.3.

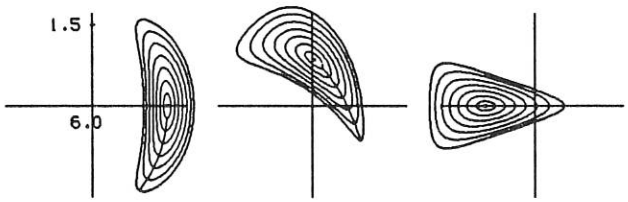

FIG. 5: An approximation to quasi-helical symmetry with 4 periods and rather low aspect ratio. The magnetic well is approximately marginal and the largest symmetry-breaking Fourier components of B in magnetic coordinates are $B_{0,1}$ and $B_{3,2}$ with $B_{0,1}/B_{0,0} \approx 0.044$ and $B_{3,2}/B_{0,0} \approx -0.03$ at the boundary.

2.2 Coil Optimizations

Coil optimizations are of particular importance for finding the lower limit on the number of coils per period, which is governed by the ripple induced by the coils, and for providing sufficient space for divertor experimentation.

2.2.1 *Coil ripple*

A systematic study on the minimum number of coils for W7-X was performed by coil optimizations with the particular goal of lowering the coil ripple for a given number of coils. Figure 6 shows the results, which indicate exponential decrease of the ripple on the magnetic axis with the number of coils. As a result, 8 coils per period will probably be the lower limit.

2.2.2 *Space for divertor experimentation*

Coil optimizations with the help of the NESCOIL code optimize the shape of the current-carrying surface under the constraints that this surface be sufficiently distant and the current lines have sufficiently large radius of curvature. The optimizations lead to the conclusion that the poloidal positions of the smallest distances encountered do not coincide with the poloidal position of the helical edge characteristic of Helias configurations

(see Secs. 2.1 and 2.6). Figure 7 illustrates this result in the low-curvature triangular cross-section.

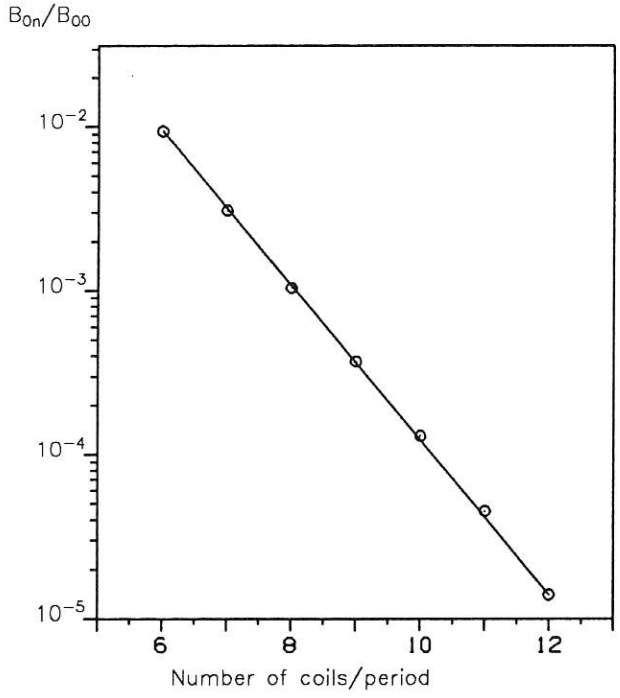

FIG. 6: The principal ripple component $B_{0,n}$ on the magnetic axis versus the number n of modular coils per period in an optimized coil configuration.

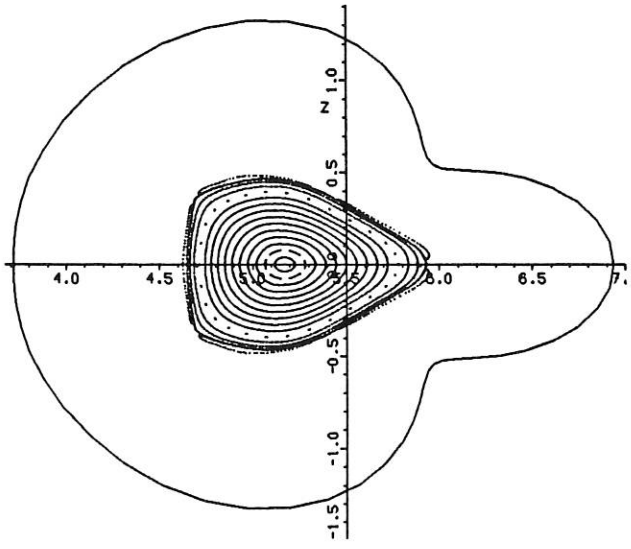

FIG. 7: Cross-section of magnetic surfaces for the Helias vacuum field obtained with a coil system of 8 coils per period which was optimized for low coil ripple and sufficient space for divertor experimentation.

2.3 Guiding Centre Physics Applications

2.3.1 Equivalent ripple calculations

Monte Carlo simulations of neoclassical transport do not need any assumptions on the structure of B in magnetic coordinates and have played an important role in calibrating other approaches such as DKES calculations and methods using the bounce-averaged kinetic equation. Good coincidence between these various approaches has been established in calculating the equivalent ripple as a measure of electron $\frac{1}{\nu}$ transport; see Fig. 8.

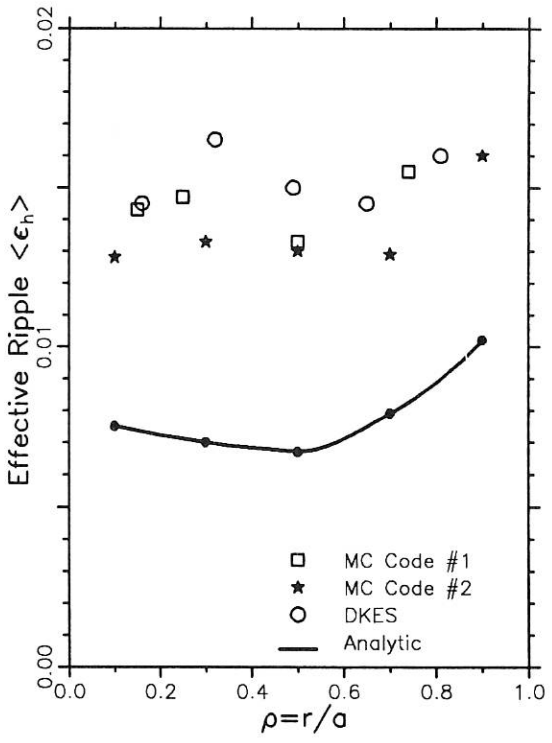

FIG. 8: The radial dependence of the equivalent ripple for case 1 of the HS5V10C coil system W7-X as determined by two different guiding-centre Monte Carlo simulations, a numerical solution of the drift-kinetic equation (DKES) and from an analytical solution of the kinetic equation. The three numerical simulations are able to account for the full complexity of the W7-X magnetic field, while the analytic theory is restricted to the lowest (0 and 1) poloidal harmonics.

2.3.2 Collisionless α losses

A simple method for assessing the collisionless α-particle confinement in general stellarator configurations[4]

was applied for determining the influence of the coil ripple of optimized coil configurations on α-particle confinement in the basic configuration for W7-X. The cases with 7 and 8 coils, for which results are shown in Fig. 9, are characterized by the following values of main coil ripple on axis $(B_{0,n}/B_{0,0})(0)$ and at the boundary $(B_{0,n}/B_{0,0})(1)$: 0.0047/0.015 and 0.0016/0.0072, respectively. For comparison see also Fig. 6.

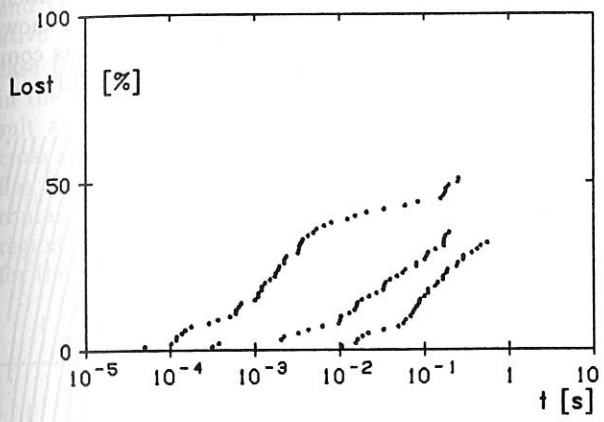

FIG. 9: Collisionless α losses in an optimized Helias configuration realized with optimized coil configurations with 7 and 8 coils. The third result with the best confinement is the 8-coil case with suppressed modular ripple. $\langle\beta\rangle = 0.046$.

Collisionless α-particle confinement was also studied in various examples of computational realizations of quasi-helically symmetric configurations. Figure 10 shows two examples with 4 periods.

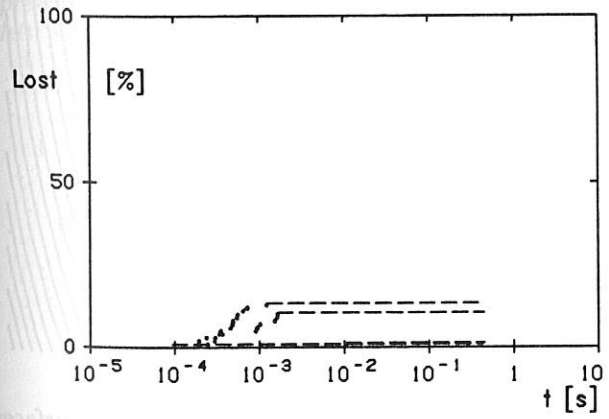

FIG. 10: Collisionless α losses in quasi-helically symmetric configurations ($\beta = 0$) with 4 periods and two different aspect ratios, the case shown in Fig. 5 and one with formal aspect ratio 8. α-particles are started at aspect ratio 40 (negligible losses) and 20 (losses about 10 %) and show good collisionless confinement.

2.3.3 *Barely passing particles*

The characteristic of the drift surfaces of barely passing particles is a qualitative measure of the bootstrap current /33/[7]: particles from regions with different densities contribute to the parallel current density. For easy visualization barely passing α-particles were used which – at the same time – characterize α-particle maximum banana widths. Figures 11 show drift surfaces at various plasma radii for axisymmetric (bootstrap current increasing the rotational transform), quasi-helical symmetry (b.c. decreasing the rotational transform), W7-AS, and the optimized Helias configurations.

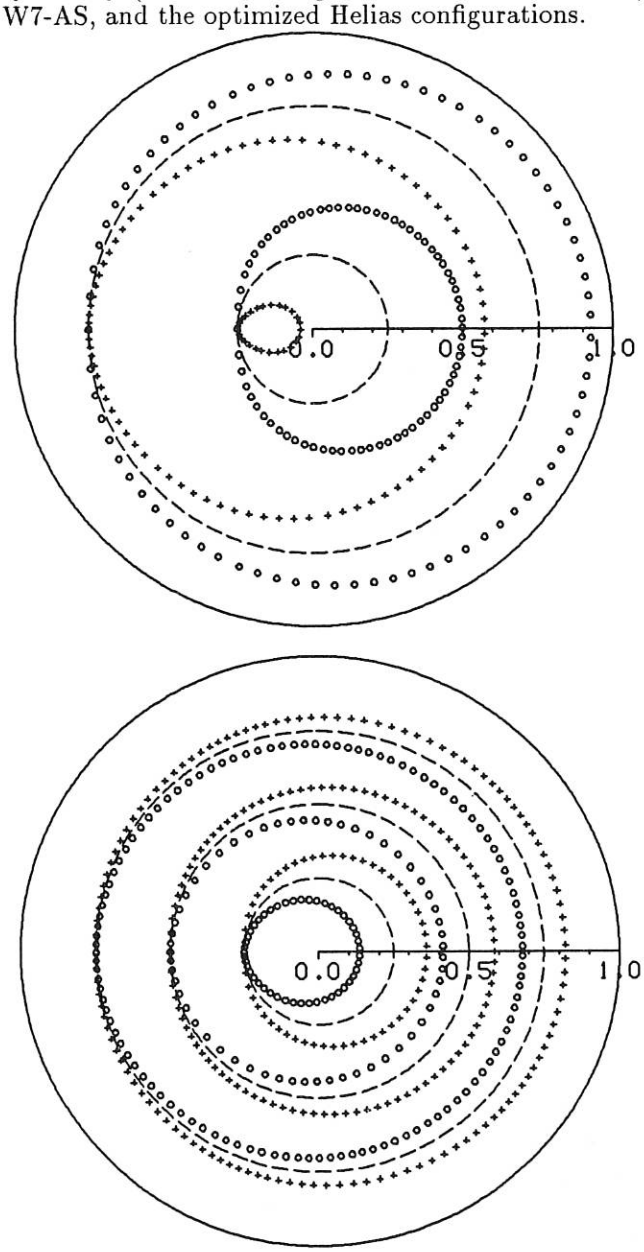

[7] Lotz, W., Third Workshop on Wendelstein 7-X, IPP 2/302 (1989) 31

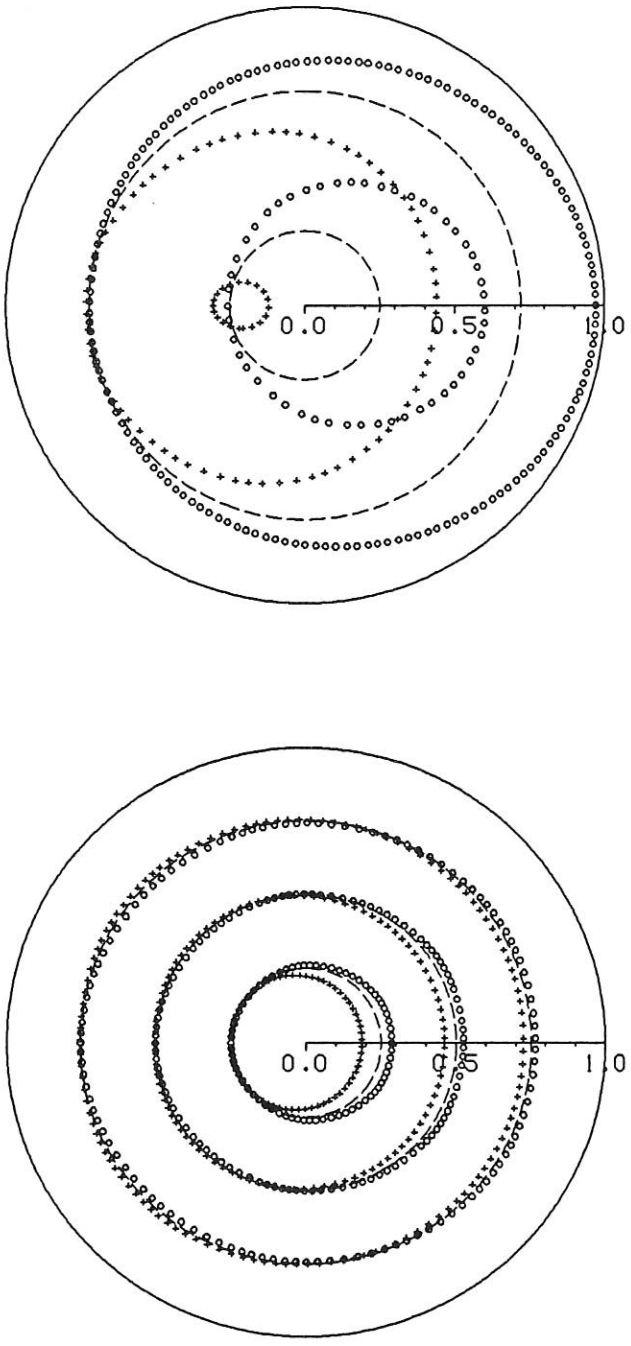

FIG. 11: Drift surfaces of barely passing α-particles in magnetic coordinates at $\frac{1}{4}$, ($\frac{1}{2}$), and $\frac{3}{4}$ of the plasma radius (dashed lines) in axisymmetry, quasi-helical symmetry, W7-AS, and the optimized Helias configuration. Crosses indicate motion into the plane, circles into the opposite direction. Note the change in sign of the deviations of the drift surfaces from the start surfaces between the axisymmetric and the quasi-helically symmetric cases.

2.4 MHD Equilibrium Calculations and Diagnostics

2.4.1 NEMEC validation

A major improvement in speed of convergence of the VMEC equilibrium code[8] was obtained in 1989/90. Incorporation of this new VMEC version into the NEMEC free-boundary code leads to a significant improvement in computing free-boundary equilibria. Figure 12 shows a cutout from a zero-β calculation for W7-AS as compared with the Poincaré plot of the vacuum field.

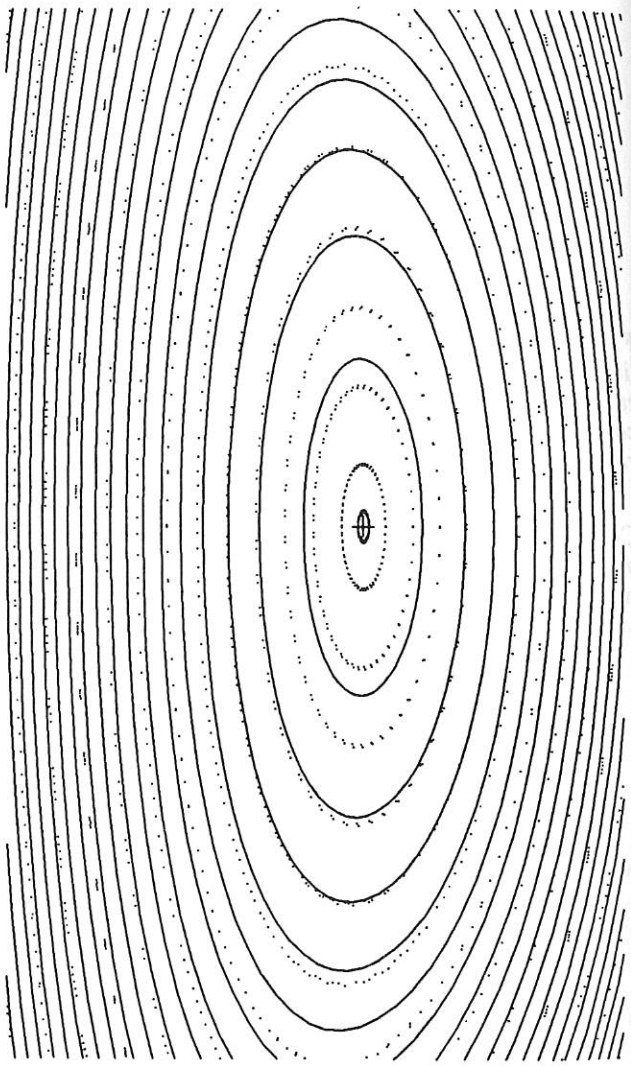

FIG. 12: Zero-β NEMEC equilibrium flux surfaces (solid lines) and Poincaré plot of the W7-AS vacuum field; (+) indicates the position of the magnetic axis obtained with NEMEC.

[8] Hirshman, S.P., Betancourt, O., to appear in J. of Comput. Physics

2.4.2 *Equilibrium diagnostics*

Previous work with the NEMEC/DIAGNO package /87/ was continued, and improved accuracy in computing the response of the diagnostic coils in W7-AS was obtained. Convergence tests showed the number M of Fourier coefficients in the poloidal direction to be critical: $M \gtrsim 12$ is needed for convergence. A typical run now takes $5 \cdot 10^3$ s and 2.7 MW (CRAY-XMP) and yields diagnostic coil responses with 5 – 10 % relative error. Figure 13 shows results for the standard case ($\iota \approx 0.39$) and a larger value of ι ($\frac{1}{2} \leq \iota \leq \frac{5}{9}$ in the vacuum field). Figure 14 shows the finite-β result at $\langle\beta\rangle = 0.009$ at the position of the triangular cross-section. The peculiar "clamped" behaviour of the flux surfaces is due to the W7-AS coil system, which contains nearly toroidally oriented coil segments in this region. This structural detail also offers an explanation for the slow convergence with M.

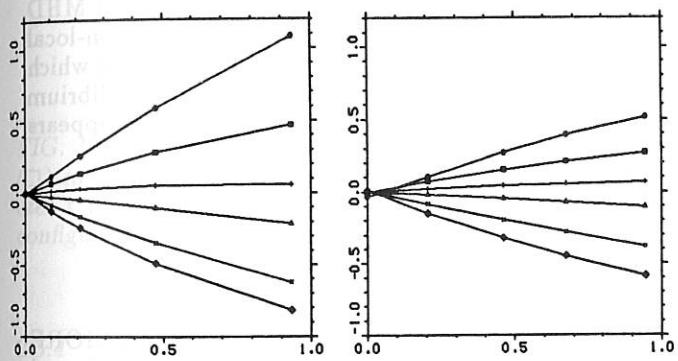

FIG. 13: Responses (B_θ in 10^{-2} T) of the diagnostic coils of W7-AS versus $\langle\beta\rangle$ (in %) for bell-shaped pressure profile and zero net toroidal current $J \equiv 0$; left: standard case, right: $\iota_0 \approx 0.5$.

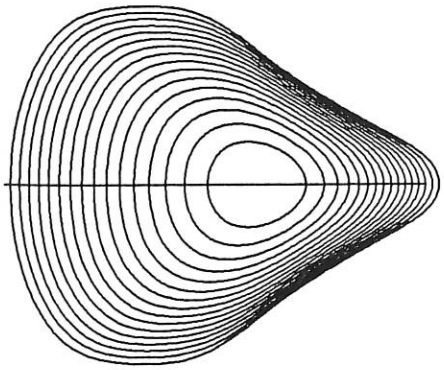

FIG. 14: Finite-β ($\langle\beta\rangle = 0.009$) flux surfaces of free-boundary W7-AS equilibrium in the triangular cross-section.

2.5 MHD Stability Studies

2.5.1 *Local ballooning including coil ripple*

Realization of stellarators with modular coils influences not only their equivalent ripple but also the local field line curvature, which influences ballooning stability. Therefore it has to be verified that this additional, often destabilizing influence is sufficiently small if the number of optimized modular coils is large enough. The example shown in Fig. 15 was obtained with 10 coils, leading to $B_{0,10}(0) \approx 0.001$ and $B_{0,10}(1) \approx 0.01$ (for comparison see also Sec.2.2.1). These ripple values are sufficiently small because the equilibrium is stable at $\langle\beta\rangle = 0.047$.

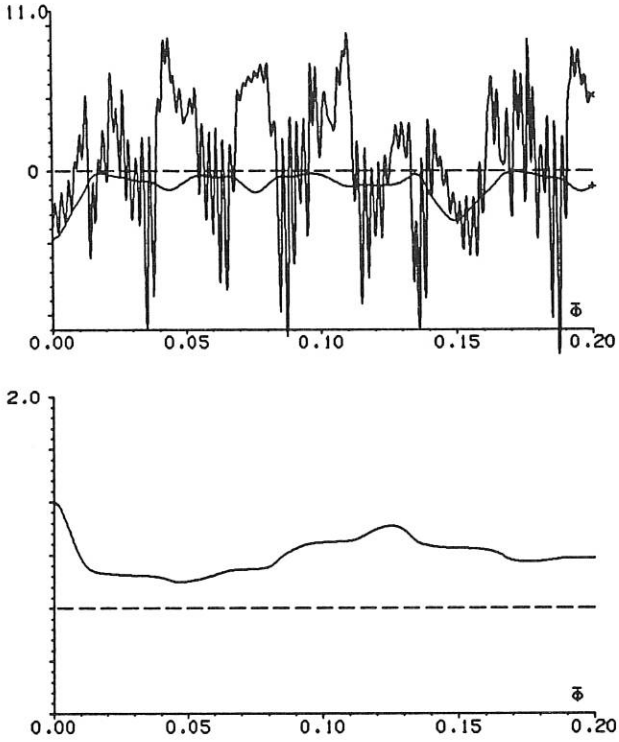

FIG. 15: The upper part of the figure shows the strongly oscillating field line curvature term and the field line bending term; the lower part of the figure the ballooning solution (indicating positive stability) along a field line. Shown is a little more than one poloidal transition; the next shorter length scale is given by the period, the shortest one by the ten modular coils. The rational value of ι considered is $\frac{7}{8}$ and occurs at 0.9 of the plasma radius.

2.5.2 *Ideal internal modes*

New steps in the development of the CAS3D Finite-Element Fourier code for global ideal MHD stability

calculations were initiated by investigating ballooning-type structures. They led to the improved code version, CAS3D1MNint[4], which comprises the following aspects. The basis is formed by an energy principle in which a rapidly varying phase factor has been extracted from the perturbation functions, so that structures with a high toroidal node number N can be investigated without need of the large amount of storage and computing otherwise required. In the incompressible case it was demonstrated with CAS3D2 that the minimizing mode is connected to vanishing field line compression, so that the two scalar components of the perturbation vector that lie within the magnetic surfaces can be eliminated from the energy functional. Thus the discrete problem is reduced to determining the third component, ξ^s. The investigation of high-shear configurations was considerably facilitated by implementing an integration-by-parts procedure that eliminates numerically destabilizing contributions to the energy integral that can occur at rational surfaces.

The transition of unstable modes from the ballooning-type structure to Mercier-type behaviour was demonstrated in a series of 3D equilibria ($N_P = 5$, $A = 10$, $\langle\beta\rangle = 0.02$ to 0.056) which connects a Mercier stable case and a Mercier unstable Helias equilibrium.

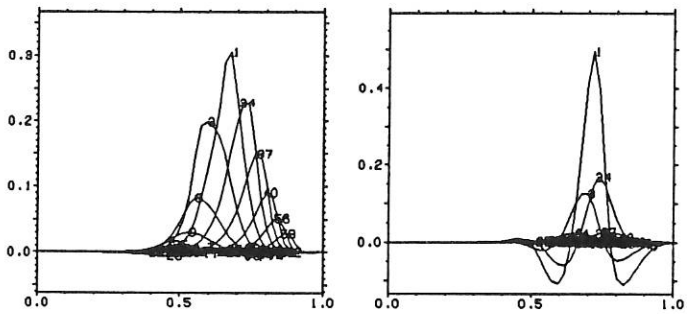

FIG. 16: Fourier coefficients of ξ^s as obtained from CAS3D1MNint. The toroidal node number is $N = 18$ and the mode is resonant at $\iota_R = 3/4$; left: 3D tokamak-type equilibrium, right: Mercier unstable Helias equilibrium.

In the Mercier stable moderately negative-shear configuration the minimizing mode is of the ballooning-type, which means that it has a radially extended structure with sidebands of competing amplitudes that are connected to the resonant component (label 1 in Fig. 16) by toroidal effects. In a low-shear Helias configuration near the Mercier marginal point the same mode, however, localizes radially and the Fourier content is dominated by the resonant component. This is characteristic of a Mercier-type structure.

A second example of mode-transformation behaviour is seen in Fig. 17: in a situation with fixed small positive shear the ballooning character of the modes becomes more prominent with increasing node number.

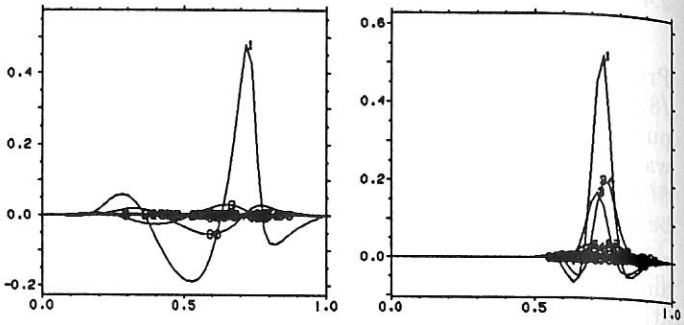

FIG. 17: Same as Fig. 16; Mercier unstable Helias equilibrium; left: toroidal node number $N = 3$; right: $N = 36$.

Parameter studies in sets of 5-period Helias configurations ($A = 10$, small shear ι-profile) – see also Sec. 2.5.3 – and various series of high shear tokamak equilibria ($A = 4.6$ to 10) show that for the fixed-boundary case a strong correlation exists between local stability criteria (Mercier and ballooning) and the non-local MHD mode analysis, and that the development of non-local mode stability codes has progressed to a stage in which the stability analysis of a given stellerator equilibrium with the exclusive use of non-local eigenmodes appears to become feasible.

2.5.3 Ideal external modes

The 3D ideal MHD stability code, TERPSICHORE /221/[9], was used for investigating global external modes in a stability study directly aimed at the behaviour of the W7-X basic configuration[10]. Eigenvalues of modes were obtained for a sequence of equilibria with $\iota \lesssim 1$ connecting unstable $\ell = 1$, 2 equilibria with the W7-X configuration at a fixed value of $\langle\beta\rangle = 0.045$. In this situation an important question is whether the mode behaviour will be dominated by the nearby resonance $\iota = 1$. This is not the case, since it turns out that a predominantly $(m, n) = (10, 9)$ (corresponding to $\iota \approx 0.9$) mode yields the lowest eigenvalues and is purely internal in mode structure. This fact is most clearly demonstrated by comparing the marginal points obtained from the internal modes studied with CAS3D1MNint and the external modes studied with TERPSICHORE; see Fig. 18.

---

[9] Anderson, D.V., Cooper, W.A., Gruber, R., Merazzi, S., Schwenn, U., The Int. J. of Supercomputer Applications, **4**, No. 3 (1990) 34

[10] Cooper, W.A., Fu, G.Y., Schwab, C., Schwenn, U., Gruber, R., Merazzi, S., Anderson, D.V., Proc. 13th Int. Conf. on Plasma Physics and Contr. Nuclear Fusion Res., Washington 1990, paper IAEA-CN-53/C-IV-20

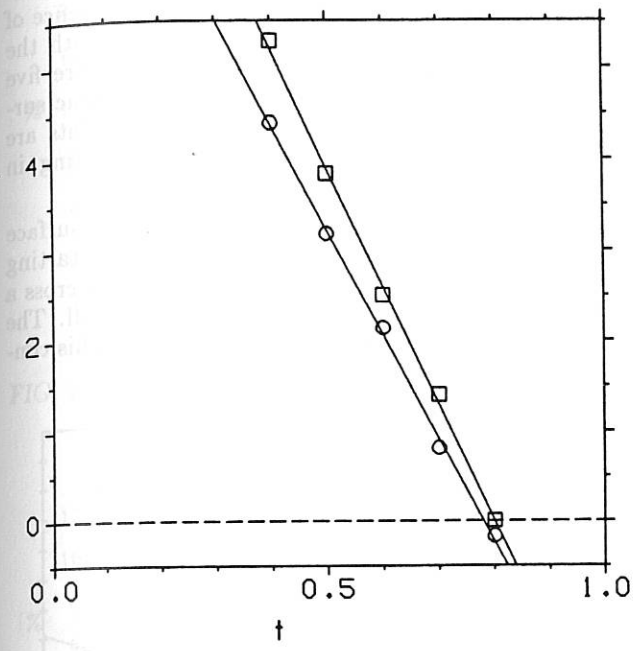

FIG. 18: Eigenvalues of internal (o) and external (□) modes in arbitrary units versus sequence parameter t in a series of unstable equilibria (t = 1 W7-X configuration).

2.5.4 *Benchmarks with TERPSICHORE and VMEC*

The TERPSICHORE code was used to benchmark various supercomputers. From the beginning the code was developed to achieve highest possible vectorization and parallelization (||).[9] Typical results are summarized in Table 1.

The code has also been successfully implemented on an INTEL ipsc2 hypercube, demonstrating a parallelization of 90 % on an 8-processor system. A simulation of the compiled code for a Kendall Square Research parallel system with 120 processors reached the CRAY-YMP/8 performance.

The VMEC equilibrium code was used to compare modern workstations with supercomputers. Table 2 gives representative results for a SUN-Sparc, an IBM-Risc 6000-520, the XMP and the YMP.

Code	Computer	CPU (s)	Mflop/s	||	
original	XMP		100	1	1)
original	CRAY-2		130	1	1)
MXM	XMP		180	1	2)
MXM	CRAY-2		300	1	2)
original	YMP8/8	157	189	1	3)
MXM	YMP8/8	137	255	1	3)
MXM	YMP8/8	20.4	1708	7.35	3)
MXM	VP400		452	1	
MXM	S400		1001	1	4)
original	SX3/12		1100	1	5)
free-boundary	YMP8/8	545	294	1	6)
free-boundary	YMP8/8	83	1930	7.45	

TABLE 1: Execution times and Mflop/s rates obtained with TERPSICHORE on various supercomputers:
1) the original version is completely written in FORTRAN 77;
2) the MXM version is based on matrix multiply modules provided by the companies;
3) this application won the 1989 CRAY Gigaflop performance award;
4) the difference between the Fujitsu/Siemens systems VP400 and S400 is due to a new efficient MXM implementation and the 4 nsec cycle time of the S400;
5) the NEC machine SX3/12 had one processor with 2 add and 2 multiply pipes and 2.9 nsec cycle time;
6) the free-boundary version allowed a further improved performance.

Computer	CPU (s)	Mflop/s	ratio	ratio	
SUN	–	1	125	204	1)
IBMR	2110	8	15.4	25.2	
XMP	163	105	1.2	1.97	2)
XMP	137	125	1	1.64	3)
YMP	82	209	0.61	1	3)

TABLE 2: Execution times and Mflop/s obtained with VMEC on workstations and supercomputers:
1) extrapolated from smaller cases;
2) CFT 1.15 compiler;
3) CFT77 compiler.

2.5.5 *Non-ideal stability*

The Braginskii two-fluid equations in the limit of negligible electron inertia and electron gyro-viscosity are used to study the finite-gyro-radius modification of ballooning modes in 3D configurations. Modes localized on a particular magnetic field line are studied in the low-frequency and vanishing-$E_{||}$ limits. The complete set of equations is then given by the two continuity and the two momentum equations supplemented by Maxwell's equations. Energy equations are not needed because the pressure response is completely determined ($\vec{B} \cdot \nabla p_e = 0$ and – in the low-frequency limit – $\vec{B} \cdot \nabla p_i = 0$). Exploiting the cancellation valid for large aspect ratio between the perpendicular inertia term and the gyro-viscous stress in the ion momentum equation, one obtains an eigenvalue equation for the displacement of magnetic field lines containing the frequency shift $\omega^2 \rightarrow \omega(\omega - \omega_{*i}^T)$ (with $\omega_{*i}^T = \vec{v}_{\nabla p_i} \cdot \vec{k}_\perp$, where $\vec{v}_{\nabla p_i}$ is the ion diamagnetic velocity) as the only modification with respect to ideal MHD theory. Thus, a variational principle is constructed which reads

$$\frac{1}{2} \int \rho\omega(\omega - \omega_{*i}^T)\xi_\perp^2 \, \mathrm{d}\tau = \delta W_{MHD}$$

where δW_{MHD} is the ideal MHD energy integral without the $\gamma p(\nabla \cdot \vec{\xi})^2$ term. Introducing the ballooning mode representation[11] one can obtain the eigenvalue equation governing the ballooning modes in 3D configurations from this variational principle:

$$\frac{\mathrm{d}}{\mathrm{d}\phi}\left\{a^{-1}[1 + (\bar{\sigma}\phi + \tilde{\sigma})^2]\frac{\mathrm{d}F}{\mathrm{d}\phi}\right\} + (\bar{D}\phi + \tilde{D})F$$
$$+ C_{\rho_i}\left(\frac{\sqrt{g}}{V'}\right)^2 \left\{a^{-1}[1 + (\bar{\sigma}\phi + \tilde{\sigma})^2]\right\} F = 0$$

with $C_{\rho_i} = \mathcal{O}[\beta N^2 \left(\frac{\rho_i}{a}\right)^2]$ and N the (large) node number and $\frac{\rho_i}{a}$ the ratio of ion gyro-radius to plasma radius.

2.6 Divertor Considerations in Helias Configurations

2.6.1 *Field line diversion in Helias configurations*

The vacuum magnetic field outside the last closed magnetic surface of Helias configurations is investigated with respect to its field line diversion properties. In a Helias configuration with N periods N half-helix like edges run on the toroidally outward side of the plasma boundary (see Sec. 2.1.1, Fig. 1) and show the possibility of separatrix formation due to the coincidence of helical edge and X-points between islands. With the choice $\iota = 1$ at the plasma boundary, there are five magnetic islands outside the last closed magnetic surface. In the case considered in Fig. 19, X-points are located in front of the helical edge at the beginning, in the middle and at the end of this edge.

With a homogeneous distribution of points on a surface outside, but very close to, the plasma surface as starting points, magnetic field lines are traced until they cross a given control surface located inside the first wall. The pattern that the intersection points create on this control surface is shown in Fig. 19.

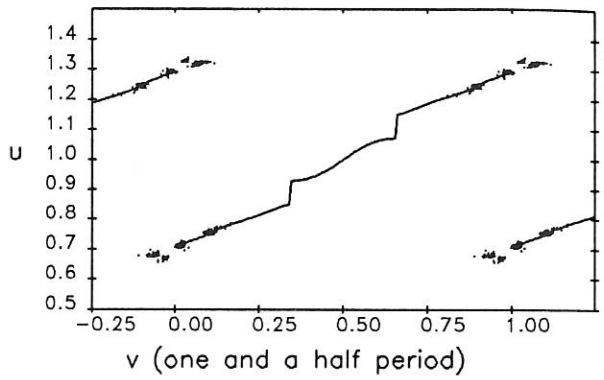

FIG. 19: Intersection pattern in u (poloidal), v (toroidal) coordinates. The solid line marks the position of the helical edge for one and a half period. The distance between plasma and control surface is approximately 10 % of the plasma radius.

The intersection points are concentrated close to the helical edge in those torus segments where an X-point lies in front of the helical edge. That is, X-points located outside the plasma surface in the region of the helical edge are positions where the field lines are diverted. The intersection points cover an area of $\lesssim 1\%$ of the control surface.

Figure 20 shows the statistics of the number of toroidal transitions of the magnetic field lines before they cross the control surface. With the average length of one transit given by ≈ 35 m ($R_0 = 5.5$ m), the mean length of the magnetic field line in this example is then given by $\langle L \rangle \approx 100$ m.

In addition, the intersection angle Ψ_{con} is determined (Fig. 21), which is the angle between the control surface and the magnetic field line at the intersection point. In this case, one obtains an average value of $\langle \Psi_{con} \rangle \approx 1.5^o$. This small angle is a consequence of the choice of the control surface, which is readily obtained from a natural coordinate system in the space between the last closed flux surface and the surface on which the coils generating the configuration are located.

[11] Correa-Restrepo, D., Z. Naturforsch. **33a** (1978) 789

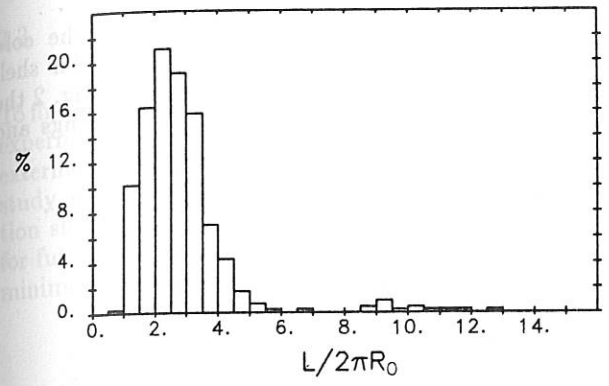

FIG. 20: Number of toroidal transitions.

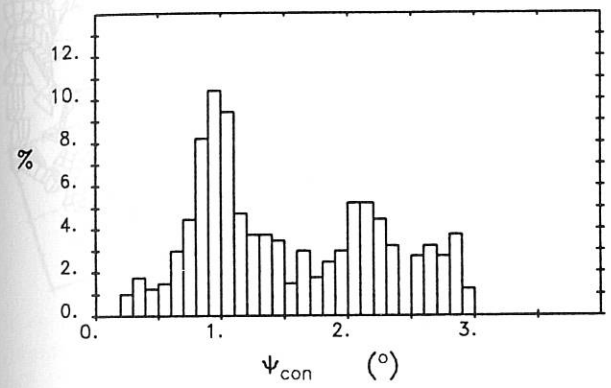

FIG. 21: Intersection angle.

Further calculations were concerned with the dependence of the intersection patterns, number of toroidal transitions, and the intersection angle on the phase of the island structure and on the distance between the plasma and control surface. Results similar to the above were obtained.

2.6.2 *SOL considerations*

The standard assumptions of SOL modelling that cross-field transport is anomalous and of order 1 m^2/s and that a characteristic velocity along field lines is the sound speed can be used for a very simplified SOL simulation with appropriately chosen "diffusion" of field lines which is achieved by random displacements during field line tracing after characteristic mean free paths ($\ll R_0$). A result is shown in Fig. 22. This exhibits a SOL thickness of approximately 2 cm, the persistence of the diversion process at the helical edge, the blurring of detailed island structures, and, consequently, the increase in plasma-control surface interaction area by approximately an order of magnitude.

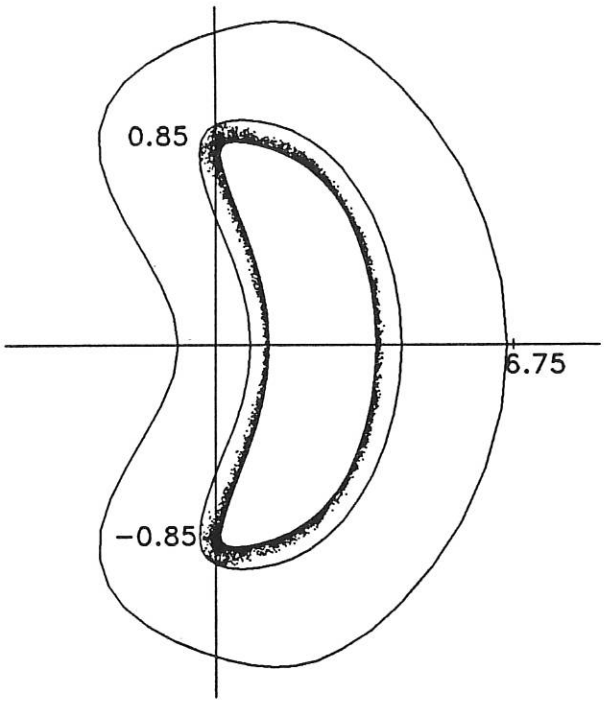

FIG. 22: SOL simulation with a field line "diffusion" model.

3. W7-X TECHNICAL STUDIES

F. Kerl[1], T. v. Larcher[1], H. Münch, J. Sapper, I. Schoenewolf

3.1 Outline

Three essential items for the engineering design of W7-X could be treated in 1990:

a) the overall design of the basic device

b) the specification of the civil engineering work

c) a more detailed layout of the prototype work and strategy together with KfK, Dept. ITP.

Applications for preferential support were worked out: one for the prototype activities (phases I and II) and another for the technical design of the whole experiment (phase I). The examination of the prototype activities took place in autumn 1990 and preferential support was granted by the Community. Except for a small sum for the beginning of the conductor development, the further support is linked to successful phase I assessment of the basic machine.

3.2 Basic machine design

For the basic machine (W7-X proper) a CAD assembly was worked out. It is shown in Fig. 1.

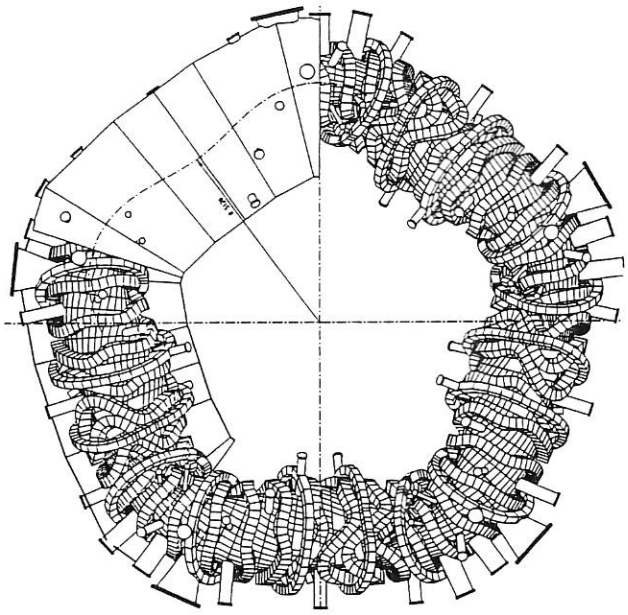

FIG. 1: Overall assembly of W7-X.

[1] from ZTE/ZK

Furthermore, a first improved planning for the cold structure was carried out, the idea of a tubular shell around the coil casings being abandoned. In Fig. 2 the integral vault design composed of the coil casings and intermediate support elements is shown.

In Table 1 the list of cold masses is presented.

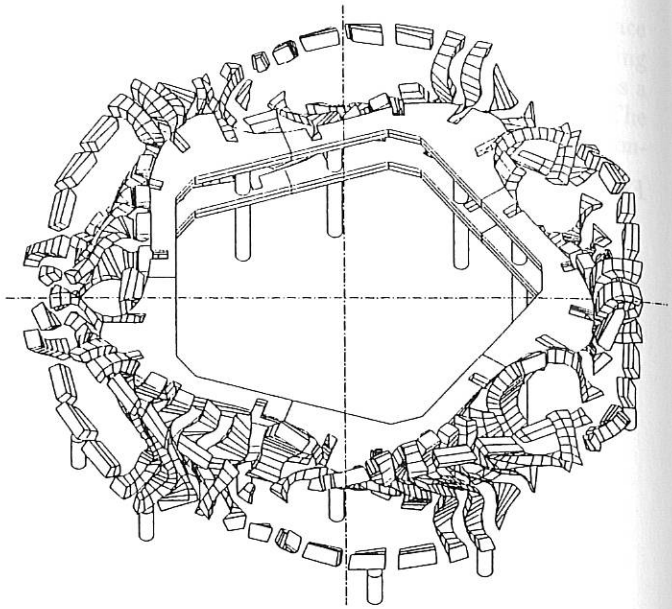

FIG. 2: Cold structure of W7-X.

Components	Mass (ton)
Coils (Al conduct.)	72
Coil housings	120
Structure	160
Inner vessel	25
Cryostat	
Outer vessel	60
Ports and ducts	17
80 K shield	15
Current distribution	12
Auxiliaries	15

TABLE 1: Mass list for the magnet system.

3.3 Civil engineering work

To find a detailed basis for the specification of the whole experimental plant, comprising all buildings also for external heating equipment and further auxiliaries, a study with four consultants was executed. The solution shown in Fig. 3 was found and is to be the basis for future planning. It was tailored to the condition of minimum space requirements.

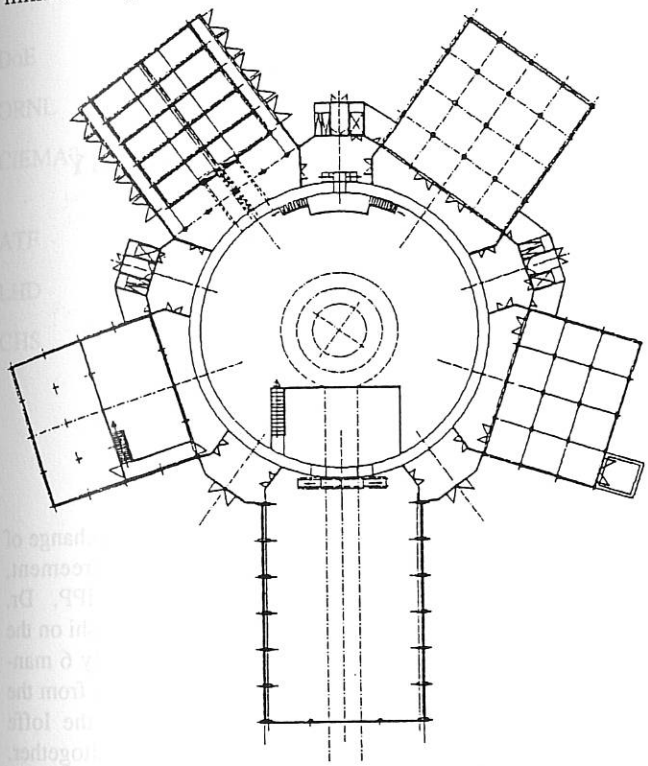

FIG. 3: W7-X buildings (proposal). Inner torus hall diameter = 34 m.

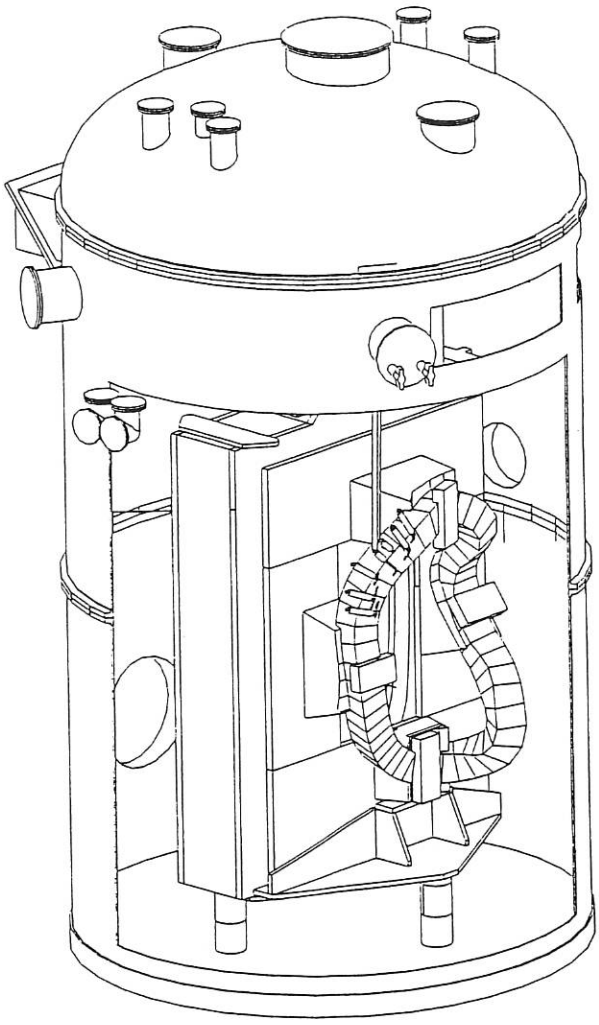

FIG. 4: TOSKA plant with Demo Coil.

3.4 Prototype work

The prototype development for W7-X will start with the procurement of a 200 m test length for the superconducting cable. A call for tender was issued in December 1990.

The cable will be wound to a cylindrical test coil to be tested electrically, magnetically and hydraulically in the STAR test bed at KfK up to the nominal data for the experimental requirements in W7-X. Then the next step can be the procurement of the prototype conductor length of 1,500 m for the "Demonstration Coil". This coil is to be tested in the TOSKA plant at KfK, as shown in Fig. 4, beyond the parameters of the normal performance of W7-X. Procurement and assembly of these components depend on phase-I approval for W7-X.

IEA IMPLEMENTING AGREEMENT
for Cooperation in Development of the Stellarator Concept
EUROPEAN ATOMIC ENERGY COMMUNITY / US DEPARTMENT OF ENERGY

1. OBJECTIVES OF THE AGREEMENT

The Implementing Agreement was first concluded in 1985 with the objective to "improve the physics base of the Stellarator concept and to enhance the effectiveness and productivity of research and development efforts related to the Stellarator concept by strengthening co-operation among Agency member countries". To achieve this, it was agreed to exchange information, conduct workshops, exchange scientists, do joint theoretical, design and system studies, coordinate experimental programmes in selected areas, exchange computer codes, and perform joint experiments. The Agreement was extended for a further five years from August 1, 1990. The contracting parties are EURATOM and the U.S. DoE. Japan having been an 'active observer' (i.e. on the working level a participant) from the beginning on plans to join the Implementing Agreement, but there are still some minor difficulties to be overcome. Also, Australia is making inquiries about the conditions for joining the Agreement.

2. STATUS OF THE AGREEMENT

In 1990, there were two meetings of the Executive Committee, the first at IPP, Garching, on July 2, 1990, the second at ORNL, Oak Ridge, on October 8, 1990. One main topic of these meetings was the pending membership of Japan. Besides this, the progress of the collaboration was reviewed and the further scientific programme discussed including the assignment of personnel.

3. REPORT ON 1990 ACTIVITIES

During 1990 fifteen physicists participated in the exchange of personnel. Within the framework of the Agreement, T. Mizuuchi and H. Zushi from Kyoto, stayed at IPP. Dr. Mizuuchi worked on plasma-wall interaction, Dr. Zushi on the energy balance. Their joint effort amounted to nearly 6 man-months. From the USSR, N. Bezedin and A. Gutarev from the Kharkov Institute as well as V. Afanasiev from the Ioffe Institute, Leningrad, worked at IPP for 5 months altogether. Besides the visits to IPP, a group of scientists from CIEMAT and also some Russian scientists worked on ATF (ORNL) mainly on fluctuation studies, global energy balance studies, and MHD issues. A regular review of the status of the various experiments is given in the 'Stellarator News', published every two months. The experimental results of W 7-AS are described in detail in the section "WENDELSTEIN 7-AS" of this annual report and the status of the planning for W 7-X is given in section "WENDELSTEIN 7-X Project".

4. WORKSHOPS

There were two workshops held in 1990. The first took place at Garching from July 2 - 6, 1990. The main topics of this workshop were: status of the experiments, confinement including turbulence, bootstrap currents, and thermal collapse with the emphasis on experimental results and their comparison with the theory. The second workshop on "Future Large Devices" was held at Oak Ridge on October 8-9, 1990. It was the third workshop on this subject. About 25 participants from the USA, Japan, FRG, Spain, Australia, and Switzerland presented papers on the physics and engineering optimization of the large next-generation stellarators, W 7-X and LHD,

stellarator reactor studies, and relevant research on present experiments (W 7-AS, CHS, AFT, Heliotron-E). For 1991, the eighth workshop on stellarators has been announced for May (27-31). It will be hosted by the Kharkov Institute.

Abbreviations

DoE	=	Department of Energy
ORNL	=	Oak Ridge National Laboratory
CIEMAT	=	Centro de Investigación Energetica Medio-Ambiental Technologíca
ATF	=	Advanced Toroidal Facility
LHD	=	Large Helical Device
CHS	=	Compact Helical System

Divisions and Groups

THE SCIENTIFIC DIVISIONS OF IPP

Experimental Plasma Physics Division 1
Director: Prof. M. Kaufmann

ASDEX Upgrade
- follow-up to the ASDEX experiment for investigating the ITER/NET divertor and a reactor relevant plasma boundary
- investigation of the magnetics of an ITER-type plasma

JET diagnostics
- operation of diagnostics at JET

Experimental Plasma Physics Division 2
Director: Dr. G. Grieger

Wendelstein 7-X
- numerical and analytical methods of investigating equilibrium, stability and transport in three-dimensional toroidal configurations incl. plasma heating, particle and power exhaust
- elaboration of concept
- engineering

Contributions to stellarator reactor systems studies

Contributions to ITER/NET studies

Experimental Plasma Physics Division 3

Director: Dr. F. Wagner

Wendelstein 7-AS (Advanced Stellarator)
- Stellarator with improved confinement conditions
- toroidal plasma confinement in the Stellarator
- net-current-free plasmas, plasma production and heating by neutral injection, and high-frequency waves
- plasma stability and impurity effects

ASDEX
- tokamak experiment with axisymmetric divertor and auxiliary heating
  in detail: energy confinement, impurity production and transport, ß-, density-, and q-limits with neutral injection, ion cyclotron heating and lower hybrid
- comparative studies of different heating and refuelling techniques

Theory Division
Director: Prof. D. Pfirsch

Theoretical basis of plasma physics
- analytical and numerical MHD computations
- models for anomalous transport
- high-frequency current drive
- turbulence theory

Tokamak Physics
Director: Prof. K. Lackner

Tokamak physics
- experiment-oriented theoretical work for the design and interpretation of tokamak experiments such as ASDEX, ASDEX Upgrade, JET and NET/ITER
- experimental work on plasma edge physics on ASDEX and ASDEX Upgrade

Surface Physics Division
Director: Prof. V. Dose

Surface Physics
- atomistic characterization of surfaces

Plasma Wall Interactions (analytical)
- interactions of atoms, ions and electrons with solid surfaces
- wall fluxes in the boundary layer of plasma devices
- limiter and wall analyses

Plasma Wall Interaction (preparative) (see also Technology Division)
- preparation and characterization of thin film coatings for plasma devices

Technology Division
Director: Prof. R. Wilhelm

Neutral Injection
- development and construction of the injection systems for W7-AS, ASDEX and ASDEX UPGRADE
- implementation of injection experiments

Electron cyclotron resonance heating
- preparation of ECRH for ASDEX Upgrade and W 7-X
- cooperation with ECRH project on W 7-AS

Lower hybrid heating on ASDEX
- operation and evaluation of LH heating and current drive experiments on ASDEX (until 1990)

Ion cyclotron resonance heating
- preparation and implementation of ICRH experiments for W7-AS, ASDEX and ASDEX Upgrade

Plasma technology (see also Surface Physics Division)
- development, characterization and modelling of low pressure plasma processes for thin film formation.

Computer Science Division
Director: Prof. F. Hertweck

Development of the AMOS/2 operating system

Development of data acquisition systems for experiments at IPP

Studies in parallel computer architectures

EXPERIMENTAL PLASMA PHYSICS DIVISION 1

(Prof. Dr. Michael Kaufmann)

Division E1 comprises two groups:

1. ASDEX Upgrade

Head: Köppendörfer W.
Deputy Head: Blaumoser M.

Ahrens P., Aubanel C., Bönisch G., Bönisch J., Bauer H., Bauer A., Behler K., Berger H.J., Berg A., Birkmeier A., Blank H., Bosch H.S., Bruhns H., Buchelt E., Buhler A., Cha S., Dietrich H., Dorn Ch., Drube R., Eberhagen A., Eicher G., Engelhardt W., Ernesti J., Ertl S., Finkelmeyer M., Fuß D., Gehre O., Georgens D., Gernhardt J., Gruber J., Haas G., Haferkamp D., Hartz F., Harnau M., Hauck F., Herppich G., Hermann J., Hohenöcker H., Huber R., Hupfloher H., Jacobi D., Kaplan E., Klement G., Kollotzek H., Kornherr M., Krüger P., Krause A., Krause H., Krieger P., Krippner J., Kudler J., Lackner E., Lindner H., Müller D., Mast K.F., Mattes K., Meisel D., Merkel R., Mertens V., Oswald J., Pachur B., Pillsticker M., Poschenrieder W., Prausner G., Preisser G., Raupp G., Reichert G., Richter H., Richter Th., Sänftl S., Söldner F.X., Salmon N., Schindler K., Schneider H., Schramm G., Schrembs G., Schweitzer U., Schindler K., Schaal J., Schmid E., Schweizer S., Seidel U., Steidl H., Stichs G., Streibl B., Teutsch H.-D., Teufl W., Troppmann M., Ulrich M., Venus G., Vernickel H., Weisbart W., Wendt T., Werner F., Wieczorek A., Wira K., Wirth H., Woyke W., Wunderer F., Zasche D., Zehetbauer T., Zimmermann G., Zohm H.

This group is concerned with the operation of the tokamak experiment ASDEX Upgrade and its peripheral installation. This group also conducts a part of the experimental investigations. ASDEX Upgrade is the follow-up experiment of ASDEX. This work is described under the ASDEX Upgrade project.

2. ASDEX Upgrade Diagnostic

Head: Röhr H.
Deputy Head: Schumacher U.

Andelfinger C., Beck W., Bessenrodt-Weberpals M., Bethmann K., Birkmeier H., Chu C., Cierpka P., Czich H., Drake W., Drechsler W., Eisgruber G., Fahrbach H.U., Feil P., Field A., Fink J., Forster K., Frischmuth H., Fußmann G., Fuchs Ch., Götsch S., Häuser R., Hausmann J., Herrmann W., Herrmann J., Hien M., Huber K., Janeschitz G., Jenichen F., Kölbl G., Kallenbach A., Knauer K.-H., Krieger K., Lang R., Lieder G., Loch R., Maier P., Mayer H.M., Murmann H., Nieder K., Oberlander E., Oswald Jos., Oswald Mat., Oswald Max, Pohl D., Roman A., Sahner K., Salzmann H., Sandmann W., Schneider H.K., Schultheiss E., Schmidtmeier O., Schwaiger M., Schilling H.B., Schmitt G., Seth R.-T., Seth T., Steuer K.H., Stimmelmayr A., Strobl J., Treske M., Weber G., Werber J., Wiesner G., Zisler J., Zölch L.

This group is responsible for the development of plasma diagnostics and pellet injectors for ASDEX Upgrade, JET and other experiments. In addition, plasma physics investigations with these diagnosics are conducted by the group. The activities are detailed under the projects ASDEX Upgrade, JET Cooperation, ASDEX, and W VII-AS.

EXPERIMENTAL PLASMA PHYSICS DIVISION 2

(Dr. Günter Grieger)

The activity of the reorganized Experimental Plasma Physics Division 2 is mainly concentrated on the Wendelstein 7-X Project (see Sec. Wendelstein 7-X Project)

The relevant team is:

W 7-X

C.D. Beidler, W. Dommaschk, G. Grieger, E. Harmeyer, F. Herrnegger, J. Junker, J. Kißlinger, W. Lotz, P. Merkel, H. Münch, J. Nührenberg, F. Rau, E. Rittger, J. Sapper, M. Spada, M. Schlüter, I. Schoenewolf, C. Schwab, U. Schwenn, E. Strumberger, H. Wobig, L. Zheng

Guests: A.H. Boozer[1)], N. Karulin[2)]

---

1) Guest from College of William and Mary, Williamsburg
2) Guest from Kurchatov Institute of Atomic Energy, Moscow

EXPERIMENTAL PLASMA PHYSICS DIVISION 3 (ASDEX)

(Dr. Friedrich Wagner)

Experimental Plasma Physics Division 3 comprises the ASDEX group, the work of which is fully reported in the section "ASDEX Project". The members of this group are as follows:

Head of Project: Dr. Friedrich Wagner
Deputy Head: Dr. Helmut Niedermeyer

R. Aratari, R. Bätzner[4], R. Bartiromo[12], G. Becker, S. Bernabei[9], B. Bomba, H.S. Bosch, R. Büchse[1], T.K. Chu[9], R. De Angelis[12], G. Dodel[3], F. Dollinger[2], A. Eberhagen, M. Endler[1], M. Engelhard[2], W. Engelhardt, G. Fussmann, O. Gehre, K.W.Gentle[11], J. Gernhardt, L. Giannone, G. Haas, T. Hartinger[2], R. Harvey[8], J.V. Hofmann, H. Hohenöcker, E. Holzhauer[3], K. Hübner[4], A. Izvozchikov[5], G. Janeschitz, E. Kakoulidis[6], F. Karger, A. Khoudoleev[5], O. Klüber†, M. Kornherr, M. Krämer[13], K. Krieger[1], J. Kucinski[17], B. Kurzan[2], G. Kyriakakis[6], S.I. Lashkul[5], U. Leinberger[2], G. Lisitano, E. Manso[10], J. Matias[10], H.-M. Mayer, K. McCormick, D. Meisel, E.R.Müller, H. Murmann, H. Niedermeyer, V. Petrzilka[18], J. Qin[14], A. Rudyj, N. Ruhs, F. Schneider, U. Schneider, R. Schubert[1], F. Serra[10], S. Sesnic[9], G. Siller, A. Silva[10], E. Simmet[1], F. Söldner, K.-H.Steuer, J. Stöckel[18], U. Stroth, G. Theimer[2], D. Thomas[8], N. Tsois[6], A. Tucillo[12], K. Ushigusa[15], J. K. Wira[16], B. Wolle[1], H.R.Yang[7], D. Zimmermann

1	Doctoral fellow
2	Undergraduate
3	Guest, University of Stuttgart, FRG
4	Guest, University of Heidelberg, FRG
5	Guest, IOFFE Institute, Leningrad, USSR
6	Guest, Demokritos, Attiki, Greece
7	Guest, Southwestern Institute of Physics, Leshan, China
8	Guest, GA Technologies Inc., San Diego, USA
9	Guest, Princeton University, USA
10	Guest, IST, Lissabon, Portugal
11	Guest, University of Texas, Austin, USA
12	Guest, ENEA, Frascati, Italy
13	Guest, University of Bochum, FRG
14	Guest, Institute of Physics, Beijing, China
15	Guest, Japan Atomic Research, Ibaraki, Japan
16	Guest, University of Washington, USA
17	Guest, Institute for Nuclear Studies, Otwock-Swierk, Poland
18	Guest, Institute of Plasma Physics, Prague, Czechoslovakia
†	03.06.90

THEORY DIVISION

(Prof. Dr. Dieter Pfirsch)

Equilibria, linear and nonlinear instabilities, RF heating, wave propagation in inhomogeneous plasmas, anomalous transport, turbulence and other nonlinear phenomena were studied within the framework of macroscopic and microscopic theories. Addressed were, in particular, the stability of tokamaks with non-circular cross-sections, the structure of separatrix x-points and their stability properties, resistive instabilities of tokamaks, especially nonlinear resistive ballooning modes and nonlinear properties of tearing modes, nonlinear drift waves, self-sustained collisional drift-wave turbulence, and nonlinear instabilities of general equilibria in the framework of Maxwell-collisionless kinetic theories and their relation to the existence of negative-energy perturbations. The studies were done analytically and numerically. The latter implies the development and use of new numerical codes. Also new analytical methods were found.

1. MHD THEORY

1.1 Axisymmetric Stability for Non-circular Cross-section Tokamaks

D. Lortz

The stability of external axisymmetric ideal MHD modes is considered. For a large aspect ratio equilibrium with linear profiles and with the wall infinitely far, it is shown that an arbitrary deviation from the circular cylinder is unstable. This proves a property which, hitherto, has merely been conjectured by several authors.

1.2 Plane Free-boundary Equilibria

D. Lortz

The free-boundary MHD equilibrium is considered for plane symmetry and a constant current profile. The external field is prescribed and the plasma current is determined such that the plasma extends up to the separatrix.

1.3 Plasma Corners

R. Kaiser, D. Lortz, G.O. Spies

Toroidal magnetohydrostatic equilibria are considered with an x-point of the poloidal magnetic field at the plasma-vacuum interface, and with plasmas filling one of the sectors formed by the separatrix. For constant toroidal plasma current densities, the structure of such "plasma corners" depends only on the multiplicity n of the x-point (defined such that the number of sectors is $2n$; simple x-points are thus characterized by $n = 2$, degenerate ones by $n > 2$) and on the orientation of the toroidal plasma current relative to the poloidal magnetic field (termed "ordinary" or "extraordinary", depending on whether it is favourable or unfavourable for confinement). Simple ordinary corners resemble simple x-points in vacuum fields in that all four sector angles are right angles, but differ in that, for small distances r from the x-point, the poloidal magnetic field is $O(r \log r^{-1})$ rather than $O(r)$, and in that the curvature of the separatrix diverges like r^{-1} rather than being bounded. All other corners have a totally different structure: At degenerate ordinary corners the plasma sector angle vanishes (cusped interface) while the vacuum sector angles are $2\pi/(2n-1)$, and at extraordinary corners the plasma sector angle is straight (smooth interface) while the vacuum sector angles are $\pi/(2n-1)$.

1.4 MHD Equilibria with Cusped Plasma-Vacuum Interfaces

R. Kaiser

The free-boundary MHD equilibrium is considered in the case of plane symmetry and constant current profile. We prove the existence of solutions in a neighbourhood of cusp singularities of the plasma-vacuum interface. In both cases – the "plasma" and "vacuum cusps"– we derive a power law describing the asymptotic shape of the cusps; the allowed exponents are half-integers. This leads to a natural classification of cusps. The solutions will be classified accordingly and their asymptotic behaviour close to the cusp is found to depend only on the class to which the solution belongs.

1.5 Plasma Corners and Interchange Instability in Z-pinches

G.O. Spies

Magnetohydrostatic Z-pinch equilibria are considered with plasma-vacuum interfaces containing magnetic stagnation points, thus having corners. The structure of the plasma corners is determined; it depends on the current density profile and the multiplicity of the stagnation point. Plane magnetic fields and special current density profiles are assumed, and a conjectured generalization to arbitrary Z-pinches is formulated. Non-degenerate corners (the stagnation point is a simple x-point) are the only corners of practical interest. Here the corner angle is a right angle, and the magnetic field approaches zero essentially like the distance from the corner, unless the current density diverges at the separatrix like some inverse power of the magnetic flux (in which case the angle is acute or even zero, and the magnetic field approaches zero faster). The interchange stability criterion is always violated at simple corners, regardless of the current density profile, implying that magnetohydrodynamic modes with few nodes remain unstable even if the plasma extends out to the separatrix.

1.6 Study of the Resistive MHD Spectrum of 2D Equilibria

S. Poedts, E. Schwarz, W. Kerner,[1)]
J.P. Goedbloed,[2)] G.T.A. Huysmans[2)]

The ideal and resistive MHD spectra of 2D fusion-relevant toroidal equilibria were investigated by means of the CASTOR normal-mode code (see Annual Report 1989). For this purpose, a new equilibrium code, HELENA, was developed. HELENA (Hermite ELement Equilibrium for Normal-mode Analysis) calculates toroidal equilibria with the use of isoparametric bicubic Hermite finite elements and maps them onto the non-orthogonal flux coordinate system used in CASTOR.

Specific JET discharges have been analyzed and both ideal and resistive instabilities were found. We also studied linear resistive internal modes in tokamak plasmas. At present, various internal modes are under investigation, such as internal kink modes, which are expected to play an important role in sawtooth oscillations, and toroidicity-induced gap modes, which may be efficiently applied to wave heating owing to their global eigenmode structure and can lead to serious instabilities when interacting with energetic α-particles.

1.7 Ideal Quasi-modes Reviewed in Resistive MHD

S. Poedts, E. Schwarz, W. Kerner[1)]

The characteristics of so-called ideal "quasi-modes" or "collective modes" were investigated in the framework of linearized compressible and resistive MHD. It was shown that ideal quasi-modes correspond to weakly-damped eigenmodes of the resistive-MHD differential operator. The damping of these modes becomes independent of the plasma resistivity in the limit of vanishing η. Hence, for the first time in the range of the Alfvén continuum, resistive eigenmodes have been found that converge to their ideal-MHD transforms as $\eta \rightarrow 0$.

1.8 Temporal Evolution of Externally Driven Plasmas

S. Poedts, E. Schwarz, W. Kerner[1)]

The time scales and the efficiency of plasma heating by resonant absorption of Alfvén waves are studied in the framework of linearized compressible and resistive MHD. The configuration considered consists of a straight cylindrical, axisymmetric plasma column surrounded by a vacuum region and a perfectly conducting shell. The plasma is excited by an external 'antenna' located in the vacuum region. The temporal evolution of this driven system is numerically simulated. It is shown that the so-called 'ideal quasi-modes' (or 'collective modes') play a fundamental role in resonant absorption and considerably affect both the temporal evolution of the driven system and the efficiency of this heating mechanism. The variation of the energetics in periodically driven resistive systems was analyzed in detail. At present, other ways of driving are under investigation, such as multi-periodic driving and random (stochastic) driving.

1.9 Localized Ideal and Resistive Instabilities in 3D MHD Equilibria with Closed Field Lines

D. Correa-Restrepo

A class of stability criteria was derived for MHD equilibria with closed field lines. The destabilizing perturbations have finite gradients along the field and are localized around a field line, the localization being stronger on the pressure surface than in the radial direction. By contrast, in sheared configurations the localization is comparable in the two directions. The derived stability criteria are less stringent than those obtained for MHD equilibria with shear for similarly localized perturbations in the limit of low shear. These results, obtained from the energy principle, are a particular case of those obtained by solving the linearized resistive MHD equations with an appropriate ansatz and subsequently taking the limit of vanishing shear and resistivity.

1.10 Nonlinear Resistive Ballooning Modes

D. Correa-Restrepo

In order to describe *nonlinear, resistive ballooning modes*, the nonlinear MHD equations for a resistive, viscous magnetofluid are studied. Considerable simplification of these equations is achieved by taking into account the spatial properties of *localized modes*, i.e. the fact that gradients transverse to the magnetic field are very large compared with the gradients along the B-field. One of the aims of this investigation is to describe the nonlinear saturation properties of toroidal resistive ballooning modes (the *linear* properties of these modes are already well understood since they have been the subject of extensive analytical and numerical investigations.) A further aim is to study the relevance of localized modes for anomalous plasma transport. This will depend crucially on the *nonlinear* behaviour. Work is in progress.

[1)] JET Joint Undertaking, Culham, U.K.

[2)] FOM-Instituut voor Plasmafysica, Rijnhuizen, The Netherlands

1.11 Nonlinear Properties of Tearing Modes

D. Biskamp and H. Welter

The nonlinear evolution and saturation of the tearing instability in plane and cylindrical configurations was reinvestigated and rendered more precise.

a) The "Rutherford" constant C in the low-amplitude regime $w = C\Delta'\eta$, w being the island size, is rederived to yield $C = 1.22$ (in contrast to previously published results $C \simeq 1, C \simeq 1.66$) and is confirmed by numerical simulations. The current distribution $j(\psi)$ in this regime is found to be singular owing to a micro sheet current at the X-point.

b) The saturation island size for helical modes in a cylindrical plasma agrees well with the semi-empirical formula $\Delta'(w) \equiv \left[\psi'(r_s + w/2) - \psi'(r - w/2)\right]/\psi(r_s) = 0$ (for fixed $\eta(r)$), in contrast to the case of a plane sheet pinch, where agreement occurs only for conditions close to marginality, while, in general, islands are much wider than predicted.

c) The effect of a dynamic resistivity profile is primarily determined by the difference of the values at the X-point (separatrix) and O-point $\Delta\eta = \eta_o - \eta_x$. While in the plane case $\Delta\eta < 0$ is destabilizing, leading to wider islands than $\Delta\eta > 0$, the reverse is true of helical islands in a cylindrical configuration, where, according to a well-known result, $\Delta\eta > 0$ ("island cooling") is destabilizing. The results can easily be explained by considering the equation

$$\frac{d(\psi_x - \psi_o)}{dt} = \eta_x j_x - \eta_o j_o$$

obtained by averaging the flux equation $\partial\psi/\partial t + \vec{v}\cdot\nabla\psi = \eta j - E$ over the surfaces $\psi = \psi_o, \psi_s$ and noting that one has $(\psi_x - \psi_o)\cdot j > 0$ in the plane case and $(\psi_x - \psi_o)\cdot j < 0$ in the helical case, where ψ is the helical flux function satisfying $\nabla^2\psi = j - 2nB_0/mR$.

1.12 Properties of MHD Turbulence

D. Biskamp, H. Welter and M. Walter

The statistical properties of 2D MHD were studied by means of high-resolution numerical simulations. As a theoretical point of reference, the β-model of intermittent turbulence was adapted to the MHD case. Comparison of simulation results for energy spectra with the β-model predictions shows intermittency corrections to be small, $\delta < 0.2$, while fourth-order correlation functions exhibit a stronger effect, $\delta \simeq 0.35$, consistent with the numerically observed Reynolds number dependence of the flatness factor $F \propto R_\lambda^{1/2}$. An argument is given that this scaling valid for $R_\lambda \sim 10^2$ is, however, not characteristic of the asymptotic regime $R_\lambda \to \infty$, where a constant value of F is to be expected. The probability distributions of the field difference $\delta\vec{v}(x,t)$, $\delta\vec{B}(x,t)$ are Gaussian for large separation x or t, approaching an approximately exponential distribution for $x, t \to 0$. This behaviour can be understood by a simple probabilistic argument.

1.13 Self-similar Statistics in MHD Turbulence

S.J. Camargo, H. Tasso

The fully developed decaying turbulence of 3D resistive, viscous, incompressible MHD is investigated by using Elsasser variables and the Hopf equation for probability distributions. The work is an extension of previous work on Navier-Stokes equations by Foias, Manley and Temam (1987). It uses essentially self-similar properties of the statistics, which allows the derivation of a decaying Kolmogorov spectrum with properly defined energies and dissipation rates.

Similarly to the Gibbs entropy principle in equilibrium statistics, some selection principle is needed to exclude any non-self-similar statistics. Such a missing principle would even allow one to prove uniquess of the Kolmogorov spectrum.

2. MICROFLUCTUATIONS AND TRANSPORT THEORY

2.1 Nonlinear Drift Waves

A. Salat

In the classical model of nonlinear drift waves the density gradient determines the phase velocity and the temperature gradient gives rise to a nonlinear term which leads to the existence of solitary waves. It was recently claimed[1] that, instead of the temperature gradient, it is the derivative of the density gradient that determines the nonlinearity. In analyzing the situation it was found that the result[1] is based on a fortuitous cancellation of terms which takes place only if the phase velocity u is treated as a constant in space. Owing to the gradients, however, which permit drift waves in the first place, u is not constant in general, and this recovers the classical results. For the special profiles which do have u = const the two theories agree with each other.

[1] Lakhin V., Mikhailovskii A., and Onishchenko O., Plasma Phys. and Controlled Fusion 30, 457 (1988).

2.2 Self-sustained Collisional Drift-wave Turbulence in a Sheared Magnetic Field

B. Scott

Although collisional drift waves in a sheared slab configuration are linearly damped, it was found in nonlinear simulations that the corresponding turbulence is self-sustaining if initialized at nonlinear amplitude. The influence of the free energy source represented by the temperature and density gradients on the turbulent system involving bi-directional spectral energy transfer is responsible for this change of regime, manifested through an identifiably self-organized mode structure. Fluctuation mode widths are determined by a competition between turbulent advective broadening and parallel dissipation. All of the features of nonlinear mode structure are thereby determined by nonlinear processes, divesting linear stability criteria of their relevance to that structure, or its amplitude. Many important features of experimentally observed tokamak edge fluctuations were

reproduced by these single-rational-surface nonlinear dynamics. Consequently, one must continue to consider drift-wave turbulence as a plausible mechanism behind such observations.

2.3 Effect of a Sheared Plasma Flow on Collisional Drift-wave Turbulence in a Sheared Magnetic Field

B. Scott

The hypothesis that a sheared flow may suppress turbulence by enhancing decorrelation was tested in computations of collisional drift-wave turbulence in a sheared slab configuration. The result was that the flow has no important effect if it does not itself cause instability. In the case of very strong flow shear, but no linear instability (no vorticity maximum), the turbulence begins to nonlinearly tap the free energy in the flow, growing further to larger saturated amplitude. Mixing-length theories predict suppression of the turbulence since the shear flow increases the vorticity of velocity perturbations throughout the spectrum. This was observed in the simulations. Nevertheless, the turbulence is not suppressed, but either remains at its old amplitude or grows to a higher one. The probable cause is the non-diffusive nature of turbulence in a sheared magnetic field. The recent suggestion that strong sheared flows at the edge of divertor plasmas have a causal role in the transition to the H-mode was thereby called into question.

2.4 Dimensional Analysis

A. Salat

The method of Grassberger and Procaccia is widely used in order to extract the dimensionality of the underlying dynamics from experimentally observed or computed time series. The series is cut into successive "window" vectors of length n, giving rise to points in n-dimensional embedding space. The number of points in a sphere of radius r versus r contains the desired information.

The merits of an alternative scheme proposed[1),2)] were tested. The matrix of window vectors is formed and the singular eigenvalue decomposition is made. The number of non-zero generalized eigenvalues is a measure of the information content. In order to get a dimension estimate, a further "neighbourhood analysis" of the eigenvectors is required. Application of this method to simple test series showed that it is not advantageous compared with the Grassberger-Procaccia algorithm. It can be automated even less and the interpretation is not always unambiguous.

1) Broomhead D. and King G., Physica D 20, 217 (1986).

2) Broomhead D., Jones R. and King G., J. Phys. A 20, L 563 (1987).

2.5 The Energy-Momentum Tensor for the Linearized Maxwell-Vlasov and Kinetic Guiding Centre Theories

D. Pfirsch and P.J. Morrison[1)]

A modified Hamilton-Jacobi formalism is introduced as a tool to obtain the energy-momentum and angular-momentum tensors for any kind of nonlinear or linearized Maxwell-collisionless kinetic theories. The emphasis is on linearized theories, for which these tensors are derived for the first time. The kinetic theories treated - which need not be the same for all particle species in a plasma - are the Vlasov and kinetic guiding centre theories. The Hamiltonian for the guiding centre motion is taken in the form resulting from Dirac's constraint theory for non-standard Lagrangian systems. As an example of the Maxwell-kinetic guiding centre theory, the second-order energy for a perturbed homogeneous magnetized plasma is calculated with initially vanishing field perturbations. The expression obtained is compared with the corresponding one of Maxwell-Vlasov theory.

2.6 Proof of a Conjecture of Morrison and Pfirsch Concerning Negative-energy Modes

H. Weitzner[1)] and D. Pfirsch

A necessary and sufficient condition for the existence of negative-energy modes in a plasma described by the Vlasov-Maxwell system is derived from an expression of Morrison and Pfirsch for the second variation of the free-energy of a steady-state solution.

2.7 Test of a Multiple Time Scale Formalism Applied to the Nonlinear Evolution of Negative-energy Modes

D. Pfirsch and F. Pohl

As a test of the use of a multiple time scale formalism in three-wave interaction with negative-energy modes the structurally similar problem of a charged particle on an axially symmetric parabolic hill ($V = -(x^2 + y^2)/2$) with a small potential perturbation $\delta V \propto x^3$ and a sufficiently strong ambient magnetic field in the z-direction is treated numerically. The linear problem allows positive and negative-energy modes. If there is resonance between these modes, given essentially by the gyrofrequency being twice the drift frequency, a multiple time scale formalism predicts explosive instability. This behaviour is also found by solving the equations of motion numerically. The approximate solutions obtained via the multiple time scale formalism and the numerical solutions agree altogether fairly well.

2.8 Nonlinear Instabilities, Negative-energy Modes and Generalized Cherry Oscillators

D. Pfirsch

In 1925 Cherry discussed two oscillators of positive and negative energy that are nonlinearly coupled in a special way, and presented a class of exact solutions of the nonlinear equations showing explosive instability independent of the strength of the nonlinearity and the initial amplitudes. In this study Cherry's Hamiltonian is transformed into a form which allows a simple physical interpretation. The

1) Department of Physics and Institute for Fusion Studies, The University of Texas at Austin

1) Courant Institute of Mathematical Sciences, New York

new Hamiltonian is generalized to three nonlinearly coupled oscillators; it corresponds to three-wave interaction in a continuum theory, like the Vlasov-Maxwell theory, if there exist linear negative-energy waves. Cherry was able to present a two-parameter solution set for his example which would, however, allow a four-parameter solution set, and, as a first result, an analogous three-parameter solution set for the resonant three-oscillator case is obtained here which, however, would allow a six-parameter solution set. Nonlinear instability is therefore proved so far only for a very small part of the phase space of the oscillators. The study gives in addition the complete solution for the three-oscillator case and shows that, except for a singular case, all initial conditions, especially those with arbitrarily small amplitudes, lead to explosive behaviour. This is true of the resonant case. The non-resonant oscillators can sometimes also become explosively unstable, but the initial amplitudes must not be infinitesimally small. A few examples are presented for illustration.

2.9 Reflection and Absorption of Ordinary Waves in a Hot Inhomogeneous Plasma

R. Croci

The usual treatment of e.m. waves in an inhomogeneous plasma only considers wavelengths much larger than the Larmor radius in order to reduce the system of Vlasov and Maxwell equations to a system of differential equations. A physically more interesting approximation is to consider wavelengths smaller than the characteristic inhomogeneity length, without limitations on the ratio of the wavelength to the Larmor radius. We have treated this problem for ordinary waves in the presence of a vacuum source, neglecting interaction of ordinary and extraordinary waves. The equilibrium plasma density depends on ηx, where η is a parameter and x is a Cartesian coordinate perpendicular to the uniform equilibrium magnetic field. The equation for the Fourier transform in space and time of the electric field is transformed to an inhomogeneous integral equation with principal part integrals coupled with a system of algebraic equations that determine the absorption and reflection coefficients. The energy conservation theorem for the reflection and transmission coefficients in an absorption–free plasma was derived without explicit knowledge of the solutions. The inhomogeneous integral equation was solved for weak absorption and sufficiently small η (essentially smaller than the vacuum wave vector) by extension of a method that we previously developed for the longitudinal waves in the same geometry. A by–product of our method is an equation for the eigenvalues that does not require complex analysis and knowledge of all solutions of the dispersion relation. We also explicitly gave the reflection and transmission coefficients and the total energy absorption; their behaviour in proximity to the eigenvalues was discussed, as well as that of the relative energy content of short–wavelength and long–wavelength waves.

2.10 Onsager's Relation and Other Results for Relativistic Electrons in Magnetic Fields

A. Holas,[1] S. Olszewski[1]) and D. Pfirsch

[1] Institute of Physical Chemistry of the Polish Academy of Sciences, Warsaw, Poland

Onsager's result concerning the quantization of the magnetic flux enclosed by the orbit of an electron moving in a static uniform magnetic field is shown to hold also in the relativistic case, and not to be restricted to the regime considered by Onsager in which the correspondence principle can be applied. The results obtained via the correspondence principle and via expectation values differ, however, in the details. It is also shown that the eigenenergies and eigenfunctions of Dirac's relativistic equation for an electron in a static non-uniform and arbitrarily strong magnetic field may be obtained direct from the solutions of Schrödinger's non-relativistic equation. In this case the expectation value of an observable depending on coordinates only equals the one calculated direct with the non-relativistic eigenfunctions.

2.11 Equal-field Solutions of Poisson's Equation

H. Tasso

Exact equal-field axisymmetric equipotentials are found for the Poisson equation in terms of elliptic integrals of the first and second kinds. The method used extends that introduced by Palumbo (1967) in the context of MHD.

The same method can be partially applied to equations more general than Poisson's equation and axisymmetric MHD equilibrium equations with side-conditions more general than the equal-field condition. Reduction to elliptic integrals is, however, not possible in the general case.

2.12 Green's Functions in WKB Approximation

D. Pfirsch and R.N. Sudan[1])

A systematic technique based on a variational principle is developed for obtaining WKB Green's functions for a non-Hermitian set of inhomogeneous, nonstationary differential equations in a space of arbitrary dimensions. A key element in this technique involves the use of the Van Vleck determinant for the amplitudes of WKB functions.

2.13 Discretization Errors at Free Boundaries of Elliptic Equations

Rita Meyer-Spasche, Bengt Fornberg[2])

The numerical error of standard finite-difference schemes was analyzed at free boundaries of elliptic equations of the Grad-Schlüter-Shafranov type. It was found that the convergence of standard schemes is slowed down by the presence of a free boundary, and that multigrid approximations do not converge in general. A simple correction strategy is devised to reduce these errors considerably, and to ensure convergence of the multigrid approximations (IPP 6/295).

[1] Laboratory of Plasma Studies, Cornell University, Ithaca, N.Y.

[2] Exxon Research & Engineering Company, Annandale, N.J., USA

THEORY DIVISION 2
(Prof. Dr. Arnulf Schlüter*)

Theory Division 2 comprises the Stellarator Physics Group, the work of which is reported in the section "Wendelstein 7-X Project".

The members of the Stellarator Physics Group are: W. Dommaschk, F. Herrnegger, W. Lotz, P. Merkel, J. Nührenberg, E. Rittger, A. Schlüter, C. Schwab, U. Schwenn, E. Strumberger, L. Zheng
Guest: A.H. Boozer[1]

*Emeritus Professor since September 1, 1990

[1] Guest from College of William and Mary, Williamsburg

TOKAMAK PHYSICS

(Prof. Dr. Karl Lackner)

The main task of this division is the support and guidance of the experimental tokamak research at our institute through applied theory. Consequently, a major fraction of the work of the division members is reported in the context of the ASDEX and ASDEX Upgrade projects. More intensive than in past years was our involvement in the NET/ITER project, where we made a major contribution to evaluating the H-mode confinement data base as a world-wide collaborative effort of all divertor tokamak teams.

During the closing phase of ASDEX and the subsequent reorganization of our institute, several physicists joined our division. As it had also recently taken on an increasing fraction of experimental work, it was renamed Tokamak Physics Division, at the end of 1990.

Team: G. Becker, M. Brambilla, M. Bessenrodt-Weberpals, K. Büchl, A. Carlson, R. Chodura, W. Feneberg, J. Geiger, O. Gruber, C. Hoffmann, O. Kardaun, K. Lackner, L. Lengyel, P. Martin, H.-P. Menzler, J. Neuhauser, U. Rang, T. Richter, R. Schneider, W. Schneider, B. Scott, R. Wunderlich, H.-P. Zehrfeld

Guests: P. McCarthy, University Cork, K. Riedel, New York University, U. Wenzel, ZIE Berlin, R. Zanino, Politecnico Torino

1. MHD EQUILIBRIUM AND STABILITY

(P. McCarthy, J. Geiger, K. Lackner, W. Schneider, R. Wunderlich, H.P. Zehrfeld)

Our main emphasis in this area is on determining plasma equilibria in ASDEX Upgrade on the basis of measured magnetic signals. This is required on a real-time basis to form the input of our plasma position and shape control system and for the aftershot analysis to afford the basis for interpreting all spatially localized measurements of plasma parameters.

Real-time applications require a very fast analysis method. Our choice for this is the method of function parametrization described in Sec. 1.1. The results of this scheme can of course also provide a useful basis for interpreting other diagnostics. To allow an independent check of the interpretation of the magnetic signals and to give a more complete picture of the structure of the flux surfaces, we are also developing, however, a complete equilibrium code which fits the free functions in the Grad-Schlüter-Shafranov equation to the measurements of magnetic field strength and flux differences (1.2.). The primary output of this code (besides macroscopic parameters such as the internal inductances (l_i) and kinetic energy content of the plasma) consists of values of the flux function on a rectangular grid spanning the vacuum vessel region. This equilibrium information is produced in a standardized form to have a clear interface to codes using the information for particular diagnostics. In particular, this interface is also of the same form for other versions of the equilibrium code (e.g. ones using prescribed rather than fitted functions in the Grad-Schlüter-Shafranov equation).

As an application paradigmatic of a variety of uses we developed a code for Abel-inverting line-integrated signals on the assumption of constant plasma parameters on flux surfaces. This code is briefly described in Sec. 1.4. The figure given (Fig.1) shows such a flux pattern resulting from the DIVA code (see Sec. 1.2.) together with structures inside the ASDEX Upgrade discharge vessel, and rays of the line of sight for one of our bolometer cameras.

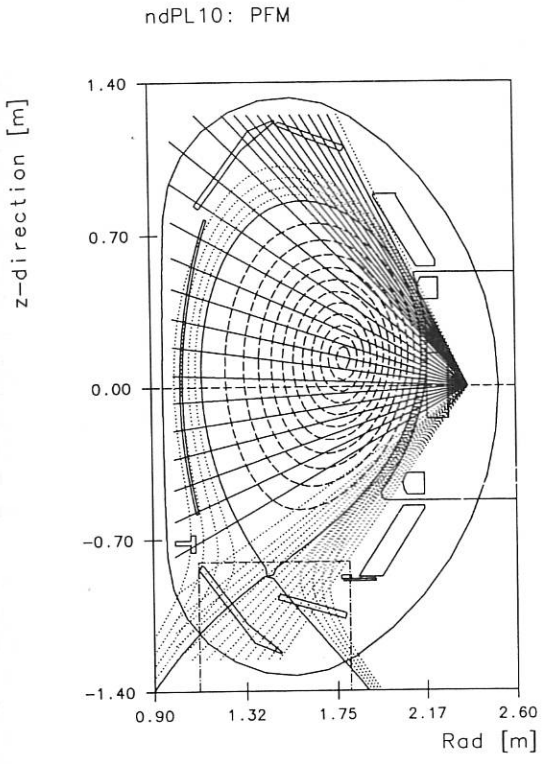

FIG.1 ASDEX Upgrade flux surfaces computed by the DIVA code, together with lines-of-sight of the outboard bolometer cameras and material structures delimiting the volume accessible to the plasma.

1.1 Function Parametrization for ASDEX Upgrade Real-Time Control

The real-time Function Parametrization (FP) algorithm, which computes equilibrium parameters from magnetic measurements for the ASDEX Upgrade (AU) feedback control system, has been implemented on the IPP-designed transputer-based R2 processor. Using regression coefficients determined by off-line analysis of a database of randomly generated AU ideal MHD equilibria, the algorithm computes a pre-selected vector of equilibrium parameters by simple algebraic operations on linear combinations of a set of real-time magnetic signal values. Up to 8 equilibrium parameters can be determined from 34 magnetic signals in approx. 1,5 ms. For initial AU operation, however, it is planned to compute only 2 parameters, namely the R and Z coordinates of the current centre. This can be achieved inside 1,0 ms. Extensive preliminary checking is done by the algorithm, including

a. detection and flagging of failed measurements or saturated integrators,

b. recovery of one failed measurement,

c. correction of flux and magnetic field measurements for ohmic stray flux,

d. correction of Mirnov probe signals for (possible) toroidal field components,

e. determination of plasma category (in/outer limiter; up/lower divertor).

1.2 Reconstruction of ASDEX Upgrade Equilibria

ASDEX Upgrade is a tokamak with elongated plasma cross-section and low aspect ratio. This makes MHD equilibrium theory as the link between measurements and interpretation a sensible instrument for investigating plasma confinement because the usually applied approximation formulas valid for large-aspect-ratio plasmas with circular cross-section cannot be used in general. We reconsidered standard plasma MHD equilibrium theory for the purposes of reconstructing ASDEX Upgrade equilibria from magnetic measurements.

In order to simulate the experimental situation, we make predictive calculations yielding particular equilibrium signatures such as conductor currents, values of flux and magnetic induction at optional diagnostic positions, and flux patterns of separatrix- and limiter-defined plasma configurations, as well as all other basic plasma parameters.

Subsequent interpretive calculations aim at reconstructing such predictions. In doing so, equilibrium-compatible function classes for current density distributions are subjected to an optimization procedure for a best fit of all magnetic signals from the prediction.

A corresponding code package, DIVA (Diagnostic Identification and Verification of Axisymmetric equilibria), running on Unix work stations was developed. For optimum system integration the main part of the code is written in C.

Auxiliary (FORTRAN) packages for plotting, data transfer, and flux surface handling and representation are under development.

1.3 Axisymmetric Equilibria with Mass Flow and Anisotropic Pressure

Stability calculations of present tokamaks are usually based on static MHD equilibria. Neutral beam injection (NBI) and efforts to understand the H-mode make it necessary to consider equilibria with substantial mass flow. This was done in several codes using the MHD equations (e.g. NIVA).

Nevertheless, the plasma parameters used in present tokamaks are in the range of low collisionality, where the MHD fluid equations are not valid parallel to the magnetic field lines. One method of overcoming this problem is to introduce an anisotropic pressure tensor and use the double adiabatic model of Chew-Goldberger-Low (CGL) to describe the anisotropy due to the inhomogeneity of the magnetic field.

We developed an equilibrium approach which takes into account toroidal and poloidal mass flows and a pressure anisotropy of the CGL-type for part of the plasma. The plasma fraction obeying the double adiabatic equations (e.g. high-energy NBI ions) is controlled by a parameter which can vary from flux surface to flux surface. The approach is the starting point for considering the stability of equilibria showing mass flow and anisotropic pressure.

In order to calculate equilibria under realistic conditions, we considered plasmas in the magnetic field produced by

the ASDEX Upgrade conductor system. Furthermore, the code is kept compatible with the existing DIVA code for static equilibria, so that they can be merged.

1.4 Abel Inversion of Diagnostic Signals in General Tokamak Geometry

A common problem arising for many diagnostics in tokamaks is the interpretation of line-integrated data on the assumption of constant plasma parameters on flux surfaces. For ASDEX this problem could be analyzed by using a model geometry of nested, but not necessarily concentric, circular flux surfaces, labelled by a coordinate ρ. For ASDEX Upgrade a very general geometry of the flux surfaces has to be allowed for. As a concrete example we used the inversion of bolometric signals. The fit function $w(\rho)$ is regularized by $\int(d^2w/d\rho^2)^2\rho d\rho$. This procedure can be physically interpreted on the assumption of dominating diffusive processes. This analogy also shows a way of extending the procedure to parameters slowly varying on flux surfaces by assuming an anisotropic diffusivity.

2. PLASMA TRANSPORT

2.1 A Fluid-Kinetic Model of Tokamak Transport. (W. Feneberg, cooperation with W. Kerner, JET)

It is well known, that neocl. transport, based on collisions between trapped and transient particles, scales like ν^* in the region of long mean freepath and is far away to explain experiments. (ν^* is of order 0.05 under reactor conditions and describes the parameter of collisionality). For this reason we have started a new approach in solving the kinetic equation which studies the effect of transient particles on transport in the region of long mean free path. The losses due to transient particles are based on the drift terms arising from the fast gyromotion in conjunction with poloidal variations of temperature, flow velocity and viscosity on a magnetic surface. As in the collisional regime, the driving term is the diamagnetic poloidal heat flow, which is in toroidal geometry not divergence free. Complementary to the usual neoclassical ordering scheme a kinetic model was set up by extending the Chapman-Enskog procedure into the long mean free path regime. For the distribution function the ansatz $f = f_m + f_1$ is appropriate, where f_m is a local Maxwellian with two temperatures $T_\parallel$ and $T_\perp$. So we preserve the basic idea of Grad's 13-moment method, but try to solve the kinetic equation directly in order to find a closed system of moment equations. The collision term of Clemmow and Dougherty

$$\frac{\partial f}{\partial t}|_c = \nu \frac{\partial}{\partial w_\parallel}\left[w_\parallel f + \frac{T}{m_e}\frac{\partial f}{\partial w_\parallel}\right],$$

which is consistent with particle, momentum and energy conservation, is applied enabling a basically analytic treatment. The basic result obtained for the electrons in this model is the electron parallel heat flux to be independent from the mean free path and thus from the collisionality. This exhibits similarity with the case of a Knudsen gas. As an immediate consequence the radial heat transport is in agreement with plateau scaling and widely exceeds the trapped particles contribution.

2.2 Determination of Off-Diagonal Transport Coefficients from Particle and Power Balance Analysis (O. Gruber, W. Schneider, K. Lackner)

In ASDEX density peaking occurs which cannot be explained by changes in the charged particle deposition profile. Besides a particular plasma boundary behaviour, distinct changes in the bulk particle transport are necessary and can be described by an increase of $-v_p/D$ (the ratio of the inward drift velocity and the diffusion coefficient used to describe in an ad-hoc way the particle transport) /1/. Common to all cases with peaked density profiles - having $\eta = (\nabla T/T)/(\nabla n/n) = L_n/L_T < 1-$ is that they show an improvement in energy and impurity particle confinement compared with flat density profile discharges ($\eta > 1$). These related changes of the bulk energy and particle transport properties point to a common change of the transport coefficients and may be interpreted in terms of a generalized non-diagonal model of particle and energy transport.

By using non-equilibrium thermodynamics linear relations between the fluxes of particles (Γ_p) and energy (Q) and the driving thermodynamic forces, i.e. the gradients of $1/T$ and $1/p$ for both electrons and ions, can be derived that satisfy the Onsager symmetry for the off-diagonal coefficients. Subtracting the convective energy flux from the total energy flux Q to get the conductive heat flux $q = Q - 2.5kT\Gamma_p$ and normalizing the energy flux equation by kT, one obtains relations between $\Gamma_p, \Gamma_{q,e}$ and $\Gamma_{q,i}$ ($\Gamma_q = q/kT$) and the recalculated forces $(-\nabla T_e/T_e, -(1 + T_i/T_e)\nabla p/p$ and $-(T_i/T_e)\nabla p_i/p_i)$ that still satisfy the Onsager symmetry for off-diagonal coefficients. If $n_i \approx n_e, T_i \approx T_e$ and a plausible relation between off-diagonal elements are assumed the following radial electron transport model results:

$$\Gamma_p = n\, D(1+\eta)(-\nabla n/n) - n\alpha(-\nabla T/T),$$

$$\Gamma_q = -n\alpha(1+\eta)(-\nabla n/n) + n\chi(-\nabla T/T), \qquad (1)$$

with $-\nabla p/p = (1+\eta)(-\nabla n/n)$ (the index e is omitted here and in the following). Contributions of the H-mode $E \times B$ drift motions are neglected, whereas the Ware pinch contribution to the particle flux is taken into account in calculating Γ_p. Connections with the often used ansatz $\Gamma_p = n\, D(-\nabla n/n) + n\, v_p$ and the simplified diagonal ansatz $\chi_{eff} = q/(nk\nabla T)$ are given below. We look for a consistent set of transport coefficients in the different confinement regimes on ASDEX taking the fluxes from radial particle and power balance analysis using the TRANSP code. The numerical procedure for solving the above equations determines Hermitian spline fits for the transport coefficients $\chi, \mu = D/\chi$ and $\varepsilon = \alpha/(\chi\sqrt{\mu})$ between several nodes by minimizing the deviations of the calculated fluxes from the input values at the grid points used.

The procedure was tested first by calculating input profiles for the fluxes and driving forces with a simulation code and assumed transport coefficients. All three quantities are recovered within 10% nearly independently of the number of nodes (3-6), while the fluxes are fitted within 10^{-3}. This result is corroborated by error analyses using

modified T and n profiles obtained from the simulated ones by changing their gradients by 110%.

First experimental results are obtained for L- and H-mode discharges. For a high-power (4 MW) L- mode case Fig.2a shows the analyzed transport coefficients χ, D and α and the ratio $\mu = D/\chi$ using the error analysis described above. The calculated $\chi's$ in the outer plasma regions are a factor of about two larger than χ_{eff} owing to the substantial off-diagonal term. A ratio of $\mu = D/\chi \approx 0.15 - 0.25$ is found, as derived from simulations of density ramp-up scenarios. The particle velocity v_p as defined above strongly increases outside $a/2$ and is inward directed. The Ware pinch contributes significantly only inside $a/4$ to Γ_p.

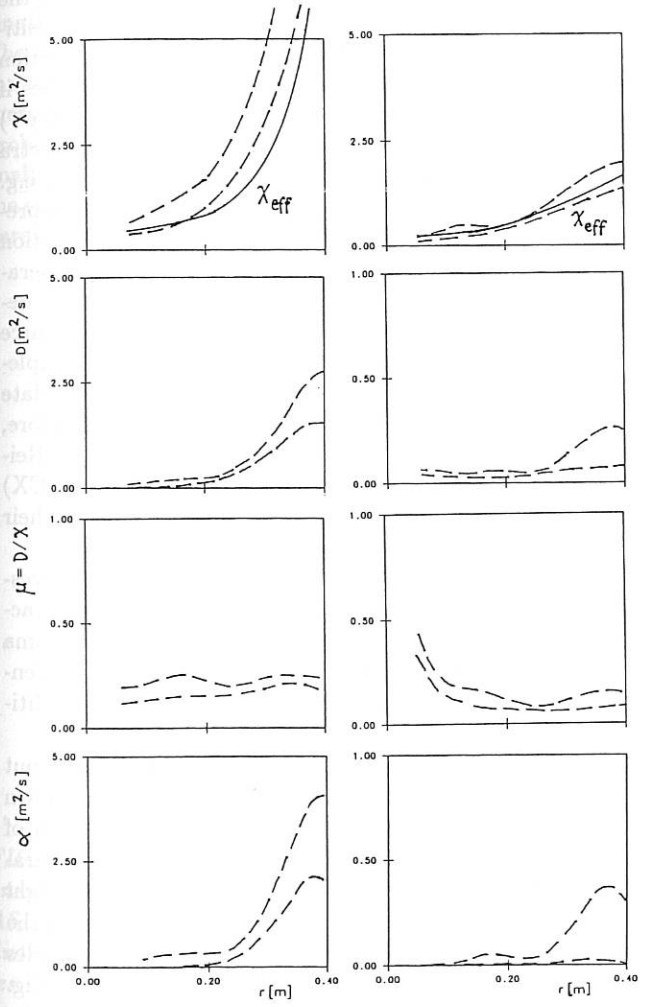

a. L-mode ($P_{NI} = 4$ MW b. H-mode ($P_{NI} = 4$ MW)

FIG.2 Calculated transport coefficients χ, D and α (off-diagonal) and the ratio $\mu = D/\chi$ for ASDEX discharges using measured n_e and T_e profiles and fluxes analyzed by TRANSP.

In the H-mode phase of the same discharge Γ_p and Γ_q are strongly reduced, as is χ in the outer plasma regions (see Fig.2b), compared with the corresponding L-mode values. Owing to the even more reduced values of α the off-diagonal contribution to the energy flux is negligible, yielding $\chi \approx \chi_{eff}$. Additionally, the anomalous particle velocity is smaller than the Ware pinch velocity up to $r/a \leq 0.8$, which may be an ingredient of the extremely flat density profiles observed in ELM-free H-mode plasmas. The fact that the Ware pinch alone can be responsible for the particle flux for $r/a < 0.6$ may also explain the increase of μ (and, accordingly,D and α) towards $r = 0$ due to larger errors in our fit procedure.

In summary, the derived transport coefficients have very similar radial profiles, pointing to the existence of a common driving mechanism for electron heat and particle transport. The proposed analysis should be considered as a complementary method to the often used perturbation analysis of heat or particle flux propagation, where coupled heat and particle flux oscillations occur too.

References: /1/ O. Gruber et al., Plasma Phys. and Contr. Fusion 30 (1988)1611

3. SCRAPE-OFF AND DIVERTOR PHYSICS

3.1 2D Multifluid Simulation of Edge Impurity Transport
(J. Neuhauser, R. Wunderlich)

The impurity transport studies in open poloidal divertor geometry relevant to tokamaks like ASDEX Upgrade, JET or ITER were continued. The Garching version of the 2D multifluid code of B. Braams was applied to a model x-point geometry. Two scenarios of specific interest for the above-mentioned experiments were considered in detail: (1) control of divertor temperature and high-Z target plate erosion by external puffing of rare gas for radiation cooling, and (2) the effect of hydrogen puffing near the x-point on impurity entrainment in the divertor. The feasibility of scenario (1) was clearly demonstated with nickel as target material and neon as the control impurity. Scenario (2) comfirmed the beneficial effect of strong divertor pumping together with an intense upstream particle source. If, however, the latter is introduced by a gas puff near the divertor throat as assumed, then charge exchange sputtering of wall material will occur at that position. It is found that a large fraction of these sputtered impurities is rapidly transported into the main chamber because of the dominant thermal force at the upstream side of the hydrogen puffing region.

3.2 Coupling of Edge Plasma and Neutral Particle Codes
(R. Schneider)

The neutral particle transport is determined by the plasma, whereas the neutral particles act as sources for the plasma. Up to now the 2D multifluid edge plasma code B2 (B. Braams) has been used at IPP with simple analytical neutral gas models. For many problems a better description of the neutral gas is necessary, which can be done by using Monte Carlo methods. For a selfconsistent description of both plasma and neutral particle transport in the edge the 2D multifluid edge plasma transport code, B2-88 (Jülich version of the Braams code), and the 3D Monte Carlo code, EIRENE (D. Reiter, Jülich), for simulating neutral

particle transport on a kinetic level were coupled (D. Reiter, P. Börner and T. Baelmans, Jülich).
EIRENE and B2-88 were installed at IPP (B2-88 in cooperation with W. D'Haeseleer, NET Team). For the coupling, which operates on an operating-system-dependent level, some technical details had to be adapted. The coupling of the two codes is done in the following way:

The same geometry input file is used in B2-88 (metric descriptions in poloidal cross-section coordinates) and EIRENE (explicit coordinates of cell vertices). Interfacing routines between B2-88 and EIRENE (including index mapping) transfer cell by cell basically plasma parameters, such as density, temperature, velocity profiles and field line pitches, from B2-88 to EIRENE.
Spatial plasma particle and energy flux distributions onto the target produced by B2-88 are translated in a kinetic source distribution function (in physical and in velocity space) for EIRENE so that the moments of this distribution function (for the initial ion distribution in front of the target plate needed for sampling the neutral particle source distribution at the plate) are consistent with the boundary conditions (Bohm criterion, sheath transmission factors) imposed in the B2-88 model at the divertor plate. The initial plasma is produced from a converged solution of the B2-88 code with analytical recycling model. With these plasma input data, a full Monte Carlo simulation of neutral particle transport is performed. At the end of the Monte Carlo simulation EIRENE produces a file output with source rate densities for B2-88.
It turned out, however, that many attempts at cycling both codes following this procedure are frustrated by severely unstable behaviour, and this especially in those cases with high recycling coefficients (small particle throughput in the system), which, however, are the ones of major interest. This could easily drive the solution too far away from the path to the converged solution of the coupled system, or at least pose intolerably low limits on the number and size of time steps to be used in one B2-88 run.
To overcome this difficulty, a more implicit source term scaling between full Monte Carlo steps was developed by factoring out those terms in a source rate which depend only on the plasma parameters and not on the neutral particle distribution function (e.g. ionisation and dissociation rate coefficients). These terms are then re-evaluated at each time step by using the full EIRENE atomic physics routines. This was efficiently achieved by a new "short call" to EIRENE at each time step, invoking only its interior atomic and molecular reaction routines for supplied plasma conditions.
Calculations with the simple model x-point geometry showed that the main problem of the coupling is to find a criterion when a full EIRENE calculation is needed or when the calculation-time-saving "short call" within B2-88 can be used. The following procedure was finally chosen: every time the flux to the target plate changes in the B2-88/"short" EIRENE more than 5% a full EIRENE calculation is done (T. Baelmans, Jülich). On this basis the qualitative behaviour of the results are in agreement with B2-88 stand-alone calculations: the midplane separatrix density increases with decreasing divertor temperature (see Annual Report 1989).
Further calculations with the coupled system are in progress, especially for comparing the results of B2-88/analytical recycling models with those of B2-88/EIRENE.

3.3 Analysis of Low-energy Time-of-flight Hydrogen Charge Exchange Neutral Spectra
(R. Schneider)

Charge exchange neutral spectroscopy combined with numerical models for neutral hydrogen gas transport is a standard procedure to determine central ion temperatures in tokamak plasmas. It has proved to be a fairly robust method even in cases in which the model assumptions at the plasma edge are quite uncertain. This valuable insensitivity to less known parameters such as surface interaction models and other typical plasma edge effects vanishes if the low-energy range (neutral energies less then 1000 eV) of neutral particle spectra is considered. These spectra have become available from time-of-flight analyzers, e.g. as applied on ASDEX (LENA). Not only is the interpretation of these data more critical because the correlation between fluxes in this energy range and the ion temperature is weaker, but also the neutral gas models now become more sensitive to geometrical effects, spatial source distribution and assumptions on recycling. This complexity has left Monte Carlo methods as the only candidate for numerical assistance in data interpretation. Therefore, we used the fully 3D Monte Carlo code EIRENE (D. Reiter, Jülich) to calculate low-energy charge exchange (CX) spectra for energies below 1000 eV and to analyse their information with respect to ion temperature profiles.
We implemented the geometrical data for the ASDEX vessel and the protection limiter located near the analyzer, acting as the dominant source of neutrals. The input plasma profiles for the electron temperature and the electron density are chosen to describe typical ASDEX ohmic conditions.
The result of a CX-spectra simulation with plasma input profiles under typical ASDEX ohmic conditions is shown in Fig. 3 as a solid line. Obviously, the information of the spectra is restricted to the region close to the separatrix because most of the particles seen by the time-of-flight analyzer originate from this region (the mean values of the distribution function of the origin of the detected particles at the calculated energies are shown as diamonds in Fig. 3, the variances of this distribution function are shown as vertical bars).
In the experiments, the CX-spectra themselves and the profiles of the electron temperature and density are measured. The simulation requires the hydrogen ion density as an input profile. This can be calculated because the impurity density is known.
By varying the ion temperature profile in the simulation and comparing the results of the simulation and the experimental CX-spectra, the ion temperature profile can be determined in the radial range from which the particles in the spectrum originate, which in our case means from the

region near the separatrix. This analysis gives very small errors for the ion temperature. However, it is very time-consuming and is only well suited to single-shot analysis. Inverting the problem is much more efficient: with all input profiles being varied and function parametrization methods being used only once a set of spectra covering the whole parameter range must be calculated and then the experimentally unknown ion temperature profiles parameters - and therefore the ion temperature profile itself - can be calculated very fast for every spectrum by multivariate regression using the spectrum and the experimentally known profiles as input values.
Statistical analysis allows determination of the separatrix ion temperature with an error of about 30 eV and the derivative of the ion temperature profile expressed as a decay length with an error of about 1.5 cm.
The main problem in applying this theoretical analysis to the experimentally relevant situation is the limitation of the number of profile parameters due to calculation-time problems. It may be solved by using principal component analysis of the input profiles and correlation analysis for the spectra and the input profiles to reduce the number of parameters. Further calculations are in progress.

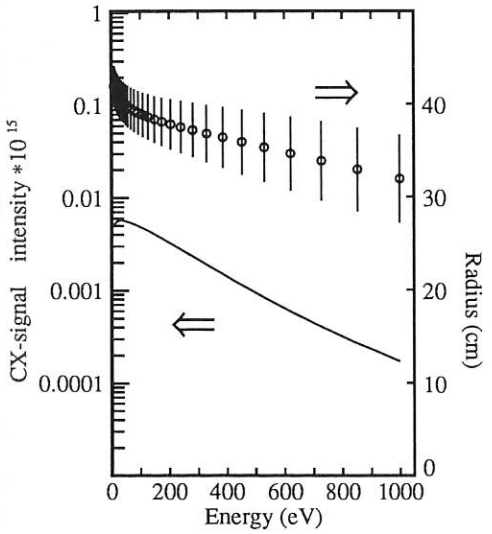

FIG.3: Calculated CX-signal intensity as a function of energy (solid line) for plasma input profiles under typical ASDEX ohmic conditions. The mean values of the radial distribution function of the origin of the detected particles at the calculated energies are shown as diamonds, the variances of this distribution function as vertical bars.

3.4 Thermoelectric Currents in the Scrape-off Layer.
(R. Chodura, R. Zanino*)

Poloidal asymmetries in the scrape off layer due to, for example, asymmetric energy influx from the core plasma lead to different plasma temperatures at the target plates. This temperature difference gives rise to a potential difference between the plates or, if they are electrically connected, to a current through the scrape-off layer along the magnetic field. The generation of this thermoelectric current was studied in a fluid model and a kinetic model. In the fluid code the driving action of the electrostatic target sheaths is modelled by prescribing the Langmuir current-voltage characteristics and the energy transfer of the sheaths as boundary conditions. In the kinetic particle model the sheaths are included. The codes were applied to cases of asymmetric energy influx, losses and recycling properties. It is shown that suitable voltage biasing of the target plates can equalize asymmetries of their power load.

3.5 Flow Properties of a 1 D Multi-component Plasma at a Neutralizing Target
(R. Chodura, R. Zanino*)

A quasineutral mixture of several ion fluids and an electron fluid flowing from a source region to a neutralizing target plate is investigated. No assumptions on the relative densities of the ion fluids are made. The equation for the characteristic velocities of the system and from the fact that all characteristic velocities at the neutralizing target should point in a direction away from the fluid allows one to derive lower limits of the flow velocities V_i of the ion components, i.e. $V_i^2 \geq (\gamma_i T_i + Z_i^2 n_i T_e/n_e)/m_i$, where $\gamma_i, Z_i, m_i, n_i and T_i$ are the adiabatic constant, charge number, mass, density and temperature of the i-th ion component, respectively. In addition, the Bohm criterion for the flow velocity at the sheath edge is generalized to a system of several ion components and gives the same result as the theory of fluid characteristics with $\gamma_i = 3$.

The velocity limits obtained allow an estimate of the impact energies of hydrogen and impurity ions at the target plate.

* Politecnico Torino

4. WAVE HEATING

4.1 Theory of Ion Cyclotron Resonance Heating
(Brambilla, C. Hoffmann)

1. We have written a new version of the ICRH code FELICE, which solves the finite Larmor radius (FLR) wave equations in a plane-layered model of the tokamak and evaluates the antenna loading and the power deposition profiles. It uses a new approach for solving the matching conditions at antenna conductors in vacuum in terms of wave impedance and admittance matrices. The new formalism has been combined with a variational principle to determine the antenna currents self-consistently instead of assuming a given distribution as previously done. Moreover, it is flexible enough to allow for an arbitrary number of antenna elements: this will make possible a more realistic modelling of ICRH experiments in ASDEX Upgrade, in which the upper and lower halves of each antenna are at different average distances from the plasma and the return conductors.

The FELICE code was further applied extensively to model experimental results in ASDEX, with particular emphasis on the investigation of electric fields near the surface of the plasma. By combining the results with the nonlinear sheath rectification model developed by Perkins and by Chodura and Neuhauser, a plausible picture of impurity production during ICR heating in ASDEX was obtained.

2. The Fokker-Planck code for investigating the evolution of the ion distribution functions during ICRH was further developed. The Fokker-Planck part of the equation was extensively tested to check its accuracy and efficiency (Spitzer resistivity, relaxation of anisotropic distributions, energy exchange between ions and electrons at different temperatures, etc.). A simplified quasilinear operator describing the time-averaged effect of resonant particle-waves interactions but not yet taking into account space inhomogeneities was used to check heating rates and evaluate the development of anisotropic distribution functions in various heating scenarios. The implementation of the appropriate surface averaged quasilinear operator taking into account the peculiarities of ICR absorption in tokamak geometry is in progress.

5. PELLET ABLATION

5.1 Pellet Shielding and Ablation Physics (L. Lengyel)

An analysis of the state of the art of studies aimed at a better understanding of phenomena that define the erosion (ablation) rate of cryogenic pellets injected into thermonuclear plasmas has been started. Particular attention was given to unsteady phenomena observed in pellet injection experiments, such as the large-amplitude fluctuations in the H_α emission trace or the field-aligned striation structure of the ablatant fan in the wake of the pellet. The ultimate purpose of this analysis is the development of a physical/numerical model that correctly describes the effect of these phenomena on the ablation rate, i.e. the development of a predictive ablation code.

5.2 Plasma Fuelling

An assessment of the physical and technological problems associated with pellet injection into tokamaks has been started in collaboration with ORNL. The analysis was commissioned by IAEA Nucl. Fusion (participants from IPP Garching: L. Lengyel and V. Mertens; from ORNL: W. Houlberg and S. Milora). The report on the state of the art shall appear as a review paper in NF. Two working sessions of the review team took place in 1990: the first one at Garching (May 1990) and the second at Oak Ridge (Sept. 1990).

The objective of a second collaborative effort (with General Atomics) is the development of a physical/numerical model with account for transient phenomena that substantially affect the physics of pellet shielding and pellet ablation. To discuss the substance and framework of this study, L. Lengyel visited GA in Sept. 1990. The project is to commence in spring 1991.

SURFACE PHYSICS DIVISION

(Prof. Dr. Volker Dose)

Scientific activities in the Surface Physics Division proceed via three routes, which we call plasma wall interaction (analytical), plasma wall interaction (preparation) and surface science. Our work on analytical problems of plasma wall interaction is for the purpose of this report further divided into two categories. Those activities which take place in intimate collaboration with fusion devices are included in the respective chapters on tokamaks and stellarators. Additional laboratory work described in this chapter is grouped under the title plasma wall interaction processes. Contributions to the field of "plasma wall interaction" (preparative) are described in a separate section entitled plasma technology. This project is a joint venture with the IPP Technology Division. More fundamental studies, resumed under the headline of surface science comprise a continuation of previous activities in magnetism and low energy electron microscopy as well as contributions to the Sonderforschungsbereich 338. The latter concentrates on adsorption at solid surfaces and integrates work at the Munich Universities and IPP and MPQ.

Surface Physics Division:

Head: V. Dose, Deputy Head: E. Taglauer;

S. Adamson[1)], M. Beckschulte[2)], R. Behrisch, E. Bertel, J. Biener[2)], U. Bischler[2)], D. Boutard[3)], K. Desinger[4)], M. Donath, R. Drube[2)] H. Dürr[2)], W. Eckstein, K. Ertl, Th. Fauster, P. Franzen[2)], E. Gauthier[1)], G. Geipel[2], H. Glatzel[2], G. Hars[5)], M. Hashmi, W.D. Hildebrandt[6)], I. Hughes[7)], R. Hytry[2)], W. Jacob[4)], C.Jandl[2)], J.Küppers, K. Lange[2)],J. Laszlo[8)], H. Liebl, A. Liegl[2)], W von der Linden[4)], C.Linsmeier[2)], V.Lossev[9)], A.P. Martinelli, M. Mayer[2)], N. Memmel[2)], W. Möller, J. du Plessis[10)], W. Poschenrieder, V. Prozesky[11)], G. Rangelov[12)], P. Reinke[2)], J. Roth, P. Sandl[2], A. Schenk[2], B. Scherzer, R. Schneider[4)], J. Schulz[13)], R. Schwörer[2)], B. Senftinger[2)], R. Siegele[2)], K. Starke[2)], G. Staudenmaier, U. Strüber[2)], M. Veprek-Heijman[14)], G. Venus, H. Verbeek, D. Voges[13)], M. Vonbank[2)], M. Wittmann[2)].

1) EURATOM stipendiary
2) Doctoral candidate
3) Guest, Laboratoire C.F.H. Chatenay Malabry, France
4) Post Doc
5) Guest, Technical University of Budapest, Hungary
6) Guest, Zentralinstitut für Elektronenphysik, Berlin
7) Guest, University of Belfast, Ireland
8) Humboldt Fellow, Technical University Budapest, Hungary
9) Guest, Inst. of Physical Chemistry, University of Moscow, USSR
10) Guest, University of Orange Free State, Bloemfontein, SA
11) Guest, Atomic Energy Corporation of SA, Pretoria
12) Guest, Bulgarian Academy of Sciences, Sofia, Bulgaria,
13) Undergraduate Student
14) Guest, Philips Res. Inst., Eindhoven, NL

1. PLASMA WALL INTERACTION PROCESSES

1.1 Recycling

Recycling of hydrogen at the first wall determines the particle balance and has important consequences on the energy balance of the plasma. Although the transport of hydrogen isotopes in and out of materials during and after exposure to hydrogenic plasmas is basically understood now, it is still difficult to explain and predict wall pumping in large fusion devices like JET with data from laboratory measurements. The main interest of our investigations therefore lay on measurements of accumulation and re-emission of hydrogen implanted in graphite and carbon-base materials, with special emphasis on high temperatures, low energies and transient effects.

1.1.1 Reemission of Deuterium from Graphite

Reemission of deuterium from graphite during bombardment with 24 keV D_3^+ was studied between room temperature and 1500 K. A quadrupole mass spectrometer was used to detect the partial pressures of the various molecules leaving the target. The main species are D_2 and HD, between 700 K and 1100 K methane (CD_4) contributes to the reemitted flux of deuterium. The contribution of higher hydrocarbons (C_nD_m) was below our detection limit in the observed temperature range.

The surprising fact is that the total reemission of deuterium atoms including all molecular species decreases with increasing target temperature. At 1200 K only 50 % - 60 % of the incident deuterium is found in the reemitted flux. The same effect is observed during the bombardment of molybdenum with deuterium, whereas it is not found during bombardment of molybdenum with helium.

The results exclude temperature variation of pumping speeds and C-D layer deposition at the walls to explain the decrease in reemitted flux. A possible mechanism could be diffusion of D into the bulk at high temperatures. Microbalance experiments show no increase in weight due to D accumulation in graphite. This may, however, be overcompensated by the weight decrease due to sputtering. Thermal desorption spectroscopy and long time implantation up to saturation of the whole target will be applied to obtain further information.
(P. Franzen, B.M.U. Scherzer, W. Möller, J. Roth).

1.1.2 Determination of the dynamic fraction of the hydrogen inventory in graphite exposed to a glow discharge

The experimental device for dynamical measurements of the hydrogen inventory in samples exposed to a RF glow discharge (26.0 MHz) has been modified to avoid plasma discharges in the RF leads and to allow for higher particle energies. The different components (mass-energy-analyzer, ERD-device, RF-plasma-chamber) have been tested successfully.

The desired improvement of the plasma-parameters was achieved: at a plasma gas pressure of 20 Pa and transmitter power ranging from 20 to 80 watt (i.e. mean H-atom energies from 18 to 70 eV) hydrogen ion fluxes up to 5×10^{15} cm^{-2} s^{-1} were obtained. In order to reduce experimental errors due to the instability of the analyzing ^4He-beam the measurements are computer controlled with frequent intermediate checks of the analyzing current.

The dynamic fraction of the hydrogen inventory in graphite (EK98) was measured at different implantation energies (Fig.1). Dynamic fractions of up to 15% werde measured depending on the mean ion energies. From the time-resolved measurements the time-constant for the release of the hydrogen inventory after plasma-implantation can be estimated to be about 100 seconds, which is in good agreement with data from fusion experiments (JET, ASDEX).

To examine the reasons of this dynamic H-inventory which may consist of C_xH_y-radicals adsorbed at the surface further experiments are in progress. One is to be the covering of the RF-electrodes by graphite to exclude the influence of near-surface impurities due to electrode-sputtering. (C. Jandl, W.Möller, B.M.U. Scherzer).

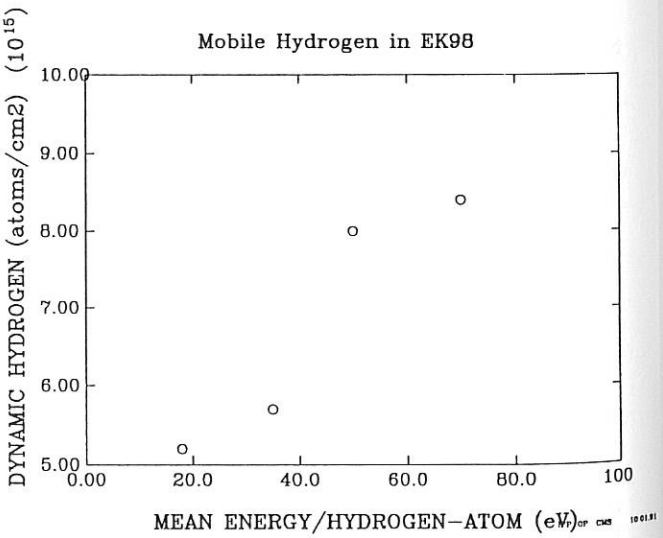

FIG.1: The dynamic fraction of RF-plasma-implanted hydrogen in graphite (EK 98) at different mean energies of the incident hydrogen atoms; the stationary hydrogen inventory amounts to 3.2×10^{16} atoms/cm^2.

1.1.3 *Trapping of hydrogen in carbon-boron compounds*

The chemical reactivity of graphite with hydrogen ions to form hydrocarbons depends strongly on doping with impurities such as boron or silicon. Therefore, the interaction of hydrogen with carbon and carbon-boron compounds containing 3 % and 15 % boron respectively, was investigated by outgassing experiments in the "High Flux Ion Source". After bombarding the samples with 3 keV H_3^+-ions at different temperatures, the thermal hydrogen emission was measured between room temperature and 1200°C using a quadrupole mass spectrometer.

The results, shown in Fig. 2, indicate great differences in the amount of hydrogen released during heating depending on the bombarding temperature and the boron concentration in the sample. Boron doped graphites show furthermore a shift of the desorption maximum from 800°C in pure carbon to 600°C, indicating different binding conditions for hydrogen.

This difference in the binding energy of hydrogen may be one reason for differences found in the formation of hydrocarbons. Another possible reason for this difference, i.e. the boron enrichment at the surface due to preferential carbon erosion, will be studied in future in situ AUGER experiments. (R. Schwörer, J. Roth, B.M.U. Scherzer).

1.1.4 *Release of deuterium from "saturated" implants in graphite*

Monoenergetic implants of hydrogen ions in graphite are known to form saturated layers with a thickness corresponding to the ion range. The saturation concentration which was originally assumed to be independent of depth, has been found to be considerably lower in the near surface part of the range than at or beyond the mean projected range. This effect can be demonstrated by observing the trapping and release behaviour during implantation with D^+-ions of changing energy. We have observed the additional trapping of 3 keV D^+-implants into layers saturated with 6 keV and the subsequent increase to reemission coefficients $R > 1$ when this layer is again bombarded with 6 keV D^+. The $R > 1$ behaviour is found in a temperature range between 300 and 700 K with a maximum near 570 K using re-emission spectroscopy of D_2, HD and CD_4. The results are in good agreement with the theoretical model for trapping and release of hydrogen in graphite by Möller and Scherzer. (B.M.U. Scherzer, W. Möller, in collaboration with J. Wang, Tsinhua University, Beijing, P.R. China).

1.1.5 *Damage and deuterium trap types in SiC due to room temperature and 770 K implantation*

In order to study the temperature dependence of trapping sites of deuterium in the SiC lattice, angular scans were obtained of both the protons from the nuclear reaction $D(^3He, p)\alpha$ as well as the backscattered ^3He yield from the Si sublattice.

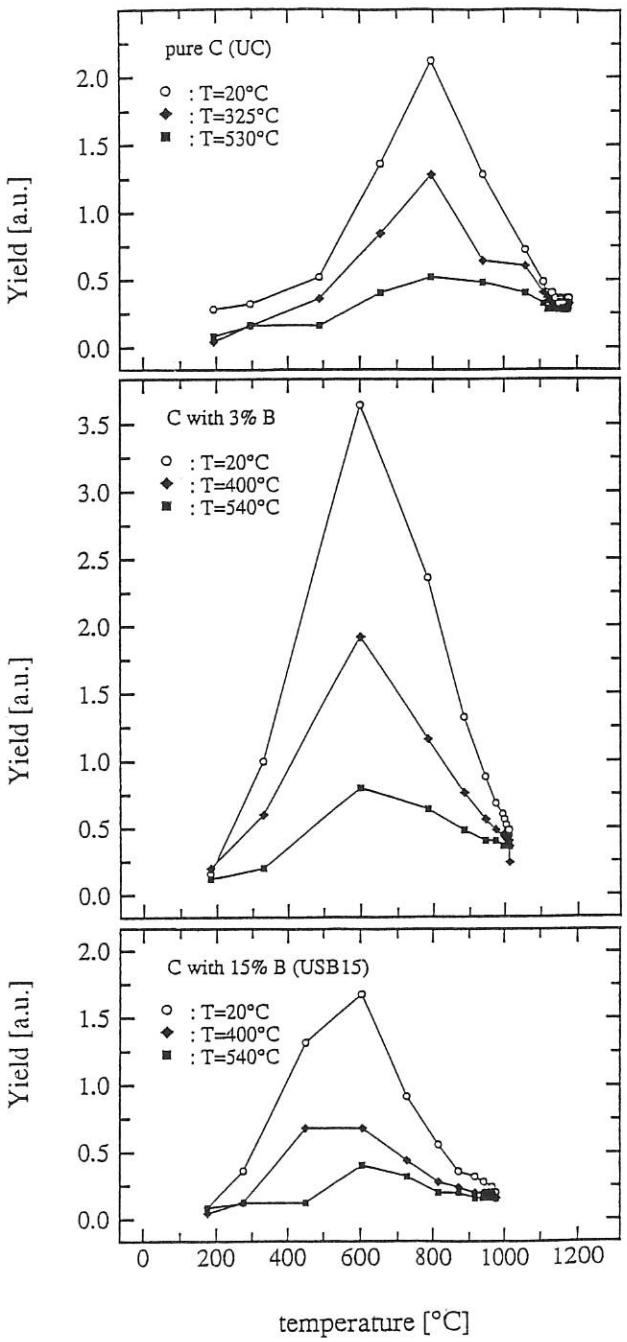

FIG.2: Thermal release of H_2 from samples with different boron content implanted with 3 keV H_3^+ at different temperatures.

Scans through the <100> axis, which is normal to the surface, following implantation of 4.0×10^{15} D/cm^2 at room temperature are shown in Fig. 3a. This low fluence allows reasonable statistical errors of the detected D

concentration while minimizing the amount of implantation damage to the SiC lattice. The proton yield shows an angular dependence with an indication of a shallow minimum in the <100> direction. The half width of this minimum is much smaller than corresponding backscattering minimum from the host lattice. The accuracy of the measurement does not allow resolution of further structures. The angular dependence with such a shallow minimum in the proton yield indicates either only slight ordering or two or more different lattice locations of the deuterium. The results of angular scans obtained following implantation at 770 K are shown in Fig.3b. In this case the proton yield shows no indication of ordering.

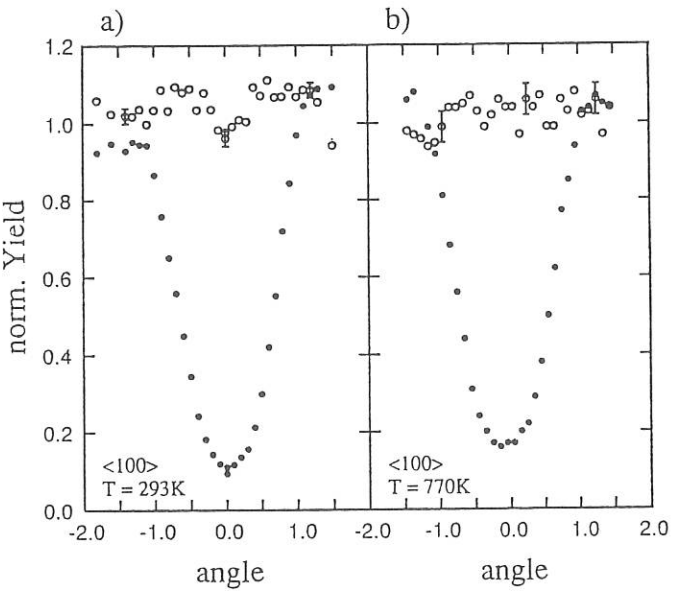

FIG. 3: The <100> axial angular distribution of the normalized proton yield from the nuclear reaction (o) and the backscattered yield from Si lattice atoms (•) following implantation with $4.0x10^{15}D/cm^2$ at a)T = RT and b)T=770 K.

The measurements indicate the existence of at least two different types of traps for D in the SiC lattice; one that leads to an ordering of the implanted D with respect to the SiC lattice, and a second type at which D is distributed randomly to the lattice.

Similar to the difference in lattice locations of D the damage introduced into the SiC lattice by the implantation at the different temperatures was found to show a difference. While most of the damage due to implantation at room temperature can easily be annealed by heating the sample up to 1000-1100 K, none of the damage due to 770 K implantation anneals at this temperature. It is expected that the damage annealing below 1000 K consists of point defects or small clusters, while the resistent damage is due to more extended defect clusters.

We assume that the different trapping sites of the deuterium are correlated to the different damage types. It is expected that D trapped at single vacancies or other simple defect structures appears ordered with respect to the lattice, while D trapped at more extended defects would not. (R. Siegele, J. Roth, B.M.U. Scherzer in collaboration with S.P. Withrow from Oak Ridge National Laboratory, Oak Ridge, TN, USA).

1.2 Sputtering

Since the finding that small amounts of dopants can significantly reduce the erosion properties of graphite, a large number of new graphitic and carbidic materials have been proposed. All these new materials are systematically tested for their sputtering yields. On special materials the basic mechanisms leading to the reduction in the sputtering yield are investigated in detail.

Metallic elemental materials, such as Be, Mo, W change their surface properties upon irradiation with typical plasma impurity ions such as C^+ and O^+. Investigations of such changes are continued as well as changes in the surface compositions of compounds and alloys.

1.2.1 Survey of the erosion properties of graphite doped with light impurities

Graphite as divertor or limiter material shows temperature regimes of enhanced erosion under ion bombardment. Around 800 K the chemical reaction of hydrogen ions to form volatile hydrocarbons has a maximum, and above 1300 K the erosion yield increases due to radiation enhanced sublimation.

In contrast to graphite carbides do not show these enhanced erosion processes. In order to retain the excellent thermal properties of graphite and reduce the erosion, graphite tiles often are protected by surface coatings such as TiC or boron . These coatings, however, only temporarily protect the graphite in view of the high ion fluxes to divertor or limiter plates. An alternative concept is the use of bulk graphite doped with small amounts of light impurities, such as boron or silicon. A large variety of graphite materials has been proposed by different manufacturers and for a quick survey of the materials the erosion yields were measured for 1 keV D^+ irradiation at 300, 800 and 1470 K to cover the different erosion mechanisms. Figure 4 shows erosion yields of test samples containing various amounts of boron and silicon compared with carbon in the form of pyrolytic graphite or diamond. Already small amounts of boron strongly reduce the chemical reactivity to form hydrocarbons, while radiation

enhanced sublimation persists until B_4C is reached. The best overall performance is found for a 15% B containing graphite (USB 15, obtained from Kurchatov Institute, Moscow) where the analysis of the chemical composition showed that B is mostly present in the form of B_4C precipitates. Si addition to graphite shows widely varying results.

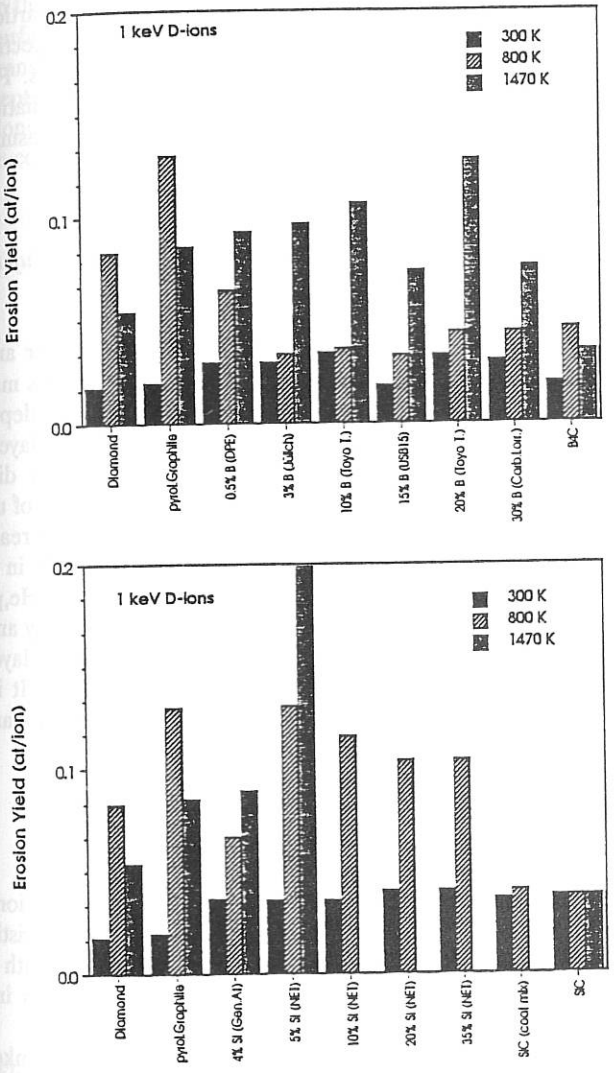

FIG.4: Erosion yields of test samples containing different amounts of B and Si for different temperatures compared to diamond and graphite.

While a graphite containing 4 % SiC inclusion shows strong reduction of the chemical reactivity, higher Si content in other samples did not result in reduction of hydrocarbon formation. The high temperature erosion is not reduced and exceeds, as measured so far, the values for pure graphite. Again, SiC did not show chemical or radiation enhanced erosion. The survey shows, that it is not the impurity content determining the erosion properties but the chemical microstructure of the material which is the dominating factor. The survey will be extended and also cover Be containing graphite.
(W. Eckstein, E. Gauthier, J. Roth).

1.2.2 Sputtering of beryllium

The sputtering of beryllium by carbon was investigated by computer simulation and experiment. For angles of incidence lower than about 40^o (with respect to the surface normal) complete carbon films build up on the beryllium target, whereas at larger angles of incidence a stationary concentration of beryllium and carbon forms in the surface layers. These calculated results are in good qualitative agreement with experimental data, although the experimentally determined range of the implanted carbon is much larger than the calculated range. This is a strong indication that diffusion processes of carbon in beryllium are important even at room temperature.
(W.Eckstein, E.Gauthier, J. Laszlo, J. Roth).

1.2.3 Sputtering of molybdenum and tungsten

The sputtering of molybdenum and tungsten by deuterium and tritium as well as selfsputtering was studied by computer simulation to provide sputtering yield data for the possible use of these refractory metals in future plasma machines. The energy range covered is from 20 eV to 5 keV. Normal incidence and oblique incidence is investigated as well as a Maxwellian distribution (including isotropic incidence) with and without a sheath potential. The most important result is the shift of the threshold for sputtering to lower plasma edge temperatures compared to a monoenergetic bombardment. An important finding is that for the hydrogen isotopes the threshold energy does not depend on the angle of incidence, whereas for selfsputtering the threshold energy is lower for oblique incidence than for normal incidence, see Fig. 5. where the sputtering yields of tungsten by deuterium and tungsten are compared at normal incidence and at 65^o. (W. Eckstein, J. Laszlo).

1.2.4 Sputtering of two-component systems

The surface composition of a series of binary alloys (PdPt, AgNi, CuTi, CuNi) under the influence of extended ion bombardment has been studied with ion scattering spectroscopy and Auger electron spectroscopy. The experimental results for the steady state surface concentrations can be reproduced by a detailed numerical model, taking preferential sputtering and radiation enhanced diffusion into account. This analysis also yields the concentration profile in the altered layer. (J. du Plessis, E. Taglauer in collaboration with G. van Wyk, University of Orange Free State, Bloemfontein, S.A.).

1.2.5. *Chemical interaction*

The cooperation between the IPP and the University of Bayreuth on fusion-relevant research on plasma-wall interaction has led to the installation of a group working on chemical erosion processes at the first wall induced by the interaction with plasma particles. The research target is a characterization of the elementary steps of the H/wall interaction in terms of the rates and energetics of these steps. The investigations concentrate on model systems of current first wall materials (C, C/B, Be) and utilize the currently available spectroscopic techniques for the characterization of surface and gas phase species respectively.
(J. Biener, V. Lossev, A. Schenk).

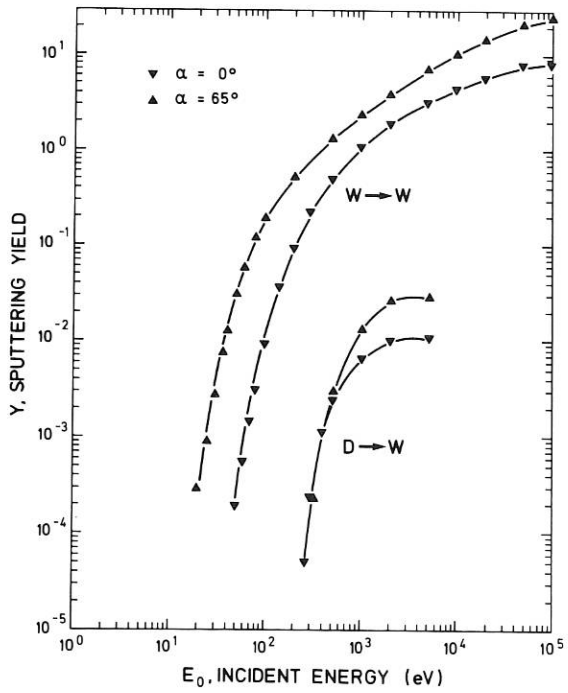

FIG.5: Sputtering yield for the bombardment of tungsten by deuterium and tungsten at normal incidence ($\alpha = 0^o$) and at an oblique angle of incidence ($\alpha = 65^o$).

1.3. Other Activities

Some activity was devoted to other topics. Among these are considerations on particle and energy fluxes to the vessel walls and on ash removal, energy levels of multiply charged ions, and on special diagnostic techniques.

1.3.1 *Particle and Energy Fluxes to the vessel walls*

In order to determine the plasma wall interactions for a burning D,T fusion plasma, the particle and energy fluxes to the vessel walls have been estimated from the condition that both the ash, i.e. the ^{4}He particles and the energy deposited in the plasma by the ^{4}He ions must be exhausted from the plasma under steady state conditions and D,T must be refuelled. These fluxes can be used to calculate the necessary average particle and energy confinement times or diffusion coefficients and D in the plasma for a given ^{4}He concentration in the plasma of typically 10 %.

Because both the exhausted particle and energy fluxes are proportional to the fusion rate, the ratio between particle and energy confinement times and or the respective diffusion coefficients must stay within narrow limits. For impurities in the plasma the extra energy losses by radiation reduce the possible operational regime for a fusion plasma.
(R. Behrisch, V. Prozesky).

1.3.2 *Depth profiling of deuterium in a Be/C layer of up to 5 μm*

After long term operation the deposits on the limiter and divertor tiles in high temperature plasma experiments may be of the order of several μm and nondestructive depth profiling of trapped hydrogen isotopes in these layers becomes very difficult. For determining the depth distribution of deuterium trapped within the Be/C layers of up to 8 μm on a JET limiter the D(^{3}He,p)^{4}He nuclear reaction using different ^{3}He ion energies was applied in a resonance-like technique. The background due to (^{3}He,p) reactions with the Be and C was determined separately and subtracted. This method extends the measurable layer thickness from several 100 nm to more than 10 μm. It is, however, much more time consuming than non-resonant techniques. (I.Hughes, R.Behrisch, A.P.Martinelli).

1.3.3 *Energy levels of multiply charged ion*

The calculations on energy levels of multiply charged ions were extended to the elements z = 46-54. A relativistic Hartree-Dirac-Fock formalism was applied to levels with a hole in one electron shell and to some excited states including all ions with one electron to the neutral state.
(W.Eckstein, in collaboration with B. Fricke and G. Blanke, Gesamthochschule Kassel).

2. SURFACE SCIENCE

Activities in the context of the "Sonderforschungsbereich 338: Adsorption on solid surfaces: Microscopic Analysis of States and Processes" focussed mainly on the investigation of adsorbate induced unoccupied electronic states by inverse photoemission (IPE) and structural investigations on clean and adsorbate covered single crystal surfaces by low energy ion scattering. An additional effort was devoted to the study of supported model catalysts.
Research on surface magnetism by spin polarized IPE was complemented by appearance potential spectroscopy.

Finally the assembly of a combined photoemission and low energy electron diffraction (LEED) microscope has been completed.

2.1 SFB 338

An inverse photoemission study (IPE) of the CO bonding to the transition metals was carried on from Ni to the (110) surfaces of Pd and Pt. The results suggest a gradual transition of the bond character from nearly pure π acceptor bonding on Ni to a cooperative π acceptor and σ donor bonding on Pt. (E. Bertel, N. Memmel, G.Rangelov, in collaboration with N. Rösch, TU Munich).

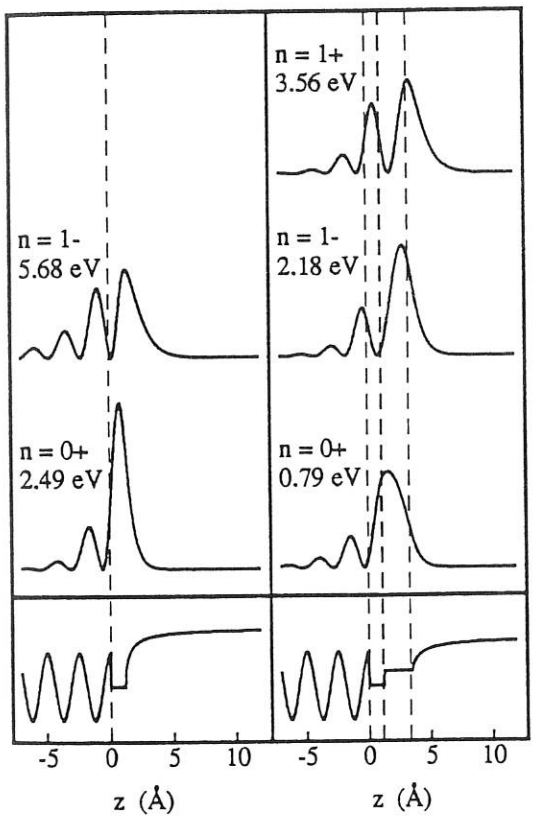

FIG.6: One dimensional surface potential model for a clean (left lower panel) and a sodium covered Ni(110) surface (right lower panel). The upper panel shows the z-dependence of the respective surface state wave functions. The energy position with reference to the Fermi level as well as the symmetry is denoted for each surface state.

An experimental and theoretical investigation of alkali induced empty states on Ag(110) and Ni(110) yielded a quantitative model for describing shifts and dispersions of surface states observed by IPE. The model allows an approximate calculation of the surface state wavefunctions and the determination of their symmetry (Fig. 6). Thereby it offers access to a chemical interpretation of the alkali induced unoccupied surface states. As a further result it was demonstrated that various types of surface reconstruction give rise to different surface state shifts and can therefore be discriminated by IPE. (E. Bertel, N. Memmel).

A new UHV system was successfully put into operation. It features complete angular resolution (i.e. independent variation of electron and photon incidence and exit angle, respectively) for both, ultraviolet and inverse photoemission spectroscopy. (E.Bertel, U.Bischler, P.Sandl, in collaboration with A.Goldmann and G.Meister, University of Kassel).

The adsorption structure of H on Ru(001) was analyzed by low-energy ion scattering and direct recoil detection. At low temperatures (138 K) H was found to adsorb in a threefold coordinated hollow position at a distance of 1.01 ± 0.07 Å above the topmost Ru layer. This distance is larger at 300 K and no lateral ordering was observed at this temperature, indicating a high mobility of hydrogen under these conditions. The experimental results were confirmed by numerical simulations using the computer code MARLOWE. (M. Beckschulte, J. Schulz, E. Taglauer, in collaboration with P. Feulner and D. Menzel, TU Munich).

The geometric structure of the oxygen covered (2x1)O-Cu(110) surface was determined with low-energy ion scattering. It was confirmed that the surface is reconstructed according to the missing row model. It could be shown that the growth of this structure proceeds via "added copper-oxygen rows" on top of the unreconstructed surface. The copper adatoms necessary for this growth mode originate from step edges. By combining low-energy ion scattering and Monte-Carlo computer simulations the mean square displacements of surface atoms could be determined as a function of temperature. The results for the (2x1)O-Cu(110) surface are shown in Fig. 7 and demonstrate that the dynamical behaviour of the surface is considerably stabilized upon oxygen adsorption. (H. Dürr, Th. Fauster, R. Schneider).

Further studies of surface structures were carried out with respect to phase transitions on single crystal surfaces. With the aim of studying the roughening transition on Cu surfaces, the structure of the stepped Cu(115) surface was investigated. Stepped metal surfaces can undergo roughening transitions well below the bulk melting temperature. Using the impact collision ion scattering method (ICISS), inner atomic distances on Cu(115) were determined . The results agree well with calculations for a three-dimensional model of the stepped surface (using the Marlowe code). Also a simplified two or three atom model calculation proved to give reliable results with considerably less computing effort. (A. Liegl, J. du Plessis, E. Taglauer).
The segregation behaviour of the (110) surface of an Fe (29 at %) Al single crystal was studied by low-energy ion scattering (ISS). Such a crystal shows an order-disorder phase transition at a critical temperature of 758 K as deduced from diffraction experiments. ISS complements

these measurements because it probes the short distance atomic arrangement and is sensitive to the topmost atomic layer. The results show an enrichment of 96 % Al on the surface at 700 K and close to 100 % at higher temperatures, with an activation energy of roughly 13 kJ/mol. The segregated surface exhibits reconstruction, the Al-Al distance being much larger than the bulk value. (J. du Plessis, E. Taglauer, D. Voges, in collaboration with H. Dosch and J.Peisl, University of Munich).

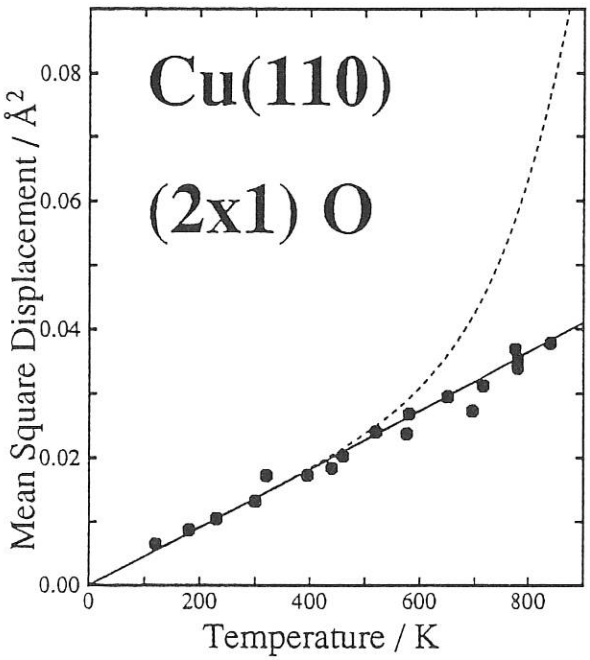

FIG.7: Mean square displacements versus temperature for the surface copper atoms on the oxygen covered Cu(110) surface. The strong anharmonic vibrations present on the clean surface (dashed line) are stabilized and the vibrations were found to be harmonic over the whole temperature range. The data are in good agreement with phonon slab calculations (full line) performed for the clean surface.

The growth mode of thin iron films deposited epitaxially on a Cu(100) surface was investigated with low energy electron diffraction, Auger electron spectroscopy and Rutherford backscattering spectroscopy. A bilayer by bilayer growth mode was found for the first four monolayers. (H. Dürr, Th. Fauster, H. Glatzel, R. Schneider).

For the investigation of the various catalytic activities of rhodium, model systems of Rh/Al_2O_3 catalysts with metal loadings of the order of one monolayer were prepared and studied with surface analytical techniques. It could be shown that alumina layers up to some hundred Ångströms thickness show a sufficiently high electrical conductivity to be examined with ion and electron beam methods. The distribution of oxygen in calcined samples is inhomogeneous in the alumina layer, changing continuously from Al_2O_3 to metallic Al.

The initially vapour deposited Rh metal is uniformly distributed over the samples, no indication of clustering or island formation was found. As an example, Fig. 8 shows a sputter-depth profile (using 2 keV He^+ ions) of a calcined Rh/Al_2O_3 sample). (Ch.Linsmeier, E.Taglauer, in collaboration with H. Knözinger, University of Munich).

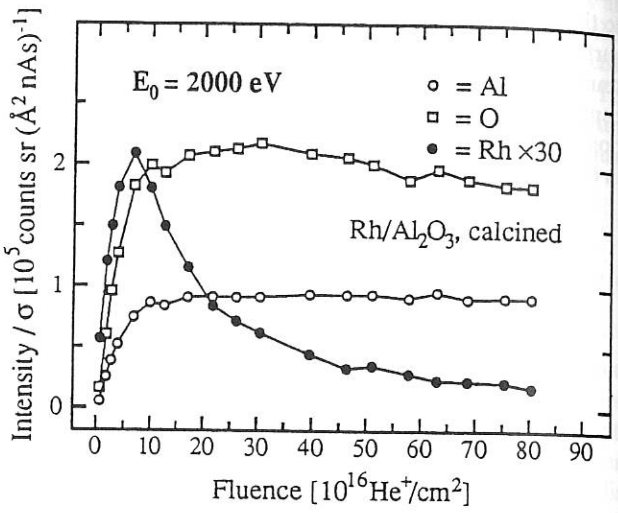

FIG.8: Depth profile of a calcined sample of an alumina film with a rhodium overlayer. 2000 eV He^+ ions were used for sputtering and ion scattering analysis. The total fluence corresponds to a depth of approximately 80 monolayers, calculated for τ-alumina. The relatively uniform distribution of oxygen is a result of calcination at 820 K.

2.2 Surface Magnetism

For interpreting results of spin-resolved electron spectroscopy of ferromagnetic samples the knowledge of the surface domain structure is essential, especially when the surface does not contain an axis of easy magnetization. In this case a complex structure of closure domains at the surface is expected at remanence.

The influence of such domains on the average surface magnetization of Ni(100) has been demonstrated with the magneto-optic Kerr effect (MOKE) and spin resolved inverse photoemission (IPE). The measurements show a strong temperature dependence of the surface domain structure. For temperatures above 440 K with small crystal anisotropy the remanent surface magnetization exhibits the same functional behaviour as the bulk saturation magnetization representing a single domain state. With decreasing temperature the anisotropy increases and closure domains are created. Consequently, the average surface magnetization is strongly reduced and at room temperature it is even reversed with respect to the bulk magnetization.

By means of spin-resolved target current spectroscopy the exchange splitting of the upper edge of the sp-band gap at

the Ni(100) Γ (X_1-point) was detected. The measured value of 230 ± 70 meV is in agreement with theoretical predictions and helps to understand the previously detected exchange splittings of surface states. In addition, the spin asymmetry of the target current can be used for a spin polarization detector.

The experimental set-up of the new apparatus for element specific studies of surface magnetism with spin-resolved appearance potential spectroscopy (APS) has been completed. First spin-resolved spectra for Cobalt in a metallic glass were obtained. The consequences of high electron correlation for the interpretation of results from Auger electron spectroscopy (AES) and APS have been studied. (M.Donath, K.Ertl, G.Geipel, K.Starke, M.Vonbank in collaboration with W. Nolting, University of Osnabrück).

2.3 LEED Microscope

All essential components have been installed and the working parameters of the electron optical columns have been explored. Both imaging columns, one for low magnification ($\sim$ 400 x) and one for high magnification ($\sim$ 2000 x) have been tested successfully in the photoemission mode. The alignment of the primary as well as the secondary beam column for imaging of the sample surface by elastically reflected low energy electrons is in progress. (H. Liebl, B. Senftinger).

TECHNOLOGY DIVISION

(Prof. Dr. Rolf Wilhelm)

The main tasks of the Technology Division are the technical development and preparation of the various plasma heating systems and their operation at the tokamak and stellarator experiments of IPP. Related details of neutral beam injection (NBI), lower hybrid heating and current drive (LHCD) and ion cyclotron resonance heating (ICRH) are described in the ASDEX, ASDEX Upgrade and W7AS-sections of this report. The following part contains further details of specific technical developments for NBI, ICRH and LHCD.

In addition, electron cyclotron resonance heating (ECRH) on ASDEX Upgrade is introduced as a newly established project of the division. Further sections describe some theoretical work on slow-wave current drive, plasma transport and reactor scaling considerations.

Film deposition by plasmachemical procedures is referred to a separate section of this report.

1. LOWER HYBRID CURRENT DRIVE AND HEATING

This experiment was constructed and conducted in cooperation with ENEA-Frascati and PPPL-Princeton.

Group leader: F. Leuterer
Deputy: M. Münich

F. Monaco, M. Zouhar (from 1.6.1990)

1.1 The Lower Hybrid System

The lower hybrid system and operational experience with it are described in previous annual reports. The system continued to work reliably up to the end of the experiments in August 1990, when ASDEX was shut down. Owing to the success of this system, the collaborating laboratories ENEA and PPPL decided to follow the same concept and technology for their couplers and the feeding systems.

It was investigated whether the system could be used on ASDEX Upgrade. A prolongation of about 50 cm of the straight section of the grill, shaping to the new plasma surface, and a new vacuum interface are necessary to install it directly in a major port. The transmitter itself can stay at its present site; only the connection to the ASDEX Upgrade control system needs to be changed. The 6 transmission lines need to be prolonged with WR 650 overmoded waveguides to reduce losses. Applying the global efficiency scaling found in ASDEX, one can expect in ASDEX Upgrade to drive close to 1 MA of current at a rather low density of 2×10^{13} cm^{-3} and the maximum magnetic field of 4T, only. Furthermore, ray tracing calculations indicate that wave penetration should be much worse than in ASDEX owing to the elongated cross-section. At higher densities, higher plasma currents and lower magnetic fields only a fraction of the current can be driven with the available power, which would still allow some modification of the current profile. In view of these ambiguous aspects of LHCD, it was decided to install an ECRH-system (see chapter 2) and to leave the lower hybrid system at ASDEX as long as this device itself is maintained as a standby machine.

1.2 Experimental Results

The experimental results are described in the chapter "ASDEX PROJECT", Sect. 1.7.

2. ELECTRON CYCLOTRON RESONANT HEATING ON ASDEX UPGRADE
(ECRH-Group)

Group leader: F. Leuterer
Deputy: M. Münich

F. Monaco, M. Zouhar (from 1.6.1990)

In view of the recent progress in gyrotron development it is planned to install ECRH on ASDEX Upgrade as a further heating method. For economic reasons the ECRH system envisaged will be of medium power level (1-2 MW) and use the highest commercially available frequency (140 GHz). Such a system should already be sufficient for some very interesting physical applications, e.g.:

- heat wave propagation for evaluation of the electron transport coefficients (by means of low-frequency power modulation at an average power of less than 0.5 MW)
- heating profile modification and related transport studies (at higher power levels)
- island stabilization (by localized heating or direct current drive in the island region)
- easier H-mode access
- density control (via edge heating).

The ECRH system envisaged will consist of 2-4 gyrotrons with about 0.5 MW each and pulse lengths of 0.5 - 1.0 s. The power will be transmitted and radiated in the HE_{11} and TEM_{11}-modes. A movable mirror system inside the torus will give access to the whole plasma cross-section perpendicularly ($k \perp B$) and obliquely ($k < B$) to the B-field.

In operation with the extraordinary harmonic wave (X_2-mode), typical parameters are:

f (GHz)	B (T)	radius of absorption (r/a)	ne_{max} 10^{20} m^{-3}
140	2.5	0 to ± 1*)	≤ 1.4
	2.7	≥ | ± 0.26 |	
	3	≥ | ± 0.66 |	

*) off-axis deposition achieved by tilting the launching mirror in the poloidal direction.

At high-field operation on AUG fundamental heating using ordinary polarization (O_1-mode) also becomes feasible:

(GHz)	(T)	(r/a)	10^{20} m^{-3}
140	< 4	< - 0.8 < - 0.45*)	≤ 2.8

*) at upshifted resonance with 2 keV electrons.

The more detailed technical planning of the ECRH system is in progress.

3. ION CYCLOTRON RESONANCE HEATING

Group leader: F. Wesner
Deputy: F. Hofmeister

J. Bäumler, M. Ballico, W. Becker, F. Braun, R. Fritsch, J.-M. Noterdaeme, S. Puri, F. Ryter, R. Schubert, H. Wedler

ICRH has been applied or is being prepared for application in the W 7-AS stellarator with a 4 MW RF system and in the ASDEX Upgrade tokamak with a separate 8 MW RF system. The special work for these experiments is reported in the sections on these projects.

In this section some general work is described.

3.1 Development of High-power Components for ICRH
(H. Wedler, W. Becker, R. Fritsch, F. Wesner)

The development work for high-power RF components, which has already been described in former Annual Reports, was continued. In 1990 the main emphasis was put on completing the development of dismountable vacuum feedthroughs and on optimizing a vacuum system for vacuum-insulated antenna feeding lines. The results will be applied first for ASDEX Upgrade.

3.2 Vacuum-insulated Feeding Lines and Vacuum Feedthroughs

In the W 7-AS and ASDEX Upgrade experiments 6 1/8", 25 Ω antenna feeding lines are used. They are fully vacuum-tight towards the torus vacuum. At their antenna side they are terminated by a 6 1/8" feedthrough, and at their generator side by a larger feedthrough representing also the transition to the 9" pressurized lines. For the feeding lines in ASDEX Upgrade new conical feedthroughs have been developed (Fig. 1):

- A feedthrough with a 6 1/8" diameter at both ends, to be used at the antenna side of the feeding line. This feedthrough, both of whose ends are in vacuum and which was already described in the Annual Report 1989, was successfully tested up to a voltage of 50.6 kV_{peak} for 9.5 s pulses (Fig. 2) and a current of 2140 A_{peak} for 10 s.

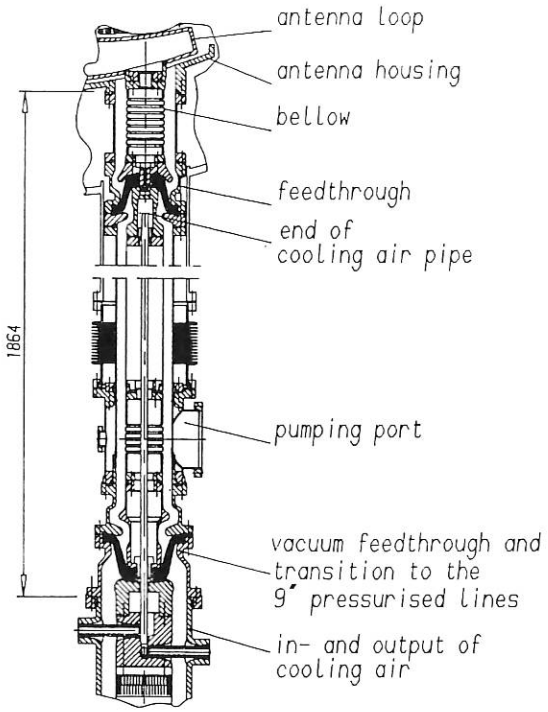

FIG.1: Vacuum-insulated antenna feeding line: 1 antenna housing, 2 antenna loop 3 bellows, 4 vacuum feedthrough, 5 end of cooling air pipe, 6 pumping port, 7 vacuum feedthrough and transition to the 9" pressurised lines, 8 input and output of cooling air

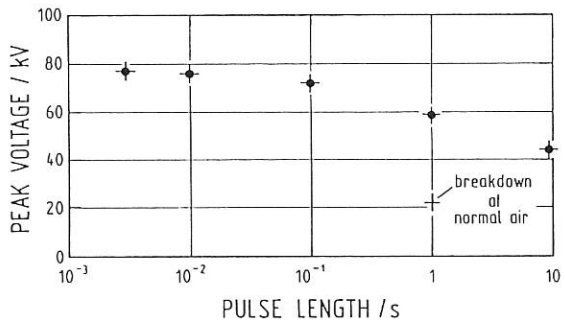

FIG.2: Voltage strength of the 6 1/8"' feedthrough versus pulse length at 67 MHz. For comparison the strength at normal air pressure is also given.

- A new feedthrough with 6 1/8" at the vacuum side and 9" at the pressurized side is used at the generator side of the feeding lines. This larger feedthrough, showing the same design principles, allows smaller values of the field strength and current density.

The two feedthrough types have similar characteristics:

- Elastic metal sealings, no brazed ceramics.
- Pronounced potential rings reducing the electric field strength at the critical metal-ceramic transitions (max. 0.7 kV/mm for a total voltage of 10 kV. For comparison, the field strength in an undisturbed 6 1/8", 25 Ω line is 0.48 kV/mm).
- The potential rings also act as baffles to prevent the ceramic surface from being coated or metallized by arcs. Arcs running towards the feedthroughs should be stopped at this. Tangential electric fields along the ceramic surfaces are minimized.
- In view of the field strength and its characteristic impedance the shape is optimized by finite-element calculations.

3.3 Vacuum System for the Antenna Feeding Lines

On the basis of tests already described in the Annual Report 1989, cryogenic pumping systems using commercial refrigerator pumps were developed. The pumps are installed directly at the feeder lines, resulting in a high effective pumping speed of 650 l/s for water vapour at the pumping port of the line.

Tests of the operational characteristics of different vacuum measuring systems within a magnetic stray field resulted in the application of Penning measuring valves. This allows the vacuum measurement to remain operational during the magnetic field pulse of ASDEX Upgrade, with errors below a factor of 3 up to a field of 200 mT. Thus, the pressure rise in the vacuum lines during RF can at least be roughly observed.

3.4 Edge Density X-mode Reflectometry of RF-heated Plasmas

(R. Schubert)

RF heating systems need special diagnostics to improve understanding of the specific wave access and wave propagation into the plasma. A critical parameter in this context is the electron density in the edge. The penetration of the heating wave to the plasma centre is strongly dependent on the edge density; conversely, the edge density can in turn be affected by the heating wave. In this situation microwave reflectometry was proven to be the appropriate diagnostic method for the density analysis just in front of an operating high-power RF antenna.

The operational principle of the reflectometer is the measurement of the phase of microwaves reflected from the cut-off layer, in comparison with a reference wave. By sweeping the frequency different density regions of the plasma are probed. Counting the interference fringes during a sweep eventually permits calculation of the electron density profile.

In principle, both polarizations, the ordinary wave with E∥B (O-mode) and the extraordinary wave with E⊥B (X-mode), can be used for reflectometry. However, the low densities in the edge region in front of the RF antennas would call for very low frequency O-mode operation, which would result in poor spatial resolution together with unacceptably large reflectometer antennas. For this reason only the X-mode is practicable for edge measurements since the X-mode cut-off is basically shifted by ω_{ce} towards higher frequency. A specific X-mode reflectometer was developed in the Technology Division which allows a frequency sweep from 60 to 80 GHz in 160 µs every 2.5 ms. Two antenna systems of the following size are installed: a) in a diagnostic hole of the NW-ICRF antenna: 10 x 8 mm^2 and 3.8 x 1.9 mm^2, b) near the LH grill: 16 x 8 mm^2 and 10 x 8 mm^2. The raw data are digitized with a sampling rate of 10 MHz.

Depending on the plasma parameters, the system can measure the ranges $n_e \approx 10^{11}$ cm^{-3} to $n_e = 1.5 \times 10^{13}$ cm^{-3} and 1.90 m $\leq R \leq$ 2.15 m for $B_o = 2.8$ T.

A major experimental problem especially for X-mode reflectometry, however, is the pronounced electron density fluctuations in the tokamak. These density fluctuations lead to strong amplitude and phase fluctuations of the reflected wave with frequencies of up to several 100 kHz typically. The obvious difficulty can only be overcome by a "moment picture", i.e. a very fast frequency scan in conjunction with a fast digitizing system (10 MHz, 12 bit, 16 channels, 1 Mword each). This rapid sweep gives a fringe frequency of more than 1 MHz, so that the fringes are not blurred out by the fluctuations. As the sweep is on the time scale of the density fluctuations, it is necessary to integrate over several sweeps ($\approx$ 40) to get the averaged density profile.

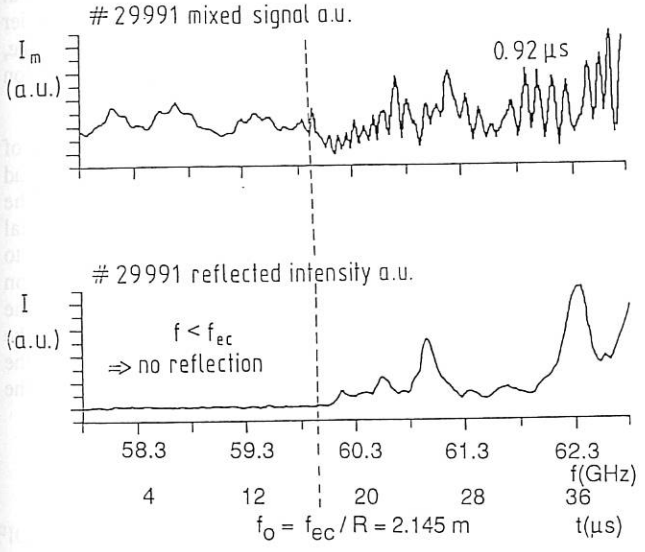

FIG.3: First 40 µs of a sweep. The mixed signal I_m and the intensity are simultaneously digitized. There is no reflection for f < f_{ce} at the antenna mouth.

Figure 3 shows the first 40 µs of a sweep. The intensity of the reflected wave and the mixed signal (reflected and reference waves) are separately digitized. The following points are to be noted:

- Since the X-mode is used, reflection does not begin till $f = f_o$ ($= f_{ce}$ at the antenna mouth), thus giving the location of the first reflection point. Hence, the absolute density profile can be calculated completely independently of any other diagnostic.
- The reflected intensity is strongly modulated in amplitude.
- The fringes appear at f > 1 MHz and are thus not perturbed by the fluctuations.

Figure 4 shows the electron density profile measured with the system near the LH grill in two stationary phases of a discharge where the plasma has been moved horizontally by 2.7 cm.

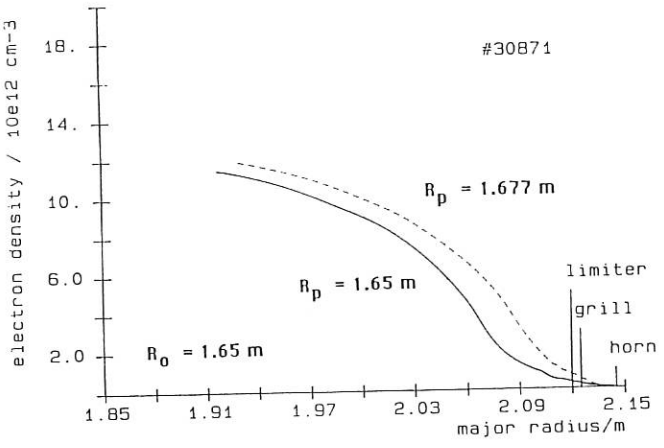

FIG.4: Density profiles measured in two stationary plasma phases in one shot, where the plasma has been moved horizontally 2.7 cm (B = 2.8T, I_p = 420kA, $n_e = 1.3 \times 10^{13}$cm^{-3}).

The system was operational in its final version from December 1989 till the shut-down of ASDEX in August 1990. The measurements confirmed the density dependence of the coupling of the LH wave to the plasma. In Fig. 4 it is seen that for $R_p \approx$ 1.68 m, the standard plasma position during LH operation, the measured electron density at the radial position of the LH grill is 5×10^{11} cm^{-3}. The Brambilla coupling theory predicts for this density a reflection coefficient for the LH wave of about 6%, which is in agreement with the experimental one. It could also be confirmed that the LH itself can create, under certain experimental conditions, a sufficiently high electron density in front of the grill for good coupling even for big grill separatrix distances (s. "ASDEX PROJECT, 1.7). The profile changes measured during LH are in agreement with those measured with other diagnostics. Finally, a strong increase of the edge turbulence during LH near the grill in high-density shots could be detected. This point is of importance for theories concerned with the propagation of the LH from the grill to the plasma centre.

3.5 Radiative Energy Transport via Electrostatic Electron Bernstein Waves (S. Puri)

Energetic electrons in a magnetic field are profuse sources of synchrotron radiation. The collective effects in the plasma channel this radiation into cyclotron-harmonic modes. Using the Rayleigh-Jeans approximation of Planck's formula, Kirchhoff's law generalized to anisotropic media gives the total radiated power density [1,2]

$$\eta = 2\pi^{-3} \int_k \eta(k)\, dk = 22(\pi)^{-3}\, T_e \int_k k_i(k) \,.\, v_g(k)\, dk\,, \qquad (1)$$

where k is the propagation vector, k_i = Im|k| and v_g is the group velocity. The integration extends over all propagating waves that satisfy the hot-plasma dispersion relation

$$D(k,\omega(k,r),r) = 0 \qquad (2)$$

Since η_T scales as the k-space volume, radiation in a plasma is dominated by the large-k electrostatic Bernstein [3] waves.

Figure 5 shows the fundamental cyclotron emissivity $\eta_\varepsilon = \eta_T/\varepsilon$, normalized with respect to the thermal energy density $\varepsilon = (3/2)\, n_e T_e$ as a function of electron temperature for $n_e = 10^{21}$ m^{-3} and $B_o = 10$ T. The corresponding $\eta_T > 0(1)$ MW m^{-3}. Large η_e values imply that a transport of the emitted radiation over a mean square distance of only $\langle r^2 \rangle \sim 0\ (10^{-3})$ m^2 would lead to an electron thermal diffusivity of $\chi = \eta_\varepsilon \langle r^2 \rangle \sim 0(.5)$.

Determination of χ is accomplished through ray tracing in accordance with the Weinberg [4] approach using the dispersion relation (2). The computational parameters consist of: major torus radius $R_o = 3$m, plasma radius a = 1 m, $n_e = n_o (1-\rho^2)$, $T_e = T_o (1-\rho^2)^2$, $n_o = 10^{21}$ m^{-3}, and $B_o = 10$ T.

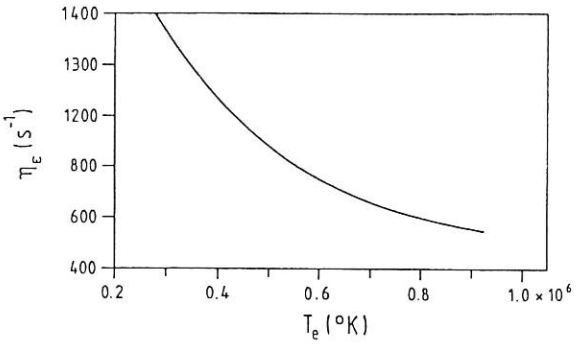

FIG.5: Normalized emissivity versus temperature.

Figure 6 shows the computed results for the case of fundamental cyclotron emission as a function of temperature. The enhanced values of $\chi \sim 0(.5)$ are of fundamental significance to thermonuclear fusion research. To our knowledge, this is the first manifestation of such a high electron thermal diffusivity which does not invoke either instabilities or non-linear turbulence.

The radiative transport of electrostatic Bernstein wave emission may hold important clues to the understanding of anomalous

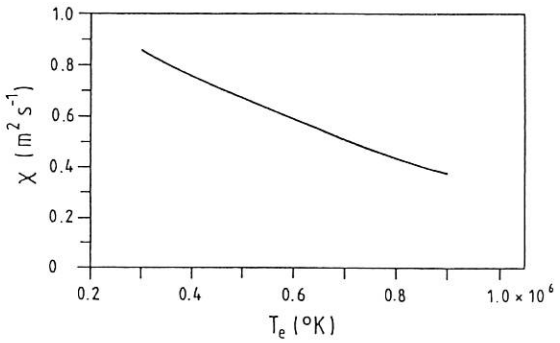

FIG.6: Diffusivity versus temperature.

thermal transport in magnetoplasmas both in the laboratory and in space.

[1] G.Bekefi, in Radiation Processes in Plasmas, John Wiley, New York (1966).
[2] M.Bornatici et al., Nuclear Fusion 9, 1153 (1983).
[3] I.B.Bernstein, Phys.Rev. 109, 10 (1958)
[4] S.Weinberg, Phys.Rev. 126, 1899 (1962)

3.6 L-H Transition via the Matsuda Anomaly (S.Puri)

Electron-ion momentum transfer collisions parallel to the magnetic field direction are anomalously enhanced if the electron gyroradius is much less than the Debye length; the collision frequency may exceed the corresponding Spitzer value by a factor of one thousand for electrons with parallel velocity of the order of the ion-thermal speed.[1,2] Trapped electrons in a torus are subject to this anomaly (henceforth referred to as the Matsuda anomaly) near their turning points, leading to the conjecture that the Matsuda anomaly might provide an additional channel for neoclassical diffusion.[1,2]

In this paper the diffusivity contribution of the Matsuda anomaly is investigated and the underlying transport mechanism is identified. The high collisionality causes the electrons to be captured near their turning points, where the parallel velocity is maintained at the ion thermal speed through continual collisions. The gradient drift occurring during the stagnation interval constitutes the mechanism for enhanced diffusivity. Under conditions of extremely large collisionality at the plasma edge, the capture time may become large enough to lead to a stagnation catastrophe signalling the onset of convective transport.

The principal conclusion of this study is that the stagnation of the trapped particles precipitated by the Matsuda anomaly can lead to considerable diffusion fluxes at the plasma edge. The stagnation catastrophe may be circumvented by a nominal increase of the ion temperature and bears a close resemblence to the L-H transition[3] in tokamaks, satisfying the transition criteria[4]: (i) The theory is capable of bifurcation, (ii) the transition has a threshold involving the edge temperature, (iii) the edge gradients would become steep at the transport barier, (iv) the asymmetry of the heat flux to the divertor is reduced, and (v) the transition is not critically dependent upon the heating method.

1 K. Matsuda, Phys. Rev. Lett. 49, 1486 (1982).
2 A.A. Ware, Phys. Rev. Lett. 62, 51 (1989).
3 F. Wagner et al., Phys. Rev. Lett. 49, 1408 (1982).
4 K.H. Burrell et al., Plasma Phys. and Contr. Fusion 31, 1649 (1989).

4. NEUTRAL INJECTION HEATING

Group leader: E. Speth
Deputy: W. Ott

R. Bilau-Faust, J. Dunne, J.-H.Feist, K.Freudenberger, B. Heinemann, W. Kraus, R.C. Kunze, H. Lohnert, W. Melkus[1)], E. Morris, F.P. Penningsfeld, F. Probst, W. Schärich, J. Sielanko[2)], B. Sombach[1)], R. Süß, A. Staebler, A. Teubel, O. Vollmer, K. Wittenbecher

1) ZTE
2) Guest scientist from the University of Lublin, Poland

4.1 Status of the Large-area RF Plasma Source (R. Bilau-Faust, J.-H. Feist, W. Kraus, E. Speth)

For two years a prototype of a powerful RF source compatible with the PINI extraction system has been developed and tested. The final version of this source is a prime candidate for the second ASDEX Upgrade neutral beam injector. In 1990 the work concentrated on further tests of the coaxial isolation transformer,

more refined beam diagnostics and plasma profile studies. The results are:

a) The HV/RF transformer, which allows the RF generator to be run at earth potential during beam extraction, worked without problems also for long pulses (plasma source only). Within the accuracy of the measurement no change of the efficiency of the source has been observed.

b) With a magnetic analyzer, a proton fraction in the beam of approx. 90 % was measured in 1989. A Doppler shift spectroscopy diagnostic installed last year resulted in a value almost 10 % lower, as shown in Fig. 7. The reason for this difference is unclear. In the original setup the backplate is made of copper. With an alumina coating of the backplate, which has a lower recombination coefficient for atomic hydrogen, an increase of 6 % was observed. Whether it is worth while to use a coating, which complicates the design of the backplate, has to be further discussed.

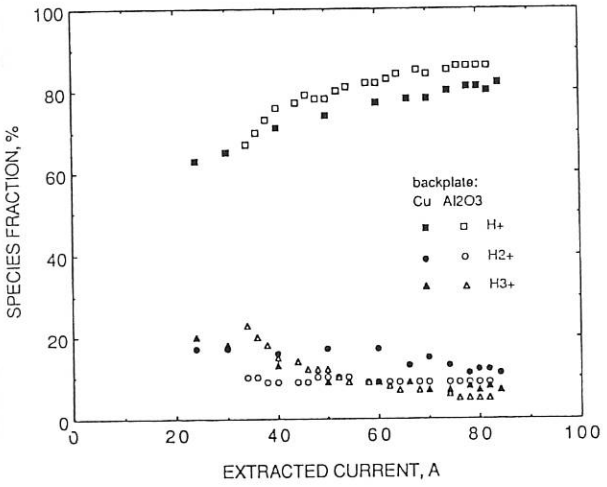

FIG.7: *Ion species distribution measured by Doppler shift spectroscopy with and without alumina coating of the copper backplate.*

c) More detailed beam profile measurements were carried out with an array of movable thermal probes. The observed beam profiles cannot be explained by a homogeneous current density across the extraction area. A change from a line-cusp to a checkerboard arrangement of the backplate magnets led to a slight improvement of the profile. Since the diagnostic is too close to the source to deliver reliable data, it is necessary to continue the measurements with a beam diagnostic at a distance corresponding to the focal length of the extraction system. This is now under construction.

d) The apparent problems with the plasma uniformity led to further experiments with disc-type Langmuir probes installed plasma density profiles for the two magnet configurations are shown in Fig. 8. With the checkerboard configuration a significant improvement has been obtained. Further experiments with additional rows of magnets placed at the side walls close to the extraction area and with a higher RF frequency yielded another slight improvement. But because of the small distance (2.6 cm) between the extraction area and the side walls of the source homogeneous profiles were not achieved over the whole extraction area. Hence this problem must be solved by enlarging the source width.

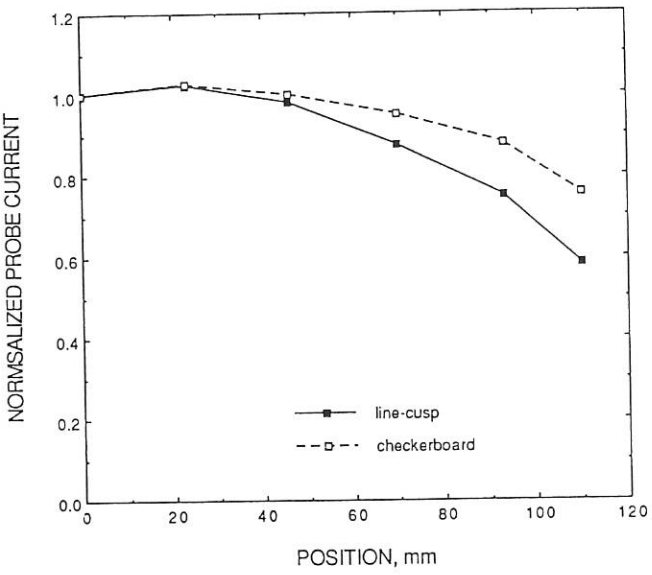

FIG.8: Normalized profiles of the probe saturation current density for different configurations of the magnets on the backplate, measured along the short axis from the centre to the edge of the extraction area.

In cooperation with KFA Jülich a new RF source was designed which meets the requirements derived from the operational experience with the first prototype and from long-pulse operation. A schematic view is shown in Fig. 9. The active cooling of the backplate allows long-pulse operation. Compared with the prototype, the new source is more compact and simpler. The width of the ground area is enlarged by 4 cm to get a greater distance between the side walls and the extraction area. The inhomogeneous part of the plasma density profiles is therefore outside the extraction area. If necessary, the distance between the

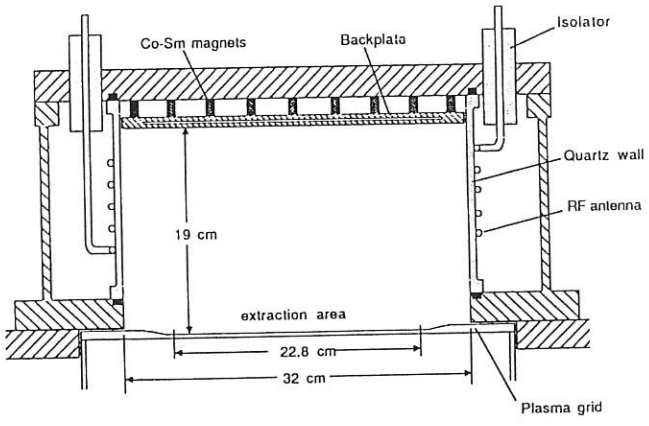

FIG.9: Schematic drawing of the future RF plasma source .

backplate and plasma grid can be varied in order to influence the plasma density profiles. The source is under construction at KFA Jülich and testing will start at the end of April. The specifications for a new 80 kW RF generator have been elaborated. It will be a self-excited oscillator with a working frequency of 1 MHz. The spezifications include control, modulation and variable rise time of the output power.

5. REACTOR ORIENTED STUDIES
(A.F. Knobloch)

The ongoing tokamak reactor configuration and power balance studies were continued with the introduction of additional conditions imposed by the present divertor model as derived by Harrison and Harbour and with respect to the impact of current drive efficiency (using physics guidelines as adopted for ITER).

The following observations were quantified, as summarized below:

a. Evaluation of the plasma power balance and the assumed confinement scaling in terms of specific plasma parameters under technical geometry constraints leads to the observation that for a given fusion power (which is practical as an approximate measure of outlay) more attractive conditions may be obtained in a higher-field compact reactor geometry. The ability to control the energy confinement time for adjustment of the plasma operating point is a necessary prerequisite for practical reactor operation.

b. The attainable level of non-inductive current drive efficiency has a marked impact on the parameter choice for a next tokamak step that includes ignition demonstration and an important technology testing programme. With high current drive efficiency, the steady-state operating point could be approximately the same as the near-ignited one (which could then be thermally stable at the associated higher plasma temperature). If properly designed for steady-state high efficiency current drive, a reactor can also be operated at reduced fusion power (lower density) with lower efficiency drivers. A rated operating density large enough to allow such a reduction can be achieved by selecting a higher toroidal field, which allows a more compact configuration and is also required for meeting the stringent edge conditions.

c. Evaluation of reactor configurations (see Annual Report 1989), including the 1D high-recycling divertor model of Harrison/Harbour, shows that the product n_eR is not only determined by the product of the Murakami parameter times the toroidal field but also depends on the divertor conditions (target plate temperature, relative edge density, expansion factor, T_e gradient safety factor, and the boundary safety factor in a certain combination). The minor radius, too, is determined by - apart from bulk plasma characteristics including the temperature - that same combination of divertor parameters. This leads to the effect that for a fixed fusion power there is a strong variation of the configuration (dimensions, aspect ratio, maximum toroidal field) within a narrow range of the plasma operating temperature assumed. The thermal divertor target load is one of the most stringent technical parameters. For the divertor model of Harrison/ Harbour the divertor target heat load, with all other plasma parameters, the fusion power and the divertor data (see above) kept fixed , can be shown to depend not only on the heat loss into the divertor channel and the attainable perpendicular heat diffusion coefficient, but also very strongly on the edge density. As shown in [1], this heat load does not seem to be readily coped with by certain conceptual reactor designs that otherwise would appear feasible .

d. It is important in any reactor parameter evaluation to obtain a large Q value, which means lower heat loads in relation to the neutron wall load and hence a lower overall recirculating power if an energy conversion system is added to provide net energy supply and the reactor auxiliary power. Depending on the parameters of blanket multiplication, power conversion, and auxiliary power, a reactor with Q = 3 - 6 is not capable of net electric power production. For a current-driven reactor one can derive the attainable $Q = P_{fus}/P_{CD}$ in terms of the plasma characteristics. It can be seen that the current drive efficiency (including the bootstrap current fraction), the dilution factor, and the plasma temperature enter in a significant manner.

e. To attain a larger Q value despite low current drive efficiency, the safety factor q could be increased, which also increases the bootstrap fraction. For given Q, reactor configuration and fusion power, for example, this entails an increase in toroidal field by a factor $X^{0.5}$ and a reduction in plasma current by the same factor when q increases by a factor X. The currrent drive efficiency then can be lower than otherwise required for the same Q. A first result of the pertaining evaluation is that (in the first stability regime) the alternative of low current drive efficiency together with large q is less attractive than the combination of high current drive efficiency together with low q for fixed Q, fusion power, and configuration, because under these constraints

   - increasing q leads to larger toroidal field and hence larger device outlay,

   - it is only possible by doubling q to replace an increase in current drive efficiency by a factor of about two. Since a desirable large overall γ value would be > 2 A/Wm^2 (which is about half that of theoretical predictions for compressional Alfvén wave current drive), the attainable γ values at larger q (including the larger bootstrap fraction for increased q) with existing drivers fall short by a factor of > 2 of becoming competitive.

   The incentive for large Q and hence for notably larger current drive efficiency than available today is very strong and calls for practical development of novel current drive methods.

f. With the neoclassical definition (there is recent work indicating further enhancement based on the neoclassical parameter relations), the bootstrap current fraction in a given plasma configuration is proportional to the attainable Troyon coefficient and the safety factor and is inversely proportional to the ratio $\beta_{tot}/\beta_{therm}$. If the Troyon coefficient is limited to 0.03, the bootstrap current fraction is limited to about 1/3 for low q. On the assumption that about 30% of the plasma current should in any case be driven (for current profile control), the maximum reasonable bootstrap current fraction amounts to 70%, regardless of what particular parameter combinations (and the recent more favourable scaling mentioned above) may promise to be attainable.

g. More compact configurations for a next-step reactor appear possible, provided some additional development can be carried out before design freezing. Such development refers to items that have to be enhanced for a subsequent DEMO reactor anyway, such as higher field magnets needed for higher plasma fusion power density (enhanced by higher relative fuel density, higher density and temperature, all within Troyon and density limits), and larger heat load components. Further necessary improvement such as the development of high-efficiency current drivers could be carried out during construction and the first operation phases.

A configuration similar to the one shown in a recent EC Reference Reactor study [2], but with lower toroidal field, can represent an ETR alternative that roughly complies with the

above features. It could be operated with current drivers of low and high current drive efficiency. The ETR alternative data set for high Q is shown in Table 1 below together with the data set for the steady-state ITER case 2d as of October 1989. It should be noted that another alternative - though limited to low current drive efficiency and low Q - was described in a recent report on a high aspect ratio ITER [3].

Table 1 Comparison of alternative ETR design parameters

		ITER 2d (1989)	Alternative (example)	
R	[m]	6.00	5.28	major radius
a	[m]	2.15	1.45	minor radius
A		2.79	3.65	aspect ratio
t_{BS}	[m]	0.91	0.96	inn. blank./shield
B	[T]	4.85	6.38	tor. field on axis
I	[MA]	19.8	14.4	plasma current
B_m	[T] (geom.)	10.4	12.1	max. tor. field
k, Δ		1.98, 0.35	1.98, 0.35	elong./triangul.
$f_{pw} = a/r_w$		0.94	0.94	minor/wall radius
q_ψ		3.57	3.10	boundary q
q_I		2.68	2.48	current q
g		0.0293	0.0293	Troyon coeff.
M $[10^{20}/Tm^2]$		0.92	1.00	Murakami param.
Z_{eff}		3.81	1.66	effective Z
γ_o $[10^{20}$ A/Wm$^2]$		0.46	1.50	CD efficiency
$\gamma = \gamma_o/(1\text{-}I_B/I)$		0.60	2.03	with bootstr. curr.
n_e $[10^{20}$ m$^{-3}]$		0.75	1.21	electron density
n_{DT}/n_e		0.622	0.731	DT content
$1 + n_i/n_e$		1.74	1.84	total density
T	[keV]	19.20	16.65	temperature
T_t	[eV]	30	35	div. target temp.
T_s	[eV]	149	148	midplane temp.
$n_s = 1/3\ n_e$		0.25	0.40	midplane density
f_s		2.36	2.95	T_e grad. safety f.
g_d		17.3	12.7	expansion fact.
$\chi_\perp$	[m^2/s]	2.2	3.0	divert. heat diff.
Δ_s	[mm]	6.1	7.0	midpl. scrape-off
Q		5.6	22.0	fus./heatg. power
τ_E	[s]	3.46	1.81	energy conf. time
$f_\tau = \tau_\alpha/\tau_E$		7.98	7.89	alpha confinem.
f_{HGO}		2.11	1.71	Goldston enh. fact.
$n_{DT}T\tau_E$		30.9	26.5	fusion product
β	[%]	5.56	4.60	total beta
P_α	[MW]	165.2	200	alpha power
P_{CD}	[MW]	147.6	45.5	curr. drive power
P_{con}	[MW]	187.4	212.1	power loss W_{th}/τ_E
P_{rad}	[MW]	119.1	26.9	bremsstr.+imp.rad.
P_{syn}	[MW]	8.6	7.4	synchr. radiation
P_f	[MW]	826	1000	fusion power
V	[m^3]	1083	431	plasma volume
pf	[MW/m^3]	0.76	2.32	fus. power density
q_w	[MW/m^2]	0.368	0.488	av. wall heat load
q_t	[MW/m^2]	8.1	12.3	peak div. heat l.
p_w	[MW/m^2]	0.78	1.59	av. neutron flux

(Density, temperature, beta are volume average values.)

[1] D. C. Robinson et al., Report CLM-P862, 1989
[2] D. A. Cooke et al., Report CLM-R298, December 1989
[3] L. J. Perkins et al., Report UCRL-ID-104178 , May 1990

6. NON-INDUCTIVE CURRENT DRIVE

(D. Eckhartt)

One of the prerequisites for operating a tokamak fusin reactor in a truly steady state is to sustain its plasma current against collisional relaxation. It has been achieved with the help of suprathermal ions or electrons having a non-symmetric velocity distribution in the toroidal direction, i.e. with respect to the main magnetic confining field. This requires the injection of toroidal momentum and energy. The suprathermal populations of ions or electrons were created by uni-directionally injecting high-power beams of energetic fuel atoms , or slow waves with frequencies in the lower hybrid range. We have compared the performances of both these schemes as observed to-day and as expected in future tokamak reactors. This comparison is made by investigating how the local figure of merit and the specific absorption of driver power are modified when plasma density and temperature are raised from present-day to reactor-relevant values, i.e. each by more than one order of magnitude. It is assumed that the fast-particle slowing-down occurs via collisions in a time that is shorter than the bulk plasma particle confinement time. The figure of merit for neutral beam current drive increases much faster with bulk electron temperature than that for lower hybrid current drive, surpassing the latter at values around 20 keV. As regards absorption, neutral beams can traverse dense plasmas provided that their beam particle energy is high enough. This is in contrast to lower hybrid slow waves, which do not at all penetrate into dense and hot plasmas owing to mode conversion and absorption effects. This limits the applicability of lower hybrid current drive to the outer plasma regions - in particular when the central plasma has already been heated by deposition of driver power. A more precise judgement can be made only after applying both drivers to some given plasma configuration. Yet theory predicts that the global current drive efficiency γ for lower hybrid waves will become only slightly higher than the values seen in present large experiments with their $N_{\parallel}$-spectrum tailored for optimum current drive. For neutral beam current drive in hot plasmas one expects γ-values of 0.3 to 0.4*). This means that the two efficiency values should come quite close to each other, whereas nowadays they are a factor of roughly ten apart.

*) D. Eckhartt. NET Physics Memo PM-90-002.

PLASMA TECHNOLOGY

(Prof. Dr. Wolfhard Möller [1])

The tasks of the Plasma Technology group, which was established in mid 1988, are threefold: Surface coatings shall be produced by means of plasma-enhanced chemical vapour deposition (PECVD) for special applications mainly in fusion plasma devices. New or improved PECVD procedures or devices are being developed for these purposes. As the scientific part of the activity, a number of plasma and thin film diagnostics shall be employed in order to correlate the discharge conditions with the properties of the resulting coatings. A final aim is to understand the deposition process to such an extent that the discharge conditions can be adjusted in a predictable way in order to optimize a desired property of the growing film.

In 1990, additional diagnostic facilities were installed and commissioned allowing further in-situ studies of the plasma, the plasma boundary layer and the growing films. SiO_2 insulating layers for bolometers have been improved and produced in larger numbers. Carbonized layers were deposited in coaxial RF guides. First boronized layers were produced under well controlled conditions.

D. Boutard[1]
V. Dose (Division Head)[1]
M. Engelhard[2]
A. Friedl[2]
R. Hytry[1]
W. Jacob[1]
A. Koch[2]
K. Lange[1]
J. Perchermeier[3]
P. Reinke[1]
M. Veprek-Heijman[1]
S. Schelz[4]
R. Wilhelm (Division Head)[2]

1) Surface Physics Division
2) Technology Division
3) Central Technical Services
4) Short-term visitor
(Univ. Basel, Switzerland)

1. INSULATING FILMS FOR BOLOMETERS (Cooperation with WVII-AS Project)

It has been shown that the insulating properties of 1 μm thick SiO_2 layers, deposited from TEOS in an rf-plasma are sufficient for use in the Ge bolometers. However, due to defects (dust, foil imperfections) the performance yield of a first series was low. It was decided to deposit in-situ, before the evaporation of the Ge layer, an additional 0.3 μm thick MgO layer. Bolometers made in this way showed extremely good insulation values (> 10 GOhm at 5 V).

A large series of 20 pieces has been deposited. Electrical measurements are not yet available. The deposition conditions could be reproduced very well, in spite of the manually operated set-up. The experimental character of the deposition apparatus limits the throughput of bolometers to 1 to 2 per day.

Measurement of the catastrophic breakdown field strength of the SiO_2 films showed that at low H-content (deposition at low rate) the films approach the value for thermally grown SiO_2 with values up to 8×10^6 V/cm.

For comparison with the standard procedure of oxygen dilution, the deposition of SiO_2 from TEOS with Ar dilution was investigated. Extremely low (< 1 %) (as compared to literature values) C-content was found. Also with Ar instead of O_2 good films can be deposited. The deposition rate is lower and, interestingly, the rate increases with increasing temperature, in contrast to the oxygen case.

Further, the dependence of the deposition rate on the rf excitation frequency was investigated. In oxygen, the rate decreases with decreasing frequency, in Ar the rate is more or less constant. To investigate the role of ions, an ion-energy analyzer was implemented in the same geometry as the substrate during deposition. Energy spectra and saturation currents were measured as function of pressure, rf-frequency and power. The maximum ion energy is always lower than the sputter threshold for SiO_2. The saturation currents in oxygen decrease with decreasing rf frequency in a similar way as does the deposition rate. It seems that at least in oxygen, the ions do not dominate the deposition process. The saturation current and deposition rate both mirror the more efficient bulk plasma excitation at higher frequency.

2. CARBONIZATION OF RF HEATING COMPONENTS (Cooperation with ICRH Group)

The PECVD device 'KESCABO' has been installed and commissioned. It allows to treat larger components up to linear dimensions of ~ 80 cm by means of DC or RF plasmas. Hydrogenated carbon coatings were deposited on RF antenna Faraday screen rods and coaxial connector elements, to be used in ASDEX UPGRADE.
For anti-multipactoring purposes, hydrogenated carbon coatings were also deposited in a 1.5 m test section of a 15 cm o.d. RF coaxial guide. A 50 Hz AC plasma in methane was used to deposit simultaneously on the inner and outer electrode.

Problems were encountered with the sticking of the deposited layers depending on the material and the curvature of the substrate components. Preliminary tests with sandblasting prior to plasma deposition were successful.

3. ECR CARBONIZATION OF ASDEX (Cooperation with W. Poschenrieder[1], F. Leuterer[2], M. Münich[2])

Carbonization tests have been performed in ASDEX with the aim to investigate possible advantages of an ECR glow discharge compared to conventional DC discharges. Microwave power at 2.45 GHz was fed into the vessel via the LH grill antenna, while the toroidal field coils at low current (~ 1.4 kA) were used to establish the ECR condition. Only pulsed operation of the microwave supply (~ 1 s with ~ 10 kW) was possible.

The optimum methane pressure is around 2×10^{-4}mbar. During the pulses, the gas is nearly completely dissociated resulting in a very high deposition rate above 10^{15}C-atoms/cm^2.s. However, this high rate cannot be extrapolated to a stationary operation with a continuous microwave supply, since the pumping speed of the vacuum system is largely insufficient for the removal of the hydrogen produced from the methane dissociation.

As expected from the low ion bombardment energies associated with microwave plasmas, the hydrogen content of the deposited layers is larger than for DC carbonization (slightly less than one hydrogen atom per carbon atom).

In summary, ECR carbonization is probably not advantageous compared to conventional carbonization, if the pumping speed of the vacuum system cannot be substantially increased.

4. OPTICAL IN SITU DIAGNOSTICS OF PLASMA DEPOSITION PROCESSES

Polymer-like hydrocarbon films have been deposited in the experimental ECR device 'PLATO'. In order to understand the deposition mechanisms and to improve the deposition techniques several optical devices have been established which are employed as in situ monitors. Nonintrusive, species-selective, spatially and temporally high-resolving diagnostics are to be preferred.

4.1 Plasma Diagnostics

Optical emission spectroscopy has been performed in the 350 to 700 nm wavelength region. A monochromator of 3 meter focal length provides good spectral resolution (< 5 pm) necessary to resolve rotational molecular spectra. CH band spectra and, for comparison, N_2 and N_2^+ band spectra have been recorded. A computer simulation of the measured spectra yields a rotational temperature of 500 degrees for N_2 and N_2^+ whereas the CH temperature is as high as 1500 degrees. The use of the actinometric technique provides density measurements of relevant species.

A pulsed dye laser system is to be employed for local and unambiguous LIF studies of particle concentrations and fluxes. First measurements have been performed with ECR-heated nitrogen plasma. A Fabry-Perot interferometer has been put into operation in order to increase the spectral resolution of the detection unit to 0.5 pm. This resolution permits the observation of particle fluxes by means of Doppler spectroscopy. The spatial resolution obtained is better than 1 mm^3. The optical setup is well suited to detect deposition-relevant species near the surface of the growing film.

4.2 Surface Diagnostics

A spectroscopic infrared ellipsometer is under construction which allows detailed studies of film parameters during the deposition process. Both film thickness and complex refractive index can be monitored as a function of the wavelength. A cascaded arc serves as a wide-band high-intensity infrared light source.

In addition, a two-beam laser interferometer at 632.8 nm has been installed and used to monitor film thicknesses and refractive indices of growing films. Multibeam numerical simulations of the time-dependant interference patterns yield information on the absorption coefficient and the lateral uniformity of the film (Figure 1). The growth rate, optical film properties, and lateral uniformity have been investigated as functions of plasma and process parameters in different devices.

5. HYDROGENATED CARBON AND BORON/CARBON FILMS

5.1 Carbonization

To gain information on the growth process of the carbonised layers and its relation to the generating plasma, glow discharges (DC or RF) were performed in various methane/hydrogen mixtures using an isotopic marker technique, i.e. dilution of CH_4 with D_2 or of CD_4 with H_2.

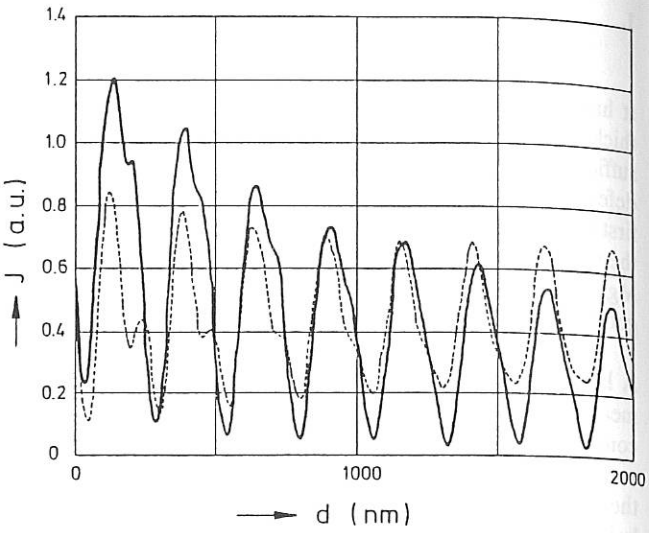

FIG.1: Thin film interferograms obtained with the two-beam laser interferometer. The reflected beam intensity J is plotted versus the thickness d of the growing film. Solid line: Experiment, dotted line: numerical simulation.

Furthermore, some experiments were done with helium as added gas. For pure methane (CH_4 or CD_4 alone), the growth rate with CD_4 is about 30 % smaller than in CH_4 under otherwise identical discharge conditions. The deuterium concentration is slightly higher (+ 10 %) than the hydrogen one in the resulting films.

In both cases, the dilution with hydrogen results in a decrease of the growth rate, which is slower than the decrease of the methane partial pressure. This suggests that the dilution gas (H_2 or D_2) improves the sticking of the carbon-carrying deposition species. This effect is mainly related to the additional ionic energy deposition since it is also observed with helium as added gas.

The dilution in H_2 or D_2 increases the total hydrogen population of the films which can be assigned to the implantation of hydrogenic ions.

5.2 Boronization

The 80 cm-diam. reactor 'KESCABO' has been equipped with gas handling and monitoring devices to allow the plasma-assisted deposition of films from discharges in toxic gases. It has been used to perform boronization with the required security level.

The initial boron-containing gas is a mixture of 10 % B_2H_6 and 90 % H_2, to which methane was added in various proportions. The depositions were performed using a largely asymmetric RF discharge, with RF power fed to the substrate electrode (self-bias about - 400 V).

The growth rates and resulting compositions of the films were measured as function of the gas composition (Fig. 2).

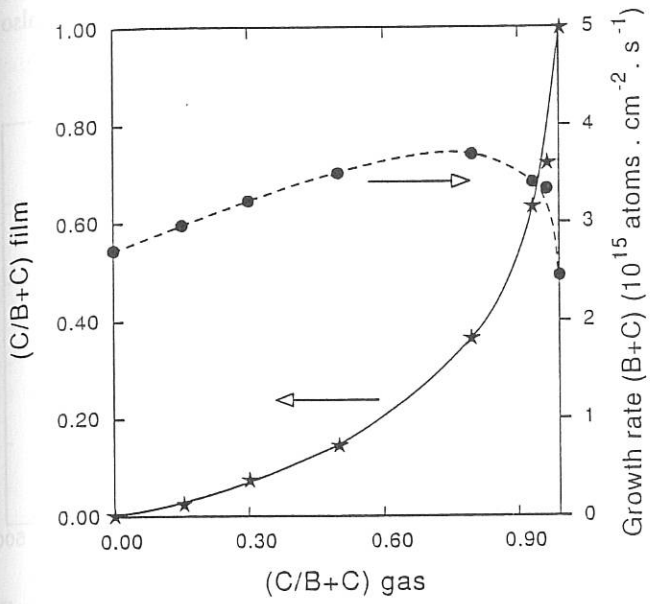

FIG.2: Growth rate (dashed line) and bulk composition (solid line) of B:C:H films as function of the composition of the process gas.

For a given total pressure (5 Pa), the growth rate displays a maximum around 3:1 carbon/boron in the gas. (Fig. 2). Over the whole range of gas composition. Boron is always incorporated preferentially with respect to carbon. IR absorption spectra show that hydrogen is bound both to boron and to carbon. At increasing carbon proportion, the CH vibration intensity increases while the BH intensity remains larger than expected from the decrease in B proportion.

6. ION ENERGIES FROM ECR PLASMAS

Mechanical properties and microstructure of hydrocarbon films deposited by plasma CVD are significantly influenced by the energies of the ions impinging on the growing film. To gain a better understanding of the ion dominated steps in the film growth process and the experimental parameters influencing the ion energies, a parallel plate retarding field analyzer was constructed. This analyzer is introduced into the cylindrical ECR reaction chamber 'PLATO' at the substrate position. It can be moved to obtain the ion energy distribution as a function of axial and radial position.

Detailed studies of the influence of gas pressure, gas composition, microwave power input and magnetic field configuration were performed. A strong dependence of the most probable energy (E_m) of the ion energy distribution (IED) on gas pressure and composition was found for Ar, CH_4 and CH_4/H_2 mixtures. An increase of the magnetic field divergence between the resonance zone and the sample location leads to an increase in E_m but also to a significant reduction of the ion current density (Fig. 3).

Another means to influence the ion energy is the application of a DC bias to a sample holder mounted on the analyzer. This results in a shift of the IED to higher energies without a broadening of the distribution. However, above a certain size of the sample holder the plasma potential is controlled by this surface and the DC bias no longer affects the IED. First polymeric and a-C:H films have been deposited on Al, Si and Ge substrates, in order to correlate the film properties with the IED.

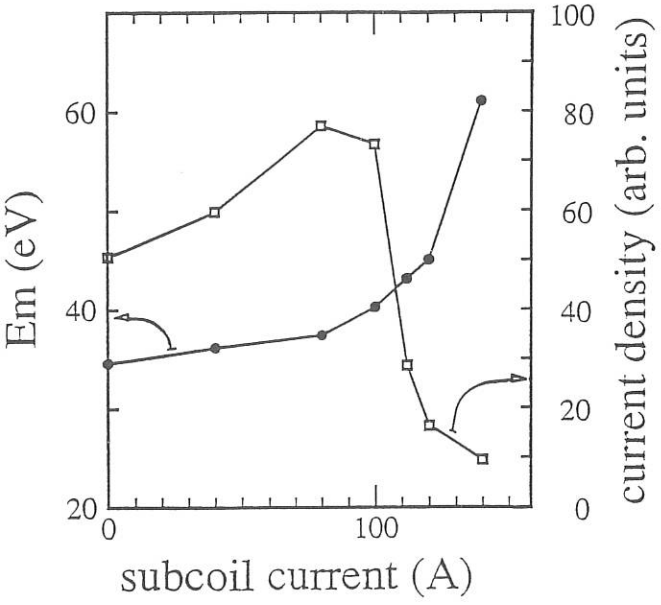

FIG.3: Dependence of the most probable ion energy E_m (filled circles) of the ion current density (open squares) on the subcoil current. An increase of subcoil current increases the magnetic field divergence.

7. ECR MICROWAVE GUIDE DISCHARGE

The ECR microwave guide discharge opens the possibility to deposit anti-multipactoring layers on the inner walls of microwave guides, which are used for heating in fusion experiments. Such films were deposited by means of plasma-assisted chemical vapour deposition from methane by the moving-coil ECR method. For further improvement of this method a thorough study of the discharge and deposition parameters was performed, by investigating the deposition rate, the composition, and the refraction index of C:H films as function of the total gas pressure, the methane flow, the absorbed microwave power and the magnetic field. A typical variation of the deposition rate along the waveguide and the corresponding distribution of magnetic field strength are shown in Fig. 4. The maximum deposition rate is found to be distinctly shifted away from

the resonance zone, where the deposition rate approaches zero. This may be explained by the motion of the ions along the magnetic field lines. In addition, the microwave enters a cut-off region when propagating in the direction of increasing magnetic field. The resonance zone can only be reached if the electron density approaches zero, that means just before ignition. Considering this, we obtain a resonant ignition, but a non-resonant microwave absorption during the steady-state discharge.

The maximum of absorbed microwave power was found to be a function of total gas pressure ($2x10^{-3}$...$4x10^{-2}$mbar) and methane flow (3.5...14 scm^3). Absorbed microwave power increases with decreasing pressure and decreasing flow, while the deposition rate (measured at the maximum of Fig. 4) decreases.

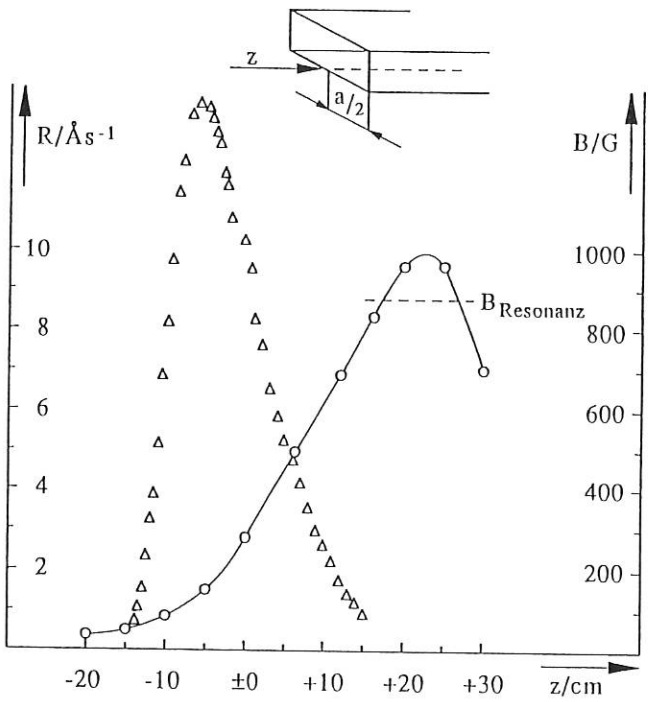

FIG.4: Comparison of C:H deposition rate R (triangles) and magnetic field B (circles) along the microwave guide, at a methane pressure of 4 x 10^{-2} mbar, a gas flow of 14 scm^3/min, and an absorbed microwave power of 25 W. The ingoing microwave travels in positive z-direction.

8. SIMULATIONS OF C:H FILM GROWTH

First computer simulations of the growth of plasma-deposited C:H films have been performed, using the dynamic binary-collision code TRIDYN. The films are modelled to grow from hydrocarbon radicals being attached to the surface, with ion bombardment being responsible for the removal of hydrogen. As seen from Fig. 5, the calculations provide information on the film/substrate interface mixing and the depth-dependent stoichiometry of the growing film. Reasonable assumptions for the impinging fluxes result in growth rates and film compositions which are in good agreement with experimental findings. Variations of the ion energy or of the bombardment species (hydrocarbon or hydrogen ions) also show the correct trends in comparison to experiments.

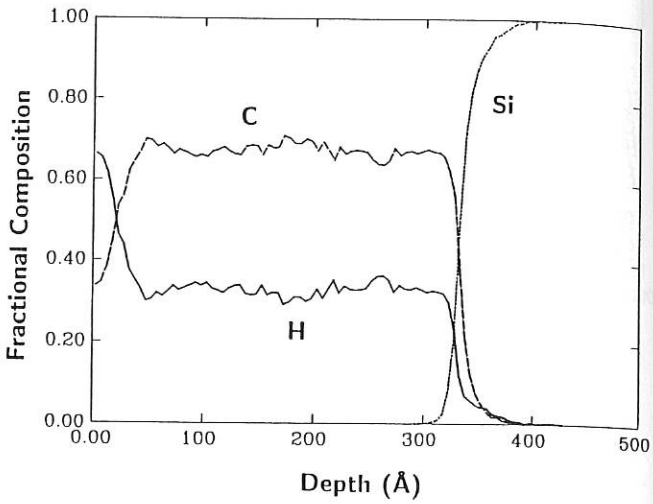

FIG. 5: Computer-simulated depth profiles for an a-C:H film deposited on a Si substrate, grown from CH_3^0 radicals and 400 eV CH_3^+ ions. The ion-to-neutral flux ratio is 0.1.

COMPUTER SCIENCE DIVISION

(Prof. Dr. Friedrich Hertweck)

Practically all activities of the division are related to the development of the AMOS/D data acquisition for ASDEX Upgrade. It was developed in close collaboration with the ASDEX Upgrade project. It is a distributed system of VMEbus workstations connected to a central computer (IBM 3090). In addition, parallel computer systems (using transputers) for the analysis of large amounts of data are also under development.

(F. Hertweck, H. Fisser, H. Friedrich, K.-H. Goihl, P. Heimann, A. Jülich, J. Maier, M.-G. Pacco-Düchs, I. Precht, Ute Schneider, D. Stolz, R. Strunz, Chr. Tichmann, R. Tisma, M. Zilker)

1. THE AMOS/D SYSTEM

After the system has been used for some years on ASDEX, its commissioning for ASDEX Upgrade began in 1990. Part of the work was performed by the ASDEX Upgrade Team itself. At present about 70 workstations have been installed, about half of them to be used as data acquisition computers connected to the CAMAC equipment.

1.1 Shot File Structure

Based on the experience with ASDEX and taking into account new requirements for ASDEX Upgrade, the structure of shot files was extended. A few new objects were added: Parameter set (for non-signal data), shot file list (to show the dependence of higher level shot files on other shot files), update set (a collection of data items for the controlled update of higher level shot files), local timer (a descriptor of the timer subsystem, local to a workstation or diagnostic). These additions, though requiring some work, were straightforward due to the designed-in extensibility of the shot file structure.

1.2 Level-n Shot Files

All shot files have a level assigned to them. As a general rule, all shot files containing measured data (known as "raw data") have level=0. Because shot files with raw data normally are of little use to others, the concept of "level-n shot files" was introduced. A level-n shot file is created by an archived program using any number of level<n shot files (an archived program normally cannot be erased). It will contain interpreted data.

1.3 Shot File Editions

Another new concept that was introduced are "file editions"; they are now a universal feature of the AMOS/2 system. They may be conveniently used for shot files or shot file headers (i.e. the templates of shot files to be supplemented with data) should the need arise to update them but still keep older versions. A file having editions, once generated, cannot be modified any more (it may only be purged). Instead, a new edition must be created (optionally by starting with the copy of an older one). This new edition may now be modified repeatedly while it is still a "working edition"; once closed with the "save" option, it becomes the current (unmodifiable) edition. This scheme permits controlled updating of shot files of level>0.

1.4 The AMOS/2 System

The AMOS/2 system is now running on an IBM 3090-150E with 32 MB of main memory. The Shot File Monitor, a process that organizes the central archiving of shot files, has been extended to use a large section of central memory as a "shared segment", accessible by user programs that want to read shot file data.

The file archiver has been extended to permit the condensation of archive tapes. The AMOS/2 archiving system creates 2 backup copies of each file of the AMOS/2 system; when a file is moved back to disk, "holes" are created on the tapes. These are removed by condensing the still valid information from two or more tapes onto one tape.

A remote function call to invoke AMOS/2 functions from a VM/CMS terminal or a UNIX workstation has also been implemented.

1.5 The AMOS/D Fiber Glass Network

The optical fiber network of AMOS/D is now connecting 70 workstations. The sustained transmission of 1.05 MByte/sec from 8 workstations to the IBM 3090 was demonstrated. Though the reliability of the network was expected to be very high, a checksum was added to messages to enhance reliablity. So far, no errors have occurred.

In order to generalize the network, the AMOS/D protocols have been embedded into the TCP/IP framework.

1.6 Shot Program Editor

The scenario of an ASDEX Upgrade discharge (a "shot") is described by a shot program file which is used for the forward control of the experiment (see sections 3.6 and 4.5 of the chapter "ASDEX Upgrade Project" in this report). A Shot Program Editor has been developed which serves to specify the shot program. It contains a graphical input subsystem that permits the entry and the update of trajectories (for the current, for instance), and a set of menu input facilities (toggle switches, numerical/alphabetical input fields, buttons, etc.)

2. PARALLEL PROCESSING

Parallel processing is the challenge of the future in the field of numerically intensive computing. We are now beginning to benefit from our experience with the transputer systems that were developed over the past few years.

2.1 Fast Control of Plasma Position

In ASDEX Upgrade it is necessary to control the position of the plasma, using a fast feed-back control device. A transputer system, consisting of 12 T800 CPUs, has been developed (see the 1988 report). It has now successfully been commissioned.

2.2 Mirnov Data Analysis Prototype

For the analysis of high data volume diagnostics, like Mirnov probes or soft X-ray, it is planned to use transputer systems. They have the advantage of permitting simple and cost-effective data input using transputer link adapters (see the 1988 report). A 16-CPU transputer system has been successfully tested on ASDEX. During the shot phase, the sixteen transputers are connected as a ring, the remaining two links on each CPU (totalling 32) being used for data collection (about 1 MByte/sec). Software was developed to scan the data in real time in order to select time windows that are most interesting from the point of view of physics and for which the data should be saved. (Note that in a 4 MByte CPU about 1 MByte/channel may be saved; for an expected shot duration of 10 sec this amounts to 10% of the shot time.)

The computer system uses a switchable topology: after the shot the ring configuration is changed to a hypercube topology (or cube-connected cycles, for larger systems) to do further data evaluation and reduction. At present a 64-transputer system is being assembled. It is obvious that the amount of data such a system may record (i.e. about 100 - 150 MBytes) must be drastically reduced in the intershot period of 5 - 10 minutes. For this the combined power of the 64-transputer system, about half of that of a Cray-1, is available.

ADMINISTRATION

(Dr. Karl Tichmann)

The administration and general services of Max-Planck-Institut für Plasmaphysik are organized in departments. Six of them are presented here:

PERSONNEL DEPARTMENT

This department is responsible for adminstrative matters relating to personnel. The personnel figures of the institute for 1990 were as follows:

Total personnel	1087
Scientists	294
Technicians	464
Directorate and Staff Representative Council	20
General services	112
Administration	68
Other personnel	129

PURCHASING AND CONTRACTS DEPARTMENT

This department handles all calls for tender, places approx. 7,500 purchase orders every year and is also responsible for all import and export formalities. A large part of the investment of IPP (1990: 40 MDM) is in the form of contracts placed after calls for tender in the European Community nations.

LEGAL AND PATENT DEPARTMENT

This department attends to patent applications and supervision, contracts of cooperation, and licensing of patents in cooperation with Garching Instrumente GmbH, a subsidiary of the Max Planck Society. In 1990 the division supervised 196 patents and similar rights.

FINANCE DEPARTMENT

The finance services are responsible for financial planning and all financial transactions and fiscal matters of IPP.

Total budget in 1990:	153.5 MDM
This budget was financed as follows:	
Federal Republic of Germany through Federal Ministry of Research and Technology (BMFT)	85.8 MDM
Free State of Bavaria	9.5 MDM
EURATOM	36.2 MDM
Other income	22.0 MDM

SOCIAL DEPARTMENT

This department gives assistance to employees seeking housing, provides accommodation for guests in IPP residences, and runs the transport pool, bus, kitchen, cafeteria and cleaning services.

SITE AND BUILDINGS DEPARTMENT

In 1990 this department, which is in charge of the planning, erection, structural alteration and reconditioning of buildings and service facilities, completed a new office and laboratory building (4 floors) adjacent to an existing test hall and replaced the central telephone switchboard with a Hicom 390 Digital System.

Publications, Conference Reports, Author Index

PUBLICATIONS AND CONFERENCE REPORTS

1 Adamson, S., M.-L. Apicella[1)], A.-P. Martinelli, E. Taglauer and ASDEX-Team[2)]:
Collector Probe Measurements of Metallic Impurity Fluxes in the Divertor Chamber of the ASDEX Tokamak. In: Selected Proc. of the 11th Internat.Vacuum Congress (IVC-11). 7th Internat. Conf. on Solid Surfaces (ICSS-7), Koeln (DE) 1989, 1545-1548 (1990).

2 Adamson, S., M.-L. Apicella[1)], A.-P. Martinelli, E. Taglauer and ASDEX-Team[2)]:
Metallic Impurities in the ASDEX Scrape-Off Layer. Nuclear Fusion 30, 5, 881-890 (1990).

3 Alimov, V.K. and B.M.U. Scherzer:
Temperature Dependence of $^4He/^3He$ Exchange in Ni. Radiation Effects and Defects in Solids 114, 137-144 (1990).

4 Andelfinger, C., H. Kollotzek, M. Ulrich, G. Weber et al.:
A Centrifuge Pellet Injector for ASDEX Upgrade. In: Selected Proc. of the 11th International Vacuum Congress (IVC-11). 7th International Conference on Solid Surfaces (ICSS-7), Koeln (DE) 1989, 1508-1509 (1990).

5 Aratari, R., S. Adamson[1)], M. Bessenrodt-Weberpals, R. Buechse, A. Carlson, C.-C. Chu, K. Desinger, G. Haas, J. Hofmann, E. Kakoulidis[1)], K. Krieger, B. Kurzan, D. Meisel, E.R. Mueller, J. Neuhauser, W. Poschenrieder, F. Ryter, G. Siller, K.-H. Steuer, J. Szigeti[1)], N. Tsois[1)], H. Verbeek, F. Wagner, ASDEX-Team[2)] and NI-Team(WVII-AS)[5)]:
Comparison of Open-Closed Divertor Geometries in ASDEX. In: ASDEX Contributions 9th Internat.Conf.Plasma Surface Interaction in Controlled Fusion Devices, Bournemouth (GB) 1990, 50-64.

6 Baetzner, R.[1)], K. Huebner[1)], L. Ingrosso[1)], R. Wagner[1)], B. Bomba, H.-S. Bosch and J. Kucinski:
Absolute Determination of High Neutron Yields for ASDEX. In: 17th EPS Conf. on Controlled Fusion and Plasma Heating, Amsterdam(NL) 1990, Eds. G. Briffod, Adri Nijsen-Vis, F.C. Schueller, 1990, ECA, 14B, Pt. 4, 1520-1523.

7 Bartiromo, R.[1)], F. Leuterer, F.X. Soeldner, H.D. Murmann, LH-Team[9)] and ASDEX-Team[2)]:
Power Absorption and Energy Confinement During LH Injection in ASDEX. In: 17th EPS Conf. on Controlled Fusion and Plasma Heating, Amsterdam(NL) 1990, Eds. G. Briffod, Adri Nijsen-Vis, F.C. Schueller, 1990, ECA, 14B, Pt. 3, 1092-1095.

8 Becker, G.:
Analysis of Energy and Particle Transport and Density Profile Peaking in the Improved Ohmic Confinement Regime. Nuclear Fusion 30, 11, 2285-2293 (1990).

9 Becker, G.:
Bootstrap Current and Ballooning Stability in ASDEX L and H Plasmas. In: Ringberg-Seminar Plasmatheorie, Ringberg, Tegernsee (DE) 1990.

10 Becker, G.:
Empirical Transport Coefficients Compared with Quasi-Linear Fluctuation Induced Transport Code. Nuclear Fusion 30, 8, 1610-1612 (1990).

11 Becker, G.:
Simulation of Density Profile Peaking and Energy and Particle Transport in the IOC Regime. In: 17th EPS Conf. on Controlled Fusion and Plasma Heating, Amsterdam(NL) 1990, Eds. G. Briffod, Adri Nijsen-Vis, F.C. Schueller, 1990, ECA, 14B, Pt. 2, 829-832.

12 Becker, G.:
Study of Possible Key Parameters for Improved Bulk Transport of H-Mode Plasmas. Nuclear Fusion 30, 11, 2377-2382 (1990).

13 Becker, G.:
Unified χ_e Scaling for the Ohmic, L and Intermediate Regimes of ASDEX. In: 17th EPS Conf. on Controlled Fusion and Plasma Heating, Amsterdam(NL) 1990, Eds. G. Briffod, Adri Nijsen-Vis, F.C. Schueller, 1990, ECA, 14B, Pt. 2, 833-836.

14 Beckschulte, M., D. Mehl[1)] and E. Taglauer:

The Adsorption of CO on Ni(100) Studied by Low Energy Ion Scattering. Vacuum 41, Nos. 1-3, 67-69 (1990).

15 Behrisch, R. and V. Prozesky[1]:
Particle and Power Exhaust for a Fusion Plasma. Nuclear Fusion 30, 10, 2166-2170 (1990).

16 Beidler, C.D., G. Grieger, E. Harmeyer, F. Herrnegger, J. Kisslinger, A. Montvai, F. Rau, R. Scardovelli and H. Wobig:
Physics and Engineering Design for Wendelstein VII-X. In: Proc. 7th Internat. Workshop on Stellarators, Oak Ridge (US) 1989, IAEA/TECDOC/558, 1990, 479-484.

17 Beidler, C.D., G. Grieger, F. Herrnegger, E. Harmeyer, J. Kisslinger, W. Lotz, H. Maassberg, P. Merkel, J. Nuehrenberg, F. Rau, J. Sapper, F. Sardei, R. Scardovelli, A. Schlueter and H. Wobig:
Physics and Engineering Design for Wendelstein VII-X. Fusion Technology 17, 1, 148-168 (1990).

18 Beidler, C.D., E. Harmeyer, F. Herrnegger, J. Kisslinger, H. Maassberg, A. Montvai, F. Rau, R. Scardovelli and H. Wobig:
Bootstrap Currents in Helias Configurations. In: Proc. 7th Internat. Workshop on Stellarators, Oak Ridge(US) 1989, IAEA/TECDOC/558, 1990, 621-625.

19 Beidler, C.D., E. Harmeyer, F. Herrnegger, J. Kisslinger, F. Rau, R. Scardovelli and H. Wobig:
On Edge Structure and Perturbations in a Helias Vaccum Field. In: Proc. 7th Internat. Workshop on Stellarators, Oak Ridge(US) 1989, IAEA/TECDOC/558, 1990, 525-533.

20 Beidler, C.D., E. Harmeyer, J. Kisslinger, P. Merkel, F. Rau, R. Scardovelli and H. Wobig:
Coil Systems, Vacuum Fields, and Parameter Range for Wendelstein VII-X Coils. In: Proc. 7th Internat. Workshop on Stellarators, Oak Ridge(US) 1989, IAEA/TECDOC/558, 507-520.

21 Beidler, C.D.:
A General Theory of LMFP Neoclassical Transport in Stellarators. In: 17th EPS Conf. on Controlled Fusion and Plasma Heating, Amsterdam(NL) 1990, Eds. G. Briffod, Adri Nijsen-Vis, F.C. Schueller, 1990, ECA, 14B, Pt. 2, 513-516.

22 Beidler, C.D., E. Harmeyer, J. Kisslinger, F. Rau, H. Wobig and WVII-AS-Team[3]:
On the Edge Structure of the WVII-AS Stellarator. In: 17th EPS Conf. on Controlled Fusion and Plasma Heating, Amsterdam (NL) 1990, Eds. G. Briffod, Adri Nijsen-Vis, F.C. Schueller, 1990, ECA, 14B, Pt. 2, 517-520.

23 Beidler, C.D., W.N.G. Hitchon, D.L. Grekov and A.A. Shishkin:
Monte Carlo Evaluation of Neoclassical Transport in Torsatrons with Different Helical Winding Laws. Nuclear Fusion 30., 3, 405-411 (1990).

24 Bengtson, R.D.[1], M. Bessenrodt-Weberpals, A. Carlson, L. Giannone, J. Neuhauser, H. Niedermeyer, A. Rudyj, N. Tsois et al.:
A Comparison of Fluctuations and Transport in the Scrape-Off Layer of a Limiter (TEXT) and Divertor Tokamak (ASDEX). In: 17th EPS Conf. on Controlled Fusion and Plasma Heating, Amsterdam(NL) 1990, Eds. G. Briffod, Adri Nijsen-Vis, F.C. Schueller, 1990, ECA, 14B, Pt. 3, 1460-1463.

25 Bessenrodt-Weberpals, M., A. Carlson, G. Haas, H.D. Murmann, J. Neuhauser, F.X. Soeldner, N. Tsois[1], H. Verbeek and ASDEX-Team[2]:
Characterizing the Edge Plasma of Different Ohmic Confinement Regimes in ASDEX. Plasma Physics and Controlled Fusion 32, 1, 21-31 (1990).

26 Bessenrodt-Weberpals, M., K. McCormick, F. Wagner and ASDEX-Team[2]:
Isotope Studies of the Edge Plasma in ASDEX. In: ASDEX Contributions 9th Internat. Conf. Plasma Surface Interaction in Controlled Fusion Devices, Bournemouth(GB) 1990, 35-49.

27 Besson, G.[1], G.G. Borg[1], J.B. Lister[1], F. Braun, A.B. Murphy, J.-M. Noterdaeme, F. Ryter, F. Wesner et al.:
Alfven Wave Heating in ASDEX. In: 17th EPS Conf. on Controlled Fusion and Plasma Heating, Amsterdam (NL) 1990, Eds. G. Briffod, Adri Nijsen-Vis, F.C. Schueller, 1990, ECA, 14B, Pt. 3, 1175-1178.

28 Biskamp, D.:
Magnetic Arcade Evolution and Instability. In: Proc. of the Cargese Workshop, Cargese (FR) 1989, Eds. M.A. Dubois, F. Bely-Duban, D. Gresillon, Ed.de Phys., Paris, 1990, Solar Plas-

ma Phenomena, 125-152.

29 Biskamp, D.:
Recent Developments in the Theory of Magnetic Reconnection. Vulcano(IT) 1989, Eds. W. Brinkmann, A.C. Fabian, F. Giovannelli, Kluwer, Dordrecht, 1990, Physical Processes in Hot Cosmic Plasmas, S. 255-269.

30 Biskamp, D. and H. Welter:
Magnetic Field Amplification and Saturation in Two-Dimensional Magnetohydrodynamic Turbulence. Physics of Fluids. B 2, 8, 1787-1793 (1990).

31 Biskamp, D., H. Welter and M. Walter:
Statistical Properties of Two-Dimensional Magnetohydrodynamic Turbulence. Physics of Fluids. B 2, 12, 3024-3031 (1990).

32 Biskamp, D. and H. Welter:
Turbulent Dissipation in Two-Dimensional MHD Turbulence. In: Proc. of the Cargese Workshop, Cargese (FR) 1989, Eds. M.A. Dubois, F. Bely-Duban, D. Gresillon, Ed.de Phys., Paris, 1990, Solar Plasma Phenomena, 37-50.

33 Boozer, A.H. and H.J. Gardner:
Bootstrap Current in Stellarators. In: Proc.7th Internat. Workshop on Stellarators, Oak Ridge (US) 1989, IAEA/TECDOC/558, 1990, 607-610.

34 Bosch, H.-S.:
Diagnostics with Charged Fusion Products in ASDEX. Rev.Sci.Instrum. 61, 6, 1699-1707 (1990).

35 Bosch, H.-S. and G.M. Hale[1]:
New Evaluation of the Fusion Cross-Sections. In: 17th EPS Conf. on Controlled Fusion and Plasma Heating, Amsterdam (NL) 1990, Eds. G. Briffod, Adri Nijsen-Vis, F.C. Schueller, 1990, ECA, 14B, Pt. 2, 873-876.

36 Bosch, H.-S., G.A. Wurden, J. Gernhardt, F. Karger and J. Perchermeier:
Electrochemical Cold Fusion Trials at IPP Garching. Journal of Fusion Energy 9, 2, 165-186 (1990).

37 Boutard, D., I. Gudowska[1], B.M.U. Scherzer and W. Moeller:
Helium Implantation Effects in Hard Hydrogenated Carbon Layers. Journal of Applied Physics 68, 5, 2068-2072 (1990).

38 Boutard, D. and W. Moeller:
Isotopic Effects in a-C:(H/D) Films Deposited from Methane/Hydrogen RF Plasmas. Journal of Materials Research 5, 11, 2451-2455 (1990).

39 Boutard, D., W. Moeller and B.M.U. Scherzer:
Hydrogen Isotope Exchange in Amorphous Hydrocarbon Layers: Plasma-Deposited a-C:H and Ion-Saturated Carbon. Radiation Effects and Defects in Solids 114, 281-289 (1990).

40 Boutard, D., W. Moeller and B.M.U. Scherzer:
Isotopic Exchange in Hard Amorphous Carbonized Layers. Journal of Applied Physics 67, 1, 163-168 (1990).

41 Brambilla, M. and J.-M. Noterdaeme:
Induction of Parallel Electric Fields at the Plasma Edge During ICRF Heating. In: 17th EPS Conf. on Controlled Fusion and Plasma Heating, Amsterdam(NL) 1990, Eds. G. Briffod, Adri Nijsen-Vis, F.C. Schueller, 1990, ECA, 14B, Pt. 3, 1056-1059.

42 Buechse, R., M. Kornherr and ASDEX-Team[2]:
Soft-X-Ray Tomography of Sawteeth and M=1 Modes in ASDEX. In: 17th EPS Conf. on Controlled Fusion and Plasma Heating, Amsterdam(NL) 1990, Eds. G. Briffod, Adri Nijsen-Vis, F.C. Schueller, 1990, ECA, 14B, Pt. 1, 391-394.

43 Bures, M., J.J. Jacquinot, D.F.H. Start and M. Brambilla:
Role of the Antenna Screen Angle During ICRF Heating in JET. Nuclear Fusion 30, 2, 251-263 (1990).

44 Camargo, S.J. and H. Tasso:
Self-Similar Statistics in MHD Turbulence. Zeitschrift fuer Naturforschung. A 45, 603-608 (1990).

45 Canobbio, E.[1] and R. Croci:
Quasilinear Theory for Spatially Delimited Wave Patterns. In: 17th EPS Conf. on Controlled Fusion and Plasma Heating, Amsterdam(NL) 1990, Eds. G. Briffod, Adri Nijsen-Vis, F.C. Schueller, 1990, ECA, 14B, Pt. 3, 1207-1210.

46 Carlson, A.:
Anti-Hebbian Learning in a Non-linear Neural Network. Biol. Cybern. 64 (2), 171-178

(1990).

47 Carlson, A., A. Rudyj and ASDEX-Team[2]:
The Limitations of Measurements of the Local Wavenumber. In: 17th EPS Conf. on Controlled Fusion and Plasma Heating, Amsterdam(NL) 1990, Eds. G. Briffod, Adri Nijsen-Vis, F.C. Schueller, 1990, ECA, 14B, Pt. 4, 1676-1679.

48 Chiu, S.C.[1], V.S. Chan[1], F.W. Perkins[1] and S. Puri:
Parasitic Coupling of the Fringing Fields of an Ion-Bernstein Wave Antenna. In: 17th EPS Conf. on Controlled Fusion and Plasma Heating, Amsterdam(NL) 1990, Eds. G. Briffod, Adri Nijsen-Vis, F.C. Schueller, 1990, ECA, 14B, Pt. 3, 1031-1034.

49 Chodura, R.:
Modelling of the Plasma at the Faraday Screen of an ICRH Antenna. Fusion Engineering and Design 12, Nos. 1-2, 111-114 (1990).

50 Chodura, R.:
Non-Local Heat Conduction Along a Scrape-Off Layer with Strong Recycling. Contrib. to Plasma Phys. 30, 1, 153-156 (1990).

51 Chodura, R.:
Thermoelectric Currents in the Scrape-Off Layer. In: 17th EPS Conf. on Controlled Fusion and Plasma Heating, Amsterdam(NL) 1990, Eds. G. Briffod, Adri Nijsen-Vis, F.C. Schueller, 1990, ECA, 14B, Pt. 3, 1443-1446.

52 Christiansen, J.P.[1], J.G. Cordey[1], O. Kardaun and K. Thomsen[1]:
Unified Physical Scaling Laws for Tokamak Confinement. In: 17th EPS Conf. on Controlled Fusion and Plasma Heating, Amsterdam(NL) 1990, Eds. G. Briffod, Adri Nijsen-Vis, F.C. Schueller, 1990, ECA, 14B, Pt. 2, 797-800.

53 Coad, J.P.[1], R. Behrisch, L. De Kock[1], A.P. Martinelli et al.:
Effect of Limiter Composition on Z_{eff} and Recycling in JET. In: 17th EPS Conf. on Controlled Fusion and Plasma Heating, Amsterdam (NL) 1990, Eds. G. Briffod, Adri Nijsen-Vis, F.C. Schueller, 1990, ECA, 14B, Pt. 3, 1357-1360.

54 Correa-Restrepo, D.:
Calculation of the Resistive Ballooning Mode Growth Rate for a Class of 3-D MHD Equilibria. Zeitschrift fuer Naturforschung. A 45, 5, 611-612 (1990).

55 Correa-Restrepo, D.:
Compressibility and Resistive Ballooning Modes. Zeitschrift fuer Naturforschung. A 45, 5, 609-610 (1990).

56 Correa-Restrepo, D.:
Localized Ideal and Resistive Instabilities in 3-dimensional MHD Equilibria with Closed Field Lines. Zeitschrift fuer Naturforschung. A 45, Nos. 9-10, 1074-1076 (1990).

57 De Angelis, R.[1], G. Fussmann, J.V. Hofmann, K. Krieger and ASDEX-Team[2]:
Impurity Transport and Production in Lower Hybrid Discharges in ASDEX. In: 17th EPS Conf. on Controlled Fusion and Plasma Heating, Amsterdam(NL) 1990, Eds. G. Briffod, Adri Nijsen-Vis, F.C. Schueller, 1990, ECA, 14B, Pt. 3, 1435-1438.

58 Diamond, P.H.[1] and D. Biskamp:
Comments on Dynamics of Decaying Two-Dimensional Magnetohydrodynamic Turbulence. Physics of Fluids. B 2, 3, 681-682 (1990).

59 Dodel, G.[1], E. Holzhauer[1], L. Giannone, H. Niedermeyer, J. Gernhardt, ASDEX-Team[2] et al.:
Investigation of Density Fluctuations in the ASDEX Tokamak via Collective Laser Scattering. In: 17th EPS Conf. on Controlled Fusion and Plasma Heating, Amsterdam(NL) 1990, Eds. G. Briffod, Adri Nijsen-Vis, F.C. Schueller, 1990, ECA, 14B, Pt. 1, 207-210.

60 Dodhy, A., G. Kuehner, H. Ringler, F. Sardei, WVII-AS-Team[3] and ECRH-Group[7]:
H_α-Spectroscopy on WVII-AS. In: 17th EPS Conf. on Controlled Fusion and Plasma Heating, Amsterdam(NL) 1990, Eds. G. Briffod, Adri Nijsen-Vis, F.C. Schueller, 1990, ECA, 14B, Pt. 2, 475-478.

61 Donath, M. and V. Dose:
Spin-Resolved Inverse Photoemission Study on the Temperature Behavior of a Magnetic Band in Nickel. In: Proc. 4th Internat. Conf. on Electron Spectroscopy, Hawaii(US) 1989, 283-286 (1990).

62 Donath, M., V. Dose, K. Ertl and U. Kolac:

Polarization Effects in Inverse-Photemission Spectra from Ni(110). Physical Review. B 41, 9, 5509-5518 (1990).

63 Donath, M., G. Schoenhense[1)], K. Ertl and V. Dose:
Influence of Surface Roughness and Chemisorption on Magnetic Hysteresis Curves of a Ni(110) Surface Observed by Spin-Resolved Inverse Photoemission. Applied Physics. A 50, 1, 49-55 (1990).

64 Dose, V.:
Inverse Photoemission Spectroscopy. Rendiconti della Scuola Internazionale di Fisica Enrico Fermi 108, 257-275 (1990).

65 Dose, V.:
Reply to Identifications of Empty Surface States on Au(110): Comment on the 1x1 to 1x2 Phase Transition of Au(110): An Inverse Photoemission Study by R. Drube, V. Dose, H. Derks and W. Heiland by N.V. Smith, C.T. Chen, R.A. Bartynski and T. Gustafsson. Surface Science Letters 227, L133 (1990).

66 Duerr, H., T. Fauster and R. Schneider:
A Compact Three-Axis Cryogenic Ultrahigh Vacuum Manipulator. Journal of Vacuum Science and Technology. A 8, 1, 145-146 (1990).

67 Duerr, H., R. Schneider and T. Fauster:
Thermal Vibrations at Copper Surfaces Studied by Low Energy Ion Scattering. Vacuum 41, Nos. 1-3, 376-378 (1990).

68 Eckhartt, D.:
Neutral Beam Current Drive with Balanced Injection. In: 17th EPS Conf. on Controlled Fusion and Plasma Heating, Amsterdam(NL) 1990, Eds. G. Briffod, Adri Nijsen-Vis, F.C. Schueller, 1990, ECA, 14B, Pt. 3, 1336-1339.

69 Eckstein, W., E.S. Mashkova[1)] and V.A. Molchanov[1)]:
Formation of Spatial Distributions of Particles Sputtered under the Ion Bombardment of Polycrystals. Poverknost 2, 55-62 (1990).

70 Elfimov, A.G.[1)] and S. Puri:
Current Drive Via Landau Damping of Kinetic Alfven Waves in Toroidal Geometry. In: 17th EPS Conf. on Controlled Fusion and Plasma Heating, Amsterdam(NL) 1990, Eds. G. Briffod, Adri Nijsen-Vis, F.C. Schueller, 1990, ECA, 14B, Pt. 3, 1315-1318.

71 Elfimov, A.G.[1)] and S. Puri:
Current Drive Via Landau Damping of Kinetic Alfven Waves in Toroidal Geometry. Nuclear Fusion 30, 7, 1215-1219 (1990).

72 Elsner, A.:
Fit Function for the Vapour Pressure of ^{3}He. Physics Letters. A 149, 4, 184-190 (1990).

73 Elsner, A.:
Phase Diagram of a Saturated Fluid. Cryogenics 30, 11, 959-967 (1990).

74 Engelmann, F. and O. Kardaun:
Tokamak Global Confinement Data with Contributions from FT, JET, JFT-2M, TFTR, T-10. Nuclear Fusion 30, 9, 1951-1956 (1990).

75 Erckmann, V., U. Gasparino, H. Maassberg, H. Renner, M. Tutter, WVII-AS-Team[3)] et al.:
Current Drive Experiments at the Electron Cyclotron Frequency. In: 17th EPS Conf. on Controlled Fusion and Plasma Heating, Amsterdam(NL) 1990, Eds. G. Briffod, Adri Nijsen-Vis, F.C. Schueller, 1990, ECA, 14B, Pt. 3, 1271-1274.

76 Erckmann, V., WVII-AS-Team[3)] et al.:
Electron Cyclotron Resonance Heating Transmission Line and Launching System for the Wendelstein VII-AS Stellarator. Fusion Technology 17, 1, 77-85 (1990).

77 Evans, T.E., J. Neuhauser, F. Leuterer, E.R. Mueller and ASDEX-Team[2)]:
Characteristics of Toroidal Energy Deposition Asymmetries in ASDEX. In: ASDEX Contributions 9th Internat.Conf.Plasma Surface Interaction in Controlled Fusion Devices, Bournemouth(GB) 1990, 81-97.

78 Fahrbach, H.-U., W. Herrmann, F.X. Soeldner, LH-Team[9)] and ASDEX-Team[2)]:
Transition from Electron- to Ion-Interaction of LH-Waves in ASDEX. In: 17th EPS Conf. on Controlled Fusion and Plasma Heating, Amsterdam(NL) 1990, Eds. G. Briffod, Adri Nijsen-Vis, F.C. Schueller, 1990, ECA, 14B, Pt. 3, 1171-1174.

79 Fajemirokun, H.[1)], C. Gowers[1)], K. Hirsch[1)], H. Salzmann et al.:

A High Resolution LIDAR-Thomson Scattering System for JET. In: 17th EPS Conf. on Controlled Fusion and Plasma Heating, Amsterdam(NL) 1990, Eds. G. Briffod, Adri Nijsen-Vis, F.C. Schueller, 1990, ECA, 14B, Pt. 4, 1692.

80 Fajemirokun, H.[1)], C. Gowers[1)], K. Hirsch[1)], P. Nielsen[1)] and H. Salzmann:
A New Method for Identifying and Estimating Systematic Error in Thomson Scattering Data. Rev. Sci. Instrum. 61, 2849 (1990).

81 Fajemirokun, H.[1)], C. Gowers[1)], P. Nielsen[1)], H. Salzmann and K. Hirsch[1)]:
A High Resolution LIDAR-Thomson Scattering Diagnostic for JET. Rev.Sci.Instrum. 61, 2843 (1990).

82 Fischer, N.[1)], S. Schuppler[1)], T. Fauster and W. Steinmann[1)]:
Intrinsic Linewidths of Image-Potential States on Ni(111). Physical Reviev. B 42, 9717-9719 (1990).

83 Franzen, P., W. Moeller and B.M.U. Scherzer:
Reemission of Deuterium from Graphite at Temperatures above 1100 K. Journal of Nuclear Materials 172, 3, 293-296 (1990).

84 Fussmann, G., J.V. Hofmann, G. Janeschitz, W. Poeffel[1)] and K.-H. Schartner[1)]:
Spectral Analysis of a Tokamak Plasma in the VUV-Range. Vulcano(IT) 1989, Eds. W. Brinkmann, A.C. Fabian, F. Giovannelli, Kluwer, Dordrecht, 1990, Physical Processes in Hot Cosmic Plasmas, S. 29-37.

85 Fussmann, G., J.V. Hofmann, G. Janeschitz and H.R. Yang[1)]:
Sputtering Flux Measurements in the ASDEX Divertor. Nuclear Fusion 30, 11, 2319-2328 (1990).

86 Fussmann, G., A. Kallenbach, K. Krieger and K.-H. Steuer:
Multi-Species Impurity Accumulation Phenomena in ASDEX. In: 17th EPS Conf. on Controlled Fusion and Plasma Heating, Amsterdam(NL) 1990, Eds. G. Briffod, Adri Nijsen-Vis, F.C. Schueller, 1990, ECA, 14B, Pt. 3, 1423-1426.

87 Gardner, H.J.:
Modelling the Behaviour of the Magnetic Field Diagnostic Coils on the WVII-AS Stellarator Using a Three-Dimensional Equilibrium Code. Nuclear Fusion 30, 8, 1417-1424 (1990).

88 Gasparino, U., V. Erckmann, H. Maassberg, WVII-AS-Team[3)] et al.:
Non-Inductive Currents in WVII-AS: Experimental Results and Theoretical Modelling. In: 17th EPS Conf. on Controlled Fusion and Plasma Heating, Amsterdam(NL) 1990, Eds. G. Briffod, Adri Nijsen-Vis, F.C. Schueller, 1990, ECA, 14B, Pt. 3, 1275-1278.

89 Gehre, O., K.W. Gentle[1)], ASDEX-Team[2)] and LH-Team[9)]:
Modifications of Density Profile and Particle Transport in ASDEX During Lower Hybrid Heating and Current Drive. In: 17th EPS Conf. on Controlled Fusion and Plasma Heating, Amsterdam(NL) 1990, Eds. G. Briffod, Adri Nijsen-Vis,, Schueller, F.C. , 1990, ECA, 14B, Pt. 1, 70-73.

90 Geisler, M.[1)], J. Kieser[1)], E. Raeuchle[1)] and R. Wilhelm:
Elongated Microwave Electron Cyclotron Resonance Heating Plasma Source. Journal of Vacuum Science and Technology 8, 908-915 (1990).

91 Giannone, L., K. Riedel, U. Stroth, A. Eberhagen, O. Gruber, V. Mertens and ASDEX-Team[2)]:
Heat and Density Pulse Propagation in ASDEX. In: 17th EPS Conf. on Controlled Fusion and Plasma Heating, Amsterdam(NL) 1990, Eds. G. Briffod, Adri Nijsen-Vis, F.C. Schueller, 1990, ECA, 14B, Pt. 1, 191-194.

92 Gottardi, N.[1)], K.F. Mast, P. Thomas[1)] et al.:
Radiation Asymmetries and H-Modes. In: 17th EPS Conf. on Controlled Fusion and Plasma Heating, Amsterdam(NL) 1990, Eds. G. Briffod, Adri Nijsen-Vis, F.C. Schueller, 1990, ECA, 14B, Pt. 1, 263-266.

93 Gowers, C.[1)], A. Gadd[1)], K. Hirsch[1)], P. Nielsen[1)] and H. Salzmann:
High Power Ruby and Alexandrite Lasers for LIDAR-Thomson Scattering Diagnostics. In: Internat. Congr. on Optical Science and Engineering, The Hague (NL) 1990, 1277.27.

94 Grassie, K. and M. Krech:

A Complete Set of Resistive Compressive Ballooning Equations for Two-Dimensional Flow Equilibria. Physics of Fluids. B 2, 3, 536-538 (1990).

95 Grassie, K. and M. Krech:
Results for Resistive Compressible Flow Ballooning Modes in a Large Aspect Ratio Expansion. Physics of Fluids. B 2, 8, 1864-1870 (1990).

96 Grieger, G. and WVII-X-Team[11]:
Status of the Wendelstein VII-X Project. In: Proc. of the First International Toki Conference on Plasma Physics and Controlled Nuclear Fusion, Toki(JP) 1989, NIFS/PROC/3, 1990, S. 7-10.

97 Gruber, O., A. Kallenbach, E. Simmet and K.-H. Steuer:
Is the Ion Confinement Improving in ASDEX H-Mode Discharges? In: 17th EPS Conf. on Controlled Fusion and Plasma Heating, Amsterdam(NL) 1990, Eds. G. Briffod, Adri Nijsen-Vis, F.C. Schueller, 1990, ECA, 14B, Pt. 1, 182.

98 Gruber, O., W. Schneider and K. Lackner:
Determination of Off-Diagonal Transport Coefficients from Particle and Power Balance Analysis. In: 17th EPS Conf. on Controlled Fusion and Plasma Heating, Amsterdam(NL) 1990, Eds. G. Briffod, Adri Nijsen-Vis, F.C. Schueller, 1990, ECA, 14B, Pt. 2, 841-844.

99 Hartfuss, H.J., J. Sanchez[1], E. Anabitarte[1], A.P. Navarro[1], WVII-AS-Team[3], NI-Team (WVII-AS)[5], Pellet-Team[10] and ECRH-Group[7]:
Observation of Density Fluctuations Associated with the Resonant q=2 Surface in Wendelstein WVII-AS Stellarator. Nuclear Fusion 30, 2383 (1990).

100 Hartfuss, H.J., M. Tutter, WVII-AS-Team[3], NI-Team(ASDEX)[4] and ECRH-Group[7]:
On Density and Temperature Fluctuations Observed by ECE Diagnostics in Wendelstein VII-AS Stellarator. In: 17th EPS Conf. on Controlled Fusion and Plasma Heating, Amsterdam(NL) 1990, Eds. G. Briffod, Adri Nijsen-Vis, F.C. Schueller, 1990, ECA, 14B, Pt. 4, 1576-1579.

101 Hellberg, M.A.[1], N.A. Frank[1], M.J. Handley[1] and W. Feneberg:
Modelling of Transport in Stochastic Magnetic Field Regions. In: 17th EPS Conf. on Controlled Fusion and Plasma Heating, Amsterdam(NL) 1990, Eds. G. Briffod, Adri Nijsen-Vis, F.C. Schueller, 1990, ECA, 14B, Pt. 2, 773-776.

102 Hermans, D.[1], W. Kerner and M. Goossens[1]:
Linearly Overstable Magnetic Convection in 1D Compressible and Non-Uniform Plasmas. Computer Physics Communications 59, 1, 127-138 (1990).

103 Herrmann, W.:
On the Possibility of Measuring the q-Profile in Dense Plasmas by Means of Molecular Hydrogen Beams. Plasma Physics and Controlled Fusion 32, 8, 605-621 (1990).

104 Herrmann, W.:
A Possible Electric Field Measurement by a Molecular Hydrogen Beam. In: 17th EPS Conf. on Controlled Fusion and Plasma Heating, Amsterdam(NL) 1990, Eds. G. Briffod, Adri Nijsen-Vis, F.C. Schueller, 1990, ECA, 14B, Pt. 4, 1672-1675.

105 Hertweck, F.:
Parallelrechner und physikalische Experimente. In: 11. ITG/GI-Fachtagung, Muenchen (DE) 1990, Ed. P. Mueller-Stoy, VDE-Verl.

106 Hertweck, F. and A. Juelich:
Transputer-Systeme fuer die Steuerung und Datenerfassung bei physikalischen Experimenten. HDM-Theorie und Praxis der Wirtschaftsinformatik 155 (1990).

107 Hirshman, S.P., U. Schwenn and J. Nuehrenberg:
Improved Radial Differences for Three-Dimensional Magnetohydrodynamic Equilibrium Calculations. J. Comput. Physics 87, 396-407 (1990).

108 Hofmann, J.V., A.R. Field, G. Fussmann and ASDEX-Team[2]:
Measurement of Poloidal Rotation on ASDEX. In: 17th EPS Conf. on Controlled Fusion and Plasma Heating, Amsterdam(NL) 1990, Eds. G. Briffod, Adri Nijsen-Vis, F.C. Schueller, 1990, ECA, 14B, Pt. 4, 1556-1559.

109 Hofmann, J.V., G. Fussmann, J.-M. Noterdaeme and F. Ryter:
Impurity Flux Measurements During ICRF Heating in ASDEX. Fusion Engineering and Design 12, Nos. 1-2, 185-191 (1990).

110 Holas, A.[1)], S. Olszewski[1)] and D. Pfirsch:
Onsager's Relation and Other Results for Relativistic Electrons in Magnetic Fields. Zeitschrift fuer Naturforschung. A 45, 7, 847-850 (1990).

111 Holzhauer, E.[1)], G. Dodel[1)] and ASDEX-Team[2)]:
Collective Laser Light Scattering from Electron Density Fluctuations in Fusion Research Plasmas (Invited). Rev.Sci.Instrum. 61, 10, Pt.2, 2817-2822 (1990).

112 Hou, M.[1)] and W. Eckstein:
Anisotropy of Momentum Distributions in Atomic-Collision Cascades Generated in Fcc Materials. Physical Review. B 42, 10, 5959-5965 (1990).

113 Jacob, W., N. Memmel, E. Bertel and V. Dose:
The Bandstructure of Pd(110) Above the Fermi Level. Applied Physics A 50, 2, 207-214 (1990).

114 Jaksic, N. and J. Simon-Weidner:
Influence of Manufactoring Tolerances of Large Helias Coils to Change in Mechanical Stresses. Finite Element News, 21-25 (1990).

115 Janeschitz, G., R. Giannella[1)], H. Jaeckel[1)] et al.:
Retention of Gaseous (Ar, He) Impurities in the JET X-Point Configuration. In: 17th EPS Conf. on Controlled Fusion and Plasma Heating, Amsterdam(NL) 1990, Eds. G. Briffod, Adri Nijsen-Vis, F.C. Schueller, 1990, ECA, 14B, Pt. 3, 1365-1368.

116 Juelich, A.:
Programmierung des Parallelrechners MULTITOP/12. In: Proc. of the 1988 Conf. on Supercomputers and Applications, Eds. H. Ehlich, K.-H. Schosser, B. Woycieszynski, Bochum, 1990.

117 Kallenbach, A., H.M. Mayer, G. Fussmann, R. Buechse, O. Gruber, O. Klueber, V. Mertens, O. Vollmer and H. Zohm:
Improvement of Angular Momentum Confinement with Density Peaking on ASDEX. Nuclear Fusion 30, 4, 645-656 (1990).

118 Kallenbach, A., H.M. Mayer, G. Fussmann, O. Gruber, U. Stroth and O. Vollmer:
Momentum Transport Studies on ASDEX. In: 17th EPS Conf. on Controlled Fusion and Plasma Heating, Amsterdam(NL) 1990, Eds. G. Briffod, Adri Nijsen-Vis, F.C. Schueller, 1990, ECA, 14B, Pt. 1, 183-186.

119 Kardaun, O., K. Thomsen[1)], J.G. Cordey[1)], F. Wagner, JET-Team and ASDEX-Team[2)]:
Global H-Mode Scalings Based on JET and ASDEX Data. In: 17th EPS Conf. on Controlled Fusion and Plasma Heating, Amsterdam(NL) 1990, Eds. G. Briffod, Adri Nijsen-Vis, F.C. Schueller, 1990, ECA, 14B, Pt. 1, 110-113.

120 Kato, S.[1)], H. Oyama[1)], H. Odagiri[1)] and E. Taglauer:
Modification of a Vacuum Surface by Carbon and its Outgassing. J. Vac. Sci. Jap. 33, 76-80 (1990).

121 Kaufmann, M.:
Zur Physik des Fusionsreaktors. Neue Ergebnisse. In: Proc. Forum '90 Wissenschaft und Technik, Trier(DE) 1990, Eds. H.-J. Friemel, G. Mueller-Schoenberger, A. Schuett (1990).

122 Kaufmann, M. et al.:
Transport Simulations of Ohmic Pellet Experiments on the TFTR, ASDEX and Alcator-C Tokamaks. Fusion Technology 18, 223 (1990).

123 Kaufmann, M., W. Sandmann, M. Bessenrodt-Weberpals, K. Buechl, O. Gruber, O. Kardaun, K. Lackner, R. Lang, V. Mertens, H.D. Murmann, J. Neuhauser and F.X. Soeldner:
Electron Temperature Profiles in Discharges with Pellet Injection and in other Mode Discharges. Plasma Physics and Controlled Fusion 32, 4, 303-308 (1990).

124 Keilmann, F., R. Brazis, H. Barkley, W. Kaparek[1)], M. Thumm[1)] and V. Erckmann:
Millimeter-Wave Frequency Tripling in Bulk Semiconductors. Europhys. Lett. 11, 337-342 (1990).

125 Kerner, W.:
Algorithms and Software for Linear and Nonlinear MHD Simulations. Computer Physics

Reports 12, 4, 135-175 (1990).

126 Kerner, W.:
Equilibrium and Stability of Tokamaks. Internat. J. for Numerical Methods in Fluids 11, 6, 791-809 (1990).

127 Klueber, O., R. Aratari, R. Buechse, M. Kornherr, H. Zohm and ASDEX-Team[2]:
ELMs as Triggered and as Triggering Relaxation Phenomena in ASDEX. In: 17th EPS Conf. on Controlled Fusion and Plasma Heating, Amsterdam(NL) 1990, Eds. G. Briffod, Adri Nijsen-Vis, F.C. Schueller, 1990, ECA, 14B, Pt. 1, 291-294.

128 Koch, A.W.:
Simultaneous Measurement of Local Drift Velocities and Electron Densities of Plasma Jets. Journal of Physics. D 23, 504-508 (1990).

129 Koeppendoerfer, W.:
ASDEX Upgrade - ein Tokamakexperiment mit reaktorrelevantem Divertor. Physikalische Blaetter 46, 8, 324-326 (1990).

130 Kraemer, M.[1], A. Carlson and ASDEX-Team[2]:
Probe Measurements of Lower-Hybrid Wavenumber Spectra in the ASDEX Edge Plasma. In: 17th EPS Conf. on Controlled Fusion and Plasma Heating, Amsterdam(NL) 1990, Eds. G. Briffod, Adri Nijsen-Vis, F.C. Schueller, 1990, ECA, 14B, Pt. 3, 1167-1170.

131 Krieger, K., G. Fussmann and ASDEX-Team[2]:
Determination of Impurity Transport Coefficients by Harmonic Analysis. Nuclear Fusion 30, 11, 2392-2396 (1990).

132 Krieger, K., G. Fussmann and ASDEX-Team[2]:
Determination of Impurity Transport Coefficients by Sinusoidal Modulated Gas Puffing. In: 17th EPS Conf. on Controlled Fusion and Plasma Heating, Amsterdam(NL) 1990, Eds. G. Briffod, Adri Nijsen-Vis, F.C. Schueller, 1990, ECA, 14B, Pt. 3, 1431-1434.

133 Kuehner, G., H. Maassberg, H. Ringler, WVII-AS-Team[3] and ECRH-Group[7]:
Statistical Analysis of Electron Heat Conduction on WVII-AS. In: 17th EPS Conf. on Controlled Fusion and Plasma Heating, Amsterdam(NL) 1990, Eds. G. Briffod, Adri Nijsen-Vis, F.C. Schueller, 1990, ECA, 14B, Pt. 2, 484-487.

134 Kueppers, J.:
Penning Spectroscopy of Alkali Metal Surfaces. Physics and Chemistry of Alkali Adsorption Materials Science Monographs 57, 45-54, Amsterdam: Elsevier (1990).

135 Lackner, K.:
Physical Equivalence of Tokamak Design. Comments on Plasma Physics and Controlled Fusion 13, 163 (1990).

136 Lackner, K. and N. Gottardi:
Tokamak Confinement in Relation to Plateau Scaling. Nuclear Fusion 30, No. 4, 767-770 (1990).

137 Lengyel, L.L.:
Physical Problems Associated with the Fuelling of Fusion Reactors. In: Proc. 5th All-Union Conf. on Eng. Problems of Fusion Reactors, Leningrad (SU) 1990

138 Lengyel, L.L. and G. Zavala:
Evolution of Pellet Clouds and Cloud Structures in Magnetically Confined Plasmas. In: 17th EPS Conf. on Controlled Fusion and Plasma Heating, Amsterdam(NL) 1990, Eds. G. Briffod, Adri Nijsen-Vis, F.C. Schueller, 1990, ECA, 14B, Pt. 1, 243-246.

139 Leuterer, F., R. Bartiromo[1], S. Bernabei[1], F. Soeldner, ASDEX-Team[2], LH-Team[9] and NI-Team(ASDEX)[4]:
Lower Hybrid Current Drive Efficiency at 2.45 GHz in ASDEX. In: 17th EPS Conf. on Controlled Fusion and Plasma Heating, Amsterdam(NL) 1990, Eds. G. Briffod, Adri Nijsen-Vis, F.C. Schueller, 1990, ECA, 14B, Pt. 3, 1291-1294.

140 Leuterer, F., F.X. Soeldner, M. Muenich, F. Monaco, M. Zouhar, ASDEX-Team[2], Pellet-Team[10] et al.:
Coupling of the 2x24 Waveguide Grill at 2.45 GHz in ASDEX. In: 17th EPS Conf. on Controlled Fusion and Plasma Heating, Amsterdam(NL) 1990, Eds. G. Briffod, Adri Nijsen-Vis, F.C. Schueller, 1990, ECA, 14B, Pt. 3, 1287-1290.

141 Liebl, H.:
On the Image Aberration of an Accelerating Central Field. Optik 85, 2, 87 (1990).

142 Liebl, H.:

Stigmatic Sector-Field Energy Analyzer Without Second-Order Angular Image Aberrations. Nuclear Instruments and Methods in Physics Research. A 292, 3, 537-540 (1990).

143 Liebl, H., B. Senftinger, P. Staib[1)] and H. Weiss[1)]:
Compact Cs^+ Ion Microsource. In: Proc. Secondary Ion Mass Spectrometry (SIMS VII), Monterey(US) 1990, Eds. A. Benninghoven et al., Wiley, 883-886.

144 Liebl, H. and B. Senftinger:
Low-Energy Electron Microscope of Novel Design. In: Proc. 12th Internat. Congress for Electron Microscopy, Seattle (US) 1990, San Francisco Press Inc. 352-353.

145 Lifshitz, Y.[1)], S.R. Kasi[1)], J.R. Rabalais[1)] and W. Eckstein:
Subplantation Model for Filem Growth from Hyperthermal Species. Physical Review. B 41, 10468-10474 (1990).

146 Linsmeier, C., E. Taglauer and H. Knoezinger[1)]:
Ion Scattering Analysis of Rh Adlayers on Alumina Films. Fundamental Aspects of Heterogeneous Catalysts by Particle Beams. NATO ASI Series, 5 (1990).

147 Loch, R., M. Kaufmann, R. Lang, R. Merkel, V. Mertens, R. Tisma and W. Sandmann:
Online Density Feedback on ASDEX for Pellet-Refuelled Discharges. In: 17th EPS Conf. on Controlled Fusion and Plasma Heating, Amsterdam(NL) 1990, Eds. G. Briffod, Adri Nijsen-Vis, F.C. Schueller, 1990, ECA, 14B, Pt. 1, 215-218.

148 Loch, R., W. Sandmann, K. Buechl, R. Lang and V. Mertens:
Scaling of Experimentally Determined Pellet Penetration Depths on ASDEX. In: 17th EPS Conf. on Controlled Fusion and Plasma Heating, Amsterdam (NL) 1990, Eds. G. Briffod, Adri Nijsen-Vis, F.C. Schueller, 1990, ECA, 14B, Pt. 1, 235-238.

149 Lortz, D.:
Axisymmetric Stability for Non-Circular Cross-Section Tokamaks. Plasma Physics and Controlled Fusion 32, 2, 117-129 (1990).

150 Lortz, D.:
Mathematical Problems in Dynamo Theory. Vulcano(IT) 1989, Eds. W. Brinkmann, A.C. Fabian, F. Giovannelli, Kluwer, Dordrecht, 1990, Physical Processes in Hot Cosmic Plasmas, S. 221-234.

151 Lotz, W., P. Merkel, J. Nuehrenberg and R. Zille:
Optimization of Helias for WVII-X. In: Proc. 7th Internat. Workshop on Stellarators, Oak Ridge (US) 1989, IAEA/TECDOC/558, 1990, 485-491.

152 Lyon, J.F.[1)], G. Grieger, F. Rau et al.:
Stellarators. Nuclear Fusion 30, 9, 1695-1715 (1990).

153 Manso, M.[1)], F. Serra[1)], A. Silva[1)], F.X. Soeldner, G. Siller et al.:
Localized Density Measurements on ASDEX Using Microwave Reflectometry. In: 17th EPS Conference on Controlled Fusion and Plasma Heating, Amsterdam (NL) 1990, Eds. G. Briffod, Adri Nijsen-Vis, F.C. Schueller, 1990, ECA, 14B, Pt. 4, 1560-1563.

154 Manso, M.[1)], A. Silva[1)], F. Serra[1)], H. Zohm, O. Klueber, F.X. Soeldner et al.:
Changes in the Density Profile Due to the m=2 Tearing Mode in ASDEX. In: 17th EPS Conf. on Controlled Fusion and Plasma Heating, Amsterdam(NL) 1990, Eds. G. Briffod, Adri Nijsen-Vis, F.C. Schueller, 1990, ECA, 14B, Pt. 2, 837-840.

155 Mathis, R. and J. Sapper:
Design and Engineering Aspects of the Main Components for the Wendelstein VII-AS Stellarator Experiment. Fusion Engineering and Design 11, 4, 399-422 (1990).

156 McCormick, K., M. Bessenrodt-Weberpals, E.R. Mueller, J. Neuhauser, H. Niedermeyer, W. Poschenrieder, F. Ryter, U. Schneider, F.X. Soeldner, K.-H. Steuer, N. Tsois[1)], O. Vollmer, F. Wagner, R. Aratari, S. Adamson[1)], G. Becker, H.-S. Bosch, R. Buechse, A. Carlson, C.C. Chu, G. Dodel[1)], A. Eberhagen, M. Endler, W. Engelhardt, H.-U. Fahrbach, G. Fussmann, O. Geh- re, J. Gernhardt, L. Giannone, O. Gruber, G. Haas, W. Herrmann, J.V. Hofmann, E. Holz- hauer, G. Janeschitz, E. Kakoulidis[1)], A. Kallenbach, F. Karger, M. Kaufmann, O. Klueber, M. Kornherr, K. Krieger, B. Kurzan, G. Kyria- kakis[1)], K. Lackner, U. Leinberger,

F. Leuterer, G. Lisitano, M.E. Manso[1)], H.M. Mayer, D. Meisel, V. Mertens, H.D. Murmann, H. Roehr, J. Roth, A. Rudyj, F. Schneider, F. Serra[1)], G. Siller, E. Simmet, A. Staebler, U. Stroth, G. Theimer, H. Verbeek, K. Wira, H. Zohm, ASDEX-Team[2)] and NI-Team (ASDEX)[4)]:
Effects of Edge Conditions on Plasma Confinement in ASDEX. In: ASDEX Contributions 9th Internat. Conf. Plasma Surface Interaction in Controlled Fusion Devices, Bournemouth (GB) 1990, 1-34 (1990).

157 McCormick, K., A. Hyatt[1)], G. Kyriakakis[1)], E.R. Mueller, H. Niedermeyer, A. Staebler, ASDEX-Team[2)], NI-Team(ASDEX)[4)] et al.:
Plasma Edge Behavior on the Way to and at the Density Limit. In: 17th EPS Conf. on Controlled Fusion and Plasma Heating, Amsterdam(NL) 1990, Eds. G. Briffod, Adri Nijsen-Vis, F.C. Schueller, 1990, ECA, 14B, Pt. 3, 1439-1442.

158 Meisel, D., G. Haas, R. Aratari and ASDEX-Team[2)]:
Evaluation of Neutral Gas Flux Measurements in the ASDEX-Divertor with Respect to Divertor-Geometry and Recycling. In: 17th EPS Conf. on Controlled Fusion and Plasma Heating, Amsterdam(NL) 1990, Eds. G. Briffod, Adri Nijsen-Vis, F.C. Schueller, 1990, ECA, 14B, Pt. 3, 1468-1471.

159 Memmel, N., G. Rangelov, E. Bertel and V. Dose:
Two-Dimensional Unoccupied Band Structure of CO on Ni(110) and Pd(110). Vacuum 41, Nos. 1-3, 729-730 (1990).

160 Merkel, P.:
Island Studies for Helias Configurations. In: Proc.First Internat.Toki Conf.on Plasma Physics and Controlled Nuclear Fusion, Toki(JP) 1989, NIFS/PROC/3, 1990, 134-137.

161 Milch, I.:
Hochtemperaturplasma im Test auf Reaktoreignung. Handelsblatt 225, 22.11.1990, B7 (1990).

162 Milch, I.:
Kernfusions-Euroreaktor. Europ.Forschung auf dem Gebiet der Kernfusion. Wirtschaft und Technik 4, 74-78 (1990).

163 Milch, I.:
Das Sonnenfeuer auf die Erde holen. Sieg Tech 5, 29-30 (1990).

164 Morrison, P.J.[1)] and D. Pfirsch:
The Free Energy of Maxwell-Vlasov Equilibria. Physics of Fluids. B 2, 6, Pt.1, 1105-1113 (1990).

165 Mueller, E.R., A. Staebler, T. Hartinger, K. McCormick, J. Neuhauser, H. Niedermeyer and ASDEX-Team[2)]:
Radiation Behaviour in ASDEX Divertor Discharges at the Density Limit. In: Proc.of the Satellite Workshop of the 9th Internat.Conf.on Plasma Surface Interactions, Cadarache(FR) 1990, EUR/CEA/FC/1403, 117-124.

166 Mueller, E.R., A. Staebler, T. Hartinger, K. McCormick, J. Neuhauser, H. Niedermeyer and ASDEX-Team[2)]:
Radiation Behaviour in ASDEX Divertor Discharges at the Density Limit. In: ASDEX Contributions. Workshop on Relevance, Realization and Stability of a Cold Layer at the Edge for Fusion Reactors, Cadarache(FR) 1990, EUR/CEA/FC/1403, 1990, 114-121.

167 Murmann, H.D., Ch. Dorn, H. Roehr and G. Schramm:
The Laser Scattering System of the Tokamak ASDEX Upgrade. The Hague (NL) 1990, 1277. 25.

168 Murmann, H.D., H. Zohm, ASDEX-Team[2)] and NI-Team(ASDEX)[4)]:
T_e Profile Invariance Under Transient Conditions on ASDEX. In: 17th EPS Conf. on Controlled Fusion and Plasma Heating, Amsterdam (NL) 1990, Eds. G. Briffod, Adri Nijsen-Vis, F.C. Schueller, 1990, ECA, 14B, Pt. 1, 54-57.

169 Murphy, A.:
Waves in the Edge Plasma During Ion Cyclotron Resonance Heating. Fusion Engineering and Design 12, Nos. 1-2, 79-92 (1990).

170 Neuhauser, J.:
Radiation Control in Poloidal Divertor Tokamaks. In: ASDEX Contributions. Workshop on Relevance, Realization and Stability of a Cold Layer at the Edge for Fusion Reactors, Cadarache (FR) 1990, 98-113.

171 Neuhauser, J.:
Radiation Control in Poloidal Divertor Tokamaks. In: Proc.of Satellite Workshop of the 9th Internat.Conf.on Plasma Surface Interactions, Cadarache(FR) 1990, EUR/CEA/FC/ 1403, 1990, S. 243-258.

172 Neuhauser, J., B. Braams, M. Krech, U. Ritschel, W. Schneider and R. Wunderlich:
Tokamak Edge Studies with a 2D Multifluid Code. Contributions to Plasma Physics 30, 1, 95-100 (1990).

174 Noterdaeme, J.-M., R. Buechse, R. Lang, R. Loch, V. Mertens, F. Ryter, W. Sandmann, F. Wesner, ICRH-Team[8)], Pellet-Team[10)] and ASDEX-Team[2)]:
Repetitive Pellet Injection Combined with Ion Cyclotron Resonance Heating in ASDEX. In: 17th EPS Conf. on Controlled Fusion and Plasma Heating, Amsterdam(NL) 1990, Eds. G. Briffod, Adri Nijsen-Vis, F.C. Schueller, 1990, ECA, 14B, Pt. 1, 239-242.

173 Noterdaeme, J.-M., ICRH-Team[8)], ASDEX-Team[2)] and NI-Team(ASDEX)[4)]:
Experimental Results on Edge Effects During ICRF Heating of ASDEX Plasmas. Fusion Engineering and Design 12, Nos. 1-2, 127-137 (1990).

175 Nuehrenberg, J.:
Optimization of Helias Configurations. In: Proc. First Internat. Toki Conf. on Plasma Physics and Controlled Nuclear Fusion, Toki(JP) 1989, NIFS/ PROC/3, 1990, 29-32.

176 Nygren, R.E.[1)], J. Bohdansky, A. Pospieszczyk[1)] et al.:
Radiation-Enhanced Sublimation of Graphite in PISCES Experiments. Journal of Vacuum Science and Technology. A 8, 3, Pt.1, 1778-1782 (1990).

177 Ott, W., F.P. Penningsfeld, WVII-AS-Team[3)], ECRH-Group[7)], NI-Group[6)] and Pellet-Team[10)]:
First Results with Neutral Injection into WVII-AS Stellarator. In: 17th EPS Conf. on Controlled Fusion and Plasma Heating, Amsterdam(NL) 1990, Eds. G. Briffod, Adri Nijsen-Vis, F.C. Schueller, 1990, ECA, 14B, Pt. 2, 483.

178 Penningsfeld, F.P., J.-H. Feist, K. Freudenberger, W. Ott and E. Speth:
Commissioning and First Operation of the W-VII-AS Neutral Beam Systems. In: IEEE 13th Symp. on Fusion Engineering, Knoxville(US) 1989, S. 288- 291 (1990).

179 Petitpierre, O., W. Moeller and B.M.U. Scherzer: Low-Temperature Dynamic Depth Profile Measurements of Implanted Deuterium in Nickel: Precipitation of Nickel Deuteride. Journal of Applied Physics 68, 7, 3169-3177 (1990).

180 Petri, A.[1)], A. Neumann[1)] and J. Kueppers:
Interaction of Oxygen and CO with Ni_2Ti Surfaces. J. Vac. Sci. Technol. A 8, 2576-2580 (1990).

181 Pfirsch, D.:
Nonlinear Instabilities, Negative Energy Modes and Generalized Cherry Oscillators. Zeitschrift fuer Naturforschung. A 45, 7, 839-846 (1990).

182 Pinkau, K.:
Gibt es eine Bringschuld der Grundlagenforschung? Muenchen(DE) 1990, S. 5-6 (1990).

183 Pinkau, K.:
Naturwissenschaft und Technik in einer Akzeptanzkrise? Muenchen(DE) 1989, S. 7-10 (1990).

184 Pinkau, K.:
Probleme der Folgenabschaetzung. Handbuch des Wissenschaftstransfers, 57-68, Berlin: Springer (1990).

185 Poedts, S., M. Goossens[1)] and W. Kerner:
Coronal Loop Heating by Resonant Absorption. Physics of Magnetic Flux Ropes, 257-262, Washington: Am.Geophys.Union (1990).

186 Poedts, S., M. Goossens[1)] and W. Kerner:
Numerical Simulation of the Stationary State of Periodically Driven Coronal Loops. Computer Physics Communications 59, 1, 75-84 (1990).

187 Poedts, S., M. Goossens[1)] and W. Kerner:
On the Efficiency of Coronal Loop Heating by Resonant Absorption. Astrophys.Journal 360, 279-287 (1990).

188 Poedts, S., M. Goossens[1)] and W. Kerner:
Temporal Evolution of Resonant Absorption in

Solar Coronal Loops. Computer Physics Communications 59, 1, 95-103 (1990).

189 Puri, S.:
Edge-Plasma Heating via Parasitic-Torsional-Mode Excitation by Faraday-Shielded Ion-Bernstein-Wave Antennas. In: 17th EPS Conf. on Controlled Fusion and Plasma Heating, Amsterdam(NL) 1990, Eds. G. Briffod, Adri Nijsen-Vis, F.C. Schueller, 1990, ECA, 14B, Pt. 3, 1158.

190 Puri, S.:
Radiative Energy Transport in Thermonuclear Plasmas. In: 17th EPS Conf. on Controlled Fusion and Plasma Heating, Amsterdam(NL) 1990, Eds. G. Briffod, Adri Nijsen-Vis, F.C. Schueller, 1990, ECA, 14B, Pt. 4, 1770-1773.

191 Rangelov, G., N. Memmel, E. Bertel and V. Dose:
The Bonding of Hydrogen on Nickel Studied by Inverse Photoemission. Surface Science 236, 3, 250-258 (1990).

192 Reichle, R., R. Behrisch and J. Roth:
Depth-Profiling of Beryllium on Graphite with Ion Beams. Nuclear Instruments and Methods in Physics Research. B 50, 68-73 (1990).

193 Richter, H.:
Multiprocessor with Dynamically Variable Topology. Computer Systems Science and Engineering 5, 1, 29-35 (1990).

194 Richter, T., S. Pfau[1)], F. Rahn[1)] and S. Werzlau[1)]:
Elektroneninduziertes Aetzen von Selen im Wasserstoffplasma einer Glimmentladung. In: Proc. 7.Tagung Physik und Technik des Plasmas, Berlin(DE) 1990, 8.

195 Ringler, H., WVII-AS-Team[3)], NI-Team(WVII-AS)[5)], ICF-Group[14)] and ECRH-Group[7)]:
Status of the WVII-AS Program. In: Proc. of the First Internat.Toki Conf.on Plasma Physics and Controlled Nuclear Fusion, Toki(JP) 1989, NIFS/PROC/3, 1990, S. 81-84.

196 Roehr, H., K.-H. Steuer, H.D. Murmann and D. Meisel:
Temperature and Density Measurement by Laser Scattering on the ASDEX Tokamak. The Hague (NL) 1990, 1277.26.

197 Rome, J.A., R.N. Morris, S.P. Hirshman, R.H. Fowler and P. Merkel:
Coil Configurations for Low Aspect Ratio Stellarators. In: Proc. 7th Internat. Workshop on Stellarators, Oak Ridge(US) 1989, IAEA/TEC-DOC/558, 1990, 545-549.

198 Roth, J., R. Behrisch, W. Moeller and W. Ottenberger:
Fusion Reactions During Low Energy Deuterium Implantation into Titanium. Nuclear Fusion 30, 3, 441-446 (1990).

199 Rudyj, A., A. Carlson, M. Endler, L. Giannone, H. Niedermeyer, G. Theimer and ASDEX-Team[2)]:
Structure of Density Fluctuations in the Edge Plasma of ASDEX. In: 17th EPS Conf. on Controlled Fusion and Plasma Heating, Amsterdam(NL) 1990, Eds. G. Briffod, Adri Nijsen-Vis, F.C. Schueller, 1990, ECA, 14B, Pt. 3, 1464-1467.

200 Ryter, F., F. Braun, F. Hofmeister, J.-M. Noterdaeme, K.-H. Steuer, F. Wesner, ICRH-Team[8)], ASDEX-Team[2)] and NI-Team(ASDEX)[4)]:
ICRF Hydrogen Minority Heating in the Boronized ASDEX Tokamak. In: 17th EPS Conf. on Controlled Fusion and Plasma Heating, Amsterdam(NL) 1990, Eds. G. Briffod, Adri Nijsen-Vis, F.C. Schueller, 1990, ECA, 14B, Pt. 3, 1052-1055.

201 Ryter, F., O. Gehre, B. Kurzan, J.-M. Noterdaeme, G. Siller, F. Wesner, ICRH-Team[8)], ASDEX-Team[2)] and NI-Team(ASDEX)[4)]:
Influence of Boronization and Carbonization on ICRF-Heated Plasmas in ASDEX. Fusion Engineering and Design 12, Nos. 1-2, 267-271 (1990).

202 Ryter, F., O. Gruber, O. Vollmer, F. Wagner, ASDEX-Team[2)] and NI-Team(ASDEX)[4)]:
ELM-Free H-Mode with CO- and CTR-Neutral Injection in ASDEX. In: 17th EPS Conf. on Controlled Fusion and Plasma Heating, Amsterdam(NL) 1990, Eds. G. Briffod, Adri Nijsen-Vis, F.C. Schueller, 1990, ECA, 14B, Pt. 1, 94-97.

203 Salzmann, H.:
Thomson Scattering in ITER Diagnostics. ITER Documentation Series 33, Vienna: IAEA (1990).

204 Sanchez, J., H.J. Hartfuss, WVII-AS-Team[3], NI-Team(WVII-AS)[5] and ECRH-Group[7]:
Reflectrometry Observations of Density Fluctuations in Wendelstein VII-AS Stellarator. In: 17th EPS Conf. on Controlled Fusion and Plasma Heating, Amsterdam(NL) 1990, Eds. G. Briffod, Adri Nijsen-Vis, F.C. Schueller, 1990, ECA, 14B, Pt. 4, 1572-1575.

205 Santaniello, A., J. Roth and F. Wagner:
Phase Transition in Fe Films on Pyrolytic Graphite During D^+ Irradiation Identified Through Moessbauer Spectroscopy. Nuclear Instruments and Methods in Physics Research. B 48, Nos. 1-4, 499-503 (1990).

206 Sapper, J.:
Overview of Engineering Design of Wendelstein VII-X. In: Proc. of the First International Toki Conference on Plasma Physics and Controlled Nuclear Fusion, Toki(JP) 1989, NIFS/PROC/3, 1990, S. 264-267.

207 Sapper, J. and H. Renner:
Stellarator Wendelstein VII-AS: Physics and Engineering Design. Fusion Technology 17, 1, 63-75 (1990).

208 Sardei, F.:
7.4 Neutral Gas Behaviour in the Plasma Edge of Wendelstein WVII-X. 7.6.5 Particle Transport (at WVII-AS). Beitraege zu WVII-X Proposal (1990).

209 Sardei, F., H. Ringler, A. Dodhy, G. Kuehner, WVII-AS-Team[3] and ECRH-Group[7]:
Particle Transport and Recycling Studies on the WVII-AS Stellarator. In: 17th EPS Conf. on Controlled Fusion and Plasma Heating, Amsterdam(NL) 1990, Eds. G. Briffod, Adri Nijsen-Vis, F.C. Schueller, 1990, ECA, 14B, Pt. 2, 471-474.

210 Scherzer, B.M.U.:
Hydrogen in the First Wall of Nuclear Fusion Plasma Devices. Nuclear Instruments and Methods in Physics Research. B 45, Nos. 1-4, 57-61 (1990).

211 Scherzer, B.M.U., J. Wang[1] and W. Moeller:
Dynamic Inventory of Implanted Deuterium in Graphite at 116-223 K. Nuclear Instruments and Methods in Physics Research. B 45, Nos. 1-4, 54-56 (1990).

212 Schneider, F. and H. Rapp:
Tokamak Plasma Control Using Thyristor Power Converters. In: Proc. CAS-CERN Accelerator School; Power Converters for Particle Acceleration, Montreux (CH) 1990, Ed. S. Turner, CERN 90/07, 325-351.

213 Schneider, R., H. Duerr, T. Fauster and V. Dose:
A Simple Method for the Determination of the Angle of Incidence for Low-Energy Electrons. Journal of Vacuum Science and Technology. A 8, 4, 3363-3364 (1990).

214 Schneider, R., H. Duerr, T. Fauster and V. Dose:
The Temperature Dependence of the Inverse Photoemission from Copper Surfaces. Vacuum 41, Nos. 1-3, 528-530 (1990).

215 Schneider, R., H. Duerr, T. Fauster and V. Dose:
Temperature Dependence of the Inverse Photoemission from Copper Surfaces. Physical Review. B 42, 1638-1651 (1990).

216 Schneider, U., W. Poschenrieder, M. Bessenrodt-Weberpals, J. Hofmann, A. Kallenbach, K. Krieger, E.R. Mueller, H. Niedermeyer, F. Ryter, J. Roth, F.X. Soeldner, A. Staebler, E.R. Mueller, K.-H. Steuer, O. Vollmer, F. Wagner, ASDEX-Team[2], ICRH-Team[8], LH-Team[9], NI-Team (ASDEX)[4] and PSI-Group[15]:
Boronization of ASDEX. In: ASDEX Contributions 9th Internat.Conf.on Plasma Surface Interaction in Controlled Fusion Devices, Bournemouth(GB) 1990, 65-80.

217 Schubert, R., F. Braun, J. Gernhardt, F. Hofmeister, F. Leuterer, M. Muenich, J.-M. Noterdaeme, F. Wesner and ASDEX-Team[2]:
Edge Density X-Mode Reflectometry of RF-Heated Plasmas on ASDEX. In: 17th EPS Conf. on Controlled Fusion and Plasma Heating, Amsterdam(NL) 1990, Eds. G. Briffod, Adri Nijsen-Vis, F.C. Schueller, 1990, ECA, 14B, Pt. 4, 1552-1555.

218 Schumacher, U. and R. Nolte:
Local Crystal Lattice Curvature Measurements for Bent-Crystal Spectrometers. Rev. Sci. Instrum. 61, 1, 121-123 (1990).

219 Schuppler, S.[1], N. Fischer[1], E. Bertel and W.

Steinmann[1]):
Two-Photon Photoemission on Ni(111) Image States. Vacuum 41, Nos. 1-3, 755-756 (1990).

220 Schuppler, S.[1]), N. Fischer[1]), W. Steinmann[1]), R. Schneider and E. Bertel:
Image-Potential States on Ni(111): A Two-Photon-Photoemission Study. Physical Review. B 42, 9403-9408 (1990).

221 Schwenn, U., D.V. Anderson[1]), W.A. Cooper[1]) et al.:
Global Ideal MHD Stability of 3D Plasmas with Pseudo-Vacuum Treatment for Free-Boundary Modes. In: 17th EPS Conf. on Controlled Fusion and Plasma Heating, Amsterdam(NL) 1990, Eds. G. Briffod, Adri Nijsen-Vis, F.C. Schueller, 1990, ECA, 14B, Pt. 2, 931-934.

222 Scott, B.D.:
A Cascade Model for Turbulent Dissipation in Convection-Accretion Disks. Astrophys.J. Lett. 357, L53-L56 (1990).

223 Scott, B.D.:
Self-Sustained Collisional Drift-Wave Turbulence in a Sheared Magnetic Field. Physical Review Letters 65, 26, 3289-3292 (1990).

224 Senftinger, B. and H. Liebl:
Performance Evaluation of a Novel Type of Low-Energy Electron Microscope. In: Proc. of the 12th International Congress for Electron Microscopy, Seattle(US) 1990, San Francisco Press Inc. 354-355.

225 Sillen, C.W.P.M.[1]), J.J.M. Ruigrok[1]), M.G.J. Veprek-Heijman, A.J.G. Bode-Fassbender[1]) and J.B. Giesbers[1]):
High-Performance Small-Track-Width Metal-in-Gap Heads Made by Reactive Ion Etching. J. of Magnetism and Magn. Materials 83, 45-47 (1990).

226 Soeldner, F.X., R.S. Bartiromo[1]), S. Bernabei[1]), F. Leuterer, K. McCormick, H.D. Murmann, LH-Team[9]), NI-Team(ASDEX)[4]) and ASDEX-Team[2]):
Profile Control with Lower Hybrid Waves on ASDEX. In: 17th EPS Conf. on Controlled Fusion and Plasma Heating, Amsterdam(NL) 1990, Eds. G. Briffod, Adri Nijsen-Vis, F.C. Schueller, 1990, ECA, 14B, Pt. 3, 1323-1326.

227 Soeldner, F.X., R. Lang, R. Loch, V. Mertens, H.-S. Bosch, F. Leuterer, Pellet-Team[10]), LH-Team[9]) and ASDEX-Team[2]):
Combined Operation of Pellet Injection and Lower Hybrid Current Drive on ASDEX. In: 17th EPS Conf. on Controlled Fusion and Plasma Heating, Amsterdam(NL) 1990, Eds. G. Briffod, Adri Nijsen-Vis, F.C. Schueller, 1990, ECA, 14B, Pt. 3, 1215-1218.

228 Spies, G.O. and J. Li[1]):
On the Kinetic Alfven Wave. Physics of Fluids. B 2, 10, 2287-2293 (1990).

229 Staebler, A., K. McCormick, E.R. Mueller, J. Neuhauser, H. Niedermeyer, N. Tsois[1]), ASDEX-Team[2]) and NI-Team(ASDEX)[4]):
Density Limit in ASDEX Under Clean Plasma Conditions. In: 17th EPS Conf. on Controlled Fusion and Plasma Heating, Amsterdam(NL) 1990, Eds. G. Briffod, Adri Nijsen-Vis, F.C. Schueller, 1990, ECA, 14B, Pt. 1, 395-398.

230 Starke, K., K. Ertl, M. Donath and V. Dose:
Exchange Splitting of Bulk and Surface States on Ni(001). Vacuum 41, Nos. 1-3, 755 (1990).

231 Steuer, K.-H., H. Roehr, W. Engelhardt, G. Fussmann, A. Kallenbach, B. Kurzan, H.D. Murmann, ASDEX-Team[2]) and NI-Team(ASDEX)[4]):
Demixing of Impurities and Hydrogen as Deduced from $Z_e$ff Profiles in the Boronized ASDEX. In: 17th EPS Conf. on Controlled Fusion and Plasma Heating, Amsterdam(NL) 1990, Eds. G. Briffod, Adri Nijsen-Vis, F.C. Schueller, 1990, ECA, 14B, Pt. 1, 62-65.

232 Steuer, K.-H., H. Roehr and B. Kurzan:
Bremsstrahlung Measurements in the Near Infrared on ASDEX. In: Proc. 8th Topical Conf. on High.Temperature Plasma Diagnostics, Hyannis(US) 1990, 3084-3086.

233 Strachan, J.D.[1]), J.M. Adams[1]), C.W. Barnes[1]), H.-S. Bosch et al.:
Neutron Calibration Techniques for Comparison of Tokamak Results. Rev.Sci.Instrum. 61 (II), 3501-3504 (1990).

234 Stroth, U., R. Buechse, W. Herrmann and K. Krieger:
Confinement Studies of Sawtooth-Free Ohmic Discharges. In: 17th EPS Conf. on Controlled Fusion and Plasma Heating, Amsterdam(NL)

1990, Eds. G. Briffod, Adri Nijsen-Vis, F.C. Schueller, 1990, ECA, 14B, Pt. 1, 66-69.

235 Taglauer, E.:
Surface Cleaning Using Sputtering. Applied Physics. A 51, 3, 238-251 (1990).

236 Tasso, H.:
Axisymmetric Equal-Field Solutions of Poisson's Equation. Nuovo Cimento 105B, 1369-1372 (1990).

237 Tasso, H.:
On the Spectra of Turbulent Fluids at Large k. Zeitschrift fuer Naturforschung. A 45, 7, 928 (1990).

238 Tasso, H.:
A Sufficient Condition in Resistive MHD. Physics Letters. A 147, 1, 28-30 (1990).

239 Tsois, N., G. Kyriakakis[1)], E. Kakoulidis[1)], A. Carlson, J. Neuhauser, W. Feneberg and ASDEX-Team[2)]:
Power Flow and Electric Current Asymmetries in the ASDEX Sol. In: 17th EPS Conf. on Controlled Fusion and Plasma Heating, Amsterdam(NL) 1990, Eds. G. Briffod, Adri Nijsen-Vis, F.C. Schueller, 1990, ECA, 14B, Pt. 3, 1427-1430.

240 Van der Linden, R.A.M.[1)], M. Goossens[1)] and W. Kerner:
A Combined Finite Element/Fourier Series Method for the Numerical Study of the Stability of Line-tied Magnetic Plasmas. Computer Physics Communications 59, 1, 61-73 (1990).

241 Veprek, S.[1)] and M.G.J. Veprek-Heijman:
The Possible Contribution of SiH_2 and SiH_2 in the Plasma-Induced Deposition of Amorphous Silicon from Silane. Appl. Phys. Lett. 56, 1766-1768 (1990).

242 Verbeek, H., W. Poschenrieder, J.K. Fu, F.X. Soeldner and ASDEX-Team[2)]:
The Particle Fluxes in the Edge Plasma During Discharges with Improved Ohmic Confinement in ASDEX. Plasma Physics and Controlled Fusion 32, 8, 651-658 (1990).

243 Vollmer, O., R. Aratari, F. Ryter, K.-H. Steuer, F. Wagner, ASDEX-Team[2)] and NI-Team(ASDEX)[4)]:
Long-Pulse Heating in ASDEX L-and H-Mode Discharges. In: 17th EPS Conf. on Controlled Fusion and Plasma Heating, Amsterdam(NL) 1990, Eds. G. Briffod, Adri Nijsen-Vis, F.C. Schueller, 1990, ECA, 14B, Pt. 1, 295-298.

244 Von Goeler, S., O. Klueber, G. Fussmann, J. Gernhardt and M. Kornherr:
Magnetohydrodynamic Activity During Edge Localized Modes on ASDEX. Nuclear Fusion 30, 3, 395-403 (1990).

245 Wagner, F., M. Bessenrodt-Weberpals, L. Giannone, A. Kallenbach, K. McCormick, F.X. Soeldner and U. Stroth:
The Isotope Dependence of Confinement in ASDEX: Part 2. In: 17th EPS Conf. on Controlled Fusion and Plasma Heating, Amsterdam(NL) 1990, Eds. G. Briffod, Adri Nijsen-Vis, F.C. Schueller, 1990, ECA, 14B, Pt. 1, 58-61.

246 Weller, A., R. Brakel, R. Burhenn, H. Hacker, A. Lazaros, WVII-AS-Team[3)], ECRH-Group[7)], ICRH-Team[8)], NI-Group[6)] and Pellet-Team[10)]:
Results from X-Ray Measurements on the Wendelstein WVII-AS Stellarator. In: 17th EPS Conf. on Controlled Fusion and Plasma Heating, Amsterdam(NL) 1990, Eds. G. Briffod, Adri Nijsen-Vis, F.C. Schueller, 1990, ECA, 14B, Pt. 2, 479-482.

247 Wesner, F., V.M. Prozesky, R. Behrisch and G. Staudenmaier:
Measurement of Fast Particles in Front of the ICRH-Antenna of ASDEX. Fusion Engineering and Design 12, Nos. 1-2, 193-196 (1990).

248 Wielunski, M. and W. Moeller:
A Simple Coincidence Method of Deuterium Profiling Using the $D(^3He,^4He)H$ Reaction. Nuclear Instruments and Methods in Physics Research. B 50, 23-26 (1990).

249 Wira, K., A. Eberhagen, V. Mertens and ASDEX-Team[2)]:
Investigation of Electron Cyclotron Emission in the ASDEX Tokamak During Lower Hybrid Current Drive and Heating. In: 17th EPS Conf. on Controlled Fusion and Plasma Heating, Amsterdam (NL) 1990, Eds. G. Briffod, Adri Nijsen-Vis, F.C. Schueller, 1990, ECA, 14B, Pt. 3, 1263-1266.

250 Wobig, H.:

Plasma Transport in Advanced Stellarators. In: Proc. of the First International Toki Conference on Plasma Physics and Controlled Nuclear Fusion, Toki(JP) 1989, NIFS/PROC/3, 1990, S. 49-56.

251 Wolle, B., B. Bomba and K. Huebner[1]:
Ion Temperature Determination from Neutron Rate Measurements During Deuterium Injection. In: 17th EPS Conf. on Controlled Fusion and Plasma Heating, Amsterdam(NL) 1990, Eds. G. Brifford, Adri Nijsen-Vis, F.C. Schueller, 1990, ECA, 14B, Pt. 4, 1516-1519.

252 Wurden, G.A.[1], K. Buechl, J. Hofmann, R. Lang, R. Loch, A. Rudyj and W. Sandmann:
Pellet Imaging Techniques in the ASDEX Tokamak. Rev. Sci. Instrum. 61, 3604-3608 (1990).

253 Yushmanov, P.N.[1], T. Takizuka[1], K. Riedel[1], O. Kardaun, J.G. Cordey[1], S.M. Kaye[1] and D.E. Post[1]:
Scalings for Tokamak Energy Confinement. Nuclear Fusion 30, 10, 1999 (1990).

254 Zanino, R. and W. Schneider:
1-D 1-Fluid SOL Modeling with Finite Elements. Contributions to Plasma Physics 30, 1, 127-132 (1990).

255 Zhang, B.[1], E. Taglauer and J. Wang[1]:
Study of Homegeneity for Surface Compositions of AgNi Allyos. J. Hunan University 17, 28-32 (1990).

256 Zohm, H., H. Bruhns, F. Leuterer, O. Klueber and F.X. Soeldner:
M=2 Mode Limit on Lower Hybrid Current Drive in ASDEX. In: 17th EPS Conf. on Controlled Fusion and Plasma Heating, Amsterdam(NL) 1990, Eds. G. Briffod, Adri Nijsen-Vis, F.C. Schueller, 1990, ECA, 14B, Pt. 3, 1223-1226.

257 Zohm, H., A. Kallenbach, H. Bruhns, G. Fussmann and O. Klueber:
Plasma Angular-Momentum Loss by MHD Mode Locking. Europhysics Letters 11, 8, 745-750 (1990).

DIPLOMA THESES

258 Engelhard, M.:
Bestimmung der effektiven Ionenladungszahl eines Plasmas aus der Bremstrahlung im nahen Infrarot Transportprozessen in Fusionsplasmen. Max-Planck-Institut fuer Plasmaphysik, Garching(DE), 1990.

259 Fischer, R.:
Erzeugung eines kurzen Wasserstoffpulses durch laserinduzierte Desorption aus Titanhydrid zur Untersuchung Transportprozessen in Fusionsplasmen. Techn. Univ. Muenchen(DE), 1990.

260 Hartinger, T.:
Bestimmung zweidimensionaler Strahlungsverteilungen in Hochtemperaturplasmen des Tokamaks ASDEX mittels bolometrischer Messungen und Computertomographie. Techn. Univ. Muenchen(DE), 1990.

261 Linsmeier, C.:
Oberflaechenanalytische Untersuchungen an Rh/Al_2O_2-Modellkatalysatoren.Univ.Muenchen(DE).

262 Loercher, M.:
Messung von Lyman-Alpha-Strahlung an Ionisationsmanometern zur Bestimmung der Wasserstoffatomdichte in Fusionsexperimenten Transportprozessen in Fusionsplasmen. Techn. Univ. Muenchen(DE), 1990.

263 Schulz, J.:
Adsorption von Wasserstoff auf Ru(001). Untersuchungen mit Ionenstreu- und Rueckstreuspektroskopie. Techn. Univ. Muenchen(DE), 1990.

264 Theimer, G.:
Methoden zur Untersuchung der raeumlichen Struktur von Dichtefluktuationen in der Randschicht von Fusionsexperimenten demonstriert am Divertortokamak ASDEX. Techn. Univ. Muenchen(DE), 1990.

265 Voges, D.:
Segregationsuntersuchungen an der Fe_2 Al(110) - Oberflaeche mit niederenergetischer Ionenstreuung. Univ. Muenchen(DE), 1990.

DOCTORAL THESES

266 Baretzky, B.:
Untersuchung der Oberflaechenzusammensetzung stoss- und segregationsbestimmter Systeme beim Beschuss von Festkoerpern mit niederenergetischen Ionen = Investigation of the Sur-

face Composition of Collison and of Segregation Dominated Systems for the Bombardment of Solids with Low-Energy Ions. Muenchen Univ.(DE), 1990.

267 Drube, R.:
Unbesetzte elektronische Zustaende rekonstruierender Einkristalloberflaechen = Unoccupied Electronic States of Reconstructing Single Crystal Surfaces. Bayreuth Univ.(DE), 1990.

268 Duerr, H.:
Geometrische Struktur und Dynamik der reinen und sauerstoffbedeckten Cu(110) Oberflaeche = Geometric Structure and Dynamics of the Clean and Oxygen Covered Cu(110) Surface. Bayreuth Univ. (DE), 1990.

269 Memmel, N.:
Chemisorption geordneter Adsorbate auf Metalloberflaechen - eine inverse Photoemissionsstudie. Bayreuth Univ.(DE), 1990.

270 Rudyj, A.:
Untersuchung transportrelevanter Fluktuationen in der Randschicht von ASDEX. Techn. Univ. Muenchen(DE), 1990.

271 Schneider, F.:
Optimierte Regelung der Plasmalage in den Tokamaks ASDEX und TCV mit Beruecksichtigung der netzgefuehrten Stromrichtersteller. Techn.Univ. Muenchen(DE). Fak. Elektrotechnik u. Informationstechnik, 1990.

272 Schneider, R.:
Temperaturabhaengigkeit direkter Uebergaenge in Inverser Photoemission.

273 Starke, K.:
Magnetische Domaenen und spinaufgeloeste elektronische Struktur von Ni(001). Bayreuth Univ. (DE), 1990.

274 Zohm, H.:
Untersuchung magnetischer Moden am Tokamak ASDEX. Heidelberg Univ. (DE), 1990.

HABILITATIONS

275 Bessenrodt-Weberpals, M.:
Analyse und Optimierung des Randschichtplasmas Ohmscher Tokamakentladungen. Duesseldorf Univ.(DE). Math.-Naturwiss.Fak., 1990.

PATENTS

276 Koch, A.W.:
Verfahren und Vorrichtung zum Beschichten von Werkstuecken durch Plasmaspritzen; BRD P 4036858.0

277 Koch, A.W.:
Verfahren und Vorrichtung zur Messung lokaler Schichtdicken und -strukturen; BRD P 40 36 857.2

278 Liebl, H.:
Kontaktionisations-Ionenstrahlquelle (12304); USA 265.056; Erteilungsbeschluss: 25.07.90

279 Liebl, H. und B. Senftinger:
Elektronenmikroskop (12537); Deutschland P 39 04 032.1; offengelegt:16.08.90; USA 476.973; angemeldet: 07.02.90; Frankreich 9001551; angemeldet: 09.02.90; Japan P 3904032.1-33; angemeldet: 09.02.90; Grossbritannien 9003080.0; angemeldet: 12.02.90

280 Mukherjee, S.:
Waermeschutzschild (12437); Deutschland 3828902.4-44; Offengelegt:08.03.90; Europa (DE,GB,FR,IT) 89115024; offengelegt:28.02.90

281 Schneider, F.:
Hybrider Regler (12606); Europa (DE,FR,IT, NL,S,GB,CH) 901 179 58.0; angemeldet: 18.09.90; USA 583.516; angemeldet: 17.09.90; Japan 248574/90; angemeldet: 18.09.90

282 Schneider, F.:
Synchronisierter Messverstaerker (12032); BRD P 36 27 610; erteilt 01.03.90

283 Schueller, P.G. und R. Wilhelm:
Mikrowellenkalorimeter (11953); Frankreich 8704951; Veroeffentlichung der Erteilung: 15.12.89

284 Spensberger, W.:
Hohlleiterelement fuer Mikrowellen (11635); Japan SHO 60-161350; Erteilungsbeschluss: 24.08.90

285 Weichselgartner, H.:
Verfahren und Einrichtung zum Entfernen von Tritium aus einem Gasgemisch (10802); Japan 76842-1981; Veroeffentlichung der Erteilung: 25.06.90

286 Wilhelm, R.:
Mikrowellen-Plasmaverfahren (12418); USA 365.424; Veroeffentlichung der Erteilung: 30.01.90

LECTURES

287 Adamson, S., M.-L. Apicella[1)], A-P. Martinelli, E. Taglauer and ASDEX-Team[2)]:
Metallische Verunreinigungen in der Plasmarandschicht von ASDEX. Verhandl. DPG (VI) 25, P17.3 (1990).

288 Andelfinger, C.:
Pellet Centrifuge for ASDEX Upgrade. I.V. Kurchatov Inst. of Atomic Energy, Moscow (SU), 1990.

289 Aratari, R., M. Bessenrodt-Weberpals, A. Carlson, C.-C. Chu, J. Hofmann, D. Meisel, W. Poschenrieder, G. Siller, H. Verbeek, ASDEX-Team[2)] and NI-Team(WVII-AS)[5)]:
Up-down Divertor Asymmetries in ASDEX. 9th Internat.Conf.Plasma Surface Interactions in Controlled Fusion Devices, Bournemouth (GB), 1990.

290 Baetzner, R.[1)], K. Huebner[1)], L. Ingrosso[1)], J. Kucinski[1)], B.V. Robouch[1)], B. Bomba, H.-S. Bosch and C. van Calker[1)].:
Absolutbestimmung der Neutronenausbeute fuer ASDEX mittels Kernspurplatten-Messungen, in Aktivierung und Monte-Carlo - Rechnungen. Verhandl. DPG (VI) 25, 412, P14.4 (1990).

291 Behrisch, R.:
Anwendung von beschleunigten Ionen zur Materialanalyse. Phys. Kolloquium, Univ. Frankfurt a.M.(DE), 1990.

292 Behrisch, R.:
Erosion of Plasma Facing Materials by Sputtering. US-Japan-Workshop on Plasma Facing Materials, Nagoya(JP), 1990.

293 Behrisch, R.:
How to Gap the Experience Gained in Today's Large Fusion Devices to the Next Step Devices. US-Japan-Workshop on Plasma Facing Materials, Nagoya(JP), 1990.

294 Behrisch, R.:
Plasma Surface Interactions in Controlled Fusion Devices. 4th Nat.Conf.on Fusion Reactor Materials, Dubna(SU), 1990.

295 Behrisch, R., R. Brakel, P. Grigull, V. Prozesky, H. Renner, J. Roth and WVII-AS-Team[3)]:
Limiterbelastung and Materialumverteilung im Stellarator Wendelstein VII-AS waehrend der ersten Experimentierphase bei 1.25 Tesla. Verhandl. DPG (VI) 25, P10.45 (1990).

296 Behrisch, R., A. Dodhy, P. Grigull, G. Kuehner, I. Lakicevic[1)], A. Martinelli[1)], H. Renner, H. Ringler, J. Roth, F. Sardei, WVII-AS-Team[3)] and ECRH-Group[7)]:
Zusammenfassung der bisherigen Randschicht-Untersuchungen am WVII-AS. ASDEX-WVII-AS Seminar, Ringberg, Tegernsee (DE), 1990.

297 Beidler, C.D.:
Helical Ripple Transport in Stellarator with Emphasis on Uragan-2M and Helias. Workshop of Stellarators Theory, Kharkov(SU), 1990.

298 Beidler, C.D., G. Grieger, E. Harmeyer, J. Kisslinger, F. Rau and H. Wobig:
Review of Advanced Stellarator Reactor and Burner Studies 1982-1990. Stellarator Workshop, Oak Ridge (US), Oct 1990.

299 Beidler, C.D., G. Grieger, E. Harmeyer, J. Kisslinger, F. Rau and H. Wobig:
Review of Advanced Stellarator Reactor and Burner Studies. Workshop of Stellarators Theory, Kharkov(SU), 1990.

300 Beidler, C.D., P. Grigull, E. Harmeyer, J. Kisslinger, F. Rau, H. Wobig and WVII-AS-Team[3)]:
On the Edge Structure and Limiter Calorimetry of the W VII-AS Stellarator. IEA Stellarator Workshop, Garching(DE), July 1990.

301 Beidler, C.D., E. Harmeyer, J. Kisslinger, F. Rau and H. Wobig:

Parameter Range of Wendelstein VII-X Fields. Workshop of Stellarators Theory, Kharkov(SU), 1990.

302 Barnsley, R.[1] and U. Schumacher:
Messungen absoluter Spektrallinien-Intensitaeten im weichen Roentgengebiet mit Doppelkristall-Monochromatoren an JET. Verhandl.DPG (VI) 25, 434, P.19.1 (1990).

303 Bessenrodt-Weberpals, M.:
Diagnostik und Modellierung der Plasmarandschicht in Tokamakentladungen. Elektrotechn. Kolloquium, Univ. Stuttgart(DE), 1990.

304 Bessenrodt-Weberpals, M.:
RAND-Bemerkungen. Seminarreihe ueber das Randschichtplasma in Fusionsmaschinen, Max-Planck-Inst. fuer Plasmaphysik, Garching(DE), 1990.

305 Bessenrodt-Weberpals, M.:
Supernova 1987A. Habilitationskolloquium, Univ. Duesseldorf(DE), 1990.

306 Bessenrodt-Weberpals, M.:
Supernova 1987A und die Elemententstehung. IPP-Kolloquium, Max-Planck-Inst. fuer Plasmaphysik, Garching(DE), 1990.

307 Bessenrodt-Weberpals, M., K. McCormick, F. Wagner and ASDEX-Team[2]:
Charakterisierung des Isotopeneffekts im Randschichtplasma von ASDEX. Verhandl. DPG (VI) 25, 375 (1990).

308 Biener, J., M. Hock[1] and J. Kueppers:
Adsorption von NO auf Pd(110)-Oberflaechen. Verhandl. DPG (VI) 25, 03.7 (1990).

309 Biskamp, D.:
Statistical Properties of MHD Turbulence. 2nd Toki Conf. on Plasma Physics and Controlled Fusion, 1990.

310 Biskamp, D.:
Theorie der magnetohydrodynamischen Turbulenz. Verhandl. DPG (VI) 25, PHV6, 410 (1990).

311 Bomba, B., F.P. Penningsfeld and A. Weller:
Vorschlaege zur Neutronendiagnostik am WVII-AS. ASDEX-WVII-AS Seminar, Ringberg, Tegernsee (DE), 1990.

312 Bosch, H.-S.:
Kritische Auswertung der Daten und Formeln fuer die Fusionsquerschnitte. Verhandl. DPG (VI) 25, P.10.34 (1990).

313 Boutard, D.:
Traitements Superficiels: Deposition Assistees par Plasmas. Ecole Normale Superieure, Univ. Paris VII(FR), 1990.

314 Brakel, R., R. Burhenn, H. Hacker, A. Weller, WVII-AS-Team[3], ECRH-Group[7] and NI-Group[6]:
Survey of Impurity Behaviour using the WVII-AS SPRED. IEA Stellarator Workshop, Garching (DE), 1990.

315 Brambilla, M.:
20 Lectures on 'H.F. Waves in Plasmas'. Advanced Seminar on Mathematical Modelling in Plasma Physics, Eteneo Veneto, Venice (IT), 1990.

316 Brambilla, M., R. Chodura, J. Hoffmann, J. Neuhauser, J.-M. Noterdaeme, F. Ryter, R. Schubert and F. Wesner:
Theoretical and Experimental Investigation of a Mechanism for Impurity Production by ICRF Fields. Proc. 13th IAEA Conf. on Plasma Phy-
sics and Controlled Nuclear Fusion Research, Washington(US), 1990.

317 Buechse, R.:
Tomographische Untersuchungen zentraler MHD Instabilitaeten an ASDEX und TFTR. ASDEX-WVII-AS Seminar, Ringberg, Tegernsee (DE), 1990.

318 Buechse, R., M. Kornherr and ASDEX-Team[2]:
M=1 Modenaktivitaet in ASDEX-Plasmen waehrend Heizung mit Lower-Hybrid-Wellen. Verhandl. DPG (VI) 25, 368, P1.2 (1990).

319 Burhenn, R., R. Brakel, H. Hacker, A. Weller, WVII-AS-Team[3], ECRH-Group[7] and NI-Group[6]:
Impurity Transport Studies in WVII-AS Using Impurity Injection. IEA Stellarator Workshop, Garching (DE), 1990.

320 Burhenn, R., R. Brakel, H. Hacker, A. Weller and WVII-AS-Team[3]:
Untersuchung der Fremdionen und deren Transport in ECRH-Plasmen in WVII-AS. Verhandl.

DPG (VI) 25, 432, P18.3 (1990).

321 Cattanei, G.:
ICRH-Theorie und WVII-AS-Alternatives Antennenkonzept 'breite Antenne'. ASDEX-WVII-AS Seminar, Ringberg, Tegernsee (DE), 1990.

322 Christiansen, J.P.[1)], J.G. Cordey[1)], O. Kardaun and K. Thomsen[1)]:
Does Global Confinement Data Satisfy the Constraints of Plasma Theory? Proc. 13th IAEA Conf. on Plasma Physics and Controlled Nuclear Fusion Research, Washington(US), 1990.

323 Christiansen, J.P.[1)], J.G. Cordey[1)], O. Kardaun and K. Thomsen[1)]:
Imposing the Plasma Physics Constraints on the L- and H-mode Global Confinement Databases. ITER Workshop on Confinement, Garching (DE), 1990.

324 Darvas, J., K. Steinmetz, R. Flowers, L. Gouni, G. Grieger, K. Koeberlein, R.S. Pease and A. Roncaglia:
Environmental, Safety-Related and Economic Potential of Fusion Power. Proc. of 13th IAEA Conf. on Plasma Physics and Controlled Nuclear Fusion Research, Washington(US), 1990.

325 Degenhardt, G.[1)], K. Huebner[1)] and M. Stams[1)]:
Sphaerische Ionisationskammer als ON-LINE-Neutronenspektrometer am Tokamak. Verhandl. DPG (VI) 25, P19.5 (1990).

326 Dodhy, A., G. Kuehner, H. Ringler, F. Sardei, WVII-AS-Team[3)] and ECRH-Group[7)]:
Spectroscopy am WVII-AS Stellarator. Verhandl. DPG (VI), 25, P10.6.

327 Donath, M.:
Inverse Photoemission and Secondary Electron Emission with Spin Resolution: Tools to Study Surface and Thin Film Magnetic Properties. Seminar, Lawrence Livermore Nat.Lab.(US), 1990.

328 Donath, M.:
Magnetic Properties of Thin Films and Surfaces from Spin-Polarized Electron Spectroscopies. AT&T Bell Laboratories, Murray Hill (US), 1990.

329 Donath, M.:
Polarization Effects in Inverse Photoemission Spectra. 5th Symposium on Surface Physics, Chlum Castle(CS), 1990.

330 Donath, M.:
Recent Developments in Surface and Interface Magnetism Studied by Spin-Polarized Techniques. Symp. on Contemporary Magnetic Issues, Pres. by the Northern Calif. Chapter of the Am. Vac. Soc. and the Santa Clara Valley IEEE Magnetics Soc., IBM Almaden Res.Center, San Jose (US), 1990.

331 Donath, M.:
Spin-Polarized Inverse Photoemissison. Gordon Research Conf.on Electron Spectroscopy, Brewster Academy, Wolfeboro (US), 1990.

332 Donath, M.:
Spin-Resolved Inverse Photoemission of Ferromagnetic Surfaces. Physical Science Seminar, IBM Almaden Res.Center, San Jose(US), 1990.

333 Donath, M.:
Surface and Thin Film Magnetism Probed by Spin-Polarized Electrons. Surf. Science Seminar, Houston(US), 1990.

334 Donath, M.:
Surface and Thin Film Magnetism Probed by Spin-Polarized Electrons. Atomic-Molec.-Optical Seminar, Texas Univ., Austin(US), 1990.

335 Donath, M.:
Surface Magnetism and Spectroscopies Involving Spin-Polarized Electrons. Adv. Topics in Magnetism and Lecture Series Lect. 3, 4 IBM Almaden Res.Center, San Jose(US), (1990).

336 Donath, M., D. Scholl[1)], H.C. Siegmann[1)] and E. Kay[1)]:
Probing Depth of the Low Energy Cascade Electrons from a Transition Metal. March Meeting of the Am. Phys. Soc., Bulletin Am.Phys.Soc. 35, 421 Anaheim(US) (1990).

337 Donath, M., D. Scholl[1)], H.C. Siegmann[1)] and E. Kay[1)]:
Effects of Film Growth Mode on Magnetic Exchange Coupling in Trilayer Structures. 35th Annual Conference on Magnetism and Magnetic Materials, San Diego(US), 1990.

338 Dose, V.:
Physik-Nobelpreis 1989. Inst. fuer Plasmafor-

schung der Univ. Stuttgart, 1990.

339 Dose, V.:
Polarization Effects in Inverse Photoemission Spectra. 14th Internat. Seminar on Surface Physics, Przesieka(PL), 1990.

340 Dose, V.:
Spin Polarized Inverse Photoemission. Internat. Seminar on Application of Inverse Photoemission Spectroscopy, Leningrad(SU), 1990.

341 Dose, V.:
Wasserstoff - Thema und Variationen. Kolloquium, IPP Garching(DE), 1990.

342 Du Plessis, J.[1)], G. Van Wyk[1)] and E. Taglauer:
Praeferentielle Zerstaeubung und strahlungsinduzierte Segregation von metallischen Legierungen. Verhandl. DPG (VI), 25, 09.8 (1990).

343 Duerr, H., T. Fauster and R. Schneider:
Geometry, Growth and Dynamics of the (2x1) O-Cu(110) Surface. 11th Europ. Conf. on Surface Science, Salamanca(ES), 1990.

344 Duerr, H., T. Fauster and R. Schneider:
Untersuchung von Geometrie und Wachstum der 2x1 Sauerstoff- Struktur auf Cu(110) mit niederenergetischer Ionenstreuung. Verhandl. DPG (VI),25, 016.10 (1990).

345 Eckstein, W.:
Computer Simulation of Backscattering and Sputtering. Acad. Sinica, Hefei (CN). Inst. Plasma Physics, 1990.

346 Eckstein, W.:
Computer Simulation of Backscattering and Sputtering. Acad. Sinica, Shanghai(CN). Inst. Nuclear Research, 1990.

347 Eckstein, W.:
Current Examples of the Use of the TRIM.SP Program. Symp. of the Physics of Ionized Gases, Dubrovnik(YU), 1990.

348 Eckstein, W.:
Fusion Plasma Interactions with First Wall Surfaces. Symp. of the Physics of Ionized Gases, Dubrovnik(YU), 1990.

349 Eckstein, W.:
Physical and Chemical Sputtering of Multiple Component Solids. 5th Workshop on Carbon Materials, Juelich(DE), 1990.

350 Eckstein, W.:
Plasma-Wall Interaction. Acad. Sinica, Hefei (CN). Inst. Plasma Physics, 1990.

351 Endler, M.:
Fluktuationen im H_α - Licht. "Rand"-Seminar von M. Bessenrodt-Weberpals, 1990.

352 Endler, M.:
Fluktuationsmessungen im H_α - Licht und mit Langmuirsonden in der ASDEX-Randschicht. ASDEX-WVII-AS Seminar, Ringberg, Tegernsee (DE), 1990.

353 Endler, M.:
H_α - Fluktuationsmessungen in der ASDEX-Randschicht. Doktorandenkolloquium des IPP, Garching (DE), 1990.

354 Erckmann, V.:
ECRH Physik und Anwendung am AS. ASDEX-WVII-AS Seminar, Ringberg, Tegernsee (DE), 1990.

355 Erckmann, V.:
Experiments with High Power, Long Pulse ECRH in the WVII-AS Stellarator. Internat. Workshop on Strang Microwaves in Plasmas, Suzdal (SU), 1990.

356 Erckmann, V.:
Long Pulse ECRH Experiments at the WVII-AS Stellarator. 2nd Joint USSR-FRG Workshop on ECRH and Gyrotrons, Kurchatov Inst., Moscow (SU), 1990.

357 Erckmann, V.:
Recent Results on ECRH and ECCD at the WVII-AS Stellarator. Lawrence Livermore Nat. Lab.(US), 1990.

358 Erckmann, V.:
Die Zukunft von 140 GHz und die Moeglichkeiten fuer WVII-AS. ASDEX-WVII-AS Seminar, Ringberg, Tegernsee (DE), 1990.

359 Erckmann, V., U. Gasparino, H. Maassberg, H. Renner, M. Tutter, WVII-AS-Team[3)], W. Kaparek[1)], G.A. Mueller[1)], P.G. Schueller[1)] and M. Thumm[1)]:
Electron Cyclotron Current Drive and Wave

Absorption Experiments in the WVII-AS Stellarator. Proc. 13th IAEA Conf. on Plasma Physics and Controlled Nuclear Fusion Research, Washington(US), 1990.

360 Ertl, K., K. Starke, M. Donath and V. Dose: Spin-Resolved Photoemission: Exchange Splitting of Bulk and Surface States on Ni(001). Symp. on Surface Science(SSS 90), La Plague (FR).

361 Ertl, K., K. Starke, M. Donath and V. Dose: Spinaufgeloeste Inverse Photoemission an Ni (100). Kolloquium "Oberflaechenmagnetismus" der DFG, Bad Honnef(DE), 1990.

362 Fauster, T.: Inverse Photoemission. 14th School of Theoretical Physics, Szczyrk(PL), 1990.

363 Fauster, T.: Struktur und Dynamik der Cu(110)-Oberflaeche. Oberseminar zur Festkoerperphysik, Muenchen (DE), 1990.

364 Fauster, T.: Struktur und Dynamik der reinen und sauerstoffbedeckten Cu(110)- Oberflaeche. Inst. fuer Physikalische Chemie, Univ. Bonn, 1990.

365 Fauster, T., H. Duerr and R. Schneider: Untersuchung des Schwingungsverhaltens von Oberflaechenatomen der reinen und sauerstoffbedeckten Cu(110)-Oberflaeche mit niederenergetischer Ionenstreuung. Verhandl. DPG (VI), 25, 018.10 (1990).

366 Field, A.R., G. Fussmann and J.V. Hofmann: Poloidal Rotation in the H-Mode of ASDEX. ASDEX-WVII-AS Seminar, Ringberg, Tegernsee (DE), 1990.

367 Fischer, N.[1)], S. Schuppler[1)], T. Fauster and W. Steinmann[1)]: Lebensdauer von Bildpotentialzustaenden an Ni(111): Zweifarbige Zweiphotonenphotoemission an Ag(100). Verhandl. DPG (VI), 25, 021.3 (1990).

368 Friedl, A.: Ellipsometrie. Ringberg-Seminar, Ringberg, Tegernsee (DE), 1990.

369 Gauthier, E.[1)], W. Eckstein, J. Laszlo and J. Roth: Physical Sputtering of Low-Z Materials. 9th Internat. Conf. Plasma Surface Interaction in Controlled Fusion Devices, Bournemouth(GB), 1990.

370 Gehre, O.: Elektronen-Teilchentransport in ASDEX mittels Gasoszillationstechnik. ASDEX-WVII-AS Seminar, Ringberg, Tegernsee (DE), 1990.

371 Giannone, L.: Saegezahnpulsanalyse in NI geheizten ASDEX Plasmen. ASDEX-WVII-AS Seminar, Ringberg, Tegernsee (DE), 1990.

372 Glatzel, H., T. Fauster, R. Schneider and V. Dose: Geometric, Electronic, and Magnetic Structure of Ultrathin Iron Films on Cu(100). 11th Europ. Conf. on Surface Science, Salamanca(ES), 1990.

373 Glatzel, H., T. Fauster and R. Schneider: Unbesetzte elektronische Zustaende von Fe-Schichten auf Cu(110). Verhandl. DPG (VI), 25, 02.5 (1990).

374 Grieger, G., C.D. Beidler, H. Maassberg, E. Harmeyer, F. Herrnegger, J. Junker, J. Kisslinger, W. Lotz, P. Merkel, J. Nuehrenberg, F. Rau, J. Sapper, A. Schlueter, F. Sardei and H. Wobig: Physics and Engineering Design Studies for Wendelstein VII-X. Proc. 13th IAEA Conf. on Plasma Physics and Controlled Nuclear Fusion Research, Washington(US), 1990.

375 Grigull, P., R. Behrisch, R. Brakel, A. Dodhy, I. Lakicevic[1)], V. Prozesky, F. Rau, H. Renner, J. Roth, F. Sardei, WVII-AS-Team[3)] and ECRH-Group[7)]: Some Aspects of the Plasma Edge Properties of the Wendelstein WVII-AS Stellarator. 9th Internat.Conf.Plasma Surface Interactions in Controlled Fusion Devices, Bournemouth (GB), 1990.

376 Hacker, H., R. Brakel, R. Burhenn, J. Hofmann and W. Ohlendorf: Spektroskopie an WVII-AS. ASDEX-WVII-AS Seminar, Ringberg, Tegernsee (DE), 1990.

377 Hacker, H., R. Brakel, R. Burhenn, WVII-AS-Team[3)], NI-Group[6)], Pellet-Team[10)] and ECRH-Group[7)]:

Studies of Light Impurities in WVII-AS with Emphasis on CXRS Measurements. IEA Stellarator Workshop, Garching (DE), 1990.

378 Harmeyer, E., R. Heller, J. Kisslinger, W. Maurer, F. Rau, H. Ulbricht, H. Wobig and G. Zahn:
Force and Stress Calculations for a Non-planar WVII-X Demonstration coil. 16th Symp. on Fusion Technology, London(GB), 1990.

379 Hartfuss, H.J.:
Beobachtungen grossraeumiger Fluktuationen der Elektronentemperatur am Stellarator WVII-AS. Verhandl. DPG (VI) 25, 404, P11.4 (1990).

380 Hartfuss, H.J.:
ECE-Radiometrie der Elektronzyklotronemission. ASDEX-WVII-AS Seminar, Ringberg, Tegernsee (DE), 1990.

381 Hartfuss, H.J.:
On Density and Temperature Fluctuations Observed by ECE Diagnostics in WVII-AS. IEA Workshop, Garching (DE), 1990.

382 Hartfuss, H.J.:
Radiometry of Electron Cyclotron Emission from Fusion Relevant Plasmas. Ferienkurs 'Coherent Detection Techniques at Millimeter Wavelengths and their Applications', Ecole de Physique Theorique, Les Houches (FR), 1990.

383 Hartfuss, H.J.:
Reflectrometry Measurements of Density Fluctuations on WVII-AS. IEA Workshop, Garching (DE), 1990.

384 Hartfuss, H.J.:
Reflektrometrische Messungen von Dichtefluktuationen am Stellarator WVII-AS. Verhandl. DPG (VI) 25, 405, P11.5 (1990).

385 Hechtl, E.[1)], H.R. Yang[1)], C.H. Wu[1)] and W. Eckstein:
An Experimental Study of Tungsten Selfsputtering. 9th Internat.Conf.Plasma Surface Interaction in Controlled Fusion Devices, Bournemouth(GB), 1990.

386 Hofmann, J.V.:
Spektroskopie an Verunreinigungen. "Rand"-Seminar ASDEX - AUG - WVII-AS, IPP Garching(DE), 1990.

387 Hofmann, J.V.:
Uebersicht ueber einige diagnostische Moeglichkeiten der sichtbaren Spektroskopie (Spiegelsystem). IPP Garching (DE), 1990.

388 Hofmann, J.V., G. Fussmann, A.R. Field, ASDEX-Team[2)], NI-Team(ASDEX)[4)], LH-Team[9)] and ICRH-Team[8)]:
On the Diagnostic Potential of Visible Spectroscopy in the ASDEX Tokamak. IPP Garching (DE), 1990.

389 Hofmann, J.V., G. Fussmann, G. Janeschitz, A.R. Field, ASDEX-Team[2)], NI-Team (ASDEX)[4)], LH-Team[9)] and ICRH-Team[8)]:
Diagnostische Moeglichkeiten der sichtbaren Spektroskopie. Verhandl. DPG (VI) 25, 434, P19.3 (1990).

390 Holzhauer, E.:
FIR-Laserlichtstreuung an ASDEX. ASDEX-WVII-AS Seminar, Ringberg, Tegernsee (DE), 1990.

391 Jacob, W.:
Plasma-unterstuetzte Deposition duenner Filme (PACVD). Kolloquium, Augsburg(DE), 1990.

392 Jaenicke, R.:
Bedeutung und Messung quasistationaerer Magnetfeldaenderungen am WVII-AS. ASDEX-WVII-AS Seminar, Ringberg, Tegernsee (DE), 1990.

393 Jandl, O., J. Sapper and J. Simon-Weidner:
Finite Element Modelling with Sliding Effects Compared to Measurements Obtained from the Non-planar Coils for the Stellarator Wendelstein VII-AS. 16th Symp. on Fusion Technology, London(GB), 1990.

394 Josek, K.[1)], R. Margraf[1)] and E. Taglauer:
Ionenstreu- und Augerelektronen-Spektroskopie an oxidischen Modellkatalysatoren. Verhandl. DPG (VI), 25, 09.5 (1990).

395 Junker, J.:
Umladung. ASDEX-WVII-AS Seminar, Ringberg, Tegernsee (DE), 1990.

396 Kallenbach, A., H.M. Mayer and G. Fussmann:
Untersuchungen zum Drehimpulstransport an ASDEX. Verhandl. DPG (VI) 25, 10.38 (1990).

397 Kardaun, O.:
The ASDEX H-mode Database. Workshop on Global H-mode Confinement, JET(GB), 1990.

398 Kardaun, O.:
Datenauswertung mit SAS. Seminar WVII-AS, IPP Garching(DE), 1990.

399 Kardaun, O.:
Regression, Collinearity and Aspects of Robustness in Global Confinement Analysis. ITER Workshop on Confinement, Garching(DE), 1990.

400 Kardaun, O.:
Regression Analysis for the ITER H-mode Database. Workshop on Global H-mode Confinement, JET(GB), 1990.

401 Kardaun, O.:
Regression Techniques for Confinement Analysis. Workshop on Global H-mode Confinement, JET(GB), 1990.

402 Kardaun, O.:
Statistische Methoden in der Plasmaphysik. 5 Lectures. IPP Garching(DE), 1990.

403 Kisslinger, J., C.D. Beidler, E. Harmeyer, F. Rau and H. Wobig:
Magnetic Field and Coil Systems of the Modular Helias Configuration HS 5-10. 16th Symp. on Fusion Technology, London(GB), 1990.

404 Kisslinger, J., F. Rau and H. Wobig:
Magnetfeldkonfiguration von Wendelstein VII-AS und Randeffekte. Workshop WVII-AS, Ringberg, Tegernsee (DE), 1990.

405 Knoezinger, H.[1)], J. Leyrer[1)], R. Margraf [1)] and E. Taglauer:
Solid-Solid Wetting in Mixtures of Oxide Powders. Symp. on Surface Science, La Plague (FR), 1990.

406 Koeppendoerfer, W.:
Completion of Assembly and Start of Technical Operation of ASDEX Upgrade. 16th Symp. on Fusion Technology, London(GB), 1990.

407 Kraus, W.:
Entwicklung und Test einer Hf-Plasmaquelle fuer die Neutralinjektion. Forschungszentrum Juelich, Inst. fuer Plasmaphysik (DE), 1990.

408 Kraus, W.:
Recent Achievements on the RF-Plasma Source. Neutral Injection Joint Development Committee Meeting, Cadarache (FR), 1990.

409 Kraus, W., R. Bilau-Faust, J.-H. Feist and E. Speth:
High Power Beam Extraction from a Large Volume Radio-Frequency Plasma Generator. 16th Symp. on Fusion Technology, London (GB), 1990.

410 Krieger, K.:
Untersuchung des Verunreinigungstransports an ASDEX mittels modulierter Gaspulse. ASDEX-WVII-AS Seminar, Ringberg, Tegernsee (DE), 1990.

411 Kueppers, J.:
Prozesse und Strukturen an Oberflaechen. Kolloquium, IPP Garching(DE), 1990.

412 Kueppers, J.:
Prozesse und Strukturen an Oberflaechen. Physikalisches Kolloquium, Bayreuth(DE), 1990.

413 Kurzan, B., K.-H. Steuer, H. Roehr and F. Schneider:
Untersuchung der Plasmabremsstrahlung im nahen Infrarot zur Bestimmung der Elektronendichte. Verhandl. DPG (VI) 25, 376 (1990).

414 Lackner, K.:
Energieeinschluss in Tokamaks: Extrapolation und Verstaendnis. Verhandl. DPG (VI) 25, PHV2 (1990).

415 Lackner, K.:
Energy Confinement in Tokamaks: Extrapolation and Understanding. Internat. Workshop on Plasma Physics, Schladming (AT), 1990.

416 Lackner, K.:
The Physical Basis of NET/ITER in the Light of Recent European Contributions. Symp. on Future Energy from Thermonuclear Fusion, Vienna (AT), 1990.

417 Lackner, K.:
Transport in Tokamaks. IAEA Stellarator Workshop, Garching (DE), 1990.

418 Lackner, K.:
Der Weg zum Fusionsreaktor: Stand der wissenschaftlichen Basis und der Systemstudien.

Jahrestagung Kerntechnik, Nuernberg (DE), 1990.

419 Lang, R.:
Impurity Transport Studies in ASDEX by Means of Ne-Seeded Pellets. I.V.Kurchatov Inst. of Atomic Energy, Moscow(SU), 1990.

420 Lang, R.:
Running Pellet Injectors on the ASDEX Tokamak and the Wendelstein-AS Stellarator. I.V. Kurchatov Inst. of Atomic Energy, Moscow (SU), 1990.

421 Laszlo, J.:
Collision Effects in Solids. Seminar, IPP Garching(DE), 1990.

422 Laszlo, J.:
Instantaneous Energy of Protons in Metals. Seminar Goethe-Universitaet, Frankfurt(DE), 1990.

423 Laszlo, J.:
Low Energy Electronic Stopping of Ions in Matter. Seminar, IPP Garching(DE), 1990.

424 Lazaros, A., A. Weller and WVII-AS-Team[3]:
Experimental Evidence for Mode Activity and Mode Simulations in WVII-AS. Verhandl. DPG (VI) 25, 396, P10.31 (1990).

425 Leinberger, U., H.-S. Bosch, U. Schumacher and U. Stroth:
Neuere Messungen von Fusions-Protonen und -Tritonen aus ASDEX. Verhandl. DPG (VI) 25, 435, P.19.4 (1990).

426 Lengyel, L.L.:
Computational Fluid Dynamics: an Introduction. Techn. Univ., Budapest (HU), 1990.

427 Lengyel, L.L.:
Discussions and Conclusions on Pellet Ablation. ITER Meetings on Fuelling and Plasma Operation Control, Garching (DE), 1990.

428 Lengyel, L.L.:
Pellet Ablation and Shielding Phenomena. I.V. Kurchatov Inst. of Atomic Energy, Moscow (SU), 1990.

429 Lengyel, L.L.:
Pellet Ablation and Shielding Phenomena: State of the Art. ITER Meetings on Fuelling and Plasma Operation Control, Garching (DE), 1990.

430 Lengyel, L.L.:
Pellet Shielding and Ablation Physics: Analysis of the Existing Ablation Models. General Atomics, San Diego (US), 1990.

431 Lengyel, L.L.:
Remarks on Scenarios on the Density Ramp-up by Pellets Combined with NB Heating. ITER Meetings on Fuelling and Plasma Operation Control, Garching (DE), 1990.

432 Leuterer, F.:
Coupling and Current Drive Efficiency in the 2.45 GHz Lower Hybrid Experiment in ASDEX. Lower Hybrid Workshop, ENEA, Frascati (IT), 1990.

433 Leuterer, F.:
Lower Hybrid Current Drive at 2.45 GHz in ASDEX. ITER-Workshop on Noninductive Current Drive, Garching (DE), 1990.

434 Leuterer, F.:
Lower Hybrid Current Drive Efficiency in ASDEX and Comparison with Theory. CEN, Cadarache (FR), 1990.

435 Leuterer, F., ASDEX-Team[2] and LH-Team[9]:
Lower Hybrid Stromtriebwirkungsgrad in ASDEX. Verhandl. DPG (VI) 25, P 11.2 (1990).

436 Leuterer, F., F.X. Soeldner, R. Bartiromo[1], R. Cesario[1], R. De Angelis[1], L. Gabellieri[1], V. Pericoli[1], A. Tuccillo[1], S. Bernabei[1], C. Forest[1] and R.W. Harvey[1]:
Lower Hybrid Experiments at 2.45 GHz in ASDEX. Internat. Workshop on Strong Microwaves in Plasmas, Suzdal (SU), 1990.

437 Liebl, H.:
Entwurf eines hochaufloesenden LEEM. Kolloquium, Darmstadt(DE), 1990.

438 Liebl, H.:
Entwurf eines hochaufloesenden Oberflaechen-Elektronenmikroskops. Kolloquium, Clausthal (DE), 1990.

439 Linsmeier, C., R. Margraf, E. Taglauer and H. Knoezinger[1]:
Untersuchung von Rh/Al_2O_2-Modellkatalysa-

toren mit Ionenstreuung. Verhandl. DPG (VI), 25, 09.7 (1990).

440 Linsmeier, C., E. Taglauer and H. Knoezinger[1]: Ion Scattering Analysis of Rh Adlayers on Alumina Films. NATO Advanced Study Institute: "Fundamental Aspects of Heterogeneous Catalysis Studied by Particle Beams", Alicante (ES), 1990.

441 Lortz, D.: Introduction to Plasma Physics. Univ. Muenchen(DE), 1989-1990.

442 Lortz, D.: Magnetohydrodynamics. Univ. Muenchen (DE), 1990.

443 Lortz, D.: TL IV Thermodynamics. Univ. Muenchen(DE), 1990-1991.

444 Madjidi, S.[1], R. Baetzner[1], K. Huebner[1] and B. Wolle: Neutronenemissionsprofil-Messungen an ASDEX. Verhandl. DPG (VI) 25, 398, P10.37 (1990).

445 Memmel, N., E. Bertel, G. Rangelov[1] and V. Dose: Alkali-Adsorption auf Uebergangs- und Sp-Band Metallen (Vergleichende Untersuchungen mit Inverser Photoemission). Verhandl. DPG (VI), 25, 07.8 (1990).

446 Meyer-Spasche, R.: Numerische Methoden fuer Bifurkationsprobleme. Techn.Univ. Muenchen(DE), 1990.

447 Moeller, W.: Computer Modeling of C:H Film Growth. NATO Advanced Study Institute on Diamond and Diamondlike Films and Coatings, Castelvecchio Pascoli(IT), 1990.

448 Moeller, W.: Deposition von wasserstoffhaltigen Kohlenstoffschichten aus Niederdruckplasmen. Stuttgart Univ. (DE), Fak.Elektrotechnik, 1990.

449 Moeller, W.: Dynamische Computersimulation von Ionenbeschuss-Phaenomenen. Friedrich-Schiller Univ. Jena (DE), Inst.Festkoerperphysik, 1990.

450 Moeller, W.: Ionenimplantation und Plasmadeposition zur Erzeugung wasserstoffhaltiger Kohlenstoffschichten. Elektrotechn. Kolloquium, Darmstadt (DE), 1990.

451 Moeller, W., W. Renz, W. Jacob, A. Koch, D. Boutard, J. Perchermeier and R. Wilhelm: C:H-Innenbeschichtung in einem metallischen Rohr mit Hilfe eines ECR-Plasmas. 4. Bundesdt. Fachtagung Plasmatechnologie, Muenchen (DE), 1990.

452 Muenich, M., F. Hassenpflug, F. Leuterer, F. Monaco, M. Pelicano, F.X. Soeldner, M. Zouhar, R. Bartiromo[1], M. D'Ortone[1], A. Marra[1], P. Papitto[1], A. Tuccillo[1] and S. Bernabei[1]: The 2.45 GHz Lower Hybrid Current Drive System on the ASDEX Tokamak. 16th Symp. on Fusion Technology, London (GB), 1990.

453 Mukherjee, S.: Thermal Deformation of Multilayer Solid Breeder Outboard Blanket. ITER Blanket Workshop, Garching(DE), 1990, ITER/TN/BL/6/03.

454 Mukhovatov, V.[1], H. Hopman[1], G.W. Pacher[1], S. Yamamoto[1], K.M. Young[1], V.A. Belyakov[1], F. Casci[1], S. Cohen[1], A. Costley[1], T. Donne[1], T. Elevant[1], F. Engelmann[1], T. Iguchi[1], S. Ishida[1], A. Izvozchikov[1], O.N. Jarvis[1], D. Johnson[1], R. Kaita[1], J. Kaellne[1], A. Kellman[1], A. Khudoleev[1], Y. Kusama[1], Yu. Kuznetsov[1], D. Manos[1], M. Martone[1], T. Matoba[1], T. Nishitano[1], D. Orlinskij[1], H.D. Pacher[1], O. Pavlichenko[1], N. Peacock[1], L.J. Perkins[1], D. Post[1], J.P. Rager[1], H. Salzmann, Y. Sano[1], M. Sasao[1], Y. Shimomura[1], M. Sironi[1], R. Snider[1], P. Stott[1], J.D. Strachan[1], B. Syme[1], P. Thomas[1] and R. Yoshino[1]: ITER Operation and Diagnostics. Proc. 13th IAEA Conf. on Plasma Physics and Controlled Nuclear Fusion, Washington(US), 1990.

455 Neuhauser, J., R. Aratari, M. Bessenrodt-Weberpals, A. Carlson, C.C. Chu, G. Fussmann, J. Gernhardt, G. Kyriakakis, K. McCormick, E.R. Mueller, H.D. Murmann, H. Niedermeyer, W. Poschenrieder, R. Schneider, U. Schneider, G. Siller, A. Staebler, N. Tsois[1], H. Verbeek, O. Vollmer, H. Zohm and ASDEX-Team[2]: Edge and Divertor Studies on ASDEX. Proc. 13th IAEA Conf. on Plasma Physics and Controlled Nuclear Fusion Research, Washington (US), 1990.

456 Niedermeyer, H.:
Fluctuation Studies on ASDEX. Second Transport Workshop, Hilton Head (US), 1990.

457 Niedermeyer, H., G. Dodel[1)], M. Endler, G. Fussmann, O. Gehre, K.W. Gentle[1)], L. Giannone, E. Holzhauer[1)], K. Krieger, A. Rudyj, G. Theimer, R.D. Bengtson[1)], A. Carlson, A. Eberhagen, W. Engelhardt, J. Gernhardt, O. Gruber, J.V. Hofmann, F. Karger, O. Klueber, M. Kraemer[1)], M.E. Manso[1)], J. Matias[1)], K. McCormick, V. Mertens, H.D. Murmann, J. Neuhauser, J. Qin[1)], N. Ruhs, F. Ryter, U. Schneider, R. Schubert, F. Serra[1)], A. Silva[1)], F.X. Soeldner, U. Stroth, N. Tsois[1)] and O. Vollmer:
Experimental Determination of the Transient Transport and of Fluctuations Relevant to Transport in ASDEX. Proc. 13th IAEA Conf. on Plasma Physics and Controlled Nuclear Fusion Research, Washington(US), 1990.

458 Noterdaeme, J.-M.:
The ASDEX Upgrade ICRH System. JET Kolloquium, Abingdon(GB), 1990.

459 Noterdaeme, J.-M.:
Experimentelle Untersuchungen zur Verunreinigungsfrage bei ICRH an ASDEX. AUG-Seminar, Garching (DE), 1990.

460 Noterdaeme, J.-M.:
Heizung mit Wellen im Ionenzyklotron-Frequenz-Bereich an ASDEX. IPF-Kolloquium, Stuttgart (DE), 1990.

461 Noterdaeme, J.-M.:
ICRH Status und Verunreinigungsproduktion im Hinblick auf W VII-AS. ASDEX-WVII-AS Seminar, Ringberg, Tegernsee (DE), 1990.

462 Noterdaeme, J.-M.:
Ionenzyklotron-Resonanzheizung. "Rand"-Seminar, IPP Garching (DE), 1990.

463 Noterdaeme, J.-M.:
Progress in the Understanding and Avoidance of Impurity Production with ICRH in ASDEX. Workshop on High Power Antenna Design, Boulder (US), 1990.

464 Noterdaeme, J.-M.:
What did we Learn from the ASDEX Antennas and what do we Plan for ASDEX Upgrade. Workshop on High Power Antenna Design, Boulder (US), 1990.

465 Nuernberg, A.[1)], R. Behrisch and U. Bauder[1)]:
Untersuchungen zum Zuendverhalten von Vakuumboegen. Verhandl. DPG (VI), 25, P10.24 (1990).

466 Ott, W.:
Leistungserhoehung der Neutralinjektion an WVII-AS. ASDEX-WVII-AS Seminar, Ringberg, Tegernsee (DE), 1990.

467 Penningsfeld, F.P.:
Simulation of H and He Injection into W VII-AS. Stellarator-Workshop, Garching (DE), 1990.

468 Pfirsch, D.:
Einfuehrung in die Theoretische Plasmaphysik 1 (Kinetische Theorie). Techn.Univ. Muenchen (DE), 1990.

469 Pfirsch, D.:
Einfuehrung in die Theoretische Plasmaphysik 2 (Makroskopische Theorie). Techn.Univ. Muenchen(DE), 1990.

470 Pfirsch, D.:
Nonlinear Instabilities, Negative Energy Modes and Generalized Cherry Oscillators. Texas Univ., Austin(US). IFS, 1990.

471 Pinkau, K.:
Fusion as an Energy Source. Spring Meeting Netherlands Physical Society, Utrecht(NL), 1989.

472 Poedts, S.:
Time-Scales and Efficiency of Alfven Wave Heating in Periodically Driven Coronal Loop Plasmas. National Center for Atmospheric Research, Boulder(US), 1990.

473 Poschenrieder, W., K. Desinger and ASDEX-Team[2)]:
Recycling of Gaseous Impurities in ASDEX. 9th Internat.Conf.Plasma Interaction in Controlled Fusion Devices, Bournemouth(GB), 1990.

474 Poschenrieder, W., U. Schneider and ASDEX-Team[2)]:
Borierung der ASDEX-Plasmakammer. Verhandl. DPG (VI), 25, P10.44 (1990).

475 Preis, R., R. Baetzner[1)], K. Huebner[1)] and B. Wolle:

Messung schneller Aenderungen der Neutronenrate an ASDEX. Verhandl. DPG (VI) 25, 412, P14.5 (1990).

476 Rangelov, G.[1)], N. Memmel, E. Bertel and V. Dose:
IPE-Untersuchung der Wasserstoff-Nickel-Bindung. Verhandl. DPG (VI), 25, 027.2 (1990).

477 Ratz, G.[1)], S. Veprek[1)] and W. Moeller:
Niedertemperatur - Silicium - Epitaxie in hochfrequenz-induzierten Plasmen. 4. Bundesdt. Fachtagung Plasmatechnologie, Muenchen (DE), 1990.

478 Reinke, P., W. Jacob and W. Moeller:
Ion Energy Distribution of the Substrate in an ECR-Reactor. NATO-ASI Summer School, 1990.

479 Renner, H.:
Ausnutzung der Flexibilitaet am WVII-AS. ASDEX-WVII-AS Seminar, Ringberg, Tegernsee (DE), 1990.

480 Renner, H., U. Gasparino, H. Maassberg, G. Kuehner, H. Ringler, F. Sardei, A. Weller and WVII-AS-Team[3)]:
Confinement Properties of the "Advanced Stellarator" WVII-AS. Proc. 13th IAEA Conf. on Plasma Physics and Controlled Fusion, Washington(US), 1990.

481 Ringler, H.:
Moeglichkeiten der diagnostischen Weiterentwicklung an WVII-AS. ASDEX-WVII-AS Seminar, Ringberg, Tegernsee (DE), 1990.

482 Ringler, H.:
Thomson-Streuung - Streuung von Laserlicht zur Bestimmung lokaler Werte von n_e und T_e. ASDEX-WVII-AS Seminar, Ringberg, Tegernsee (DE), 1990.

483 Roehr, H.:
Thomson Scattering and Z_{eff}-Measurements on ASDEX. Hungarian Academy of Sciences, Central Research Institute for Physics, Dept. of Plasma Physics, Budapest(HU), 1990.

484 Roehr, H.:
Thomsonstreuung und Bremsstrahlungsdiagnostik am Garching Tokamak ASDEX. Akad.der Wissenschaften. Phys.-Techn.Inst., Jena(DE), 1990.

485 Roth, J.:
Aspects of Sputtering at Low Energies in Fusion Research. Univ. of Salford, Manchester (GB), 1990.

486 Roth, J.:
Erosion of Divertor and Limiter Materials. General Atomics, San Diego(US). Fusion Div., 1990.

487 Roth, J.:
Low-Energy Ion Sputtering. Univ. of Warwick, 1990.

488 Roth, J.:
Oberflaechenprobleme in Fusionsplasmen. Univ. Augsburg(DE), 1990.

489 Roth, J.:
Sputtering of Limiter and Divertor Materials. 9th Internat.Conf.Plasma Interaction in Controlled Fusion Devices, Bournemouth(GB), 1990.

490 Rudyj, A., A. Carlson, H. Niedermeyer and ASDEX-Team[2)]:
Profile und raeumliche Struktur der Fluktuationen in der Randschicht von ASDEX. Verhandl. DPG (VI) 25, 396, P10.32 (1990).

491 Rudyj, A., A. Carlson, H. Niedermeyer and ASDEX-Team[2)]:
Teilchentransport und Fluktuationen in der Randschicht von ASDEX. Verhandl. DPG (VI) 25, 369, P1.4 (1990).

492 Ruhl, G.[1)], S. Veprek[1)] and M.G.J. Veprek:
Plasmaaetzen von Mangan-Zink-Ferriten. 4. Bundesdt. Fachtagung Plasmatechnologie, Muenchen (DE), 1990.

493 Ryter, F.:
ICRH-Experimente an ASDEX: eine Zusammenfassung der Ergebnisse. IPP Kolloquium, Garching (DE), 1990.

494 Ryter, F., ASDEX-Team[2)] and NI-Team(ASDEX)[4)]:
Recent H-Mode Results on ASDEX: Meeting the H-Mode ITER Data Bank. JET Abingdon (GB), 1990.

495 Ryter, F., O. Gruber, O. Vollmer, F. Wagner, ASDEX-Team[2)] and NI-Team(ASDEX)[4)]:
ELM-Free H-Mode Confinement in ASDEX. ITER Technical Workshop on Confinement, Garching (DE), 1990.

496 Saffert, J.:
Allgemein zugaengliche AS-Software. ASDEX-WVII-AS Seminar, Ringberg, Tegernsee (DE), 1990.

497 Salat, A.:
Is the Temperature Gradient or the Derivative of the Density Gradient Responsible for Drift Solitons? Plasma Physics and Controlled Fusion, 32, No.14, 1337-1348 (1990).

498 Salzmann, H.:
LIDAR-Thomson Streuung an JET. Techn.Univ. Festkoerper-Laser-Inst. Berlin (DE), 1990.

499 Sandmann, W.:
Density Profile Control by Pellets and Related Particle Transport. ITER Meetings on Fuelling and Plasma Operation Control, Garching (DE), 1990.

500 Sandmann, W.:
Double-Feedback Controlled Pellet Refuelled Plasmas. ITER Meetings on Fuelling and Plasma Operation Control, Garching(DE), 1990.

501 Sapper, J.:
Basic Engineering Design of WVII-X. IEA Workshop on Next Generation Experiments, Nagoya (JP), 1989.

502 Sapper, J. and WVII-X-Team[11]:
The Wendelstein VII-X Stellarator. Technical Design and Engineering. 16th Symp. on Fusion Technology, London(GB), 1990.

503 Sardei, F. and M. Richter-Gloetzl:
TRANS Code. ASDEX-WVII-AS Seminar, Ringberg, Tegernsee (DE), 1990.

504 Sardei, F., H. Ringler, A. Dodhy, G. Kuehner, R. Scardovelli[1] and WVII-AS-Team[3]:
Neutralgasverhalten und Teilchentransport am WVII-AS. Anwendungen auf WVII-X. Seminar "Rand"-Bemerkungen, IPP Garching (DE), 1990.

505 Scherzer, B.M.U.:
The Trapping and Release Behaviour of Hydrogen with Respect to Fuel Recycling in Tokamaks. Conf. on the Effects of Irradiation on Materials of Fusion Reactors, Leningrad(SU), 1990.

506 Schneider, F.:
Neuere Entwicklungen zur analogen Feedback Steuerung. ASDEX-WVII-AS Seminar, Ringberg, Tegernsee (DE), 1990.

507 Schneider, R.:
Temperaturabhaengigkeit direkter Uebergaenge in Inverser Photoemission. Kollqu. Schwerpunkt: 'Hochenergetische Spektroskopie elektronischer Zustaende in Festkoerpern und Molekuelen' der DFG. Physikzentrum, Bad Honnef (DE), 1990.

508 Schneider, U., ASDEX-Team[2], ICRH-Team[8], LH-Team[9], NI-Team(ASDEX)[4] and PSI-Group[15]:
Boronization Experience in ASDEX. IEA Workshop on Stellarators, Garching (DE), 1990.

509 Schulz, J. and E. Taglauer:
Adsorption von Wasserstoff auf Ru(001) - Untersuchungen mit Ionenstreu- und Rueckstossspektroskopie. Verhandl. DPG (VI), 25, 027.4 (1990).

510 Schumacher, U.:
Energie heisst Leben - Wie koennen wir unseren Energiebedarf langfristig sichern? Kaemmerertagung, Fuerstenfeldbruck(DE), 1990.

511 Schumacher, U.:
Forschung zur langfristigen Energiesicherung. Vorstandsseminare der Sparkassenakademie Bayern, Ringberg, Tegernsee (DE), 1990.

512 Schumacher, U.:
Kernfusion - Stand der Forschung und Aussichten der Anwendung. Mitgliederversammlung der FDBR Duesseldorf, Mayschoss(DE), 1990.

513 Schumacher, U.:
Spektroskopie an heissen Plasmen mit Doppelkristall-Monochromatoren. Sektion Physik der Friedrich-Schiller-Univ. Jena(DE), 1990.

514 Schumacher, U.:
Stand und Entwicklung der Fusionsforschung. Physikalisches Kolloquium, Univ. Konstanz (DE), 1990.

515 Schumacher, U.:
Teilchenbeschleunigung mit Plasmen. Elektrotechnisches Kolloquium, Univ. Stuttgart (DE), 1990.

516 Schuppler, S.[1)], N. Fischer[1)], T. Fauster and W. Steinmann[1)]:
Intrinsic Linewidth of Image States on Ni(111); Intrinsic Linewidth of Image States on Ag(100). 14th Internat. Seminar on Surface Physics, Przesieka(PL), 1990.

517 Schuppler, S.[1)], N. Fischer[1)], T. Fauster and W. Steinmann[1)]:
Linewidths of Image Potential States on Ni(111) and Ag(100) by High-Resolution Two-Photon Photoemission Spectroscopy. 37th Nat. Symp. of the American Vacuum Society, Toronto(CA), 1990.

518 Scott, B.D.:
Collisional Drift-wave Turbulence in a Sheared Magnetic Field. CEN, Cadarache (FR), 1990.

519 Scott, B.D.:
Collisional Drift-wave Turbulence in a Sheared Magnetic Field. MIT, Cambridge (US), 1990.

520 Scott, B.D.:
Collisional Drift-wave Turbulence in a Sheared Magnetic Field. PPPL, Princeton (US), 1990.

521 Scott, B.D.:
Self-sustained Collisional Drift-wave Turbulence in a Sheared Magnetic Field. Joint Varenna-Lausanne Internat. Workshop on Theory of Fusion Plasmas, Varenna (IT), 1990.

522 Scott, B.D.:
Thermal and Dissipative Stability of Convection-Accretion Disks. 129th I.A.U. Colloq. on Structure and Emission Properties of Accretion Disks, Paris (FR), 1990.

523 Scott, B.D.:
Thermal Stability of Convection-accretion Disks. Ruhr Univ. Bochum (DE), 1990.

524 Scott, B.D.:
Turbulent Convection in Accretion Disks. MPI fuer Astrophysik, Garching (DE), 1990.

525 Scott, B.D.:
Universal Nonlinear Drift-wave Turbulence. Internat. Sherwood Fusion Theory Conf., Williamsburg (US), 1990.

526 Siegele, R., S.P. Withrow[1)], J. Roth and B.M.U. Scherzer:
Trapping of D and SiC and Damage due to Implantation. 9th Internat.Conf.Plasma Surface Interaction in Controlled Fusion Devices, Bournemouth(GB), 1990.

527 Simmet, E., U. Stroth and H.-U. Fahrbach:
Transport der Ionenenergie in Plasmaentladungen an ASDEX. Verhandl. DPG (VI) 25, 431, P18.2 (1990).

528 Simon-Weidner, J., N. Jaksic and E. Harmeyer:
On Mechanical Stresses in Large Helias Coil Systems and the Influence of Contact Effects. 16th Symp. on Fusion Technology, London (GB), 1990.

529 Soeldner, F.X.:
Combined Operation of Pellet Injection and Low- er Hybrid Current Drive on ASDEX. ITER-Workshop on Fuelling and Density Control, Garching (DE), 1990.

530 Soeldner, F.X.:
Confinement and Profile Modification with Lower Hybrid Wave on ASDEX. Kolloquium, Cadarache (FR), 1990.

531 Soeldner, F.X.:
Confinement with Lower Hybrid Heating. LH-Workshop, Frascati (IT), 1990.

532 Soeldner, F.X.:
Current Profile Control with Lower Hybrid Waves. LH-Workshop, Frascati (IT), 1990.

533 Soeldner, F.X.:
Energieeinschluss und Profilkontrolle mit Lower-Hybrid-Wellen. Kolloquium, IPP Garching(DE), 1990.

534 Soeldner, F.X.:
Plasmaheizung mit Hochfrequenz-Wellen. Kolloquium, Univ. Regensburg (DE), 1990.

535 Soeldner, F.X.:
Profile Control, MHD-Stabilization, Confinement with Lower Hybrid Waves on ASDEX. ITER-Workshop on Physics and Modelling of LH, 1990.

536 Soeldner, F.X.:
Profile Control with Lower Hybrid Waves on ASDEX. ITER-Workshop on Current Profile Control, Garching (DE), 1990.

537 Soeldner, F.X.:

Review of Lower Hybrid Experiments on ASDEX. Proc. 13th IAEA Conf. on Plasma Physics and Controlled Fusion, Washington(US), 1990.

538 Soeldner, F.X., ASDEX-Team[2)], LH-Team[9)] and NI-Team(ASDEX)[4)]:
Heizung und Energieeinschluss mit Lower-Hybrid-Wellen. DPG (VI) 25, P10.41, 399 (1990).

539 Staebler, A.:
Density Limit Studies on ASDEX. 9th Europ. Tokamak Programme Workshop, Arles (FR), 1990.

540 Starke, K., K. Ertl and V. Dose:
Temperature and Field Dependence of the Magnetization at Ni(001). 11th Europ. Conf. on Surface Science, Salamanca(ES), 1990.

541 Steuer, K.-H.:
Laserlichtstreuung und ihre neueren Anwendungen in der Plasmaphysik. Physik. Kolloquium, Univ. Augsburg(DE), 1990.

542 Steuer, K.-H.:
Physik der Kernfusion. Verhandl. DPG (VI) 25, FB2 (1990).

543 Steuer, K.-H.:
Welchen Beitrag kann die Physik zur Loesung des Energieproblems leisten? 2 Schulvortraege, MPG Hauptversammlung, Luebeck (DE), 1990.

544 Steuer, K.-H.:
YAG-Thomsonstreuung und die Infrarotkontinuumsdiagnostik an ASDEX. WVII-AS Seminar, Ringberg, Tegernsee (DE), 1990.

545 Steuer, K.-H.:
T_e, n_e und Z_{eff} Messungen an ASDEX mit dem YAG System. ASDEX-WVII-AS Seminar, Ringberg (DE), 1990.

546 Streibl, B.:
Design, Manufactoring and Assembling of the ASDEX-Upgrade Turn over Structure. 16th Symp. on Fusion Technology, London (GB), 1990.

547 Taglauer, E.:
Impurity Flux Measurements in the Scrape-Off Layer of ASDEX. Hokkaido Univ., Sapporo(JP), 1990.

548 Taglauer, E.:
Impurity Flux Measurements in the Scrape-Off Layer of ASDEX. Univ. Nagoya(JP), 1990.

549 Taglauer, E.:
Ion Scattering Studies of Ordered and Amorphous Surface Layers. RIKEN Inst., Wako(JP), 1990.

550 Taglauer, E.:
ISS and AES Studies of Compound and Alloy Surfaces under Ion Bombardment. Univ. Osaka(JP), 1990.

551 Taglauer, E.:
Low-Energy Ion Scattering Investigations of Catalysts. NATO Advanced Study Institute "Fundamental Aspects of Heterogenous Catalysis Studied by Particle Beams", Alicante(SP), 1990.

552 Taglauer, E.:
Surface Investigations Using Low Energy Ions. Symp.on Surface Science, La Plague(FR), 1990.

553 Taglauer, E., J. Schulz, P. Feulner[1)] and D. Menzel[1)]:
Structure Analysis of Light Adsorbates by Recoil Detection. 8th Internat. Workshop on Inelastic Ion-Surface Collisions, Wiener Neustadt (AT), 1990.

554 Tasso, H.:
Lyapunov Stability of Large Systems of van der Pol - like Oscillators and Connection with Statistics and Turbulence. Dynamics Days, Austin (US), 1990.

555 Tasso, H. and S.J. Camargo:
On the Nonlinear Stability of Dissipative Fluids. School on Qualitative Aspects and Applications of Nonlinear Evolution Equations, Triest (IT), 1990.

556 Theimer, G., M. Endler, H. Niedermeyer and A. Rudyj:
Raeumliche Struktur der Fluktuationen in der Randschicht des Tokamak ASDEX. Verhandl. DPG (VI) 25, 369, P1.5 (1990).

557 Veprek-Heijman, M.G.J.:
The H-Content of SiO_2-Films Deposited from TEOS in RF-Plasma. AT&T Bell Laboratories, Murray Hill(US), 1990.

558 Veprek-Heijman, M.G.J.:

The H-Content of SiO_2-Films Deposited from TEOS in RF-Plasmas. Gordon Conf.on Plasma Chemistry, Tilton(US), 1990.

559 Veprek, M.G.J., D. Boutard and W. Moeller: Die Abscheidung von Isolatorschichten aus TEOS im HF-Plasma. 4. Bundesdt. Fachtagung Plasmatechnologie, Muenchen(DE), 1990.

560 Veprek, S.[1] and M.G.J. Veprek-Heijman: Mechanismus plasmainduzierter Abscheidung von Silicium: SiH_2, hoehere Silane und die SiH_2-Story. 4. Bundesdt. Fachtagung Plasmatechnologie, Muenchen(DE), 1990.

561 Veprek, S.[1], M.G.J. Veprek-Heijman, F. Glatz[1], R. Konwitschny[1], G. Ratz[1] and M. Rueckschloss[1]: The Mechanism of Plasma Induced Deposition of Silicon and Germanium: The Rate Controlling Steps, Amorphicity and Crystallization. Gordon Conf. on Plasma Chemistry, Tilton (US), 1990.

562 Verbeek, H., U. Stroth, M. Bessenrodt-Weberpals, J.K. Fu[1], H.D. Murmann and ASDEX-Team[2]: Determination of Edge Ion Temperatures at ASDEX Using a Low Energy Neutral Particle Analyzer. 9th Internat.Conf.Plasma Surface Interactions in Controlled Fusion Devices, Bournemouth (GB), 1990.

563 Volz, T.[1], G. Degenhardt[1] and K. Huebner[1]: Numerische Simulation der Response der sphaerischen Ionisationskammer. Verhandl. DPG (VI) 25, 411, P14.2 (1990).

564 Wagner, F.: "Rand"-Bemerkungen ueber Plasmaeigenschaften von ASDEX. Kolloquium, IPP Garching (DE), 1990.

565 Wagner, F.: Isotope Effects on Confinement on ASDEX. Second Transport Workshop, Hilton Head (US), 1990.

566 Wagner, F.: Stand der Fusion. Elektrotechnisches Kolloquium, Univ. Stuttgart(DE), Univ. Muenchen (DE), 1990.

567 Wagner, F.: Summary on Isotope Studies in ASDEX. PPPL-IAEA Tokamak Transport Meeting, Princeton (US), 1990.

568 Wagner, F.: 10 Years of ASDEX Operation. 9th European Tokamak Programm Workshop, Arles (FR), 1990.

569 Wagner, F., F. Ryter, A.R. Field, G. Fussmann, J.V. Hofmann, M.E. Manso[1] and O. Vollmer: Recent Results of H-Mode Studies on ASDEX. Proc. 13th IAEA Conf. on Plasma Physics and Controlled Fusion, Washington(US), 1990.

570 Wagner, R.[1], R. Baetzner[1], S. Helbig[1], H.-J. Husel[1], H. Hinsch, K. Huebner[1], S. Guldbakke[1] and H. Klein[1]: Kalibrierung von Kernspurplatten fuer die Neutronendiagnostik. Verhandl. DPG (VI) 25, 411, P14.3 (1990).

571 Weller, A.: Soft X-Ray Diagnostik an Wendelstein WVII-AS. ASDEX-WVII-AS Seminar, Ringberg, Tegernsee (DE), 1990.

572 Weller, A., R. Brakel, R. Burhenn, H. Hacker, A. Elsner, A. Lazaros and WVII-AS-Team[3]: Integrated Radiation Analysis of Intrinsic Impurities in WVII-AS. IEA Stellarator Workshop, Garching (DE), 1990.

573 Weller, A., A. Elsner, H. Jaeckel, A. Lazaros and WVII-AS-Team[3]: Spektroskopische Interpretation von totalen Strahlungs-Messungen in WVII-AS. Verhandl. DPG (VI) 25, 376, P4.5 (1990).

574 Wesner, F.: ICRH an WVII-AS Seminar - Technologische Fragen. ASDEX-WVII-AS Seminar, Ringberg, Tegernsee (DE), 1990.

575 Wesner, F., J. Baeumler, W. Becker, F. Braun, R. Fritsch, F. Hofmeister, J.-M. Noterdaeme, H. Wedler, H.-U. Boksberger[1], B. Rossa[1] and J. Wyss[1]: The 4x2 MW ICRH System for ASDEX Upgrade. 16th Symp. on Fusion Technology, London (GB), 1990.

576 Wieczorek, A.: Power Supply and Protection System for Plas-

ma Stabilization Coils of ASDEX Upgrade Commissioning Results. 16th Symp. on Fusion Technology, London (GB), 1990.

577 Wittmann, M. and J. Kueppers:
Wechselwirkung von CO und O_2 mit duennen Ag-Schichten auf Ti. Verhandl. DPG (VI), 25, 03.2 (1990).

578 Wobig, H.:
Neoclassical Transport in General Toroidal Equilibria. Workshop of Stellarators Theory, Kharkov (SU), 1990.

579 Wobig, H.:
Status of Wendelstein VII-X Including Technology. Workshop of Stellarators Theory, Kharkov (SU), 1990.

580 Wobig, H.:
Der Stellarator - Perspektiven im Lichte heutiger Ergebnisse. Verhandl. DPG (VI) 25, 382 (1990).

581 Wolle, B., L.G. Eriksson[1)] and K. Huebner[1)]:
Neutronenproduktion in Hot-Ion-Mode-Entladungen in JET. Verhandl. DPG (VI) 25, P10.36 (1990).

582 Wu, C.H.[1)], E. Hechtl[1)], H.R. Young[1)] and W. Eckstein:
Erosion of Beryllium by Oxygen. 9th Internat.Conf.Plasma Surface Interaction in Controlled Fusion Devices, Bournemouth (GB), 1990.

583 Zohm, H.:
Locked Mode Studies in the ASDEX Tokamak. Europ.Tokamak Programme Workshop, Arles (FR), 1990.

584 Zohm, H.:
MHD Behaviour of Lower Hybrid Discharges in ASDEX. LH-Workshop IPP-Garching - ENEA Frascati, Frascati(IT), 1990.

585 Zohm, H.:
The Physics of Mode Locking. CIT Workshop on Field Errors, Princeton(US), 1990.

586 Zohm, H., R. Buechse and O. Klueber:
M=2 Aktivitaet waehrend Lower Hybrid Current Drive. Verhandl. DPG (VI) 25, 368, P1.1 (1990).

587 Zohm, H., A. Kallenbach, H. Bruhns, G. Fussmann and O. Klueber:
MHD Mode Locking in ASDEX. Verhandl. DPG (VI) 25, 369, P1.3 (1990).

LABORATORY REPORTS

IPP 1/252 Bosch, H.-S.: Review of Data and Formulas for Fusion Cross-Sections. (1990)

IPP 1/253 Herrmann, W.: The Paramagnetic Electron Ring. (1990)

IPP 1/254 Zohm, H.: Untersuchung magnetischer Moden am Tokamak ASDEX. (1990)

IPP 1/255 Kallenbach, A., H.M. Mayer, G. Fussmann, V. Mertens, U. Stroth, O. Vollmer, ASDEX-Team[2)]: Characterisation of the Angular Momentum Transport in ASDEX. (1990)

IPP 1/256 Bessenrodt-Weberpals, M.: Analyse und Optimierung des Randschichtplasmas Ohmscher Tokamakentladungen. (1990)

IPP 2/306 Mahn, C.: Far Forward Scattering of CO_2 Laser Radiation by Plasma Density Fluctuations in the W VII-A Stellarator. (1990)

IPP 2/310 Harmeyer, E., J. Kisslinger, F. Rau, J. Sapper, H. Wobig: Studies on Normal-Conducting Coils for Wendelstein VII-X. (1990)

IPP III/155 Fischer, R.: Erzeugung eines kurzen Wasserstoffpulses durch laserinduzierte Desorption aus Titanhydrid zur Untersuchung Transportprozessen in Fusionsplasmen. (1990)

IPP III/156 Loercher, M.: Messung von Lyman-Alpha-Strahlung an Ionisationsmanometern zur Bestimmung der Wasserstoffatomdichte in Fusionsexperimenten. (1990)

IPP III/157 Engelhard, M.: Bestimmung der effektiven Ionenladungszahl eines Plasmas aus der Bremstrahlung im nahen Infrarot. (1990)

IPP III/158 Development of Diagnostics and Data Analysis. (Jahresbericht 1989). (1990)

IPP III/159 Lazaros, A., A. Weller: Equilibrium and Stability Studies by the X-Ray Diagnostics in the WVII-AS Stellarator. (1990)

IPP III/160 Rudyj, A.: Untersuchung transportrelevanter Fluktuationen in der Randschicht von ASDEX. (1990)

IPP III/161 Bessenrodt-Weberpals, M., K. McCormick, F.X. Soeldner, F. Wagner, H.-S. Bosch, O. Gehre, E.R. Mueller, H.D. Murmann, J. Neuhauser, W. Poschenrieder, K.-H. Steuer, N. Tsois, ASDEX-Team[2)]: The Multiple Facets of Ohmic Confinement in ASDEX. (1990)

IPP III/162 Soeldner, F.X.: Lower Hybrid Experiments on ASDEX in 1989. (1990)

IPP III/163 Max-Planck-Institut fuer Plasmaphysik, Garching(DE): ASDEX Contributions to the 9th Internat. Conf. on Plasma Surface Interaction in Controlled Fusion Devices and Workshop on Relevance, Realization and Stability of a Cold Layer at the Edge for Fusion Reactors. (1990)

IPP III/164 ASDEX Contributions to the 17th EPS Conference on Controlled Fusion and Plasma Heating. (1990)

IPP III/165 Field, A.R., G. Fussmann, J.V. Hofmann: Measurement of the Radial Electric Field in the ASDEX Tokamak. (1990)

IPP III/166 Schneider, U., W. Poschenrieder, M. Bessenrodt-Weberpals, J. Hofmann, A. Kallenbach, K. Krieger, E.R. Mueller, H. Niedermeyer, F. Ryter, J. Roth, F.X. Soeldner, A. Staebler, K.-H. Steuer,

O. Vollmer, F. Wagner, ASDEX-Team[2)], ICRH-Team[8)], LH-Team[9)], NI-Team(ASDEX)[4)], PSI-Group[15)]: Boronization of ASDEX. (1990)

PP III/167 Soeldner, F.X., V. Mertens, R. Bartiromo, H.S. Bosch, M. Kornherr, R. Lang, F. Leuterer, R. Loch, W. Sandmann, K. Ushigusa: Combined Operation of Pellet Injection and Lower Hybrid Current Drive on ASDEX. (1990)

PP III/168 Schneider, F.: Optimierte Regelung der Plasmalage in den Tokamaks ASDEX und TCV mit Beruecksichtigung der netzgefuehrten Stromrichtersteller. (1990)

PP III/169 Theimer, G.: Methoden zur Untersuchung der raeumlichen Struktur von Dichtefluktuationen in der Randschicht von Fusionsexperimenten demonstriert am Divertortokamak ASDEX. (1990)

PP III/170 Hartinger, T.: Bestimmung zweidimensionaler Strahlungsverteilungen in Hochtemperaturplasmen des Tokamaks ASDEX mittels bolometrischer Messungen und Computertomographie. (1990)

IPP 4/241 Chiu, S.C.: Investigation of Current Drive Possibilities with the Present ICRH System in Wendelstein VII-AS. (1990)

IPP 4/242 Eckhartt, D.: Non-Inductive Current Drive with Suprathermal Ions and Electrons in Reactor-Grade Tokamak Plasmas: A Comparison. (1990)

IPP 4/243 Petrzilka, V.[1)], F. Leuterer: Nonlinear Coupling of Lower Hybrid Grills and Comparison with Experimental Data from ASDEX. (1990)

IPP 4/244 Puri, S.: Toroidal Transport via the Magnetic-Field Collisonal Anomaly. (1990)

IPP 5/34 McCarthy, P.J., K.S. Riedel, O. Kardaun, H.D Murmann, K. Lackner, ASDEX-Team[2)]: Scalings and Plasma Profile Parameterisation of ASDEX High Density Ohmic Discharges. (1990)

IPP 5/35 Kardaun, O., K.S. Riedel, P.J. McCarthy, K. Lackner: A Statistical Approach to Plasma Profile Analysis. (1990)

IPP 5/36 Riedel, K.S.: A Special Covariance Structure for Random Coefficient Models with Both between and within Covariates. (1990)

IPP 5/39 Lengyel, L.L., G. Zavala, O. Kardaun, P. Lalousis[1)]: Evolution of Pellet Clouds and Cloud Structures in Magnetically Confined Plasmas. (1990)

IPP 6/287 Salat, A.: Is the Temperature Gradient or the Derivative of the Density Gradient Responsible for Drift Solitons? (1990)

IPP 6/288 Camargo, S.J., H. Tasso: Self-Similar Statistics in MHD Turbulence. (1990)

IPP 6/289 Pfirsch, D., P.J. Morrison[1)]: The Energy-Momentum Tensor for the Linearized Maxwell-Vlasov and Kinetic Guiding Center Theories. (1990)

IPP 6/290 Pfirsch, D.: Generalized Cherry Oscillators and Negative Energy Waves. (1990)

IPP 6/291 Salat, A.: On the Roles of the Density and Temperature Gradients in the Theory of Nonlinear Drift Waves. (1990)

IPP 6/292 Croci, R.: Asymptotic Solution of a Class of Inhomogeneous Integral Equations. (1990)

IPP 6/293 Pfirsch, D.: Complete Solution of the Modified Cherry Oscillator Problem. (1990)

IPP 6/294 Weitzner, H.[1)], D. Pfirsch: Proof of a Conjecture of Morrison and Pfirsch. (1990)

IPP 6/295 Meyer-Spasche, R., B. Fornberg[1)]: Discretization Errors at Free Boundaries of the Grad-Schlueter-Shafranov Equation. (1990)

IPP 6/296 Croci, R.: Reflection and Absorption of Ordinary Waves in an Inhomogeneous Plasma. (1990)

IPP 9/76 Baretzky, B.: Untersuchung der Oberflaechenzusammensetzung stoss- und segregationsbestimmter Systeme beim Beschuss von Festkoerpern mit niederenergetischen Ionen = Investigation of the Surface Composition of Collison and of Segregation Dominated Systems for the Bombardment of Solids with Low-Energy Ions. (1990)

IPP 9/77 Laszlo, J.: Report on Models of Low Energy Neutralization near Surfaces. (1990)

IPP 9/78 Drube, R.: Unbesetzte elektronische Zustaende rekonstruierender Einkrisalloberflaechen = Unoccupied Electronic States of Reconstructing Single Crystal Surfaces. (1990)

IPP 9/79 Schneider, R., V. Dose: Neuere Entwicklungen in der niederenergetischen inversen Photoemission = Topics in Low-Energy Inverse Photoemission. (1990)

IPP 9/80 Duerr, H.: Geometrische Struktur und Dynamik der reinen und sauerstoffbedeckten Cu(110) Oberflaeche = Geometric Structure and Dynamics of the Clean and Oxygen Covered Cu(110) Surface. (1990)

IPP 9/81 Laszlo, J., W. Eckstein: Deduction of Electronic Stopping Coefficients from the Transmission of H^+, D^+ and He^+ through Non-Crystalline Gold Foils. (1990)

IPP 9/83 Memmel, N.: Chemisorption geordneter Adsorbate auf Metalloberflaechen - eine inverse Photoemissionsstudie. (1990)

EXTERNAL LABORATORY REPORTS

IAEA/CN/53 Cordey, J.G.[1)], J.P. Christiansen[1)], K. Thomsen[1)], A. Tanga[1)], J. De Boo[1)], D. Schissel[1)], T. Taylor[1)], O. Kardaun, F. Wagner, F. Ryter, S.M. Kaye[1)], D.E. Post[1)], Y. Miura[1)], N. Suzuki[1)], M. Mori[1)], T. Matsuda[1)], H. Tamai[1)], T. Takizuka[1)], S.-I. Itoh[1)], K. Itoh[1)]: A Preliminary Analysis of the ITER Energy Confinement H-mode Data Base. (1990)

IFSR 420 Pfirsch, D., P.J. Morrison[1)]: The Energy-Momentum Tensor for the Linearized Maxwell-Vlasov and Kinetic Guiding Center Theories. Texas Univ., Austin(US). Inst.for Fusion Studies (1990)

IFUSP P/786 Viana, R.L.[1)], I.L. Caldas[1)], H. Tasso: Periodic Behaviour in a Class of Periodically Forced Dissipative Integrable Systems. Sao Paulo Univ. (BR), Inst. de Fisica (1990)

JET/P(90)09 Gowers, C., A. Gadd, K. Hirsch, P. Nielsen, H. Salzmann: High Power Ruby and Alexandrite Lasers for LIDAR-Thomson Scattering Diagnostics. JET, Abingdon(GB) (1990)

JET/P(90)36 Weisen, H., A. Pasini, A. Weller, A.W. Edwards: Measurements of Light Impurity Densities and Z_{eff} in JET using X-Ray Tomography. JET, Abingdon(GB) (1990)

LPS 90/14 Pfirsch, D., R.N. Sudan[1)]: Green's Functions in WKB Approximations. Cornell Univ. Ithaca, NY, (US) (1990)

ORNL TM/11558 Lyon, J.F.[1)], G. Grieger, F. Rau, et al.: Stellarator Status-1989. Oak Ridge National Lab.,TN(US) (1990)

REP. 11/90 Petrzilka, V.[1)]: A Comparison of the Results of the nonlinear LH-Coupling Theory with the Measurements of the Reflection Coefficient on the ASDEX Tokamak. Czech.Acad.Sciences, Praha(CS). Inst.Plasma Physics (1990)

1) No Member of Max-Planck-Institut für Plasmaphysik

2) **ASDEX-Team:** R. Aratari, G. Becker, M. Bessenrodt-Weberpals, B. Bomba, H.-S. Bosch, K. Buechl, R. Buechse, A. Carlson, C.C. Chu, G. Dodel, A. Eberhagen, M. Endler, W. Engelhardt, H.-U. Fahrbach, G. Fussmann, O. Gehre, J. Gernhardt, L. Giannone, O. Gruber, G. Haas, T. Hartinger, W. Herrmann, J.V. Hofmann, H. Hohenoecker, E. Holzhauer, K. Huebner, G. Janeschitz, A. Kallenbach, O. Kardaun, F. Karger, M. Kaufmann, O. Klueber, M. Kornherr, K. Krieger, J. Kucinski, K. Lackner, R. Lang, F. Leuterer, G. Lisitano, R. Loch, H.M. Mayer, K. McCormick, D. Meisel, V. Mertens, E.R. Mueller, H.D. Murmann, J. Neuhauser, H. Niedermeyer, J.-M. Noterdaeme, W. Poschenrieder, H. Roehr, J. Roth, A. Rudyj, N. Ruhs, F. Ryter, W. Sandmann, F. Schneider, U. Schneider, R. Schubert, G. Siller, E. Simmet, F.X. Soeldner, E. Speth, A. Staebler, K.-H. Steuer, U. Stroth, E. Taglauer, N. Tsois, H. Verbeek, O. Vollmer, F. Wagner, K. Wira, F. Wesner, D. Zimmermann, H. Zohm

3) **WVII-AS-Team:** V. Afanasiev, J. Baldzuhn, N. Besedin, R. Brakel, R. Burhenn, G. Cattanei, A. Dodhy, D. Dorst, A. Elsner, K. Engelhardt, V. Erckmann, U. Gasparino, S. Geissler, S. Grebenchtchikov, P. Grigull, U. Gutarev, H. Hacker, H.J. Hartfuss, A. Izvozchikov, R. Jaenicke, S. Jiang, J. Junker, F. Karger, M. Kick, J. Kholnov, K. Kondo, H. Kroiss, G. Kuehner, I. Lakicevic, A. Lazaros, H. Maassberg, C. Mahn, P. Mizuuchi, A. Navarro, H. Niedermeyer, M. Ochando, W. Ohlendorf, F. Rau, H. Renner, H. Ringler, J. Saffert, J. Sanchez, F. Sardei, U. Schneider, M. Tutter, F. Wagner, A. Weller, H. Wobig, E. Wuersching, M. Zippe, S. Zoepfel, H. Zushi

4) **NI-Team(ASDEX):** R. Bilau-Faust, E. Speth, A. Staebler, O. Vollmer

5) **NI-Team(WVII-AS):** J.-H. Feist, K. Freudenberger, M. Liniers, W. Ott, F.P. Penningsfeld, E. Speth, W. Melkus

6) **NI-Group:** E. Speth, R. Bilau-Faust, J. Dunne, J.-H. Feist, K. Freudenberger, B. Heinemann, W. Kraus, R.-C. Kunze, H. Lohnert, E. Morris, W. Ott, F.P. Penningsfeld, F. Probst, J. Sielanko, A. Staebler, R. Suess, A. Teubel, O. Vollmer, K. Wittenbecher

7) **ECRH-Group:** W. Kasparek, G. Mueller, P.G. Schueller, M. Thumm

8) **ICRH-Team:** J. Baeumler, M. Ballico, W. Becker, F. Braun, R. Fritsch, F. Hofmeister, J.-M. Noterdaeme, S. Puri, F. Ryter, H. Wedler, F. Wesner

9) **LH-Team:** F. Leuterer, F. Brandl, M. Muenich, F. Monaco, M. Zouhar

10) **Pellet-Team:** K. Buechl, R. Lang

11) **WVII-X-Team:** C.D. Beidler, W. Domaschk, G. Grieger, E. Harmeyer, F. Herrnegger, J. Junker, J. Kisslinger, W. Lotz, P. Merkel, H. Muench, J. Nuehrenberg, F. Rau, E. Rittger, J. Sapper, M. Schlueter, I. Schoenewolf, C. Schwab, U. Schwenn, M. Spada, E. Strumberger, H. Wobig, L. Zheng

12) **ASDEX-Upgrade-Project-Group:** C. Aubanel, A. Bauer, H. Bauer, K. Behler, A. Berg, H.J. Berger, A. Birkmeier, H. Blank, M. Blaumoser, H. Bruhns, E. Buchelt, S. Cha, C. Dorn, R. Drube, A. Field, D. Georgens, J. Gernhardt, J. Gruber, D. Haferkamp, M. Harnau, F. Hartz, E. Herrmann, H. Hohenoecker, D. Jacobi, E. Kaplan, G. Klement, H. Kollotzek, A. Krause, E. Lackner, G. Lieder, H. Lindner, K. Mattes*, R. Merkel, V. Mertens, E. Oswald, B. Pachur, M. Pillsticker, G. Prausner, G. Raupp, G. Reichert, H. Richter, T. Richter, S. Saenftl, N. Salmon, J. Schaal, K. Schindr, H. Schneider, G. Schramm, G. Schrembs, S. Schweizer, U. Schweitzer, U. Seidel, H. Steidl, B. Streibl, W. Teufl, M. Troppmann, H. Vernickel, T. Wendt, F. Werner, A. Wieczorek, W. Wirth, W. Woyke, F. Wunderer, D. Zasche, T. Zehetbauer, G. Zimmermann

13) **ASDEX-Upgrade-Diagnostic-Group:** H. Roehr, U. Schumacher, C. Andelfinger, M. Bessenrodt-Weberpals, H.-S. Bosch, K. Buechl, A. Carlson, C.C. Chu, A. Eberhagen, H.-U. Fahrbach, D. Fieg*, A. Field, C. Fuchs, G. Fussmann, O. Gehre, J. Gernhardt, S. Goetsch, G. Haas, W. Herrmann, G. Janeschitz, F. Jenichen, A. Kallenbach, M. Kornherr, H. Krause, K. Krieger, R. Lang, G. Lieder, R. Loch, K.-F. Mast, H.M. Mayer, D. Meisel, V. Mertens, H.D. Murmann, J. Neuhauser, H. Richter, N. Salmon, H. Salzmann, W. Sandmann, H.-B. Schilling, J. Schweinzer, F.X. Soeldner, K.-H. Steuer, M. Ulrich, H. Vernickel, K. Wira, H. Zohm, W. Beck, H. Birkmeier, J. Boenisch, P. Cierpka, W. Drechsler, J. Fink, H. Frischmuth, J. Herrmann, J. Krippner, E. Oberlander, M. Oswald, D. Pohl, A. Roman, K. Schindler, E. Schmid, G. Schmitt, G. Stichs, A. Stimmelmayr, G. Weber, L. Zoelch

14) **ICF-Group:** J. Baeumler, W. Becker, F. Braun, R. Fritsch, F. Hofmeister, A. Murphy, J.-M. Noterdaeme, S. Puri, F. Ryter, H. Wedler, F. Wesner

15) **PSI-Group:** R. Behrisch, A.-P. Martinelli, V. Prozesky, J. Roth, E. Taglauer

AUTHOR INDEX

University Contributions to IPP Programme

Lehrstuhl für Experimentalphysik VI der Universität Bayreuth

(Prof. Dr. Jürgen Küppers)

- Activities noted in the section: Surface Physics Division

Ruhr-Universität Bochum

INSTITUT FÜR EXPERIMENTALPHYSIK AG VI
AKUSTIK UND OPTIK DER FESTKÖRPER
(Prof. Dr. J. Pelzl, B. K. Bein)

he final report of the project on Thermo-
hysical Properties of Technical Graphite
resented here is devoted to the IR radio-
etric detection of small-amplitude ther-
al waves on a relatively high temperature
ackground. In this Thermal Wave Radiome-
ry, thermal waves are excited in solids
y intensity modulated heating, e.g. by
ocussed light or laser beams. The related
hermal response, which depends on the
hermophysical properties of the solid, is
easured by detecting the periodic varia-
ions of the total radiant emittance of
he sample. This radiometric detection is
n absolutely non-contact technique for
easuring thermal waves, most suitable for
emote sensing. It can be applied for in-
situ measurements of thermal properties in non accessible, hostile environments, e.g. at high temperatures or under irradiation by energetic particles or X-rays.

In contrast to the usual IR radiometry, which serves to detect larger radiation contrasts at a low temperature background, and in contrast to the IR thermography in tokamaks /1/, which is able to resolve temperature differences of several Kelvin at average limiter temperatures up to about 1000 K, the thermal radiometry here has been developed in order to detect small-amplitude thermal waves of the order of 0.01 K - 1 K at average sample temperatures from 500 K - 1000 K. The complete experimental arrangement (Fig.1) to test

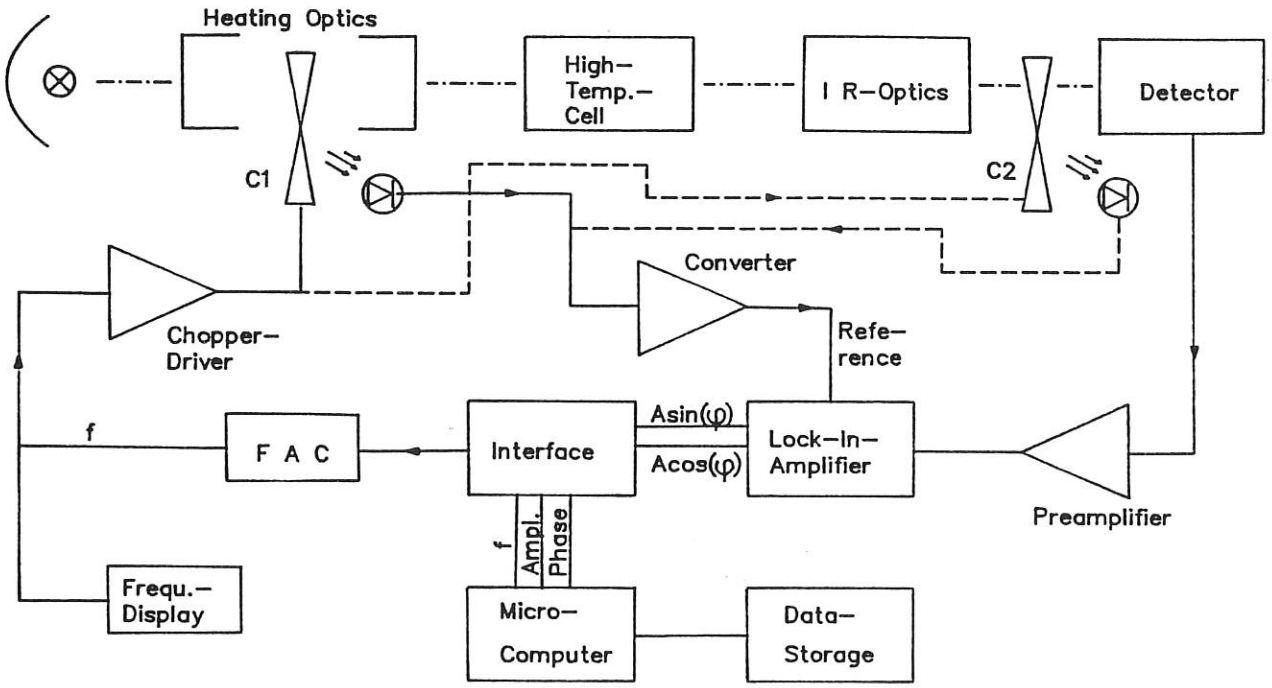

Fig. 1: Schematic of the IR experiment, which allows to measure both the signals related to thermal waves and the radiation level corresponding to the average sample temperature.

the radiometric detection and to measure thermal properties of fusion reactor materials at high temperatures consists of three main components: The high-temperature cell to heat the samples to the required average temperature and to protect them against oxidation and corrosion, the heating system for the excitation of thermal waves, and the IR detection system. Thermal waves are excited in the sample by absorption of a light beam modulated by chopper C1. The related radiometric response, which can be considered as a small fluctuation of the high radiation level corresponding to the average sample temperature, is filtered from the detector signal using a lock-in amplifier. The chopper C2 (Fig.1) is used to measure the total radiant emittance at the average sample temperature. This second signal yields information about the emissivity of the sample surface and can be used for the calibration of the radiometric signals related to the thermal waves.

The signal generation process for thermal waves has been studied using a wavelength-independent pyroelectric detector and an InSb photon detector. The radiometric signal related to the thermal wave $\sigma M(T)$ and the signal $M(T)$ corresponding to the total emittance at the average sample temperature T, which were measured with the help of the pyroelectric detector, show the temperature dependences predicted by Stefan-Boltzmann's law (Fig. 2). For signals measured with the more sensitive InSb detector the observed temperature dependences are affected by the limited detectable wavelength interval which has to be considered in the interpretation of the radiometric signals /2/. Figure 3 shows radiometric signals σM measured with the InSb detector as a function of the modulation frequency f of the thermal wave. The smallest thermal wave amplitudes detected at an average sample temperature T = 775 K were σT = 0.2 K and 0.07 K for the thin and the thicker sample /2/.

Figure 4 shows measurements for metal test samples and first results for graphite /3/. The measured values of the thermal diffusivity, deduced from the theoretical approximations of the measured normalized phase shift, are in good agreement with literature values of the metal samples, respectively confirm the values measured for graphite at high temperatures with the help of the photoacoustic technique /4/.

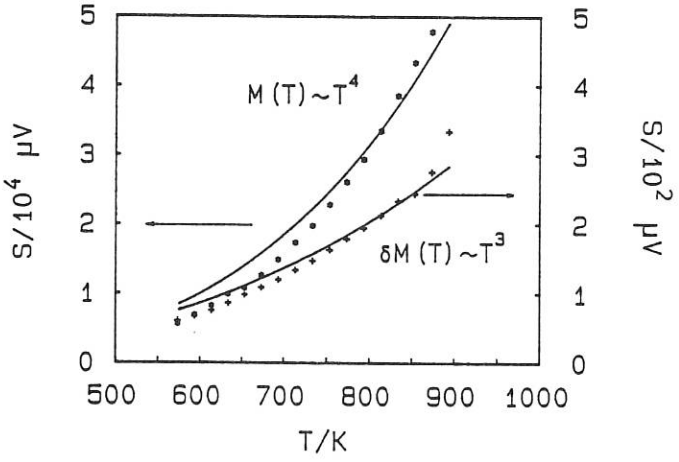

Fig.2: Signals related to thermal waves and total emittance of a W sample.

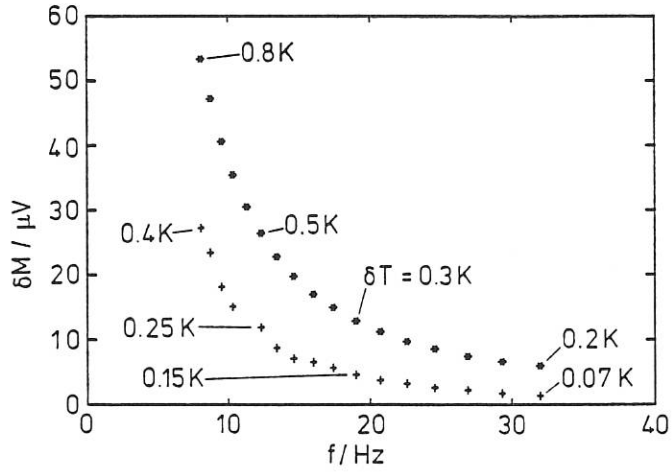

Fig.3: Radiometric signals related to thermal waves in Ta samples of 0.5 and 1 mm thickness.

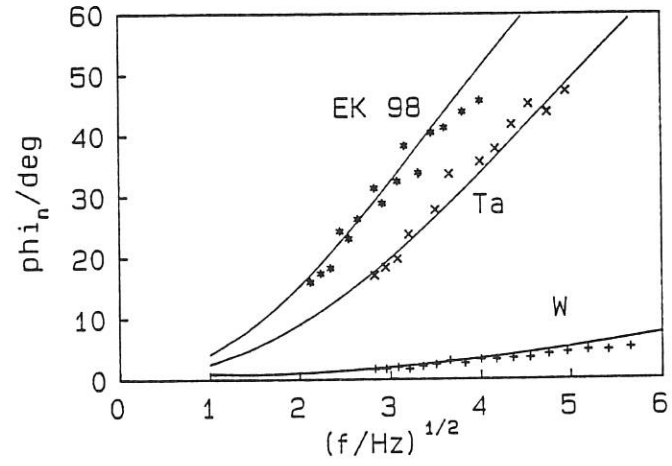

Fig.4: Normalized phases for metal samples and graphite at 775 K.

/1/E.R. Müller, B.K. Bein, K. Steinmetz, 'Time and space-resolved energy flux measurements in the divertor of the ASDEX tokamak by computerized IR thermography', Report IPP III/97, (1984).
/2/B.K. Bein, R.Hüttner, J.H.Gu, J.Pelzl, D.L. Balageas, A.A. Deom, 'Radiometric Detection of Small-Amplitude Thermal Waves at Background Temperatures between 500 K -1000 K', to be publ. 1991.
/3/B.K.Bein, J.H.Gu, R.Hüttner, J.Gibkes, H.W. Schmidt, J. Pelzl, 'Thermal-Wave Characterization of Plasma-Facing Materials from 500 K to 1000 K by an IR Radiometric Technique' in: The Proc. of 16th SOFT, London, Sept. 3-7, 1990, (Eds. B.E. Keen, M.Huguet) Elseviers Science Publ., Amsterdam, (1991).
/4/J. Pelzl and B.K. Bein, IPP Annual Report 1989.

INSTITUT FÜR KERNPHYSIK, STRAHLENZENTRUM
JUSTUS-LIEBIG-UNIVERSITÄT GIESSEN
(Prof.Dr.E.Salzborn)

ne emittance of ion beams produced by the new 10 GHz Giessen ECRIS was evaluated by a slotted late - Faraday cup system. This allowed the measurement of the 80% emittance ($\epsilon_{80\%}$).

ne use of a slotted plate-Faraday cup system to easure the emittance of ion beams extracted from CRIS plasmas

R.Trassl, M.Schlapp, M.Liehr, F.Melchert)

n order to measure the emittance of ion beams we uilt a device consisting of a slotted plate and ovable Faraday cup.
ig. 1 is a schematic representation of the set-p. It consists of a plate with 21 parallel lots, each of 40 mm length. The width of the lots is 0.2 mm and the distance between two lots is 1.8 mm. Ions passing through the slots re detected in a Faraday cup positioned 50 mm ehind the plate. The entrance of the cup is 0 mm long and 0.2 mm wide. The Faraday cup can e moved perpendicular to the slots within a otal range of 40 mm. The pattern of the beam-ntensity distribution obtained from this set-up s illustrated in Fig. 2. The ion beam measured as extracted from an Argon plasma at 10 kV ex-raction voltage. The emittance was then calcu-ated from the intensity distribution and the imensions of the slotted plate - Faraday cup ystem. Fig. 3 shows the results obtained. The alue of the emittance at 80% of total ion beam ntensity can be derived from Fig. 3. The yield s $\epsilon_{80\%} = 102\pi$ mm mrad.

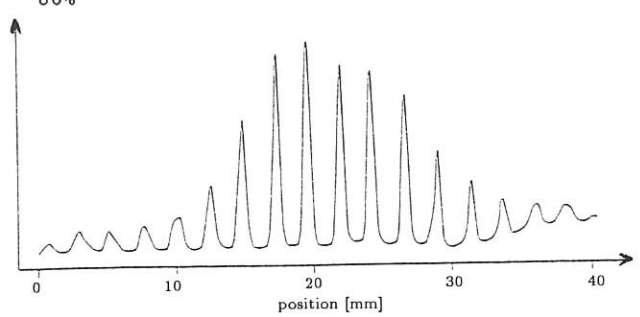

ig. 2: Ion intensity distribution obtained behind the slotted plate.

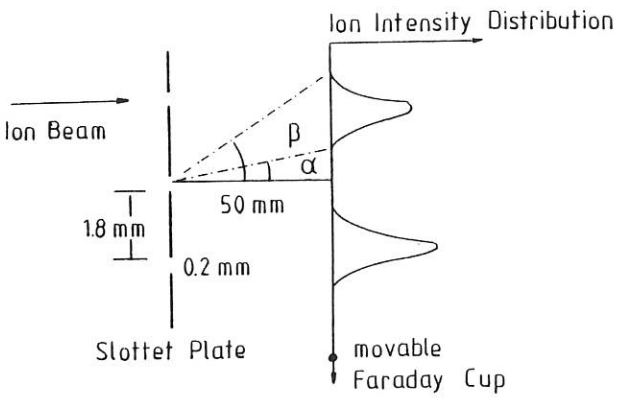

Fig. 1 Schematical set-up of the slotted plate-Faraday cup system.

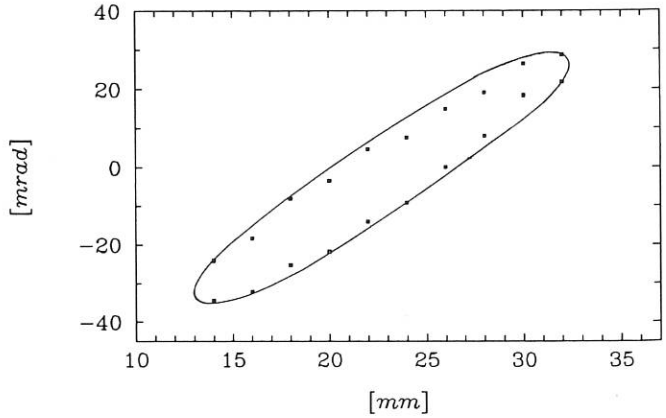

Fig. 3: Ion beam emittance $\epsilon_{80\%}$ obtained from an ECRIS plasma at 10 kV-extraction voltage.

INSTITUT FÜR ANGEWANDTE PHYSIK II
DER UNIVERSITÄT HEIDELBERG
(Prof. Dr. Klaus Hübner)

Cooperation with IPP in the field of neutron diagnostics was continued in 1990. This comprises neutron measurements on ASDEX and their interpretation, numerical simulation of neutron transport, and automated scanning of nuclear emulsions.

1. FAST FOKKER-PLANCK NEUTRON INTERPRETATION CODE

(B. Wolle)

Neutron rate measurements are often used to determine the ion temperature or deuteron density in tokamak fusion plasmas. This can easily be done during ohmic heating or H injection since the velocity distribution function of the plasma deuterons is Maxwellian. However, during D injection the distribution function is highly non-Maxwellian and thus needs to be calculated explicitly to determine the temperature or density.

In our fast interpretation software, the 2-dimensional distribution function $f(v,\mu)$, where μ is the cosine of the pitch angle of the particle, is calculated by means of a steady-state solution of the Fokker-Planck equation:

$$\frac{\partial f(v,\mu)}{\partial t} = C(f(v,\mu)) + S(v,\mu) - L(v) = 0,$$

where $C(f(v,\mu))$ is the collision operator with the classical Rosenbluth potentials, $S(v,\mu)$ is the source of injected particles, and $L(v)$ is a particle loss term. To solve this equation numerically, the distribution function is expanded in Legendre polynomials P_n: $f(v,\mu) = \sum a_n(v)P_n(\mu)$. In most cases it is sufficient to simplify the collision operator by using a Maxwellian in the Rosenbluth potentials. As an option, the Fokker-Planck equation can also be solved self-consistently by taking into account the distribution function itself in the collision potentials.

The neutron rate and, hence, the distribution function depend on many different plasma parameters, the most important of which are the electron temperature T_e, the ion temperature T_i, the deuteron density n_D, and the number s_0 of injected particles per unit volume and time. In order to discuss the effect of variations of these input data on the neutron rate and to determine the range of application of our interpretation code, a sensitivity study was carried out. The relative change of the neutron rate Y is given by

$$\frac{dY}{Y} = \frac{\partial Y}{Y\partial T_e}\,dT_e + \frac{\partial Y}{Y\,\partial T_i}\,dT_i + \frac{\partial Y}{Y\,\partial n_D}\,dn_D + \frac{\partial Y}{Y\,\partial s_0}\,ds_0.$$

The sensitivity factors K_e, K_i, K_D, and K_s, which in general are functions of all plasma parameters themselves, are defined by

$$\frac{\partial Y}{Y\partial T_e} = K_e, \quad \frac{\partial Y}{Y\,\partial T_i} = K_i, \quad \frac{\partial Y}{Y\,\partial n_D} = K_D, \quad \frac{\partial Y}{Y\,\partial s_0} = K_s.$$

We used 1,200 data points to obtain analytical approximation formulas for the sensitivity factors. It should be pointed out that, in order to perform an interpretation calculation, the sensitivity factor of the plasma parameter of interest has to be as large as possible in relation to the others. In Fig. 1 some of the sensitivity functions are plotted in a n_D-T_i diagram together with the approximate range of operation of several fusion experiments. For example, $K_i = 0.2$ means a 20% change in the neutron rate is caused by a change of 1 keV in temperature or 10^{19} m^{-3} in density. Points below the line $K_i = K_e$ are more strongly influenced by T_e points above more strongly by T_i. The picture indicates that the ion temperature can be determined for plasmas with

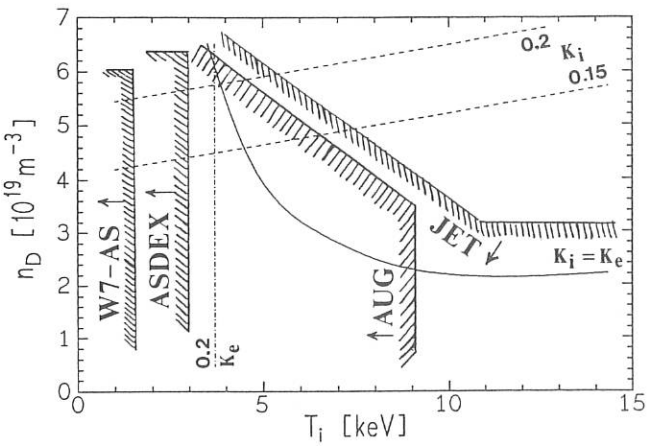

FIG. 1: Range of applications for interpretive calculations for several fusion experiments.

medium or high densities and temperatures below approximately 5-7 keV. On the other hand, determination of T_i from neutron rate measurements during D injection is not possible for low-density plasmas, while determination of n_D is possible for all plasmas, with increasing accuracy for low-density plasmas.

This work was performed in collaboration with the Theory Division of JET.

2. SPHERICAL IONIZATION CHAMBER AS ON-LINE NEUTRON SPECTROMETER AT ASDEX
(G. Degenhardt, M. Stams)

A spherical ionization chamber as described by Hoenen[1] was tested under the working conditions at ASDEX. We used a tangential, collimated observation of the plasma, but limited space did not allow an optimized observation direction and a suitable collimator size. For this reason we were restricted to measurements during H injection and the scattered neutron background was relatively high. - The collimator consisted of polyethylene and lead to shield against scattered neutrons and γ rays. The distance to the plasma axis was about 1.5 m. In this position we needed typically more than 10 ohmic discharges or about 5 discharges with H injection into deuterium plasma to obtain a reasonable result.

Figures 2 and 3 give the results for shot series 31891 to 31902 with H injection. The directly measured signal is the recoil proton spectrum (Fig. 2), which has to be smoothed and differentiated to get the neutron energy spectrum (Fig. 3). The edge in the proton energy spectrum between channels 130 and 145 contains the information about the direct neutrons from the plasma and produces the peak centred at 2.45 MeV in the neutron spectrum. Owing to the large scattered background only the high-energy wing of the measured neutron spectrum represents these direct neutrons. A Gaussian fit - also shown in Fig. 3 - gives a deuteron temperature of 1.3 ± 0.3 keV, which is averaged over the volume observed. This value is in good agreement with the central value of 1.65 ± 0.15 keV determined by CX measurements during this shot series. - The broadening of the low-energy wing is caused by elastic scattering of neutrons, and the low-energy contributions are due to inelastic scattering. The structure in this low-energy part of the spectrum is mainly caused by statistical errors in the count rates.

This work was done in collaboration with Dr. F. Hoenen, IPP, KFA Jülich.

[1] F. Hoenen, Nucl. Instr. and Meth. 259 (1987) 529

3. PNEUMATIC TRANSPORT SYSTEM FOR ASDEX
(R. Bätzner)

The transport system for our position 6 described in previous annual reports was extensively used for indium activation, nuclear emulsion measurements, and in-situ calibration. It proved to be highly reliable and simple to use. In order to ensure exact positioning of the samples or emulsions during exposure, an optical end position detector was installed.

4. IMPROVED MONTE CARLO SIMULATION OF NUCLEAR EMULSION RESPONSE
(St. Helbing)

We extended our NEPMC software (see Annual Report 1986, p. 189) to treat uncollimated measurements, especially in position 6 at ASDEX. Here we have to consider that scattered neutrons hit the emulsion from the back, causing proton tracks running in a direction opposite to the usual tracks produced by direct neutrons. As the scanning routines cannot distinguish between the beginning and end of a proton track, this leads to distortion of the emulsion response which depends on the amount and direction of the scattered neutron fluence entering the emulsion.

Furthermore, by higher computing accuracy of the coordinates the simulation now also takes into account the losses due to protons escaping from the emulsion through its surfaces.

5. AUTOMATIC SCANNING OF NUCLEAR EMULSIONS
(M. Hermann, H. Hinsch)

We improved the new evaluation method for detecting and measuring proton tracks in nuclear emulsion plates mentioned in the Annual Report 1989. In order to get shorter execution times, the programs were implemented on a VME cpu board with the RISC processor 88000. We started to divide the whole procedure in two parts in order to control the scanning and video equipmemt with a separate VME cpu board with a 68020 processor. The video data is to be transferred from this processor board into the dual-ported memory of the 88000 processor board. Unfortunately, there are a lot of hardware and software problems to overcome with the 88000, the UNIX operating system, and the dual processor concept, which need still some effort.

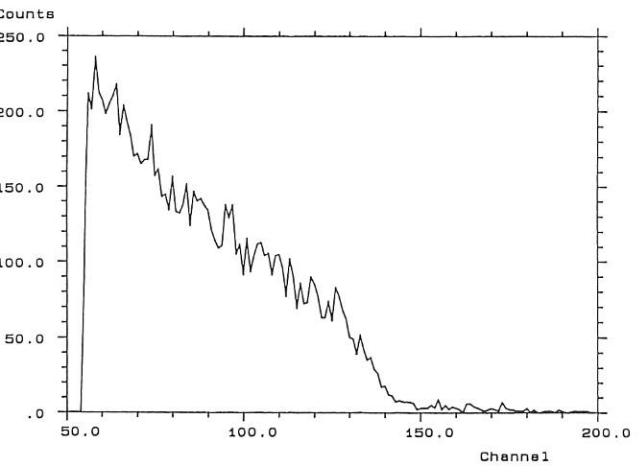

FIG. 2: Raw data of proton recoil spectrum.

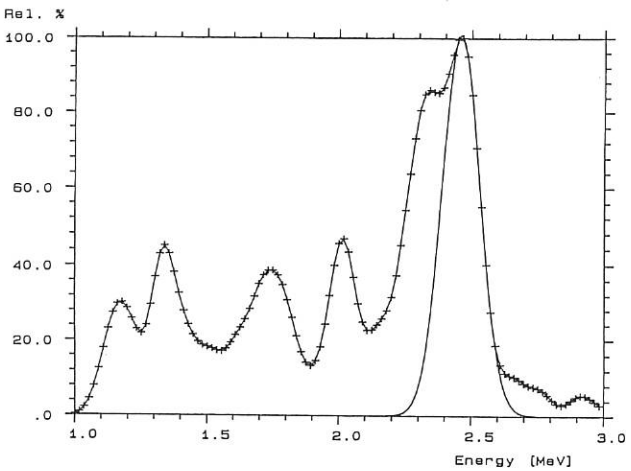

FIG. 3: Evaluated neutron energy spectrum.

ISOTOPE SEPARATOR LABORATORY, PHYSICS DEPARTMENT,
TECHNICAL UNIVERSITY OF MUNICH
(Dr. E. Hechtl)

Sputtering yields of beryllium bombarded with oxygen and self-sputtering yields of tungsten were measured.

Sputtering of Solid Surfaces with Heavy Ions
(E. Hechtl, A. Mazanec)

The low-Z material beryllium was bombarded with oxygen ions and sputtering yields in the energy range from 10^2 to 10^4 eV were measured at room temperature and at 900 K. Comparisions with TRIM.SP code calculations were made, showing the following results. The calculated sputtering yields of beryllium bombarded with oxygen are higher than those measured. At the lowest energy the discrepancy is a factor of six continously decreasing to a factor of 1.3 at 10^4 eV. On the other hand, the calculated yields of beryllium oxide bombarded with oxygen agree very well with the experimental results. This suggests that beryllium is converted to beryllium oxide during oxygen bombardment. Sputtering yields taken at the target temperature of 900 K show no significant difference to the room temperature data.

The measurement of self-sputtering yields of tungsten was carried out at room temperature for energies between 10^2 and 10^4 eV. The results are shown in Fig. 1, where the self-sputtering yield data for normal incidence are plotted versus the ion energy. The curve drawn is the yield calculated with the TRIM.SP program. The correspondence between the measured and calculated data is almost perfect, especially in the medium-energy range. The recently built ion optical system for obliquely impinging ions was used to measure self-sputtering yields of tungsten as a function of the angle of ion incidence. Since the method applied for measuring the sputtering yields is the weight loss method, one cannot distinguish between sputtered and reflected particles. The yield found is therefore the sum of the sputtering yield and reflection losses. Comparision with the TRIM code calculation for the sum of these values shows good agreement up to an angle of incidence of 50° to normal incidence. At higher angles of incidence the measured values show lower values owing to the roughness of the surface.

The low-Z materials boron and boron carbide are in the process of being investigated with respect to self-sputtering and simulated self-sputtering, respectively, in the relevant energy range.

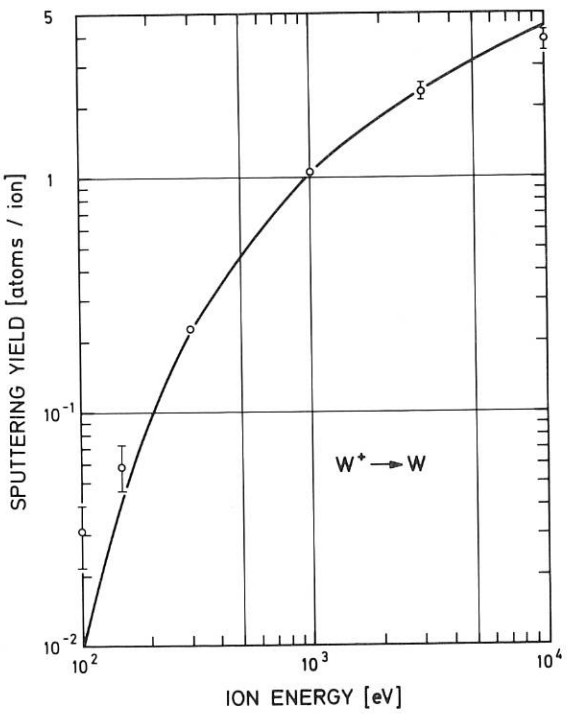

Fig. 1. Self-sputtering yield of tungsten versus the ion energy at normal incidence. The curve drawn is not a fit but is calculated with the TRIM.SP code.

Conference Contributions

Hechtl, E., Yang, H.R., Wu, C.H., and Eckstein, W.: An experimental study of tungsten self sputtering, 9th Int. PSI Conf., Bournemouth, UK, 20-25 May 1990.

Wu, C.H., Hechtl, E., Yang, H.R., and Eckstein, W.: Erosion of beryllium by oxygen, 9th Int. PSI Conf., Bournemouth, UK, 20-25 May 1990.

Institut für Plasmaforschung (IPF)
der Universität Stuttgart
(Prof. Dr. R. Wienecke)

1. ELECTRON CYCLOTRON RESONANCE HEATING (ECRH)

(R. W i e n e c k e , V. Erckmann[1], W. Henle[2], A. Jacobs[2], W. Kasparek, H. Kumrić, H. Li[3], G.A. Müller, J. Pretterebner, P.G. Schüller, M. Thumm[4], D. Wagner)

In 1990 the W7-AS stellarator, after reinforcement of the coil structure, was ready to operate at the full magnetic field B = 2.5 T. ECRH experiments at 70 GHz were therefore performed with O-mode wave launch, for which an electron density of up to $6 \cdot 10^{13}$ cm^{-3} is accessible. A quasi-stationary plasma could be produced in long pulses of up to 1.5 s duration. A plasma with a central electron temperature T_{e0} = 2 keV at an electron density of $n_{e0} = 3.5 \cdot 10^{13}$ cm^{-3} was generated with a microwave power of 670 kW. In experiments with NBI heating the plasmas produced by ECRH were used as target plasmas. The study of non-inductive plasma current drive by ECR wave absorption (ECCD) was continued; in particular, the Doppler up- and down-shifted resonance condition in ECCD was investigated and compared with numerical calculations.

The details of the physical results are discussed in the stellarator part of this Annual Report. Technical experiments with the 70 GHz system and improvements of some components are described in the following.

Owing to the density increase by NBI heating the 70 GHz microwave does not penetrate to the plasma centre. To investigate combined heating by NBI and ECR, a microwave system at 140 GHz with X-mode launch at 2nd-harmonic resonance was planned and constructed. This project is a collaboration between IPP Garching, IPF Stuttgart and KfK Karlsruhe. The development of a 140 GHz gyrotron with a pulsed power of 100 kW for 100 ms was successful at KfK Karlsruhe. The tube was delivered to IPP and tested in the 2nd half of 1990 with the assistance of IPP and IPF. The tube, which emits the microwave power in a TE03 output mode, is ready for plasma experiments in 1991. The microwaves are guided from this gyrotron to the plasma by a quasi-optical mirror transmission line consisting of imaging mirror optics, mode converter for the gyrotron output mode, polarizer, and beam monitor. The components of this transmission line have been designed and manufactured. New developments and test results on these components are described in the following. Such quasi-optical transmission lines are of importance for future multi-megawatt ECRH systems.

---

1) IPP Garching
2) until April 1990
3) guest from University of Electronic Science and Technology of China, Chengdu, P. R. China
4) until June 1990

1.1 Microwave Technology for ECRH at 70 GHz

1.1.1 *Microwave generator system*

For plasma generation and heating in the W7-AS stellarator the four long-pulse gyrotron generator modules generate a total power of up to 760 kW at 70 GHz with pulse lengths of up to 1.5 s. An additional 70 GHz, 200 kW gyrotron with a pulse length of 100 ms was used for special current drive experiments. These five modules running in parallel operation allowed flexible programming of injected power with a high degree of reliability.

1.1.2 *Transmission line system*

The transmission line for the additional 70 GHz 100 ms pulse tube was completed and successfully tested. This line launches the wave into the plasma at a position where the magnetic field of the stellarator increases from the plasma inside to the outside. This results in the cyclotron resonance condition being matched not only at the plasma centre but also somewhere outside the confined plasma region. To avoid unwanted plasma production at this location, the wave is guided there in a differentially evacuated HE11 waveguide section between two microwave barrier windows. The first experiments with this line showed that in spite of the evacuated waveguide a plasma breakdown occurred in this critical section. This waveguide was not baked out in vacuum and therefore there may be a possibility of gas release from the surface by microwave heating. Successful wave launching to the plasma centre was achieved by removing this special waveguide and making use of free space transmission through the second resonance zone without any gas breakdown.

At pulse lengths exceeding 1 s some of the transmission lines suffered from microwave-induced arcing in the TE11 part of the TE01-TE11 mode transformer. This device proved to be the most critical because of the high electric field (4.6 kV/cm) and the high surface current density at the TE11 output, where the flange contacts are a source of trouble. The ultimate solution of this problem will be to replace the two-step TE01-TE11-HE11 mode converter by a newly designed, direct, one-step TE01-HE11 mode transducer which avoids the problem of high wall current density in the TE11 section.

Direct, high-power TE01-HE11 mode converters in an overmoded, circular corrugated waveguide (70 GHz, I.D. = 27.79 mm) with periodic curvature distortions in one plane were optimized by numerically integrating the corresponding coupled-mode differential equations with new, generalized coupling coefficients. Since at appropriate corrugation depth the unwanted mode conversion to surface modes TE11-EH11 and TE21-EH21 is negligible, it is possible to design short mode transducers with high conversion efficiency. Both the input mode TE01 and the output mode HE11 have very low currents and electric fields at the waveguide wall (volume modes).

The efficiency of rippled-wall mode converters with simple perturbation profiles (pure cosine or sine shape) depends on the starting phase of the wall distortions. It can be further improved by using various combinations of:

(1) slightly changed perturbation period (wall perturbation period $L_w = \lambda_B$) resulting in continuous phase rematching within the converter,

(2) proper placement of phase delay sections of straight corrugated waveguide,

(3) superposition of additional, small and phase-matched perturbation amplitudes on the main wall distortion, tapered along the mode converter.

Efficiency optimization was studied by numerically solving the coupled-mode differential equations for eight coupled hybrid

Number of periods	3	4
length L	1.435 m	1.854 m
mode purity	97.99 %	99.14 %
ohmic losses	0.06 %	0.07 %
phase delay section	yes	no
period correction	no	0.994

TABLE 1: *Calculated data of improved 3 λ_B and 4 λ_B long 70 GHz TE01-HE11 mode transducers (I.D. = 27.79 mm).*

modes in a corrugated waveguide with a slot depth of $0.2 \cdot (\lambda/4)$, where the mode conversion to the unwanted surface mode is sufficiently removed. Ohmic attenuation is included in the analysis. The results of optimization on an $L = 3\lambda_B$ and $L = 4\lambda_B$ TE01-HE11 mode converter are shown in Table 1 and Fig. 1. The overall conversion efficiency was calculated as 97.44% for a $3\lambda_B$ mode converter, and 98.40% for a $4\lambda_B$ mode converter.

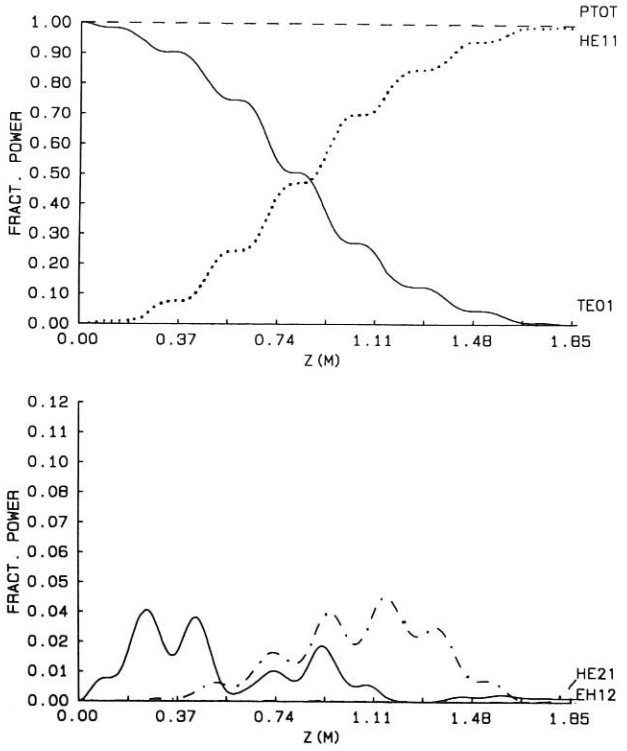

FIG. 1: *Calculated power in desired and main spurious modes as a function of z along the improved optimized 4 λ_B long 70 GHz mode converter.*

The sensitivity to frequency change in the range of frequency tolerances of commercial 70 GHz gyrotrons was calculated. The overall conversion efficiency stays in the range of ± 4% for the optimized short mode transducer, and ± 2% for the long one.

For temperature compensation and vacuum pumping special cylindrical slotted sections were developed. Theoretical considerations[5] on the losses and spurious modes for a slot (length L) in an oversized waveguide (radius r) lead to the following predictions:

Total losses for the TE01 mode: $P_{(dB)} = 2.4\ (L \cdot \lambda/2r^2)^{3/2}$

and for the HE11 mode: $P_{(dB)} = 1.3\ (L \cdot \lambda/2r^2)^{3/2}$

Measurements on a waveguide slot with variable length were made at 70 GHz and I.D. = 27.79 mm with the TE01 and HE11

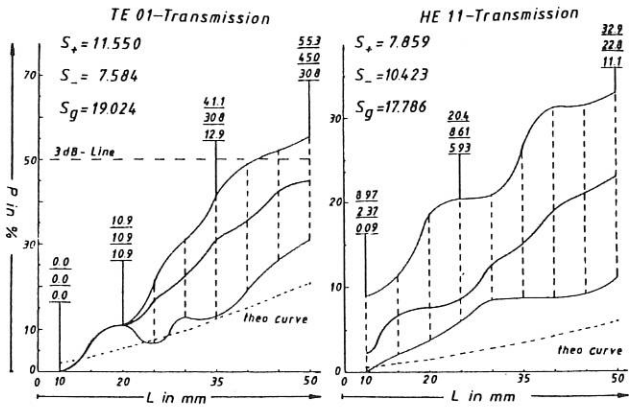

FIG. 2: *Calculated and measured losses as a function of the slot length for the TE01 mode (left) and HE11 mode (right).*

as input modes by means of a k-spectrometer. Figure 2 shows a comparison between the predicted and measured losses as a function of the slot length for the TE01 and HE11 mode, respectively. For small slots there is good agreement between theoretical and measured values. Wide slots lead to higher losses owing to the radiation out of the slot, which is not included in the theoretical calculations. The measurements show that it is possible to use slotted waveguides with small slot lengths.

Since the arc length of corrugated bends for TE01 and HE11 modes in oversized waveguides becomes very large, the use of corner bends (mitre elbows) containing simple flat mirrors was investigated. Phase distortions due to diffraction on the mirror aperture lead to the generation of unwanted parasitic waves. By combining diffraction theory in open systems and ordinary waveguide theory a theoretical description of the passage of the circular TE01 mode through an overmoded elbow bend with flat mirror is given. The lost power is nonuniformly distributed among the parasitic waves. One quarter travels backward in the form of several high-order spurious waves close to cut-off, and an equal fraction goes forward in the form of similar modes. Half of the lost power is transmitted as unwanted spurious modes with a broad mode spectrum. This predicted spectral

[5] Katsenelenbaum, B.Z., Radio Eng. Electron. Phys. 8, (1963) 1098.

energy distribution was checked by using a wave number spectrometer. The measured spectra are shown in Fig. 3.

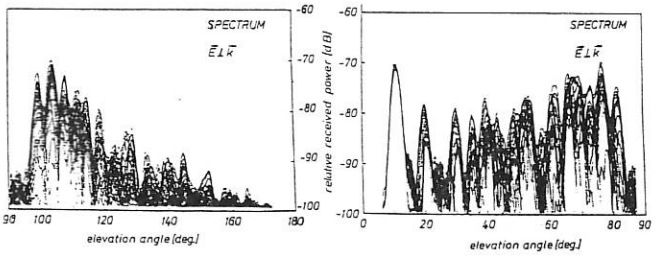

FIG. 3: *Backward (left) and forward (right) spectrum for a flat mirror TE01 bend.*

A comparison between the theoretical losses in spurious waves in a flat TE01 and HE11 mirror and the experimental results is given in Tab. 2. The spectral distributions of forward and

		theor. losses	meas. losses	trans-mitted	re-flected
TE01		6 %	(5.3±0.5) %	4 %	1.3 %
HE11	H-plane	5 %	(5.4±0.5) %	4.1 %	1.3 %
	E-plane		(5.7±0.5) %	4.2 %	1.5 %

TABLE 2: *Comparison between theoretical and measured mode conversion losses in TE01 and HE11 mitre bends.*

backward travelling parasitic modes in the HE11 mitre bend correspond to those of the TE01 elbow bend.

The losses involved in the conversion into such undesirable modes can be reduced if the mirror is slightly curved and thus becomes a phase corrector. The quasi-optical Gaussian beam approximation for the radiation from an open-ended HE11 waveguide leads to an elliptically curved mirror which partially compensates for the phase distortions caused by diffraction. Since the wave field in a mitre bend is partially guided by the walls, a cylindrical shape of the mirror (2-dimensional) is sufficient. Finally, the shape of an optimally curved cylindrical HE11 mirror was numerically designed with respect to the requirement of minimum diffraction. The experimentally determined losses of the improved mirrors are shown in Table 3. The mirrors with a quasi-optical phase correction reduce the diffraction losses by 25 % and the optimally curved cylindrical HE11 mirror by approx. 50 %, which is in good agreement with the theory.

phase correction		total losses	trans-mitted	re-flected
elliptical	H-plane	(4.3±0.5)%	3.2%	1.1%
	E-plane	(3.9±0.5)%	2.9%	1.0%
cylindrical	H-plane	(4.1-0.5)%	3.0%	1.1%
	E-plane	(4.0±0.5)%	3.0%	1.0%
optimum	H-plane	(2.7±0.5)%	1.9%	0.8%
	E-plane	(2.8±0.5)%	1.9%	0.9%

TABLE 3: *Mode conversion losses in oversized HE11 mitre bends for 70 GHz and I.D. = 27.79 mm with different phase correcting mirrors.*

1.2 Microwave Technology for ECRH at 140 GHz

The investigations on systems and components for the two high-power transmission concepts at 140 GHz, namely highly oversized tubular HE11 waveguide and quasi-optical TEM00 beam waveguides using focusing reflectors, were continued in 1990.

For closed HE11 waveguide transmission, the studies were mainly conducted in the context of the planned upgrade of the ECRH system on W7-AS, the ECRH system on ASDEX-U, the α-particle scattering diagnostic now being constructed at JET and the ECRH/ECCD system envisaged for NET/ITER. The TEM00 transmission techniques were further investigated on the basis of the 140 GHz ECRH system now being built at W7-AS, and the launching antenna systems for JET and NET/ITER.

1.2.1 *Quasi-optical 140 GHz transmission system for W7-AS*

The construction of all optical components for the transmission line was completed. The TE03 gyrotron from KfK was installed at IPP and successfully operated. In short-pulse operation, the output power exceeded 200 kW; at 100 ms pulses, reliable operation was demonstrated with an output power of 100 kW. Measurements showed that the mode purity was generally good; however, it could be influenced by the load. The transmission

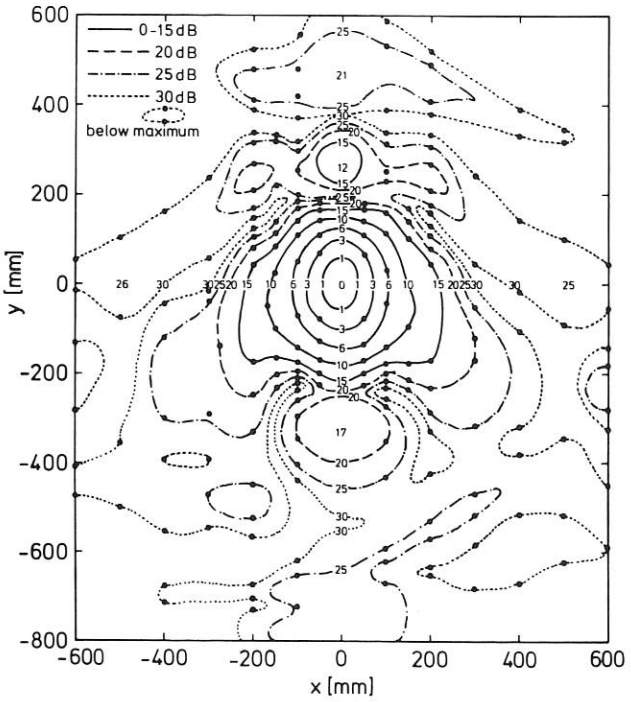

FIG. 4: *Far-field pattern of the quasi-optical mode converter.*

line now consists of the quasi-optical TE03-TEM00 converter, five curved mirrors for matching and transmission of the beam, two plane corrugated mirrors for polarization adjustment, one plane focusing grating for power monitoring and the steerable launching antenna. As a first step, a conventional Vlasov-type converter was constructed for the transformation of the gyrotron mode into a Gaussian beam. For an input w.g. diameter of 70 mm (= diameter of the gyrotron output w.g.), the device has a cut length of 705 mm, and the length of the parabolic mirror is 1600 mm for a focal length of 53 mm. Measurements of the far field (see Fig. 4) of this converter yield an efficiency for the conversion from the TE03 mode to the linearly polarized Gaussian beam of approx. 80 %; as this element is the main source of transmission loss, intense investigations are under way to improve its efficiency (see Sec. 1.2.2).

The guiding mirrors of the transmission line were machined into a light-weight grid structure with a surface roughness of typ. 2-3 μm. Eight coupling holes allow adjustment with the help of the microwave beam.

For polarization adjustment, an alternative device was built which consists of a combination of two grooved mirrors, namely a polarization twister (electrical groove depth λ/4) and an elliptical polarizer (el. groove depth λ/8). By adjusting the angle between the groove directions, any output polarization can be obtained. To allow a high power density on the polarizer surfaces, corrugations with a sinusoidal profile are used. For a corrugation period of 1.28 mm, measurements yielded corrugation depths of 0.79 mm and 0.61 mm for 180° and 90° phase shift, respectively.

The bi-directional coupler comprises two focusing gratings with a nominal depth of 25 μm, which were milled into the surface of the last plane reflector and which diffract a small portion of the transmitted (and possibly reflected) beams into first-order focused beams. Thus the diffracted beams can be perfectly coupled to matched horns to give the forward and backward power signals, and a quite compact bi-directional coupler is feasible. Additionally, the diffracted field in the focal plane of the grating is an image of the main beam and thus allows estimates of the mode purity of the transmitted main beam. A test of the prototype of the coupler is shown in Fig. 5, where the intensity of 140 GHz radiation was measured in the plane of incidence at a distance from the grating equal to its focal length. One clearly sees the difference between the beam widths of the unfocused main beam and the focused monitor beams. The coupling factors are approx. -30 and -40 dB for the forward and backward monitor beams, respectively, owing to the different groove depths of the gratings. The measured directivity was better than 25 dB.

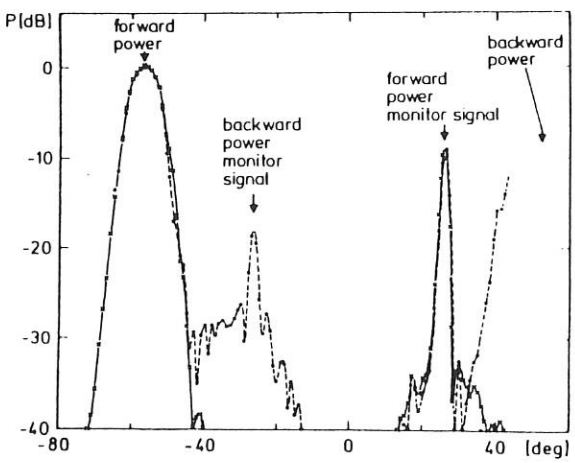

FIG. 5: *Intensity of the main and monitor beams of the grating coupler, measured at a distance equal to the focal length.*

The antenna was installed in the stellarator vessel, but the Varian vacuum barrier window has not yet been delivered. Most of the components were mounted at their positions; some of them have already been adjusted by laser beams.

1.2.2 *Development of quasi-optical mode converters for rotating high-order TE modes*

The transformation of high-order circular waveguide modes into the linearly polarized free-space Gaussian beam can be done with the help of a quasi-optical mode converter and with one or more reflectors. A standard converter consists of a helical and a straight cut of the waveguide and a reflector. In this antenna the energy is radiated from the straight cut and hits the reflector.

In a first step several types of waveguide cuts were analyzed at 140 GHz with a right-hand rotating TE15,2 mode. The contour plots of the intensities (Poynting vector) of the different antenna types showed that the "Vlasov cut" antenna radiates energy along the straight cut and the helical cut which cannot hit the reflector. The "rectangular cut" antenna avoids this problem (see Fig. 6). To increase the efficiency to values of ~ 95 %, several methods are possible:

(1) Wave beam shaping by diffraction at convex cylindrical surfaces (flared cut): A rotating high-order TE_{mn} mode with a low second index n (whispering-gallery mode (WGM)) propagating near the surface with variable curvature in the axial direction can change the transverse mode structure. Following the procedure of IAP-Gorky, we analyzed several convex surfaces. The efficiency for the transformation into the Gaussian beam decreases when the mode changes to a volume mode (high second index), e.g. 98 % for TE15,1 and 93 % for TE15,2.

(2) Operation of a corrugated quasi-optical antenna (in collaboration with A. Möbius, KfK Karlsruhe): All balanced hybrid modes propagating in a corrugated waveguide with a slot depth of $\lambda/4$ have very low wall fields and thus lead to lower edge diffraction losses if radiated from a waveguide launcher. Theoretical considerations and measurements at IPF Stuttgart showed that the radiated Gaussian beam is circularly and not linearly polarized.

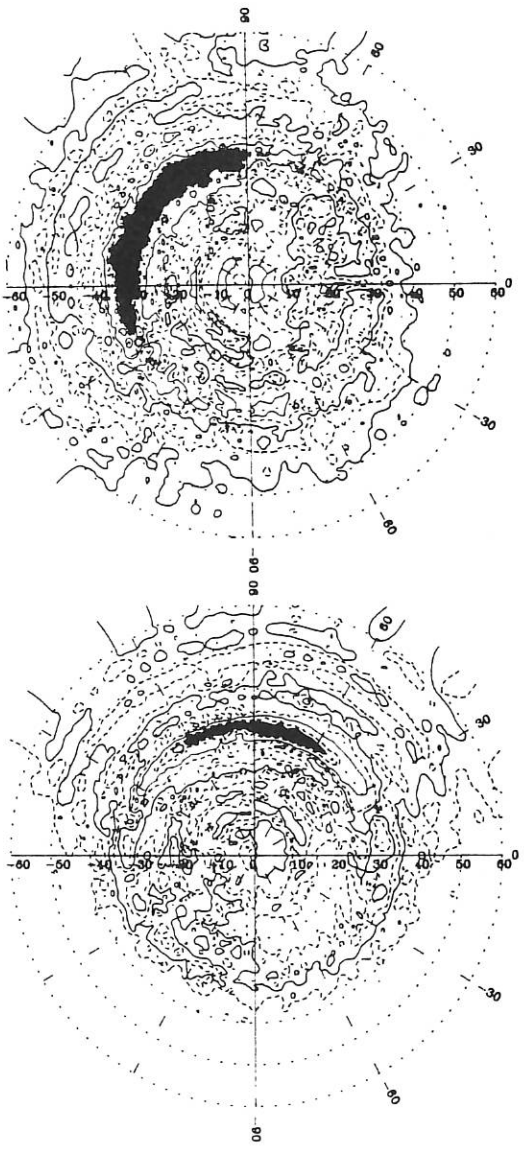

FIG. 6: *Far field pattern for a TE15,2 mode with rectangular cut (top) and Vlasov cut (bottom).*

(3) The first reflector (sub-reflector) is connected with the straight waveguide cut: "visor" design (in collaboration with M. Sato et al., PPL Kyoto University). The approach here is to determine the shape of the sub-reflector and the main reflector by decomposing waveguide modes into rays. For the design of the two reflectors the classical decomposition of rotating TE and TM modes into rays grazing one caustic is used. The resulting far-field pattern was analyzed with geometric optics (GO) which also includes the curvature of the reflector for the amplitude calculation of the far field (see Fig. 7).

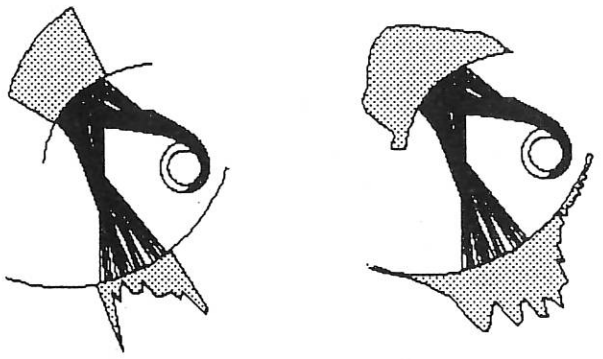

FIG. 7: *Reflector and far field amplitude calculated with ray optics (left) and discrete Franz formula (right).*

A new exact description of waveguide modes in terms of rays was developed ("continuous caustics") which also allows description of volume modes with GO. For the calculation of the main field and the edge-diffraction effects at the waveguide opening a general description (discrete Franz formula) of the transformation: waveguide → visor → reflector → far field was derived (see Fig. 7). The calculations showed that the main problem of the quasi-optical antenna for a high efficiency is the amplitude distribution over the aperture of the opened waveguide or, equivalently, the amplitude distribution of the caustic before opening the waveguide.

1.2.3 *Waveguide mode converters for rotating high-order TE_{mn} modes*

The mode transformers were optimized by numerically solving the appropriate coupled-mode differential equations. The manufactured mode converters for the TE07 → TE15,2 mode at 140 GHz were tested with a wave number spectrometer. The result is shown in Fig. 8. The predicted mode purity of the TE15,2 output mode and the measured value of (97±3) % are in good agreement.

1.3 Investigation of Materials for High-power Microwave Applications

Use of materials in high-power microwave applications requires in most cases accurate knowledge of their dielectric properties. Several methods of determining the complex permittivity, i.e.

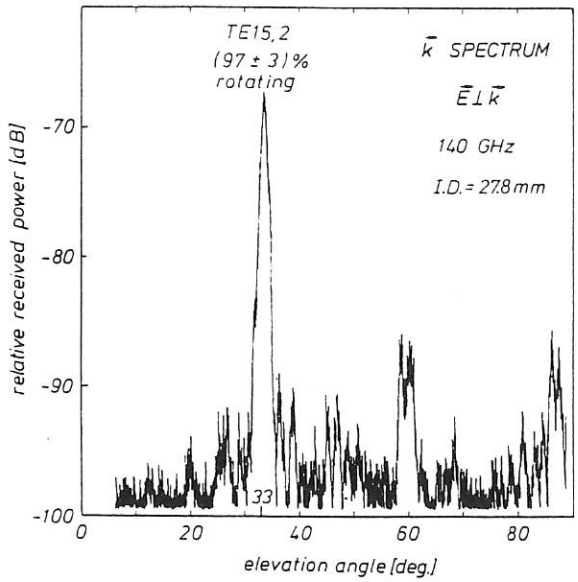

FIG. 8: *k-spectrum of the TE15,2 mode.*

relative dielectric constant and loss factor, are therefore employed.

Our investigations up to now have been concentrated on measurements by mainly two methods, the open resonator and the free-space microwave bridge with, respectively, low-loss and lossy solid materials. In addition, data of fluid and pulverized matters are also of great interest, especially for window cooling or microwave sintering applications. An experimental arrangement was therefore set up in which the short-circuited waveguide measurement method is applied. In this method the sample of unknown permittivity, either solid, pulverized or fluid, is placed against a short-circuit termination at the end of a vertical waveguide. If the applied frequency and the length of the sample are known, the only measurements required to determine the permittivity are the standing-wave ratios in the waveguide with the sample in place and the sample removed, and the positions of the voltage standing-wave modes under these two conditions. The shift of the mode position due to the presence of the sample depends mainly upon the relative dielectric constant ε_r, and the change in the standing-wave ratio depends mainly on the loss tangent tan δ.

First experience with this method shows that it may be well suited to application to high-temperature measurements because the waveguide with the sample can easily be placed in a vacuum oven and heated to temperatures exceeding 1600 °C.

2. LASER DIAGNOSTICS

(H. Alius[6], G. Dodel, K. Hirsch, E. Holzhauer)

2.1 LIDAR Thomson Scattering on JET

(in collaboration with the JET-LIDAR team:
H. Fajemirokun, A. Gadd, C. Gowers, P. Nielsen, and
H. Salzmann, IPP Garching)

During the past year the LIDAR diagnostic was routinely operated by the JET-LIDAR team, who were also developing a LIDAR-type edge diagnostic and designing a divertor diagnostic for T_e and n_e. In collaboration with the JET-LIDAR team the complete LIDAR system - including laser input beam path, collection system (new collection mirrors were installed at the end of 1989) and spectrometer - was realigned in May 1990. Recalibration in time (space) response and spectral characteristic was done. Stray light test measurements and absolute calibration via Raman scattering completed the whole procedure of recalibration. On the basis of this recalibration the accuracy of the results of measurements performed early in 1990 was improved.

2.2 Far-infrared Collective Scattering on ASDEX

The 119 μm laser scattering device was operated in the heterodyne mode to investigate the direction of propagation of density fluctuations. The local oscillator of the heterodyne system could be shifted in frequency up to ≈700 kHz by using a rotating cylindrical diffraction grating. Making use of the different pitch of the magnetic field lines in the inner and outer halves of the equatorial chord, spatial resolution was obtained for $k > 10\ cm^{-1}$ by appropriate alignment of the scattering device (scattering vector perpendicular to the magnetic field). Fast sampling of the scattering signals allowed frequency spectra to be deduced by Fourier transformation and the change of the fluctuation spectra during the L-H transition to be studied with high temporal resolution.
Results are described in section "ASDEX PROJECT" of this Annual Report.

2.3 Far-infrared Modulation

The 119 μm radiation of an H_2O laser was modulated in amplitude, phase and frequency by optical generation of free carriers in a silicon wafer. Two compact, diode-pumped CW Nd:YAG-lasers (λ=1.06 μm, P=40 mW each) electrically tunable in frequency and power were used for optical excitation. A maximum intensity modulation efficiency of 70 % and maximum phase modulation of 74 degrees were achieved. Modulation frequencies for amplitude and phase up to 80 kHz have been realized, the degree of modulation decreasing with increasing modulation frequency. FIR frequency modulation was accomplished by generating an optically induced "travelling" grating using two Nd:YAG lasers. Frequency shifts up to 15 MHz were achieved in reflection from and transmission through the wafer. With an effective excitation power of 26 mW the maximum efficiency was $1.5 \cdot 10^{-3}$ with a 3 dB roll-off frequency of 35 kHz for the Si wafer used. The results are published in the reference given in the footnote [7].

2.4 Far-infrared Laser Components

A radio-frequency excited H_2O laser operating at a wavelength of 119 μm was built to test output couplers using metallic echellete gratings machined in the IPF workshop. These couplers are selective with respect to polarization and wavelength.
Numerical calculations to solve Maxwell's equations in two dimensions were made to investigate the properties of reflectors with corrugated surfaces in the FIR and microwave regimes.

---

6) doctoral student
7) Alius, H. and G. Dodel, Infrared Phys. 32 (1991) 1

3. PLASMA EDGE DIAGNOSTICS

(K. Behringer , H. Jentschke, T. Schütte, K. Hublé, U. Fantz)

3.1 Chemical Impurity Production

Chemical reactions of hydrogen or deuterium and of oxygen impurities with graphite target and protection plates, leading to chemical erosion of these surfaces, is still an important problem in the development of future fusion reactors. The respective impurity fluxes are released in the form of molecules (CH_4 /CD_4 or higher hydrocarbons and CO) and can possibly be diagnosed by means of emission bands of these molecules or their dissociation products. In pursuit of this idea, spectra of ASDEX and JET edge plasmas were studied with the aim of measuring the chemical carbon production from CH/CD, CO or CO^+ molecular bands. Laboratory experiments were performed to provide the necessary background information about the appearance of the molecular spectra and their correct theoretical description. To some extent, these plasmas have already confirmed the present ideas about the molecular dissociation processes. In the future, they will also be used for measurement of molecular excitation rate coefficients. The interpretation of CH/CD spectra is almost complete and has already been published[8]. Only a brief summary will therefore be given here.

3.1.1 *Measurement of CH_4 /CD_4 fluxes and of chemical carbon erosion from CH/CD band emission*

The CH_4 /CD_4 production in tokamaks or stellarators can be measured in situ from molecular CH or CD band spectra around 431 nm in the visible. These are prominent features in the spectra of many tokamaks with carbon limiters, e.g. JET or TEXTOR, but are also seen in divertor tokamaks like ASDEX. Their intensity has been related to an externally controlled CH_4 influx by empirical calibration for a number of electron temperatures and related electron densities[9], but without the influence of particle transport in the plasma being known.

The observed molecular bands consist of the $A\,^2\Delta$ - $X\,^2\Pi$ electronic transition of the CH and CD molecules and involve the upper and lower vibrational levels v'-v' = 0-0, 1-1 and 2-2. On the basis of known molecular data - and some empirical fitting for CD-computer programs were set up to calculate the respective $F_{1/2,c/d}$ term values, the term differences and the wavelengths in air. The rotational and vibrational level populations, which are given by the rotational and vibrational temperatures T_r and T_v in the case of thermal equilibrium, were taken from the measured spectra. Theoretical line strengths and the apparatus profile of the respective spectrometer were used to calculate band spectra which are practically identical with those measured with arbitrary spectral resolution.

For the purpose of developing and testing these simulation programs, spectra emitted from CH_4 /CD_4 microwave discharges were investigated. The respective plasma parameters are known from spectroscopic and probe diagnostics[10], namely the electron temperature $T_e \approx 3$ eV and the electron density $n_e \approx 10^{11}$ cm^{-3}. The kinetic temperature T_g of the heavy particles, which is usually believed to be responsible for the rotational level population, is about 500 K, as demonstrated by nitrogen molecular bands, when a trace of N_2 is added. Nevertheless, $T_r \approx 3000$ K is required to explain the measured CH/CD rotational intensity distribution, indicating rotational excitation during the chemical decomposition in the plasma. In the case of CD, the population of the lower 10 rotational levels was observed to fall off more steeply, corresponding only to $T_r \approx 1200$ K. The relative populations in v'=1 and v'=2 with respect to v'=0 were found to be 0.4/0.3 and 0.08/0.04 for CH/CD. It is also interesting that the kinetic temperature of the hydrogen atoms in microwave discharges, as derived from the H_α spectral width, is again about 3000 K and not equal to T_g. The H atoms are a 1 % minority in this case and originate only from the methane dissociation. They obviously gain energy from the CH_4 dissociation process. More details of these investigations will be published[10].

---

8) Behringer, K., J. Nucl. Mater. (1991), in print
9) Pospieszczyk, A. et al., Report UCLA-PPG-1251, Dec. 1989
10) Behringer, K., submitted to Plasma Phys. and Contr. Fusion, Nov. 1990

Surprisingly, CH/CD tokamak spectra are very similar in appearance to the ones described above, in spite of completely different plasma parameters. Because of this fortunate fact, the described modelling of the spectra can immediately be applied to fusion plasmas, e.g. ASDEX, after a minor change of T_r (3500 K instead of 3000 K). As a first application, the H/D isotope ratio in the relevant carbon surfaces was measured in ASDEX by analyzing the CH/CD intensity ratio (and assuming that the molecular break-up is the same for CH_4 and CD_4[11]) Measured and calculated JET carbon limiter spectra (flat-top phase of pulse #5361) are shown in Fig. 9.

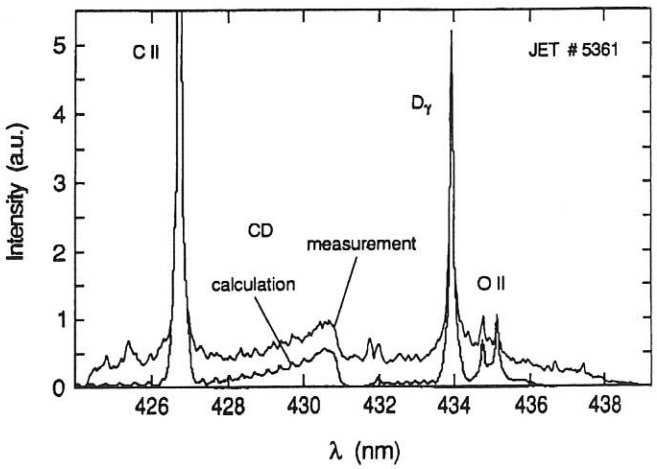

FIG. 9: *Visible JET carbon limiter spectrum, containing D_γ, C II and O II lines, as well as CD molecular bands.*

A comprehensive list of CH_4 dissociation processes in tokamak plasmas and respective rate coefficients has been compiled by Ehrhardt and Langer[12], these being available in the form of convenient fit functions. In our case, electron impact processes play the most important role, i.e. electron collisions leading to the stripping off of another electron or an electron and a hydrogen atom, to the loss of a neutral H atom or a H^+ ion, or to the capture of the electron with concurrent ejection of one or two H atoms. Charge exchange reactions with protons/deuterons are also of some importance. On the basis of these rate coefficients, the densities of the different dissociation products CH_4^+, CH_3, etc. can easily be calculated, starting from a given CH_4 density. If transport losses are negligible, the dissociation balance is independent of the electron density n_e and the hydrogen ion density n_i. Transport can be included in a global sense by defining particle confinement times τ_i and τ_n for molecular ions and neutral molecules, respectively, but then the electron density must be known. These confinement times characterize average particle losses across the plasma boundary, i.e. redeposition, but also losses along the magnetic field lines.

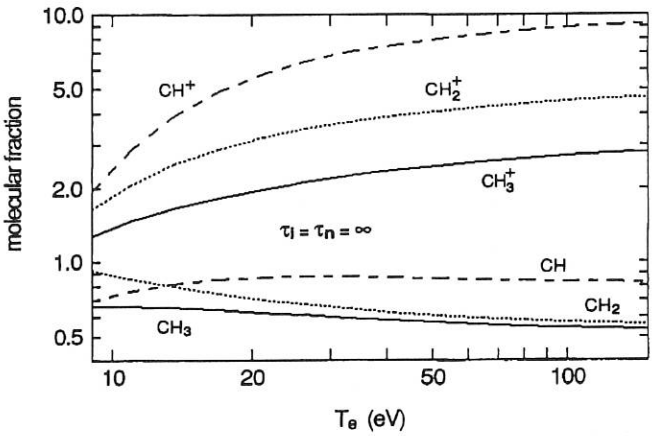

FIG. 10: *Densities of CH_4 dissociation products, normalized to $n(CH_4) = 1$, calculated from dissociation rate coefficients without transport losses.*

Figure 10 shows densities of CH_4 dissociation products as a function of T_e, calculated from the above rate coefficients by another computer program for $n(CH_4)=1$ and $\tau_i=\tau_n=\infty$. For charge exchange reactions with deuterons, $n_i=n_e$ and $T_i=T_e$ have been adopted, which are not crucial assumptions, and the rate coefficients[12] have been adjusted to the deuterium mass. As shown in Fig. 10, the CH density is comparable to the CH_4 density, while n_{CH^+} is expected to be much higher at higher electron temperatures. A finite transport time for either neutrals or ions leads to a reduction in the CH fraction particularly at low electron density and temperature. The CH_4 flux density $\Gamma(CH_4)$ required to sustain steady state is given by $n(CH_4)$, n_e and the sum of all CH_4 loss rate coefficients integrated over the dissociation zone near the plasma boundary. These calculations should also be valid for CD_4.

Because it is an optically allowed transition, and because the electron energy in tokamaks is much higher than the excitation energy, the electron excitation rate coefficient from the $X\ ^2\Pi$ ground state to the upper CH $A\ ^2\Delta$ level can be calculated according to the Bethe-Born theory[13] using the optical

[11] IPP Annual Report IPP AR/1989, p.25
[12] Ehrhardt, A.B., W.D. Langer, Report PPPL-2477, Sept. 1987
[13] Bethe, H., Ann. Physik 5 (1930) 325

f-value of 0.0068[14]. However, there is at least one more possibility to produce excited CH, namely by dissociation of CH_4 into CH A $^2\Delta$, H_2 and H[15]. The reported cross-section[15] as a function of energy was converted to the respective excitation rate coefficient, which must obviously be multiplied by the CH_4 and the electron density and is mainly responsible for the CH band emission from microwave discharges. It could therefore be verified to a large extent under these conditions. In tokamak plasmas, CH_4 and CH densities are comparable, and the second process is a relatively small contribution. It is not known whether other reactions also lead to the formation of excited CH, but they should be of minor importance.

These excitation rate coefficients and calculations for the molecular CH_4 /CD_4 break-up were used to calculate the number of CH_4 dissociation processes associated with each CH photon, a quantity which is usually called S/XB in the case of atoms or ions. Within the framework of the usual approximations, the line-of-sight intensity of the integrated molecular bands, observed perpendicularly to the plasma periphery, can be converted into the local CH_4 influx density by multiplication by the relevant S/XB value.

The molecular bands were integrated over the wavelength by fitting simulated computer spectra to the observed ones. However, in order to compare the calculated S/XB values with experimental data[9] the CH/CD band intensities were only

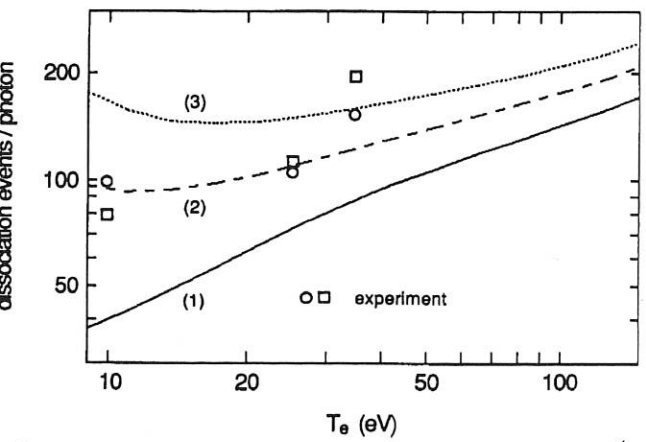

FIG. 11: *CH_4 flux per CH photon. $\tau_i=\tau_n=\infty$ (1), $\tau_i=\tau_n=10^{-4}$ s and $n_e=10^{12}$ (2) or $5\cdot10^{11}$ cm^{-3} (3).*

ntegrated over a 1.5 nm wavelength interval starting at the band heads, which typically contains 75 % of the total intensity.

The respective results for S/XB are shown in Fig. 11 as a function of T_e. Their dependence on the molecular confinement times in the plasma is demonstrated by plotting three different cases, namely, assuming $\tau_i=\tau_n=\infty$, and using $\tau_i=\tau_n=10^{-4}$ s at electron densities of $5\cdot10^{11}$ and 10^{12} cm^{-3}. A confinement time of 10^{-4} s is considered to be a lower limit, and electron densities will usually be closer to 10^{12} cm^{-3}; the uncertainty margin is therefore not very wide. At the usual plasma edge temperatures, about 80 to 100 dissociation events per CH/CD photon should be expected. Experimental results for two different CH_4 fluxes[9] also shown in Fig. 11, are in good agreement with the present calculations if a small confinement time is assumed (the two experimental points at $T_e\approx35$ eV may actually correspond to higher temperatures[9]).

The above results were applied to the JET carbon limiter situation of Fig. 9. If a value of 800 is adopted for the number of deuterium ionization events/D_γ photon[16] the explanation of the CD spectrum of Fig. 9 requires a CD_4 /D flux ratio of 0.08. This is a relatively high yield, considering the fact that part of the escaping flux, which is measured here, is already due to the four D atoms of CD_4, i.e. the production yield is about 12 %. On the other hand, this is the highest molecular intensity which could be found in many JET limiter spectra, and the typical situation (e.g. pulse #5427) is probably better characterized by a yield of 0.05. In order to gain more confidence in these results, the molecular spectrum of CD^+ must also be analyzed, which is emitted in the same spectral range as CD, but is blended with the above CD bands and therefore requires better spectral resolution and more modelling.

It may be worth noting that the dissociation of CH_4 also leads to quite intense molecular lines in the red and infrared parts of the spectrum, presumably from CH_2. Since this radiation may disturb the results of other diagnostics, e.g. laser light scattering techniques, some documentation of the appearance of these spectra is being made.

---

[14] Hinze, J., G. C. Lie, B. Liu, Astrophys. J. 196 (1975) 621
[15] Aarts, J.F.M., C.I.M. Beenakker and F.J. de Heer, Physica 53 (1971) 32
[16] Johnson, L. C., E. Hinnov, JQSRT 13 (1973) 333

3.1.2 *Molecular spectra of CO, CO^+ and H_2.*

CO molecular spectra are not so obvious in fusion plasmas and their intensities are more difficult to interpret than those of CH. In addition, since oxygen is efficiently removed by the recently available wall conditioning techniques, CO formation may be of less importance in future fusion experiments. Nevertheless, investigations have begun of CO laboratory plasmas in order to eventually provide diagnostic possibilities similar to those for CH_4. Figure 12 shows part of CO and CO^+ spectra emitted

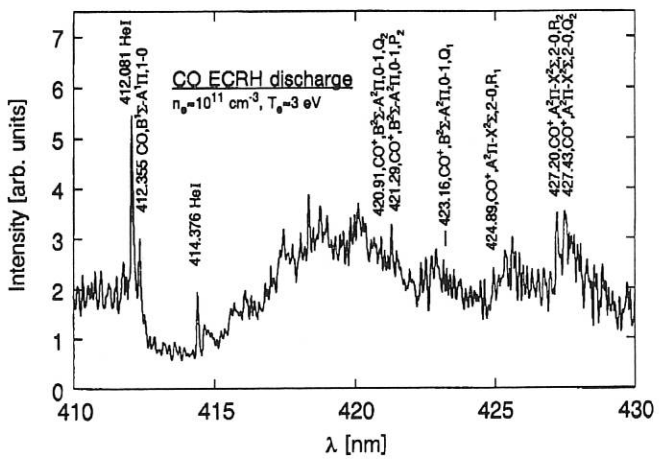

FIG. 12: *Measured spectrum of an ECRH microwave discharge in a CO/He mixture (2/18 Pa, 100 W). Band heads of CO and CO^+ are annotated.*

from an ECRH microwave discharge in a mixture of CO and He at a pressure of 20 Pa. Some details of these spectra are annotated in the figure. It will obviously not be simple to identify weak CO or CO^+ bands in a more complex tokamak spectrum, but respective analyses are still in progress.

In the spectra of both fusion plasmas (e.g. ASDEX) and

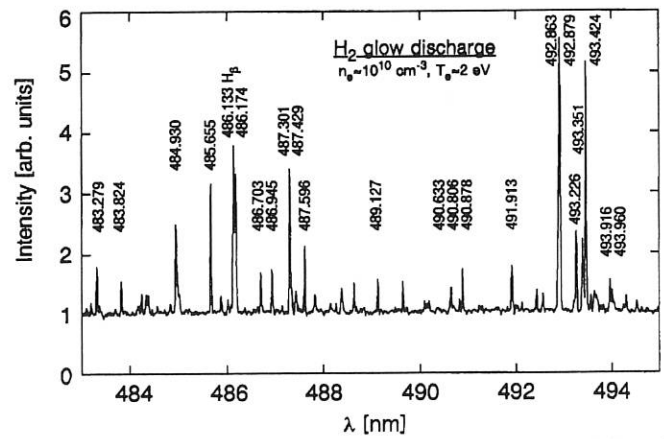

FIG. 13: *Measured H_2 molecular spectrum in the vicinity of H_β. There is a strong continuous H_2 background.*

laboratory discharges, well-known H_2 molecular lines have been observed, which are particularly strong in the vicinity of H_β. An example is shown in Fig. 13, which also demonstrates the existence of strong continuous H_2 background radiation. Further analysis of such spectra (and those of D_2) may provide useful diagnostic methods for the investigation of cold, dense divertor plasmas in fusion devices. Moreover, the respective information is essential for standard fusion plasma spectroscopy with filters of relatively large spectral bandwidth.

3.2 Atomic Rate Coefficients

For the interpretation of radiation from edge or divertor plasmas, atomic rate coefficients or population calculations are required, which can, to a large extent, be taken from experimental work[16), 17), 18)]. However, the accuracy of such data is still an open question. As an example, Fig. 14 shows the population of the n=3 and n=4 levels of atomic hydrogen

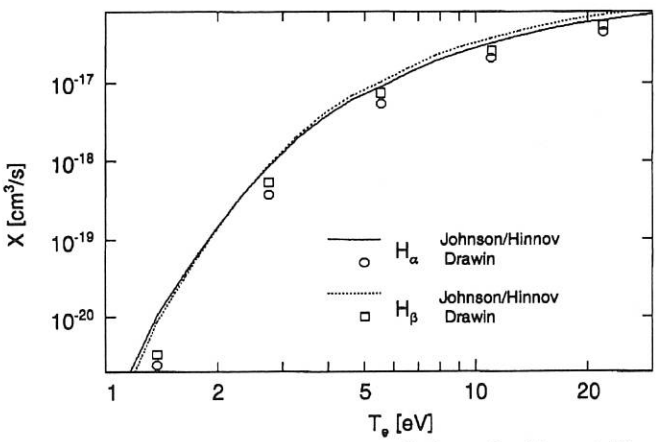

FIG. 14: *Effective excitation rate coefficients for H_α and H_β.*

relative to the ground state n_1 and the electron density n_e, i.e. the effective excitation rate coefficient. Two models are applied, namely those of Johnson-Hinnov[16)] and Drawin[18)]. Apparently, even in this relatively simple case, the two calculations give quite different results, particularly at lower electron temperatures. Furthermore, different H_α /H_β ratios are predicted. Such discrepancies will be further investigated on the basis of more recent theories and by comparison with experimental results from laboratory plasmas.

[17)] Behringer, K., H.P. Summers, B. Denne, M. Forrest, M. Stamp, Plasma Phys. and Contr. Fusion 31 (1989) 2059.

[18)] Drawin, H.W. and F. Emard, Report EUR-CEA-FC-534 (1970)

PUBLICATIONS AND CONFERENCE REPORTS

Alius, H., and G. Dodel: "Far-infrared frequency modulation by optically induced gratings in silicon". Appl. Phys. Lett. 57 (1990) 16.

Erckmann, V., W7-AS Team, W. Kasparek, G.A. Müller, P. G. Schüller, M. Thumm: "Electron cyclotron resonance heating transmission line and launching system for the Wendelstein W7-AS stellarator". Fusion Technol. 17 (1990) 76.

Keilmann, F., R. Brazis, H. Barkley, W. Kasparek, M. Thumm, V. Erckmann: "Millimetre-wave frequency tripling in bulk semiconductors". Europhys. Lett. 11 (1990) 337.

Titz, R. U., H. P. Röser, G. W. Schwaab, H. J. Neilson, P. A. Wood, T. W. Crowe, W. C. B. Peatman, J. Prince, B.S. Deaver, H. Alius and G. Dodel: "Investigation of GaAs Schottky barrier diodes in the terahertz range". Int. J. Infrared and Millimetre Waves 11 (1990) 809.

Holzhauer, E., G. Dodel, and ASDEX Team: "Collective laser light scattering from electron density fluctuations in fusion research plasmas". Rev. Sci. Instrum. 61 (1990) 2817.

Fajemirokun, H., C. Gowers, K. Hirsch, P. Nielsen and H. Salzmann: "A high resolution LIDAR Thomson scattering system for JET". Rev. Sci. Instrum. 61 (1990) 2843.

Fajemirokun, H., C. Gowers, K. Hirsch, P. Nielsen and H. Salzmann: "A method for identifying and estimating systematic errors in Thomson scattering data". Rev. Sci. Instrum. 61 (1990) 2849.

Ringler, H., U. Gasparino, G.Kühner, H. Maassberg, H. Renner, F. Sardei, W7-AS Team, ECRH-Group (W. Kasparek, G. A. Müller, P. G. Schüller, M. Thumm, R. Wienecke): "Confinement studies on the Wendelstein VII-AS stellarator". Plasma Phys. and Contr. Fusion 32 (1990) 933.

Conference on Optical Science and Engineering, Le Hague, March 12-15, 1990.

Gowers, C., A. Gadd, K. Hirsch, P. Nielsen, H. Salzmann: High power Ruby- and Alexandrite-lasers for LIDAR-Thomson scattering diagnostics.
Proc., SPIE 1277, p. 162

Frühjahrstagung der Deutschen Physikalischen Gesellschaft, Fachausschuß Plasmaphysik, München, March 12-16, 1990.

Kasparek, W., G. A. Müller, P. G. Schüller, M. Thumm, V. Erckmann, WVII-AS Team:
Experimente zur Plasmaheizung und zum nichtinduktiven Stromtrieb durch Elektronen-Zyklotronwellen im Stellarator WVII-AS.
Verhandl. DPG (VI) 25 (1990) P 11.3

Behringer, K., K. Hublé:
Spektroskopische Diagnostik von CH_4-Mikrowellenplasmen.
Verhandl. DPG (VI) 25 (1990) P 14.23

Dodel, G., E. Holzhauer, L. Giannone, H. Niedermeyer, J. Gernhardt, ASDEX-Team:
Skalierung von Dichtefluktuationen für ohmsche Entladungen in ASDEX.
Verhandl. DPG (VI) 25 (1990) P 18.7

9th Int. Conf. on Plasma Surface Interactions, Bournemouth, UK, May 20-25, 1990.

Behringer, K.:
Measurement of CH_4/CD_4 fluxes and of chemical carbon erosion from CH/CD band emission.
Contributed paper.

2nd Joint USSR-FRG Meeting on ECRH and Gyrotrons, Gorky, USSR, June 18 - 22, 1990.

Kasparek, W., G. A. Müller, P. G. Schüller, M. Thumm, V. Erckmann:
Microwave technology of the quasi-optical 140 GHz system on stellarator WVII-AS at Garching.

Erckmann, V., WVII-AS Team, ECRH-Group (W. Kasparek, G. A. Müller, P. G. Schüller, M. Thumm):
Long-pulse ECHR and ECCD experiments at the WVII-AS.

Thumm, M., A. Jacobs, W. Kasparek, J. Pretterebner et al.:
Low-power measurements on improved quasi-optical high-power mode converters for rotating high-order TE modes.

17th European Conf. on Controlled Fusion and Plasma Physics, Amsterdam, June 25 - 29, 1990.

Dodel, G., E. Holzhauer, L. Giannone, H. Niedermeyer, J. Gernhardt, ASDEX-Team:
Investigation of density fluctuations in the ASDEX tokamak via collective laser scattering.
Proc. ECA 14B, Part I, p. 207.

Erckmann, V., U. Gasparino, H. Maaßberg, H. Renner, M. Tutter, WVII-AS Team, W. Kasparek, G. A. Müller, P. G. Schüller, M. Thumm:
Current drive experiments at the electron cyclotron frequency.
Proc. ECA 14B, Part III, p. 1271.

Gasparino, U., V. Erckmann, H. Maaßberg, WVII-AS Team, ECRH-Group (W. Kasparek, G. A. Müller, P.G. Schüller, M. Thumm):
Non-inductive currents in WVII-AS.
Proc. ECA 14B, Part III, p. 1275.

16th Symp. on Fusion Technology (SOFT), London, September 3 - 7, 1990.

Henle, W., A.Jacobs, W.Kasparek, H.Kumrić, G.A.Müller, P. G. Schüller, M. Thumm, F. Engelmann, L. Rebuffi:
Conceptional study of multi-Megawatt millimetre wave transmission and antenna systems for electron cyclotron wave applications in NET/ITER.
Contributed paper O. 09.

Henle, W., W. Kasparek, H. Kumrić, G. A. Müller, P. G. Schüller, M. Thumm, V. Erckmann:
Microwave technology of the quasi-optical 140 GHz ECRH on the advanced stellarator WVII-AS.
Contributed paper R. 34.

Pochelon, A., T. Goodman, D. Whaley, M. Q. Tran, A. Perrenoud, D. Reinhard, B. Jödicke, H. G. Mathews, W. Kasparek, M. Thumm:
39 GHz ECRH system for break-down studies on the TCA tokamak.
Contributed paper R. 18.

13th Int. Conf. on Plasma Physics and Controlled Nuclear Fusion Research, Washington D.C., October 1 - 6, 1990.

Erckmann, V., U. Gasparino, H. Maaßberg, H. Renner, M. Tutter, WVII-AS-Team, W. Kasparek, G. A. Müller, P. G. Schüller, M. Thumm:
Electron cyclotron current drive and wave absorption experiments in the WVII-AS stellarator.
IAEA-CN-53/C-3-1.

International Workshop on ECH Transmission Systems, Cocoa Beach, Florida, December 6 - 8, 1990.

Thumm, M., W. Kasparek, H. Kumrić, G. A. Müller, J. Pretterebner, P. G. Schüller, D. Wagner:
Transmission and diagnostic of high-power mm-wave radiation, status and prospects.

Kasparek, W., H. Kumrić, G. A. Müller, P. G. Schüller: Quasi-optical 140 GHz ECRH system on the Garching Stellarator WVII-AS.

Pretterebner, J:
Design of quasi-optical mode converters at 140 GHz.

5th Int. Conf. on Infrared and Millimetre Waves, Orlando, Florida, December 10 - 14, 1990.

Henle, W., H. Kumrić, H. Li, M. Thumm:
Direct TE01-HE11 mode converters in corrugated circular waveguide with periodic curvature perturbation.
Proc., SPIE 1514, p. 440.

Thumm, M., A. Jacobs, H. Kumrić, J. Pretterebner:
Generation of rotating high-order TE_{mn} modes for cold-test measurements on high-power quasi-optical gyrotron output mode converters.
Proc., SPIE 1514, p. 204.

Wagner, D., M. Thumm, W. Kasparek:
Spectrum of unwanted spurious modes generated by flat and phase correcting HE11 and TE01 mirrors in highly-oversized elbow bends.
Proc., SPIE 1514, p. 437.

Kasparek, W., K. Kopp:
Bi-directional couplers for highly oversized HE11 waveguides and TEM00 beam waveguides.
Proc., SPIE 1514, 310.

Pretterebner, W., M. Thumm:
Design of improved Bragg reflectors for resonators in overmoded high-power microwave oscillators.
Proc., SPIE 1514, p. 298.

Hogg, J.P., H. Cao, W. Kasparek, T.M. Tran, M.Q. Tran:
Output coupling of a quasi-optical Fabry-Perot resonator by mean of a diffractive grating in the mm wave range.
Proc., SPIE 1514, p. 535.

DIPLOMA THESES

Hammann, K.:
Aufbau eines Pulsgenerators für das "Gating" eines MCP-Photomultipliers, Untersuchung seiner Empfindlichkeit beim CW- und geschalteten Betrieb.

Hublé, K.:
Spektroskopische Untersuchungen von Methan-Niederdruckplasmen.

Leipold, F.:
Spektroskopische Untersuchungen der Molekülstrahlung von Stickstoffniederdruckentladungen.

Wagner, D.:
Spektrum der unerwünschten Wellentypen, hervorgerufen durch ebene und phasenkorrigierte HE11- und TE01-Spiegel in stark überdimensionierten Hohlleiterkrümmern.

LABORATORY REPORTS

Henle, W., A. Jacobs, W. Kasparek, H.Kumrić, G.A. Müller, P.G. Schüller, M. Thumm:
Study on ECW transmission lines for ITER/NET.
Report ITER IL-HD-6-0-5/-22/-23, 1990.

Nave, M.F.F., A. Edwards, K. Hirsch, M. Hugon, A. Jacchia, E. Lazarro, H. Salzmann, P. Smeulders:
Observation of MHD structures in JET temperature profiles.
Report JET-P(90)57, 1990.

INVITED TALKS

Behringer, K.:
Diagnostik und Modellierung von Methan-Mikrowellenplasmen. 4. Bundesdeutsche Fachtagung Plasmatechnologie, München, April 24, 1990.

Kasparek, W.:
Electron cyclotron resonance heating at 70 GHz on the stellarator WVII-AS and technological developments at 140 GHz. CRPP Lausanne, August 1990.

How to reach
Max-Planck-Institut für Plasmaphysik (IPP)

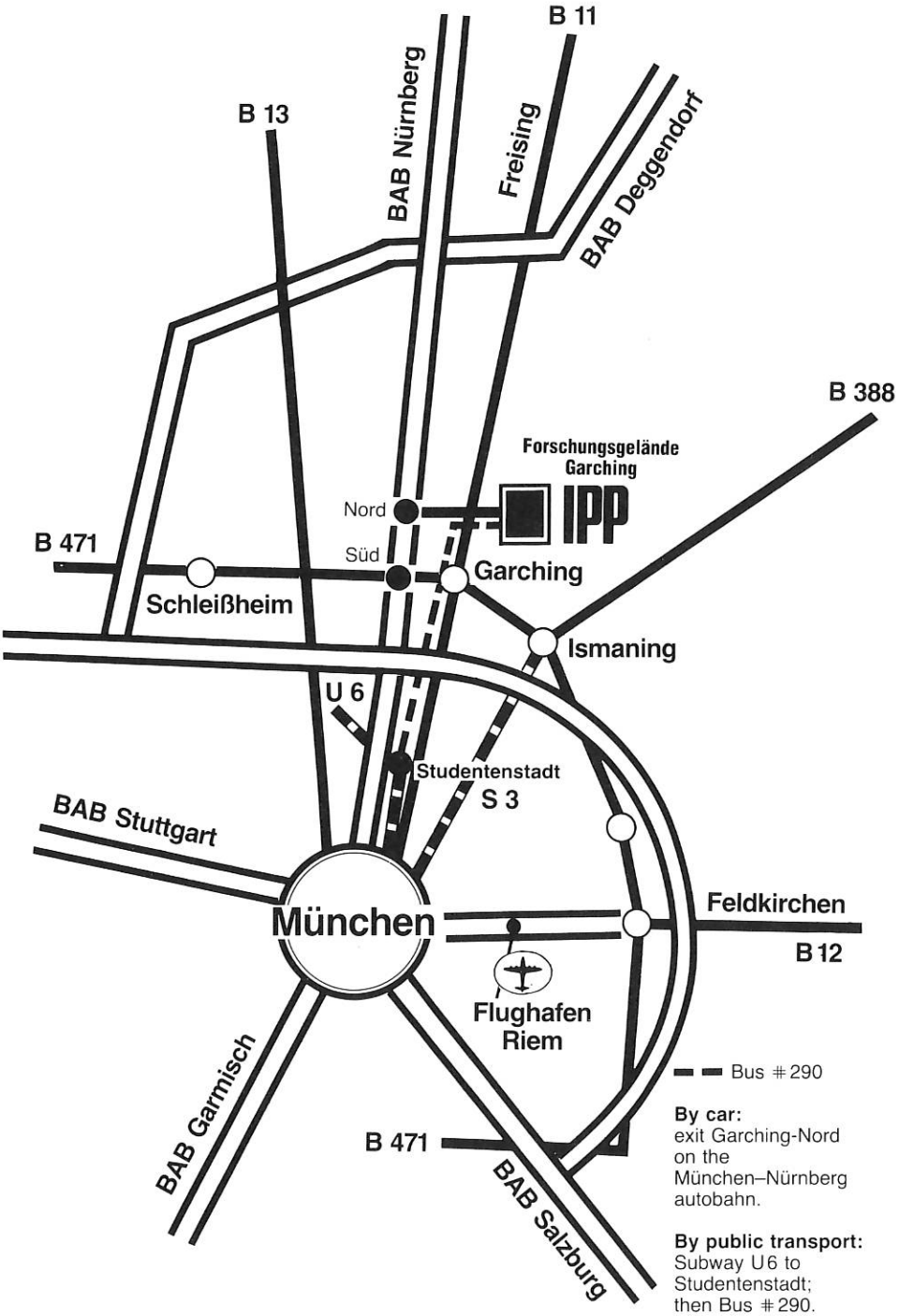

ANNUAL REPORT 1990

Max-Planck-Institut für Plasmaphysik (IPP) · 8046 Garching bei München
Telephone (0 89) 32 99 - 01 · Telefax (0 89) 32 99 - 22 00

Editing and Layout: Dr. Werner Dyckhoff, Isabella Milch
Printing: SV-Kommunalschriften-Druckerei, München

Printed in Germany
ISSN 0179-9347

This work was performed under the terms of the agreement between Max-Planck-Institut für Plasmaphysik and the European Atomic Energy Community to conduct joint research in the field of plasma physics.

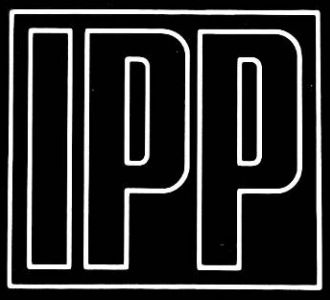
IPP